

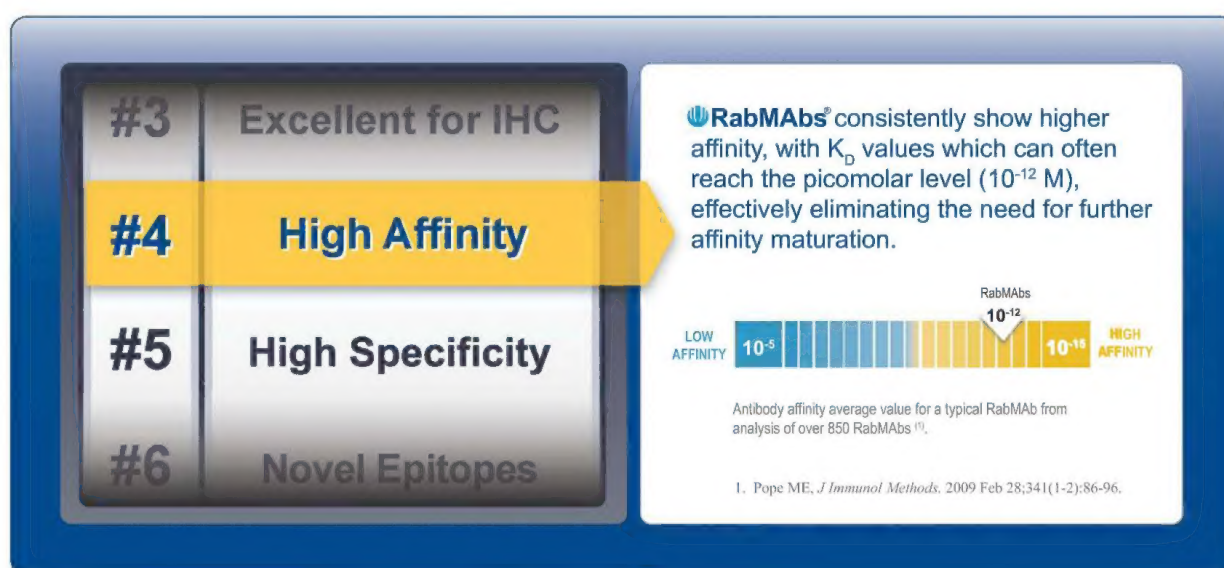
7 June 2013 | \$10

Science



Morphogenesis

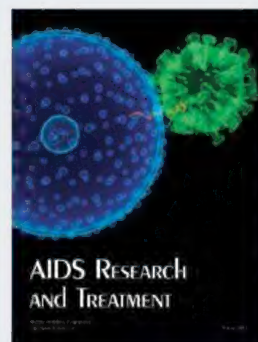
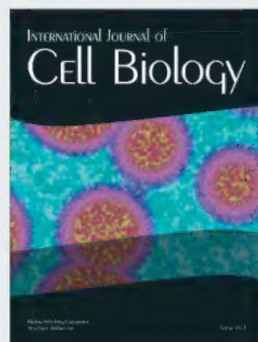
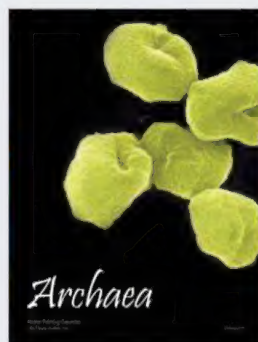
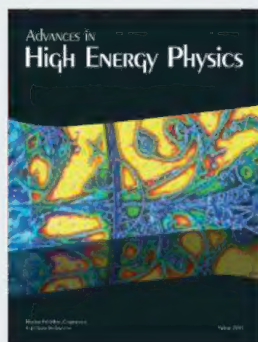
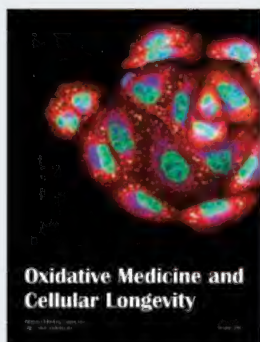
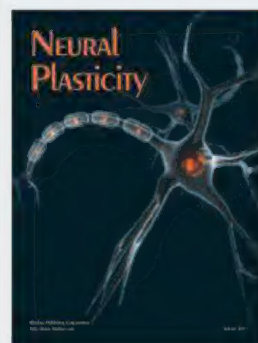
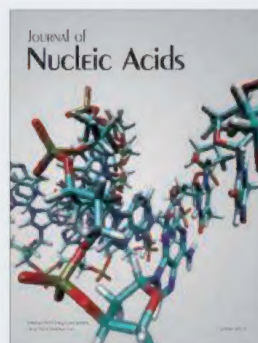
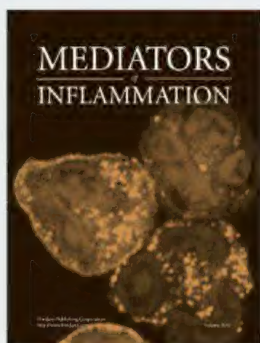
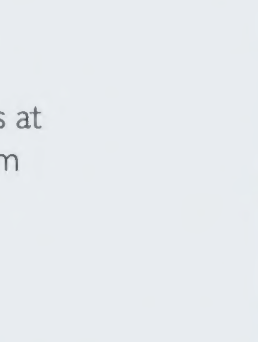
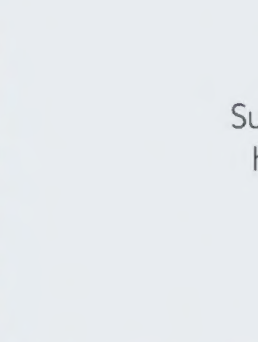
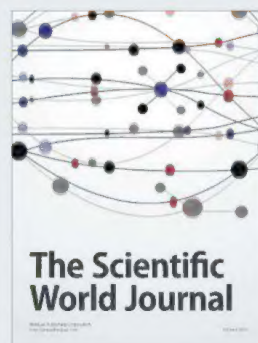
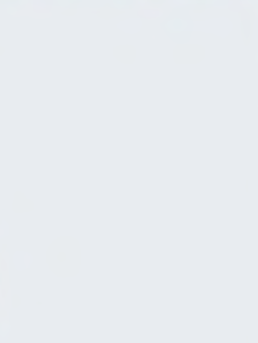
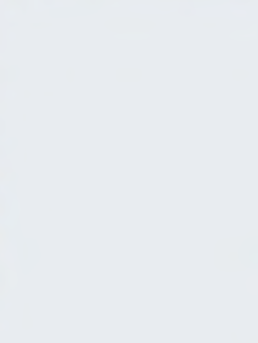
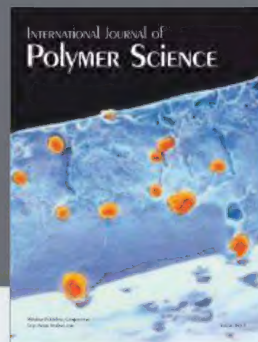
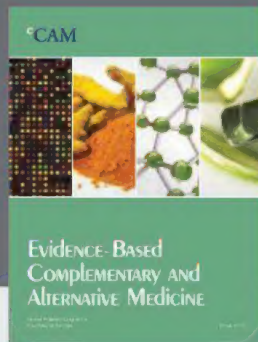
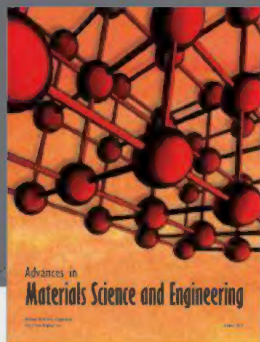
What can **RabMAbs[®]** do for you?



Rabbit Monoclonal Antibodies (RabMAbs[®]) offer multiple advantages to bring you the highest quality antibody possible.

Discover more at abcam.com/RabMAbs





Hindawi

Submit your manuscripts at
<http://www.hindawi.com>

Cultivating knowledge.

The 2013•14 NEB Catalog & Technical Reference

New England Biolabs introduces the latest edition of its award-winning Catalog & Technical Reference, featuring over 100 new products, up-to-date selection charts, protocols and troubleshooting tips. The new catalog's thought-provoking collection of mini-reviews explore methods for sustainable development.

Featured Products:

- > 200 restriction enzymes now 100% active in CutSmart[™] Buffer
- OneTaq[®] and Q5[®] High-Fidelity DNA Polymerases – robust amplification of a wide range of templates (AT- and GC-rich)
- NEBNext[®] reagents for NGS library preparation – now includes Ultra[™] kits for fast workflows and lower inputs

To request a copy, visit

www.neb.com/newcatalog

SPECIAL SECTION

Morphogenesis

INTRODUCTION

- 1183 Getting into Shape

REVIEWS

- 1184 Imaging Morphogenesis: Technological Advances and Biological Insights
P. J. Keller
Review Summary; for full text:
<http://dx.doi.org/10.1126/science.1234168>

- 1185 Mechanics of Epithelial Tissue Homeostasis and Morphogenesis
C. Guillot and T. Lecuit
- 1190 Growing Self-Organizing Mini-Guts from a Single Intestinal Stem Cell: Mechanism and Applications
T. Sato and H. Clevers
>> Science Podcast
- >> News story p. 1156; and Science Careers at www.sciencemag.org/special/morph

EDITORIAL

- 1141 Passing the Baton
Marcia McNutt
>> Policy Podcast

NEWS OF THE WEEK

- 1148 A roundup of the week's top stories

NEWS & ANALYSIS

- 1151 Europe Opens Door to Global Approach on Megaprojects
- 1152 Fading Academy Stakes Future on Reforming President
- 1153 Authenticity of China's Fabulous Fossils Gets New Scrutiny
- 1155 Accelerator Leak Halts Japanese Physics Experiments

NEWS FOCUS

- 1156 Mysteries of Development
How Do Organs Know When They Have Reached the Right Size?
Why Do So Many Neurons Commit Suicide During Brain Development?
How Do Microbes Shape Animal Development?
How Does Fetal Environment Influence Later Health?
Under Development
>> Morphogenesis section p. 1183;
Science Podcast

- 1162 The Cyborg Era Begins

LETTERS

- 1167 Rhino Poaching: Supply and Demand Uncertain
A. Collins et al.
Rhino Poaching: Unique Challenges
H. H. T. Prins and B. Okita-Ouma
Rhino Poaching: Apply Conservation Psychology
C. A. Litchfield
Response
D. Biggs et al.

1168 CORRECTIONS AND CLARIFICATIONS

BOOKS ET AL.

- 1170 The Cambrian Explosion
D. H. Erwin and J. W. Valentine,
reviewed by C. J. Lowe
- 1171 Spam
F. Brunton, reviewed by J. Golbeck

POLICY FORUM

- 1172 Uncapping Conflict of Interest?
S. F. Wood and J. K. Mador

PERSPECTIVES

- 1174 Illuminating the Neural Circuitry of Compulsive Behaviors
S. L. Rauch and W. A. Carlezon Jr.
>> Reports pp. 1234 and 1243



page 1162

- 1175 Interfacing Atoms and Light—The Smaller the Stronger
M. Keller
>> Report p. 1202
- 1176 Seas of Superoxide
Y. Shaked and A. Rose
>> Report p. 1223
- 1177 Bayes' Theorem in the 21st Century
B. Efron
- 1179 A Trap for Planet Formation
P. J. Armitage
>> Report p. 1199
- 1180 What the Bomb Said About the Brain
G. Kempermann
- 1181 Deserts and Waves in Gene Expression
A. R. Rodrigues and C. J. Tabin
>> Research Article p. 1195

CONTENTS continued >>

ON THE WEB THIS WEEK

- >> Policy Podcast
Listen to an interview with Science's new editor-in-chief, Marcia McNutt.
- >> Find More Online
Check out Science Express, our podcast, videos, daily news, our research journals, and Science Careers at www.sciencemag.org.



COVER

Intestinal organoids (red) derived in vitro from single intestinal stem cells display cryptlike structures with stem and Paneth cells (stem cells, green). Infused mini-guts fill in the ulcerated area of an inflamed colon. Reviews in this special issue on morphogenesis describe recent mini-gut technology, as well as advances in light microscopy of live organisms and mechanical analyses of cell dynamics during development. See the special section on page 1183 and at www.sciencemag.org/special/morph.

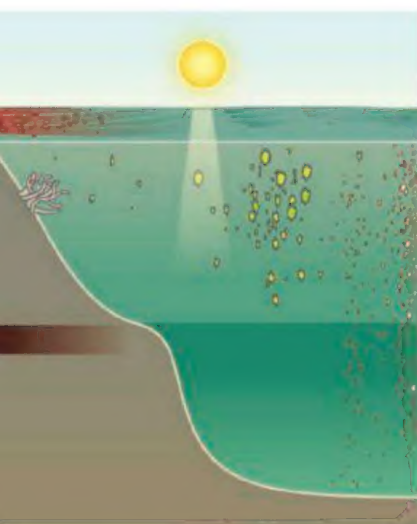
Image: Hans Clevers, Hubrecht Institute

DEPARTMENTS

- 1139 This Week in Science
- 1142 Editors' Choice
- 1144 Science Staff
- 1247 New Products
- 1248 Science Careers



page 1171



pages 1176 & 1223

RESEARCH ARTICLE

- 1195 A Switch Between Topological Domains Underlies *HoxD* Genes Collinearity in Mouse Limbs**
G. Andrey et al.
Regulation of the *HoxD* gene cluster switches from one side of the cluster to the other in parallel with limb development.
Research Article Summary; for full text:
<http://dx.doi.org/10.1126/science.1234167>
>> *Perspective p. 1181*

REPORTS

- 1196 Probing the Solar Magnetic Field with a Sun-Grazing Comet**
C. Downs et al.
Observations of a comet's motion through the solar corona constrain this region's magnetic field and plasma properties.
>> *Video*
- 1199 A Major Asymmetric Dust Trap in a Transition Disk**
N. van der Marel et al.
Radio interferometry observations reveal a highly asymmetric distribution of millimeter-sized grains surrounding a young star.
>> *Perspective p. 1179*
- 1202 Coupling a Single Trapped Atom to a Nanoscale Optical Cavity**
J. D. Thompson et al.
A single rubidium atom is positioned in close proximity to an optical cavity so they can interact.
>> *Perspective p. 1175*
- 1205 Entanglement Polytopes: Multiparticle Entanglement from Single-Particle Information**
M. Walter et al.
An algebraic geometry approach provides insight into the nature of entanglement of many particles.
- 1208 From Sub-Rayleigh to Supershear Ruptures During Stick-Slip Experiments on Crustal Rocks**
F. X. Passelègue et al.
Rupture fronts propagate faster than shear waves following experimental microearthquake nucleation.
- 1211 Stepwise Evolution of Essential Centromere Function in a *Drosophila* Neogene**
B. D. Ross et al.
How does a recently evolved gene come to encode an essential function?

- 1215 Density Triggers Maternal Hormones That Increase Adaptive Offspring Growth in a Wild Mammal**
B. Dantzer et al.
Mothers' stress levels in free-ranging red squirrels increase baby growth in anticipation of overcrowding.
- 1217 The Cross-Bridge Spring: Can Cool Muscles Store Elastic Energy?**
N. T. George et al.
A temperature gradient in a locked-spring lattice in insect muscle stores energy during locomotion.
- 1220 Structural Systems Biology Evaluation of Metabolic Thermotolerance in *Escherichia coli***
R. L. Chang et al.
As summer approaches, protein structures and network analysis pinpoint heat-sensitive metabolic nodes in a bacterium.
- 1223 Widespread Production of Extracellular Superoxide by Heterotrophic Bacteria**
J. M. Diaz et al.
A broad range of bacteria produce substantial amounts of reactive oxygen species in aquatic ecosystems.
>> *Perspective p. 1176*
- 1227 Structural Basis for Effector Control and Redox Partner Recognition in Cytochrome P450**
S. Tripathi et al.
The redox partner of P450cam stabilizes it in an open conformation to facilitate proton-coupled electron transfer.
- 1230 Role of Tissue Protection in Lethal Respiratory Viral-Bacterial Coinfection**
A. M. Jamieson et al.
Reduced immune tolerance, rather than resistance, increases the susceptibility of mice to a secondary bacterial infection.
- 1234 Repeated Cortico-Striatal Stimulation Generates Persistent OCD-Like Behavior**
S. E. Ahmari et al.
Hyperactivation of projections from the orbitofrontal cortex to the striatum increases repetitive grooming in mice.
>> *Perspective p. 1174; Report p. 1243*
- 1239 Geniculocortical Input Drives Genetic Distinctions Between Primary and Higher-Order Visual Areas**
S.-J. Chou et al.
Neural activity in the developing visual system dictates differential gene expression in the primary and higher-order areas.
- 1243 Optogenetic Stimulation of Lateral Orbitofronto-Striatal Pathway Suppresses Compulsive Behaviors**
E. Burguière et al.
Normal behavior can be rescued in a mouse model of obsessive-compulsive disorder.
>> *Perspective p. 1174; Report p. 1234*

SCIENCE (ISSN 0036-8075) is published weekly on Friday, except the last week in December, by the American Association for the Advancement of Science, 1200 New York Avenue, NW, Washington, DC 20005. Periodicals Mail postage (publication No. 484460) paid at Washington, DC, and additional mailing offices. Copyright © 2013 by the American Association for the Advancement of Science. The title SCIENCE is a registered trademark of the AAAS. Domestic individual membership and subscription (S1 issues): \$149 (\$74 allocated to subscription). Domestic institutional subscription (S1 issues): \$990; Foreign postage extra: Mexico, Caribbean (surface mail) \$55; other countries (air assist delivery) \$85. First class, airmail, student, and emeritus rates on request. Canadian rates with GST available upon request, GST #1254 88122. Publications Mail Agreement Number 1069624. Printed in the U.S.A.

Change of address: Allow 4 weeks, giving old and new addresses and 8-digit account number. Postmaster: Send change of address to AAAS, P.O. Box 96178, Washington, DC 20090-6178. Single-copy sales: \$10.00 current issue, \$15.00 back issue prepaid includes surface postage; bulk rates on request. Authorization to photocopy material for internal or personal use under circumstances not falling within the fair use provisions of the Copyright Act is granted by AAAS to libraries and other users registered with the Copyright Clearance Center (CCC) Transactional Reporting Service, provided that \$30.00 per article is paid directly to CCC, 222 Rosewood Drive, Danvers, MA 01923. The identification code for Science is 0036-8075. Science is indexed in the Reader's Guide to Periodical Literature and in several specialized indexes.

From Dust Grains to Planets

Almost 900 extrasolar planets have been identified, but we still struggle to understand exactly how planets form. Using data from the Atacama Large Millimeter Array, **van der Marel *et al.*** (p. 1199; see the Perspective by **Armitage**) report a highly asymmetric distribution of millimeter-sized grains surrounding a young star. Modeling suggests that these particles—the material from which planets form—are being trapped within a protoplanetary disk by an anticyclonic vortex. Localized concentration of large grains within a protoplanetary disk is thought to be a step in planet formation.

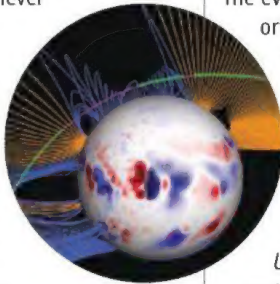
Trapped and Coupled

Trapped single atoms are ideal for storing and manipulating quantum information. **Thompson *et al.*** (p. 1202, published online 25 April; see the Perspective by **Keller**) were able to control single atoms interacting coherently with a field mode of a photonic crystal cavity. An optical tweezer was used to trap the single atom, which enabled positioning of the atom in close proximity to the photonic crystal waveguide, coupling the atom to the optical mode of the cavity. Such coupling should prove useful in quantum measurement, sensing, and information processing.

A Comet in the Sun

In 2011, comet Lovejoy plunged into the solar atmosphere and survived its flight through a region of the Sun that has never been visited by spacecraft.

Downs *et al.* (p. 1196) used spacecraft observations of this Sun-grazing comet, combined with advanced magnetohydrodynamic simulations, to constrain the magnetic field of the solar atmosphere—a quantity that has been very difficult to measure directly.



Sonic Boom from Below

Seismic shear waves released by an earthquake typically far outpace motion along the fault surface. Occasionally, however, earthquakes along strike-slip faults appear to propagate so that the rupture velocity is faster than shear waves, creating a sort of sonic boom along the fault surface. **Passelègue *et al.*** (p. 1208) were able to reproduce and measure these so-called supershear ruptures in stick-slip experiments with two pieces of granite under high applied normal stress. Much like during a sonic boom



Thank Your Mother

Maternal effects and influence can sometimes prepare unborn offspring for some of the environmental conditions they may face. **Dantzer *et al.*** (p. 1215, published online 18 April) monitored a population of red squirrels and found that both natural and artificially induced increases in the number of conspecific calls increased the growth rate of pups because of increased glucocorticoid levels in the mother. The density stress experienced by mothers thus appears to stimulate them to produce pups that will grow faster and hopefully outcompete the many other pups expected to be produced in the dense population.

when a plane travels faster than the speed of sound, the ruptures created a shock wave in the form of a Mach cone around the rupture front.

Essential Novelty

The evolution of essential function for newly originated genes presents a conundrum, in that prior to the gene's origin either the essential function was absent or else performed by another gene or set of genes. In order to better understand how new genes acquire essential function, **Ross *et al.*** (p. 1211) investigated the origin of the *Drosophila* gene *Umbrea*. *Umbrea* became an essential protein in certain *Drosophila* species through the gain of localization at the centrosome and a role in chromosome segregation.

Tolerance Needed

It's a common enough occurrence: You're sick as a dog with a cold, but the person in the office next door just has a few sniffles. What accounts for this difference? Most commonly, these sorts of differences are chalked up to differences in resistance—perhaps you have higher viral loads than your office mate. But such differences can also involve differences in the ability to tolerate the same amount of virus. Deciphering the contribution of resistance versus tolerance, however, is difficult.

Jamieson *et al.* (p. 1230, published online 25 April) studied a mouse model of viral and bacterial co-infection where tolerance and resistance could be separated. Mice infected with influenza virus were more likely to succumb to a secondary infection with *Legionella pneumophila* as a result of impaired tolerance to tissue damage, rather than because of a difference in bacterial burden.

What Causes Obsessive Compulsive Disorder?

Obsessive compulsive disorder is a severe, chronic mental illness that affects millions of individuals. However, the mechanisms underlying this disease are still largely unknown (see the Perspective by **Rauch and Carlezon Jr.**). **Ahmari *et al.*** (p. 1234) stimulated glutamatergic pathways between the orbitofrontal cortex and the ventromedial striatum and used grooming to assess obsessive compulsive behavior in mice. Repetitive stimulation over days triggered changes in the neuronal responses of the ventromedial striatum. Over time, the behavior of the animals became independent of stimulation and could be prevented by the antidepressant fluoxetine. **Burguière *et al.*** (p. 1243) investigated the neural basis of obsessive compulsive symptoms in a mutant mouse that showed excessive expression of a conditioned form of grooming.



Finally, one application that syncs your PDF articles, your lab group, and your **next manuscript**.

ACS ChemWorx is a free, single-source solution designed to increase productivity in research management, collaboration, and publishing.

Find out how you can spend less time organizing and more time researching.



Search.



Import.



Annotate.



Collaborate.



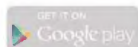
Store.



Publish.

Format and insert citations, generate bibliographies, and submit your ACS manuscripts using the ACS ChemWorx Publishing Center.

Login today at www.acschemworx.org





Marcia McNutt is Editor-in-Chief of *Science*.

Passing the Baton

IT IS WITH AWE AND DEEP RESPECT FOR THE WEIGHTY ACCOMPLISHMENTS OF THOSE WHO HAVE passed before me that I assume the title of Editor-in-Chief of *Science*, one of less than a handful of journals that can claim to represent the spectrum of scientific endeavors and a truly international audience of authors and readers. Each editor-in-chief has come to this position with his (and now her!) own vision of how to use this opportunity to benefit the scientific community. Bruce Alberts has left an important legacy that I hope to continue and build upon.

To begin with, Bruce raised the visibility of the science education community and its myriad challenges. A sizable fraction of researchers are also science educators and care deeply about improving STEM (science, technology, engineering, and mathematics) education. By providing a forum for their issues, Bruce energized those within and outside the education community to pursue essential reforms. He also increased the globalization of *Science* by reaching out to developing countries. Bruce, a tireless traveler, was forever striving to make *Science* more accessible to aspiring researchers no matter where they might be found. Himself a respected researcher, Bruce brought the perspective of the individual scientist to discussions of publication format, open access, the review process, and other publication matters. He addressed these issues with integrity in the forefront. He immediately recognized that access to the information provided by nonclassified research papers on H5N1 (avian flu) was critical for world health concerns and insisted on their controlled release in a manner that would neither compromise the integrity of publication nor present a potential health threat. Indeed, having the scientist's perspective "at the top" helps ensure that *Science* evolves to serve the best interests of the scientific community, which depends on rapid communication of the most important results.

Without backing off on any of the priorities of my predecessor, my own top goal is to make *Science* the premier communications platform for accelerating advances in science, using the latest in modern technologies. Many excellent journals are geared toward disciplinary audiences. My view is that a journal such as *Science* that is read by researchers across a broad spectrum of fields has a special responsibility to publish papers that need to be communicated to scientists in fields outside of a narrow specialty, because new observations, technologies, processes, models, and results have the potential to revolutionize other areas of research. I would like to see *Science* publish even more of the best papers, that those papers are written so that their significance is broadly understood, and that computational methods, such as machine learning and natural language processes, can be harnessed to connect members of AAAS (the publisher of *Science*) to studies of interest.

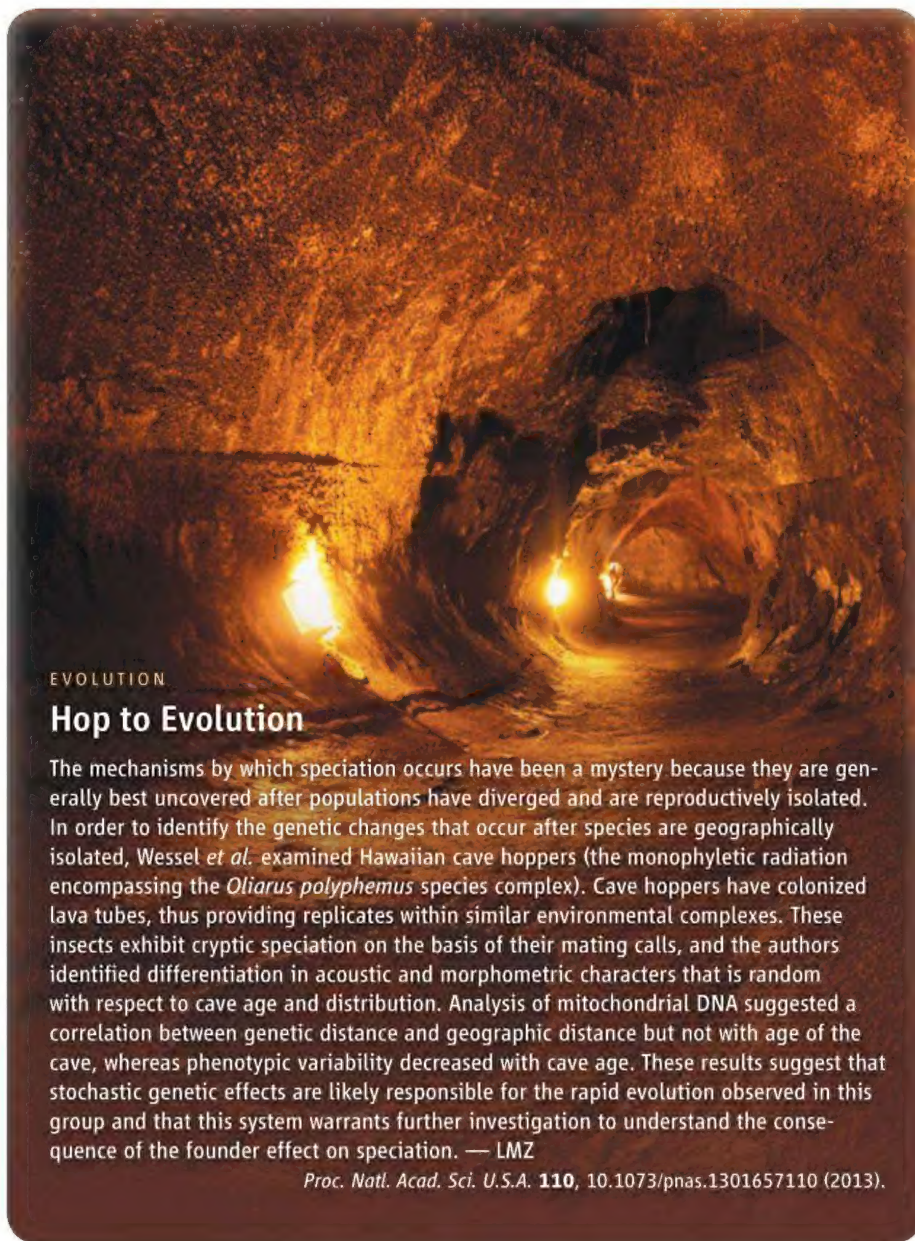
The recently released report *ARISE 2** (Advancing Research in Science and Engineering) from the American Academy of Arts and Sciences makes recommendations for breaking down barriers to collaboration across sectors to promote fundamental advances in science and their translation into new products and services. Their number-one recommendation is that a "knowledge network" be developed that "enables investigators from different disciplines to identify opportunities, establish collaborative efforts, and focus disparate expertise and approaches on problems of common interest." My hope is that *Science* can contribute to that knowledge network by promoting communication styles, technologies, and approaches that transcend individual disciplines. Clearly, *Science* cannot achieve recommendation number one alone, but I believe it is in a great position to be an important part of the solution.

— Marcia McNutt

10.1126/science.1240779

**ARISE 2: Unleashing America's Research & Innovation Enterprise* (American Academy of Arts and Sciences, Cambridge, MA, 2013), p. xiii; www.amacad.org/arise2.pdf.





EVOLUTION

Hop to Evolution

The mechanisms by which speciation occurs have been a mystery because they are generally best uncovered after populations have diverged and are reproductively isolated. In order to identify the genetic changes that occur after species are geographically isolated, Wessel *et al.* examined Hawaiian cave hoppers (the monophyletic radiation encompassing the *Oliarus polyphemus* species complex). Cave hoppers have colonized lava tubes, thus providing replicates within similar environmental complexes. These insects exhibit cryptic speciation on the basis of their mating calls, and the authors identified differentiation in acoustic and morphometric characters that is random with respect to cave age and distribution. Analysis of mitochondrial DNA suggested a correlation between genetic distance and geographic distance but not with age of the cave, whereas phenotypic variability decreased with cave age. These results suggest that stochastic genetic effects are likely responsible for the rapid evolution observed in this group and that this system warrants further investigation to understand the consequence of the founder effect on speciation. — LMZ

Proc. Natl. Acad. Sci. U.S.A. **110**, 10.1073/pnas.1301657110 (2013).

CHEMISTRY

Bridging Color

The ability to solution-process small light-emitting molecules makes it possible to fabricate organic light-emitting devices using large-scale methods and onto a wide range of substrates. In order to get reasonable values for the photoluminescence efficiency, larger oligomeric molecules are required; however, the increased size rapidly decreases the solubility. Solubility can be increased through the addition of alkyl side groups while also decreasing intermolecular quenching, but this often also diminishes the intermolecular charge transfer, which is the key step in converting electrical charge into

light. Christensen *et al.* reacted a series of chromophore molecules to form Ar-S-Ar symmetrically bridged sulfides, where the Ar ligand was either bithiophene, terthiophene, naphthalene, or pyrene, and where the sulfur bridge could be subsequently oxidized to form a sulfoxide or sulfone. The addition of the sulfur bridge enhanced the solubility of the molecules; however, it was the oxidation of the sulfur that was the key to the enhanced photoluminescence seen in all cases. The authors speculate that the electron deficiency of the sulfoxide or sulfone groups enhances the formation of charge-transfer states. Interestingly, the photoluminescence yields of the bithiophene and terthiophene sulfone molecules were greater than the values

seen for nonbridged thiophenes with an equivalent number of aromatic units. — MSL

J. Am. Chem. Soc. 10.1021/ja401383q (2013).

GEOCHEMISTRY

The Nd of the Innocence

There are few remaining geologic clues about the structure and geodynamics operating on Earth from its initial differentiation around 4.5 billion years ago until modern plate tectonics began. Debaille *et al.* analyzed the geochemistry of an ancient layered lava flow from Ontario, Canada, that serves as a window into a partially melted mantle plume from around 2.7 billion years ago. Excess ^{142}Nd contents, which are daughter products of now extinct radiogenic ^{146}Sm , imply that the mantle contained heterogeneities generated by relatively sluggish mixing—especially when considering that the temperatures and convection rates at that time would have been much higher than they are in the modern mantle. Using numerical models, the authors show that the preservation of this signature could occur in a stagnant regime of plate tectonics independently of high convection rates, meaning that early subduction events occurred only in brief and sporadic episodes. Combined with other geochemical data, the ancient lava flow data are consistent with the onset of modern (i.e. continuous) plate tectonics around 2.7 to 3.0 billion years ago. — NW

Earth Planet Sci. Lett. 10.1016/j.epsl.2013.04.016 (2013).

BIOMEDICINE

Misplacing RAS (Again)

The discovery that the mutational activation of RAS proteins drives the growth of human cancer cells catalyzed a dogged—but ultimately unsuccessful—search for drugs that inhibit RAS activity. Interest in pharmacologically targeting RAS has been revived by cancer genome studies, which revealed *KRAS* to be the most frequently mutated gene in the cancer types that are most common in the population and/or most refractory to therapy, such as pancreatic, lung, and colorectal cancer.

Because *KRAS* signaling activity is dependent on the protein's localization at the cell membrane, Zimmermann *et al.* investigated whether compounds that interfere with *KRAS* localization have anticancer activity. In a high-throughput screen, they identified small molecules that prevent *KRAS* from binding to PDE- δ , a protein that facilitates *KRAS* trafficking to the membrane. An optimized compound, deltarasin, was found to inhibit *KRAS* signal-

ing and growth of KRAS-mutant human pancreatic cancer cells in vitro and in mice. Although these results are promising, the bar for deltarasin and its derivatives will be high, because previous drugs designed to disrupt KRAS membrane localization in a different way proved to be ineffective in clinical trials. — PAK

Nature 10.1038/nature12205 (2013).



CELL BIOLOGY

Seeing the Light

The ability to visualize live cells using genetically encoded bioluminescent and fluorescent proteins has provided insight into many biological processes. Sellmyer *et al.* report a strategy to visualize cell-cell interactions in live animals using bioluminescence, which occurs when luciferase enzymes are activated by a luciferin substrate. One cell population (the reporter cells) expressed luciferase, whereas a different cell population (the activator cells) expressed an uncaging enzyme and luciferin. The uncaging of activator cells allowed the release of luciferin, which could then diffuse into nearby reporter cells, react with luciferase, and cause the emission of light that was dependent on the distance between the activator and reporter cells. The method was shown to assay cellular proximity in cultured cells and was able to identify metastatic sites in a mouse breast cancer model. Further improvements in the technique will likely allow the visualization of many other cellular interactions, which could lead to new insight into processes such as adaptive immunity or stem cell niche development. — VV

Proc. Natl. Acad. Sci. U.S.A. **110**, 8567 (2013).

EVOLUTION

Cooperative Yeast Break Free

Cooperation is pervasive in nature, but how it remains a successful evolutionary strategy in the face of defectors and free riders is not yet fully understood. This is especially true in models of the classical Prisoner's Dilemma game, in which, theoretically, cooperators should always lose to defectors.

Van Dyken *et al.* engineer baker's yeast, *Saccharomyces cerevisiae*, into cooperators and

defectors and pit them against each other in a Prisoner's Dilemma game. They are mutated so they cannot take up sucrose from the medium. Cooperators secrete invertase, which breaks sucrose down into monosaccharides. Defectors are mutant for invertase. Neither cooperators nor defectors can take up sucrose, but both can take up monosaccharides. When a growth cost is imposed for cooperation, and defectors are able to achieve limited monosaccharide-inde-

pendent growth, defectors initially outcompete cooperators. But as the colonies grow, the cooperator populations expand at the expense of the defectors. The cooperators form genetically demixed sectors, analogous to "genetic surfing" seen in frontier populations. Simulations support the idea that an expanding colony frontier favors (cooperative) genotypes that maximize group productivity and that this could apply to range expansions seen in many species, including humans. — GR

Curr. Biol. **23**, 919 (2013).

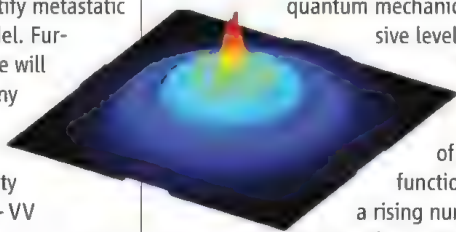
PHYSICS

Seeing Nuclei

A hundred years ago, Niels Bohr introduced the concept of discrete, or quantized, electronic energy levels in hydrogen atoms to account for the discrete lines in their optical spectra.

Within a couple of decades, the model had been elaborated to establish the framework for quantum mechanics, with succes-

sive levels corresponding to spatial probability distributions of electronic wave functions manifesting a rising number of nodes.

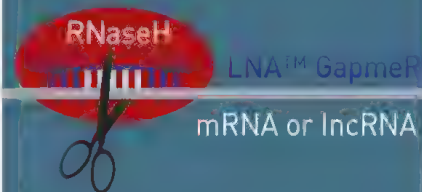


Since then, a vast and diverse array of physical and chemical phenomena has bolstered the validity of this framework. Yet visualization retains a special power to elucidate. Stodolna *et al.* have now directly projected the nodal pattern of a hydrogen atom's electronic wave function onto a detector. Theory had predicted that the preparation of Stark states, in a static electric field, would foster direct imaging upon ionization. The authors note that the addition of a magnetic field to the experimental setup could probe further intricacies of atomic electron dynamics. — JSY

Phys. Rev. Lett. **110**, 213001 (2013).

More efficient
gene silencing?

LNA™ GapmeR



RNase H mediated
antisense inhibition of
mRNA and lncRNA

- Low toxicity and superior potency
- Less off-target effects with short, single stranded oligos
- High flexibility – use *in vitro* or *in vivo*

Learn more:
exiqon.com/gapmers

EXIQON
Seek Find Verify

1200 New York Avenue, NW
Washington, DC 20005

Editorial: 202-326-6550, FAX 202-289-7562
News: 202-326-6591, FAX 202-371-9227

Bateman House, 82-88 Hills Road

Cambridge, UK CB2 1LQ

+44 (0) 1223 326500, FAX +44 (0) 1223 326501

SUBSCRIPTION SERVICES For change of address, missing issues, new orders and renewals, and payment questions: 866-434-AAAS (2227) or 202-326-6417, FAX 202-842-1065. Mailing addresses: AAAS, P.O. Box 96178, Washington, DC 20090-6178 or AAAS Member Services, 1200 New York Avenue, NW, Washington, DC 20005

INSTITUTIONAL SITE LICENSES please call 202-326-6755 for any questions or information

REPRINTS: Author Inquiries 800-635-7181

Commercial Inquiries 803-359-4578

PERMISSIONS 202-326-6765, permissions@aaas.org

MEMBER BENEFITS AAAS Travels: Betchart Expeditions 800-252-4910; Apple Store www.store.apple.com/us/go/epstore/aaas; NASA Federal, 1-888-NASA-FCU (1-888-627-2328) or www.nasa.fcui.com; Cold Spring Harbor Laboratory Press Publications www.cshlpress.com/affiliates/aaas.htm; GEICO Auto Insurance www.geico.com/landingpage/go51.htm?logo=17624; Hertz 800-654-2200 CDP#343457; Office Depot https://bsd.officedepot.com/portalLogin.do; Seabury & Smith Life Insurance 800-424-9883; Subaru VIP Program 202-326-6417; VIP Moving Services www.vipmayflower.com/domestic/index.html; Other Benefits: AAAS Member Services 202-326-6417 or www.aaasmember.org.

science_editors@aaas.org (for general editorial queries)
science_letters@aaas.org (for queries about letters)
science_reviews@aaas.org (for returning manuscript reviews)
science_bookrevs@aaas.org (for book review queries)

Published by the American Association for the Advancement of Science (AAAS), *Science* serves its readers as a forum for the presentation and discussion of important issues related to the advancement of science, including the presentation of minority or conflicting points of view, rather than by publishing only material on which a consensus has been reached. Accordingly, all articles published in *Science*—including editorials, news and comment, and book reviews—are signed and reflect the individual views of the authors and not official points of view adopted by AAAS or the institutions with which the authors are affiliated.

AAAS was founded in 1848 and incorporated in 1874. Its mission is to advance science, engineering, and innovation throughout the world for the benefit of all people. The goals of the association are to: enhance communication among scientists, engineers, and the public; promote and defend the integrity of science and its use; strengthen support for the science and technology enterprise; provide a voice for science on societal issues; promote the responsible use of science in public policy; strengthen and diversify the science and technology workforce; foster education in science and technology for everyone; increase public engagement with science and technology; and advance international cooperation in science.

INFORMATION FOR AUTHORS

See pages 716 and 717 of the 8 February 2013 issue or access www.sciencemag.org/about/authors

SENIOR EDITORIAL BOARD

A. Paul Alivisatos, Lawrence Berkeley Nat'l Laboratory
Ernst Fehr, Univ. of Zurich
Michael S. Turner, University of Chicago

BOARD OF REVIEWING EDITORS

Adriano Aguzzi, Univ. Hospital Zürich
Takuzo Aida, Univ. of Tokyo
Leslie Aiello, Wenner-Gren Foundation
Sonia Altizer, Univ. of Georgia
Virginia Armbrust, Univ. of Washington
Sebastião Amigorena, Institut Curie
Angelika Amon, MIT
Kathryn Anderson, Memorial Sloan-Kettering Cancer Center
Shy G. E. Andersson, Uppsala Univ.
Peter Andolfatto, Princeton Univ.
Meinrat O. Andreae, Max Planck Inst., Mainz
Paola Ariotti, Harvard Univ.
Johan Auwerx, EPFL
David Auschulom, Univ. of California Santa Barbara
Ben Barres, Stanford Medical School
Jordi Bascompte, Estación Biológica de Doñana, CSIC
Facundo Batista, London Research Inst.
Ray H. Baughman, Univ. of Texas, Dallas
David Baum, Univ. of Wisconsin
Mark Bear, Massachusetts Inst. of Technology
Yasmine Belkaid, NIAID, NIH
Philip Benfey, Duke Univ.
Stephen J. Benkovic, Penn State Univ.
Christophe Bernard, Aix-Marseille Univ.
Gregory C. Berzosa, Stanford Univ.
Gabriele Bergers, Univ. of California, San Francisco
Peer Bork, EMBL
Bernard Bourdon, Ecole Normale Supérieure de Lyon
Chris Bowley, Ecole Normale Supérieure
Ian Boyd, Univ. of St. Andrews
Christian Büchel, Universitätsklinikum Hamburg-Eppendorf
Joseph A. Burns, Cornell Univ.
William P. Butz, Population Reference Bureau
Grzegorz Buzsáki, New York Univ., School of Medicine
Mats Carlsson, Univ. of Oslo
Mildred Cho, Stanford Univ.
David Clapham, Children's Hospital, Boston
David Clark, Univ. of Oxford
Jonathan D. Cohen, Princeton Univ.
Robert Cook-Deegan, Duke Univ.
James Collins, Boston Univ.
Alan Cowman, Walter & Eliza Hall Inst.
Robert H. Crabtree, Yale Univ.
Wolfgang Cramer, Max Planck Inst. of Biodiversity and Ecology
Jeff J. Dangel, Univ. of North Carolina
Tom Daniel, Univ. of Washington
Frans de Waal, Emory Univ.
Stanislav Dehaene, Collège de France

Robert Desimone, MIT
Claude Desplan, New York Univ.
Ap Dijksterhuis, Radboud Univ. of Nijmegen
Dennis Discher, Univ. of Pennsylvania
Gerald W. Dorn II, Washington Univ. School of Medicine
Jennifer A. Doudna, Univ. of California, Berkeley
Julian Downward, Cancer Research UK
Bruce Dunn, Univ. of California, Los Angeles
Christopher Dye, WHO
Todd Ehlers, University of Tuebingen
David Ehardt, Carnegie Inst. of Washington
Tim Elston, Univ. of North Carolina at Chapel Hill
Gerhard Ertl, Fritz Haber Institute, Berlin
Barry Everitt, Univ. of Cambridge
Paul G. Falkowski, Rutgers Univ.
Ernst Fehr, Univ. of Zurich
Tom Fenchel, Univ. of Copenhagen
Michael Feuer, The George Washington Univ.
Alain Fischer, INSERM
Susan Fiske, Princeton Univ.
Anne C. Ferguson-Smith, Univ. of Cambridge
Peter Fratzl, Max Planck Inst.
Elaine Fuchs, Rockefeller Univ.
Wulfraam Gerstner, EPFL Lausanne
Daniel Geschwind, UCLA
Andrew Gewirth, Univ. of Illinois
Karl-Heinz Glassmeier, TU Braunschweig
Elizabeth Grove, Univ. of Chicago
Kip Guy, St. Jude's Children's Research Hospital
Taek-Hyung Ha, Univ. of Illinois at Urbana-Champaign
Christian Haass, Ludwig Maximilians Univ.
Steven Hahn, Fred Hutchinson Cancer Research Center
Gregory J. Hannan, Cold Spring Harbor Lab.
Martin Heimann, Max Planck Inst., Jena
Vika Helariutta, Univ. of Finland
Isaac Held, NOAA
James A. Hendler, Rensselaer Polytechnic Inst.
Susan G. Hering, Swiss Fed. Inst. of Aquatic Science & Technology
Ray Hilborn, Univ. of Washington
Michael E. Himmel, National Renewable Energy Lab.
Kai-Uwe Hinrichs, Univ. of Bremen
Kei Hirose, Tokyo Inst. of Technology
David Hodell, Univ. of Cambridge
David Holden, Imperial College
Lara Hooper, UT Southwestern Medical Ctr at Dallas
Jeffrey A. Hubbell, EPFL Lausanne
Thomas Hudson, Ontario Inst. for Cancer Research
Raymond Huey, Univ. of Washington
Steven Jacobsen, Univ. of California, Los Angeles
Kai Johnson, EPFL Lausanne
Peter Jonas, Inst. of Science & Technology (IST) Australia
Matthäus Kaeblerlein, Univ. of Washington
William Kaelin Jr., Dana-Farber Cancer Inst.
Daniel Kahne, Harvard Univ.

Daniel Kammen, Univ. of California, Berkeley
John Kingsolver, Univ. of North Carolina at Chapel Hill
Robert Kingston, Harvard Medical School
Roberto Kolter, Harvard Medical School
Alberto R. Kornblitt, Univ. of Buenos Aires
Leonid Kruglyak, Princeton Univ.
Thomas Lange, Univ. of Cologne
Mitchell A. Lazar, Univ. of Pennsylvania
David Lazer, Harvard Univ.
Virginia Lee, Univ. of Pennsylvania
Stanley Lemmon, Univ. of North Carolina at Chapel Hill
Ottoline Leyser, Cambridge Univ.
Marcia C. Lin, Univ. of California, Berkeley
Jiang Liu, Michigan State Univ.
Luis Liz-Marzan, CNRS bioMAG
Jonathan Losos, Harvard Univ.
Ke Lu, Chinese Acad. of Sciences
Christian Lüscher, Univ. of Geneva
Laura Mackey, CRUK Beatson Inst. for Cancer Research
Anne Magurran, Univ. of St. Andrews
Oscar Marin, CSIC & IIS, Miguel Hernández
Charles Marshall, Univ. of California, Berkeley
Chris Marshall, Inst. of Cancer Research
Martin M. Matzuk, Baylor College of Medicine
C. Robertson McClung, Dartmouth College
Graham Medley, Univ. of Warwick
Yasushi Miki, Univ. of Tokyo
Richard Morris, Univ. of Edinburgh
Edward Moser, Norwegian Univ. of Science and Technology
Sean Munro, MRC Lab. of Molecular Biology
Thomas Murray, The Hastings Center
Naoki Nagasawa, Univ. of Tokyo
James Nelson, Stanford Univ. School of Med.
Daniel Neumark, Univ. of California, Berkeley
Stuart Newman, New York Medical College
Timothy W. Nilsen, Case Western Reserve Univ.
Pär Nordlund, Karolinska Inst.
Helga Nowotny, European Research Advisory Board
Luke O'Neill, Trinity College, Dublin
Stuart Newman, New York Medical College
N. Phuan Ong, Princeton Univ.
Joe Overstelt, Univ. of California, Berkeley & Lawrence Berkeley National Lab
Harry Orr, Univ. of Minnesota
Andrew Oswald, Univ. of Warwick
Steve Palumbi, Stanford Univ.
Jane Parker, Max-Planck Inst. of Plant Breeding Research
Donald R. Paul, Univ. of Texas at Austin
P. David Pearson, Univ. of California, Berkeley
John H. J. Petrini, Memorial Sloan-Kettering Cancer Center
Simon Philip, Univ. of Florida
Joshua Plotkin, Univ. of Pennsylvania
Phillippe Poulin, CNRS
Colin Renfrew, Univ. of Cambridge
Trevor Robbins, Univ. of Cambridge

EXECUTIVE PUBLISHER Alan I. Leshner
PUBLISHER Beth Rosner

FULFILLMENT SYSTEMS AND OPERATIONS (membership@aaas.org); CUSTOMER SERVICE SUPERVISOR Pat Butler; SPECIALISTS LaToya Casteel, Michelle Ofordire, April Marshall; MANAGER, DATA ENTRY Mickie Napoleoni; DATA ENTRY SPECIALISTS JJ Regan, Jaimee Wise, Fiona Giblin

BUSINESS OPERATIONS AND ADMINISTRATION Director Deborah Rivera-Wienhold; BUSINESS SYSTEMS AND FINANCIAL ANALYSIS Director Randy Yi; MANAGER OF FULFILLMENT SYSTEMS Neal Hawkins; SYSTEMS ANALYST Nicole Mehmedovich; MANAGER, BUSINESS ANALYSIS Eric Knott; MANAGER, BUSINESS OPERATIONS Jessica Tierney; BUSINESS ANALYST Cory Lipman, Cooper Tilton, Celeste Troxler; FINANCIAL ANALYST Jeremy Clay; RIGHTS AND PERMISSIONS: ASSISTANT DIRECTOR Emilie David; ASSOCIATE Elizabeth Sandler; MARKETING DIRECTOR Ian King; MARKETING MANAGERS Allison Chandler, Julianne Wielga, Justin Sawyers; MARKETING ASSOCIATES Mary Ellen Crowley, Elizabeth Sattler, Rebecca Rikliff; SENIOR MARKETING EXECUTIVE Jennifer Reeves; DIRECTOR, SITE LICENSING Tom Ryan; DIRECTOR, CORPORATE RELATIONS Eileen Bernadette Moran; SENIOR PUBLISHER RELATIONS SPECIALIST Kiki Forsythe; PUBLISHER RELATIONS MANAGER Catherine Holland; PUBLISHER RELATIONS, EASTERN REGION Keith Layson; PUBLISHER RELATIONS, WESTERN REGION Ryan Rexroth; CUSTOMER RELATIONS MANAGER Iquo Edim; CUSTOMER RELATIONS ANALYST Simon Chong, Lana Gu; ASSOCIATE DIRECTOR, MARKETING Christina Schlecht; MARKETING ASSOCIATES Paulina Curto, Mitchell Edmund; ELECTRONIC MEDIA DIRECTOR Elizabeth Harman; ASSISTANT MANAGER Lisa Stanford; PRODUCTION SPECIALISTS Antoinette Hodal, Nichole Johnston, Lori Murphy, Kimberly Oster; WEB AND NEW MEDIA: SENIOR PROJECT MANAGER Trista Smith, PROJECT LEADER Luke Johnson COMPUTER SPECIALISTS Walter Jones, Kai Zhang, WEB DEVELOPER Chris Coleman; PROGRAM DIRECTOR, AAAS MEMBER CENTRAL Peggy Mihelich

DIRECTOR, GLOBAL COLLABORATION, CUSTOM PUBLICATIONS, ADVERTISING Bill Moran

EDITOR, CUSTOM PUBLISHING Sean Sanders; 202-326-6430

ASSISTANT EDITOR, CUSTOM PUBLISHING Tianna Hicklin 202-326-6463

SPONSORED CONTENT SPECIALIST Candice Nulsen 202-256-1528

ASSOCIATE DIRECTOR, COLLABORATION, CUSTOM PUBLICATIONS/CHINA/TAIWAN/KOREA/SINGAPORE Ruolei Wu +86-1367-101-5294

PRODUCT (science_advertising@aaas.org); MIDWEST Rick Bongiovanni: 330-405-7080, FAX 330-405-7081; EAST COAST/ CANADA Laurie Faraday: 508-747-9395, FAX 617-507-8189; WEST COAST/ CANADA Lynne Stickrod: 415-931-9782, FAX 415-520-6940; UK EUROPE/ASIA Roger Goncalves: TEL/ FAX +41 43 243 1358; JAPAN, Makiko Hara: +81 (0) 3 6802 4616, FAX +81 (0) 3 6802 4615; ads@sciencemag.jp; CHINA/TAIWAN Ruolei Wu: +86 1367 1015 294 ruw@aaas.org

WORLDWIDE ASSOCIATE DIRECTOR OF SCIENCE CAREERS Tracy Holmes: +44 (0) 1223 326525, FAX +44 (0) 1223 326532

CLASSIFIED (advertise@sciencemag.org); U.S./CANADA/SOUTH AMERICA

Tina Burks: 202-326-6577; U.S. CORPORATE Candice Nulsen 202-256-1528;

SALES ADMINISTRATOR Marci Gallun; EUROPE/ROW SALES Axel Gesatzki;

SALES ASSISTANT Kelly Grace; JAPAN Yuri Kobayashi +81 (0)90-

9110-1719; careerads@sciencemag.jp; CHINA/TAIWAN

Ruolei Wu: +86 1367 1015 294 ruw@aaas.org; ADVERTISING

SUPPORT MANAGER Karen Foote: 202-326-6740; ADVERTISING PRODUCTION

OPERATIONS MANAGER Deborah Tompkins; SENIOR PRODUCTION SPECIALIST/GRAPHIC

DESIGNER Amy Hardcastle; PRODUCTION SPECIALIST Yuse Lajimimuh; SENIOR

TRAFFIC ASSOCIATE Christine Hall; SALES COORDINATOR Shirley Young; MARKETING

MANAGER Allison Pritchard; MARKETING ASSOCIATE Alimee Aponte

AAAS BOARD OF DIRECTORS RETIRING PRESIDENT, Chair William H. Press; PRESIDENT Phillip A. Sharp; PRESIDENT-ELECT Gerald R. Fink; TREASURER David Evans Shaw; CHIEF EXECUTIVE OFFICER Alan I. Leshner; BOARD BONNIE L. Bassler, May R. Berenbaum, Claire M. Fraser, Elizabeth Loftus, Stephen L. Mayo, Raymond Orbach, Sue V. Rosser, Inder M. Verma



ADVANCING SCIENCE SERVING SOCIETY

Jim Roberts, Fred Hutchinson Cancer Research Ctr.
Barbara A. Romanowicz, Univ. of California, Berkeley
Jens Rostrup-Nielsen, Aarhus Univ.
Mike Ryan, Univ. of Texas, Austin
Shimon Sakaguchi, Kyoto Univ.
Miquel Salmeron, Lawrence Berkeley National Lab
Jürgen Sandkühner, Medical Univ. of Vienna
Alexander Schlier, Harvard Univ.
Randy Seeley, Univ. of Cincinnati
Vladimir Shalaya, Purdue Univ.
Joseph Silk, Institut d'Astrophysique de Paris
Dennis Simons, Arizona State Univ.
Allison Smith, John Innes Centre
Davor Solter, Inst. of Medical Biology, Singapore
Peter Sorger, Harvard Medical School
John Speakman, Univ. of Aberdeen
Allan C. Spradling, Carnegie Institution of Washington
Jonathan Sprent, Garvan Inst. of Medical Research
Eric Steig, Univ. of Washington
Paula Stephan, Georgia State Univ. and National Bureau of Economic Research
Elisbeth Stern, ETH Zürich
V. S. Subrahmanian, Univ. of Maryland
Ira Tabas, Columbia Univ.
Yoshiko Takahashi, Kyoto University
Sarah Teichmann, Cambridge Univ.
John Thomas, North Carolina State Univ.
Christopher Tyler-Smith, The Wellcome Trust Sanger Inst.
Herbert Virsik, Washington Univ.
Bernd Vogelstein, Johns Hopkins Univ.
Cynthia Volpert, Univ. of Göttingen
Bruce D. Walker, Harvard Medical School
Douglas Wallace, Oathouse Univ.
Ian Walsley, Univ. of Oxford
David A. Wardle, Swedish Univ. of Agric. Sciences
David Waxman, Fudan Univ.
Jonathan Weissman, Univ. of California, San Francisco
Kathy Willis, Oxford Univ.
Ian A. Wilson, The Scripps Res. Inst.
Timothy D. Wilson, Univ. of Virginia
Rosemary Wyse, Johns Hopkins Univ.
Jan Zaenen, Leiden Univ.
Kenneth Zaret, Univ. of Penn. School of Medicine
Jonathan Zehr, Univ. of California, Santa Cruz
Maria Zuber, MIT

BOOK REVIEW BOARD

John Aldrich, Duke Univ.
David Bloom, Harvard Univ.
Angela Creager, Princeton Univ.
Richard Shwartz, Univ. of Chicago
Ed Wasserman, DuPont
Lewis Wolpert, Univ. College London



Join the Conversation!

Twitter is a great way to connect with AAAS members and staff about the issues that matter to you most. Be a part of the discussion while staying up-to-date on the latest news and information about your personal member benefits.

**Follow us @AAASmember
and join the conversation
with #AAAS**



MemberCentral.aaas.org



**At Atlas Antibodies we
have a very singular focus.
It's the complete human.**

From our facilities in Stockholm, Sweden, we manufacture and distribute highly characterized antibodies targeting all human proteins. All of our antibodies are manufactured using a standardized production process to ensure the most rigorous levels of quality.

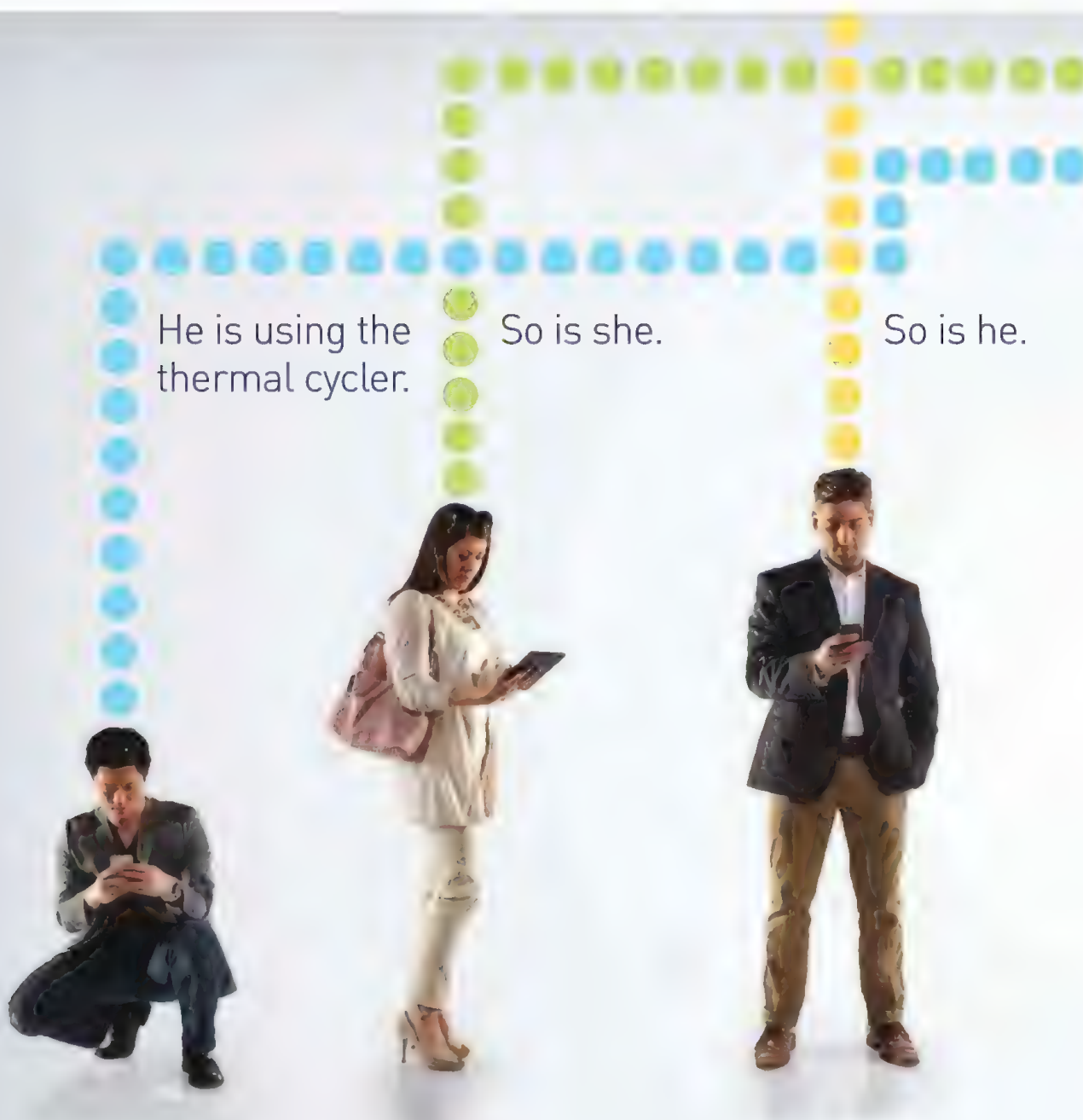
Working in close partnership with the Human Protein Atlas project, we are looking to complete the systematic exploration of the human proteome using antibodies. Of the possible 20,000 protein coding genes in the human body we already have over 15,000 antibodies covering 13,000 gene products. This is of course supported by millions of images available on our websites.

So, if you're interested in some human dialogue, why not talk with us.

atlasantibodies.com/totallyhuman



Atlas Antibodies AB Stockholm, Sweden
atlasantibodies.com, proteinatlas.org



He is using the
thermal cycler.

So is she.

So is he.

3 different users. 3 different experiments. 3 different times. All connected remotely to one high-performing and flexible instrument built for today's PCR laboratory.

Applied Biosystems®

Buy one at lifetechnologies.com/proflexpcr

For Research Use Only. Not for use in diagnostic procedures. ©2013 Life Technologies Corporation. All rights reserved. The trademarks mentioned herein are the property of Life Technologies Corporation and/or its affiliate(s) or their respective owners. C0113461 0513

Introducing the ProFlex™ PCR System



life
technologies™

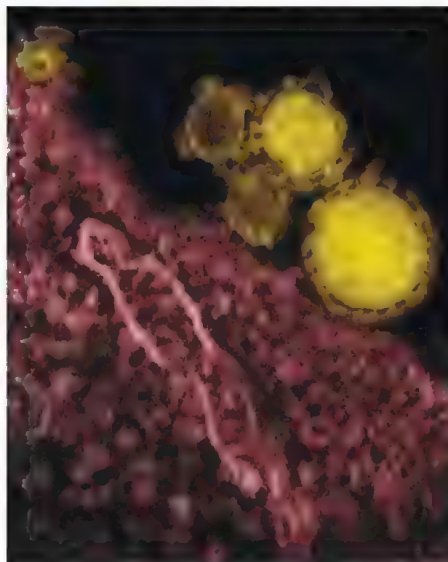
AROUND THE WORLD



Florence, Italy

Three MERS Cases in Italy

A deadly new virus that originated in the Middle East has made another jump to Europe. Italian health authorities have reported three cases of Middle East respiratory syndrome (MERS), the first of whom was a 45-year-old man who fell ill



after a 40-day trip to Jordan, where he is assumed to have picked up the virus. A 2-year-old girl and a 42-year-old woman who were in close contact with the man became infected in Italy.

The cluster is another clear sign that the virus can spread between people, although not very efficiently so far. That's worrisome to scientists and public health experts, who fear that MERS may start spreading more rapidly and trigger a pandemic. Caused by a distant cousin of the SARS virus, MERS is known to have occurred in Jordan, Saudi

Arabia, Qatar, and the United Arab Emirates; people infected in those countries had previously brought the virus to the United Kingdom, Germany, France, and Tunisia. So far, there have been 53 recorded cases, including 30 deaths.

Tokyo 2

Joining the Fight Against Neglected Diseases

Japan is joining global efforts to contain malaria, tuberculosis, and a variety of tropical diseases in a big way. On 1 June, a recently formed public-private partnership announced agreements to screen tens of thousands of drug candidates from Japanese private and public sector compound libraries for treatments for illnesses that primarily afflict the poor in developing countries.

The 11 initial agreements are the first fruits of a recently formed public-private Global Health Innovative Technology Fund (GHIT Fund), which brings together Japan's foreign affairs and health and welfare ministries, five pharmaceutical companies, and the Bill & Melinda Gates Foundation. The Japanese government is putting up a bit over one-half of the \$100 million committed to GHIT over the next 5 years; the drugmakers and the Gates Foundation are contributing the rest.

Even though Japan is a major producer of new pharmaceuticals, the country has been a bit behind other nations in contributing to the global health R&D effort, says BT Slingsby, the fund's CEO and executive director. GHIT is working with established nonprofits—the Global Alliance for TB Drug Development, the Medicines for Malaria Venture, and the Drugs for Neglected Diseases initiative—to help develop candidate drugs.

<http://scim.ag/GHITJapan>

Paris 3

Can Science Help France's Economy?

On 28 May, France's National Assembly approved a law that aims to simplify the national landscape for research and higher education, making it more efficient and more competitive at the European level. The bill, which comes hand in hand with a new strategic plan called France Europe 2020, also gives the government a greater role in coordinating research. The bill and the strategic plan have been sharply criticized by various groups of researchers and university professors.

The new national priorities include health, food security, climate change, sustainable energy, urban systems, digital technologies, and space; they will be periodically revised by a newly created strategic research council. The strategic plan is partly designed to reinvigorate industry through pathbreaking areas such as nanotechnologies and by promoting industry-academia partnerships.

But trade unions say that the government can't make science responsible for rescuing the economy and worry that the new plan will erode basic research. "There is a big concern because [the government] wants research to solve an economic problem and an industry problem," says Patrick Monfort, a marine ecologist with CNRS in Montpellier and the general secretary of SNC-SFSU, the national trade union for scientific researchers.

<http://scim.ag/Franceecon>

Oregon and Berlin 4

Furor Over U.S. GM Wheat

News that genetically modified wheat plants—last deliberately planted years ago—were found growing on an Oregon farm touched off an international uproar last week. Japan postponed wheat imports from Oregon, while South Korea and the European Union called for stepped up testing to ensure that GM wheat hasn't entered the food supply. Oregon's wheat crop, valued at up to \$500 million a year, now stands in jeopardy.

Science LIVE

Join us on Thursday, 13 June, at 3 p.m. EDT for a live chat with experts on **bioelectronics**.
<http://scim.ag/science-live>



Frown for the Camera

For decades, psychologists have used "Pictures of Facial Affect" (conceived by psychologist Paul Ekman) to examine human responses to "universal" facial expressions and emotions: anger, fear, sadness, happiness, surprise, and disgust. But these photos have a drawback: They're primarily of Caucasian adults, and reactions to the expressions can depend on both race and age, says psychologist Vanessa LoBue of Rutgers University, Newark, in New Jersey.

So over the last 5 to 6 years, LoBue, with the help of photographer and former research assistant Cat Thrasher, has created her own set of more than 1200 photos, featuring 190 children of multiple demographics and ages (including the 4- to 6-year-olds shown here). Last month, LoBue received a National Science Foundation grant to conduct validation experiments of her new photo set, in which adults and children of different age groups will try to identify the expressions in each photo, and each photo will then get a "validity score" that researchers can use to design their own experiments. "Ultimately, the goal is to release the set for anyone to use for free," LoBue says. "We spent so many years working on it, we feel like anyone should be able to use it."

The latest GM row touched off in April after a farmer noticed wheat plants growing on his farm, although it had been sprayed with enough of the herbicide glyphosate to kill normal wheat. He contacted researchers at Oregon State University, Corvallis, who tested plant samples and discovered that they contain an introduced gene for glyphosate resistance, a GM technology field-tested by Monsanto in Oregon and 15 other states from 1998 to 2005. Monsanto dropped the project when it became clear there was little market for GM wheat.

Monsanto has come to a similar conclusion in Europe: It will not apply for new E.U. product licenses for GM varieties or conduct new field trials, a spokesperson told German newspaper *Die Tageszeitung* last week.

NEWSMAKERS

Storm Chasers Killed in Tornado

Tim Samaras, 55, an engineer and tornado researcher and "storm chaser," was one of 13 people killed by a cluster of tornadoes that swept through central Oklahoma on 31 May. Two other storm chasers—Samaras's

son **Paul**, 24, and researcher **Carl Young**, 45, were also killed, in the first known fatalities of storm interceptors during a tornado.

Samaras designed and built weather probes that he deployed in the path of tornadoes in order to gain scientific insight into their inner workings. He founded the Tactical Weather Instrumented Sampling in/near Tor-



nadoes Experiment, consisting of a caravan of vehicles equipped with thermodynamic and video probes that deployed each spring during tornado season.

"We are terribly saddened by this news," said a spokesperson for the National Oceanic and Atmospheric Administration in a statement on 3 June. "Samaras was a respected

tornado researcher and friend of NOAA who brought to the field a unique portfolio of expertise in engineering, science, writing and videography."

First Fresenius Award To Immunologist

Yale University immunologist **Ruslan Medzhitov** has been awarded the first Else Kröner Fresenius Immunology Award. The scientist will receive \$650,000 for past achievements, plus an additional \$4.5 million for his ongoing research. The Fresenius Foundation plans to award the prize, which commemorates the 25th anniversary of the death of German pharmaceutical entre-



preneur Else Kröner, every 4 years; each award will single out promising research in a different field.

"We wanted to single out the most innovative work in immunology done in the past that promises

to have the highest impact on future clinical immunology," said immunologist Stefan Kaufmann, head of the selection committee, in a statement.

Medzhitov, who was born in Tashkent, Uzbekistan, worked with Yale immunologist Charles Janeway to elucidate how the human body fights infectious agents. Together, they showed that molecules called toll-like receptors recognize pathogens in the human body and activate the immune system. Medzhitov was controversially left out when the Nobel Committee recognized work in this field in 2011.

New Award to Target Young Scientists

Ukrainian billionaire **Leonard Blavatnik** and the New York Academy of Sciences (NYAS) this week announced the creation of a new national award specifically geared to help young scientists still working to establish their careers. Three unrestricted cash prizes of \$250,000 in three categories (physical sciences and engineering, chemistry, and life sciences) will be awarded annually by NYAS and the Blavatnik Family Foundation.

The award grew from a regional awards program that, beginning in 2007, recognized young scientists in New York, New Jersey, and Connecticut. The scientific advisory

council for the national award includes a number of heavy-hitters, including Ellis Rubinstein, the chair and CEO of the NYAS, and Tim Appenzeller, incoming news editor of *Science*. Institutions can choose nominees for the 2014 program from October to December 2013.

"The long-term goal of the Awards is to create a pipeline of scientific support, in which established scientists choose the most outstanding young faculty-rank scientists, who then go on to mentor the next generation of would-be scientists and award winners," Rubinstein said in a statement.

FINDINGS

OK, Cupid: Online Dating Can Lead to Love

Once considered "creepy" by many, online dating has become mainstream with the rise of dating websites such as Match and OkCupid. Now, a new survey of nearly 20,000 Americans suggests that spouses who met online have marriages that are at least as stable and satisfying as those who met in the real world—possibly more so.

Curious about the impact of online dating, John Cacioppo, a psychologist at the University of Chicago in Illinois and a scientific adviser to eHarmony, convinced the company to pay for the survey. (Two statisti-

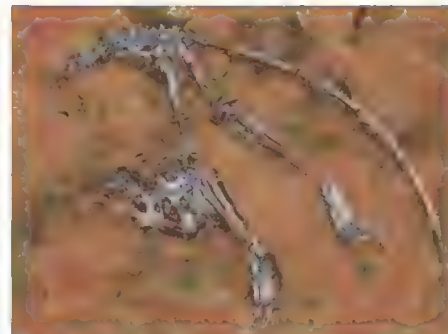
cians with no connection to the company, Elizabeth Ogburn and Tyler VanderWeele of the Harvard School of Public Health in Boston, analyzed the answers). In 2012, 19,131 people out of 200,000 who responded to an e-mail survey request were chosen; of those, more than a third reported meeting their spouse online. Still-married participants answered questions such as, "Please indicate the degree of happiness, all things considered, of your marriage."

Online marriages, it turns out, were durable. In fact, people who met online were slightly less likely to divorce and scored slightly higher on marital satisfaction, the team reports online this week in the *Proceedings of the National Academy of Science*. <http://scim.ag/Onlinelove>

'Crucial Link' in Primate Evolution

A tiny fossil skeleton excavated from an ancient lakebed in central China is among the earliest known primates, a team reports this week in *Nature*. Dubbed *Archicebus achilles*, the creature lived 55 million years ago and probably weighed less than an ounce. Its discovery supports a once-controversial hypothesis: Primates first evolved in Asia and only later migrated to Africa.

A. achilles is likely a very early ancestor of modern tarsiers, a group of small,



big-eyed nocturnal primates with long heel bones that help them take powerful leaps. The fossil "sits at that critical part of the [evolutionary] tree right where the tarsier branch is splitting away from the anthropoid branch," which includes monkeys, apes, and humans, says K. Christopher Beard, a paleontologist at the Carnegie Museum of Natural History in Pittsburgh, Pennsylvania, and a co-author of the study. Indeed, *A. achilles* has several anthropoid-like features, including relatively small eyes and a short heel bone.

"You don't get these kind of complete fossils very often," says John Fleagle, a paleontologist at Stony Brook University in New York who was not involved in the research. "It documents an aspect of primate evolution that we didn't have much documentation for." <http://scim.ag/Archicebus>

Random Sample

Red Meets White Atop Mont Blanc

By the time this issue of *Science* appears, 25 Dutch scientists and volunteers should be climbing Europe's highest mountain, Mont Blanc in the French Alps, seeking to better understand the effects of hypoxia and low blood oxygen levels on blood coagulation. The mission, called "the red meets white study," was scheduled to begin on 5 June in the French village of Chamonix near the base of the mountain (expedition logo, inset). Led by Dutch mountain guide Edward Bekker, the climbers plan to attain the summit, 5000 meters above sea level, by 14 June. Every thousand meters, each climber will offer up a drop of blood.

Previous alpine expeditions have sought a direct link—if one exists—between lowered blood oxygen levels and an increased risk of thrombosis, the formation of blood clots within blood vessels. But those efforts were unsuccessful, due to the failure of regular blood coagulation tests at high altitudes: At lower atmospheric pressures, not enough blood enters the catalyst-filled test tubes to get conclusive results.

But, expedition leader biochemist Bas de Laat of Maastricht University has a secret weapon—a new coagulation test specially adapted for the expedition that requires just a single drop of blood. De Laat divided his team into two groups—one hiking and one taking a cable car—to track how physical activity affects coagulation. Then, each team's medical staff, consisting of cardiologists, a hematologist, and anesthesiologists, will use the new test, adapted from a standard test by Synapse BV (a Maastricht University spinoff company of which de Laat is the current CEO) that measures thrombin, a key blood clotting component that forms within 10 minutes after coagulation begins.





PARTICLE PHYSICS

Europe Opens Door to Global Approach on Megaprojects

In particle physics, as in fashion, Europe could be setting the trend. Last week, European particle physicists unveiled an updated strategy for delving deeper into the building blocks of matter. Their road map could have sway well beyond the continent—particularly in the United States and Japan—as it sows the seeds of a global strategy for building the expensive megaprojects that define the field. “They’re looking at the world picture,” says Pier Oddone, director of Fermilab National Accelerator Laboratory (Fermilab) in Batavia, Illinois.

Presented on 30 May in Brussels, the plan builds on a strategy formulated in 2006. Predictably, it says that Europe’s first priority is to fully exploit the world’s biggest atom smasher, the Large Hadron Collider (LHC) at the European particle physics laboratory, CERN, near Geneva, Switzerland. Last year, the LHC coughed up the long-sought Higgs boson, the particle that is key to physicists’ explanation of how other fundamental particles get their masses. Researchers plan to run LHC until 2030 in hopes of discovering other new particles.

The plan breaks new ground, however, in stating for the first time Europe’s willingness to participate in massive experiments on other continents “once they have a clear plan,” says Rolf-Dieter Heuer, director-general of CERN and a member of the panel that produced the update.

That statement could have outsized implications for sharing the three big projects now at the center of physicists’ dreams. The first is the LHC. The second is a proposed 30-kilometer-long straight-shot International Linear Collider (ILC). By creating

relatively “clean” electron-positron collisions, the collider would study in detail any new particles that the LHC unearths in its messy proton-proton collisions. The third project would be a far-bigger version of current experiments in which physicists shoot elusive particles called neutrinos hundreds of kilometers through Earth to underground detectors. The goal is to study how the three types of neutrinos morph into each other as they zing along. Such “neutrino oscillations” could help explain how the universe generated so much more matter than antimatter, although a bigger detector is needed for such studies.

Physicists haven’t agreed on who should build the two proposed machines. U.S. researchers had hoped to host the linear collider, but in 2007 the U.S. Department of Energy (DOE) said that it couldn’t afford the estimated \$7 billion that a 50% share would cost. Many scientists then thought that CERN would be the likely site. But last year, Japanese officials expressed interest in hosting the ILC, proposing to pay for it, in part, with funds for rebuilding after the 2011 Tohoku disaster (*Science*, 14 December 2012, p. 1404). The plan for the neutrino experiment is murkier, with competing concepts from Japan, Europe, and the United States.

The updated European strategy could help clarify matters. It says that Japan’s bid “to host the ILC ... is most welcome,” and that Europe “looks forward to a proposal from Japan to discuss a possible participation.” Europe should also “explore the possibility of major participation” in a U.S. or Japanese neutrino experiment, it says. That suggests a scenario in which Japan builds

Foreign aid. With Europe’s help, U.S. physicists could better realize their ambitions for the proposed Long-Baseline Neutrino Experiment.

the ILC and the United States builds the neutrino experiment.

There’s no guarantee that the Japanese government would agree to that road map. Still, Europe’s cooperative stance could give a big boost to U.S. physicists pushing for the proposed Long-Baseline Neutrino Experiment (LBNE). It would fire neutrinos from Fermilab 1300 kilometers to a detector filled with frigid liquid argon at the abandoned Homestake gold mine in Lead, South Dakota.

Until recently, researchers had envisioned LBNE as the definitive neutrino oscillation experiment, with a 34,000-tonne detector 1480 meters underground. But DOE balked at the project’s \$1.9 billion cost and asked for a cheaper plan to build it in stages (*Science*, 30 March 2012, p. 1553). Physicists now plan to start with a 10,000-tonne surface detector at Homestake, at a cost of \$867 million, says Milind Diwan, a physicist at Brookhaven National Laboratory in Upton, New York, and co-spokesperson for the LBNE collaboration. To make the experiment sing, however, the detector would need to be built underground to shield it from cosmic rays. To do that, Fermilab officials hope that countries such as India will kick in more than \$100 million.

A financial contribution from Europe could help LBNE researchers more fully realize their ambitions. But LBNE researchers could find themselves in a chicken-or-egg bind: Europe may open its wallet only if the United States has already committed to a top-flight experiment. “The ball is in the U.S.’s court,” Heuer says. “LBNE has to be a world-class project that will do the physics that you want to do—and that means it has to go underground.” Diwan agrees. “The Europeans want Americans to play for something big,” he says. “They won’t participate if it is an attenuated, miserly experiment. They want America to be America.”

—ADRIAN CHO

RUSSIA

Fading Academy Stakes Future on Reforming President

MOSCOW—Over the past 2 decades, Vladimir Fortov has nimbly moved between the worlds of plasma physics and science policy. Now, he faces his greatest challenge yet: saving one of the world's largest scientific organizations. Last week, the Russian Academy of Sciences (RAS), fiercely independent but diminished in stature, elected Fortov as its president with a mandate to urgently reform the 289-year-old institution. "Academy members have finally understood that the 'business as usual,' or 'give us more money and then shut up,' approach is not working anymore," says Mikhail Gelfand, a bioinformatics professor and a member of the Ministry of Education and Science's Public Council. "It remains to be seen whether he'll have sufficient power and resolve to carry it through."

The election ended the 22-year-long reign of Yuri Osipov, a mathematician whose personal links to former President Boris Yeltsin protected RAS during the financial chaos that followed the breakup of Soviet Union in 1991. But as Russia emerged as a modern economy in the 21st century, the academy, a sprawling behemoth with more than 400 institutes and nearly 100,000 scientific staff members, stagnated. Osipov refused to embrace funding by competitive grants and weighing scientific productivity according to publication prowess, says Alexei Khokhlov of the RAS Nesmeyanov Institute of Organoelement Compounds and vice rector of Moscow State University. "Many reasonable suggestions were bluntly rejected by him. He claimed that these are the signs of 'Western influence,' and that Russian science has to find its own way."

More importantly for grassroots scientists, government funding for RAS—\$1.9 billion in 2012—is a small fraction, in terms of purchasing power, of budgets during the Soviet era. The steady erosion of resources, combined with Osipov's reluctance to close institutes or fire researchers, has meant that in some years, rank-and-file academy scientists were paid less than construction workers. Many researchers struggle to scrape together money to buy instruments or research materials; often they hold second jobs to supplement their salaries. The RAS workforce has grayed as young peo-

ple turn their backs on a career in science (*Science*, 19 November 2010, p. 1036).

Fortov seems destined for the role of savior. The plasma physicist trained at the Moscow Institute of Physics and Technology, then in the 1970s and 1980s split his time between there, the Institute of Chemical Physics in Chernogolovka, and the Joint Institute for High Temperatures (JIHT) in Moscow, becoming JIHT's director in



Looking forward. Can Vladimir Fortov revitalize an aging academy?

1992. He still runs a research group at JIHT that's probing the dynamics of plasmas and extreme states of matter. Fortov "does not have to prove that he is a world-recognized scientist," Khokhlov says.

Fortov's academic record makes his success as a science manager all the more surprising. From 1993, during the tumultuous early years of the Russian Federation, Fortov chaired the Russian Foundation for Basic Research (RFBR), a government body set up as an alternative funding channel outside RAS. Despite strong opposition from the academy, Fortov built up RFBR as a Western-style agency based on peer review and competitive funding, tripling its financial resources during his 4-year tenure to 6% of the government science budget. "Fortov contributed tremendously to the development of a grant system of research funding, which was totally new for Russia," says physicist Aleksei Zheltikov of Moscow State University and the RAS Photochemistry Center in Moscow.

In 1996, Yeltsin promoted Fortov to science minister and deputy prime minister. For 2 years, the physicist was part of the government while also serving as a RAS vice presi-

dent. This put him in the awkward position of defending the academy's interests while promoting the ministry's effort to curb RAS authority and boost grant-based research funding. "The conflict between the ministry and the academy was a real vendetta, a battle of annihilation," Fortov said during his recent election campaign. That animosity had flowered under his predecessor as science minister, Boris Saltykov, but

Fortov managed to ease tensions and establish a truce in which RAS was acknowledged as Russia's pre-eminent research organization and the ministry was accepted as the leader in science policy.

That formula worked for nearly 15 years, until last year when Dmitry Livanov became science minister. Livanov has vowed to transfer research activity from RAS institutes to universities and to create a scientific council at the ministry that many see as a move to undermine RAS's authority. The new ministerial body "will coordinate all the basic research both in higher education institutions and the RAS research institutes. This council will become the voice of Russian science," Livanov said in March.

Things were looking bleakest for RAS that month, when Livanov told the Echo of Moscow radio station that the academy "is not viable" and "without prospects." Fortov and several other RAS academicians sent an open telegram to the minister demanding an apology. Livanov publicly backed down at a meeting with journalists, but still insisted that "in general, the system of organization of RAS researchers is not modern, efficient, and does not meet world standards." Fortov immediately resigned from a ministry advisory body, telling an online Russian news service, Gazeta.ru, that it was impossible for him to continue working there.

Renewed tensions with the science ministry cast a pall over the academy elections, which pitted Fortov against Zhores Alferov, a 2000 Nobel Prize winner in physics and head of the RAS St. Petersburg Scientific Center, and Alexandr Nekipelov, an economist who chairs the board of directors of Russia's biggest oil company Rosneft. Fortov's triumph in the 29 May election was resounding—he won 58% of the vote. "Fortov has a mandate to go ahead with the

CREDIT: VISHINSKY DENIS/TASS PHOTO/CORBIS

reforms,” Zheltikov says. “Among all three candidates,” Khokhlov adds, “Fortov has formulated the clearest program that emphasizes the necessity for changes in the Russian Academy of Sciences.”

Fortov faces an uphill struggle to persuade Livanov to grant him time to reform RAS from within. “During the election campaign, Fortov repeatedly emphasized that relations with the ministry have to be normalized,” Khokhlov says. Livanov, like his predecessors in the administrations of Vladimir Putin and Dmitry Medvedev, dislikes the academy’s independence and emphasis on basic

research; he wants more research that is relevant to industry. To an extent, Fortov agrees. In his electoral program he states: “the Academy must actively and in various ways participate in the creation and implementation of large-scale targeted programs for the benefit of the state, education, and business.”

During the campaign, Fortov suggested that young scientists should be offered contracts of 3 to 5 years—instead of the current RAS system guaranteeing lifetime employment—“to create a competitive environment and raise the mobility” of researchers. Fortov says he will ensure that

scientists get paid as much as twice the average salary of all workers in the region in which an institute is based, and provide emeritus scientists with “decent conditions for life and work.” To shake up the ossified management, Fortov has proposed limiting senior RAS officials, including the president, to two 5-year terms in office.

“By any measure,” Zheltikov says, Fortov “is the right person at the right time to do the job—to find the right tone, lead a dialogue, and work out the right solutions.”

—VLADIMIR POKROVSKY AND DANIEL CLERY
Vladimir Pokrovsky is a writer in Moscow.

PALEONTOLOGY

Authenticity of China’s Fabulous Fossils Gets New Scrutiny

Last week, when paleontologists unveiled a fossil purporting to be the earliest known bird, media outlets rapidly spread the news. Most relayed the team’s contention, published in *Nature*, that the 160-million-year-old fossil from China dubbed *Aurornis* “resolves” long-standing controversies about the early evolutionary history of birds, which nearly all researchers now believe descended from feathered dinosaurs.

But the picture is murkier. Few media reports noted that *Aurornis*, or “dawn bird,” had not been found during the team’s excavations in China, but had been acquired from a fossil dealer. This key information was not in the main body of the *Nature* paper, but rather in online supplementary information (SI) that accompanied it. The authors acknowledge the possibility that the specimen may be 35 million years younger than reported; they are conducting additional tests to verify its provenance.

Suspensions dog any specimens from the fabulous fossil fields in northeast China’s Liaoning province, where *Aurornis* and dozens of other new species of feathered dinosaurs and early birds have been found over the past 15 years. Some of the country’s leading paleontologists have been outspoken about a growing number of fake and composite specimens from Liaoning and other fossil-rich areas of China (*Science*, 24 December 2010, p. 1740). “This is a big concern,” says Zhou Zhonghe, director of the Institute of Vertebrate Paleontology and Paleoanthropology (IVPP) in Beijing. “Illegal and unscientific collecting and commercial trading,” he says, have flooded the market with fake fossils and caused an “irretrievable loss” of crucial information, such as where authentic fossils came from

and how old they really are.

Many scientists in Western countries have been slow to express concern about the provenance of Chinese fossils, possibly to avoid antagonizing Chinese colleagues. But the publication of *Aurornis*, the latest of a flurry of recent papers in *Science* and *Nature* describing fossils purchased from Chinese commercial dealers or acquired from collectors, has emboldened several leading Western paleontologists to speak their minds.

“We usually think of guns and drugs when we think of the black market, but there is a black market for fossils, too, and China is an epicenter,” says Stephen Brusatte, a paleontologist at the University of Edinburgh in the United Kingdom. “Some of these fakes are masterful.” Kevin Padian, a paleontologist at the University of California (UC), Berkeley, says that researchers should be prepared to

subject any fossil of uncertain provenance to extra tests, such as computed tomography (CT) scanning, to prove that specimens are genuine. “We have experienced scientists squawking when the integrity of their specimens has been impugned, but sometimes the suspicions have been vindicated,” he says.

An infamous case is “Archaeoraptor,” billed in *National Geographic* in 1999 as a “missing link” between dinosaurs and birds. “Archaeoraptor was a clumsy fake,” says Timothy Rowe, a paleontologist at the University of Texas, Austin, who led the team that cracked the case. But that conclusion came only after extensive forensic examination. High-resolution x-ray CT revealed that what at first appeared to be a complete skeleton was a mosaic of 88 separate pieces mounted onto a shale slab and glued into place with builder’s grout.



True or false? A Beijing-based paleontologist checks a fossil in a dealer’s shop in Liaoning province.

CREDIT: R. STONE/SCIENCE

"Authentication is not easy," says Lawrence Witmer, a paleontologist at Ohio University in Athens. "High-quality fossil forgeries can fool paleontologists just as easily as forgeries in the art community." Luis Chiappe, an early bird expert at the Natural History Museum of Los Angeles County in California, says that he will "always be skeptical of any specimen that is so neatly arranged, so well preserved in a single slab with little bone missing." *Aurornis*'s exquisite preservation should raise eyebrows, Chiappe asserts, although he stresses that he has no evidence to suggest that it is not authentic. The fossil trade in China "is not a black-and-white story," he adds, because "we've benefited enormously from specimens acquired in this way," even if important information about where the fossils came from is lost.

The economy of Liaoning province has also significantly benefited, Chinese and Western scientists point out, because local farmers—who vastly outnumber paleontologists—have become better and better at finding fossils and working with intermediaries and dealers to create composites that can be sold for higher prices. "We can't blame the farmers for this," Padian says. "It's money."

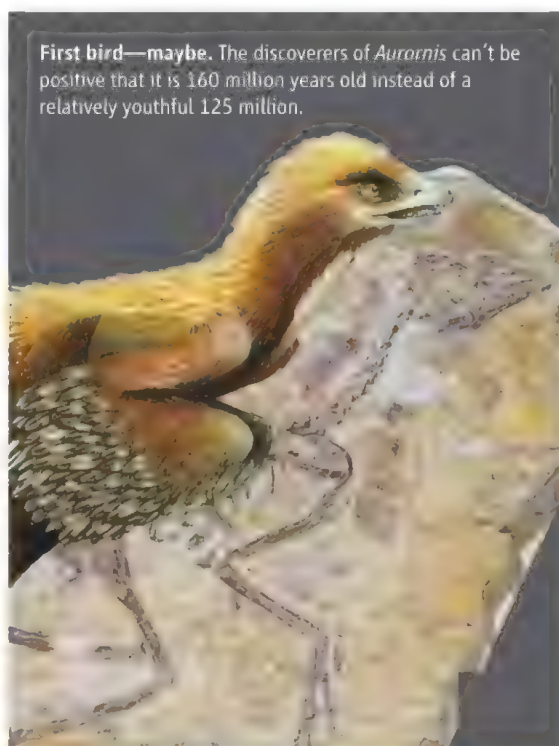
Indeed, says IVPP paleontologist Deng Tao, creating composite fossils has become a small-scale industry in fossil-rich areas of China. "I have personally seen these composite fossils being constructed in workshops or little factories" across several counties in Gansu province, Deng says. "In each workshop, there are bones on shelves like parts in factories."

Museums and other institutions often get fooled by specimens that turn out to be too good to be true. Or, with genuine fossils, they can't be sure where the specimens came from. "In China this is especially bad," says Paul Sereno, a paleontologist at the University of Chicago in Illinois. "There are so many [layers] that are beginning to yield ... fossils across 50 million years of time and a half dozen provinces. There can be as many as 20 specimens of a well-known and named taxon, and yet scientists may be in the dark" about what time period they are from.

For example, the team that reported *Aurornis*, led by paleontologist Pascal Godefroit of the Royal Belgian Institute of Natural Sciences in Brussels, is not entirely

sure whether the fossil came from Liaoning province's 160-million-year-old Tiaojishan Formation, as the information provided by the fossil dealer indicated, or from the province's 125-million-year-old Yixian Formation, the mother lode of many other ancient bird fossils. Most other specimens acquired from dealers have similarly uncertain ages, researchers say.

Godefroit and his co-workers acknowledge the possibility that *Aurornis* may have come from Yixian. He says that his team is trying to confirm the specimen's provenance using botanical and mineralogical tests on the shale slab that it is embedded in and



First bird—maybe. The discoverers of *Aurornis* can't be positive that it is 160 million years old instead of a relatively youthful 125 million.

that the results of these tests will be published later. Godefroit adds that x-rays and CT scanning reveal no evidence that the fossil was forged, although these data were not included in the *Nature* paper's SI.

Journals take different approaches to fossil origins. Recent *Nature* reports on feathered dinosaurs and early birds have included at least a minimum of provenance information, as that journal's rules for authors require, but some papers in *Science* have left it out. For example, the publication earlier this year of 11 specimens of early birds by the IVPP's Xing Xu, one of China's most successful dino hunters—a report suggesting that the earliest birds were biplanes that used all four limbs as wings (*Science*, 15 March, p. 1261)—did not include an acknowledgement that the specimens had

come from fossil collectors.

Andrew Sugden, *Science*'s deputy editor for biology, says that the journal's instructions to authors do not require them to provide information about the provenance of fossils. "We may have to review" those policies, he says, and develop "an internal checklist or something of that kind."

Xu says that researchers do not have to solely rely on the information that dealers and collectors provide. For example, before publishing a beautifully preserved skeleton of *Anchiornis*—a feathered dinosaur thought to have lived around the time of the dinosaur-bird transition—in *Nature* in 2009, Xu's team organized a field trip to the site where a farmer claimed to have found it. During that expedition, the team found other specimens of *Anchiornis*, although none as complete as the original.

So what is to be done? Lacking a consensus, some researchers have developed innovative approaches to the problem. For example, Chiappe's colleague Xiaoming Wang, a mammalian paleontologist at the L.A. County museum, says that the group he leads has worked out an arrangement with dealers "specifically trained to watch out for every specimen they buy and record exactly where it came from." His team also instructs dealers to pass along the fossils, even if fragmentary, without altering them to enhance their value.

Some researchers say that more drastic steps are required. "Everything that has passed through commercial hands should be CT scanned" before it is published, Rowe insists, adding that the scans should be included in the SI or placed in a public repository. Some paleontologists agree that such a course has become necessary, at least for high-profile specimens on which major evolutionary claims are being based. "In the case of things like *Aurornis*, CT scanning is essential," Brusatte argues. "Without it, there will always be lingering doubt that the specimen is genuine."

But others think this is "going too far," as Sereno puts it, and that it is impractical in many cases. "Most authors do not have access to a CT scanner of appropriate caliber," says paleontologist Ryosuke Motani of UC Davis, "and most institutions will be against making 3D data of their specimens available to everyone." Witmer agrees: "Blanket policies about scanning all fossils probably aren't workable."

Until researchers hammer out a solution, controversies like the one over *Aurornis* are likely to become more frequent. The flood of fossil fakes, Wang says, "is going to haunt Chinese vertebrate paleontology for the next 100 years."

—MICHAEL BALTER

CREDIT: THIERRY HUBIN/RSNB



RADIATION SAFETY

Accelerator Leak Halts Japanese Physics Experiments

A minor radiation leak at a particle accelerator in Japan last month is causing a major headache for researchers. The facility is shut down indefinitely, putting a world-class neutrino experiment and nuclear physics studies in limbo. The handling of the accident raises new questions about safety procedures in a nation still nervous about radiation following the 2011 Fukushima nuclear power plant disaster. An ongoing investigation could lead a new regulatory agency to impose remedial safety measures.

The accident occurred at the Japan Proton Accelerator Research Complex (J-PARC) in Tokai, 110 kilometers northeast of Tokyo. The centerpiece of the facility is a 50 giga-electronvolt synchrotron that produces a proton beam for use in three experimental halls, focusing on exotic particles known as hadrons, ephemeral entities called neutrinos, and materials and life sciences.

According to an explanation posted on the J-PARC website, just before noon on 23 May, a malfunction in the beam extraction system directed a pulse of protons 400 times stronger than planned at a gold target used to produce hadrons. The powerful beam appears to have vaporized part of the target. Some of the resulting radioactive material then leaked from the experimental apparatus into the hall, the explanation said, exposing 34 workers to small amounts of radiation. The beam automatically shut down. However, a researcher who was apparently unaware of any danger restarted the experiment 13 minutes later. Monitors in the hall showed radiation exposure rising to

4 microsieverts per hour, 10 times greater than normal. Workers shut down the experiment. But they also vented the hall, releasing contamination into the environment.

The accident “is a surprise,” says Robert Tschirhart, a particle physicist at Fermi National Accelerator Laboratory (Fermilab) in Batavia, Illinois, who sits on the J-PARC International Advisory Committee and has visited the site several times. “The care in construction [of the facility] with regard to radiation safety is world-class.” He speculates that the leak is due to a “training issue with some individuals.”

The two most exposed workers received doses of about 1.7 millisieverts, equivalent to a high-dose medical x-ray but far below the Japanese allowable maximum of 50 millisieverts per year for nuclear industry workers. Off-site monitoring posts in the area showed a measurable but small and transient increase in radiation the afternoon of 23 May. The experimental hall remains contaminated and off-limits.

J-PARC officials did not report the accident to the Nuclear Regulation Authority (NRA), a legal requirement, until 10:40 p.m. on 24 May, more than 34 hours after it occurred. In a statement on its website, the authority acknowledged that the amount of radiation spreading beyond the facility was low and does not pose a risk to the general public. But the statement adds that venting the hall was “not appropriate management of radioactive materials and shows the lack of a culture of safety.”

It is the latest black eye for the Japan

Offline. A radiation leak in a nuclear physics experiment (left) has shut down all work at Japan’s leading particle accelerator.

Atomic Energy Agency (JAEA), which jointly runs J-PARC with the High Energy Accelerator Research Organization. JAEA also operates the trouble-plagued Monju experimental fast breeder reactor, which has been idle almost continuously since a 1995 massive leak of sodium coolant and resulting fire that officials tried to cover up. Just a few days before the J-PARC leak, JAEA President Atsuyuki Suzuki resigned over a separate scandal involving inadequate inspections of key Monju components. NRA has ordered JAEA to halt work toward restarting Monju pending a safety review.

As for J-PARC, “it is very difficult to predict how long the shutdown will be,” says Takashi Kobayashi, a KEK physicist who is the spokesperson for T2K, the facility’s neutrino experiment. “We need to recover the trust of the general public by investigating the cause of the accident thoroughly and taking all necessary measures before resuming accelerator operations,” he says. He adds that the Ministry of Education has called for an external review of conclusions and recommendations. “From the point of view of the T2K experiment, we would like to restart taking data as soon as possible,” Kobayashi says.

Tschirhart says that if the facility can be brought back online next January after upgrades scheduled for this fall, the current halt would have only a “marginal impact.” But he says that suspending the hadron experiments for a long time would broadly affect research.

The T2K experiment directs a stream of neutrinos produced at J-PARC to the Super-Kamiokande detector, 300 kilometers west, to investigate neutrino mass. Christos Touramanis, a physicist at the University of Liverpool in the United Kingdom who is a member of T2K, says that the team has already published some groundbreaking results and is now analyzing previously collected data for presentation at summer conferences. But so far they have less than 10% of the data expected for the duration of the experiment. “We are eager to see the end of this disruption,” he says. The T2K results will complement findings expected to start coming in later this year from the NOvA experiment, which will send neutrinos 800 kilometers from Fermilab to a detector in Ash River, Minnesota. “A significant delay in T2K will be detrimental not only to us but to the field as a whole,” he says.

—DENNIS NORMILE

With reporting by Adrian Cho.

Mysteries of Development

DEVELOPMENT IS, LITERALLY, THE JOURNEY OF A LIFE time, and it is a trip still as mysterious as it is remarkable. Despite new methods to probe how an animal or plant forms from a single cell, biologists have much to learn about the unimaginably complex process. To identify some of the field's persistent riddles, Senior Editors Beverly Purnell and Stella Hurtley and the news staff of *Science* have consulted with developmental biologists on our Board of Reviewing Editors and elsewhere. The mysteries offered here are a humbling reminder that our knowledge of development remains to a great extent embryonic.

—JOHN TRAVIS

Fly balls. Images of fruit fly embryos, revealing locations of different microRNA molecules.

How Do Organs Know When They Have Reached the Right Size?

In the 1920s, biologists began exploring a new way of studying development: surgically removing rudimentary tissues that would form organs and limbs from embryos of one species and transplanting them into those of a related species. In one visually striking example, Yale University zoologists Victor C. Twitty and Joseph L. Schwind removed embryonic tissue that would become a leg in the large salamander species, *Ambystoma tigrinum*, and transplanted it into the embryo of a smaller species, *Ambystoma punctatum*. Despite the early stage of the transplant—before limb buds even appear in the subsequent larvae—the legs grew to the size that they would have on their original body; small salamanders ended up with a longer-than-normal leg, and large salamanders with a short leg. The result, published in 1931 and considered a classic experiment today, suggested that something intrinsic in the leg, rather than signals from the rest of the body, determines a limb's final size.

Since then, developmental biologists have found dozens of proteins and genes that play a role in the growth of plants and animals. But how growing organs and organisms can sense their size and know when to stop is still a mystery.

Developmental biologists continue to explore that mystery today, although most of their experiments now use fruit flies instead of salamanders. The current objects of their attention are imaginal discs, flattened sacs of cells that grow during the fly's larval stages. During the pupal stages and morphogenesis, specific discs differentiate to form the adult wings, legs, eyes, antennae, or other structures. Although they seem undifferentiated in the larval stages, the cells of the different discs are already destined to become a particular body part. Scientists can transplant a wing imaginal disc from a larva into the abdomen of an adult fly, leaving it there for months, and if it is transplanted back into a larva, it will still form wing tissue during pupation and morphogenesis.

A variety of experiments have shown that both the size of imaginal discs and the organs they form are very tightly controlled. When researchers transplant the wing imaginal disc from an early fly larva to a later one or vice versa, the wing still reaches normal size despite having different growing times. If researchers kill a portion of the imaginal disc cells with radiation or other techniques, the insect can boost cell division and still form a normal-size adult. If a fly receives just a fragment of a disc as a transplant, the animal won't move to the next stage of development until the disc has reached the correct size—pausing overall development to allow the disc to catch up. The transplanted disc “will know what size it should be,” says developmental biologist Savraj Grewal of the University of Calgary in Canada.

Scientists can also change the rate at which imaginal disc cells divide, prompting either too many or not enough cells to form, but the cell size adjusts so that organ size remains the same. “The organ isn't counting cell divisions. It's measuring something about dimension,” Grewal says. “What does the organ sense? I think the answer is still unclear.”

There are a few clues, however. A protein called Hippo is part of a cascade of signals that plays a role in the growth of insect imaginal discs and some mammalian organs. (The name comes from the appearance of flies that lack the gene for Hippo in their eye imaginal discs; their over-

CREDIT: ERIC LÉCUYER/IRCM/UNIVERSITÉ DE MONTRÉAL, RONIT WILK AND HENRY KRAUSE/DONNELLY CENTRE/UNIVERSITY OF TORONTO

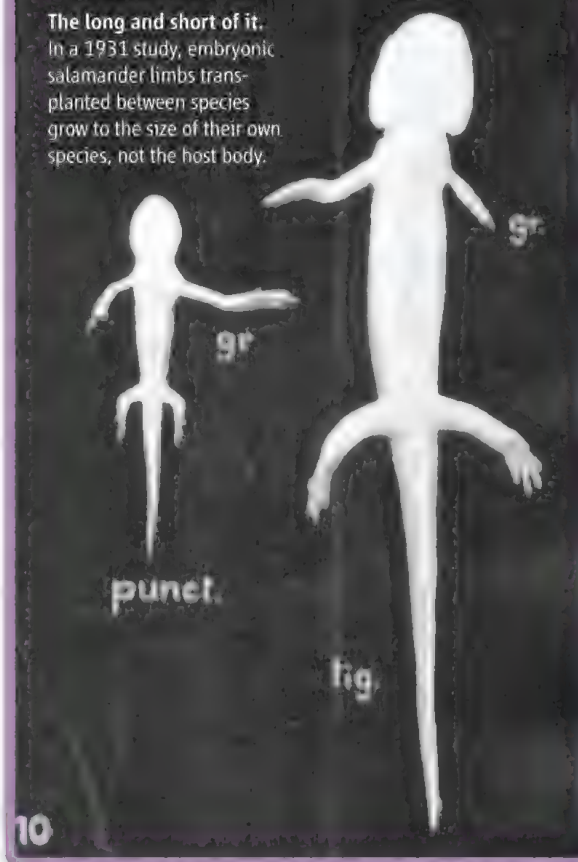
grown heads have a wrinkled surface that resembles a hippopotamus hide.) Disruptions in the Hippo signaling pathway can lead to overgrowth, suggesting that it plays some role in controlling size. But recent studies suggest that it probably isn't the whole answer, says developmental biologist Georg Halder of the KU Leuven in Belgium.

Another set of genes that help with size sensing are ones that produce proteins called morphogens. These molecules originate from a single source in an embryo and diffuse across cells. They are best known for helping determine patterns during development. But some also influence the size of organs, tissues, and limbs. One theory is that when a morphogen gradient is steep—that is, there is a large difference in its concentration from one cell to another—then cells continue to divide. As cells divide, the gradient becomes more gradual. Once it has flattened out to a particular level, cells stop dividing.

There is also evidence that a cell's sense of which direction is up—called planar cell polarity—helps control growth. When certain genes involved in determining cell polarity are disrupted or missing, body parts tend to grow larger, suggesting that they can't sense when they should stop. "It's no coincidence that some of these polarity genes may act as tumor suppressors," Grewal says, and are suspected of playing a role in some cancers.

Many researchers suspect that a developing organ somehow senses the mechanical forces on its growing and dividing cells. One theory is that relative crowding and stretching of cells helps determine whether a cell continues to divide or stops.

The long and short of it.
In a 1931 study, embryonic salamander limbs transplanted between species grow to the size of their own species, not the host body.



The size of an organ depends not only on how many cells it has, but also how big those cells are. Some developing organs—plant leaves, for example, and fruit fly wings—can compensate when fewer cells are available by making the individual cells larger. How a leaf knows when to expand its cells is also unclear, says Hirokazu Tsukaya, a developmental biologist at the University of Tokyo who was among the first to characterize the phenomenon in leaves. He and his team have evidence that some sort of cell-to-cell communication drives the process. Here, too, the evidence suggests that a plant doesn't count cells but can somehow assess the overall size of a leaf,

says plant biologist Beth Krizek of the University of South Carolina in Columbia. "But the mechanism of how that works is another mystery."

The size of tissues, and ultimately an overall organism, also clearly depends on signals from the environment, which researchers call extrinsic factors. Those size control systems are connected to, but different from, the intrinsic systems that help ensure an organism is correctly proportioned. In plants, growth can be especially sensitive to such outside factors, Krizek notes, because they can't move. Plants growing in shade, for example, concentrate on stem growth—to reach the sun—instead of leaf development. In animals, the amount of nutrition available can strongly influence the final size of some organs. One dramatic instance is the horn on a rhinoceros beetle. The horn is a sexually selected trait; males with bigger horns get access to more females. Recent studies have shown that the size of the horn is particularly sensitive to insulin signaling, which is related to the beetle's nutrition.

That, in turn, signals the animal's overall fitness (*Science*, 27 July 2012, p. 408).

The problem of size control is still a fundamental one for developmental biologists, says Peter Lawrence of the University of Cambridge in the United Kingdom. Together with shape, size "is the material that evolution largely works on." But the field is still mostly in the dark. Despite hundreds of papers on what happens when the Hippo signaling pathway is interrupted, Lawrence notes, what scientists really need to understand is what it does when it is working properly. "That is not something we know." —GRETCHEN VOGEL

Why Do So Many Neurons Commit Suicide During Brain Development?

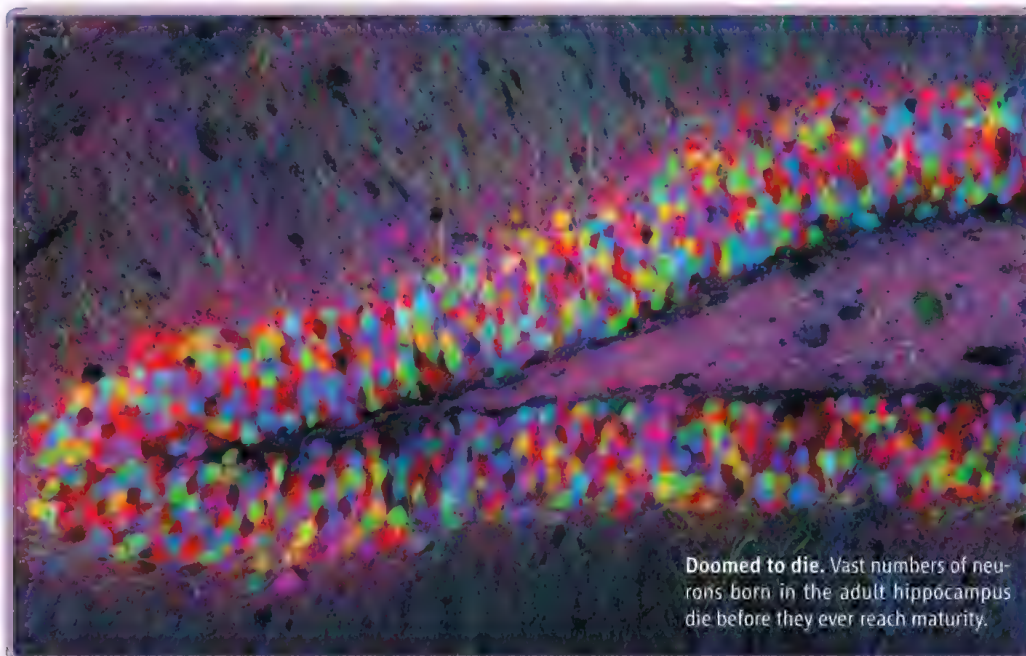
With a few notable exceptions, the roughly 100 billion neurons we have at birth are the only ones we'll ever have. Unlike skin and immune cells, which continuously self-renew, once a neuron has differentiated from its parent stem cell it will never divide again. Given this finite supply, why do so many neurons—more than half in some brain regions—kill themselves during embryonic brain development?

For roughly 50 years, many scientists

focused on a single explanation for this rampant cellular suicide. Their hypothesis was rooted in research on the peripheral nervous system, which connects the nerves of the brain and spinal cord to limbs, organs, and sensory systems. To survive in the developing brain, researchers thought, neurons must compete for limited quantities of a chemical "trophic" factor released by the targets they aim to innervate. Without this signal, the cells self-destruct in a pro-

cess known as programmed cell death, or apoptosis. Called the neurotrophic hypothesis, the concept neatly explained how an overabundance of neurons could attach where needed, or be culled.

"We were all carried away by this observation," says neuroscientist Yves-Alain Barde of the University of Basel in Switzerland. Inspired by the discovery of nerve growth factor in the 1950s, a protein essential to the growth and survival of sensory and motor neurons in the peripheral nervous system, Barde hunted for a single "survival" molecule for neurons in



the brain. Although he hoped that his discovery in the 1980s of brain-derived neurotrophic factor would be that molecule, “this turned out not to be the case,” he says. The protein does promote neuron survival in some parts of the brain, but it is more widely involved in stimulating their growth and shaping their connections.

Today, researchers recognize that the neurotrophic hypothesis alone cannot explain why so many cells die in the brain. “There’s a complexity that we didn’t appreciate,” says Kevin Roth, a neuroscientist at the University of Alabama, Birmingham, School of Medicine. From the moment a neuron is born, he says, the cell is influenced not just by trophic factors, but also by a barrage of environmental and genetic cues that will ultimately determine whether it ever becomes a mature neuron.

Thanks to the invention of antibodies that can detect neurons as they self-destruct, scientists have identified at least two, and possibly three, waves of neuronal cell death in the embryonic mammalian brain during development, each tightly regulated by different enzymatic pathways. The first wave strikes down cells before they are fully differentiated neurons. Evidence suggests that this stage of cell death helps sculpt the size and shape of the nervous system, says neuroscientist Rae Nishi of the University of Vermont in Burlington.

Interfering with this process can have serious consequences. For example, by blocking the activity of caspases, a family of enzymes that aids in killing off young neurons, “you get really ugly, big brains,”

and the embryos soon die, Nishi says. Some caspases appear to target embryonic neurons with extra or missing chromosomes, suggesting that the programmed cell death culls abnormal cells, according to recent work from neuroscientist Jerold Chun at the University of California, San Diego.

A second wave of cell suicide occurs after neurons have begun to differentiate and extend their axons to make contact with other cells. Although some researchers have tried to “shoe-horn” the die-off at this later stage into the neurotrophic hypothesis, Nishi says, she believes her group’s work on neurons that innervate eye muscles suggests that lack of a survival molecule is not what triggers death at this time. Supporting this idea are new studies on cells in the cerebral cortex called inhibitory interneurons. Derek Southwell, a neuroscientist at Stanford University in Palo Alto, California, and colleagues transplanted a group of developing mouse interneurons into tissue where similar cells had already established themselves. In mice, 40% of inhibitory interneurons normally die during development after they migrate out of their birthplace in the forebrain to the cortex. Precisely 40% of the transplanted cells also died, suggesting that they acted of their own accord and not in response to their environment, Southwell says. “It seems there is some kind of developmental clock that times this decision about survival versus death,” he concludes.

This strictly programmed cell death could prevent abnormal cells from being

cancerous or remove cells that served some transient role. The cells might also require direct stimulation from other cells to survive and die off if they are isolated, Southwell suggests. “The truth of the matter is that we have no idea.”

Such massive neuronal suicide could also have no purpose. In some cases, “blocking cell death doesn’t have any dramatic consequences,” Barde says. In 2006, for example, neuroscientist Ronald Oppenheim at the Wake Forest School of Medicine in Winston-Salem, North Carolina, was chagrined at the result of creating mice with absolutely no programmed cell death after neuronal differentiation. (He and his colleagues blocked the activity of a gene necessary for

apoptosis.) “The most striking thing was that despite having all these tens of thousands of excess neurons throughout the nervous system, [the mice] seemed really quite normal,” he says. “That was an embarrassing revelation. I thought, why have I been spending most of my career studying this?”

Although the excess cells look like motor neurons and have axons, they don’t work. “They just hang around,” Oppenheim says.

“You might call them undead.” He suggests that the developing nervous system compensates for the extra cells by simply not linking them in to neural circuits. Another possibility is that the effects of excess cells are too subtle to easily detect,

Nishi says, adding that similar studies that have prevented normal cell death during the brain’s development in mice have uncovered heightened anxiety and defensiveness.

Understanding the brain’s profligate ways has become paramount. Overturning conventional wisdom, scientists now know that adults generate new neurons throughout their lives in a few select brain regions, such as the hippocampus. Many of these newcomers have short lifespans. “Of the immature neurons born in the hippocampus [during adulthood], the vast majority die before they’re ever integrated into any kind of circuitry,” Roth says. “Any time you have neurogenesis, the counter side is cell death.” For now, however, why these processes are so deeply intertwined remains a mystery.

—EMILY UNDERWOOD

Online

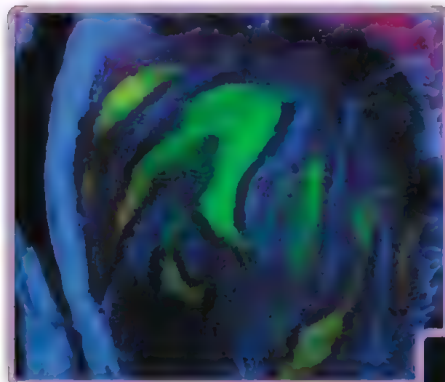
sciencemag.org



Podcast interview with editor John Travis (http://scim.ag/pod_6137).

How Do Microbes Shape Animal Development?

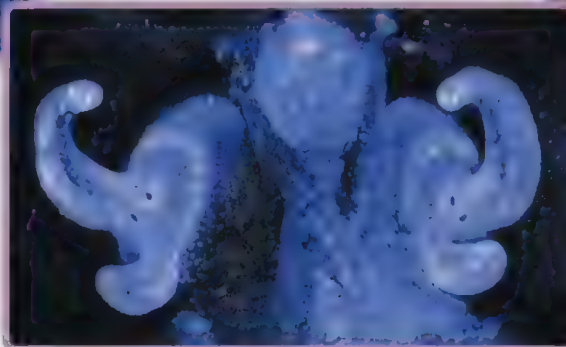
As the other mysteries in this package attest, developmental biologists have long had their hands full trying to fathom the transformation of a single cell into a full-fledged adult animal. They have concerned themselves primarily with deciphering the internal, genetically guided programs that take each species through specific stages to come out the right size and shape with a predetermined number of limbs, fins, eyes, and noses. But they were missing an elephant in the room, says Margaret McFall-Ngai, a developmental biologist at the University of Wisconsin, Madison: The world of microbes that live in, on, and around every animal.



dressed question: How much do microbes shape normal development?

Animals and plants have always shared space with bacteria, fungi, viruses, and other microbes, coevolving through many millennia. In the mid-1800s, however, scientists came to view microbes primarily as enemies and fought hard with antibiotics, vaccines, and good hygiene to get the best of them. But the microscopic world is so intertwined with macroscopic life that the idea that each multicellular animal exists as a separate individual defined by its genome is falling by the wayside. There is a growing realization that microbes and their genes are partners in each animal's journey from egg through adulthood. "What we understand to be the 'individual' develops as a consortium of animal cells and microbes," says Scott Gilbert, a developmental biologist from Swarthmore College in Pennsylvania.

Partners in development. The developing light organ (below) of the bobtail squid (right) temporarily has mucus-covered surfaces to gather symbiotic bacteria (left, green).

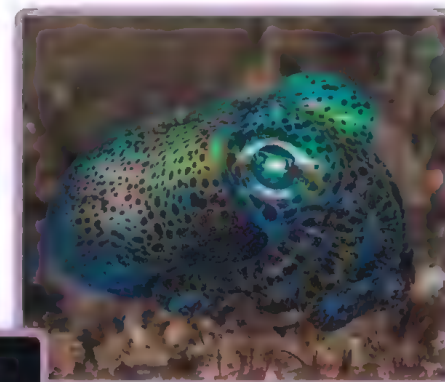


The more she and other scientists get to know this world, the more they realize how big an influence microbes have on all aspects of animal and plant life—and not just as infectious pathogens. Take McFall-Ngai's research focus, the Hawaiian bobtail squid *Euprymna scolopes*. A nighttime hunter, it has evolved a way to acquire the bioluminescing bacterium *Vibrio fischeri* from surrounding seawater to light its underside so that predators below don't see its shadow in the moonlight. Squid embryos temporarily develop a mucus-laden ciliated patch inside the body cavity, where *Vibrio* selectively accumulate and eventually migrate into crypts destined to become the squid's so-called light organ. The presence of the bacteria affects squid gene activity, causing the ciliated patch to disintegrate and the light organ to differentiate. If there are no bacteria, the light organ fails to fully develop.

This example of *Vibrios* as midwives for the formation of an animal organ raises the provocative and, until recently, largely unad-

microbes, they may still rely on microbes to set in motion or complete certain aspects of postnatal development. Like McFall-Ngai's squid, mammals acquire microbial partners after birth and seem to have evolved strategies to encourage the right species to settle in specific places. Human milk, for example, contains complex sugars that infants cannot digest but which promote the growth of intestinal bifidobacteria.

But what do these microbial partners do? Germfree mice have finally allowed researchers to begin addressing this question. These are mice that lack the usual complement of gut bacteria because they are bred and raised in sterile environments and eat sterilized food. Studies of such mice make an increasingly strong case that bifidobacteria and other gut bacteria guide the postnatal maturation of the intestinal and immune systems, and even parts of the brain, in mammals. The microbes



turn on mammalian genes important for cellular differentiation and produce metabolic products that may also affect development. Gut-associated lymphoid tissue and the capillary beds of the villi of the intestine fail to adequately develop in germfree mice, for example. With respect to the immune system, mouse studies also show that a polysaccharide produced by the symbiont *Bacteroides fragilis* helps establish the right balance between helper 1 and helper 2 T cells. B cells also need symbiotic bacteria to develop normally.

The evidence for a role for symbionts in the postnatal developing brain is more preliminary but nonetheless intriguing. More and more connections are being found between the gut microbiota and behavior (*Science*, 12 October 2012, p. 198). In 2011, Pettersson and his colleagues tested anxiety levels and locomotor activity in germfree mice and found that the rodents are hyperactive and have a decreased level of anxiety compared with mice with a healthy microbiota. There

"Microbes came before us, so all development that takes place in all organisms has basically been taking place in the presence of the microbiota," adds Sven Pettersson of the Karolinska Institute in Stockholm.

The evidence for coevolution in developmental processes is coming from far corners of the animal kingdom. Whereas marine biologists once thought that drifting larvae of coral, snails, and other oceangoing invertebrates randomly settled down to become adults, they now know that many respond to cues from bacterial biofilms to pick their new homes. And while many animals develop in wombs or eggs apparently free of

were also differences in the activity of genes associated with motor activity and anxiety. There seems to be a window of opportunity for the microbiota to influence behavior patterns: Colonizing germfree mice with normal mouse microbes negated these differences in young, but not older, mice, they reported.

Some work suggests that gut microbes influence behavior through the vagus nerve, which connects the brain with the digestive system, but Pettersson and others suspect a role for blood-borne bacterial products as well. These products, which make up 10% or more of the metabolites in blood,

may extend the reach of the gut microbiota throughout the body.

That realization may mean that prenatal development in mammals isn't as free from microbial influence as everyone has thought. In mammals, the developing fetus is virtually bacteria-free; hence, researchers have focused on finding a role for bacteria in development after birth. Yet blood-borne metabolites from a mother's gut germs could exert an effect on a growing fetus. "That was one of the assumptions, that pregnancy did not involve microbes," Gilbert says. "But it probably does."

As such assumptions are overturned, researchers are addressing new issues. What is the molecular dialogue that enables the microbial world to influence development? How did that dialogue evolve and how often is it a friendly one? "The big questions are now exposed," says Michael Hadfield, a developmental biologist at the University of Hawaii, Manoa. "After all the years we tended to ignore the bacteria, most people who are studying development should be looking for where the bacteria are and what roles they are playing."

—ELIZABETH PENNISI

How Does Fetal Environment Influence Later Health?

Parents pore over their newborn's face, drinking in the fuzz of her eyebrows, the shape of the chin, searching for themselves in her smile. But they're not thinking about what they can't see, and what ultimately matters more: the heft of her heart, the hormones churning from the liver, all those invisible features that influence her health into adulthood.

While their baby's biology of course reflects a mingling of the mother's and father's DNA, there's more to her than that. In a peculiar way, all newborns are "an expression of the mother," in the words of David Barker, a physician and epidemiologist at the University of Southampton in the United Kingdom. He believes that people are shaped, inside and out, by the maternal environment that sustained them before they were born.

In the late 1980s, Barker scrutinized thousands of birth and death certificates of people from Hertfordshire, U.K., and concluded that those whose birth weight fell on the low end of normal were much more likely to die of heart disease as adults. Since then, Barker has promulgated his theory that maternal environment controls a baby's destiny in more ways than we yet understand.

These days, there's broad agreement that the fetal world, the most rapid period of human growth and devel-

opment, shapes one's risk of future disease, although how much influence it has remains uncertain. A key missing link is in the mechanism. What switches in the fetus, or the placenta that nourishes it, are flipped by a mother's diet or stress levels? In other words, how does fetal environment mold development?

Those exploring this fundamental mystery have at least one intriguing discovery to follow up. No matter what the stressor on the fetus, studies of people and animals suggest that the output is similar: a higher risk of type 2 diabetes, obesity, heart disease, insulin resistance, and high blood pressure. In rodents, "anything that could be a nutritional stressor seems to have the same effect," says

Simon Langley-Evans of the University of Nottingham in the United Kingdom, suggesting that the fetus is implementing a universal response to stress, perhaps to ensure its survival.

The early focus of the field that Barker spawned was on birth weight, a crude reflection of a fetus's surroundings: Smaller babies tended to reflect poorly nourished or highly stressed mothers. But what a mother eats when she's pregnant is only a small part of the fetal environment, Barker notes. "The mother's body is the product of her lifetime nutrition," he says—and even her own mother's nutrition, too, because most or all of her eggs are formed before birth.

Scientists are now striving for greater sophistication in exploring the black box of the womb. Animal studies have found that without good nutrient flow across the placenta, the offspring responds "by building its organs on the cheap," says Kent Thornburg, a cardiac physiologist at Oregon Health & Science University in Portland. Hearts have fewer muscle cells. Kidneys have fewer nephrons for filtering urine. There's less skeletal muscle in limbs and fewer insulin-producing cells in the pancreas.

Peeling back the layers, scientists are also finding differences in DNA patterns in the offspring, depending on whether their mothers were properly fed or malnourished. One long-running effort examines men and women who developed in utero during the Dutch Hunger Winter of 1944 to 1945, when the Germans cut off food and fuel shipments to part of the Netherlands. A birthday soon



Prebirth world. The fetal environment correlates with health later on, but researchers are still disentangling exactly how one connects to the other.

CREDIT: CAROLINA BIOLOGICAL SUPPLY CO./VISUALS UNLIMITED INC.

Under Development

The journey from single cell to mature organism is full of intrigue. Far too much of what we know about development involves what happens when things go awry, says Peter Lawrence of the University of Cambridge in the United Kingdom. "If a mutant gene causes an organism's head to fall off, the conclusion is that the gene's function is to hold the head on," he says. "People have applied this logic, inappropriately, to complex phenomena like the building of an organism." The focus on mutations, he says, has distracted the field from some of the most important questions in development, which require understanding what genes do when they are working as they should. Here are five more mysteries of development.

—GRETCHEN VOGEL

The shape of things to come. Despite exciting progress reported in this issue (see p. 1183), how cells use genetic instructions to form the shapes that organisms ultimately take is a conundrum. "The shape of your nose? That's all written very precisely somewhere in some form," Lawrence says. "We have no idea where."

Not carbon copies. Although they share the same genome, identical twins are different—sometimes subtly, sometimes dramatically. They show how chance events can influence developing organisms, but many questions remain about just how much of development is due to chance.

Millennial naps. Researchers recently coaxed seeds to sprout after being buried in frozen tundra for thousands of years. How do seeds remain in a state of suspended animation, waiting for the right moment to start putting down roots and pushing up shoots?

Pick your progeny. How do stem cells—which can both replicate themselves and give rise to other cell types—know when to switch from one kind of daughter cell to another?

New parts from old. During evolution, new structures such as turtle shells or bat wings arise through a process that repurposes existing parts. Tracing the genetic changes that lead to new structures as species evolve is a passion of evolutionary developmental biologists; advances in genomics may help solve such mysteries.

after was correlated with more obesity and impaired glucose metabolism in adulthood, along with higher rates of other health issues. In 2008, a group at Columbia University and Leiden University Medical Center added a genetic twist to that well-documented story. They reported that almost 60 years after the famine, those born at the time had different patterns of methylation, a chemical coating of DNA that influences gene expression, in the gene *IGF2* as compared with their siblings who arrived in flusher times. The researchers also found that as adults, men had more differences in methylation than women born at the same time. They are continuing to explore methylation patterns on a genomewide scale among their cohort.

One problem with this work is that no one knows for sure whether the DNA changes occurred in utero in response to the famine, or came about later in life for entirely dif-

ferent reasons. Nor do scientists yet know whether these genetic changes, which are often modest, play a role in disease susceptibility. "It's so damn difficult" to do this research, says Bastiaan T. Heijmans of Leiden University Medical Center, who led these methylation studies of the Dutch Hunger Winter cohort along with his Columbia colleague, Lambert H. Lumey. "There's some quite compelling evidence that indeed this relationship is there" between the fetal environment, the DNA changes, and later health problems. But "it's hard for me to put my finger on" exactly what's going on.

Animal work can help clear up the confusion. And it, too, is identifying striking sex differences in how fetuses react to their surroundings. Ten years ago, Lubo Zhang of Loma Linda University School of Medicine in California began depriving pregnant rats of oxygen, mimicking the effects of a mom-

to-be with heart disease, or women whose placentas are poorly formed. Then he studied the hearts of the offspring when they reached adulthood.

The organs, Zhang found, functioned normally. That is, until he induced stress in the animals that mimicked a heart attack. The males lost far more heart muscle tissue than females or than animals whose gestation had been healthy. "They become much more vulnerable to the second hit," he says. "If the heart is not stressed later in life, [the animals] cannot tell the difference."

Over the ensuing years, Zhang traced this effect to dampened expression in a gene called Protein Kinase C epsilon. Protecting fetuses from low oxygen, for example with a compound called N-acetylcysteine, kept this gene's activity up during development and hearts healthy long-term. He hypothesizes that extra estrogen in the placentas of female animals protects them.

Then there are the myriad studies suggesting that pregnant women (or pregnant rodents) who suffer from common infections like the flu or a days-long fever are more likely to have offspring who develop autism or schizophrenia. Here, too, the findings are still tenuous, and researchers are only beginning to address how a woman's immune system battling infection can influence the developing nervous system in her womb.

One underexplored piece of gestation is the placenta. Its morphology varies tremendously—perhaps related to a mother's body composition and diet—and studies have found that the state of the placenta at a baby's birth can predict how the child fares later on. Barker, Thornburg, and others have probed this connection via the Helsinki Birth Cohort Study of more than 20,000 people born in the 1930s and '40s. The hospitals kept detailed measurements of each baby's placentas, and the researchers have linked placental measurements to later adult health, everything from sudden cardiac death to lung cancer to insulin resistance. As with so many fetal environment studies, though, the choreography—the pattern of dance steps that occur between fetus and placenta—is largely unknown.

Solving these mysteries is daunting. "We try to link time points that are so far apart," Heijmans says. "There's no study that goes from preconception to 100 years of age." While "a good part of healthy aging starts in the womb," Heijmans believes, it's just the beginning to a hopefully long life that will mold health and disease.

—JENNIFER COUZIN-FRANKEL

BIOELECTRONICS

The Cyborg Era Begins

Advances in flexible electronics now make it possible to integrate circuits with tissues

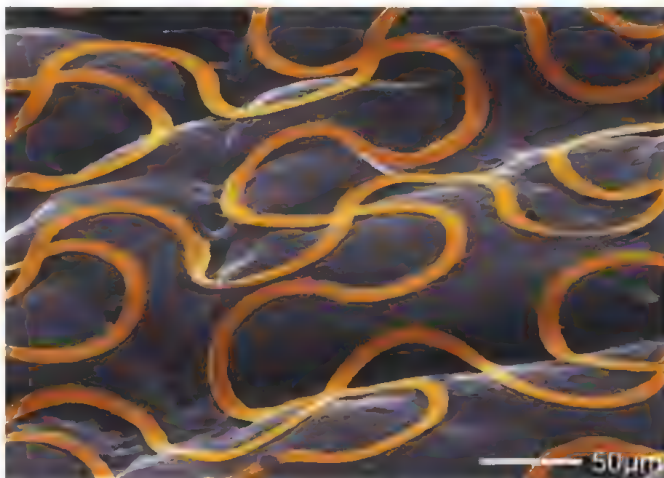
Life plus. Nanocircuitry (yellow-green) integrated into nerve cells.

John Rogers doesn't look like a cyborg yet, but his transformation has begun. As he delivered a talk at a recent conference in San Francisco, Rogers, a materials scientist at the University of Illinois, Urbana-Champaign, picked up a penlike microscope connected to the projector that beamed the PowerPoint slides on his computer for all in the audience to see. As Rogers pressed the pen-scope against his forearm, viewers got a close-up view of the craggy hills and valleys of his skin, as well as an array of squiggly gold lines and square pads. The lines and pads, it turns out, were components of arrays of circuits—not the Intel or ARM variety found in your laptop or cell phone, but a postage stamp-sized collection of flexible, stretchable, and nearly transparent devices that molded perfectly to the contours of Rogers' skin.

That intimate contact, Rogers explained, will allow his team to use flexible circuitry to monitor body temperature, heart rate, and blood pressure and wirelessly transmit the data to a nearby computer. Using similar arrays, Rogers's team has also been able to track arm motion, allowing researchers to control a toy helicopter's flight path with a wave of the arm. Through a startup company that he founded called MC10, Rogers has teamed up with NBA and NFL stars such as Grant Hill and Matt Hasselbeck to use the technology to monitor head impacts during sports. Working with the stars "is pretty cool," Rogers says. "It gives you a lot of credibility

with your 10-year-old son."

Fanciful as such technology sounds, it's just the beginning. Additional devices shown by Rogers and others at the Materials Research Society (MRS) meeting went even further. Cling wrap-like circuitry draped over the hearts of test animals can not only independently track the activity of each of the heart's four chambers, but it can also emit pulses of heat that kill tiny patches of tissue that initiate potentially deadly arrhythmias. Other arrays penetrate brain tissue to



Rise and fall. Electrode arrays flexible enough to hug the contours of human skin make it possible to measure temperature and muscle contraction.

monitor the abnormal nerve firing patterns in epilepsy or induce gene expression in the brain tissue of mice and monitor the results to study developmental biology. One team has even made a 3D printed bionic ear com-

plete with cartilage cells and wiring able to tune in to both Beethoven's "Für Elise" and ultrasonic bleats that humans cannot hear.

Meet your future self. The beginnings of a cyborg world have arrived. These early prototypes are pale shadows of the Hollywood versions, such as the humanoid Cylons in *Battlestar Galactica* or the Borg in *Star Trek* who claim that resistance to incorporation into their collective is futile. Nevertheless, research progress is real, as a mix of biologists, materials scientists, and nanotechnology experts are chipping away at a host of challenges. "I see it as building a seamless interface between cells, tissues, and electronics," says Aleksandr

Noy, a bionanoelectronics expert at Lawrence Livermore National Laboratory and the University of California, Merced. For now, most of these efforts focus on providing better health care and quality of life for patients. But over time, expect devices that will make us better athletes and soldiers, or even improve our complexion.

"A few years ago these things were science fiction. Now we are seeing the emergence of real devices and applications," Noy says. And fast, says Zhenan Bao, an organic electronics expert at Stanford University in California: "The competition is furious."

Stretching the limits

The idea of fusing man and machine has long tantalized humanity. Over the past century, Rogers points out, researchers have pioneered myriad efforts to use electronics to measure biological activity and sometimes even alter it. They tailored metal electrodes that could be taped to the skin for use in electrocardiograms. They devised brain stimulators that can be inserted deep within brain tissue to disrupt the neural firing

patterns that cause debilitating tremors in patients with Parkinson's disease. And they created cochlear implants capable of converting sound to electrical impulses that can be registered by the inner ear.

The early technologies were crude: rigid devices that were strapped and glued to the skin or stabbed through soft tissue. The latest iterations are more about tailoring electronics to mimic the body's pliability. Efforts range from the macroscale of things we can see to the microscopic scale at which electronics are being entwined with individual cells.

At the upper end of the scale, Michael McAlpine, a mechanical engineer at Princeton University, and colleagues reported in the 1 May issue of *Nano Letters* that they've made the first 3D printed functional organ: a bionic ear that hears acoustic sound and ultrasound. "We're trying to see if one could introduce augmented functionality that a human wouldn't ordinarily have," McAlpine says.

Three-dimensional printers work by using a computer-driven laser printer to build up layers of material-based inks, usually made from plastics. McAlpine's team started with three different inks: one made from silicone; another with silicone infused with silver nanoparticles; and a third with chondrocytes, cells that produce cartilage, along with a gel to promote their growth. Numerous groups have used 3D printing to make tissues, but they have typically printed only scaffolding material and cells. McAlpine's team added a level of sophistication to the technology. The researchers printed out a metal coil in the center of the engineered ear that serves as an antenna capable of picking up acoustic signals and converting them to electrical pulses for the inner ear, à la a conventional cochlear implant. The antenna can also detect ultrasonic waves that dogs and other animals can hear but humans cannot.

Another macroscopic project is electronic skin, complete with tactile, temperature, and even chemical sensors. Such skin could potentially be integrated into prosthetic limbs, enabling users to feel and touch their world again, and perhaps give robots a new sense of their surroundings. For electronic skin to work, it must be soft, flexible, and stretchable, much like our own. That rules out conventional computer electronics made from rigid glass and ceramic chips.

But such skin is around the corner thanks to progress in organic electronics. Nearly all organic solids are insulators: They don't readily conduct electricity. But in the 1970s and 1980s, researchers discovered how to

tweak the structures of some organic compounds to make them metal-like conductors or semiconductors, with the ability to switch a current on and off—a property critical to transistors and other devices. That advance opened the door to creating electronics on soft, flexible substrates. By the 2000s, researchers had honed their skills to make arrays of devices and pattern them cheaply. Compared with top-shelf electronics in computers and cell phones, flexible electronics remained big and slow. But they could now go places that rigid silicon could not.

In the past few years, numerous groups have unveiled flexible and stretchable arrays of touch and temperature sensors. For example, 2 years ago Bao and her colleagues at Stanford made an array of flexible organic pres-

web, as well as monitoring time, temperature, and fitness information such as how many calories a jogger wearing the device is burning up. Apple isn't alone. MC10 and fitness giant Reebok have developed prototypes of wearable sensors to monitor concussion risk in athletes playing contact sports like football or hockey. If the device senses strong enough head impacts—as determined by measurements of rotational acceleration, multidirectional acceleration, and the location and duration of the blow—it lights up a panel of light-emitting diodes (LEDs) that alerts the coach to take the player out of the game.

Other researchers are shrinking devices to pack more into a patch. One technology at this frontier is touch sensors. Most touch sensors work by spotting how pres-



Feel that? Flexible electronic sensors could give robots and prosthetic limbs more realistic ways of detecting touch, temperature, and strain.

sure sensors so sensitive that it could detect the weight of a butterfly sitting on top. More recently, at the MRS meeting, Bao reported how she and her colleagues had used a miniature array, roughly 144 square millimeters in area, to detect heartbeat and blood pressure from a simple watch-style wristband. Bulky wristwatch heart rate monitors exist, but the Stanford team's devices are paper-thin. "Human skin is a great inspiration," says Bao, whose group has also produced flexible chemical sensors and devices in which metal nanoparticles can move to fill in cracks so that damaged devices can heal themselves.

According to the online rumor mill that follows everything that the electronics giant Apple has in the works, the company is testing the use of flexible electronics in a sleek iWatch that will have a screen for surfing the

web, as well as monitoring time, temperature, and fitness information such as how many calories a jogger wearing the device is burning up. Apple isn't alone. MC10 and fitness giant Reebok have developed prototypes of wearable sensors to monitor concussion risk in athletes playing contact sports like football or hockey. If the device senses strong enough head impacts—as determined by measurements of rotational acceleration, multidirectional acceleration, and the location and duration of the blow—it lights up a panel of light-emitting diodes (LEDs) that alerts the coach to take the player out of the game.

Other researchers are shrinking devices to pack more into a patch. One technology at this frontier is touch sensors. Most touch sensors work by spotting how pres-

sure changes the electrical resistance of current flowing through a device array. Chemist Zhong Lin Wang of the Georgia Institute of Technology in Atlanta and his colleagues have come up with an alternative based on piezotronics, in which increasing the strain on a material changes its polarization, or the distribution of positive and negative charges, which can be read out as a signal. Unlike the conventional transistor approach, Wang notes, piezotronics enable researchers to fashion tiny devices, making it possible to create arrays with ultrahigh resolution. In the 24 May issue of *Science* (p. 952), the group reported packing piezotronic transistors at the density of 8464 devices per 1 centimeter square—thousands of times denser than tactile sensors in human skin. Such arrays, Wang says, could eventu-

eppendorf
& Science
PRIZE FOR
NEURO
BIOLOGY



2012 Winner
Dr. Marlene R. Cohen
Assistant Professor
University of Pittsburgh

Call for Entries

Application Deadline
June 15, 2013

Eppendorf & Science Prize for Neurobiology

The annual Eppendorf & Science Prize for Neurobiology, an international award, honors young scientists for their outstanding contributions to neurobiological research. The winner and finalists are selected by a committee of independent scientists, chaired by Science's Senior Editor, Dr. Peter Stern. To be eligible, you must be 35 years of age or younger.

You could be next to win this prize and to receive

- > Prize money of US\$25,000
- > Publication of your work in Science
- > Full support to attend the Prize Ceremony held in conjunction with the Annual Meeting of the Society for Neuroscience in the USA
- > An invitation to visit Eppendorf in Hamburg, Germany

It's easy to apply!

Learn more at: www.eppendorf.com/prize

eppendorf





Big and small. Bioelectronic advances include using tiny light emitters to study brain development (*left*) and engineering a functional ear (*above*).

ally be useful in providing high-resolution touch sensing to prosthetic limbs, or giving robots a tactile sense sharp enough to identify what they're touching, or making signature readers capable of sensing not only the swoops of a handwritten signature but characteristic changes in pressure as well.

Flexible sensors are going way past skin deep. Rogers's team reported last year in the *Proceedings of the National Academy of Sciences* that ultraflexible circuitry could cling to the surface of beating hearts of pigs and rabbits and, at each of more than a dozen points in the array, continuously register the electric signals that fire muscle cells in the beating heart. This allowed them to image waves of muscle fiber contraction as blood is pumped throughout different chambers. The fine detail also makes it possible to map patches of heart tissue that misfire during arrhythmia, a condition that affects up to 5% of people in the United States.

Rogers and his colleagues also integrated temperature sensors and tiny heating pads into their array. By turning on the pads—emitting heat instead of measuring it—they ablated tiny tissue patches in their test animals, opening the door to using similar arrays to cure arrhythmia.

Going deep

Perhaps the boldest direction in bioelectronics is the emerging effort of marrying tissue and electronics at the cellular level. At Harvard University, chemist Charles Lieber and

his colleagues have spent much of the past 2 decades pioneering efforts to grow ultra-thin nanowires from the atomic scale up and to design them to work as transistors and other electronic devices. Nanoscale devices are the right size to monitor and influence biology inside cells. "It's really the natural length scale for electrical interface," Lieber says. Ion channels in neurons are less than 10 nanometers in width, synaptic connections between nerves are less than 100 nanometers across, and neurons themselves are on the order of a micrometer. Devices at those scales could be revolutionary.

Using nanowires, Lieber's team has made nanoscale computer memories, LEDs, and photovoltaics. In a series of recent papers, Lieber and his colleagues used their devices to track nerve firing. And they've placed multiple transistor-based recorders on nanowire probes that can be inserted inside neurons, making it possible for the first time to track neural signals as they traverse the interior of a cell. Patch clamp probes have made it possible to monitor the firing of individual cells since the late 1970s, but that approach can't track action potentials inside a cell. The new nanowire approach "is really the first fundamentally new recording method since the patch clamp," Lieber says.

Another new device in the nano tool chest is one that uses pulses of light to control gene expression in mice. Optogenetic tools of late have become a valuable way for biologists to initiate the expression of tar-

get genes in lab animals and track the effect. To use them, however, researchers typically must tether animals to complex electronic gear that distorts their natural behavior. In the 12 April issue of *Science*, Rogers and his colleagues described patterning nanoscale LEDs on the end of a flexible nanoscale filament (p. 211). These nano LEDs were then injected deep within the brain tissue of mice engineered to turn on particular genes in response to light. The nanoribbons were designed to pick up nearby radio waves and convert them to electricity. By placing a radio source next to the heads of the mice, the researchers turned on the LEDs, which, in turn, triggered gene expression. The new technique, Rogers says, foreshadows applications in which self-powered bioelectronics embedded in a variety of organs will regulate their function.

Some of the latest work by Lieber's group makes that day seem close at hand. As described in the November 2012 issue of *Nature Materials*, his team created a 3D mesh of silicon nanowires with built-in transistors. They used the mesh as scaffold for growing tissue, either heart muscle cells or neurons. The transistor array could monitor the electrical activity of the growing tissues and track their response to drugs such as noradrenaline, which stimulates cardiac cell contraction.

Such devices are only the beginning of a brave new world of bioelectronics. Better hope that it is more benign than *Star Trek's* soulless collective, because make no mistake: With so much to gain, we *will* be assimilated.

—ROBERT F. SERVICE



SCIENTIFIC **2013**
SESSIONS

Exhibits: November 17–19

Sessions: November 16–20

Resuscitation Science Symposium: November 16–17

Cardiovascular Nursing Symposium: November 19–20

Dallas, Texas

Dallas|2013

The American Heart Association's Scientific Sessions is the leading cardiovascular conference for basic, translational, clinical and population science. Lead the way to discovery in the fight against heart disease and stroke. Register today!

Key Dates

Nov. 17–19 | Exhibits

Nov. 16–20 | Scientific Sessions

Nov. 16–17 | Resuscitation Science Symposium

Nov. 19–20 | Cardiovascular Nursing Symposium

Registration and Housing Opens

June 12 | FAHA and VIP

June 19 | Members and Media

June 26 | Nonmembers

AHA/ASA Professional Membership

Members **SAVE \$400** on Sessions 2013



Leading Discovery.
Global Impact.

scientificsessions.org

Tackling a
grand puzzle

1170

700 new
neurons a day

1180



LETTERS | BOOKS | POLICY FORUM | EDUCATION FORUM | PERSPECTIVES

LETTERS

edited by Jennifer Sills

Rhino Poaching: Supply and Demand Uncertain

IN THEIR POLICY FORUM "LEGAL TRADE OF AFRICA'S RHINO HORNS" (1 MARCH, P. 1038), D. Biggs *et al.* point out that the trade ban on rhino horn has not been successful in reducing rhino poaching, which reached a record high of 668 in 2012. They argue that trade bans support illegal organizations, whereas a regulated legal market could reduce poaching effort and provide much-needed income for conservation. In making their case, Biggs *et al.* overlook a few important points.

Biggs *et al.* write that legal trade can only work if, among other things, "the demand does not escalate to dangerous levels as the stigma associated with the illegality of the product is removed." It is unclear whether any stigma is associated with rhino horn usage in eastern countries, but the phenomenally high price for the horn, along with rising real income and population growth in the major consumer markets, is likely to indicate rising demand.

Biggs *et al.* point out that the technology to profile rhino DNA is now affordable. In the past, illegal buyers have been unable to determine easily whether they are using real or fake products. With affordable DNA profiling, however, the supply of fake rhino horns [which is, by some accounts, extensive (1)] will diminish, thus further increasing demand pressure for the genuine horn.

On the supply side, there is currently insufficient evidence as to whether farmed rhinos would breed at the same rate as in the wild. An additional concern is that South Africa's white rhino population is based on a very small gene pool. After nearly being hunted to extinction in the 19th century, with only a small number of white rhinos surviving in one South African park (Hluhluwe-Umfolozi), the population grew to 840 in 1960 (2). These white rhinos were used to populate national and private game reserves. Intensive breeding programs would thus have to consider this potential genetic weakness.

According to the Africa Guide (3), the gestation period of a rhino is 15 to 16 months and the calf stays with the cow for 2 to 3 years in the case of the white rhino and 2.5 to 4 years for the black rhino. It thus would take up to 5 years for an adult rhino population to produce a generation sufficiently mature for regular harvesting of horn.

Biggs *et al.* acknowledge that there are well-resourced criminal syndicates currently engaged in illegal horn trade. However, they fail to take into account the reaction of illegal



traders to the establishment of legal suppliers. The extent to which illegal organizations will retaliate is contingent on the effectiveness of auction releases in reducing horn price. If prices remain high, illegal suppliers will remain in business and vigorous turf wars are likely to emerge (4). It is unlikely that such criminal syndicates will respond passively; rather, they would seek to interrupt the regulated supply chain through acts of sabotage and even stronger poaching effort.

The characterization of the supply chain as a single body—the Central Selling Organization (CSO)—is oversimplified. In practice, the supply side consists of a disparate mix of public and private "providers" with different objectives and motives. Regulation and management are unlikely to be simple, as a CSO represents only one stage of the supply chain. More research is needed in terms of what such a CSO would do. For example, would it be able to provide adequate enforcement and incentives to prevent private suppliers from selling outside the legal market?

ALAN COLLINS,^{1,2} GAVIN FRASER,¹
JEN SNOWBALL^{1*}

¹Department of Economics and Economic History, Rhodes University, Grahamstown, 6140, South Africa. ²Economics and Finance, Portsmouth Business School, University of Portsmouth, Portsmouth PO1 3DE, UK.

*Corresponding author. E-mail: j.snowball@ru.ac.za

References

1. T. Milliken, J. Shaw, "The South Africa–Viet Nam rhino horn trade nexus: A deadly combination of institutional lapses, corrupt wildlife industry professionals and Asian crime syndicates" (TRAFFIC, Johannesburg, South Africa, 2012).
2. M. 't Sas-Rolfes, "Saving African rhinos: A market success story" (PERC Case Studies, Bozeman, MT, 2010); <http://perc.org/sites/default/files/Saving%20African%20Rhinos%20final.pdf>.
3. The Africa Guide, Rhinoceros (www.africaguide.com/wildlife/rhino.htm).
4. A. C. Carpenter, *Conflict Resolution Quart.* **27**, 401 (2010).

Rhino Poaching:
Unique Challenges

IN THEIR POLICY FORUM "LEGAL TRADE OF Africa's rhino horns" (1 March, p. 1038), D. Biggs *et al.* advocate legalizing trade in rhino horn through harvesting horns of 5000 white rhinos in South Africa as the panacea to the current rhino poaching crisis. Their arguments were based on the law of supply and demand and supported by the example of crocodile farming.

The law of supply and demand only applies to commodities for which supply is independent of demand. It does not apply specifically to white rhino horn because the mar-

Letters to the Editor

Letters (~300 words) discuss material published in *Science* in the past 3 months or matters of general interest. Letters are not acknowledged upon receipt. Whether published in full or in part, Letters are subject to editing for clarity and space. Letters submitted, published, or posted elsewhere, in print or online, will be disqualified. To submit a Letter, go to www.submit2science.org.

ket does not differentiate between horns of the five extant rhinoceros species, and therefore the supply exceeds the quantity of horns of the white rhino alone. Because the rhino horn has no medicinal properties (1, 2), drug producers can dilute it at will, making the price formation normally dictated by the law of supply and demand unpredictable. Furthermore, legal access to rhino horn risks reawakening demand in older markets, such as Taiwan, Japan, Singapore, and Yemen, where demand for rhino horn was prevalent in the 1970s and 1980s and has since decreased (3). If demand grows again in these markets, indiscriminate poaching may increase accordingly, putting look-alike black, Indian, Javan, northern white, and Sumatran rhinoceros species at even higher risk. The costs of securing horns for the proposed Central Selling Organization for legal trade might make poaching even more lucrative.

The comparison with the crocodile skin market is unjustified. Farmed crocodiles occur in millions, whereas the five rhino species number about 30,000 animals and reproduce much more slowly. Crocodile-skin trade involves processing and was established in well-regulated industries; rhino horn is used unprocessed in China and Vietnam (3, 4), known for weak control of their drugs industries. Unlike rhino horn, crocodile skin has substitutes, is not consumed, and is not believed to have medicinal or religious applications.

The Convention on International Trade in Endangered Species of Wild Fauna and Flora (CITES) upheld the ban on trade in rhino horn by enacting tighter controls in March 2013 (5). We propose education, awareness, and diplomacy (5, 6) for squashing horn demands in China and Vietnam that continue to destabilize rhino conservation globally and undermine national security (7) in source countries.

HERBERT H. T. PRINS¹ AND BENSON OKITA-OUA^{1,2,*}

¹Resource Ecology Group, Wageningen University, Droevendaalsesteeg 3a, 6708 PB Wageningen, Netherlands.

²Kenya Wildlife Service, P.O. Box 40241-00100, Nairobi, Kenya.

*Author for correspondence. E-mail: bokita@kws.go.ke

References

1. R. Shamloul, *J. Sexual Med.* **7**, 39 (2009).
2. H. P. Laburn, D. Mitchell, *J. Basic Clin. Physiol. Pharmacol.* **8**, 1 (2011).
3. T. Milliken, J. Shaw, "The South Africa-Viet Nam rhino horn trade nexus: A deadly combination of institutional lapses, corrupt wildlife industry professionals and Asian crime syndicates" (TRAFFIC, Johannesburg, South Africa, 2012).
4. D. Graham-Rowe, *Nature* **480**, 5101 (2011).
5. CITES, "Rhinoceroses: Draft decisions of the Conferences of the Parties" (16th meeting of the Conference of the Parties, Bangkok, Thailand, 2013); www.cites.org/common/cop/16/com/E-CoP16-Com-II-24.pdf.
6. S. M. Ferreira, B. Okita-Ouma, *Pachyderm* **51**, 52 (2012).
7. J. Ayling, *J. Int. Wildlife Law Pol.* **16**, 57 (2013).

Rhino Poaching: Apply Conservation Psychology

THERE IS NO DOUBT THAT THE ILLEGAL TRADE in rhino horns is a lucrative industry and is contributing to their extinction in the wild ("Legal trade of Africa's rhino horns," D. Biggs *et al.*, Policy Forum, 1 March, p. 1038). Conservation psychology can play a role in preventing people from consuming rhino horn (1). Psychological principles of persuasion, attitude, and behavior change have been used effectively for many decades, but they have been largely ignored or underutilized within biodiversity conservation (2).

Investigation of consumer behavior must not be restricted to economic theory of market and individual demands, but rather should recognize human psychology in all its complexity. First, we must understand rhino horn consumption patterns in east and Southeast Asia, and possibly elsewhere, given that rhino horn is used for different purposes. Exploring the "dark side" of rhino horn consumption is necessary (consumption of illegal products may be considered "cool"). Global and country-specific public marketing campaigns can

raise awareness about the negative impacts of illegal (or perhaps one day, legal) trade in rhino horns and debunk the myth of their healing properties. The most effective communicators about rhino conservation may be children, naturalists, specialist tour guides, field assistants, trackers, religious leaders, or even ex-poachers or ex-hunters. Saving rhinos is the responsibility of everyone, and effective conservation is based on moral values as well as economic ones.

CARLA A. LITCHFIELD

School of Psychology, Social Work, and Social Policy, University of South Australia, Magill, Adelaide, SA 5172, Australia. E-mail: carla.litchfield@unisa.edu.au

References

1. S. D. Clayton, *The Oxford Handbook of Environmental and Conservation Psychology* (Oxford Univ. Press, Oxford, 2012).
2. S. K. Jacobson, *Communication Skills for Conservation Professionals* (Island Press, Washington, DC, ed. 2, 2009).

Response

COLLINS *ET AL.* AGREE WITH OUR OBSERVATION that the trade ban has failed and that a legal trade in Africa's rhino horn will be an important contributor to tackling the current poaching crisis. A skillfully regulated legal trade, in which horn is harvested renewably from live animals, will offer financial incentives for the conservation of rhinos and deliver benefits to local communities. Moreover, we concur with Collins *et al.* that the institutional and market arrangements for the management for a legal trade require in-depth discussion and evaluation. This deliberation is particularly important as the South African government has indicated that it is seriously exploring this contentious issue in the build-up to the next CITES Conference of Parties in 2016 (1, 2).

We acknowledged the uncertainties inherent in estimating demand under a trade ban and in the functioning of a legal trade. We discussed how risks can be minimized and explained that the trade must be monitored closely and managed adaptively, with possible restructuring required over time. Under a well-enforced legal trade, the demand for horn more broadly will be met in a sustainable way. In addition, more resources should be available for stronger enforcement against illegal trade in horn of all rhino species. As we wrote in our Policy Forum, technology exists to track horns from the source through the market chain to the buyer (3). The presence of fake horn, which appears to originate in Asia (4), is unlikely to have an impact on a well-regulated and enforced legal trade, nor on the illegal killing of rhinos in Africa.

Collins *et al.* raise the critical issue of the structure of a legal trade. A Central

CORRECTIONS AND CLARIFICATIONS

New Focus: "Hubs aim to reinvent DOE research culture" by A. Cho (24 May, p. 914). The caption for the photograph on page 918 incorrectly identifies the leaders of the five Department of Energy-funded hubs. They are, from left to right, Douglas Kothe of CASL, Nathan Lewis of JCAP, Henry Foley of EEB, George Crabtree of JCESR, and Alexander King of CMI. The HTML and PDF versions online have been corrected.

Reports: "A reconciled estimate of glacier contributions to sea level rise: 2003 to 2009" by A. S. Gardner (17 May, p. 857). In the last paragraph of the text, the first sentence should have included "(2.50 ± 0.54 mm year⁻¹)" after the phrase "the observed sea-level rise." The last sentence of the text should read as follows (total numbers have been changed): "To avoid double counting, we subtracted our estimates for peripheral glacier mass loss from this total to obtain a total ice-sheet mass budget of -290 ± 50 Gt year⁻¹ (11) and a total land ice (all glaciers + ice sheets) mass budget of -549 ± 57 Gt year⁻¹, amounting to a sea-level rise of 1.51 ± 0.16 mm of SLE year⁻¹ which is 61 ± 19% of the total global sea-level rise (11)." The HTML and PDF versions online have been corrected.

Editorial: "Improving education standards" by J. Coffey and B. Alberts (1 February, p. 489). The doi was incorrect. It is 10.1126/science.1235590. The HTML and PDF versions online have been corrected.

Selling Organization (CSO) is one option for institutionalizing a legal trade; the costs and benefits of alternative structures need to be evaluated. It is critical that the governments of the main demand countries, including Vietnam and China, support and actively police the legal trade. In particular, Vietnam has been criticized for its lack of enforcement of the current trade ban (5). The strong actions by China and Vietnam against the illegal drug trade (6) suggest that if these governments actively support a legal trade in horn, they may be capable of enforcing compliance. The inception of a legal trade would imply international acknowledgment and respect for the long history of use of rhino horn in their societies. This may be an important factor in gaining their active participation and cooperation in designing a workable market structure at the outset. Some of the potential risks can be informed by research and scientific input; others, such as managing possible turf wars with illegal horn traders, require input from security experts and the use of tools such as scenario analyses (7, 8).

Prins and Okita-Ouma question our application of the law of supply and demand.

Basic economics dictates that the price of a product continually changes and is determined by the interaction of supply and demand, in addition to factors such as regulation (9). Our comparison with the crocodile trade was to show how a legal trade can usurp an illegal trade by enabling a more profitable, safer, and easier way to supply the market (10). Prins and Okita-Ouma claim we should try to reduce demand and crush the illegal markets. Litchfield argues that it is possible to convince people to stop consuming horn. However, the current poaching crisis affirms the persistent failure of these strategies (11). Evidence and logical argument suggest that Africa's rhinos are more likely to be conserved through instituting a skillfully regulated and enforced legal trade.

DUAN BIGGS,^{1*} FRANCK COURCHAMP,²
ROWAN MARTIN,³ HUGH P. POSSINGHAM¹

¹Australian Research Council Centre of Excellence for Environmental Decisions, Centre for Biodiversity and Conservation Science, University of Queensland, Brisbane, QLD 4072, Australia. ²Ecologie, Systematique et Evolution, Universite Paris-Sud, UMR CNRS 8079, Orsay, France. ³Independent Consultant, Harare, 00263, Zimbabwe.

*Author for correspondence. E-mail: ancientantwren@gmail.com

References

1. J. Rademeyer, "Environmental Affairs Minister Edna Molewa throws her weight behind controversial calls for the legalisation of trade in rhino horn," *Mail & Guardian* (22 March 2013).
2. S. Blaine, "CITES meeting is SA's next step in setting up rhino horn trade," *Business Day* (29 March 2013).
3. R. Martin, *A Legal Trade In Rhino Horn: Hobson's Choice* (Rhino Survival Trust, Johannesburg, South Africa, 2012).
4. K. Nowell, "Species trade and conservation. Rhinoceroses: Assessment of rhino horn as a traditional medicine" (CITES and TRAFFIC, 2012); www.cites.org/eng/com/sc/62/E62-47-02-A.pdf.
5. CITES, "Interpretation and implementation of the Convention: Species trade and conservation: Rhinoceroses. Sixteenth meeting of the Conference of the Parties, Bangkok (Thailand), 3–14 March 2013" (CITES, 2013).
6. W. Schabas, "The death penalty and drug offences" (NUI Galway and the International Centre on Human Rights and Drug Policy, 2010); www.humanrightsanddrugs.org/wp-content/uploads/2010/10/Prof-Schabas-Death-Penalty-for-Drug-Offences-Oct-2010-EN.pdf.
7. N. Bunnefeld, E. Hoshino, E. J. Milner-Gulland, *Trends Ecol. Evol.* **26**, 441 (2011).
8. G. D. Peterson, G. S. Cumming, S. R. Carpenter, *Conserv. Biol.* **17**, 358 (2003).
9. G. N. Mankwi, *Principles of Economics* (South-Western Cengage Learning, Mason, OH, 2008).
10. J. Hutton, G. Webb, in *Crocodiles: Proceedings of the 16th Working Meeting of the Crocodile Specialist Group, IUCN—The World Conservation Union, Gland, Switzerland and Cambridge UK* (IUCN, Gland, Switzerland, 2002), pp. 1–10.
11. K. Conrad, *Trop. Conserv. Sci.* **5**, 245 (2012).

ScienceClassic

Digital Archives
of Science
1880–1996

Fully integrated with
Science Online
(1997–Current Issue)

Recommend Science Classic
to your institution's library.
ScienceOnline.org/recommend



ScienceClassic.org

LAMBDA VF-5 Tunable filter changer

NEW!



Introducing the world's first filter changer to use tunable thin-film optical filters. The Sutter **LAMBDA VF-5** allows you to quickly access any center bandpass from 330 to 800nm in nanometer increments. Building on the VersaChrome® filters from Semrock®, the **LAMBDA VF-5** maintains transmission over the tuning range of each filter.

Easy Wavelength Selection

Wavelength range as wide as 330–800nm
Keypad or computer interface (USB or serial)

Flexible

Suitable for excitation or emission
Easily switch between fluorophore combinations
Optional liquid light guide offers absolute vibration isolation
Images pass through filters

Thin filter advantage

High transmission
Steep spectral edges
High out-of-band blocking
Polarization independence
(s and p nearly identical)

SUTTER INSTRUMENT

PHONE: 415.883.0128 | FAX: 415.883.0572
EMAIL: INFO@SUTTER.COM | WWW.SUTTER.COM

EVOLUTION

What Led to Metazoa's Big Bang?

Christopher J. Lowe

The Ediacaran and Cambrian periods witnessed a phase of morphological innovation in animal evolution unrivaled in metazoan history, yet the proximate causes of this body plan revolution remain decidedly murky. The grand puzzle of the Cambrian explosion surely must rank as one of the most important outstanding mysteries in evolutionary biology. Evidence of early representatives of all the major animal phyla first appear abruptly in the Cambrian (starting 542 million years ago). This spectacular morphological diversity contrasts strongly with Precambrian deposits, which have yielded a sparse fossil record with small, morphologically ambiguous trace fossils or the enigmatic but elegant creatures of the Ediacaran fauna. Following the Cambrian, despite a rich fossil record that documents impressive morphological diversification among animals, no new body plans have been revealed, leaving the Cambrian as the apparent crucible of metazoan body plan innovation. Although it is only in the various Cambrian fossil assemblages that this exuberance of animal life first makes an appearance, molecular clock calculations estimate divergence times of the major metazoan lineages well before the Cambrian. That suggests a prolonged period of cryptic evolution in the Ediacaran not well represented in fossils, adding further intrigue to the puzzle.

The range of hypotheses proposed to explain the Cambrian explosion is as diverse and broad as the fossils they seek to explain. Researchers from a wide range of sciences (including geology, ecology, developmental biology, and genomics) have all made substantial contributions toward unraveling the causes of this key puzzle of animal evolution. Yet in most cases, their findings have been consid-

ered independent of one another. In *The Cambrian Explosion*, paleontologists Douglas Erwin (National Museum of Natural History) and James Valentine (University of California, Berkeley) make a heroic attempt to synthesize these disparate fields. In the process, they have distilled a unique contribution that should be a required addition to any biologist's bookshelf.

The book's first two sections set the stage. The authors introduce the geological and environmental contexts of the Cambrian and Ediacaran and then the animal phyla and fossils. They strip the characteristics of each phylum down to the basics, not burdening readers with too much detail but providing enough for them to appreciate how recent modifications to animal phylogeny have strongly revised our understanding of early animal diversification. This section is well illustrated with clear and simple diagrams. I found the fossil chapters particularly compelling, as they brought together key Ediacaran and Cambrian fossils, discussed within the framework of contem-

porary hypotheses of animal relationships. Quade Paul's vivid color reconstructions, displayed next to photos of the fossils, bring to life the stunning morphological diversity and ecological context that are often lost in the rather clinical descriptions of these mysterious fossils from the primary literature.

The authors also review molecular biology's substantial contributions to solving the grand puzzle of the Cambrian explosion, which have at times been at odds with interpretations derived from fossil data. Comparative developmental genetic studies and genome sequencing projects from diverse metazoan phyla have revealed some of the genetic innovations that were likely responsible, in part, for the increase in animal complexity. These new data may help us reconstruct ancestral morphological features of the mysterious stem lineages of the Ediacaran, by reconstructing ancestral gene complements and by inferring gene regulatory networks that have key roles in setting up the body plans of extant animals. However, our understanding of how to relate genomic and developmental regulatory complexity to organizational and morphological complexity remains in its infancy.

In the book's last section, Erwin and Valentine begin to integrate and synthesize the introductory material. They hold that many previous attempts at developing hypotheses to explain the Cambrian explosion focused on a single cause, which was often inconsistent with data available from other fields.

They argue convincingly that complete understandings of animal origins and the explosion's "great evolutionary puzzle" can only be achieved by considering the relative importance of three main aspects: substantial change in the environment, which differed greatly from the present day; the sequential acquisition of genetic and developmental innovations that gradually increased body plan complexity during the Ediacaran and Cambrian; and the establishment of ecological relationships among animals that ensured that new metazoans with novel body plans succeeded in their new environments. Ecological opportunities for novel morphological innovations were not just provided by physical changes to the environment but also driven by changes produced by the activities of animals themselves.

The Cambrian Explosion The Construction of Animal Biodiversity

by Douglas H. Erwin and
James W. Valentine
Roberts and Company,
Greenwood Village, CO, 2013
416 pp., illus. \$60.
ISBN 9781936221035.



Difficult to interpret. *Herpetogaster collinsi*, a tentaculate soft-bodied fossil from the Burgess Shale, is a possible stem Ambulacraria.

The reviewer is at the Hopkins Marine Station, Stanford University, 120 Oceanview Boulevard, Pacific Grove, CA 93950, USA. E-mail: clowe@stanford.edu

CREDIT: QUADE PAUL/COURTESY ROBERTS AND COMPANY

Readers of *The Cambrian Explosion* will likely have either little background or some expertise in one of the disciplines covered. Falling into the latter camp, I have largely considered causes of the Cambrian explosion from the perspective of molecular genetics and genomics. Erwin and Valentine illuminate clear links between seemingly disparate disciplines, and they make a compelling case that substantial progress toward understanding the origins of animal diversity will not be achieved through adding isolated gains in individual fields. It is futile to hope to explain such a major evolutionary event without embracing an interdisciplinary approach.

10.1126/science.1237431

COMPUTERS

Lovely Spam! Wonderful Spam!

Jennifer Golbeck

In the 1970s and 1980s, spam was that annoying co-worker who comes into your office when you're up against a deadline to give you his take on the last episode of *Battlestar Galactica* when you don't watch *Battlestar Galactica*. Today, spam is a horde of zombies, beating against the walls of the old farmhouse you're holed up in, bent on eating your brains.

The world has changed a lot over the past few decades. Finn Brunton's *Spam: A Shadow History of the Internet* traces spam's history—from its early days, as annoying messages taking up valuable bandwidth, to the present, when it accounts for the overwhelming majority of all e-mail and CAPTCHAs (*I*) routinely demand that we prove our humanity.

Brunton (a digital media researcher who is moving to New York University) breaks the story of spam into three eras: the largely pre-Web days from 1971 to 1994, Web and e-mail spam from 1995 to 2003, and botnets and powerful spam filters since 2003. His descriptions of the three eras are deeply engaging, and together they provide a fascinating account of the history of the Internet, as the book's subtitle implies.

The reviewer is at the Human-Computer Interaction Lab, University of Maryland, College Park, MD 20742, USA. E-mail: golbeck@cs.umd.edu



Right from the start, and using great storytelling, Brunton immerses readers in the early days of the Internet. A community of computer scientists and techies were learning to interact in a new medium. Through a series of vignettes, the author paints a picture of the Internet's infancy: the technological and bandwidth limitations (now all but forgotten), the communities that sprang into existence, and key moments and figures in the history of spam.

His play-by-play account of early abuses offers an entertaining tour through the past. Brunton discusses the misbehaving scammers on USENET, including

the person whose 1988 message asked everyone on the Internet to donate one dollar to "JJ's College Fund" and the dramatic response of the (then) small community to punish that abuser. He also describes early attempts at technical solutions and their resulting failures. For

example, the Automated Retroactive Minimal Moderation program (ARMM) trapped bad messages on USENET, but unfortunately it then sent notifications that were themselves identified as spam, touching off a chain reaction of bad posts.

This early era ended as commercial use of the Internet exploded, accompanied by unabashed use of spam for marketing. In describing the second era, Brunton relays how community-oriented solutions failed to stop the growing spam problem and how their failure fueled the development of increasingly sophisticated technical solutions and government policies.

Eventually, spam matured into a largely criminal enterprise. Brunton documents the world of botnets, link spam, and social spam. This shift in spammers' strategy cor-

responds to a change in victims and how they are targeted. Only the most naïve users are expected to respond to the pitches, while other victims are exploited to build legions of botnets to distribute spam. The fundamentally decentralized nature of the botnets means the spamming cannot be shut down at the source.

The book began its life as a dissertation, and in some places that origin shows. The text occasionally strays from its otherwise excellent flow of narrative, delving into some unnecessary detail. An early five-page discussion of *charivari* (a sort of harassing

mob) versus vigilantism is one such example; the longish, nontechnical overview of Google's PageRank algorithm is another. Such rough spots occur a bit more frequently later in the book. Nonetheless, they are only noticeable because the rest of the text flows so smoothly, and they do not detract from the book's value.

One of Brunton's core messages is that spam is both a social and technical problem. The recent explosive growth of social media leads many to think that social interaction and communities are a relatively new phenomenon online. The book shows, however, that communities were around on (and, indeed, defined) the Internet from its earliest days. Spam, by its nature, is a reflection of the community's standards, as they have progressed with the technology.

Spam will fascinate readers who aren't experts in the subject matter by shedding new light on the culture and function of their Internet experience. But it has plenty to offer computer scientists and online-community researchers as well. As someone who was born after the Internet, Brunton's account has transformed what was in my mind a collection of dates and rather bland history into a richer, much more vivid image of community and interactions. More important, the book made me realize just how in flux these systems are. As we live with the fact of spam and antispam technology, it's easy to lose track of how the landscape is shifting around us. This masterful telling of the history illustrates just how much has changed and how we fit into the larger story.

References and Notes

1. The acronym, based on "capture," stands for "Completely Automated Public Turing test to tell Computers and Humans Apart."

10.1126/science.1239398

Uncapping Conflict of Interest?

Susan F. Wood* and Jillian K. Mador

The U.S. Food and Drug Administration (FDA) calls on advisory committees (ACs) to provide external expert advice and recommendations to “enhance FDA’s ability to protect and promote the public health and maintain the public trust” (1). The FDA Safety and Innovation Act (FDASIA) (2) was signed into law in 2012 primarily to reauthorize user-fee programs for drugs, devices, and biosimilars. We discuss concerns about how FDASIA also changes AC financial conflict of interest (COI) requirements.

Waivers may be granted so that experts with financial COIs can serve on FDA ACs. Generally, waivers are granted if one of the following is true: (i) the COI is unlikely to “affect the integrity of the services,” (ii) the “need for the individual’s services outweighs the potential for a COI,” or (iii) they will contribute “essential expertise.” Experts may not participate if financial COI is over \$50,000. COI disclosures and waivers must be publicly available on the FDA Web site (1).

In response to concerns of conflicted AC members influencing the objectivity and scientific scrutiny of the ACs (3, 4), the 2007 FDA Amendments Act (FDAAA) established “caps” on the number of COI waivers FDA can grant. The number decreased by 5% over 5 years to the 2012 limit of 11.5% of AC members each year (5). FDAAA also directed the FDA to recruit nonconflicted experts from academic institutions, professional societies, and patient and consumer groups (6).

A waiver-free AC does not mean it is necessarily conflict-free. The FDA only considers a member conflicted and requiring a waiver if he or she has a financial relationship within the past 12 months. Many institutions and journals require COI disclosure back 36 months (7, 8); the European Medicines Agency assigns experts a “risk level” based on declared COIs within 5 years (9).

Amending COI Requirements

New provisions in FDASIA relax limitations on COI waivers and establish new priorities and mechanisms for recruiting AC members.

Waiver limitations. COI waiver caps were removed. Members must still disclose COIs and be granted a waiver, but an unlimited number of waivers may be granted.

Recruitment. Although AC recruitment will continue to target patient groups, disease advocacy organizations, professional societies, medical societies, academic organizations, and governmental organizations, the new legislation now calls for member referrals every 180 days to also include “product developers” but does not identify “consumer” or “patient safety” organizations.

Expertise. AC member selection criteria changed from including both expertise and financial disclosures to simply requiring “the most current expert advice.” COIs are not prioritized when evaluating potential AC members.

Annual report. In addition to reporting numbers of AC vacancies, nominees, and disclosures, the Annual Report on the FDA Advisory Committee Vacancies and Public Disclosures must now include the number of nominees who did not participate because of a disqualifying COI.

The 2012 scaling back of limits on FDA advisory panel financial conflicts had no clear basis and may have unanticipated impacts.

Reasons for Removing COI Caps

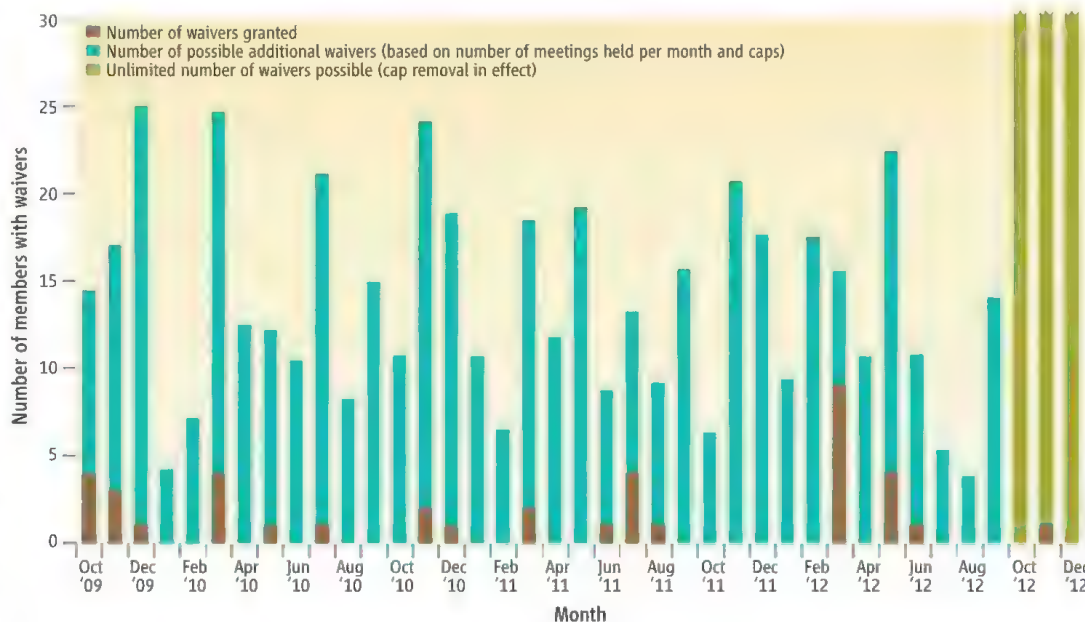
COIs may not affect voting patterns. A 2006 study did not show a statistically significant relation between conflict rates and voting patterns (10). An FDA-contracted study also found no statistically significant relation between disclosed COIs and voting outcomes (11).

Experts with COIs may have higher expertise. A 2007 FDA-contracted study created a composite expertise index combining number of publications, years of experience, and scientific productivity. AC members with COI waivers had a somewhat higher expertise composite (0.40) compared with nonconflicted members (0.31) (12).

Increased effort in finding nonconflicted members. The 2007 FDA study concluded “the ability to create a conflict-free panel is speculative,” arguing that it is more difficult to find highly qualified nonconflicted members and doing so would have negative impacts on FDA. It might worsen the high number of vacancies in ACs and could require additional recruiting efforts from the already burdened FDA, which could affect productivity (12). This argument has been made by pharmaceutical representatives critical of COI caps (13).

Support for Keeping COI Limits in Place

Scientific integrity. COI limitations were put



Conflict of interest waivers allowed and granted by month. Data from U.S. FDA. See SM for details.

Health Policy, George Washington University, Washington, DC 20006, USA. *Corresponding author: sfwood@gwu.edu

in place by FDAAA in 2007 in part because of longstanding concern for the scientific validity and objectivity of the ACs; the FDA Science Board concluded “science at the FDA is in a precarious position” (3). A 2009 Institute of Medicine report determined that COIs “threaten the integrity of scientific investigations, the objectivity of medical education, and the quality of patient care, ... [and] jeopardize public trust in medicine” (14). Other studies have identified that AC members “describe pressure to conform and to recommend approval” (4), which compromises the integrity of the recommendations.

COIs may affect AC decisions. Although detecting a direct impact of COIs on voting patterns is difficult (10, 11), specific cases have raised concerns. An AC voted 15 to 11 that the risk of blood clots from Yaz and Yasmin contraceptives was outweighed by benefits. Four members of the AC had undisclosed COIs, enough to change the voting outcome (15). In separate votes on painkillers Celebrex, Bextra, and Vioxx, 93% of votes cast by the 10 conflicted AC members favored the drugs’ approval, compared with 56% of votes by the 22 nonconflicted members (16, 17).

Vacancies are decreasing, and FDA productivity is increasing. Public FDA data show that vacancies in AC positions have decreased or remained stable, despite the caps [see fig. S1, supplementary materials (SM)]. The FDA’s goal is to have 10% or less of AC positions vacant. December 2012 vacancy rates were 22% versus 33% in October 2009.

FDA approval of new drugs is not declining, contrary to claims that COI caps would slow FDA functionality. As one measure of productivity, in fiscal year 2011, the FDA Center for Drug Evaluation and Research (CDER), with a workload of 39 applications, approved 30 new molecular entities, similar to approval rates since 2002 (18). Within the FDA, CDER has the highest number of AC members and most meetings each year (19).

Caps have never been reached. Since their establishment, financial COI waiver caps have never been reached, which implies that conflicted experts identified through the waiver process have not been denied membership solely because of waiver limitations. According to FDA data from October 2009 to December 2012, the average percentage of AC members granted waivers each month was only 0.78%, of the allowable 11.5 to 13.0% (see SM). From October 2009 until September 2012 (the date the caps were removed), an additional 455 waivers could have been granted, which would have allowed FDA to fill vacant positions with conflicted members while remaining well within FDAAA

waiver limits (10) (see the chart). This is not to argue that the FDA should use more conflicted members to fill vacancies or that the caps serve no purpose. Rather, there is no reason to proactively remove the caps if they are not being reached. Caps can provide protection from overly conflicted ACs, while allowing waived, conflicted experts to serve.

Nonconflicted experts are out there. A 2009 study of academic life science researchers found that 47.2% declared no relationship with industry. The study concluded that “it is difficult, but not impossible, to find academic scientists without industry relationships to serve in advisory roles for organizations such as [FDA] ...” (20). With roughly 139,000 faculty at U.S. medical, pharmacy, and public health schools (21–23), there is capacity to fill AC positions with nonconflicted experts.

Support for a nonconflicted FDA. A 2012 U.S. public poll found that 92% of respondents expressed some concern, and 66% expressed high concern about “recommendations made by expert committees that included doctors who had current financial relationships with medical device makers” (24). In 2010, FDA Commissioner Hamburg wrote “it is clearly better for the agency in fulfilling its public health mission when advisors have no [COI]” (25). In 2011, she supported weakening COI regulation, but reaffirmed her original position in 2012: “... we are not bumping up against our cap in terms of waivers, and we have actually been making an aggressive effort to fill empty slots on our advisory committees and have made progress... We don’t at the moment see major areas where a legislative fix is required” (13).

Appearance of a Threat to Integrity

Evidence we have identified does not support the need to remove the COI limitations. Removal of the caps weakens the system for managing COIs and creates potential for an unlimited number of conflicted AC members. At a minimum, this could create the appearance of a threat to scientific integrity.

Removing the 2007 COI restrictions did not occur by accident but in response to advocacy by interested parties. Long-term impacts of this legislation could include more conflicted members voting on FDA recommendations, with unforeseen consequences on the safety and efficacy of FDA-regulated products and, thus, on the health of consumers. Reauthorization of FDASIA is scheduled for 2017, with discussions beginning much sooner. Increased engagement of the scientific and medical communities is crucial to ensure a strong and effective FDA advisory system.

References and Notes

1. FDA, *Guidance for the Public, FDA Advisory Committee Members, and FDA Staff: Public Availability of Advisory Committee Members’ Financial Interest Information and Waivers, Final Guidance* (FDA, Silver Spring, MD, 2012).
2. Food and Drug Administration Safety and Innovation Act of 2012, PL 112-144, (2012).
3. Science Board to the FDA, *FDA Science and Mission at Risk* (FDA, Silver Spring, MD, 2007).
4. D. M. Zuckerman, *FDA Advisory Committees: Does Approval Mean Safety?* (National Research Center for Women and Families, Washington, DC, 2006).
5. FDA, Percent of FDA advisory committee members participating in meetings in the month who were granted waivers. Data available online through the FDA, details available in the SM.
6. S. F. Wood, K. L. Perosino, *Public Health Rep.* **43**, 409 (2008).
7. P. B. Fontanarosa *et al.*, *JAMA* **304**, 1496 (2010).
8. Science, Science/AAAS Authorship Form and Statement of Conflicts of Interest (AAAS, Washington, DC, 20013).
9. European Medicines Agency, “European Expert List”; www.ema.europa.eu/ema/index.jsp?curl=pages/about_us/landing/experts.jsp&mid=WCObd1ac058043244a.
10. P. Lurie *et al.*, *JAMA* **295**, 1921 (2006).
11. N. Ackerley *et al.*, *Financial Conflict-of-Interest Disclosure and Voting Patterns at FDA Advisory Committee Meetings* (Eastern Research Group, Arlington, VA, 2009).
12. N. Ackerley *et al.*, *Measuring Conflict of Interest and Expertise on FDA Advisory Committees* (Eastern Research Group, Lexington, MA, 2007); www.fda.gov/oc/advisory/ergcolreport.pdf.
13. Health Subcommittee Hearing on Reauthorization of the Prescription Drug User Fee Act, Hearing before the Subcommittee on Health of the House Committee on Energy and Commerce, 112th Congress (1 February 2012).
14. B. Lo, M. J. Field, Eds., *Conflict of Interest in Medical Research, Education and Practice* (National Academy Press, Washington, DC, 2009).
15. J. Lenzer, K. Epstein, “The Yaz men: Members of FDA panel reviewing the risks of popular Bayer contraceptive had industry ties.” *Wash. Mon.* 9 January 2012.
16. Center for Science in the Public Interest, Conflict of Interest on COX-2 Panel (Center for Science in the Public Interest, Washington, DC, 2005); www.cspinet.org/new/200502251.html.
17. G. Harris, A. Berenson, *New York Times*, 25 February 2005.
18. CDER, *2011 Novel New Drugs* (FDA, Silver Spring, MD, 2012); www.fda.gov/downloads/Drugs/ucm293663.pdf.
19. FDA, Annual report on the FDA: AC vacancies and public disclosures (FDA, Silver Spring, MD, 2011).
20. D. E. Zinner *et al.*, *Health Aff.* **28**, 1814 (2009).
21. Association of American Medical Colleges, About the AAMC (AAMC, Washington, DC, 2012); <https://www.aamc.org/about/membership/>.
22. American Association of Colleges of Pharmacy, AACP Institutional Members (AACP, Alexandria, VA, 2012); www.aacp.org/about/membership/institutionalmembership/Pages/usinstitutionalmember.aspx.
23. Association of Schools of Public Health, Member Schools (ASPH, Washington, DC, 2012); www.asph.org/document.cfm?page=200.
24. Consumer Reports National Research Center, Poll: Public wants strong medical device safety oversight (Consumer Reports, Yonkers, NY, 2012); <http://consumersunion.org/news/poll-public-wants-strong-medical-device-oversight/>.
25. M. A. Hamburg, Commissioner’s letter to FDA staff on disclosure of financial conflicts of interest (FDA, Silver Spring MD, 2010); www.fda.gov/AdvisoryCommittees/AboutAdvisoryCommittees/ucm209001.htm.

Supplementary Materials

www.sciencemag.org/cgi/content/full/340/6137/1172/DC1

10.1126/science.1231955

Illuminating the Neural Circuitry of Compulsive Behaviors

Scott L. Rauch and William A. Carlezon Jr.

Obsessive-compulsive disorder (OCD) is characterized by unwanted intrusive thoughts (obsessions) and ritualized repetitive behaviors (compulsions) that are often unpleasant and time-consuming; those afflicted feel tormented and can be functionally disabled. Classic examples include obsessions about contamination, which are associated with anxiety and lead to washing compulsions. Compulsive behaviors are not unique to OCD but are a feature of numerous neuropsychiatric disorders, including autism, substance use disorders, and Tourette's disorder (1). The complexity of OCD is emblematic of the challenges inherent in developing animal models of psychiatric disorders, in that repetitive behavior is readily measured, whereas intrusive thoughts are exceedingly difficult to quantify. On pages 1234 and 1243 of this issue, Ahmari *et al.* (2) and Burguière *et al.* (3) describe, respectively, the use of optogenetics (4) to produce and relieve compulsive-like behaviors in animal models. Their pioneering work highlights how models that link genetics, neuroanatomy, physiology, and behavior in ways that cut across disorders (5) can provide promising opportunities for developing diagnostics and treatments in the field.

There are essentially no biomarkers or assays that serve as diagnostic tests in psychiatry (6). Findings from people with OCD support a circuitry model focused on a network of brain regions comprising the orbitofrontal and anterior cingulate cortex, striatum, and thalamus (7). Decades of functional brain imaging data indicate that in OCD, the nodes of this network exhibit hyperactivity at rest that is exacerbated during symptom induction and attenuated by successful treatment (8). These are, however, correlations;



Brain circuitry for repetitive behavior. Hyperactivation (by optogenetic stimulation) of a glutamatergic (GLU) pathway between the orbitofrontal cortex and ventromedial striatum can produce repetitive behavior (extensive grooming) in wild-type mice, presumably by elevating the activity of medium spiny neurons (MSNs). A genetic mouse model of OCD that exhibits repetitive behavior (grooming) shows deficits in the suppression of MSN activity; both can be normalized by activating (through optogenetic stimulation) fast-spiking striatal interneurons (FSIs) that inhibit MSN neurons. A classic example of OCD in humans is an obsession about contamination, which is associated with anxiety and leads to washing compulsions.

we lack the ability to induce the signs and symptoms of the disorder by manipulating activity within specific circuits. Moreover, the imaging data were obtained at modest spatial resolution, making it impossible to test hypotheses regarding specific microcircuitry of interest.

There are corresponding limitations in OCD therapeutics. Although treatments, including pharmacotherapy with selective serotonergic reuptake inhibitors, have modest efficacy, many patients are refractory, and responders are often left with residual symptoms (9). OCD is a prime example of how advances in circuitry models are fueling interest in regional neurostimulation, such as by deep brain stimulation (10) and transcranial magnetic stimulation (11). Unfortunately, these methods of gross regional stimulation to modulate circuits lack specificity at the cellular level. Although some efforts have enabled differential modulation of cells and neuronal fibers according to scale, size, orientation, direction, and myelination status (12), they pale in comparison to the neuroanatomic and cellular specificity possible with optogenetics (2–4). Optogenetics combines genetics and optics to allow temporally and spatially precise manipulation of

Optogenetics is used to delineate and control a brain circuit that drives repetitive behavior in an animal model, opening up new possibilities for the treatment of compulsive disorders.

electrical and biochemical events using fiber-optic light in living organisms.

Ahmari *et al.* and Burguière *et al.* use optogenetics to identify the specific circuits involved in regulating repetitive behavior (excessive grooming) in mice. Ahmari *et al.* found that hyperstimulation of an excitatory circuit between glutamatergic neurons in the orbitofrontal cortex and the ventromedial striatum triggers compulsive behavior (see the figure). Burguière *et al.* discovered that in a genetic mouse model of OCD, excessive grooming was caused by an impaired pathway in the ventromedial striatum (the inhibition of medium spiny neurons by fast-spiking striatal interneurons) within this same neural circuit. This delineation

has broad implications for understanding the neural basis of OCD and other disorders that include compulsivity as a clinical feature. For example, repetitive behavior is a core feature of autism spectrum disorders, and studies in rodents (13) have used animal models similar to those used by Ahmari *et al.* and Burguière *et al.* The striatal regions identified by Ahmari *et al.* and Burguière *et al.* have also been implicated in repetitive behaviors seen with addiction that, through drug-induced neuroplasticity, become habits (14). These “transdiagnostic” behaviors may have common underlying circuitry, and therapeutics that target this circuitry may have broad indications that cut across conditions previously conceptualized as unrelated.

Optogenetics provides a glimpse of highly selective means to control brain circuits, but there are obstacles for its use in nonhuman primate models of disease or clinical settings (15). These include logistical issues (an optical fiber that tethers the subject to the stimulator), ethical and pragmatic concerns (use of viral vectors to express proteins in target cells that create neural sensitivity to light stimulation), and—given that these disorders often arise in childhood and adolescence (1)—the largely unaddressed

Department of Psychiatry, Harvard Medical School, McLean Hospital, Belmont, MA 02478, USA. E-mail: srauch@partners.org

question about how this type of intervention affects the developing brain. A lesson of the Ahmari *et al.* study is that acute stimulation does not produce repetitive behaviors; multiple exposures to stimulation are needed for the phenotype to develop, which suggests that signs of compulsive disorders can be acquired through neuroplasticity. More work is needed to examine how optogenetic manipulation of key circuits early in life affects developmental trajectories to ensure no unintended effects. These current limitations notwithstanding, the cutting-edge and insightful research of Ahmari *et al.* and Burguière *et al.* illuminates the neurocircuitry of compulsive behavior with unprecedented clarity. Although there is still

far to go, these discoveries represent a major leap forward toward eventual methods for “flipping the off-switch” on pathological compulsive behaviors.

References and Notes

1. *Diagnostic and Statistical Manual of Mental Disorders* (American Psychiatric Association, Washington, DC, ed. 4, 2000).
2. S. E. Ahmari *et al.*, *Science* **340**, 1234 (2013).
3. E. Burguière *et al.*, *Science* **340**, 1243 (2013).
4. K. M. Tye, K. Deisseroth, *Nat. Rev. Neurosci.* **13**, 251 (2012).
5. S. E. Morris, B. N. Cuthbert, *Dialogues Clin. Neurosci.* **14**, 29 (2012).
6. E. J. Nestler, W. A. Carlezon Jr., *Biol. Psychiatry* **59**, 1151 (2006).
7. M. R. Milad, S. L. Rauch, *Trends Cogn. Sci.* **16**, 43 (2012).
8. S. Saxena, S. L. Rauch, *Psychiatr. Clin. North Am.* **23**, 563 (2000).
9. W. K. Goodman, R. B. Lydiard, *J. Clin. Psychiatry* **68**, e30 (2007).
10. B. H. Kopell, B. D. Greenberg, *Neurosci. Biobehav. Rev.* **32**, 408 (2008).
11. M. S. George *et al.*, *Neurosurg. Clin. N. Am.* **14**, 283 (2003).
12. C. B. McCracken, A. A. Grace, *J. Neurosci.* **29**, 5354 (2009).
13. N. V. Malkova *et al.*, *Brain Behav. Immun.* **26**, 607 (2012).
14. G. F. Koob, N. D. Volkow, *Neuropsychopharmacology* **35**, 217 (2010).
15. I. Diester *et al.*, *Nat. Neurosci.* **14**, 387 (2011).

Acknowledgments: Supported by National Institute of Mental Health grants MH063266 and MH097860 (W.A.C.). S.L.R. has received research funding from Cyberonics and Medtronic, which develop devices for treating psychiatric illnesses such as OCD. W.A.C. has a U.S. patent covering the use of κ -opioid receptor antagonists in the treatment of depressive disorders.

10.1126/science.1239652

PHYSICS

Interfacing Atoms and Light— The Smaller the Stronger

Matthias Keller

Most of us use the Internet to exchange information in everyday life. The ever-increasing rate at which Internet connections transmit data requires faster and faster conversion of local information into signals that can be easily transmitted over long distances. For example, the information sent by your computer is converted from electronic signals into optical signals, which are then sent through a network of optical fibers. Without the reliable and high-speed conversion of information from electronic to optical form, modern communication would not be possible. With the emergence of quantum technologies, most notably quantum information technology, the way we communicate is about to change fundamentally. On page 1202 of this issue, Thompson *et al.* (1) describe a system that has the potential to become an interface between atoms and optical signals and provide local information storage and transmission in the quantum domain.

In recent years, the processing of quantum information, where quantum-mechanical effects are used to potentially speed up computations, has been demonstrated in several systems (2–6). With these achievements, the question of long-distance communication in the quantum realm arises (7). As in

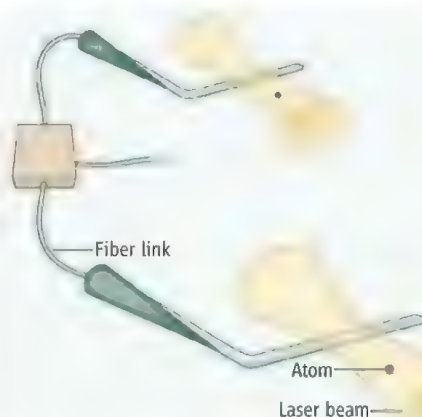
the classical communication domain, a crucial building block consists of converters that can transform quantum information from one form into another, so-called quantum hybrid systems or quantum interfaces. Currently, the most successful implementation for such quantum interfaces for long-distance quantum communication is cavity quantum elec-

The strong interaction of neutral atoms with photons in a waveguide cavity may provide a way to create quantum information networks.

trodynamic, where atoms interact with light in a cavity.

Recently, the transfer of information between atomic states by single light particles (photons) or the entanglement of their states has been demonstrated (8–10). However, a technological challenge is still the fast, efficient, and faithful transfer of information between atoms and photons. To enhance the interaction between photons and atoms, both need to be tightly confined at the same location, and trapped for a sufficiently long time to allow the information transfer. The smaller the space in which both are confined, the stronger the interaction is, and the faster the interface operates.

In 1999, Ye *et al.* (11) trapped atoms in an optical cavity and demonstrated the control of the interaction between atoms and single photons. This technique was later used by Stute *et al.* (8) to demonstrate a quantum network. In a quest to increase the coupling strength between atoms and photons, Colombe *et al.* (12) combined a cavity, formed by laser-machined optical fiber ends with high reflective coating, with magnetically trapped atoms on a chip. Because of the small volume of such a cavity,



Toward quantum networks. Thompson *et al.* trapped atoms with laser beams in the vicinity of photonic waveguide cavities, as shown in the expanded view. The coupling interaction was determined by measuring the emission of photons that escaped the trap through the tip of a tapered optical fiber. These photons, guided by optical fibers, could potentially interact with other trapped atoms. The interactions in these quantum networks could provide a way to store and send quantum information.

Department of Physics and Astronomy, University of Sussex, Brighton, UK. E-mail: m.k.keller@sussex.ac.uk

the coherent coupling was greatly enhanced compared to conventional systems. In an alternative approach, Alton *et al.* (13) investigated monolithic microresonators in which photons were confined in whispering-gallery modes within a toroidal glass structure.

Thompson *et al.* have demonstrated the coupling of trapped neutral atoms with a photonic waveguide cavity (PWC). They have confined single atoms to a volume smaller than $0.007 \mu\text{m}^3$ at a distance of 260 nm away from the PWC. In order to trap a single atom near the PWC structure, they used the reflection of a tightly focused laser on the waveguide structure. The reflected beam together with the incident beam forms a standing wave in whose maxima the atom is trapped. The exact position of the atom is determined by the reflected laser beam and depends on the structure of the waveguide itself.

To probe the interaction between the light trap (PWC) and the atom, Thompson

et al. attached the waveguide to the tip of a tapered fiber through which the photons can escape the trap. Thus, by measuring the photon emission from the fiber, the interaction between atom and photon could be probed. The authors observed a coupling strength of 600 MHz, which measures the rate at which excitation between the waveguide structure and the atom is exchanged and thus constitutes the upper limit of the information transfer between atom and light. The atom was held in the vicinity of the PWC for 250 ms before it left the trap and was lost.

The combination of a single atom coupled to a waveguide structure is a promising implementation of a quantum interface between atomic and photonic quantum states. It opens the possibility to couple atoms, either to the same PWC, or to remote fiber-linked PWCs, through photon exchange (see the figure). Although there are still many technological challenges to overcome, such as to

increase substantially the trap lifetime near the surface of the PWC, or the improvement of the PWC quality, the work of Thompson *et al.* constitutes an important demonstration of a quantum hybrid system.

References

1. J. D. Thompson *et al.*, *Science* **340**, 1202 (2013); 10.1126/science.1237125.
2. F. Schmidt-Kaler *et al.*, *Nature* **422**, 408 (2003).
3. D. Leibfried *et al.*, *Nature* **422**, 412 (2003).
4. A. Politi *et al.*, *Science* **325**, 1221 (2009).
5. L. M. K. Vandersypen *et al.*, *Nature* **414**, 883 (2001).
6. L. DiCarlo *et al.*, *Nature* **460**, 240 (2009).
7. J. I. Cirac, P. Zoller, H. Kimble, H. Mabuchi, *Phys. Rev. Lett.* **78**, 3221 (1997).
8. A. Stute *et al.*, *Nat. Photonics* **7**, 219 (2013).
9. T. Wilk, S. C. Webster, A. Kuhn, G. Rempe, *Science* **317**, 488 (2007).
10. S. Ritter *et al.*, *Nature* **484**, 195 (2012).
11. J. Ye, D. Vernooy, H. Kimble, *Phys. Rev. Lett.* **83**, 4987 (1999).
12. Y. Colombe *et al.*, *Nature* **450**, 272 (2007).
13. D. J. Alton *et al.*, *Nat. Phys.* **7**, 159 (2011).

10.1126/science.1239500

MICROBIOLOGY

Seas of Superoxide

Yeala Shaked¹ and Andrew Rose²

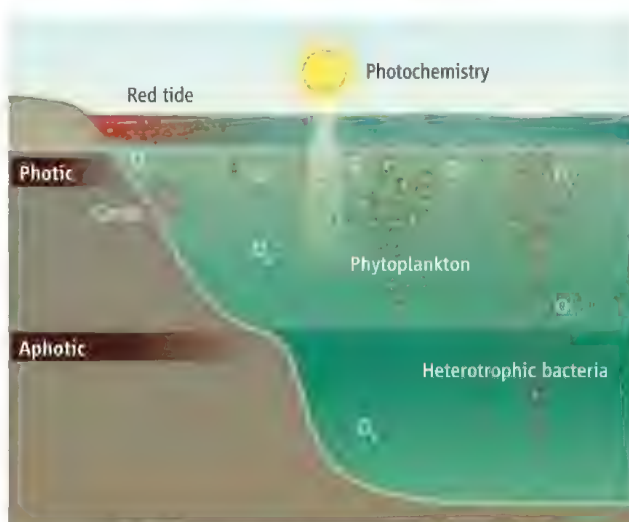
In the past decade, sensitive analytical techniques have enabled a new look at the distributions, sources and chemical reactivity of superoxide (O_2^-) in the ocean. Until recently superoxide was thought to form solely through photochemical reactions in the surface ocean, but now biological processes are considered to be equally important in generating superoxide. On page 1223 of this issue, Diaz *et al.* (1) show that heterogeneous bacteria produce superoxide and potentially represent a substantial source of superoxide in the sea.

Superoxide is a reactive oxygen species that is highly toxic within biological cells, contributing to oxidative stress and cell death pathways, cellular aging, and pathologies, including cancer and Alzheimer's disease. Yet it is also vital for gene expression, intracellular signaling, and immune defense. Intracellular superoxide concentrations in biological systems are therefore tightly regulated, and its lifetimes within cells are extremely short. By contrast, in seawater, superoxide can persist long enough to

diffuse well away from its source and react with organic and inorganic compounds.

Abiotic photochemistry in sunlit surface waters was long considered the major source of superoxide and other reactive oxygen spe-

Superoxide in seawater may be produced by heterotrophic bacteria, with implications for trace metal cycling in the sea.



Superoxide in the ocean. In the photic zone, superoxide (O_2^-) is generated via photolysis of organic matter or by biological processes. In coastal waters, corals, macroalgae, and toxic red tide phytoplankton are potential sources of superoxide. In the open ocean, phytoplankton were regarded thus far as the dominant source of biologically produced superoxide. Diaz *et al.* show that extracellular superoxide is widespread among heterotrophic bacteria and may be an additional source of superoxide.

cies in natural waters (2, 3). Recently, superoxide has been measured in a range of marine environments at picomolar to nanomolar concentrations (4–8). Unexpectedly, superoxide was found not only in the well-illuminated surface water but also in the deep ocean and at nighttime, albeit at lower concentrations (see the figure). That and the finding of particle-associated superoxide production (4–7) showed that there must be additional, possibly biological, sources of superoxide.

Enzymatic superoxide production on the outer cell membranes or plasma membranes is ubiquitous among plants, fungi, macroalgae, phytoplankton, corals, and bacteria (6, 9–12). Toxic red tide algae of the genera *Chattonella* and *Heterosigma* produce superoxide at extraordinary rates (10) but only in coastal waters (see the figure). Other nontoxic rep-

¹InterUniversity Institute for Marine Sciences, Eilat 88103, Israel, and Institute of Earth Sciences, Hebrew University, Jerusalem 91904, Israel. ²Southern Cross GeoScience, Southern Cross University, Lismore, NSW 2480, Australia. E-mail: yeala.shaked@mail.huji.ac.il

representatives from the major phytoplankton classes in the ocean—diatoms, dinoflagellates, and cyanobacteria—can also produce extracellular superoxide (6, 9, 10). Moreover, field studies have found elevated superoxide concentrations in areas of high phytoplankton abundance (5, 7). Hence, it is now accepted that phytoplankton are the main source of particle-associated superoxide in the upper, photic, oceanic water column (see the figure).

Diaz *et al.* show that extracellular production of superoxide is widespread among taxonomically divergent heterotrophic bacteria from a range of different environments. Some of their bacterial cultures are marine isolates; these bacteria can potentially generate superoxide in marine sediments and in the vast expanses of the deep ocean that do not receive sunlight. Of course, heterotrophic bacteria are not restricted to the deep ocean and may thus also contribute to particle-associated biological superoxide production close to the ocean surface (see the figure).

Superoxide interacts with many chemical elements and compounds. For example, it alters the redox states of iron, copper, and manganese and modulates their chemical reactivity, solubility, bioavailability, and toxicity (8, 9, 13, 14). These metals control the abundance and distribution of marine phytoplankton, which in turn drive the cycling of

major nutrients, such as carbon and nitrogen. Superoxide also oxidizes dissolved manganese to solid manganese oxides, which are efficient trace metal sorbents and powerful oxidants of organic materials (12). When these minerals settle out of the water column, they influence the distribution of trace elements and nutrients. Furthermore, superoxide promotes the degradation of dissolved organic matter, with implications for the marine carbon cycle. Further interactions and biogeochemical roles of superoxide in the ocean are likely.

Given its functions in other systems, superoxide may play a role in the chemical interactions among microorganisms at sea. Superoxide is potentially toxic to organisms and can be used as a first line of defense against viral or bacterial attacks. At low levels, it may also assist communication among marine microbes. So far, the only demonstrated role of superoxide production by phytoplankton is of increased iron availability, shown for a filamentous cyanobacterium (14). However, another study with a diatom found that iron acquisition was unaffected by superoxide production (9).

We are still a long way from a full assessment of superoxide concentrations across oceanic environments and their link to bacterial activity. Given the potential influence of superoxide on trace metal and carbon cycling

in the ocean, these are exciting times to study the dynamics of superoxide in seawater. The analytic capabilities exist, correspondence with other disciplines provides a good stream of ideas and hypotheses, and there are still more questions than answers.

References and Notes

1. J. M. Diaz *et al.*, *Science* **340**, 1223 (2013); 10.1126/science.1237331.
2. R. M. Baxter, J. H. Carey, *Nature* **306**, 575 (1983).
3. E. Micinski, L. A. Ball, O. C. Zafiriou, *J. Geophys. Res.* **98**, 2299 (1993).
4. S. P. Hansard, A. W. Vermilyea, B. M. Voelker, *Deep Sea Res.* **57**, 1111 (2010).
5. A. L. Rose, A. Godrant, M. Furnas, T. D. Waite, *Limnol. Oceanogr.* **55**, 1521 (2010).
6. A. L. Rose, E. A. Webb, T. D. Waite, J. W. Moffett, *Environ. Sci. Technol.* **42**, 2387 (2008).
7. S. A. Rusak, B. M. Peake, L. E. Richard, S. D. Nodder, W. J. Cooper, *Mar. Chem.* **127**, 155 (2011).
8. Y. Shaked, R. Harris, N. Klein-Kedem, *Environ. Sci. Technol.* **44**, 3238 (2010).
9. A. B. Kustka, Y. Shaked, A. J. Milligan, D. W. King, F. M. M. Morel, *Limnol. Oceanogr.* **50**, 1172 (2005).
10. J.-A. Marshall, M. de Salas, T. Oda, G. Hallegraeff, *Mar. Biol.* **147**, 533 (2005).
11. E. Saragosti, D. Tchernov, A. Katsir, Y. Shaked, *PLoS ONE* **5**, e12508 (2010).
12. D. R. Learman, B. M. Voelker, A. I. Vazquez-Rodriguez, C. M. Hansel, *Nat. Geosci.* **4**, 95 (2011).
13. S. P. Hansard, H. D. Easter, B. M. Voelker, *Environ. Sci. Technol.* **45**, 2811 (2011).
14. A. L. Rose, *Front. Microbiol.* **3**, 124 (2012).

Acknowledgments: Supported by Israel Science Foundation grant 248/11 (Y.S.).

10.1126/science.1240195

MATHEMATICS

Bayes' Theorem in the 21st Century

Bradley Efron

The term “controversial theorem” sounds like an oxymoron, but Bayes' theorem has played this part for two-and-a-half centuries. Twice it has soared to scientific celebrity, twice it has crashed, and it is currently enjoying another boom. The theorem itself is a landmark of logical reasoning and the first serious triumph of statistical inference, yet is still treated with suspicion by most statisticians. There are reasons to believe in the staying power of its current popularity, but also some signs of trouble ahead.

Here is a simple but genuine example of Bayes' rule in action (see sidebar) (1). A physicist couple I know learned, from sonograms, that they were due to be parents of twin boys.

They wondered what the probability was that their twins would be identical rather than fraternal. There are two pieces of relevant evidence. One-third of twins are identical; on the other hand, identical twins are twice as likely to yield twin boy sonograms, because they are always same-sex, whereas the likelihood of fraternal twins being same-sex is 50:50. Putting this together, Bayes' rule correctly concludes that the two pieces balance out, and that the odds of the twins being identical are even. (The twins were fraternal.)

Bayes' theorem is thus an algorithm for combining prior experience (one-third of twins are identicals) with current evidence (the sonogram). Followers of Nate Silver's FiveThirtyEight Web blog got to see the rule in spectacular form during the 2012 U.S. presidential campaign: The algorithm updated prior poll results with new data on

Bayes' theorem plays an increasingly prominent role in statistical applications but remains controversial among statisticians.

a daily basis, correctly predicting the actual vote in all 50 states. “Statisticians beat pundits” was the verdict in the press (2).

Bayes' 1763 paper was an impeccable exercise in probability theory. The trouble and the subsequent busts came from overenthusiastic application of the theorem in the absence of genuine prior information, with Pierre-Simon Laplace as a prime violator. Suppose that in the twins example we lacked the prior knowledge that one-third of twins are identical. Laplace would have assumed a uniform distribution between zero and one for the unknown prior probability of identical twins, yielding 2/3 rather than 1/2 as the answer to the physicists' question. In modern parlance, Laplace would be trying to assign an “uninformative prior” or “objective prior” (2), one having only neutral effects on the output of Bayes' rule (3). Whether or not this

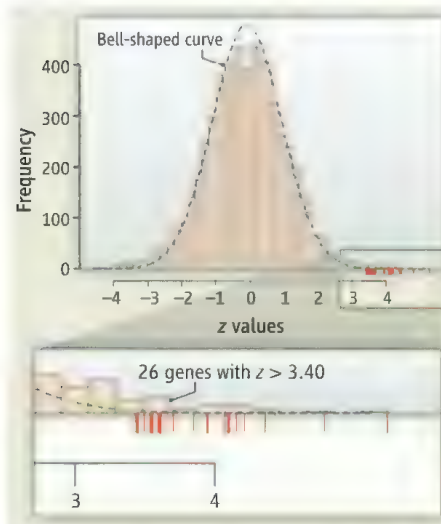
Department of Statistics, Stanford University, Stanford, CA 94305, USA. E-mail: brad@stat.stanford.edu

can be done legitimately has fueled the 250-year controversy.

Frequentism, the dominant statistical paradigm over the past hundred years, rejects the use of uninformative priors, and in fact does away with prior distributions entirely (1). In place of past experience, frequentism considers future behavior. An optimal estimator is one that performs best in hypothetical repetitions of the current experiment. The resulting gain in scientific objectivity has carried the day, though at a price in the coherent integration of evidence from different sources, as in the FiveThirtyEight example.

The Bayesian-frequentist argument, unlike most philosophical disputes, has immediate practical consequences. Consider that after a 7-year trial on human subjects, a research team announces that drug A has proved better than drug B at the 0.05 significance level. Asked why the trial took so long, the team leader replies “That was the first time the results reached the 0.05 level.” Food and Drug Administration (FDA) regulators reject the team’s submission, on the frequentist grounds that interim tests of the data, by taking repeated 0.05 chances, could raise the false alarm rate to (say) 15% from the claimed 5%.

A Bayesian FDA regulator would be more forgiving. Starting from a given prior distribution, the Bayesian posterior probability of drug A’s superiority depends only on its final evaluation, not whether there might have been earlier decisions. This is a corollary of



True and false discoveries. Test statistic z for 6033 genes in a microarray study of prostate cancer. The 28 genes having $z \geq 3.40$ are likely to be “true discoveries,” that is, genes that are more active in prostate cancer patients than in controls. These results are based on Bayes’ rule, but with “prior” information obtained from the current data, an example of empirical Bayes methodology.

SIDEBAR: BAYES’ THEOREM IN ACTION

If $P(A)$ is the probability of A and $P(B)$ is the probability of B, then the conditional probability of A given B is $P(A|B)$ and the conditional probability of B given A is $P(B|A)$. Bayes’ theorem says that

$$P(A|B) = \frac{P(B|A)P(A)}{P(B)}$$

In the twins example, A is “twins identical” and B is “sonogram shows twin boys.” The doctor’s prior says $P(A) = 1/3$; genetics implies $P(B|A) = 1/2$ and $P(B|\text{not } A) = 1/4$, so $P(B) = (1/2)(1/3) + (1/4)(2/3) = 1/3$. Bayes’ theorem then gives

$$P(A|B) = (1/2)(1/3)/(1/3) = 1/2$$

The two pieces of evidence thus balance out, and the likelihood of the boys being fraternal is equal to that of the boys being identical.

Bayes’ theorem, convenient but potentially dangerous in practice, especially when using prior distributions not firmly grounded in past experience.

I recently completed my term as editor of an applied statistics journal. Maybe a quarter of the papers used Bayes’ theorem. Almost all of these were based on uninformative priors, reflecting the fact that most cutting-edge science does not enjoy FiveThirtyEight-level background information. Are we in for another Bayesian bust?

Arguing against this is a change in our statistical environment. Modern scientific equipment pumps out results in fire hose quantities, producing enormous data sets bearing on complicated webs of interrelated questions. In this new scientific era, the ability of Bayesian statistics to connect disparate inferences counts heavily in its favor.

An example will help here. In a microarray prostate cancer study (4), 102 men—52 patients and 50 healthy controls—each had their genetic activity measured for 6033 genes. The investigators were hoping to find genes expressed differently in the patients than in the controls. To this end, they calculated a test statistic z for each gene, with a standard normal (“bell-shaped”) distribution in the null case of no patient/control difference, but with bigger values for genes expressed more intensely in patients.

The histogram of the 6033 z values (see the figure) does not look much different than the bell-shaped curve that would apply if all genes were null. However, there is a suggestion of interesting non-null genes in the heavy right tail of the distribution. We have to be careful, though. With 6033 genes to consider at once, a few of the z ’s are bound to look big even under the null hypothesis, an example

of selection bias or regression to the mean. These would be “false discoveries.”

False discovery rates (FDRs) (5) are a recent development that takes multiple testing into account (6). Here, it implies that the 28 genes with z values above 3.40 (red dashes in the figure) are indeed interesting, with the expected proportion of false discoveries among them being less than 10%. This is a frequentist 10%: how many mistakes we would average using the algorithm in future studies. We expect only 2.8 of the z values exceeding 3.40 to be null, that is, only 10% of the actual number observed. Larger choices of the cutoff would yield smaller FDRs.

This brings us back to Bayes. Another interpretation of the FDR algorithm is that the Bayesian probability of nullness given a z value exceeding 3.40 is 10%. What prior evidence are we using? None, as it turns out! With 6033 parallel situations at hand, we can effectively estimate the relevant prior from the data itself. “Empirical Bayes” is the name for this sort of statistical jujitsu, suggesting a fusion of frequentist and Bayesian reasoning (7). Empirical Bayes is an exciting new statistical idea, well-suited to modern scientific technology, saying that experiments involving large numbers of parallel situations carry within them their own prior distribution. The idea was coined in the 1950s (8), but real developmental interest awaited the vast data sets of the 21st century.

I wish I could report that this resolves the 250-year controversy and that it is now safe to always employ Bayes’ theorem. Sorry. My own practice is to use Bayesian analysis in the presence of genuine prior information; to use empirical Bayes methods in the parallel cases situation; and otherwise to be cautious when invoking uninformative priors. In the last case, Bayesian calculations cannot be uncritically accepted and should be checked by other methods, which usually means frequentistically.

References and Notes

1. B. Efron, *Bull. Am. Math. Soc.* **50**, 129 (2013).
2. S. Wang, B. Campbell, *Science* **339**, 758 (2013).
3. J. Berger, *Bayesian Anal.* **1**, 385 (2006).
4. D. Singh et al., *Cancer Cell* **1**, 203 (2002).
5. Y. Benjamini, Y. Hochberg, *J. R. Stat. Soc. B* **57**, 289 (1995).
6. See chapter 4 of (7) for a careful exposition of false discovery rate theory.
7. B. Efron, *Large-Scale Inference: Empirical Bayes Methods for Estimation, Testing, and Prediction* (Institute of Mathematical Statistics Monographs, Cambridge Univ. Press, Cambridge, UK, 2010).
8. H. Robbins, in *Proceedings of the Third Berkeley Symposium on Mathematical Statistics and Probability, 1954–1955, Vol. 1* (Univ. of California Press, Berkeley/Los Angeles, 1956), pp. 157–163.

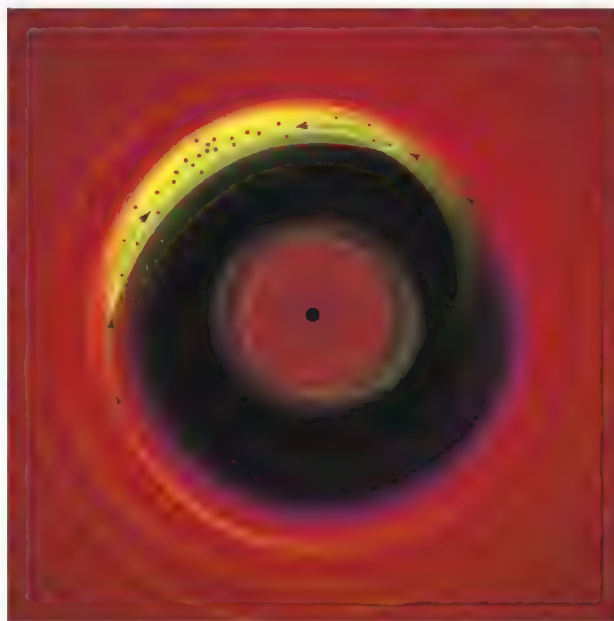
ASTRONOMY

A Trap for Planet Formation

Philip J. Armitage^{1,2}

The raw material for forming planets is micrometer to millimeter-sized particles of dust that orbit along with gas in protoplanetary disks around young low-mass stars. These disks are known to be common and to persist for several million years (1). The Kepler mission (2) showed that mature planetary systems are also common. What is not known, however, is the full sequence of steps that allows the dust within protoplanetary disks to grow into planets. On page 1199 of this issue, van der Marel *et al.* (3) report observations from the Atacama Large Millimeter/submillimeter Array (ALMA) that hint at how the most problematic step may be surmounted—millimeter-sized particles are seen to be accumulating into a giant trap that acts as a holding pen for growth into larger bodies.

Planet growth (4) is dominated at the smallest scales by aerodynamic interactions between dust particles and the surrounding gas disk, which orbit the star at slightly different speeds. Once kilometer-sized bodies form, their larger ratio of mass to surface area means that aerodynamic forces become negligible and gravitational forces dominate. Growth through the size range between these extremes is the hardest to explain (5). At any distance from the star, there is a critical particle size [about a meter at 1 astronomical unit (AU), a millimeter at several tens of AU] for which aerodynamic drag leads to rapid inspiral through the gas disk (6). A trapping or concentrating mechanism is needed to allow particles to surmount this radial drift barrier and avoid the loss of solids into the star. Many possibilities have been suggested: Disks could trap solids in vortices (7) or zonal flows (8), which are analogs of the anticyclones and jets observed in planetary atmospheres, or at radial locations where the density and pressure within the disk change abruptly (9). Concentration could occur on these large scales, or on smaller scales



From dust to planet. Illustration of the proposed mechanism that creates a dust trap in the disk of IRS 48. A massive planet (plus symbol) creates an annular gap in the gas disk, whose surface density is shown as a color map. A high-pressure vortex (contours) forms at the gap edge, collecting and trapping millimeter-sized dust particles that would otherwise spiral rapidly inward through the disk.

metric distribution. The emission from smaller dust particles, measured separately at infrared wavelengths, is also distributed uniformly around the orbit (11). These observations are consistent with theoretical expectations for a dust trap, in which a modest peak in gas pressure is able to strongly concentrate the millimeter-sized solid particles that would otherwise experience rapid orbital decay. The smaller dust particles can escape the trap due to the action of turbulence that spreads them azimuthally around the orbit.

Van der Marel's interpretation of the nature of the trap is motivated by the transitional nature of the disk around IRS 48 (see the figure) and starts from the assumption that there is a massive planet (or brown dwarf) orbiting interior to the observed peak in millimeter emission. The planet holds back the inward flow of gas and dust through the disk, creating the cavity inferred to be present in transitional sources (12, 13). If the planet is massive enough and the disk not too turbulent, then a persistent anticyclonic vortex can form at the edge of the cavity (14); the high-pressure core of the vortex then acts as a particle trap. A quantitative model of vortex formation for IRS 48 (3) provides a reasonable but not perfect match to the observed morphology of the millimeter emission.

Does the observational detection of a particle trap in IRS 48 imply that traps are the answer to surmounting the radial drift barrier and allowing planet formation? Not immediately. Particle traps solve theoretical problems in planet formation that exist at millimeter to meter scales, and they are no solution at all if the only way to form them requires that gas giant planets already exist. The trap observed in the IRS 48 disk might instead catalyze the formation of additional

where instabilities are triggered by the aerodynamic interaction between gas and solids (5). Because calculations of trapping mechanisms have large uncertainties, observations that shed light on whether these processes occur are of great value.

The star Oph IRS 48 is a member of one of the nearest star-forming regions at a distance of 120 parsec from the Sun. Its exact mass and age are uncertain, but it is estimated to have a mass about twice that of the Sun and an age of 15 million years (10). Previous observations of the radial distribution of circumstellar matter showed that it belonged to the class of "transition disks," with a substantial mass of gas and dust orbiting at large radii surrounding an inner cavity that in this case extends to about 25 AU (11). The new data show that the distribution of millimeter-sized dust in the outer disk is strikingly asymmetric. Van der Marel *et al.* show that the emission at a wavelength of 0.44 mm is concentrated into a crescent-shaped structure that extends for less than a third of the way around the orbit. No emission at this wavelength is detected on the side of the star opposite the crescent down to a level that is more than a hundred times weaker. In contrast to the lopsided millimeter emission, the molecular gas in the outer disk (measured as part of the same observing campaign) follows a roughly axisym-

¹JILA, University of Colorado and National Institute of Standards and Technology, Boulder, CO 80309–0440, USA.

²Department of Astrophysical and Planetary Sciences, University of Colorado, Boulder, CO 80309, USA. E-mail: pja@jilau1.colorado.edu

planets, or a massive debris disk (15) similar to the Kuiper Belt, at larger radii than would otherwise be possible. Future observations will be needed to determine whether traps are also present in younger disks where there is no evidence for preexisting planets. Such traps could be important even if they are substantially weaker than that observed in the IRS 48 disk. The sensitivity and image fidelity of ALMA has been improved further since the Early Science phase observations executed last year, so answers should soon be forthcoming.

References and Notes

1. K. E. Haisch Jr., E. A. Lada, C. J. Lada, *Astrophys. J.* **553**, L153 (2001).
2. A. W. Howard *et al.*, *Astrophys. J.* **201** (suppl.), 15 (2012).
3. N. van der Marel *et al.*, *Science* **340**, 1199 (2013).
4. P. J. Armitage, *Astrophysics of Planet Formation* (Cambridge Univ. Press, Cambridge, UK, 2010).
5. E. Chiang, A. N. Youdin, *Annu. Rev. Earth Planet. Sci.* **38**, 493 (2010).
6. S. J. Weidenschilling, *Mon. Not. R. Astron. Soc.* **180**, 57 (1977).
7. P. Barge, J. Sommeria, *Astron. Astrophys.* **295**, L1 (1995).
8. A. Johansen, A. Youdin, H. Klahr, *Astrophys. J.* **697**, 1269 (2009).
9. K. A. Kretke, D. N. C. Lin, *Astrophys. J.* **664**, L55 (2007).
10. J. M. Brown, G. J. Herczeg, K. M. Pontoppidan, E. F. van Dishoeck, *Astrophys. J.* **744**, 116 (2012).
11. V. C. Geers *et al.*, *Astron. Astrophys.* **469**, L35 (2007).
12. N. Calvet *et al.*, *Astrophys. J.* **568**, 1008 (2002).
13. W. K. M. Rice, K. Wood, P. J. Armitage, B. A. Whitney, J. E. Bjorkman, *Mon. Not. R. Astron. Soc.* **342**, 79 (2003).
14. R. V. E. Lovelace, H. Li, S. A. Colgate, A. F. Nelson, *Astrophys. J.* **513**, 805 (1999).
15. M. C. Wyatt, *Annu. Rev. Astron. Astrophys.* **46**, 339 (2008).

Acknowledgments: I thank A. Pisconti for helpful discussions. This work was supported by NASA's Origins of Solar Systems and Astrophysics Theory Programs, and by grant HST-AR-12814 awarded by Space Telescope Science Institute.

10.1126/science.1239404

NEUROSCIENCE

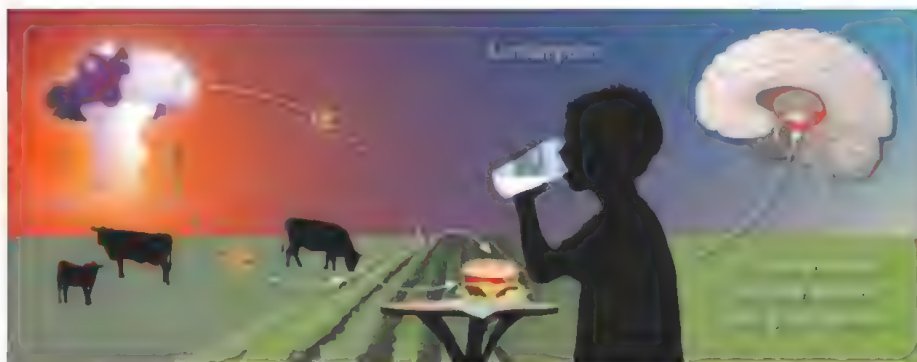
What the Bomb Said About the Brain

Gerd Kempermann

There are few positive things to be said about above-surface nuclear bomb tests, but one of their most unexpected fallouts will be the proof of neurogenesis in the adult human brain. With help from atomic-age history, Spalding *et al.* (1) have derived a model predicting that neurogenesis-based plasticity in humans reaches much greater levels than previously assumed.

The hippocampal region of the brain in most, if not all, mammals, including humans, generates new neurons. A landmark study 15 years ago applied a method routinely used in animal research to human subjects and revealed new neurons in the adult human brain in five individuals up to 72 years of age (2). But this classical method involved injecting a label that permanently integrates into the DNA of dividing cells. The compound, bromodeoxyuridine (BrdU), can be recognized with antibodies and used to visualize cells that originate from a cell that took up the label when it was injected, and subsequently divided. For a short time, BrdU was used in clinical studies for tumor-staging purposes. The 1998 study relied on the availability of a cohort of patients that had received BrdU injections and were willing to donate their brains after death. This situation will not occur again, as BrdU is no longer given to patients for safety reasons.

Deutsches Zentrum für Neurodegenerative Erkrankungen (DZNE) and the Center for Regenerative Therapies Dresden, Technische Universität Dresden, Fetscherstrasse 105 Dresden, 01307 Germany. E-mail: gerd.kempermann@dzne.de



The brain, time-stamped. Atmospheric ^{14}C that was released during nuclear bomb tests between 1945 and 1963 has been incorporated into the DNA of dividing cells, providing a time-stamp. This has been used to prove adult hippocampal neurogenesis in humans, thereby confirming a particular type of structural and functional brain plasticity involved in higher cognitive function.

Thus, information on adult hippocampal neurons in humans has relied on this one influential study, although there has been some additional indirect evidence since then. For example, the characteristic molecular markers that identify adult hippocampal neurogenesis in the mouse are also present in the adult and old human hippocampus (3).

The long-awaited, more direct proof has finally been provided by Spalding *et al.* through an ingenious approach (see the figure). Their strategy makes use of the extreme peak of carbon isotope 14 (^{14}C) that was released into the atmosphere during the aboveground nuclear bomb tests between 1945 and 1963. Following the Limited Test Ban Treaty of 1963, most aboveground blasts ceased. Since then, the

amount of atmospheric ^{14}C has declined. Dividing cells require carbon, and as this carbon is ultimately taken from the atmosphere, ^{14}C finds its way into the DNA of proliferating cells, where the atoms are stably integrated into chromosomes as they are being duplicated. Conveniently, the amount of incorporated ^{14}C correlates with the atmospheric ^{14}C at the time of cell division. So one “only” has to measure ^{14}C in the DNA to estimate, quite precisely, the age of a cell, based on the age of its DNA (the decline in ^{14}C over time is used to calculate the age). The technical realization of this kind of cellular carbon dating turned out to be a tremendous challenge (4), but over the years, it has been used to study the cellular turnover in several tissues, such as adipose (5).

CREDIT: H. McDONALD/SCIENCE

Spalding *et al.* not only confirm that adult brain neurogenesis is restricted to the hippocampus, but the size of their data set (genomic DNA was isolated from hippocampal neurons from subjects 19 to 92 years of age) enabled the authors to attempt a quantitative estimate on the dynamics of the process. Based on a sophisticated modeling approach, they conclude that contrary to some expectations, humans have at least as much adult hippocampal neurogenesis as mice. They calculate a considerable turnover of neurons in the dentate gyrus portion of the hippocampus and put forth a model of how the composition of this hippocampal structure changes over the course of life. In the proposed model, “turn-over” does not imply that specific neurons are renewed one-by-one. Rather, a subpopulation of neurons renews consistently and continually, whereas another population is non-renewing. Spalding *et al.* estimate that one-third of adult hippocampal neurons are turning over. This amounts to 700 new neurons added per day, for an annual turnover rate of 1.75% (or 0.004% of dentate gyrus neurons). This turnover rate was not significantly different between men and women and declined only modestly with age. The author’s modeling suggests that nonrenewing neurons in the hippocampus die without being replaced and account for the slow decrease in total neuron number throughout life. By contrast, adult-born neurons in the renewing population do not survive as long and are preferentially lost. The half life of the latter is about 7 years, 10 times shorter than that of the former.

The big question is whether adult-born neurons contribute to brain function. Indeed, other models already have suggested that such continual turnover is highly efficient for meeting some of the particular computational needs that the hippocampus has to face (6). It is the young, immature neurons that seem to play a critical role in the function of the dentate gyrus (7, 8); essentially all long-term potentiation (which underlies learning and memory) measurable under normal conditions can be attributed to the newborn cells. Adult neurogenesis would not only provide plasticity but also add to stability because some new neurons are also integrated for a longer amount of time, presumably resulting in relatively long-lasting adaptations of the local network. Acute benefits from neurogenesis might be translated into lasting ones, depending on actual activity and cognitive demand.

At the behavioral level, adult neurogenesis adds a particular type of cognitive flexibility to the hippocampus (8). Adult neurogenesis does not appear to be required for

hippocampal function per se, even though tampering with adult neurogenesis affects the efficiency of hippocampal functions such as “pattern separation” (which allows storing similar representations in a nonoverlapping manner) (9). Perhaps, the advantage of having a dentate gyrus, as mammals do, lies in the ability it provides to cope with change and novelty (10). Adult neurogenesis in this region might add a particular functionality not achievable by other types of plasticity. By staying “forever young,” the dentate gyrus could command unique solutions to computational problems only found in the brain region central to learning, memory, and many higher cognitive functions considered essential for humans.

The evolutionary advantage attributable to the mammalian dentate gyrus compared to the analogous structures in other vertebrates might result from adult hippocampal neurogenesis and might even prominently

contribute to the individualization of the brain and thus the shaping of personality (11). In such context, Spalding *et al.* provide a confirmation with the highest possible impact. Neurogenesis researchers can stop worrying and love the bomb.

References

1. K. Spalding *et al.*, *Cell* 10.1016/j.cell.2013.05.002 (2013).
2. P. S. Eriksson *et al.*, *Nat. Med.* **4**, 1313 (1998).
3. R. Knoth *et al.*, *PLoS ONE* **5**, e8809 (2010).
4. R. D. Bhardwaj *et al.*, *Proc. Natl. Acad. Sci. U.S.A.* **103**, 12564 (2006).
5. K. L. Spalding *et al.*, *Nature* **453**, 783 (2008).
6. A. Appleby, G. Kempermann, L. Wiskott, *PLoS Comput. Biol.* **7**, e1001063 (2011).
7. J. S. Snyder, N. Kee, J. M. Wojtowicz, *J. Neurophysiol.* **85**, 2423 (2001).
8. A. Garthe, J. Behr, G. Kempermann, *PLoS ONE* **4**, e5464 (2009).
9. J. B. Aimone, J. Wiles, F. H. Gage, *Neuron* **61**, 187 (2009).
10. G. Kempermann, *Nat. Rev. Neurosci.* **13**, 727 (2012).
11. J. Freund *et al.*, *Science* **340**, 756 (2013).

10.1126/science.1240681

DEVELOPMENTAL BIOLOGY

Deserts and Waves in Gene Expression

Alan R. Rodrigues^{1,2} and Clifford J. Tabin¹

A gene cluster that regulates limb development is controlled in two phases by regulatory elements that flank the cluster and operate independently.

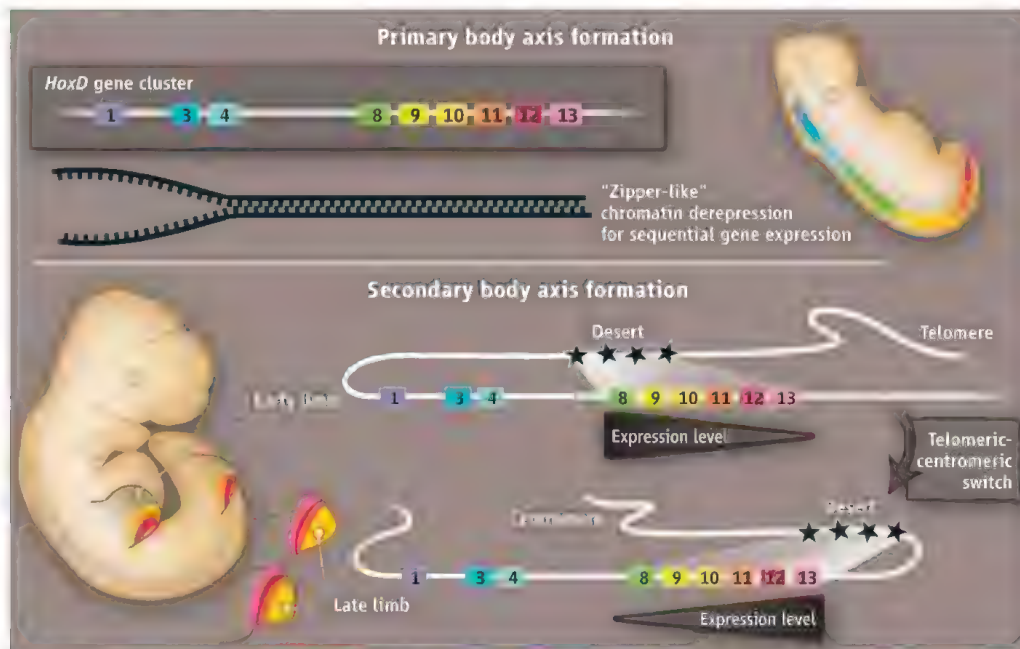
The homeotic genes, or *Hox* genes, encode transcription factors that are situated in tight clusters within the genome of broadly divergent taxa. In invertebrates and vertebrates, *Hox* genes specify differences along the anteroposterior body axis in the same order as their physical order in the cluster (1–3), but in the latter, this collinearity has also been co-opted for constructing secondary body axes such as the limb (4). On page 1195 in this issue, Andrey *et al.* (5) elucidate the complex regulatory mechanisms responsible for the collinearity of *Hox* genes in patterning such secondary axes.

Establishment of the primary body axis is attributable to the chromosomal organization of *Hox* genes in concert with two regulatory features. One is that the genes become accessible for transcription gradually from one end of the cluster to the other through chromatin

derepression (see the figure). This mechanism, postulated over two decades ago (6), is supported by profiles of chromatin epigenetic marks that reflect changing states of gene expression (7). Another feature is that *Hox* genes activated at the lagging end of the cluster are functionally dominant over those activated at the leading end (8). To reemploy these genes for specifying the secondary body axes, however, new mechanisms are required.

In vertebrates, duplication of the *Hox* cluster has produced the *HoxA*, *B*, *C*, and *D* clusters. Of these, the *HoxA* and *HoxD* clusters pattern the limb buds (4). Within the limb, *HoxD* cluster expression is manifested in two discrete phases. In the early distal limb, when forearm elements are specified, *Hoxd1–9* are broadly expressed whereas *Hoxd10–13* are expressed in smaller spatial domains, similar to the collinearity that constructs the primary body axis (9, 10). A second phase of expression arises in the late distal limb when the hand is specified, during which the order of collinearity is reversed—*Hoxd13* is

¹Department of Genetics, Harvard Medical School, Boston, MA 02115, USA. ²Department of Molecular and Cellular Biology, Harvard University, Cambridge, MA 02138, USA. E-mail: tabin@genetics.med.harvard.edu



Controlling collinearity. Genes in the *HoxD* cluster are expressed from one end to the other, through sequential opening of the chromosome, to construct the vertebrate primary body axis (mouse embryo shown). Later in development, when limbs emerge (secondary body axes), the same cluster is redeployed through a different regulatory mechanism. During early limb development, a regulatory region flanking one end of the cluster (telomeric enhancers) controls *HoxD* gene expression. As limb development progresses, the telomeric enhancers are switched off while centromeric enhancers flanking the other end of the cluster are switched on.

expressed most broadly, whereas *Hoxd12-10* are expressed in smaller domains (9, 11).

To articulate how the second wave of *Hox* gene expression follows the first, it is necessary to know where in the genome the responsible regulatory regions lie. The main sources are likely the gene-poor yet highly conserved regions (“gene deserts”) that flank both sides of the *HoxD* cluster (12). To pinpoint specific regulatory elements within these large (~1 MB) gene deserts, Andrey *et al.* used chromosomal capture, transient transgenic, and genomic deletion techniques, approaches that previously identified a series of enhancer elements in a neighboring telomeric gene desert that controls *Hoxd* gene expression in the presumptive digits of the late limb (13). Focusing on *Hoxd9* in the mouse, which is transcribed in the first phase of expression, the authors observed that the gene is not in physical contact with the telomeric desert but contacts a centromeric desert on the opposite end of the cluster, where two enhancers robustly drive expression in the early limb bud.

Are individual genes within the cluster regulated by only one or both of the two distinct regulatory landscapes? Andrey *et al.* found that genes at the extremes of the cluster only contact the deserts they are adjacent to, regardless of developmental stage or transcriptional activity. By contrast, genes within

the center of the cluster (*Hoxd9-11*) have a more dynamic interaction profile. During the early phase of limb development, these central *HoxD* genes contact the centromeric gene desert; both regions possess chromatin marks of active enhancers and genes, indicating that their interaction results in early-phase *HoxD* expression. During the late phase of limb development, *Hoxd9-11* no longer contact the centromeric desert but contact the telomeric desert instead. This shift in contact also correlated with the presence of active chromatin marks on the telomeric desert.

Intriguingly, the centromeric desert is shut down at the appropriate time, when the switch normally takes place, even if the telomeric desert is deleted. Hence, Andrey *et al.* conclude that the two deserts are functionally independent. However, even if the repressive epigenetic marks can be laid down on the centromeric desert in the absence of the telomeric desert, the signaling input that causes the centromeric desert to shut down could be the same as that which activates the telomeric desert. The nature of the signals orchestrating the switch remains an important open question.

Another interesting aspect of *Hoxd* gene regulation is the gap that lies between the forearm domain, where the *Hoxd* genes are under the control of the centromeric desert, and the distal domain, where they are regu-

lated by telomeric enhancers. The chromatin state in this gap, where *Hoxd* genes are inactive, is not known. The cluster may continue to make centromeric contacts without maintaining expression, or it may have switched to telomeric contacts without activating transcription. Regardless of the mechanism, this gap in *Hoxd* expression seems important as it corresponds to the domain of the future wrist, which appears to be specified either in response to low *Hoxd* activity, or through the directed action of *Hoxa13* (which is expressed there) in the absence of *Hoxd13* input (14). Another unique *Hox* code is found in the region of the presumptive thumb, where *Hoxd13* is expressed but *Hoxd11* and *Hoxd12* are silent. Perhaps this too is regulated at the level of the specific chromatin contacts in the telomeric desert.

In addition to the *HoxD* cluster, the *HoxA* cluster also has been coopted to regulate limb patterning. *Hoxa11* and *Hoxd11*

are roughly coexpressed in the proximal limb and *Hoxa13* and *Hoxd13* overlap extensively in the distal limb. It will be interesting from a comparative standpoint to unravel the chromosomal mechanisms used in the *HoxA* context.

The serial duplication of *Hox* genes potentiated a simple mechanism for their collinear expression along the main body axis. Andrey *et al.* have revealed how this organization also allowed new regulatory mechanisms to be superimposed on the clusters to direct collinear expression in new secondary locations and under new controls.

References

1. E. B. Lewis, *Nature* **276**, 565 (1978).
2. S. J. Gaunt, *Development* **103**, 135 (1988).
3. A. Graham, I. McGonnell, *Curr. Biol.* **9**, R630 (1999).
4. B. Turchini, D. Duboule, M. Kmita, *Nature* **443**, 985 (2006).
5. G. Andrey *et al.*, *Science* **340**, 1195 (2013).
6. M. Peifer, F. Karch, W. Bender, *Genes Dev.* **1**, 891 (1987).
7. N. Soshnikova, D. Duboule, *Science* **324**, 1320 (2009).
8. D. Duboule, G. Morata, *Trends Genet.* **10**, 358 (1994).
9. P. Dollé, J. C. Izpisua-Belmonte, H. Falkenstein, A. Renucci, D. Duboule, *Nature* **342**, 767 (1989).
10. C. E. Nelson *et al.*, *Development* **122**, 1449 (1996).
11. J. Zákány, M. Kmita, D. Duboule, *Science* **304**, 1669 (2004).
12. P. Tschoopp, D. Duboule, *Annu. Rev. Genet.* **45**, 145 (2011).
13. T. Montavon *et al.*, *Cell* **147**, 1132 (2011).
14. Y. Yokouchi *et al.*, *Genes Dev.* **9**, 2509 (1995).

INTRODUCTION

Getting into Shape

AS DEVELOPMENT PROGRESSES FROM A SINGLE FERTILIZED EGG TO 2, 4, 6, 8, 16 cells, and so on, the early apparent homogeneity soon transitions to cells displaying varied sizes and shapes. Cell adhesion and cortical tension, with their associated forces, contribute to such changes. Crowded cells are pushed and pulled, but some make their own way via cell-autonomous migration or chemotaxis. These events proceed in an amazingly precise, choreographed manner, both temporally and spatially. Distinct germ layers and ultimately the stereotypic body form result, with amazing robustness. This special issue presents exciting advances in understanding morphogenesis, or the development of body shape.

Morphogenetic events are quickly coming into focus through new imaging techniques. *Science's* online Review by Philipp Keller (p. 1184) looks at recent advances, with numerous figures and movies exemplifying the exciting possibilities to detail the dynamics of development as seen by light microscopy of live organisms. Morphogenesis can be viewed at short or long temporal scales to fit with fast subcellular rearrangements or slow organismal events, respectively, and at ever-expanding tissue depth. By combining imaging techniques with computational approaches and mathematical models, new facets of developmental discovery are made possible.

Epithelia are characterized by layers of densely packed cells that are joined by strong adhesive contacts. These tissues provide structural integrity to developing embryos and adult organs and serve as barriers to pathogens and protection from dehydration. Despite what appears to be a set structural form, epithelial cells display active dynamics with fluid behavior. Guillot and Lecuit (p. 1185) review mechanical aspects of epithelial cell junctions in cell division, cell extrusion, and cell intercalation, in which cells change shape and location to drive local tissue deformation.

Stem cells are uniquely able to self-renew and differentiate. Recent work shows that when certain stem cells are placed in the right environment, they can self-organize to form organlike structures. Sato and Clevers (p. 1190) review research in which single *Lgr5* stem cells develop into epithelial organoids that resemble *in vivo* intestinal epithelium. This *in vitro* morphogenesis provides complex structures that can be used for stem cell and organ research as well as disease modeling and regenerative medicine.

A collection of News articles on Mysteries of Development (p. 1156) explores what we don't yet understand about how growing organisms control size, how symbionts help drive development, why brains lose so many cells as they mature, and how the fetal environment shapes later health. By continuing to probe the components, movements, and mechanics involved in development, a deeper understanding of the makings of organismal life is gained, with expanded opportunities to address events when things go awry.

— BEVERLY A. PURNELL

Morphogenesis

CONTENTS

Reviews

- 1184 **Imaging Morphogenesis: Technological Advances and Biological Insights**
P. J. Keller
- 1185 **Mechanics of Epithelial Tissue Homeostasis and Morphogenesis**
C. Guillot and T. Lecuit
- 1190 **Growing Self-Organizing Mini-Guts from a Single Intestinal Stem Cell: Mechanism and Applications**
T. Sato and H. Clevers

See also *News Focus* p. 1156; *Science Careers*; and *Science Podcast* at www.sciencemag.org/special/morph

Science

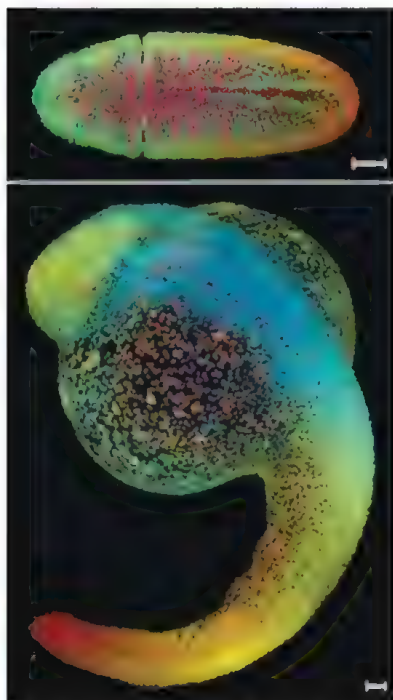
Imaging Morphogenesis: Technological Advances and Biological Insights

Philipp J. Keller

Background: Our understanding of developmental processes relies fundamentally on their in vivo observation. Morphogenesis, the shaping of an organism by cell movements, cell-cell interactions, collective cell behavior, cell shape changes, cell divisions, and cell death, is a dynamic process on many scales, from fast subcellular rearrangements to slow structural changes at the whole-organism level. The ability to capture, simultaneously, the fast dynamic behavior of individual cells, as well as their system-level interactions over long periods of time, is crucial for an understanding of the underlying biological mechanisms. Arriving at a complete picture of morphogenesis requires not only observation of single-cell to tissue-level morphological dynamics, but also quantitative measurement of protein dynamics, changes in gene expression, and readouts of physical forces acting during development. Live-imaging approaches based on light microscopy are of key importance to obtaining such information at the system level and with high spatiotemporal resolution.

Advances: Live imaging with light microscopy requires carefully balancing competing parameters, among which spatiotemporal resolution and light exposure of the living specimen are chief. To maximize the quantity and quality of information extracted from the specimen under observation, optimal use must be made of the limited number of photons that can be collected under physiological conditions. Emerging techniques for noninvasive in vivo imaging can record morphogenetic processes at temporal scales from seconds to days and at spatial scales from hundreds of nanometers to several millimeters, with minimal energy load on the specimen. These approaches are able to capture cellular dynamics in entire vertebrate and higher invertebrate embryos throughout their development. It has become possible to follow cell movements, cell shape dynamics, subcellular protein localization, and changes in gene expression simultaneously, for the entire undisturbed living system. The application of these methods to the study of morphogenesis in the fly, fish, and mouse has led to fundamental insights into the mechanisms underlying epithelial folding, the control of tissue morphogenesis by signaling pathways, and the role of physical forces in local and tissue-wide morphogenetic changes.

Outlook: Current efforts in microscopy technology development are aimed at advancing deep-tissue in vivo imaging, improving spatial resolution, and increasing temporal sampling. To unlock their full potential, these methods need to be matched with new computational approaches and physical models that help convert the resulting, highly complex image data sets into biological insights. With the availability of system-level data on cell behavior and gene expression, and the potential for a system-level analysis of biophysical tissue properties, we are reaching the point at which it will be feasible to develop computational approaches that incorporate these data into a single model capable of dissecting morphogenesis at the whole-organism level.



Live imaging of embryonic development. Nuclei-labeled *Drosophila* (top) and zebrafish (bottom) embryos were imaged with a simultaneous multiview light-sheet microscope (SiM-View). The embryos are shown at 3 and 22 hours postfertilization, respectively. Color indicates depth in the image. Scale bars: 50 μ m.

READ THE FULL ARTICLE ONLINE
<http://dx.doi.org/10.1126/science.1234168>

Cite this article as P. J. Keller, *Science* **340**, 1234168 (2013). DOI: 10.1126/science.1234168

ARTICLE OUTLINE

Challenges in the Live Imaging of Morphogenesis

Novel Approaches and Recent Advances in Light Microscopy

Advancing Our Understanding of Morphogenesis with Live Imaging

Computational Image Analysis and Modeling of Morphogenesis: The Next Frontier

Future Directions

BACKGROUND READING

J. Mertz, Optical sectioning microscopy with planar or structured illumination. *Nat. Methods* **8**, 811 (2011). doi:10.1038/nmeth.1709

A. C. Oates, N. Gorfinkel, M. González-Gaitán, C. P. Heisenberg, Quantitative approaches in developmental biology. *Nat. Rev. Genet.* **10**, 517 (2009). doi:10.1038/nrg2548

S. G. Megason, S. E. Fraser, Imaging in systems biology. *Cell* **130**, 784 (2007). doi:10.1016/j.cell.2007.08.031

K. Khairy, P. J. Keller, Reconstructing embryonic development. *Genesis* **49**, 488 (2011). doi:10.1002/dvg.20698

M. Behrndt *et al.*, Forces driving epithelial spreading in zebrafish gastrulation. *Science* **338**, 257 (2012). doi:10.1126/science.1224143

F. Bosveld *et al.*, Mechanical control of morphogenesis by Fat/Dachsous/Four-jointed planar cell polarity pathway. *Science* **336**, 724 (2012). doi:10.1126/science.1221071

Y. C. Wang, Z. Khan, M. Kaschube, E. F. Wieschaus, Differential positioning of adherens junctions is associated with initiation of epithelial folding. *Nature* **484**, 390 (2012). doi:10.1038/nature10938

REVIEW

Imaging Morphogenesis: Technological Advances and Biological Insights

Philipp J. Keller

Morphogenesis, the development of the shape of an organism, is a dynamic process on a multitude of scales, from fast subcellular rearrangements and cell movements to slow structural changes at the whole-organism level. Live-imaging approaches based on light microscopy reveal the intricate dynamics of this process and are thus indispensable for investigating the underlying mechanisms. This Review discusses emerging imaging techniques that can record morphogenesis at temporal scales from seconds to days and at spatial scales from hundreds of nanometers to several millimeters. To unlock their full potential, these methods need to be matched with new computational approaches and physical models that help convert highly complex image data sets into biological insights.

Vertebrates and higher invertebrates start as a single cell that develops into a fully functional organism comprising tens of thousands to trillions of cells, which are arranged in tissues and organs able to perform highly complex tasks. Understanding development as a

function of cell behavior at this system-wide level is a central goal of biology. This investigation, however, faces fundamental challenges, because morphogenesis—i.e., the shaping of an organism by cell movements, cell-cell interactions, collective cell behavior, cell shape changes, cell divisions, and cell death—is a dynamic process on multiple spatial and temporal scales: from submicrometer and subsecond dynamics of macromolecules inside each cell, to changes of cell shape that occur on the scale of micrometers within seconds, to cell movements that take place over distances of tens to hundreds of micrometers within minutes to hours, to structural changes on the tissue- and whole-organism level encompassing millimeter to centimeter length scales and hours to days of development (Fig. 1). Thus, the ability to capture, simultaneously, the fast dynamic behavior of individual cells, as well as their system-level interactions over long periods of time, is crucial for an understanding of the underlying biological mechanisms.

Howard Hughes Medical Institute, Janelia Farm Research Campus, 19700 Helix Drive, Ashburn, VA 20147, USA.

E-mail: kellerp@janelia.hhmi.org

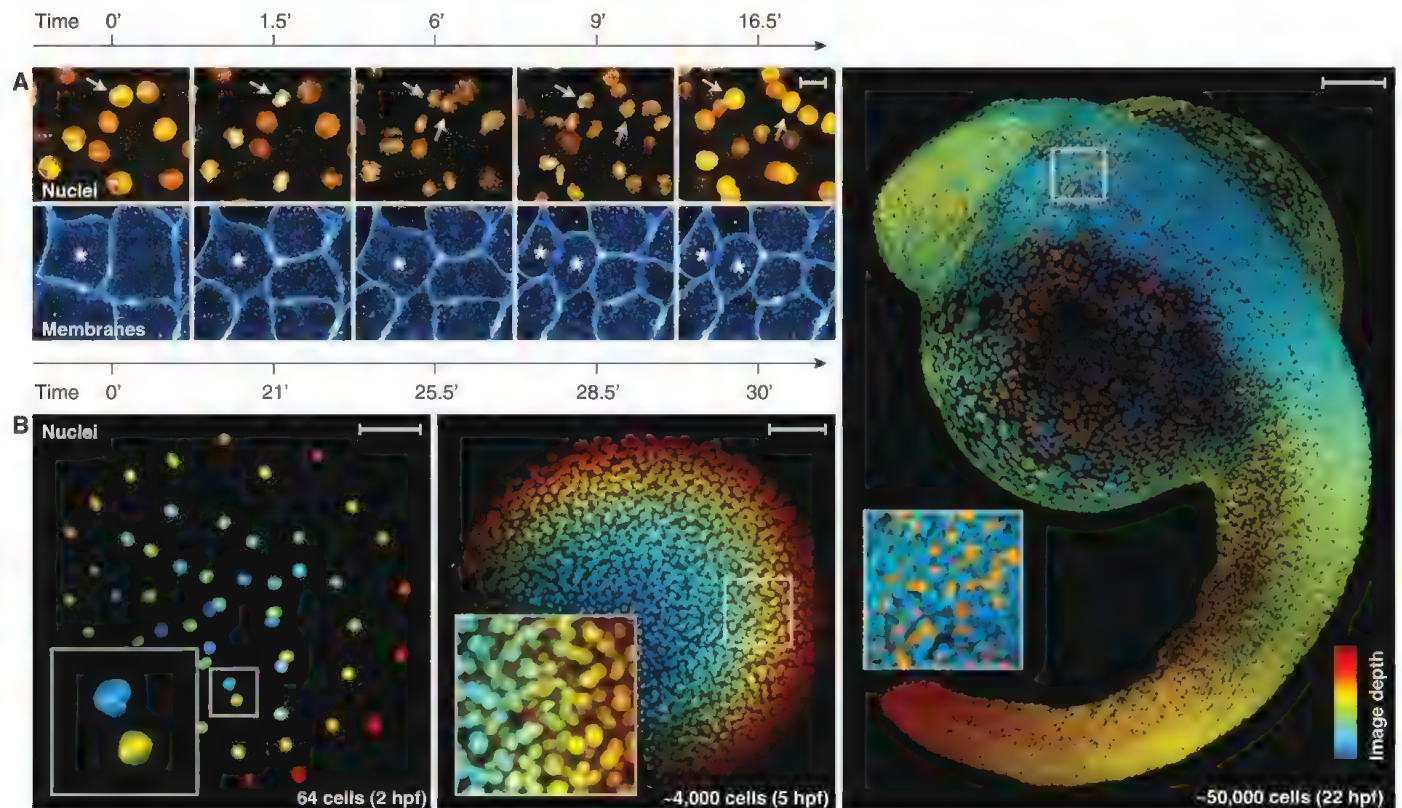


Fig. 1. Spatiotemporal scales of morphogenesis. Morphogenesis, illustrated here for the zebrafish embryo, involves multiple spatial and temporal scales: from fast, local cell shape changes and cell movements (A) to slow but large-scale structural changes on the tissue- and whole-embryo level (B). Images were recorded with digital scanned laser light-sheet microscopy (DSLMM) and simultaneous multiview light-sheet microscopy (SiMView) (2, 25). (A) Nuclei

(top) and membrane (bottom) dynamics in two different locations of a 2-hour-old zebrafish embryo. Arrows and asterisks highlight examples of dividing cells. (B) Whole-embryo projections of nuclei-labeled zebrafish embryos at different developmental stages, showing the rapid increase in cell count and morphological complexity in early embryogenesis. Insets: enlarged views of highlighted areas. Scale bars: 20 μm (A), 100 μm (B).

Morphogenesis

In addition to tackling the spatial and temporal challenges associated with the observation of single-cell to tissue-level morphological dynamics (1–3), a comprehensive understanding of morphogenesis requires quantitative measurements of protein dynamics (4), changes in gene expression (5–7), and (direct or indirect) readouts of physical forces acting during development (8). Knowing the spatiotemporal relationship of these core constituents is often the key to elucidating developmental mechanisms. Live-imaging approaches based on light microscopy are of central importance to obtain such information at the system level and with high spatiotemporal resolution (Fig. 2).

The development of advanced microscopy technology for noninvasive in vivo imaging is indispensable for advancing our understanding of morphogenesis. It is now feasible to obtain comprehensive information on the cellular dynamics in entire developing vertebrate and higher invertebrate embryos throughout their development (movies S1 to S10). It is possible to record cell movements, cell shape dynamics, cell divisions, and gene expression information simultaneously, for the entire undisturbed living system. At the same time, substantial efforts are underway to experimentally characterize the biophysical properties of tissues, in particular the parameters describing their responses to external mechanical forces and the adhesive behavior of their cellular components (9).

With the emergence of powerful, new imaging techniques that produce large image data sets of complex developmental processes at unprecedented detail, it is equally important to devise new computational methods to analyze such microscopy data in a biologically meaningful way. By integrating biological material properties with comprehensive live-imaging data of entire developing embryos at the subcellular level, computational models of morphogenesis with predictive power—projecting the tissue- or even embryo-wide morphogenetic consequences of genetic or mechanical perturbations—are finally within reach.

Challenges in the Live Imaging of Morphogenesis

Live-imaging applications require carefully balancing competing parameters (Fig. 3). High imaging speeds are required to capture fast cellular processes and to facilitate effective live imaging of large biological specimens. High spatial resolution is needed to follow intracellular processes or to resolve structural details of cell-cell interactions. High signal-to-noise ratios are crucial to obtain interpretable images and to robustly automate computational image analysis. Long observation periods are needed to capture continuous data sets of nonstereotypic processes over relevant developmental time scales. Comprehensive physical coverage is required to follow developmental events on the whole-organism level. Finally, low levels of light exposure are essential to

reduce photobleaching of fluorescent markers and minimize phototoxic effects that may impact normal development.

These key parameters are limited by fundamental physical and biological constraints that are independent of microscope design. For example, with a given amount of fluorescent proteins, spatial resolution can be improved only at

the expense of temporal sampling, signal-to-noise ratio, or maximum observation length, owing to the higher light exposure of the sample and increased rate of fluorescent protein consumption (Fig. 3A). The optimal imaging method thus makes maximum use of the parameter space that is allowed. The requirement of practical applicability to live observations of biological processes

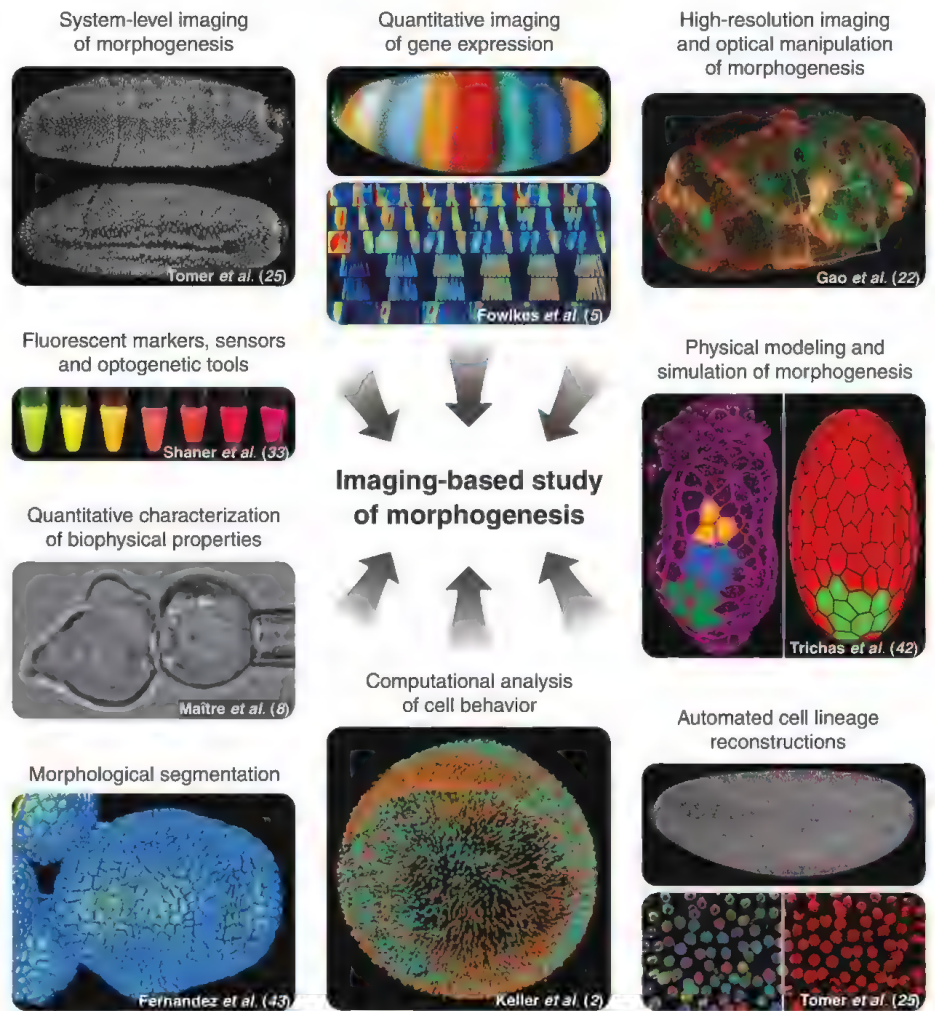


Fig. 2. Imaging-based study of morphogenesis. The imaging-based study of morphogenesis involves optical methods, biotechnology, and biophysical measurements, as well as physical modeling and computational approaches to image analysis. Specific examples of these general classes of techniques are depicted in each box. Often, most—if not all—of these approaches are combined to arrive at a quantitative understanding of morphogenetic processes. Clockwise, from top right panel: High-resolution Bessel SR-SIM live imaging of myosin (green) and membranes (orange) in an early *C. elegans* embryo [reprinted from (22)]; imaging (left, examples of groups of cells that share a central vertex highlighted in color) and modeling (right, anterior visceral endoderm cells shown in green) of an early mouse embryo [reprinted from (42)]; automated cell lineage reconstruction in the *Drosophila* syncytial blastoderm (top: whole embryo, bottom: enlarged view) [reprinted from (25)]; global cell tracking in the early zebrafish embryo [reprinted from (2)]; cell segmentation in an *Arabidopsis* flower [reprinted from (43)]; assay for measuring mechanical parameters controlling cell-cell contact formation by ex vivo adhesion of progenitor cell doublets [reprinted from (8)]; fluorescence image of purified proteins mHoneydew, mBanana, mOrange, tdTomato, mTangerine, mStrawberry, and mCherry (from left to right) [reprinted from (33)]; SIMView live imaging of a nuclei-labeled *Drosophila* embryo at the onset of gastrulation (top: dorsal view, bottom: ventral view) [reprinted from (25)]; visualization of gene expression data obtained by two-photon imaging of early *Drosophila* embryos (top: expression of gap genes *fkh*, *gt*, *hb*, *kni*, and *Kr*; bottom: expression of *kni*, *gt*, *hb*, *eve*, *ftz*, and *slp1* at different time points) [reprinted from (5)].

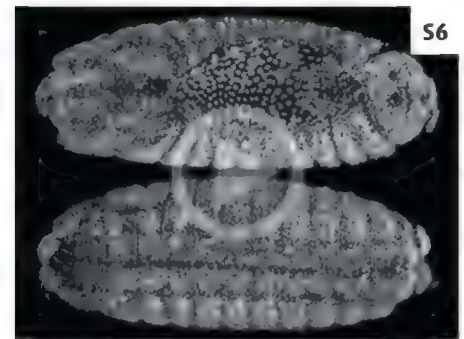
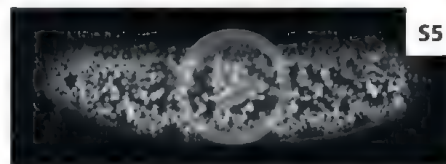
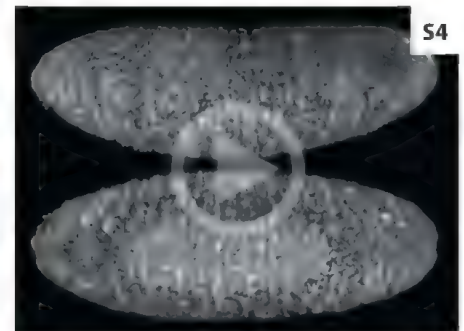
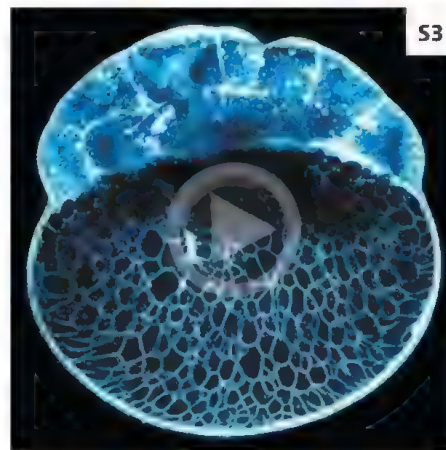
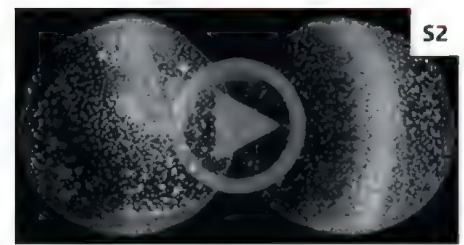
(Figs. 3B and 4 and movies S11 to S15) often favors an overall optimization of performance over a microscope design that provides a substantial improvement in a single parameter at the expense of others. Although different live-imaging techniques are qualitatively constrained by the same fundamental trade-offs, they often exhibit substantial performance differences as the direct result of their methodological design.

Confocal fluorescence microscopes are currently the most commonly used imaging systems with optical sectioning capability [the ability to resolve three-dimensional (3D) structures]. This mature, commercially available technology represents a state-of-the-art approach to studying morphogenesis by live imaging and can resolve biological processes on a multitude of spatial scales, from subcellular to whole-tissue level (Fig. 4, B to D, and movies S7, S9, S11 to S13, and S15).

In point-scanning confocal fluorescence microscopy, a beam of laser light is focused into the specimen to excite fluorescent molecules. Fluorescence light is generated especially, but not exclusively, at the focus. To ensure that only fluorescence light originating from the small focal volume is detected, a small pinhole in the detection system is used to block out-of-focus signal. An entire 3D image can thus be recorded by scanning the laser focus through the sample and measuring the signal sequentially at each focus position.

A major drawback of this concept is the very inefficient use of light and fluorescent markers, as well as the very high light exposure of the sample. At the same time, the point-scanning approach introduces a fundamental imaging speed limit. The discovery of two-photon excitation presents an effective approach to address the first issue: Laser light at approximately twice the conventional wavelength is used to excite fluorescence only in the focal volume, where the power density is high enough to efficiently trigger multiphoton absorption. The use of this longer-wavelength light also allows penetrating deeper into biological tissues (10) (Figs. 4A and 5, A and B, and movies S1 and S14). However, in the conventional implementation of this approach as a point-scanning technique, it suffers from the same limitations in speed and signal-to-noise ratio as confocal fluorescence microscopy.

To address these limitations, a new fluorescence imaging method was developed that combines intrinsic optical sectioning with wide-field detection. This method, known as light-sheet microscopy (11, 12), allows entire multimegapixel images to be acquired in a single, spatially confined illumination step: In contrast to the point excitation approach in confocal microscopy, an entire micrometer-thin volume is illuminated with laser light entering the sample from the side. The fluorescence emitted by reporter molecules in this thin volume is collected with an objective lens oriented at a right angle to the light sheet.



Movie S1. Imaging mesoderm spreading in the *Drosophila* embryo with point-scanning two-photon microscopy. Dorsal (part 1) and posterior (part 2) views of a H2A-GFP expressing embryo are shown. This movie was published previously (1). [Credit: McMahon *et al.* 2008 (1)]

Movie S2. Multiview imaging of zebrafish embryonic development with digital scanned laser light-sheet microscopy (DSLM). The H2B-eGFP mRNA injected zebrafish embryo was imaged from the 64-cell stage for 25 hours in intervals of 90 s (453,620 high-resolution images, 3.5 TB). This movie was published previously (2). [Credit: Keller *et al.* 2008 (2)]

Movie S3. Third-harmonic generation (THG) imaging of the early zebrafish embryo. THG imaging (1200 nm excitation wavelength) started in the one-cell stage. A sagittal thick slice is displayed. Scale bar: 100 μ m. This movie was published previously (50). [Credit: Olivier *et al.* 2010 (50)]

Movie S4. Imaging *Drosophila* embryogenesis with two-photon light-sheet microscopy (2p-SPIM). 3D-rendered views of a fly embryo with GFP-labeled nuclei are shown over a period of 18 hours. Scale bar: 100 μ m. This movie was published previously (24). [Credit: Truong *et al.* 2011 (24)]

Movie S5. Imaging a stage 16 *Drosophila* embryo with simultaneous multiview two-photon light-sheet microscopy (2p-SiMView). The volume of a nuclei-labeled *Drosophila* embryo is shown slice by slice. This movie was published previously (25). [Credit: Tomer *et al.* 2012 (25)]

Movie S6. Imaging *Drosophila* embryogenesis with simultaneous multiview light-sheet microscopy (SiMView). The fly embryo with GFP-labeled nuclei was imaged for 17 hours in intervals of 30 s (1,066,520 high-resolution images, 11 TB). This movie was published previously (25). [Credit: Tomer *et al.* 2012 (25)]

Although this approach is derived from a more than 100-year-old idea (13), its outstanding practical performance has been demonstrated only recently (12). Light-sheet fluorescence microscopy provides substantially improved imaging

speed and signal-to-noise ratio, while minimizing the light exposure of the specimen (14) (Figs. 1 and 5, C to F, and movies S2, S4 to S6, S8, and S10). It is thus particularly well suited to biological live-imaging applications (15) and has an

Morphogenesis

outstanding potential in the systematic, quantitative study of development (2, 12) and function (16, 17) of complex biological systems.

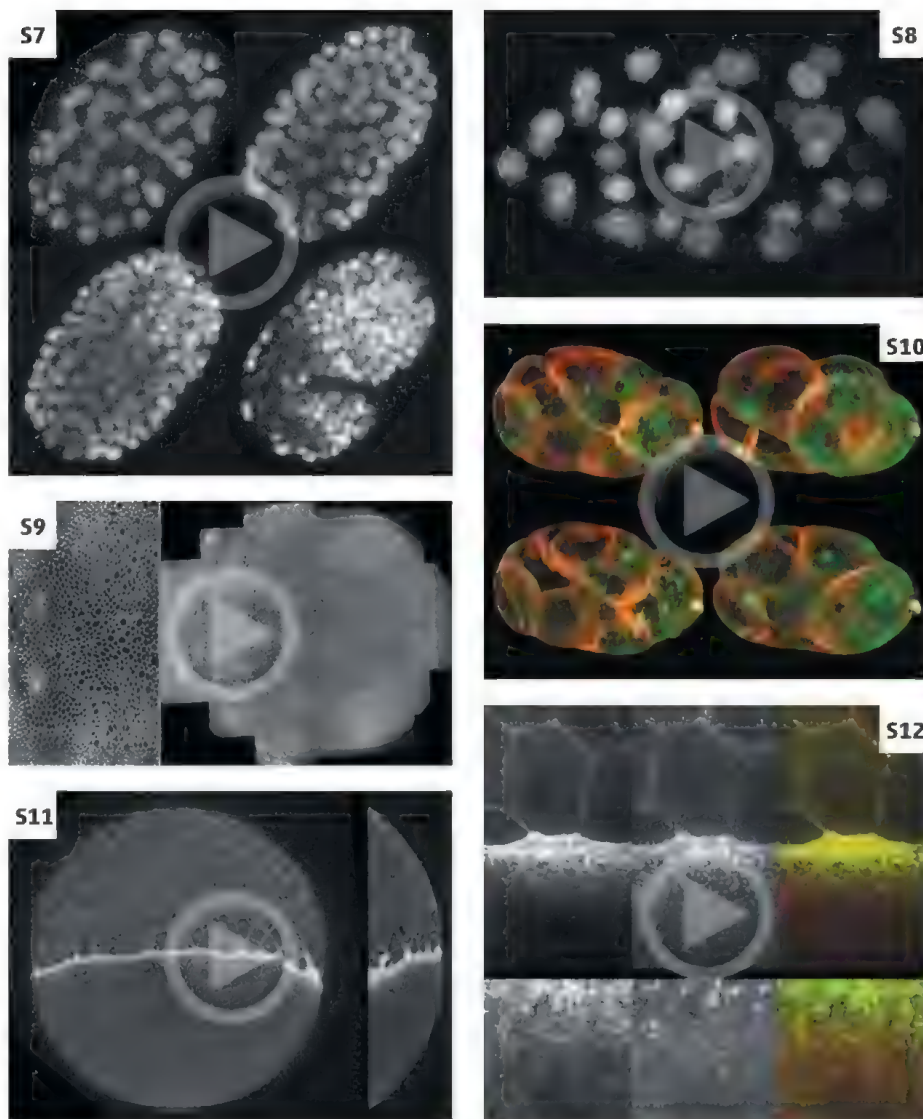
Novel Approaches and Recent Advances in Light Microscopy

Confocal and two-photon fluorescence imaging approaches have gone through numerous iterations of refinement and optimization over the course of several decades. Powerful commercial systems are readily available, and recent conceptual advances in light microscopy may soon open the door to an entirely new generation of these methods (18–20). By contrast, the emerging field of light-sheet microscopy still largely relies on custom-built instruments, some of which have been crafted as highly affordable hybrids by extending basic commercial imaging platforms with custom light-sheet illumination modules (3). In the past 2 years, the development of light-sheet-based fluorescence microscopy has experienced rapid progress, which is of particular relevance to the imaging-based study of morphogenesis. These advances address the most critical limitations of conventional techniques; namely, spatial resolution (21, 22) (Fig. 5D and movie S10), imaging speed (3, 16, 23) (Fig. 5C and movies S7 and S8), and optical access to developmental processes in nontransparent living organisms (24–26) (Fig. 5, E and F, and movies S4 to S6). By virtue of these new capabilities, state-of-the-art light-sheet microscopes enable the design of live-imaging experiments that were previously not possible.

Spatial Resolution

Bessel beam light-sheet microscopy provides substantially improved spatial resolution (21). In conventional scanned light-sheet microscopy, a thin volume section of the sample is illuminated by rapidly moving a weakly focused Gaussian laser beam across the field-of-view (2). Because the laser beam is oriented parallel to the recorded plane, its thickness directly influences the axial resolution of the microscope, which is typically on the order of a few micrometers. By using Bessel beams with a thinner central intensity peak for specimen illumination, the axial resolution can be substantially improved, to the point where it becomes comparable to the typically much better lateral resolution—on the order of 300 nm—of the microscope (21). In addition, the use of Bessel beams has been shown to reduce the overall amount of scattering-induced image artifacts and improve penetration of biological tissues (27).

The Bessel beam's thin core is surrounded by a series of concentric rings, which, if left unaccounted for, will degrade image quality compared to a recording made with Gaussian beams. However, this issue can be mitigated, for example, by using structured illumination (i.e., patterned light for specimen illumination) (28, 29) or two-photon excitation (21). Structured illumina-



Movie S7. Imaging *C. elegans* embryogenesis with spinning-disk confocal microscopy. An embryo of the BV24 GFP-histone strain was imaged at 1 volume/min. This movie was published previously (3). [Credit: Wu *et al.* 2011 (3)]

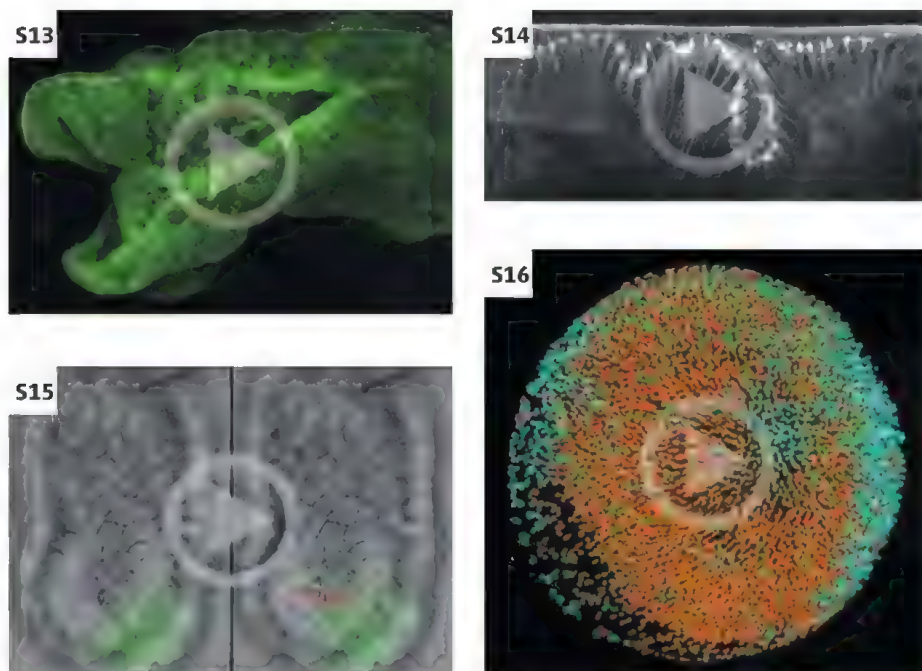
Movie S8. Imaging *C. elegans* embryogenesis with inverted selective plane illumination microscopy (iSPIM). An embryo of the BV24 GFP-histone strain was imaged at 30 volumes/min from the two-cell stage until hatching. This movie was published previously (3). [Credit: Wu *et al.* 2011 (3)]

Movie S9. Imaging epithelium morphogenesis in the *Drosophila* dorsal thorax with spinning disk confocal microscopy. Dorsal thorax tissue expressing E-Cad:GFP was imaged between 11 and 35 hAPF in 5 min intervals. The positions of macrochaetae and midline are indicated by white circles and by a black dotted line, respectively. This movie was published previously (36). [Credit: Bosveld *et al.* 2012 (36)]

Movie S10. Imaging early *C. elegans* embryogenesis with Bessel beam super-resolution structured plane illumination microscopy (SR-SIM). Membrane dynamics during early embryonic development (part 1) and relationship between membrane morphology and myosin expression (part 2) are shown. This movie was published previously (22). [Credit: Gao *et al.* 2012 (22)]

Movie S11. Imaging zebrafish epiboly with confocal fluorescence microscopy. *Tg(actb1:GFP-utrCH)* labeling F-Actin was imaged throughout the course of epiboly (40–90% epiboly). Left: Lateral view. Right: Orthogonal view. Scale bar: 100 μ m. This movie was published previously (37). [Credit: Behrndt *et al.* 2012 (37)]

Movie S12. Imaging actomyosin flows in zebrafish epiboly with spinning-disk confocal fluorescence microscopy. *Tg(actb1:myl12.1-eGFP)* labeling Myosin-2 (left), injected with lifeact-RFP mRNA labeling F-Actin (middle), was imaged at 60 to 70% epiboly. Right: Dual-color merge. White rectangle indicates region of magnified view (bottom). Scale bars: 10 μ m. This movie was published previously (37). [Credit: Behrndt *et al.* 2012 (37)]



Movie S13. Imaging neural tube closure in the mouse embryo with confocal fluorescence microscopy. Movie shows dorsal side of a 13-somite wild-type embryo expressing *Ven^{Myr}* highlighting cell membranes. Scale bar: 100 μm . This movie was published previously (51). [Credit: Massarwa and Niswander 2013 (51)]

Movie S14. Imaging the dynamics of adherens junctions during *Drosophila* dorsal fold formation with point-scanning two-photon microscopy. An optical mid-sagittal section of the dorsal epithelium expressing E-Cadherin-GFP was imaged every 5 s from late cellularization to early gastrulation. This movie was published previously (39). [Credit: Wang *et al.* 2012 (39)]

Movie S15. Imaging mouse development with confocal fluorescence microscopy. Time-lapse movie shows rosettes forming in the visceral endoderm during anterior visceral endoderm (AVE) migration. AVE cells are marked by Hex-GFP fluorescence (green). DIC images were acquired with the confocal's transmitted light PMT. Scale bar: 50 μm . This movie was published previously (42). [Credit: Trichas *et al.* 2012 (42)]

Movie S16. Reconstructing zebrafish embryonic development from DSLM image data. Orthographic rendering of the computational reconstruction of the data set shown in movie S2. Color-code indicates movement speed of each nucleus (cyan to orange: 0 to 1.2 $\mu\text{m}/\text{min}$). This movie was published previously (2). [Credit: Keller *et al.* 2008 (2)]

tion in scanned light-sheet microscopy has been shown to enable contrast enhancement in non-transparent living specimens (30), where image quality usually suffers from light scattering. By combining Bessel beam light-sheet microscopy with this type of illumination strategy, exceptionally high spatial resolution, image contrast, and signal strength can be achieved through subsequent image reconstruction with algorithms previously developed for superresolution structured illumination microscopy (SR-SIM) (22). In contrast to typical superresolution approaches, this method minimizes the energy load on the specimen, provides acquisition rates of hundreds of images per second, and is applicable to living multicellular specimens. Recently, this method has been used to image cell shape dynamics in entire developing *Caenorhabditis elegans* embryos at 200-nm lateral resolution and 400-nm axial resolution (22), demonstrating its potential for the study of morphogenesis (Fig. 5D and movie S10, study “h” in Fig. 3B).

Penetration Depth

Another key challenge in all light-based imaging techniques is the fundamentally limited penetration depth of light in biological tissues, which constrains imaging of large living specimens. Even in relatively transparent tissues, conventional methods generally only reach depths of several tens to a few hundreds of micrometers when using visible light. Strategies being developed to address this limitation include the use of adaptive optics (18, 31) and deep-tissue penetration by acousto-optic fluorescence imaging (19, 32). For example, through use of an approach to adaptive optics in which the rear pupil of the objective lens is segmented, substantial improvements in resolution and signal strength have been achieved at depths up to 400 μm into mammalian tissue, thereby addressing typical limitations in penetration depth arising from optical aberrations (18). Moreover, fluorescence imaging up to 2 mm deep inside highly scattering media has recently been demonstrated

by modulating light propagation through the tissue with ultrasound pulses (19).

Penetration depth can also be increased by the use of fluorescent probes excitable with light of longer wavelengths (33, 34), in particular in the far red or even infrared, where biological tissues generally scatter and absorb considerably less light and thus appear more transparent. The concept of nonlinear excitation in two-photon microscopy takes this idea one step further and constitutes a powerful and well-established strategy to facilitate observations inside living specimens at greater depths than are possible with conventional imaging approaches (Fig. 5, A and B, and movies S1 and S14). The recent introduction of nonlinear excitation in scanned light-sheet microscopy combines the strengths of both methods, enabling, for example, a twofold increase in penetration depth in live imaging of *Drosophila* embryos (24) (Fig. 5E and movie S4).

Imaging Speed and Spatial Coverage

By simultaneously recording multiple complementary views of the sample in a light-sheet microscope, fast cellular dynamics can be rapidly imaged even for large, nontransparent biological specimens (25, 26) (Fig. 5F). This approach synergizes with the use of nonlinear excitation (movie S5) and enables quantitative analyses of biological processes at the system level, such as comprehensive cell tracking through the cell division waves in the blastoderm-stage *Drosophila* embryo (25). In addition, light-sheet-based simultaneous multiview imaging greatly improves volumetric imaging speeds, providing sustained image acquisition rates on the order of 175 million voxels per second. This performance exceeds that obtained with state-of-the-art point-scanning imaging techniques by a factor of 10 to 100 and enabled, for example, recording the morphogenesis of entire *Drosophila* embryos at 30-s intervals throughout their development (25) (movie S6, study “b” in Fig. 3B). Considering that light-sheet microscopy benefits directly from advances in high-speed camera technology, such as the recent progress in scientific complementary metal oxide semiconductor (sCMOS) technology, a further increase in imaging speed by at least a factor of 10 can be expected in the near future (16).

The techniques discussed in this section have been implemented only recently and, for the most part, only proof-of-principle experiments have been performed. Considering the high relevance of their new capabilities for biological live-imaging applications, these methods are likely to quickly find their way into studies of morphogenesis.

Advancing Our Understanding of Morphogenesis with Live Imaging

The use of live-imaging strategies and their combination with optical sample manipulation, computational modeling, and quantitative image analysis are indispensable for advancing our understanding of the key mechanisms driving morphogenesis. Imaging-based investigations enable, for example,

Morphogenesis

cell lineage tracing in the developing organism (35), analyzing the role of signaling pathways in directing morphogenetic events (36), and studying the role of physical forces in local and tissue-wide morphogenetic changes (8, 37). The most frequently used model systems in such studies include the fruit fly, zebrafish, and mouse (Fig. 4).

Fruit Fly

Drosophila melanogaster is a well-established model system in developmental biology, owing to the exceptionally wide spectrum of readily available genetic tools. However, resolving cellular dynamics in early development requires imaging approaches with excellent optical penetration (Fig. 5A), because light is strongly scattered and absorbed in the *Drosophila* embryo (38).

Live imaging with two-photon fluorescence microscopy is well suited to revealing dynamic processes deep inside the embryo. Using this method, a link between differential positioning of adherens junctions and the initiation of epithelial folding was recently uncovered (39) (Fig. 4A and movie S14). These observations (study “d” in Fig. 3B) showed that by modulating epithelial apical-basal polarity, adherens junctions shift basally in those cells that are about to initiate dorsal transverse folds in the early *Drosophila* embryo. This basal shift alters the shape of initiating cells and forces the lateral membrane of adjacent cells to bend toward the initiating cells (39).

For imaging superficial tissues, one-photon excitation strategies are advantageous, as they have the potential to yield excellent signal-to-noise ratios at higher image-acquisition speeds. Fast time-lapse imaging of the entire *Drosophila*

dorsal thorax with spinning-disk confocal microscopy (study “f” in Fig. 3B), in combination with quantitative image analysis and physical modeling, provided new insights into the control of tissue morphogenesis by signaling pathways (36) (Fig. 4B and movie S9). This imaging-based approach revealed how the Fat/Dachsous/Four-Jointed planar cell polarity (PCP) pathway controls morphogenesis of the thorax. It linked the planar polarization established via this pathway to the generation of anisotropy of junction tension by the myosin Dachs and demonstrated that this anisotropy leads to oriented cell rearrangements (36).

Zebrafish

Zebrafish embryos and larvae lend themselves particularly well to live-imaging studies using light microscopy, owing to their optical transparency.

A recent multidisciplinary study combining live imaging of zebrafish gastrulation with confocal fluorescence microscopy (Fig. 4C and movies S11 and S12), computational modeling, and optical manipulation through laser ablation (Fig. 4C’) revealed the mechanism that allows the contractile actomyosin ring to drive the spreading of the enveloping cell layer over the yolk cell (37). Detailed modeling of the forces acting during this morphogenetic process, and time-lapse imaging after local disruption of the actomyosin ring by laser cutting (study “g” in Fig. 3B), showed that this ring functions not only by circumferential contraction but also by a flow-friction mechanism. This investigation thus advanced our understanding of the function of actomyosin rings in epithelial morphogenesis and shed new light on the role of cortical flows in morphogenetic pattern formation (37).

A related study in the zebrafish model system investigated cell-cell contact formation of progenitor cells and combined these biophysical measurements with in vitro and in vivo imaging experiments of progenitor cell sorting (8). This approach helped to clarify the different roles of cell adhesion and cell cortex tension in driving cell sorting during gastrulation: Cell adhesion is needed to mechanically couple cortices at cell-cell contacts and allows cell cortex tension to control expansion of such contacts (8).

Mouse

The study of morphogenesis in mammalian model systems is another field exhibiting rapid progress. The mouse constitutes a leading model system in this respect, owing to its close genetic and physiological similarities to humans and the powerful tools available for manipulating its genome. However, preparation and ex utero culturing of mouse embryos for live imaging with light microscopy are challenging, and sophisticated imaging assays are required for light-based analysis of this exceptionally light-sensitive organism (40) (movies S13 and S15). Consequently, many basic questions about the developmental dynamics underlying mouse embryogenesis are currently unanswered (41). When do morphogen gradients form and start to act on cells? How do the germ layers form on the cellular level? Are the tissue boundaries evident in late stages already established in the pool of early precursor cells?

Whole-embryo live-imaging assays have a high potential to shed new light on mammalian morphogenesis. For example, a recent study examined the role of rosettes—groups of five or

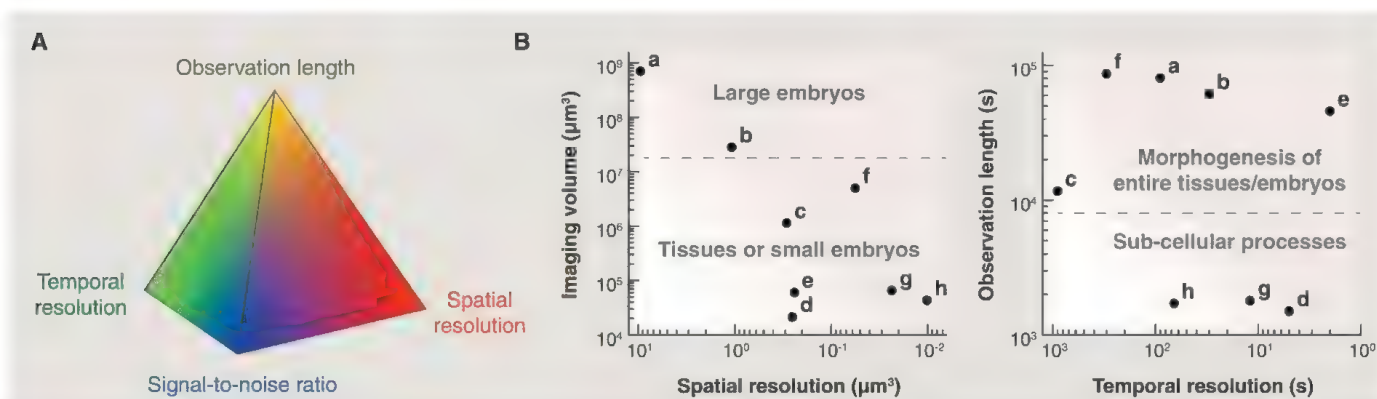


Fig. 3. Parameter space in light-based live imaging of biological specimens. (A) The design of in vivo imaging experiments is fundamentally constrained by the light-induced damage capacity of the biological system (maximum allowed amount of light exposure before impacting the biological process) and, for fluorescence microscopy, the total photon yield of the fluorescent markers in the specimen. Many imaging parameters, of which the four most important ones are shown as the corners of the tetrahedron, compete for these two resources and need to be carefully balanced to obtain optimal results in a given experiment. Increasing one parameter intrinsically reduces the maximum performance achievable for at least one of the other

parameters. (B) Examples of specimen size, spatial resolution (provided as theoretical size of focal volume), observation length, and temporal resolution from eight imaging studies of morphogenetic processes: cell dynamics in entire embryos [a, (2); b, (25); e, (3)], anterior visceral endoderm migration [c, (42)], dynamics of adherens junctions [d, (39)], morphogenesis of pupal thorax [f, (36)], actomyosin flows in the yolk syncytial layer [g, (37)], and membrane dynamics in early embryos [h, (22)]. These examples involve different model systems [zebrafish (a,g), fruit fly (b,d,f), mouse (c), nematode (e,h)] and imaging techniques [DSLM (a), SiMView (b), confocal (c), two-photon (d), iSPIM (e), spinning disk (f,g), Bessel SR-SiM (h)].

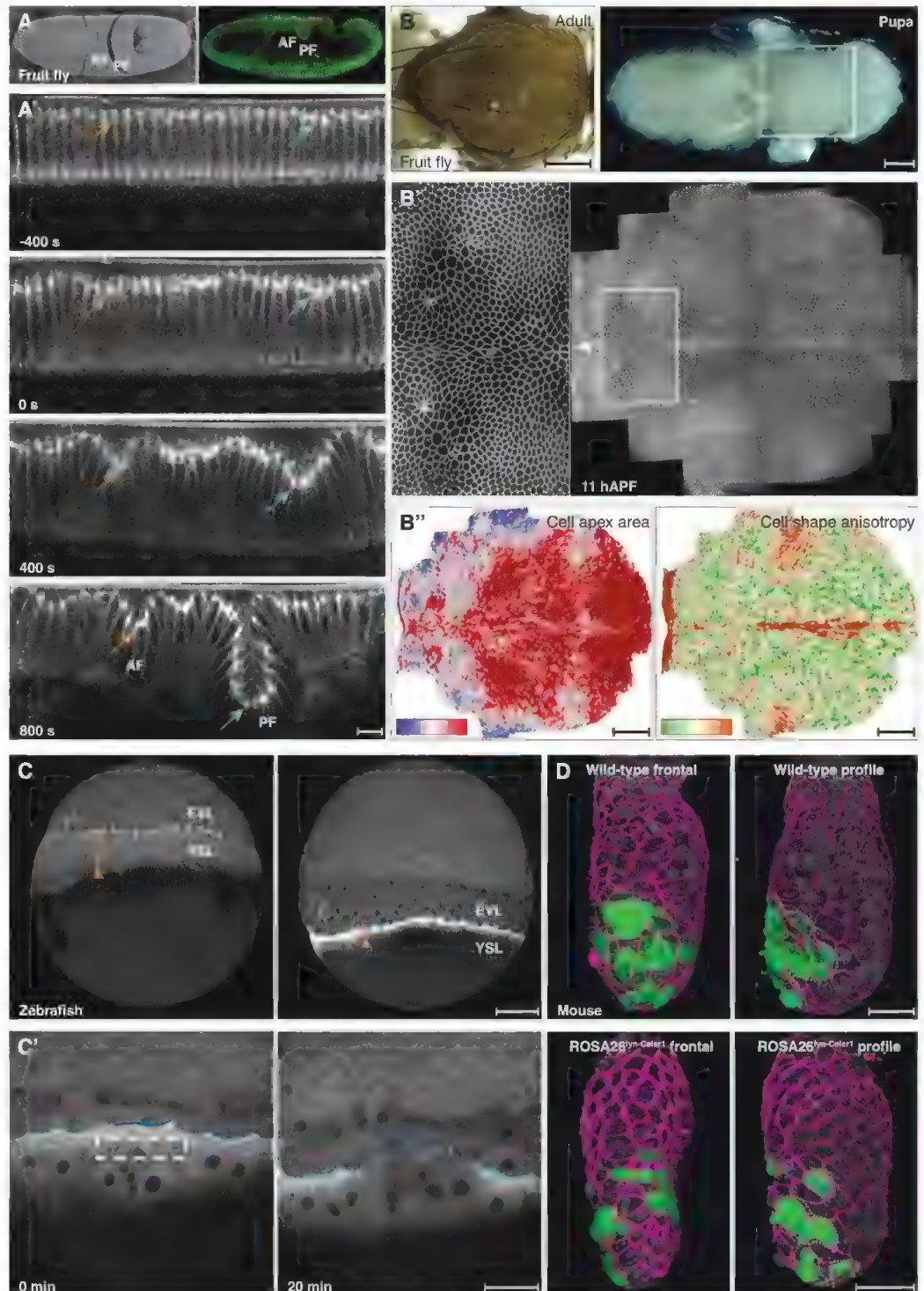
more cells that share a common central vertex—during migration of the anterior visceral endoderm (Fig. 4D and movie S15) (42). The visceral endoderm in the egg-cylinder-stage mouse embryo is a continuous epithelial sheet consisting of two

regions with very different cellular behaviors: One exhibits cell movement and intercalation, whereas the other is essentially static. By using time-lapse imaging with confocal microscopy (study “c” in Fig. 3B) and computational mod-

eling, rosettes were found to facilitate ordered migration of the anterior visceral endoderm cells within the dynamic region of the epithelium. Interestingly, the rosettes are not formed passively but rather as a result of PCP signaling and buffer the

Fig. 4. Advancing our understanding of morphogenesis with live imaging.

(A) Morphology and cellular dynamics during *Drosophila* dorsal fold formation. Left: Scanning electron micrographs of the dorsal surface in a late *Drosophila* gastrula. Right: Confocal mid-sagittal sections of Neurotactin (green) and Runt (red) immunofluorescence. (A') Two-photon time-lapse mid-sagittal section of E-Cad:GFP (green fluorescent protein). Arrows, junctions of initiating cells in the anterior (AF, orange) and posterior (PF, cyan) folds undergo basal shift. See movie S14. [Reprinted from (39)] (B) *Drosophila* dorsal thorax in adult (left) and pupa [right, 11 hours after pupa formation (hAPF), without pupal case]. White box indicates position of thorax. (B') *Drosophila* pupa dorsal thorax tissue expressing E-Cad:GFP to label apical cell junctions, imaged by multiposition confocal microscopy (24 positions at 5-min resolution). The scutellum is magnified at the left (boxed region). (B'') Cell-level measurements at 11 hAPF. Colors: cell apex area, blue ($10 \mu\text{m}^2$) to red ($60 \mu\text{m}^2$); cell shape anisotropy, green (0.1) to brown (0.6). See movie S9. [Reprinted from (36)] (C) Actomyosin ring morphogenesis and function in zebrafish. In *Tg(actb1:myl12.1-eGFP)* embryos at 40% epiboly (left), an initially diffuse and broad actomyosin band (orange bar) narrows along the animal-vegetal axis to form a distinct cable-like structure at 70% epiboly (right). (C') Local disruption of the actomyosin ring in *Tg(actb1:myl12.1-eGFP)* embryos at 60% epiboly by consecutive ultraviolet-laser ablation (white dashed rectangle, left) reduces advancement of the adjacent EVL margin (dark blue, right). EVL, enveloping cell layer; YSL, yolk syncytial layer. See movies S11 and S12. [Reprinted from (37)] (D) Abnormal migration of anterior visceral endoderm (AVE, marked with dotted line in panels to the right) and cellular geometry in mouse mutants with disrupted PCP signaling. Top: En face and profile view of a representative wild-type embryo, illustrating stereotypical ordered migration of AVE cells. Bottom: En face and profile views of an equivalent stage *ROSA26^{lyn-Celsr1}* mutant, showing abnormal AVE migration. AVE cells appear to have broken into several groups and are spread much more broadly. Magenta: cell outlines (staining for ZO-1); green: AVE cells (Hex-GFP); gray: nuclei (DAPI, 4',6-diamidino-2-phenylindole). See movie S15. [Reprinted from (42)] Scale bars: 250 μm (B), 100 μm (B'', C), 50 μm (C', D), 10 μm (A').



Morphogenesis

disequilibrium in cell packing generated by movement of cells in only one part of the epithelium (42).

With the demonstrations of system-level imaging of morphogenesis in fruit fly (24–26) and

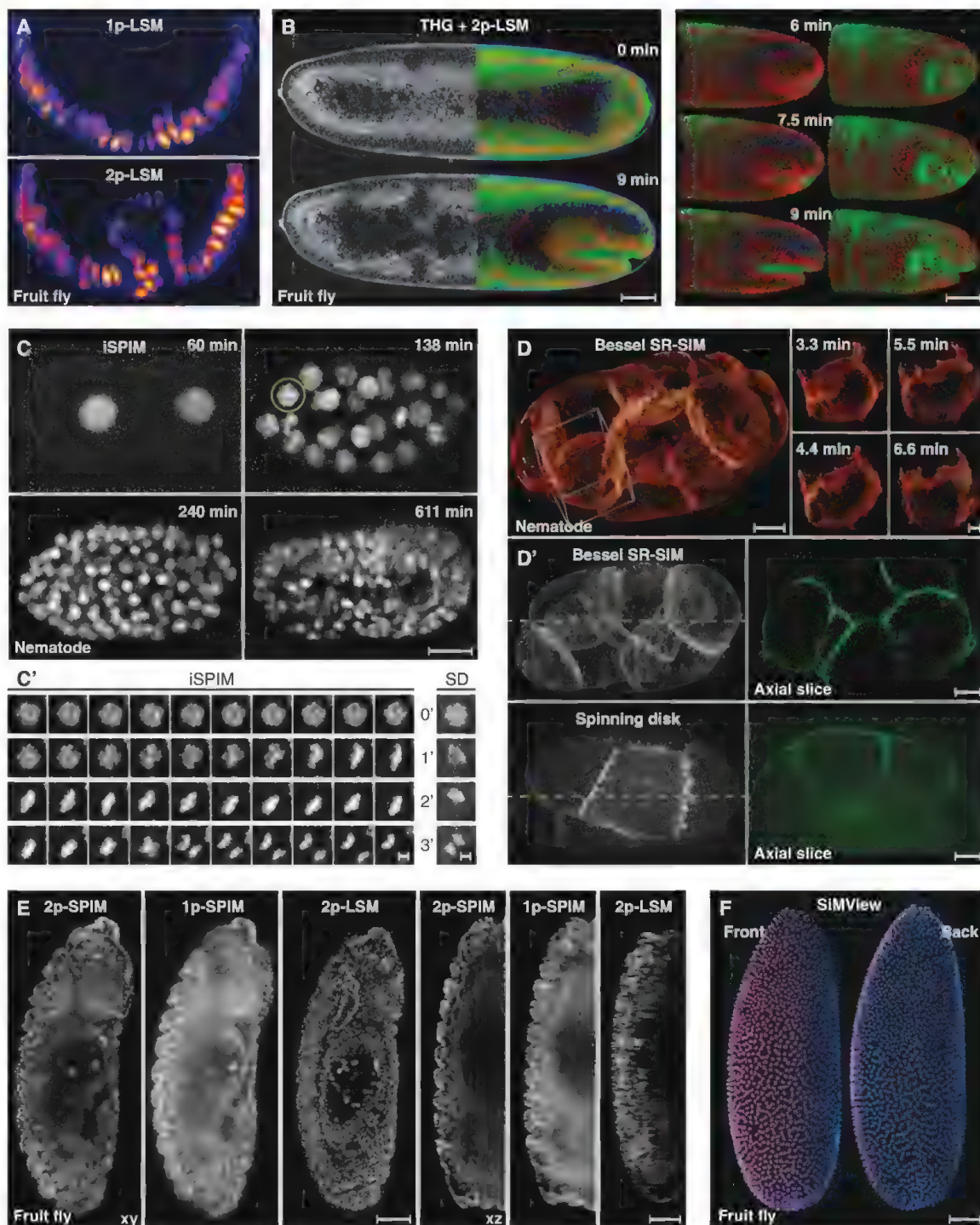
zebrafish (2), the combination of powerful mammalian embryo culture systems with emerging in vivo imaging technologies will open the door to similar approaches also for mammalian model systems.

Computational Image Analysis and Modeling of Morphogenesis: The Next Frontier

The emergence of powerful live-imaging techniques has turned the generation of large information-rich image data sets of complex biological processes

Fig. 5. Emerging imaging techniques for the study of morphogenesis.

(A) In contrast to one-photon laser-scanning confocal microscopy (1p-LSM, top), two-photon laser-scanning microscopy (2p-LSM, bottom) captures internalized mesoderm cells in histone-GFP-expressing *Drosophila* embryos. See movie S1. [Reprinted from (2)] (B) Simultaneous multicolor two-photon [2p-LSM, blue: endogenous fluorescence, green: GFP, red: RFP (red fluorescent protein)] and third-harmonic generation (THG) imaging of a developing *Drosophila* embryo. Panels to the right show inner (left) and outer (right) views of the posterior pole region. [Reprinted from (20)] (C) High-speed inverted selective plane illumination microscopy (iSPIM) imaging (30 volumes/min) of a nuclei-labeled *C. elegans* embryo. (C') Comparison of iSPIM (sampled every 2 s, shown every 6 s) and spinning disk (SD) confocal microscopy (sampled every 60 s) images. See movies S7 and S8. [Reprinted from (3)] (D) Bessel plane SR-SIM high-resolution imaging of a membrane-labeled *C. elegans* embryo. Box in top left panel highlights region shown to the right. (D') In contrast to Bessel plane SR-SIM, spinning disk confocal microscopy images show rapid loss of signal and resolution at depth. See movie S10. [Reprinted from (22)] (E) Comparison of two-photon light-sheet microscopy (2p-SPIM), one-photon light-sheet microscopy (1p-SPIM) and two-photon laser-scanning microscopy (2p-LSM) images of nuclei-labeled *Drosophila* embryos (left/right: lateral/axial slices). See movie S4. [Reprinted from (24)] (F) SiMView of an entire nuclei-labeled *Drosophila* embryo. In contrast to single-view light-



sheet microscopy, which captures only ~30% of the embryo (red), SiMView provides full physical coverage (blue). See movies S5 and S6. [Reprinted from (25)] Scale bars: 50 μ m (B, E, F), 10 μ m (C), 5 μ m (D, left; D', D, right).

into a routine task. Advanced light-sheet microscopes can record dozens of terabytes of data and millions of high-resolution images per day (25). The size of a single whole-embryo imaging experiment obtained with this methodology is comparable to that of the entire book collection of the U.S. Library of Congress. The sheer volume of these recordings thus demands automated approaches of computational image analysis to convert the raw image data into biologically meaningful representations.

However, the tasks needed to extract quantitative information about cell morphology and cell behavior from such data are usually complex and technically challenging. Typical requirements include 3D cell shape segmentation (43), accurate cell tracking over time and through cell divisions (25, 44), quantification of expression levels of genes of interest (5, 45), and subcellular localization of proteins (39). For example, to quantitatively follow the formation and arrangement of the tens of thousands of cells in a one-day-old zebrafish or fruit fly embryo (Fig. 1B), ~100 million cell positions need to be determined from several thousand volumetric whole-embryo image stacks (movie S16, study “a” in Fig. 3B), considering that a temporal sampling of at most 30 to 60 s is needed to keep up with the speed of cell movements (2, 25). Even when focusing only on morphogenetic processes in a single tissue, the computational challenges are still immense. Speed and scalability of computational methods have thus become as important as their accuracy and robustness.

This first layer of image analysis typically marks only the beginning of the postexperiment analysis. Powerful visualization tools (46, 47) and physical modeling (48) are subsequently needed to interpret the resulting data and test mechanistic hypotheses. To reach a system-level understanding of morphogenesis and its multiscale character, the transition from qualitative to quantitative analyses of the underlying biological processes is of key importance. Thus, to keep up with fundamental advances in imaging capabilities, it is now equally important to conceive of new concepts and powerful computational methods to mine the resulting high-content data sets. With the availability of system-level data on cell behavior, gene expression, and likely soon also biophysical tissue properties, we are reaching the point at which it will be feasible to develop computational approaches that incorporate these data into a single model capable of dissecting morphogenesis on the whole-organism level (15).

Future Directions

The nature of key breakthroughs in developmental biology in recent years demonstrates that further advancing our understanding of morphogenesis is intrinsically linked to advances in live-imaging technology, development of new approaches to computational data analysis, and seamless inte-

gration of physical modeling. It has finally become possible to image entire vertebrate and higher invertebrate embryos throughout their development at a spatiotemporal resolution that enables comprehensive cell tracking, systematic analysis of cell fate determination, reconstruction of single-cell to whole-tissue morphologies, and systematic dissection of the role of physical forces in shaping the developmental building plan.

In coming years, further advances in microscopy technology are expected with high relevance to a wide spectrum of applications in the study of morphogenesis. Ongoing efforts are aimed at advancing deep-tissue in vivo imaging, improving spatial resolution, and increasing temporal sampling. These capabilities will open up exciting new possibilities. For example, resolving the fine spatiotemporal dynamics of subcellular processes on the whole-tissue level will help to elucidate the molecular mechanisms underlying tissue morphogenesis. High-speed volumetric imaging will give access to both development and function of complex biological systems at the same time, from individual tissues and organs, such as the developing heart (17), to entire organ systems, such as the nervous system (16). Existing assays in light-sheet microscopy already reveal cell behavior on the whole-embryo level, but further improvements, in particular with respect to imaging speed, will make it possible to also systematically measure functional properties of developing tissues, and thus, to determine the reciprocal effect on development.

Combining advanced imaging methods with powerful computational tools will enable not only system-level analyses of morphogenesis but also entirely new experimental approaches. Real-time cell segmentation and cell lineage reconstructions during live imaging of embryonic development could guide functional interference—for example, by using cell positions and computationally predicted cell identities for targeted optical manipulation with laser ablation or optogenetics. Such approaches could be used for the systematic dissection of functional relationships in the developmental building plan on the whole-embryo level.

Imaging-based studies of morphogenesis will also greatly benefit from the development of new fluorescent probes and sensors, including highly photostable and bright infrared fluorescent proteins for deep-tissue imaging, novel fluorescent timer proteins for visualizing signaling and other processes based on protein age and turnover (4), and genetically encoded sensors for the quantitative in vivo measurement of physical forces (49).

Combining the experimental capabilities and theoretical approaches of these different disciplines will be an indispensable step toward the establishment of a quantitative model of the developing embryo and, thus, a system-level understanding of morphogenesis.

References and Notes

1. A. McMahon, W. Supatto, S. E. Fraser, A. Stathopoulos, Dynamic analyses of *Drosophila* gastrulation provide insights into collective cell migration. *Science* **322**, 1546–1550 (2008). doi: 10.1126/science.1167094; pmid: 19056986
2. P. J. Keller, A. D. Schmidt, J. Wittbrodt, E. H. K. Stelzer, Reconstruction of zebrafish early embryonic development by scanned light sheet microscopy. *Science* **322**, 1065–1069 (2008). doi: 10.1126/science.1162493; pmid: 18845710
3. Y. Wu, A. Ghitani, R. Christensen, A. Santella, Z. Du, G. Rondeau, Z. Bao, D. Colón-Ramos, H. Shroff, Inverted selective plane illumination microscopy (ISPIM) enables coupled cell identity lineage and neurodevelopmental imaging in *Caenorhabditis elegans*. *Proc. Natl. Acad. Sci. U.S.A.* **108**, 17708–17713 (2011). doi: 10.1073/pnas.1108494108; pmid: 22006307
4. A. Khmelinskii, P. J. Keller, A. Bartosik, M. Meurer, J. D. Barry, B. R. Mardin, A. Kaufmann, S. Trautmann, M. Wachsmuth, G. Pereira, W. Huber, E. Schiebel, M. Knop, Tandem fluorescent protein timers for in vivo analysis of protein dynamics. *Nat. Biotechnol.* **30**, 708–714 (2012). doi: 10.1038/nbt.2281; pmid: 22729030
5. C. C. Fowlkes, C. L. Hendriks, S. V. Keränen, G. H. Weber, O. Rübner, M. Y. Huang, S. Chatoor, A. H. DePace, L. Simirenko, C. Henriquez, A. Beaton, R. Weizmann, S. Celniker, B. Hamann, D. W. Knowles, M. D. Biggin, M. B. Eisen, J. Malik, A quantitative spatiotemporal atlas of gene expression in the *Drosophila* blastoderm. *Cell* **133**, 364–374 (2008). doi: 10.1016/j.cell.2008.01.053; pmid: 18423206
6. B. Wu, K. D. Piatkevich, T. Lionnet, R. H. Singer, V. V. Verkhusha, Modern fluorescent proteins and imaging technologies to study gene expression, nuclear localization, and dynamics. *Curr. Opin. Cell Biol.* **23**, 310–317 (2011). doi: 10.1016/j.ceb.2010.12.004; pmid: 21242078
7. G. T. Reeves, N. Trisnadi, T. V. Truong, M. Nahmad, S. Katz, A. Stathopoulos, Dorsal-ventral gene expression in the *Drosophila* embryo reflects the dynamics and precision of the dorsal nuclear gradient. *Dev. Cell* **22**, 544–557 (2012). doi: 10.1016/j.devcel.2011.12.007; pmid: 22342544
8. J. L. Maître, H. Berthoumieux, S. F. Krens, G. Salbreux, F. Jülicher, E. Paluch, C. P. Heisenberg, Adhesion functions in cell sorting by mechanically coupling the cortices of adhering cells. *Science* **338**, 253–256 (2012). doi: 10.1126/science.1225399; pmid: 22923438
9. C. Guillot, T. Lecuit, Mechanics of epithelial tissue homeostasis and morphogenesis. *Science* **340**, 1185 (2013).
10. W. Denk, J. H. Strickler, W. W. Webb, Two-photon laser scanning fluorescence microscopy. *Science* **248**, 73–76 (1990). doi: 10.1126/science.2321027; pmid: 2321027
11. A. H. Voie, D. H. Burns, F. A. Spelman, Orthogonal-plane fluorescence optical sectioning: Three-dimensional imaging of macroscopic biological specimens. *J. Microsc.* **170**, 229–236 (1993). doi: 10.1111/j.1365-2818.1993.tb03346.x; pmid: 8371260
12. J. Huiskens, J. Swoger, F. Del Bene, J. Wittbrodt, E. H. K. Stelzer, Optical sectioning deep inside live embryos by selective plane illumination microscopy. *Science* **305**, 1007–1009 (2004). doi: 10.1126/science.1100035; pmid: 15310904
13. H. Siedentopf, R. Zsigmondy, Über Sichtbarmachung und Größenbestimmung ultramikroskopischer Teilchen, mit besonderer Anwendung auf Goldrubingläser. *Annalen der Physik* **315**, 1–39 (1902). doi: 10.1002/andp.19023150102
14. J. Mertz, Optical sectioning microscopy with planar or structured illumination. *Nat. Methods* **8**, 811–819 (2011). doi: 10.1038/nmeth.1709; pmid: 21959136
15. K. Khairy, P. J. Keller, Reconstructing embryonic development. *Genesis* **49**, 488–513 (2011). doi: 10.1002/dvg.20698; pmid: 21140407

16. M. B. Ahrens, M. B. Orger, D. N. Robson, J. M. Li, P. J. Keller, Whole-brain functional imaging at cellular resolution using light-sheet microscopy. *Nat. Methods* **10**, 413–420 (2013). doi: [10.1038/nmeth.2434](https://doi.org/10.1038/nmeth.2434); pmid: 23524393
17. A. B. Arrenberg, D. Y. Stainier, H. Baier, J. Huisken, Optogenetic control of cardiac function. *Science* **330**, 971–974 (2010). doi: [10.1126/science.1195929](https://doi.org/10.1126/science.1195929); pmid: 21071670
18. N. Ji, D. E. Milkie, E. Betzig, Adaptive optics via pupil segmentation for high-resolution imaging in biological tissues. *Nat. Methods* **7**, 141–147 (2010). doi: [10.1038/nmeth.1411](https://doi.org/10.1038/nmeth.1411); pmid: 20037592
19. K. Si, R. Fiolka, M. Cui, Fluorescence imaging beyond the ballistic regime by ultrasound pulse guided digital phase conjugation. *Nat. Photonics* **6**, 657–661 (2012). doi: [10.1038/nphoton.2012.205](https://doi.org/10.1038/nphoton.2012.205); pmid: 23241552
20. P. Mahou, M. Zimmerley, K. Loulier, K. S. Matho, G. Labroille, X. Morin, W. Supatto, J. Livet, D. Débarre, E. Beaurepaire, Multicolor two-photon tissue imaging by wavelength mixing. *Nat. Methods* **9**, 815–818 (2012). doi: [10.1038/nmeth.2098](https://doi.org/10.1038/nmeth.2098); pmid: 22772730
21. A. A. Planchon, L. Gao, D. E. Milkie, M. W. Davidson, J. A. Galbraith, C. G. Galbraith, E. Betzig, Rapid three-dimensional isotropic imaging of living cells using Bessel beam plane illumination. *Nat. Methods* **8**, 417–423 (2011). doi: [10.1038/nmeth.1586](https://doi.org/10.1038/nmeth.1586); pmid: 21378978
22. L. Gao, L. Shao, C. D. Higgins, J. S. Poulton, M. Peifer, M. W. Davidson, X. Wu, B. Goldstein, E. Betzig, Noninvasive imaging beyond the diffraction limit of 3D dynamics in thickly fluorescent specimens. *Cell* **151**, 1370–1385 (2012). doi: [10.1016/j.cell.2012.10.008](https://doi.org/10.1016/j.cell.2012.10.008); pmid: 23217717
23. J. Capoulade, M. Wachsmuth, L. Hufnagel, M. Knop, Quantitative fluorescence imaging of protein diffusion and interaction in living cells. *Nat. Biotechnol.* **29**, 835–839 (2011). doi: [10.1038/nbt.1928](https://doi.org/10.1038/nbt.1928); pmid: 2182256
24. T. V. Truong, W. Supatto, D. S. Koos, J. M. Choi, S. E. Fraser, Deep and fast live imaging with two-photon scanned light-sheet microscopy. *Nat. Methods* **8**, 757–760 (2011). doi: [10.1038/nmeth.1652](https://doi.org/10.1038/nmeth.1652); pmid: 21765409
25. R. Tomer, K. Khairy, F. Amat, P. J. Keller, Quantitative high-speed imaging of entire developing embryos with simultaneous multiview light-sheet microscopy. *Nat. Methods* **9**, 755–763 (2012). doi: [10.1038/nmeth.2062](https://doi.org/10.1038/nmeth.2062); pmid: 22660741
26. U. Krzic, S. Gunther, T. E. Saunders, S. J. Streichen, L. Hufnagel, Multiview light-sheet microscope for rapid in toto imaging. *Nat. Methods* **9**, 730–733 (2012). doi: [10.1038/nmeth.2064](https://doi.org/10.1038/nmeth.2064); pmid: 22660739
27. F. O. Fährbach, P. Simon, A. Rohrbach, Microscopy with self-reconstructing beams. *Nat. Photonics* **4**, 780–785 (2010). doi: [10.1038/nphoton.2010.204](https://doi.org/10.1038/nphoton.2010.204)
28. M. A. Neil, R. Juskaitis, T. Wilson, Method of obtaining optical sectioning by using structured light in a conventional microscope. *Opt. Lett.* **22**, 1905–1907 (1997). doi: [10.1364/OL.22.001905](https://doi.org/10.1364/OL.22.001905); pmid: 18188403
29. M. G. Gustafsson, L. Shao, P. M. Carlton, C. J. Wang, I. N. Golubovskaya, W. Z. Cande, D. A. Agard, J. W. Sedat, Three-dimensional resolution doubling in wide-field fluorescence microscopy by structured illumination. *Biophys. J.* **94**, 4957–4970 (2008). doi: [10.1529/biophysj.107.120345](https://doi.org/10.1529/biophysj.107.120345); pmid: 18326650
30. P. J. Keller, A. D. Schmidt, A. Santella, K. Khairy, Z. Bao, J. Wittbrodt, E. H. Stelzer, Fast, high-contrast imaging of animal development with scanned light sheet-based structured-illumination microscopy. *Nat. Methods* **7**, 637–642 (2010). doi: [10.1038/nmeth.1476](https://doi.org/10.1038/nmeth.1476); pmid: 20601950
31. M. J. Booth, Adaptive optics in microscopy. *Philos. Trans R Soc A* **365**, 2829–2843 (2007). doi: [10.1098/rsta.2007.0013](https://doi.org/10.1098/rsta.2007.0013); pmid: 17855218
32. X. Xu, H. Liu, L. V. Wang, Time-reversed ultrasonically encoded optical focusing into scattering media. *Nat. Photonics* **5**, 154–157 (2011). doi: [10.1038/nphoton.2010.306](https://doi.org/10.1038/nphoton.2010.306); pmid: 21532925
33. N. C. Shaner, R. E. Campbell, P. A. Steinbach, B. N. Giepmans, A. E. Palmer, R. Y. Tsien, Improved monomeric red, orange and yellow fluorescent proteins derived from *Discosoma* sp. red fluorescent protein. *Nat. Biotechnol.* **22**, 1567–1572 (2004). doi: [10.1038/nbt1037](https://doi.org/10.1038/nbt1037); pmid: 15558047
34. D. M. Chudakov, M. V. Matz, S. Lukyanov, K. A. Lukyanov, Fluorescent proteins and their applications in imaging living cells and tissues. *Physiol. Rev.* **90**, 1103–1163 (2010). doi: [10.1152/physrev.00038.2009](https://doi.org/10.1152/physrev.00038.2009); pmid: 20664080
35. P. B. Abitua, E. Wagner, I. A. Navarrete, M. Levine, Identification of a rudimentary neural crest in a non-vertebrate chordate. *Nature* **492**, 104–107 (2012). doi: [10.1038/nature11589](https://doi.org/10.1038/nature11589); pmid: 23135395
36. F. Bosveld, I. Bonnet, B. Guirao, S. Tlili, Z. Wang, A. Petitlot, R. Marchand, P. L. Bardet, P. Marq, F. Graner, Y. Bellaïche, Mechanical control of morphogenesis by Fat/Dachsous/Four-jointed planar cell polarity pathway. *Science* **336**, 724–727 (2012). doi: [10.1126/science.1221071](https://doi.org/10.1126/science.1221071); pmid: 22499807
37. M. Behrndt, G. Salbreux, P. Campinho, R. Hauschild, F. Oswald, J. Roensch, S. W. Grill, C. P. Heisenberg, Forces driving epithelial spreading in zebrafish gastrulation. *Science* **338**, 257–260 (2012). doi: [10.1126/science.1224143](https://doi.org/10.1126/science.1224143); pmid: 23066079
38. W. Supatto, A. McMahon, S. E. Fraser, A. Stathopoulos, Quantitative imaging of collective cell migration during *Drosophila* gastrulation: Multiphoton microscopy and computational analysis. *Nat. Protoc.* **4**, 1397–1412 (2009). doi: [10.1038/nprot.2009.130](https://doi.org/10.1038/nprot.2009.130); pmid: 19745822
39. Y. C. Wang, Z. Khan, M. Kaschube, E. F. Wieschaus, Differential positioning of adherens junctions is associated with initiation of epithelial folding. *Nature* **484**, 390–393 (2012). doi: [10.1038/nature10938](https://doi.org/10.1038/nature10938); pmid: 22456706
40. A. Piliszek, G. S. Kwon, A. K. Hadjantonakis, Ex utero culture and live imaging of mouse embryos. *Methods Mol. Biol.* **770**, 243–257 (2011). doi: [10.1007/978-1-61779-210-6_9](https://doi.org/10.1007/978-1-61779-210-6_9); pmid: 21805267
41. S. Nowotschin, A. K. Hadjantonakis, Cellular dynamics in the early mouse embryo: From axis formation to gastrulation. *Curr. Opin. Genet. Dev.* **20**, 420–427 (2010). doi: [10.1016/j.gde.2010.05.008](https://doi.org/10.1016/j.gde.2010.05.008); pmid: 20566281
42. G. Trichas, A. M. Smith, N. White, V. Wilkins, T. Watanabe, A. Moore, B. Joyce, J. Sugnaseelan, T. A. Rodriguez, D. Kay, R. E. Baker, P. K. Maini, S. Srinivas, Multi-cellular rosettes in the mouse visceral endoderm facilitate the ordered migration of anterior visceral endoderm cells. *PLoS Biol.* **10**, e1001256 (2012). doi: [10.1371/journal.pbio.1001256](https://doi.org/10.1371/journal.pbio.1001256); pmid: 22346733
43. R. Fernandez, P. Das, V. Mirabet, E. Moscardi, J. Traas, J. L. Verdeil, G. Malandain, C. Godin, Imaging plant growth in 4D: Robust tissue reconstruction and lineageing at cell resolution. *Nat. Methods* **7**, 547–553 (2010). doi: [10.1038/nmeth.1472](https://doi.org/10.1038/nmeth.1472); pmid: 20543845
44. Z. Bao, J. I. Murray, T. Boyle, S. L. Ooi, M. J. Sandel, R. H. Waterston, Automated cell lineage tracing in *Caenorhabditis elegans*. *Proc. Natl. Acad. Sci. U.S.A.* **103**, 2707–2712 (2006). doi: [10.1073/pnas.0511111103](https://doi.org/10.1073/pnas.0511111103); pmid: 16477039
45. J. I. Murray, Z. Bao, T. J. Boyle, M. E. Boeck, B. L. Mericle, T. J. Nicholas, Z. Zhao, M. J. Sandel, R. H. Waterston, Automated analysis of embryonic gene expression with cellular resolution in *C. elegans*. *Nat. Methods* **5**, 703–709 (2008). doi: [10.1038/nmeth.1228](https://doi.org/10.1038/nmeth.1228); pmid: 18587405
46. H. Peng, Z. Ruan, F. Long, J. H. Simpson, E. W. Myers, V3D enables real-time 3D visualization and quantitative analysis of large-scale biological image data sets. *Nat. Biotechnol.* **28**, 348–353 (2010). doi: [10.1038/nbt.1612](https://doi.org/10.1038/nbt.1612); pmid: 20231818
47. K. W. Eliceiri, M. R. Berthold, I. G. Goldberg, L. Ibáñez, B. S. Manjunath, M. E. Martone, R. F. Murphy, H. Peng, A. L. Plant, B. Roysam, N. Stuurman, J. R. Swedlow, P. Tomancak, A. E. Carpenter, Biological imaging software tools. *Nat. Methods* **9**, 697–710 (2012). doi: [10.1038/nmeth.2084](https://doi.org/10.1038/nmeth.2084); pmid: 22743775
48. A. C. Oates, N. Gorfinkel, M. González-Gaitán, C. P. Heisenberg, Quantitative approaches in developmental biology. *Nat. Rev. Genet.* **10**, 517–530 (2009). doi: [10.1038/nrg2548](https://doi.org/10.1038/nrg2548); pmid: 19584811
49. C. Grashoff, B. D. Hoffman, M. D. Brenner, R. Zhou, M. Parsons, M. T. Yang, M. A. McLean, S. G. Sligar, C. S. Chen, T. Ha, M. A. Schwartz, Measuring mechanical tension across vinculin reveals regulation of focal adhesion dynamics. *Nature* **466**, 263–266 (2010). doi: [10.1038/nature09198](https://doi.org/10.1038/nature09198); pmid: 20613844

Acknowledgments: I thank K. Branson for helpful discussions and help with preparing the figures; Y. Wan and W. Lemon for help with recording the zebrafish SiMView data set; and F. Amat, Y. Bellaïche, E. Betzig, M. Handberg-Thorsager, B. Hoeckendorf, K. Khairy, M. Knop, W. Lemon, J. Liu, K. McDole, S. Srinivas, D. Stern and Y. Wan for helpful comments on the manuscript. This work was supported by the Howard Hughes Medical Institute.

Supplementary Materials
www.sciencemag.org/content/340/6137/1234168/suppl/DC1
 References (50, 51)
 Movies S1 to S16
[10.1126/science.1234168](https://doi.org/10.1126/science.1234168)

REVIEW

Mechanics of Epithelial Tissue Homeostasis and Morphogenesis

Charlène Guillot and Thomas Lecuit*

Epithelia are robust tissues that support the structure of embryos and organs and serve as effective barriers against pathogens. Epithelia also chemically separate different physiological environments. These vital functions require tight association between cells through the assembly of junctions that mechanically stabilize the tissue. Remarkably, epithelia are also dynamic and can display a fluid behavior. Cells continuously die or divide, thereby allowing functional tissue homeostasis. Epithelial cells can change shape or intercalate as tissues deform during morphogenesis. We review the mechanical basis of tissue robustness and fluidity, with an emphasis on the pivotal role of junction dynamics. Tissue fluidity emerges from local active stresses acting at cell interfaces and allows the maintenance of epithelial organization during morphogenesis and tissue renewal.

Epithelia form sheets of cells organized in a monolayer, as in developing embryos and the gut, or multilayered, as in the skin. Epithelial cohesion requires the formation of adhesive contacts supported mainly by E-cadherin molecules. E-cadherin forms cis and trans homophilic clusters that are stabilized by actin filaments via catenin molecules such as β -catenin and α -catenin, vinculin, and other proteins (1, 2) (Fig. 1A). E-cadherin clusters concentrate in the adherens junctions and form an adhesive belt that stitches cells together. From a mechanical point of view, the extent of cell contacts depends on adhesion forces that stabilize cell-cell interfaces, balanced against cortical tension exerted by the actomyosin network that tends to reduce cell contacts [reviewed in (3)]. At the molecular level, adhesion reflects both the ligation of E-cadherin ectodomains (4, 5) and the mechanical coupling to the cortical actomyosin network via α -catenin and vinculin (6–10), which stabilizes E-cadherin complexes. As a consequence, adhesion complexes are under tension and transmit subcellular forces exerted by actomyosin networks to the cortex (Fig. 1A) (6, 7). By virtue of their symmetrical organization at cell contacts, E-cadherin clusters mechanically couple cells in a tissue. The interplay between E-cadherin complexes and actomyosin networks controls two key features of junction mechanics and dynamics: the ability to deform and remodel cell contacts by transmitting cell tension, and the resistance to cell deformation by cell adhesion. Thus, the balance between tension transmission and adhesion controls local junction dynamics.

Epithelial cell packing is responsible for characteristic polygonal cell geometries, in which edges are junctions between two cells, and vertices

mark points of contact among three or more cells (Fig. 1A'). One can describe the organization of an epithelium according to the number and distribution of edges and vertices. A brief (less than a minute) external stress will elastically deform (elongate by stretching) this cellular array by cell shape changes where edges lengthen or shorten, while preserving the integrity of the epithelium (Fig. 1B, upper right). These deformations are geometrical and reversible, and they reflect the amplitude of intercellular adhesion forces together with the active response of the contractile cell cortex. When the stress is applied on longer time scales (tens of minutes), the tissue exhibits a fluid behavior where cells move much like particles that diffuse in a liquid. This requires topological changes by remodeling of cell contacts (elongation by rearrangement): Some edges disappear and others form (Fig. 1B, lower right). Epithelial cells not only respond actively

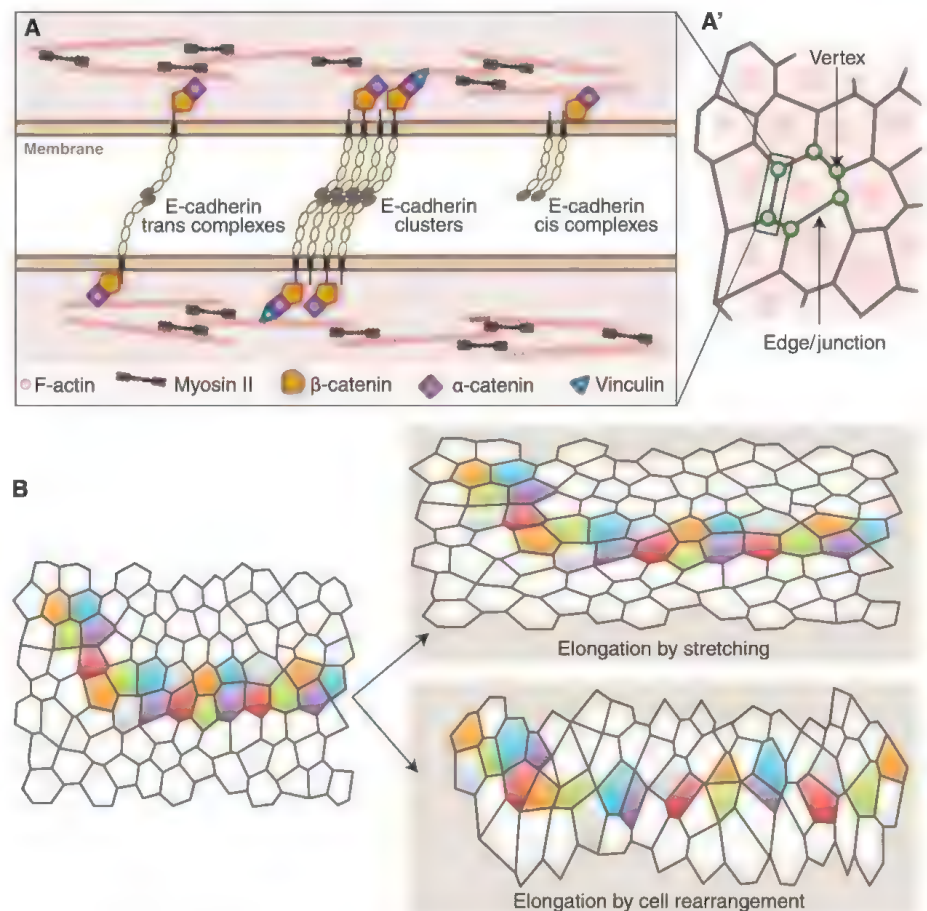


Fig. 1. Structure and plasticity of epithelial junctions during tissue stretching and remodeling. (A) E-cadherin forms cis and trans clusters stabilized by interaction between extracellular domains and actin filaments (F-actin, pink) via β -catenin, α -catenin, and vinculin (gold, purple, and light blue elements, respectively). (A') These complexes control adhesion and tension transmission at cell junctions. Epithelial junctions form a polygonal network of edges (black) and vertices (green). (B) A tissue deforms elastically if it is stretched on short time scales (less than a few minutes); cells change their geometry (upper right). On longer time scales (tens of minutes), cells change their position by remodeling the topology of cell contacts and thereby dissipate the stress like a viscous fluid (lower right).

Aix-Marseille Université, CNRS UMR 7288, IBDM, Campus de Luminy, Case 907, 13009 Marseille, France.

*Corresponding author. E-mail: thomas.lecuit@univ-amu.fr

Morphogenesis

to externally applied stress (e.g., coming from another tissue), but also generate their own internal stress through the regulation of subcellular actomyosin networks.

The source of epithelial plasticity and fluid behavior thus resides in the ability to actively remodel cell junctions. We review three main types of remodeling and extract general principles underlying these diverse processes (Fig. 2). First, cell division produces new cell junctions (11). Second, live cell extrusion and cell death remove cell junctions (12). Last, cell movement by intercalation changes the position of junctions (13, 14). Remarkably, in all cases, junction dynamics is an active and multicellular process.

Formation of New Contacts During Division

Cell division profoundly affects the organization of epithelial tissues (Fig. 3A). Cell division is responsible for the rapid emergence of a robust equilibrium pattern of cell topologies (11). This results from simple empirical rules of cell division, shared among animals and plants, in particular, the fact that a division produces a new edge and two new vertices with minimal cell rearrangement. In turn, the cell topology affects the shape of its neighbors and thereby affects the orientation of cell division in this cell. If all cells are hexagonal, then cell shapes are similar and isotropic and cell divisions are randomly oriented. However, a hexagonal cell that contacts a four-sided cell will elongate parallel to the contact between the two cells. In turn, the cleavage plane of this elongated cell will be biased perpendicular to the contact between the two cells (15). The interplay among cell topology, cell shape, and cell division orientation is a striking manifestation of how cell proliferation participates in the steady-state organization of an epithelium by controlling how cell contacts are distributed locally and globally.

It has remained unclear how cell division occurs in an epithelium—in particular, what enables a new adhesive interface to form during division (Fig. 3B). This is a fundamental problem because division must preserve the integrity of an epithelium, in particular its barrier function. Do cells lose their adhesive contacts with neighbors as they divide? What is the link between junction formation and cell cleavage during cytokinesis? Cytokinesis requires the formation of a contractile actomyosin ring that deforms the dividing cells (16). If cells remain adhesive during division, such deformations will be resisted by cell adhesion with neighbors and the effective tension exerted by neighbors via cell junctions on the dividing cell. Madin-Darby canine kidney (MDCK) epithelial cells have been reported to maintain adhesion and apico-basal polarity as they divide (17). This is also observed in *Drosophila* epithelial cells at different stages of development and in the mouse neuroepithelium, so it is likely to be a general mechanism

(18–20). Partitioning of the polarized cell progresses from basal to apical, and requires apical anchoring of the cytokinetic ring to cell junctions (Fig. 2B).

In most cases reported so far, dividing cells remain in contact during and immediately after division, although one cell may later exchange neighbors (see below). As a consequence, the clonal descendants of an epithelial cell are not scattered and tend to form a cohesive clone, as seen in early zebrafish (21) and *Drosophila* tissues (22). Further investigations in other systems will be useful in determining whether this is always the case, especially when cell polarity and a columnar epithelial organization are not evident.

Recent studies in *Drosophila* provide a simple model for understanding how formation of the new junction is coupled to cleavage in the plane of junctions (Fig. 3C) (18–20). Contraction of the ring deforms the cell junctions during cleavage up to a point where local disengagement of E-cadherin complexes in the cleavage furrow causes the separation of the membranes of the dividing cell and its neighbors (Fig. 3C and movie S1). A new membrane interface forms between the two daughter cells, which restores E-cadherin clusters, thereby maintaining adhesion. The length of the membrane interface requires nonautonomous actomyosin tension in the *Drosophila* pupa, which forces annealing between the surfaces of the two daughter cells (18, 20). Local adhesion disengagement is also an active process. It requires tension exerted by the ring (which depends on septin and anillin) together with the tension exerted by neighboring cells pulling orthogonally to the junction (18, 19). However, it is possible that adhesion disengagement is also the result of local biochemical regulation. E-cadherin clusters transmit and integrate intrinsic and extrinsic tension. In pupal epithelia,

another remarkable active process is involved: Arp2/3-dependent actin polymerization causes maintenance of the newly formed interface (20), although the exact mechanism is still unclear. When these active processes are perturbed, either new junction formation is strongly delayed and ultimately fails, or the new junction is short and not stabilized, sometimes causing intercalation with neighbors.

During epithelial cell division, the addition of new junctions and the control of junction length is thus an active and multicellular process that preserves the tissue barrier function. It will be interesting to investigate these mechanisms in other organisms and see whether cells can escape this mechanism during tumor progression, and if so, how this is accomplished.

Removal of Junctions and Cells by Extrusion

Cell division increases the number of cells and cell contacts in a tissue. When division is associated with cell growth, the tissue expands, such as in developing embryos and organs or during regeneration. Once the tissue has attained its final adult size, however, the epithelium reaches a steady state (homeostasis) where cell divisions are balanced by cell death or live cell extrusion. A striking example is the mammalian gut. Cell divisions are concentrated in the crypt where stem cells produce progenitors (23). Cells then migrate along the side of microvilli and reach their tip (Fig. 4A). Remarkably, at the tips of microvilli, the majority of cells that extrude from the epithelium are nonapoptotic. Live cell extrusion was observed in other systems, such as in MDCK cell monolayers, developing fins in the zebrafish (24), or the midline of the developing dorsal adult *Drosophila* epithelium, called the notum (Fig. 4B) (25). In all but the *Drosophila* notum, extrusion is apical (24, 25). Recent studies have shed light on the mecha-

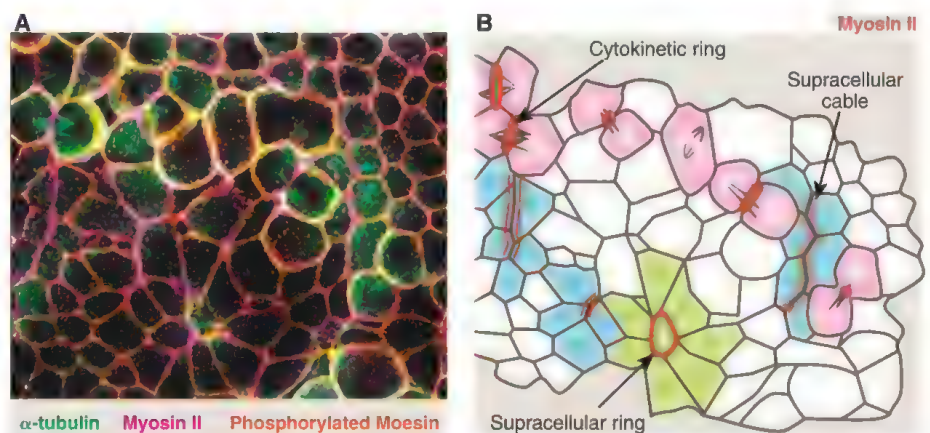


Fig. 2. Plasticity of epithelia is due to cell division, extrusion, and intercalation. (A) Immunostaining shows microtubule (green), myosin II (pink), and phosphorylated moesin marking the cell cortex (orange) of a *Drosophila* embryo. (B) Schematic of (A) showing cell division (pink), cell extrusion (green), and intercalation (blue) events in the tissue. Cell boundaries are in gray; myosin II is in orange.

nisms of cell junction removal during live cell extrusion. They reveal interesting differences with apoptotic extrusion but also show evidence of conserved pathways.

The trigger for nonapoptotic cell extrusion appears to be a buildup of tissue compression due to tissue growth and/or active cell movements. Although tissue pressure is difficult to measure directly, a series of observations supports this view. Reducing or increasing proliferation respectively inhibits or induces cell extrusion in the *Drosophila notum* (25). Cell extrusion also happens in regions where cells converge, such as in zebrafish fins (24). In addition, as MDCK cells are grown on a stretched elastic matrix, when the substra-

tum is released and relaxes back, cell density increases within the first 30 min; after a few hours, cells extrude and restore the original cell density (24).

Because a whole cell disappears during extrusion, an average of six junctions must be removed. Cell extrusion proceeds in two main steps. First, two to three junctions disappear as neighbors are pushed away from the extruding cell by local cell intercalation events called T1 swaps (Fig. 4C). This step is most likely dependent on tissue compression and resultant differential junction tension: In *Drosophila*, cell-cell junctions relaxed more slowly after focal laser ablation in the dorsal midline than away from it

(25). Once cells have about three junctions, an actomyosin supracellular ring is assembled in surrounding cells (Fig. 2B) and its contraction completes cell extrusion by a so-called T2 process, as reported in apoptotic cell extrusion or during wound closure (26). In zebrafish, cell extrusion requires stress-activated ion channels (called Piezo) and sphingosine-1-phosphate signaling, which could control the final step of the process through regulation of the Rho1-myosin II pathway (24).

Junction removal thus allows cell extrusion when tissue compression is too high. This contributes to maintaining a steady state in the epithelium. The inhibition of growth by contact inhibition is also a major component of homeostasis (27). Junction removal is an active and collective process that requires non-local forces emerging from a buildup in tissue pressure, as well as local forces produced by immediate neighbors.

Moving Cells by Intercalation and Junction Exchange

Local neighbor exchange, or cell intercalation, is a driving force during convergent extension movements in different organisms (1, 28–32) and enables stress dissipation in a growing tissue (Fig. 1). During morphogenesis, it also participates in the extensive tissue remodeling as epithelia acquire their complex three-dimensional (3D) shapes. As imaging methods become more powerful to track cells in complex 3D environments (33), the cellular bases of tissue morphogenesis are gradually emerging in a variety of systems. A striking example of tissue morphogenesis is the elongation of an epithelium (Fig. 5, A and B). Cell intercalation allows cells to rearrange their positions, such as in the mouse visceral endoderm (34), in the *Xenopus* (30) and chick neural tube (35), and in the *Drosophila* germ band (36, 37) (Fig. 5C and movie S2).

In essence, cell intercalation enables cell movement by changing the position of cell junctions in the tissue (Fig. 5C). In a first step, cell junctions are removed. This brings four or more cells together, producing a high-order vertex in a tetrad (36) or a rosette (37). Tetrads and rosettes have been described in a variety of systems (34–37). They are transient (and possibly unstable) structures that resolve through the formation of new junctions orthogonal to those that were removed. Intercalation is an irreversible process that is also planar-polarized when it drives tissue extension: The set of junctions that is removed is dependent on its orientation with respect to the tissue. For instance, in the *Drosophila* germ band, contacts between anteroposterior neighbors disappear selectively. The new junctions are formed at the interface between dorsal-ventral neighbors. As a result, the tissue elongates along the anteroposterior axis (36, 37). In the chick neural tube, similar cell rearrangements have been described (35).

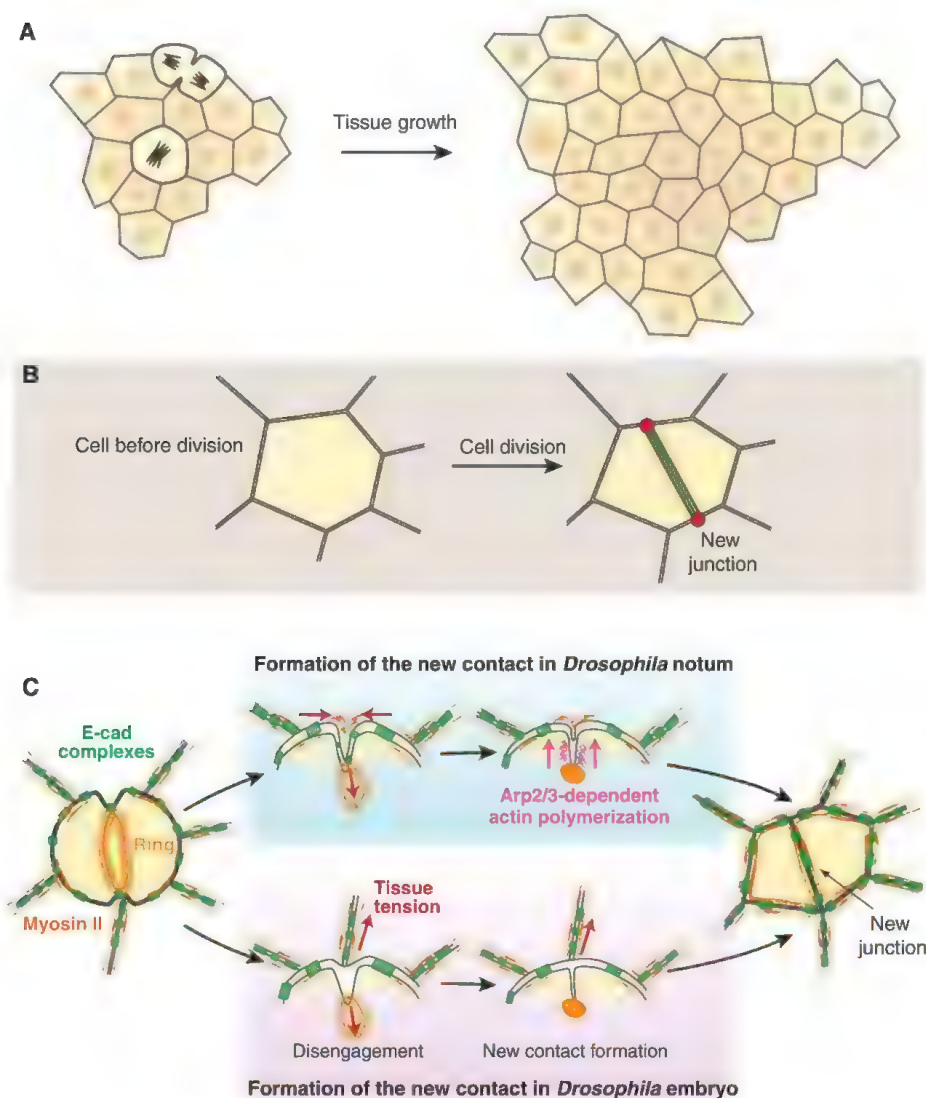


Fig. 3. Cell division in an epithelial layer. (A) Expansion of an epithelium by cell division. (B) Cell division produces a new cell junction (green) and two new vertices (red). (C) Successive stages of cell division in the *Drosophila notum* (top) and embryo (bottom), showing how intrinsic tension (due to ring contraction, red arrow) and extrinsic tension (red arrows) control disengagement of E-cadherin (E-cad) complexes and annealing of cell surfaces (top). Arp2/3-dependent polymerization controls new contact formation and/or stability (purple arrow, top).

Morphogenesis

In principle, cell junction remodeling and intercalation could be controlled by external constraints acting on the tissue. In the *Drosophila* pupal wing, this is likely to be the case, as hinge contraction drives cell rearrangements (38). However, in several systems, cells locally produce the energy used to remodel contacts by forming planar-polarized actomyosin cables connecting two or more vertices together (Fig. 5, A and B). This process is both active and to a certain degree collective, as it involves a minimum of four cells, and as many as seven or eight cells, connected by supracellular contractile cables (Fig. 2B).

Studies in *Drosophila* and chicken delineate a similar pathway for polarized regulation of actomyosin contractility by the Rho1 pathway (Fig. 5D). RhoGEFs (35, 39), ROCK (40, 41), and myosin II regulatory light chain (35–37) are recruited and activated in a planar-polarized manner by surface receptors. Although these remain unknown in *Drosophila*, in the chick, PDZ-RhoGEF is activated by the planar cell polarity pathway, namely Celsr2, the ortholog of *Drosophila* Fmi (35). The increased bond tension at cell interfaces (42, 43) could explain cell contact remodeling as shown using computational methods (35, 43). Adhesion is also likely lower in anteroposterior contacts of the *Drosophila* germ band, because there are fewer and smaller E-cadherin adhesion clusters in these contacts (37, 39). Cell intercalation was recently shown to depend on interfacial tension controlled by another myosin called Dachs, which is involved in planar cell polarization (44).

Cell intercalation drives tissue extension when the process is planar-polarized. The polarity is imposed by the orientation of interfacial stresses controlled by actomyosin networks. It is unclear how extension of the new junction occurs and whether this is an active or a passive process.

Toward a Multiscale Model of Tissue Dynamics

General principles of tissue homeostasis and morphogenesis emerge from the comparison of how junctions are formed, removed, or exchanged in epithelia. Junction dynamics is not a passive response to external and internal forces; it is an active process at cell contacts, whereby cells act collectively to remodel the junctions. On long time scales, junction dynamics confer fluid behavior through the dissipation of active stresses propagating in the tissue from its boundaries or internally controlled. This fluid behavior may explain how large-scale deformations, such as morphogenesis, arise. In some cases, junction remodeling is prevented and cells are stretched by multicellular actomyosin cables. This is the case at compartment boundaries, which prevent miscibility between two large groups of cells (45, 46). In the chick neural tube, similar large-scale supracellular cables may allow tissue buckling by accumulating stress in the tissue as it closes (35). It will be important to investigate the

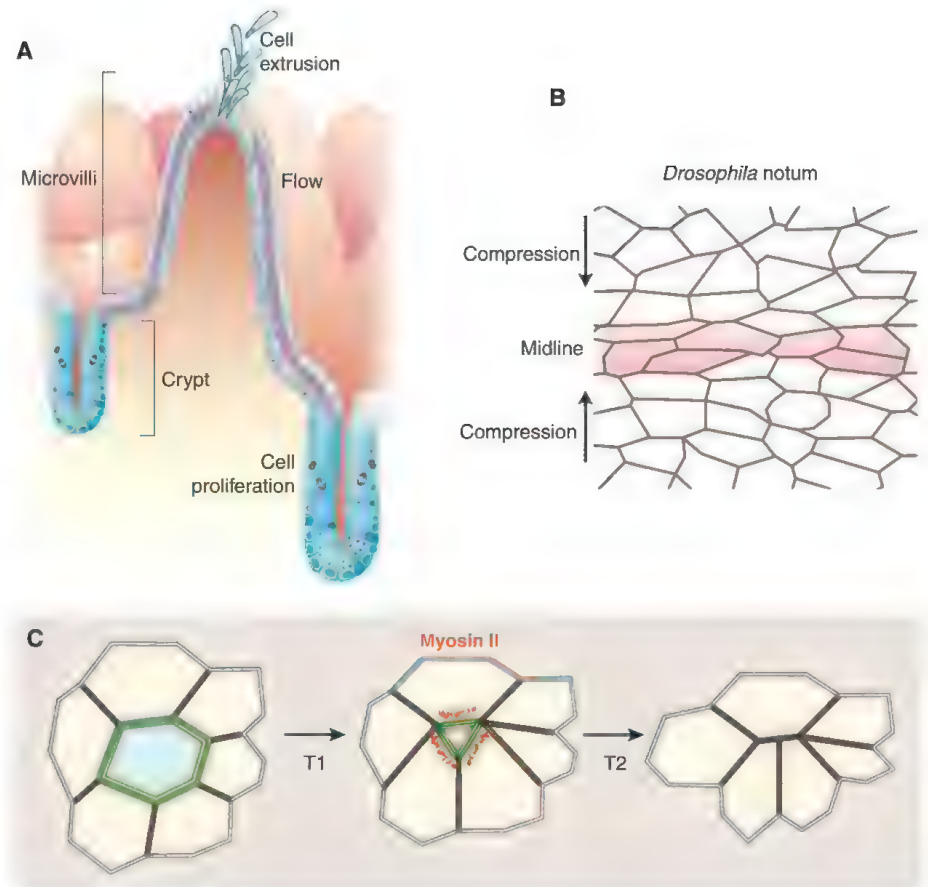


Fig. 4. Cell extrusion in epithelia can be mechanically induced. (A) In the mammalian gut, cells divide in the crypt and move to the top of microvilli, where they die or extrude while alive. (B) In *Drosophila*, cell compression due to tissue growth changes cell shape (red) and causes live cell extrusion. (C) Live cell extrusion requires displacement of two or three cell neighbors by junction removal using T1 swaps (see Fig. 5C). This is followed by accumulation of myosin II in a ring in neighboring cells (orange), producing T2 events and complete cell extrusion.

cellular mechanisms controlling whether a cell can or cannot remodel cell contacts in response to internal stresses and the compressive forces acting from the tissue boundaries into the whole tissue. The adaptive response of E-cadherin adhesive complexes to actomyosin stresses, namely their ability to remodel or to reinforce, is likely an important area of future study. Cell junction dynamics requires dynamics of vertices where interplay occurs between actomyosin tension and adhesive clusters. Whether vertices are subject to a specific regulation relative to junctions will be an important consideration in determining how cell mechanics drives tissue dynamics.

Cell division, cell death, and cell intercalation modify the distribution of cell stresses in an epithelium. It is unclear how these local phenomena affect the global properties of the tissue (such as its global stress pattern), or how changes in global properties may in turn affect these local processes (47, 48). For instance, polarized cell division would result in an effective polarized growth and stress that could potentially affect tissue organization.

Whether cells can dissipate this stress by live cell extrusion or intercalation will have a profound impact on tissue organization and morphogenesis. Likewise, an overgrowth could affect the accumulation of stress in a tissue depending on whether cells can extrude. We are just beginning to see what sort of mechanical interplay exists between local and tissue scales in epithelia, and this will be an important avenue of investigation.

As we have seen, cell and tissue behaviors are also controlled by biochemical signals that control, for instance, actomyosin network dynamics and contractility. Biomechanical feedbacks operate on two different scales. At the cellular scale, cell deformation and actomyosin flows in cells transport polarity proteins and regulators of actomyosin contractility, thereby explaining to some extent how cell deformations and polarization are self-organized (49). At the tissue level, signals that are produced and exchanged at cell interfaces, and that coordinate cell contractility, may be influenced by the very cell deformation they control. Changes in the orientation or number

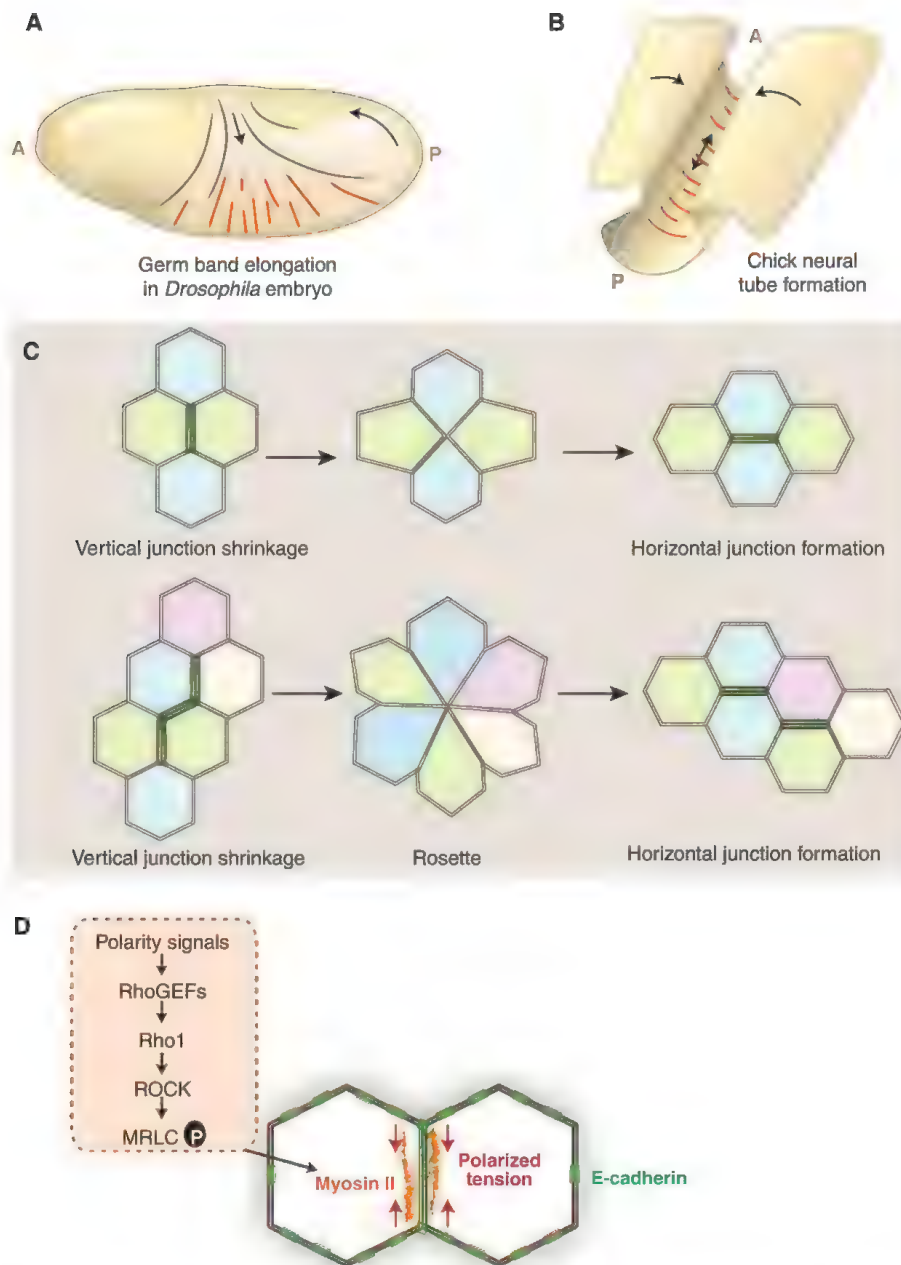


Fig. 5. Epithelial remodeling by cell intercalation. (A and B) *Drosophila* germ band extension (A) and chick neural tube closure (B) require cell intercalation (T1 swap) driven by polarized myosin II accumulation at cell contacts. (C) Planar junction remodeling consists of two steps: junction shrinkage to produce tetrads (top) or rosettes (bottom), and junction growth at a perpendicular. This process is planar-polarized in elongating tissues. (D) Junction shrinkage requires polarized phosphorylation of myosin II regulatory light chain (MRLCp), enrichment of myosin minifilaments, and polarized interfacial tension.

of cell junctions may affect the flow of information through the tissue; whether this information is in the form of polarity complexes that interact locally and propagate by proxy (38, 50) and/or whether it is in the form of long-range morphogens (51) remains to be elucidated.

We are entering an exciting time when interdisciplinary research enables us to understand the fundamental properties of tissue functional

homeostasis and morphogenesis by considering the interplay between biochemical and mechanical signals across different scales of organization.

References and Notes

- G. A. Gomez, R. W. McLachlan, A. S. Yap, *Trends Cell Biol.* **21**, 499 (2011).
- S. Yonemura, *Curr. Opin. Cell Biol.* **23**, 515 (2011).
- T. Lecuit, P. F. Lenne, *Nat. Rev. Mol. Cell Biol.* **8**, 633 (2007).

- J. Brasch, O. J. Harrison, B. Honig, L. Shapiro, *Trends Cell Biol.* **22**, 299 (2012).
- P. Katsamba et al., *Proc. Natl. Acad. Sci. U.S.A.* **106**, 11594 (2009).
- N. Borghi et al., *Proc. Natl. Acad. Sci. U.S.A.* **109**, 12568 (2012).
- M. Cavey, M. Rauzi, P. F. Lenne, T. Lecuit, *Nature* **453**, 751 (2008).
- R. Desai et al., *Nat. Cell Biol.* **15**, 261 (2013).
- S. Huveneers et al., *J. Cell Biol.* **196**, 641 (2012).
- J. L. Maître et al., *Science* **338**, 253 (2012).
- M. C. Gibson, A. B. Patel, R. Nagpal, N. Perrimon, *Nature* **442**, 1038 (2006).
- Y. Gu, J. Rosenblatt, *Curr. Opin. Cell Biol.* **24**, 865 (2012).
- T. Nishimura, M. Takeichi, *Curr. Top. Dev. Biol.* **89**, 33 (2009).
- A. Vichas, J. A. Zallen, *Semin. Cell Dev. Biol.* **22**, 858 (2011).
- W. T. Gibson et al., *Cell* **144**, 427 (2011).
- M. Glotzer, *Science* **307**, 1735 (2005).
- S. Reinsch, E. Karsenti, *J. Cell Biol.* **126**, 1509 (1994).
- N. Founounou, N. Loyer, R. Le Borgne, *Dev. Cell* **24**, 242 (2013).
- C. Guillot, T. Lecuit, *Dev. Cell* **24**, 227 (2013).
- S. Herszterg, A. Leibfried, F. Bosveld, C. Martin, Y. Bellaiche, *Dev. Cell* **24**, 256 (2013).
- N. Olivier et al., *Science* **329**, 967 (2010).
- A. L. Knox, N. H. Brown, *Science* **295**, 1285 (2002).
- B. D. Simons, H. Clevers, *Exp. Cell Res.* **317**, 2719 (2011).
- G. T. Eisenhoffer et al., *Nature* **484**, 546 (2012).
- E. Marinari et al., *Nature* **484**, 542 (2012).
- K. J. Sonnemann, W. M. Bement, *Annu. Rev. Cell Dev. Biol.* **27**, 237 (2011).
- A. Puliafito et al., *Proc. Natl. Acad. Sci. U.S.A.* **109**, 739 (2012).
- J. P. Trinkaus, M. Trinkaus, R. D. Fink, *J. Exp. Zool.* **261**, 40 (1992).
- K. D. Irvine, E. Wieschaus, *Development* **120**, 827 (1994).
- L. A. Davidson, R. E. Keller, *Development* **126**, 4547 (1999).
- R. Keller et al., *Philos. Trans. R. Soc. London Ser. B* **355**, 897 (2000).
- E. M. Munro, G. M. Odell, *Development* **129**, 13 (2002).
- P. J. Keller, *Science* **340**, 1184 (2013).
- G. Trichas et al., *PLoS Biol.* **10**, e1001256 (2012).
- T. Nishimura, H. Honda, M. Takeichi, *Cell* **149**, 1084 (2012).
- C. Bertet, L. Sulak, T. Lecuit, *Nature* **429**, 667 (2004).
- J. T. Blankenship, S. T. Backovic, J. S. Sanny, O. Weitz, J. A. Zallen, *Dev. Cell* **11**, 459 (2006).
- B. Aigouy et al., *Cell* **142**, 773 (2010).
- R. Levayer, A. Pelissier-Monier, T. Lecuit, *Nat. Cell Biol.* **13**, 529 (2011).
- T. Nishimura, M. Takeichi, *Development* **135**, 1493 (2008).
- S. M. Simões et al., *Dev. Cell* **19**, 377 (2010).
- R. Fernandez-Gonzalez, S. M. Simoes, J. C. Röper, S. Eaton, J. A. Zallen, *Dev. Cell* **17**, 736 (2009).
- M. Rauzi, P. Verant, T. Lecuit, P. F. Lenne, *Nat. Cell Biol.* **10**, 1401 (2008).
- F. Bosveld et al., *Science* **336**, 724 (2012).
- K. P. Landsberg et al., *Curr. Biol.* **19**, 1950 (2009).
- B. Monier, A. Pelissier-Monier, A. H. Brand, B. Sanson, *Nat. Cell Biol.* **12**, 60 (2010).
- B. I. Shraiman, *Proc. Natl. Acad. Sci. U.S.A.* **102**, 3318 (2005).
- T. Aegerter-Wilmsen et al., *Development* **137**, 499 (2010).
- N. W. Goehring et al., *Science* **334**, 1137 (2011).
- D. Ma et al., *Proc. Natl. Acad. Sci. U.S.A.* **105**, 18800 (2008).
- O. Wartlick, A. Kicheva, M. González-Gaitán, *Cold Spring Harb. Perspect. Biol.* **1**, a001255 (2009).

Acknowledgments: We thank members of our group, as well as R. Le Borgne and B. Shraiman, for useful comments, and C. Collinet for contributing movie S2. Supported by CNRS, ANR (Programme Blanc, Archiplast, and Labex INFORM, ANR-11-LABX-0054 under the A*MIDEX program ANR-11-IDEX-0001-02), ERC (grant 323027-Biomecamorph), and ARC (grant SL220120605305).

10.1126/science.1235249

Growing Self-Organizing Mini-Guts from a Single Intestinal Stem Cell: Mechanism and Applications

Toshiro Sato^{1*} and Hans Clevers^{2*}

Recent examples have highlighted how stem cells have the capability to initiate morphogenesis *in vitro*; that is, to generate complex structures in culture that closely parallel their *in vivo* counterparts. *Lgr5*, the receptor for the Wnt-agonistic R-spondins, marks stem cells in multiple adult organs of mice and humans. In R-spondin-based three-dimensional cultures, these *Lgr5* stem cells can grow into ever-expanding epithelial organoids that retain their original organ identity. Single *Lgr5* stem cells derived from the intestine can be cultured to build epithelial structures that retain hallmarks of the *in vivo* epithelium. Here, we review the mechanisms that support this notable example of self-organization and discuss applications of this technology for stem cell research, disease modeling (e.g., for colorectal cancer and cystic fibrosis), and regenerative medicine.

The epithelium of the small intestine has a higher self-renewal rate than any other mammalian tissue, with a turnover time of less than 5 days. Intestinal stem cells reside near the bottom of the intestinal crypt. Their rapidly dividing, transit-amplifying (TA) daughter cells oc-

cupy the remainder of the crypts and flow onto the flanks of the villi, where they differentiate, absorb nutrients, and eventually die at the villus tips (Fig. 1A). The differentiated cell types include absorptive enterocytes, multiple secretory cells (Paneth cells, goblet cells, enteroendocrine

cells, and tuft cells), and the M cells of Peyer's patches (1).

Stem Cells of the Intestinal Crypt

Cheng and Leblond (2) were the first to describe the slender crypt base columnar (CBC) cells at the crypt bottom, intercalated between the post-mitotic Paneth cells (Fig. 1B). The Wnt target gene *Lgr5* is an excellent marker for CBC cells, in turn allowing the assessment of their position in the self-renewal hierarchy by genetic lineage tracing (3). Marked *Lgr5*⁺ cells persist for the lifetime of a mouse, whereas their progeny include all differentiated cell lineages of the epithelium. Thus, *Lgr5*⁺ cells represent cycling, long-lived, multipotent stem cells. A second, quiescent stem cell type is proposed to reside at position four (directly above the Paneth cells): These “+4 cells” (1) were originally identified as DNA label-retaining cells (4). Several markers have been described for these cells, such as *Bmi-1*, *Hopx*, *mTert*, and *Lrig1* (5–8). Because the stem cell niche (microenvironment) and culture condition for +4 cells have

¹Department of Gastroenterology, Keio University School of Medicine, Tokyo 160-8582, Japan. ²Hubrecht Institute–Koninklijke Nederlandse Akademie van Wetenschappen and University Medical Centre Utrecht, Uppsalalaan 8, 3584CT, Utrecht, Netherlands.

*Corresponding author. E-mail: t.sato@a7.keio.jp (T.S.); hclevers@hubrecht.eu (H.C.)

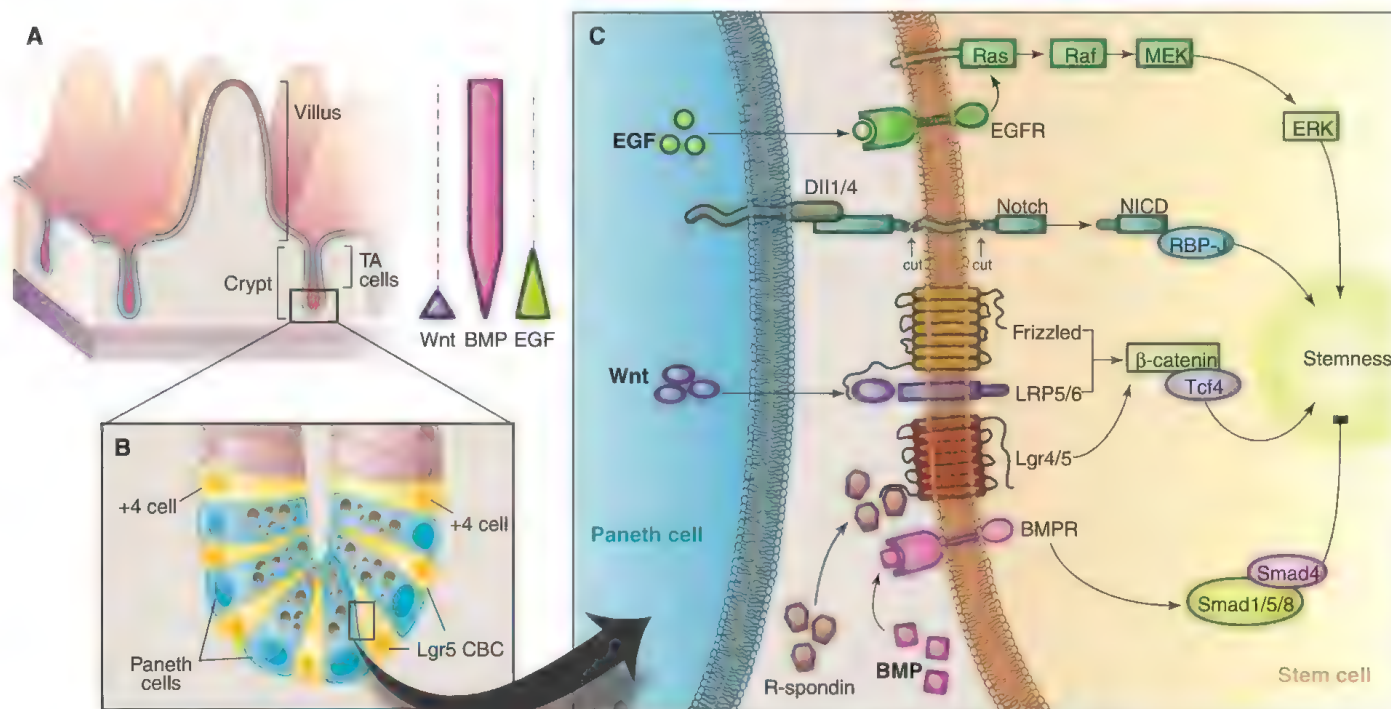


Fig. 1. Histological location and biological interaction of intestinal stem cells and their niche. (A) Scheme of intestinal epithelial structure and stem cells. Spatial gradients of Wnt, BMP, and EGF signals are formed along the crypt axis. (B) Cartoon of the stem cell niche. *Lgr5*⁺ intestinal CBC cells intimately adhere to Paneth

cells and receive signals for stem cell maintenance. (C) Three signals (EGF, Notch, and Wnt) are essential for intestinal epithelial stemness, whereas BMP negatively regulates stemness. For full Wnt activation in the intestinal epithelium, R-spondin–Lgr4/5 signal is required. Currently, the source of R-spondin is unknown.

not yet been defined, we will not discuss them further. Very recently, genetic marking of DNA label-retaining cells has identified a rare, nondividing secretory precursor that coexpresses *Lgr5* and all +4 markers. Located near crypt bottoms, this precursor undergoes terminal differentiation over periods of weeks. Upon tissue damage, it reverts into a cycling, *Lgr5*⁺ stem cell CBC cell (9). Hereafter, we refer to the dividing *Lgr5*⁺ stem cells as *Lgr5*-CBC cells to distinguish them from these much rarer, label-retaining, nondividing *Lgr5*⁺ cells.

Every murine crypt contains ~15 *Lgr5*-CBC cells (10). An *Lgr5*-CBC cell divides every 24 hours and, through its TA daughters, generates 16 to 32 differentiated epithelial cells per day. Cell division generally occurs in a symmetrical fashion, after which individual daughter cells stochastically adopt stem cell or TA cell fates, depending on available niche space (10, 11).

The Intestinal Stem Cell Niche

Intestinal homeostasis is tightly controlled by four well-characterized signaling pathways (Fig. 1, A and C). Wnt constitutes the key pathway to maintain stem cell fate and drive proliferation of stem- and TA cells (12). Paradoxically, Wnt also drives terminal differentiation of Paneth cells, that

are always in direct contact with the stem cells (13). Wnt factors, when engaging their Frizzled-Lrp5/6 co-receptors, will induce stabilization of β -catenin. The latter molecule can then bind and activate the transcription factor Tcf4, thus activating a genetic program that supports stemness (Fig. 1C). Notch is also essential to maintain the undifferentiated state. When Notch signaling is blocked in proliferative stem and TA cells, these cells differentiate into secretory lineage cells (14). *Dll1*⁺ *Dll4*⁺ Paneth cells trigger signaling by Notch1/2 on neighboring stem cells, thus keeping them from secretory differentiation (15). Each day, stem cell daughters lose contact with the *Dll1/4*-expressing Paneth cells. Some of these cells down-regulate Notch and up-regulate *Dll1*, setting their own secretory fate (16). Such a secretory precursor presents *Dll1* to six to eight neighboring Notch⁺ TA cells, which will experience active Notch signals and stay fated toward the enterocyte lineage. In sum, Notch lateral inhibition controls the enterocyte-secretory switch. Figure 1C depicts how engagement of Notch by its ligand *Dll1/4* leads to release of the Notch intracellular domain, which subsequently interacts with the nuclear effector RBP-J to suppress the gene program for secretory differentiation. Epidermal growth factor (EGF) signals exert strong mitogenic effects

on stem and TA cells upon engagement of their EGF receptors (EGFRs). Indeed, the Ras/Raf/Mek/Erk signaling axis is active in crypt epithelium. Inhibition of Mek ablates intestinal stem cells (17). Finally, bone morphogenetic protein (BMP) signals are active in the villus compartment. When BMP signaling in the villus is inhibited by transgenic Noggin, cryptlike structures appear along the flanks of the villi (18), implying that BMP inhibition creates a crypt-permissive environment. Figure 1C shows how engagement of BMP receptors by BMP leads to complexes between Smad1/5/8 and Smad 4 to repress stemness genes in the nucleus.

The *Lgr5*-CBC cells are in intimate contact with Paneth cells. Paneth cells secrete bactericidal products as well as EGF and Wnt3. Moreover, they express the Notch ligands *Dll1* and *Dll4* on their surface (Fig. 1C). Paneth cell depletion in vivo results in concomitant loss of *Lgr5*-CBC cells in several animal models (19, 20), with the exception of a conditional *Math1* mutant, which eliminates Paneth cells yet retains its stem cells (21). It was then pointed out that *Math1* deletion in *Lgr5*-CBC cells relieves the in vivo dependence on Notch ligands, which are normally provided by Paneth cells and that are essential for *Lgr5*-CBC cell maintenance (22). Durand *et al.* noted

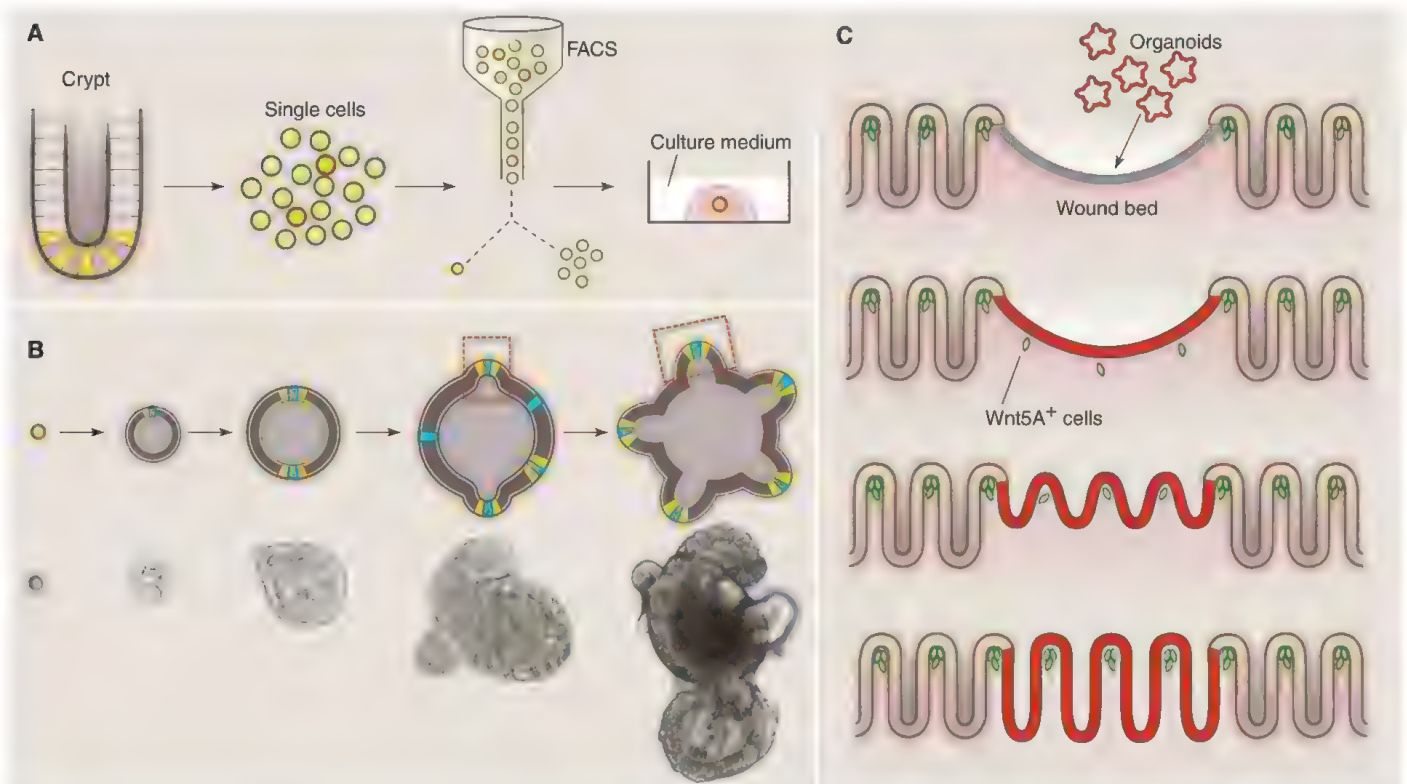


Fig. 2. Mini-gut culture system. (A) *Lgr5*⁺ CBC cells genetically labeled by EGFP are sorted and embedded in Matrigel. The culture medium consists of EGF, Noggin, and R-spondin. FACS, fluorescence-activated cell sorting. (B) Time course of organoid growth. A single stem cell forms a symmetric cyst structure. The symmetry is broken by bud formation. The budding structure resembles a

crypt. *Lgr5*⁺ CBC cells are depicted in yellow, and Paneth cells are shown in blue. (C) Scheme showing the engraftment of intestinal organoids. Organoids adhere to a de-epithelialized wound bed. Organoids form a flat epithelial layer, followed by crypt reconstruction. Wnt-5A⁺ mesenchymal cells support crypt structure formation in the damaged area. Donor organoids are depicted in red.

Morphogenesis

that *Math1*-mutant mini-guts (see below) fail to grow in vitro, which implies a crucial in vitro dependence on another signal provided by Paneth cells, probably Wnt3. Indeed, *Wnt3*^{-/-} crypts grow normally in vivo but fail to grow in vitro (13). Together, Paneth cells fulfill a stem cell niche function. In vivo, Wnts are also provided by surrounding mesenchyme (13), whereas R-spondins and BMP inhibitors are distinctly provided from nonepithelial sources.

Epithelial Mini-Gut Culture

It has generally been thought impossible to establish long-term cultures from primary adult tissues without inducing genetic transformation. Indeed, the Hayflick limit indicates that somatic cells have a limited proliferative potential (23). Yet, we have recently established an in vitro culture system to grow three-dimensional (3D) intestinal epithelial organoids ("epithelial mini-guts") from a single *Lgr5*-CBC cell for periods greater than 1.5 years (24). We employed R-spondin-1, a Wnt signal enhancer, that was later discovered as the physiological ligand of *Lgr5*: The R-spondin-*Lgr5* interaction augments Wnt signal strength initiated by the interaction of Wnt with Frizzled and Lrp (25, 26) (Fig. 1C). R-spondins are crucial in vivo. Gut-specific depletion of *Lgr4* and -5 leads to the demise of crypts (26, 27), whereas exogenous R-spondin-1 induces hyperplasticity of crypts (28). The isolated crypts require Matrigel (BD Biosciences, San Jose, CA), a 3D laminin- and collagen-rich matrix that mimics the basal lamina. A cocktail of R-spondin, EGF, and Noggin represents the minimal, essential stem cell maintenance factor cocktail. For colon crypt culture, Wnt ligand is an additional factor required to maintain *Lgr5*-CBC cells, because the epithelium

makes little, if any, Wnt. Of note, this approach also allows derivation of intestinal organoids from induced pluripotent stem cells (29). In an alternative approach, intestinal fragments containing epithelial and mesenchymal components from neonatal mice were grown for several months in a collagen gel with air-liquid interface in the presence of serum. The expanding cystic structures consisted of a simple epithelium of all cell types surrounded by myofibroblasts and were responsive to R-spondin-1 and Notch inhibition. They did not develop defined crypt- and villus-like domains (30).

Single crypts can be readily isolated from mouse or human intestine by EDTA-based $\text{Ca}^{2+}/\text{Mg}^{2+}$ chelation. Such crypts grow into 3D organoids under the culture conditions described. Culturing of single stem cells is inefficient at 1 to 2% plating efficiency, whereas up to half of the stem cell-Paneth cells doublets form organoids in vitro (19). This doublet assay has allowed demonstration that Paneth cells monitor the metabolic state to fine-tune stem cell activity (31).

In vitro-generated organoids occur as cysts with a central lumen flanked by a simple, highly polarized villus epithelium. Multiple cryptlike structures project outward (Fig. 2B). The basal side of the cells is oriented toward the outside, touching the matrigel, whereas enterocyte brush borders form the luminal surface. Secretion by Paneth and goblet cells occurs toward the lumen. The organoids can be passaged weekly at a 1:5 ratio for at least 1.5 years, with a phenotype and karyotype that remain unchanged. Mechanically disrupted organoids rapidly reseal. Self-renewal kinetics and cell-type composition closely resemble the in vivo situation. Notably, a timer of unknown molecular nature remains active in the absence of the in vivo

wear-and-tear: 2 to 3 days after terminal differentiation, the cells exfoliate into the lumen.

How normal are the epithelial mini-guts? To test this, large numbers of organoids were grown in vitro from a single *Lgr5* stem cell (Fig. 2B) that was marked by a red fluorescent protein in the adult colon (32). These in vitro-expanded colon organoids were reintroduced per anum into the colons of multiple mice with chemical-induced mucosal lesions (Fig. 2C). The engrafted epithelial mini-guts regenerated epithelial patches that were indiscernible from surrounding recipient epithelium. The patches persisted for at least 6 months without changing their histologic appearance.

How Does an *Lgr5* Stem Cell Establish Epithelial Mini-Gut Architecture?

When epithelial mini-guts derived from a Wnt reporter mouse (*Axin2-LacZ*) are grown under standard conditions, strong Wnt signals only occur adjacent to Paneth cells (19) (Fig. 3A). This fits with the notion that Paneth cells are the only source of Wnt in culture (13) and that R-spondin-1 that is ubiquitously present in the medium enhances these focal Wnt signals. Thus, sharp Wnt gradients surround Paneth cells. In a medium containing Wnt3A in addition to R-spondin-1, the Wnt gradient is lost and epithelial mini-guts become symmetric, round cysts, consisting of a homogeneous population of stem and progenitor cells (19). Epithelial mini-guts grown from adenomatous polyposis coli (APC)-mutant adenoma cells display the same symmetric shape (19), which is not surprising, because APC loss leads to constitutive Wnt pathway activation. These observations imply that the typical crypt-villus architecture is suppressed under conditions of homogeneous (rather than focal) Wnt signaling.

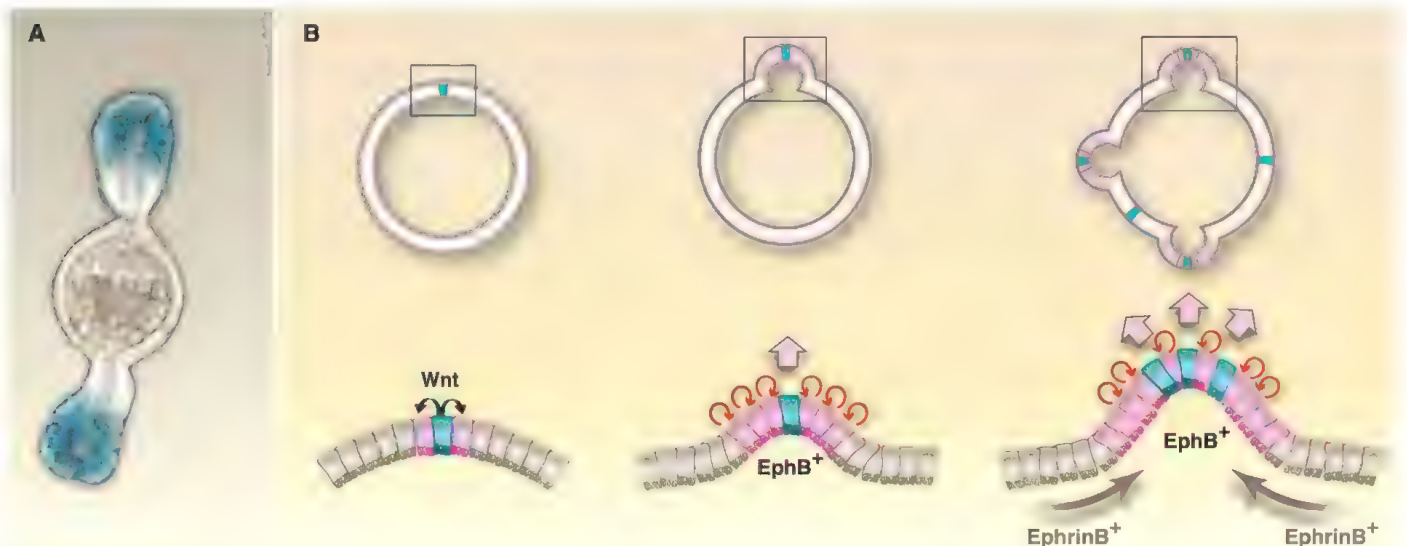


Fig. 3. Mechanism of the self-organizing architecture of a mini-gut. (A) An organoid derived from *Axin2-LacZ* knock-in mice. *Axin2-LacZ* (blue) expression recapitulates Wnt activation. (B) Wnt activation induces local pro-

liferation and EphB expression. Local cell expansion and Eph-Ephrin repulsive force generate bud formation. Wnt-producing Paneth cells are depicted in blue; Wnt-activated cells are shown in pink.

When a single cultured stem cell is followed over time, a small symmetric cyst forms. The stochastic appearance of a Paneth cell constitutes the “symmetry-breaking” event (Fig. 3B): A bud forms around the cell; within 2 to 3 days, this bud develops into a cryptlike structure with stem and Paneth cells. Every nondifferentiated cell that touches a Paneth cell is (or becomes) an Lgr5-CBC cell (16, 19), presumably driven by potent Wnt and Notch signals from the Paneth cell.

The proliferative stem cell–Paneth niche pushes itself outward from the central cyst (movie S1). This process is most likely driven by repulsive EphB–EphrinB interactions, as described in vivo (33). EphB2 and -B3 are Wnt target genes, expressed by Paneth and stem cells. When TA cells move toward the villus in vivo, they travel down the Wnt gradient. As a consequence, they differentiate and gradually replace EphB expression by expression of the counterstructures, EphrinBs. Translated to the situation in the mini-gut, cells that sit at the Wnt source (Paneth cells and their direct neighbors, the Lgr5-CBC cells) are EphB⁺. Because all other cells in the central cyst do not experience Wnt signals and express the counterstructure EphrinB, the EphB⁺ stem cells and Paneth cells are expelled from the cyst and create a bud (Fig. 3B). In these cryptlike buds, the Wnt3-producing (and, therefore, EphB3⁺) Paneth cells are sorted toward the bottom. Thus, a Wnt-gradient is automatically created along the crypt axis. Proliferating TA cells are mechanically pushed toward the lumen by younger TA cells, thus experiencing rapidly decreasing Wnt levels. This drives their

terminal differentiation into one of the villus-epithelial cell types, with Notch lateral inhibition acting as the enterocyte-secretory fate switch.

How Stem Cell Numbers Are Controlled

Touching a Paneth cell appears necessary and sufficient to acquire and maintain the Lgr5-CBC cell phenotype. Thus, a key parameter that controls crypt homeostasis is the number of Paneth cells. Strong Wnt signals, in the absence of Notch signals, drive formation of new Paneth cells (13, 34). Because Paneth cell–derived Wnt can, in turn, generate more stem and Paneth cells, a Wnt-driven positive-feedback loop could potentially induce ever-expanding crypts. Two E3 ligases (Rnf43 and Znf3) are encoded by stem cell–specific Wnt target genes (35). These two E3 ligases down-regulate Wnt receptors, thus serving as feedback inhibitors of the Wnt pathway (35, 36). When this negative-feedback loop is broken by deletion of the two E3 ligase genes, a rapidly expanding Paneth–stem cell zone is observed (35). Thus, Rnf43 and Znf3 serve in the homeostatic control of crypt size by negatively regulating Wnt signal strength. The strength of the EGF signal also affects stem cell numbers. Deletion of Lrig1, a negative regulator of EGFR family members, leads to increased stem cell numbers in vivo and in culture (17).

Epithelial Mini-Guts as Experimental Tools

The ability to grow epithelial mini-guts from single cells can be used as a surrogate marker of stemness, allowing the study of (the interrelation-

ship of) intestinal stem cell types (6, 37–39, 40). Although cycling Lgr5-CBC cells grow under standard conditions (24), the addition of Wnt3A can coerce proliferative progenitors, such as the Dll1⁺ secretory precursor (16), or even the non-dividing Paneth precursors (9, 41), to revert to a stem cell phenotype and generate epithelial mini-guts.

Organoids that are grown from mouse intestine are amenable to all standard experimental manipulations used for cell lines, including long-term storage by freezing, transfection of DNA and of small interfering RNA, and infection with recombinant retro- and lentiviruses (42). They can be analyzed by immunohistochemistry and confocal immunofluorescence, gene expression microarray, and mass spectrometry. Floxed alleles can be deleted in culture (for instance, using CreERT2 in conjunction with tamoxifen) and the effect followed in real time. The identification of Lgr4 and -5 as receptors of R-spondins has rested on the generation of organoids mutant in these genes (26, 27, 43). Other genes studied in organoids include Toll-like receptor 4 (44), Troy (45), and YAP (46).

The organoid technology is well suited to the study of cell-biological phenomena that require a closed epithelial structure with a physiological, polarized topology. Mizutani *et al.* studied P-glycoprotein (an efflux transporter acting at the intestinal epithelium) in mini-guts. The transporter was observed at the apical (luminal) membrane in organoids and actively pumped rhodamine 123 toward the luminal space (47).

Organoids recapitulate the complete stem cell differentiation hierarchy and allow the in vitro

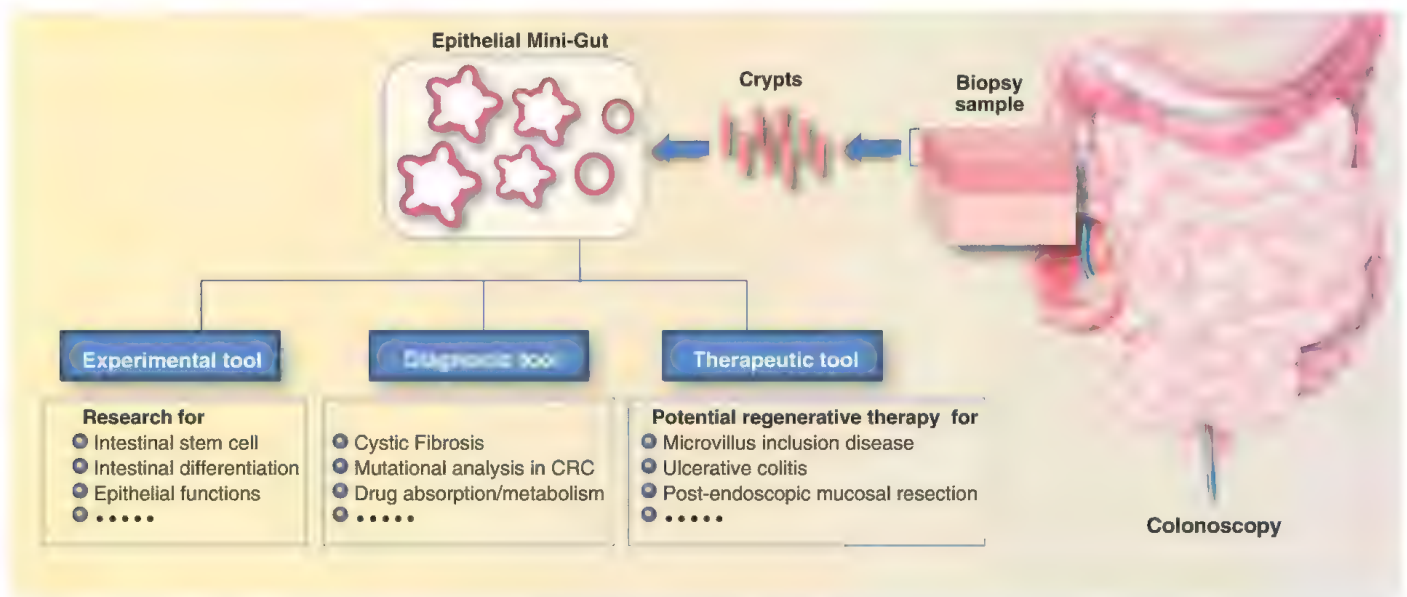


Fig. 4. Basic and clinical applications of an epithelial mini-gut. An epithelial mini-gut is efficiently established from a single (3 to 5 mm²) endoscopic biopsy sample. EDTA chelation releases ~3000 crypts from a biopsy sample. An epithelial mini-gut grows logarithmically and expands 1000-fold within a month. Three applications of epithelial mini-guts are as follows: (i) As an experimental tool. Genetic manipulation, gene expression analysis, live imaging,

and other standard biological analyses can be employed for normal and patient-derived epithelial mini-guts. (ii) As a diagnostic tool. Patient-derived epithelial mini-guts recapitulate in vivo intestinal epithelial functions and genetic signatures. Efficient expansion of pure epithelial cells provides a high-quality source for deep sequencing or functional assays. (iii) As a therapeutic tool. Epithelial mini-gut transplantation may become a feasible regenerative therapy.

study of cell fate determination. Inhibition of Notch signaling in vitro (42, 48), for instance, phenocopies the effects of the same manipulation in vivo (14), resulting in the massive production of goblet cells. Local, retrovirally driven production of Wnt3 converts the recombinant Wnt3-expressing cells into Paneth cells (13). Peyer's patch M cells are normally absent in organoid culture. Simple addition of RANKL, essential for M cells in vivo (49), robustly induces M cell formation. The minute numbers of M cells in the gut have previously precluded their detailed study. This may now be overcome by this in vitro system.

The technology described here has been used to study how a regenerating colon reestablishes its repetitive crypt architecture. Wnt5a is focally expressed by intercrypt mesenchyme, driving the overlying epithelium to differentiate (Fig. 2C). Wnt5a-soaked beads block local growth when placed onto organoids (50). Malignant transformation can also be studied in organoids. Introduction of activating Wnt pathway mutations generates organoids that are spheroid and no longer require R-spondin-1 (19, 35, 51, 52). Along these lines, deletion of the EGF inhibitor *Lrig1* allows the mutant organoids to grow without EGF (17).

Epithelial Mini-Guts as Disease Models

Protocols have been developed to grow human epithelial mini-guts from biopsies (53) or single human EphB2⁺ stem cells (54). Human intestinal epithelial cells are more difficult to grow and require small-molecule inhibitors for activin-like kinase and p38 mitogen-activated protein kinase, in addition to the mouse colon epithelial mini-gut culture condition. The protocol has been applied for the study of cystic fibrosis (CF), a disease caused by mutations in the cystic fibrosis transmembrane conductance regulator (CFTR) chloride channel. Raising adenosine 3',5'-monophosphate levels by forskolin opens the channel and results in membrane depolarization of wild-type mice, but not of *Cftr*-knockout mice (55). Along these lines, forskolin induces a robust swelling of wild-type mini-guts, but not of mini-guts derived from CF patients (56). The function of the common, temperature-sensitive CFTR-F508del mutant is restored at 27°C and by addition of experimental CFTR corrector compounds. The simple and robust assay can be performed within weeks after biopsy. It may facilitate diagnosis, drug development, and personalized medicine approaches in CF.

The culture protocol also allows the establishment of organoids from primary human adenomas and colorectal cancers (53). Because the success rate of establishing the cultures from individual

patient samples is near 100%, this allows the prospective generation of large "living biobanks," side-by-side with healthy tissue from the same individual. This presents the opportunity to bridge the current experimental gap between deep-sequencing efforts in human colon cancer (57) and patient outcome.

The notable ability of single intestinal Lgr5-CBC cells to grow into structures that faithfully recapitulate the self-renewing intestinal epithelium offers a broad range of experimental approaches. In its current guise, the technology is restricted to epithelial phenomena. Future applications may include the study of immune-mediated diseases (by reconstitution with components of the immune system) or infectious diseases (by coculture with pathogens). Because intestinal organoids can be expanded indefinitely from single stem cells, the technology may present a safe venue for gene therapy approaches: The offspring of individual stem cells, transduced in culture, can be analyzed at the clonal level. This allows the selection of individual mini-guts with safe integrations, which can then be expanded for subsequent transplantation. Because biopsies taken from live donors can serve as the tissue source, this approach could solve ethical and logistical issues associated with organ transplantation and may represent a safe complement to embryonic or induced pluripotent stem cell-based strategies.

In sum, intestinal stem cells possess the notable capacity to form epithelial structures in vitro that closely resemble the self-renewing crypt-villus architecture of the gut. These mini-guts can be expanded for periods of years and are amenable to essentially all experimental technologies that have been developed for cell lines. A variety of applications of mini-guts have been reported in studies of stem cell behavior, gene function, and disease modeling (Fig. 4). Thus, mini-guts present an opportunity to exploit in a variety of ways the distinct morphogenetic characteristics of adult stem cells.

References and Notes

1. L. G. van der Flier, H. Clevers, *Annu. Rev. Physiol.* **71**, 241 (2009).
2. H. Cheng, C. P. Leblond, *Am. J. Anat.* **141**, 537 (1974).
3. N. Barker et al., *Nature* **449**, 1003 (2007).
4. C. S. Potten, *Nature* **269**, 518 (1977).
5. E. Sangiorgi, M. R. Capecchi, *Nat. Genet.* **40**, 915 (2008).
6. N. Takeda et al., *Science* **334**, 1420 (2011).
7. R. K. Montgomery et al., *Proc. Natl. Acad. Sci. U.S.A.* **108**, 179 (2011).
8. A. E. Powell et al., *Cell* **149**, 146 (2012).
9. S. J. Buczacki et al., *Nature* **495**, 65 (2013).
10. H. J. Snippert et al., *Cell* **143**, 134 (2010).
11. C. Lopez-Garcia, A. M. Klein, B. D. Simons, D. J. Winton, *Science* **330**, 822 (2010).

12. V. Korinek et al., *Nat. Genet.* **19**, 379 (1998).
13. H. F. Farin, J. H. Van Es, H. Clevers, *Gastroenterology* **143**, 1518, e7 (2012).
14. J. H. van Es et al., *Nature* **435**, 959 (2005).
15. L. Pellegrinet et al., *Gastroenterology* **140**, 1230, e1 (2011).
16. J. H. van Es et al., *Nat. Cell Biol.* **14**, 1099 (2012).
17. V. W. Wong et al., *Nat. Cell Biol.* **14**, 401 (2012).
18. A. P. Haramis et al., *Science* **303**, 1684 (2004).
19. T. Sato et al., *Nature* **469**, 415 (2011).
20. J. Geiser, K. J. Venken, R. C. De Lisle, G. K. Andrews, *PLoS Genet.* **8**, e1002766 (2012).
21. T. H. Kim, S. Escudero, R. A. Shivdasani, *Proc. Natl. Acad. Sci. U.S.A.* **109**, 3932 (2012).
22. A. Durand et al., *Proc. Natl. Acad. Sci. U.S.A.* **109**, 8965 (2012).
23. L. Hayflick, *Exp. Cell Res.* **37**, 614 (1965).
24. T. Sato et al., *Nature* **459**, 262 (2009).
25. K. S. Carmon, Q. Lin, X. Gong, A. Thomas, Q. Liu, *Mol. Cell Biol.* **32**, 2054 (2012).
26. W. de Lau et al., *Nature* **476**, 293 (2011).
27. R. C. Mustata et al., *EMBO Rep.* **12**, 558 (2011).
28. K. A. Kim et al., *Science* **309**, 1256 (2005).
29. J. R. Spence et al., *Nature* **470**, 105 (2011).
30. A. Ootani et al., *Nat. Med.* **15**, 701 (2009).
31. O. H. Yilmaz et al., *Nature* **486**, 490 (2012).
32. S. Yui et al., *Nat. Med.* **18**, 618 (2012).
33. E. Battle et al., *Cell* **111**, 251 (2002).
34. J. H. van Es et al., *Nat. Cell Biol.* **7**, 381 (2005).
35. B. K. Koo et al., *Nature* **488**, 665 (2012).
36. H. X. Hao et al., *Nature* **485**, 195 (2012).
37. A. D. Gracz, S. Ramalingam, S. T. Magness, *Am. J. Physiol. Gastrointest. Liver Physiol.* **298**, G590 (2010).
38. R. J. von Furstenberg et al., *Am. J. Physiol. Gastrointest. Liver Physiol.* **300**, G409 (2011).
39. K. S. Yan et al., *Proc. Natl. Acad. Sci. U.S.A.* **109**, 466 (2012).
40. H. Tian et al., *Nature* **478**, 255 (2011).
41. S. Roth et al., *PLoS ONE* **7**, e38965 (2012).
42. B.-K. Koo et al., *Nat. Methods* **9**, 81 (2012).
43. H. Ruffner et al., *PLoS ONE* **7**, e40976 (2012).
44. C. P. Sodhi et al., *Gastroenterology* **143**, 708 (2012).
45. B. Fafulek et al., *Gastroenterology* (2012).
46. E. R. Barry et al., *Nature* **493**, 106 (2013).
47. T. Mizutani et al., *Biochem. Biophys. Res. Commun.* **419**, 238 (2012).
48. K. L. VanDussen et al., *Development* **139**, 488 (2012).
49. W. de Lau et al., *Mol. Cell Biol.* **32**, 3639 (2012).
50. H. Miyoshi, T. S. Stappenbeck, *Cell Cycle* **12**, 387 (2013).
51. A. G. Schepers et al., *Science* **337**, 730 (2012).
52. S. Schmitalla et al., *Cell* **152**, 25 (2013).
53. T. Sato et al., *Gastroenterology* **141**, 1762 (2011).
54. P. Jung et al., *Nat. Med.* **17**, 1225 (2011).
55. J. Liu, N. M. Walker, M. T. Cook, A. Ootani, L. L. Clarke, *Am. J. Physiol. Cell Physiol.* **302**, C1492 (2012).
56. J. F. Dekkers et al., *Nat. Med.* (2013).
57. H. Ledford, *Nature* **464**, 972 (2010).

Acknowledgments: We thank I. Nathke and P. Appleton (University of Dundee) for providing a movie of mini-guts and A. Takano (Keio University) for figure preparation. T.S. and H.C. are inventors on several patent applications pertaining to the organoid technology (WO/2010/090513 and WO/2012/168930).

Supplementary Materials

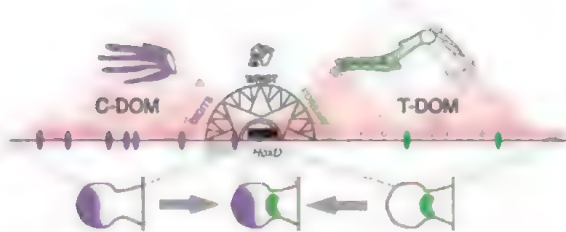
www.sciencemag.org/cgi/content/full/340/6137/1190/DC1
Movie S1

10.1126/science.1234852

A Switch Between Topological Domains Underlies *HoxD* Genes Collinearity in Mouse Limbs

Guillaume Andrey, Thomas Montavon, Bénédicte Mascres, Federico Gonzalez, Daan Noordermeer, Marion Leleu, Didier Trono, François Spitz, Denis Duboule*

Introduction: During vertebrate limb development, gene members of the *HoxD* cluster are transcribed in two subsequent waves, following a collinear strategy. Early on, genes located in the center of the cluster are transcriptionally activated and pattern a "central" part of the limbs, such as the forearm and part of the arm. Subsequently, a partially overlapping group of genes, located at one extremity of the cluster, are activated in a distal territory, which will expand and organize the distal pieces of our limbs: the hands. Although enhancer sequences controlling the latter phase have been characterized and mapped in a gene desert centromeric to the gene cluster, the location of the early enhancers, as well as the mechanism underlying the transition from the early to the late phases of transcription, remained elusive.



Regulation of *HoxD* gene collinear expression in developing limb buds. The *HoxD* cluster is flanked by two topological domains containing distinct regulatory capacities. The telomeric domain regulates early transcription in the arm and forearm. The centromeric domain subsequently patterns the hands. During limb development, a switch occurs between landscapes as specific *Hoxd* genes swing from one regulatory domain to the other through a conformational change. This modular organization creates a domain in between, which will form the wrist.

In situ hybridizations and reverse transcription quantitative real-time fluorescence polymerase chain reaction analyses were used as readouts for gene transcription.

Results: We show that the early phase of transcription requires enhancers located in the telomeric gene desert. Therefore, the early and late phases of *Hoxd* gene transcription in limb buds are controlled by two opposite deserts flanking the cluster on either side and corresponding to two adjacent topological domains. The transition between early and late regulation involves a functional and conformational switch between these domains, as reflected by a subset of genes mapping centrally into the cluster, which initially interact with the telomeric domain and subsequently shift to establish new contacts with the opposite side. This polarization of the cluster between the two domains ensures a proper collinear distribution of HOX products in both proximal and distal limb structures.

Discussion: The intriguing collinear correspondence between *Hoxd* gene topology and the patterning of proximal versus distal limb structures relies on the sequential implementation of two regulatory landscapes flanking the gene cluster. Genes located around the boundary between these two topological domains will swing from one to the other, along with the switch in regulation. The existence of independent regulation allows for cellular offset to occur between the two expression domains, where a reduced HOX protein dose is present, and which will develop into the wrist. Therefore, the mechanism patterning vertebrate proximal and distal limb pieces also contains the intrinsic capacity to build the necessary articulation in between—an adaptive value presumably explaining the selection of this complex regulatory system in tetrapods.

READ THE FULL ARTICLE ONLINE
<http://dx.doi.org/10.1126/science.1234167>

Cite this article as G. Andrey *et al.*, *Science* **340**, 1234167 (2013). DOI: 10.1126/science.1234167

FIGURES IN THE FULL ARTICLE

Fig. 1. Early phase of *Hoxd* gene transcription in forelimb buds

Fig. 2. Interaction profiles and forelimb bud enhancers.

Fig. 3. Allelic series over the telomeric gene desert.

Fig. 4. Transcriptional connectivity of the early and late domains.

Fig. 5. A conformational switch underlies collinearity in limbs.

Fig. 6. Functional independence of the regulatory landscapes.

Fig. 7. Disrupting the equilibrium between telomeric and centromeric interactions.

Fig. 8. A regulatory model for *Hoxd* gene collinearity in limbs.

SUPPLEMENTARY MATERIALS

Materials and Methods

Figs. S1 to S4

Tables S1 to S5

References

BACKGROUND READING

M. Kmita, D. Duboule, Organizing axes in time and space: 25 years of colinear tinkering. *Science* **301**, 331 (2003). doi:10.1126/science.1085753

C. Tabin, L. Wolpert, Rethinking the proximodistal axis of the vertebrate limb in the molecular era. *Genes Dev.* **21**, 1433 (2007). doi:10.1101/gad.1547407

F. Spitz, E. E. Furlong, Transcription factors: From enhancer binding to developmental control. *Nat. Rev. Genet.* **13**, 613 (2012). doi:10.1038/nrg3207

E. P. Nora *et al.*, Spatial partitioning of the regulatory landscape of the X-inactivation centre. *Nature* **485**, 381 (2012). doi:10.1038/nature11049

J. R. Dixon *et al.*, Topological domains in mammalian genomes identified by analysis of chromatin interactions. *Nature* **485**, 376 (2012). doi:10.1038/nature11082

The list of author affiliations is available in the full article online.

*Corresponding author. E-mail: denis.duboule@unige.ch; denis.duboule@epfl.ch

Stem Cell Lawsuit Finally Over. Russian Team Retrieves First Sample from Lake Vostok. Surprise Choices Mark New Leadership on U.S. House Science Panel. India Unveils Ambitious Science Policy.



Now, more than ever, developments in the lab are directly connected to decisions made in the halls of government.

*Science*Insider, the policy blog from the journal *Science*, is your source for news from the intersection of science and policy. From budget debates in the United States Congress, to climate change agreements at the United Nations, *Science*Insider covers the issues that have an impact on your work, your field, and your world.

Keep up to date and keep informed. Go inside the issues at www.ScienceInsider.org



*Science***Insider**

Breaking news and analysis from the world of science policy



A Switch Between Topological Domains Underlies *HoxD* Genes Collinearity in Mouse Limbs

Guillaume Andrey,¹ Thomas Montavon,^{1*} Bénédicte Mascrez,² Federico Gonzalez,^{2†} Daan Noordermeer,¹ Marion Leleu,¹ Didier Trono,¹ François Spitz,³ Denis Duboule^{1,2‡}

Hox genes are major determinants of the animal body plan, where they organize structures along both the trunk and appendicular axes. During mouse limb development, *Hoxd* genes are transcribed in two waves: early on, when the arm and forearm are specified, and later, when digits form. The transition between early and late regulations involves a functional switch between two opposite topological domains. This switch is reflected by a subset of *Hoxd* genes mapping centrally into the cluster, which initially interact with the telomeric domain and subsequently swing toward the centromeric domain, where they establish new contacts. This transition between independent regulatory landscapes illustrates both the modularity of the limbs and the distinct evolutionary histories of its various pieces. It also allows the formation of an intermediate area of low HOX proteins content, which develops into the wrist, the transition between our arms and our hands. This regulatory strategy accounts for collinear *Hox* gene regulation in land vertebrate appendages.

During animal embryonic development, various axial structures must be patterned along the major body axis, such as the spine, the central nervous system, or the intestinal tract. This critical function is achieved by genes such as those in the *Hox* gene family, a set of transcription factors conserved throughout animal evolution. The pioneering work of Lewis using *Drosophila* genetics (1) revealed that these genes are colocalized in the genome and that the relative order within this cluster corresponds to the relative position of the structures they instruct along the anterior-to-posterior body axis. This intriguing correspondence is referred to as “collinearity,” and its underlying molecular mechanisms have remained elusive [see, e.g., (2)].

Although *Drosophila* contains a single copy of the *Hox* gene cluster in two pieces, there are four copies of an ancestral *Hox* gene complex (the *HoxA* to *HoxD* clusters) in terrestrial vertebrates. As for *Drosophila*, the relative position of each vertebrate gene within its cluster determines the axial distribution of its future functional territory (3), reflecting the evolutionary conservation of this patterning mechanism (4, 5). The availability of multiple *Hox* clusters at the root of vertebrates made it possible for novel functions to emerge, associated with any one of these gene

complexes, which likely participated in the appearance of several vertebrate-specific features. For example, the *HoxA* gene cluster is particularly important for the proper function of neural crest cells (6).

Such neofunctionalization events often coopted several genes from the same cluster, using their collinear properties. Consequently, vertebrates display collinear *Hox* gene expression in a variety of developmental contexts, generally associated with axial structures (7). However, the mechanisms leading to these collinear distributions of HOX protein products may be different from case to case, because only the final combinatorial display of proteins was selected for, rather than the underlying process (8). This is illustrated by the comparison between the trunk and the appendicular axes, where distinct collinear mechanisms are implemented. During axial extension of the trunk, *Hox* genes are activated in a strict, progressive time sequence associated with a stepwise transition from a repressed chromatin configuration to a transcriptionally competent context (9, 10). However, the situation is distinct in vertebrate appendages.

During limb development, gene members of the *HoxD* cluster are transcribed following a clear collinear strategy (8, 11–13). Yet, unlike in the trunk, collinearity occurs through two subsequent waves of transcription, which split the pool of limb mesenchymal cells into two distinct domains along the limb proximodistal axis. Early on, genes located in the center of the cluster are transcriptionally activated and pattern the proximal part of the limbs leading to the prospective arm and the forearm (13). Subsequently, a partially overlapping group of genes, located at the centromeric extremity of the cluster, are turned on in the most distal aspect of the early domain. This subapical domain will then expand and organize the most distal pieces of our limbs: the hands [Fig. 1A and

(14)]. In this latter case, a set of enhancer sequences lying in a gene desert located immediately centromeric to the gene cluster controls transcription in digits through long-range interactions (Fig. 1B) (12).

In the present work, we addressed the mechanism for controlling both the early phase of transcription and the transition between the early and late regulations. We show that the proximodistal collinear transcription of *Hoxd* genes during limb development relies on a regulatory switch between two opposite regulatory landscapes, overlapping over a common subset of *Hoxd* loci. These landscapes correspond to topological domains (15, 16), and we show that each *Hoxd* gene displays a specific tropism for either domain, depending on its relative genomic position in the cluster.

Results

Early Phase of *Hoxd* Gene Transcription

To understand the transcriptional control of *Hoxd* genes during the early phase of expression, we quantified the level of steady-state *Hoxd* gene expression at three consecutive stages of forelimb bud development. We used embryonic day 9.5 (E9.5) early budding limbs, which is soon after the onset of *Hoxd* gene transcription, as well as entire E10.5 limb buds. We also analyzed microdissected proximal parts of E12.5 forelimbs (Fig. 1C). This latter domain contains those cells directly derived from early bud progenitor cells, which will remain at a proximal location during subsequent limb development. These cells are the remnants of the early expression phase (13) and will pattern the arm and forearm (Fig. 1A, green domains). Reverse transcription quantitative real-time fluorescence polymerase chain reaction (RT-qPCR) analyses revealed that *Hoxd9* was expressed the strongest in early E9.5 limb buds. At later stages, however, its mRNA level decreased, whereas *Hoxd11* transcription was strongly up-regulated (Fig. 1C). A comparison between the transcript profiles and the distributions of specific chromatin modifications confirmed that *Hoxd8* to *Hoxd11* are the main targets of this early phase of transcriptional regulation. These genes were indeed enriched in both H3K4me3 and H3K27ac chromatin marks, known to label actively transcribed genes (Fig. 1, D to F) (13, 17–20). In addition, the progression in time of H2K27 acetylation toward the centromeric end of the gene cluster, combined with the delayed transcription of *Hoxd11*, reflected the step-wise activation of these genes occurring during this early phase (13).

As previously observed during trunk development (10), low transcription signals were scored over *Hoxd13* in early E9.5 limb buds, before *Hoxd12* was switched on. Although this may reflect the activity of a spurious enhancer, it might also come from a few cells already implementing the second phase of transcription, because this latter phase primarily targets *Hoxd13* (14). Also, although both transcripts and H3K27ac marks were

¹School of Life Sciences, Federal Institute of Technology, Lausanne, 1015 Lausanne, Switzerland. ²National Research Centre “Frontiers in Genetics,” Department of Genetics and Evolution, University of Geneva, 1211 Geneva 4, Switzerland. ³Developmental Biology Unit, European Molecular Biology Laboratory, 69117 Heidelberg, Germany.

*Present address: Department of Epigenetics, Max Planck Institute of Immunobiology and Epigenetics, Stübeweg 51, 79108 Freiburg, Germany.

†Present address: Developmental Biology Program, Sloan-Kettering Institute, New York, NY 10065, USA.

‡Corresponding author. E-mail: denis.duboule@unige.ch; denis.duboule@epfl.ch

detected over the *Hoxd4* to *Hoxd3* region at the earliest stage, their amounts progressively decreased subsequently (Fig. 1, C, D, and F). In contrast, the *Polycomb*-associated mark H3K27me3

(21–23) was depleted from the telomeric half of the cluster in early limb buds, whereas it displayed a maximal coverage toward the centromeric extremity, peaking over *Hoxd13* (Fig. 1G). Lower amounts of

H3K27me3 signals were also detected over the promoter regions of both *Hoxd11* and *Hoxd10*, which presumably reflects the presence of nonexpressing cells located in the anterior-most aspect of forelimb

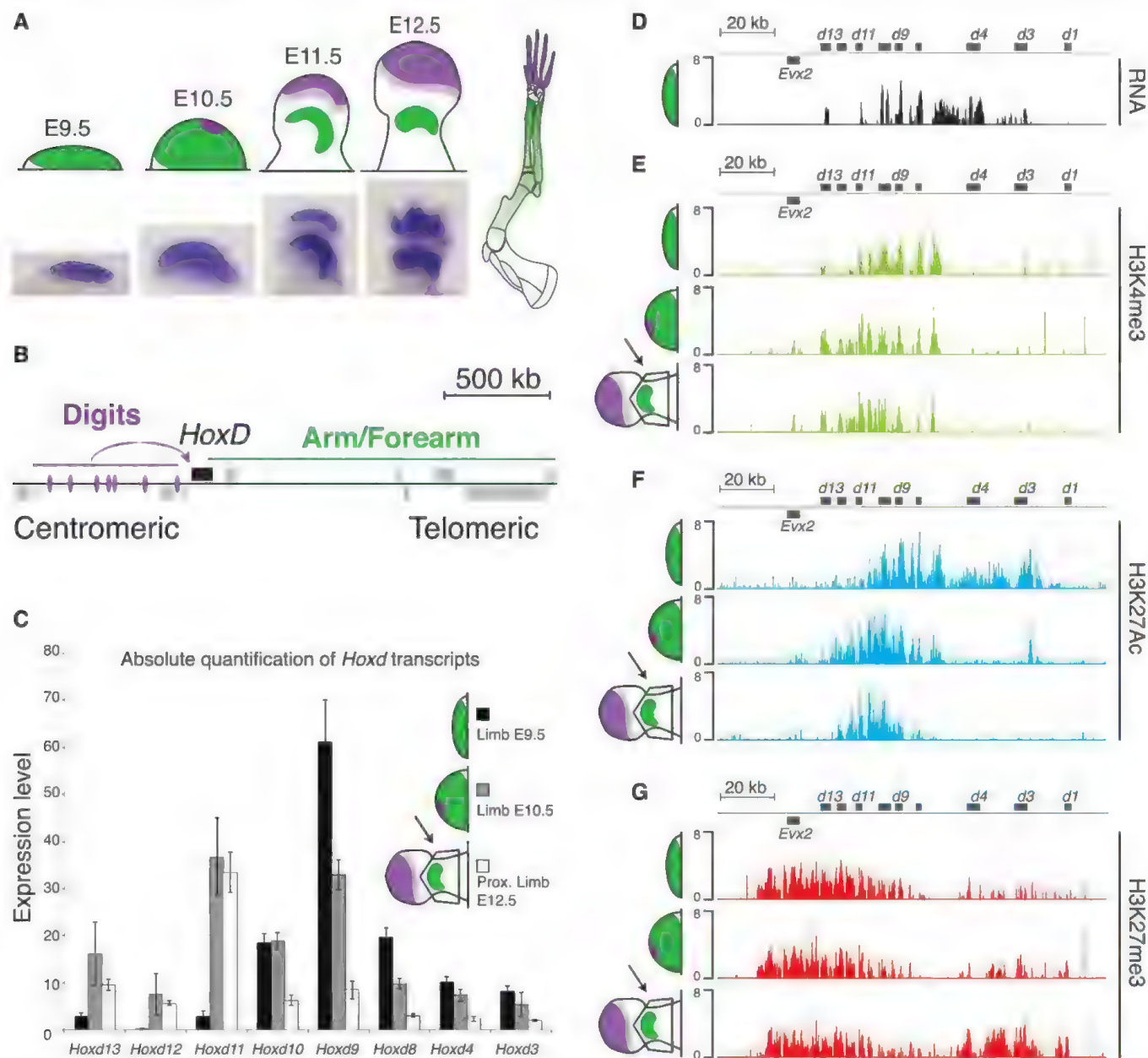


Fig. 1. Early phase of *Hoxd* gene transcription in forelimb buds. (A) Expression of *Hoxd10* during bud outgrowth (bottom) with a schematic illustration of the early (green) and late (purple) phases of expression (top). Early on, *Hoxd10* expression involves most cells of the forelimb bud. Subsequently, a small group of distally located cells starts to implement the late regulation (purple at E10.5). The two domains eventually separate from one another (E11.5). The skeleton on the right shows the fate of the two domains. (B) Schematic of the *HoxD* locus, with its centromeric regulatory landscape (purple ovals) controlling expression in digits and hypothetical arm/forearm enhancers located telomeric to the cluster (29). Genes are indicated as gray rectangles. Centromeric (5') and telomeric (3') sides are indicated. (C) Absolute quantification of steady-state levels of *Hoxd* transcripts in entire forelimb buds at E9.5 and E10.5, as well as in proximal forelimbs (without digits) at E12.5 (schemes on the right). *Hoxd9* is the most robustly expressed gene at E9.5, whereas *Hoxd11* mRNA content is strongly increased at E10.5. Error bars, mean \pm SD ($N = 4$ pairs of limbs). (D) Tiling array hybridization of

E9.5 forelimb bud mRNAs showing the robust transcription of the central part of the gene cluster. The y axis represents a log2 scale of cDNA/gDNA (genomic DNA) signal intensity. (E) Centrally located *Hoxd* genes (*Hoxd8* to *Hoxd11*) are decorated with the active mark H3K4me3 at all stages. The y axis represents a log2 scale of chromatin immunoprecipitation (ChIP)-enriched/input gDNA signal intensity. (F) Profiles of H3K27Ac marks, which label both active enhancers and promoters. Together with the *Hoxd8* to *Hoxd10* region, the 3'-located promoters (e.g., *Hoxd3* and *Hoxd4*) are acetylated at the earliest stage, likely due to their transcription in lateral plate mesoderm. They become progressively deacetylated over time, as *Hoxd11* becomes acetylated. The y axis represents the ChIP-enriched minus input gDNA normalized read count. (G) The H3K27me3 repressive mark decorates early on the inactive, centromeric part of the gene cluster. These marks are subsequently gained in the *Hoxd1* to *Hoxd4* region, when these latter genes are no longer transcribed. The y axis represents a log2 scale of ChIP-enriched/input gDNA signal intensity.

buds and included in our dissections. At later developmental stages, the *Hoxd4* to *Hoxd3* region became also decorated with this mark, in agreement with the loss of both transcriptional activity and H3K27 acetylation (Figs. 1C, F, and G) (13).

A Telomeric Regulatory Landscape

We used circular chromosome conformation capture (4C) to identify contacts established either by active or inactive genes during this early phase (9, 24). *Hoxd13*, which was mostly repressed, interacted preferentially with the centromeric gene desert. The extent of this interaction domain (Fig. 2A, upper track, gray-shaded area) precisely matched a topological

domain—i.e., a domain of preferential enhancer-promoter interactions (25) reported to cover this gene desert and described in (16). Conversely, the actively transcribed *Hoxd9* gene contacted a 1.5-Mb region, telomeric to the cluster and also containing a large gene desert (Fig. 2A, middle track). Again, this desert together with a large part of the gene cluster matched a reported topological domain (Fig. 2A, middle track, gray-shaded area) directly adjacent to the former (16). In early forelimb buds, the telomeric desert was specifically labeled with H3K27ac marks, which are generally associated with active enhancers (Fig. 2A, lower track) (18, 19). The amount of this histone H3 modification, however, severely de-

creased over developmental time (fig. S1), likely reflecting the transient activity of potential enhancers located within this gene desert and active mostly during the early stages of limb bud development.

We selected 72 conserved noncoding sequences (CNS) located within this telomeric landscape (table S1) and assayed them for enhancer activity using lentivector-mediated transgenesis (26, 27). Two regions elicited a robust expression in early limb buds (Fig. 2B, CNS 39 and 65). CNS 39 triggered *lacZ* transcription in very early limb buds, as expected for a proximal regulation. However, expression localized more distally at later developmental stages. CNS 65 induced transcription in a broader domain, also at an early stage, which remained restricted to the proximal limb, subsequently (Fig. 2B). Both regions are located within the telomeric gene desert, 385 and 670 Kb away from the *HoxD* cluster, respectively. The contacts established by these sequences with the target *Hoxd* genes were verified by using both CNS 39 and 65 as viewpoints in 4C experiments (Fig. 2C). This reverse 4C approach confirmed that both sequences interact specifically with the transcribed *Hoxd* genes. In these two instances, the overall extent of the interaction landscapes, as defined by using the enhancers as baits, precisely matched the reported telomeric topological domain (Fig. 2C, gray-shaded area). These interactions between the two enhancers and the *HoxD* cluster were abruptly lost over the *Hoxd12* to *Hoxd13* region (Fig. 2C, arrows, and fig. S1). As expected from such a conformational insulation from both enhancers, these latter two genes are not transcribed (or are poorly transcribed) at this stage.

Genetic Analysis of the Telomeric Gene Desert

We assessed the function of this telomeric landscape, including both CNS 39 and 65, by engineering several deletions in vivo, as well as an inversion containing the entire gene desert (Fig. 3 and tables S2 and S3). The targeted deletion in vivo of CNS 65 alone led to a 30 to 40% decrease in the steady-state levels of *Hoxd8* to *Hoxd11* mRNAs in proximal forelimb buds at E12.5 [Fig. 3, white arrow, and fig. S2, *del(65)*]. We also used targeted meiotic recombination (TAMERE) and sequential targeted recombination (STRING) in vivo recombinant strategies (28, 29) to engineer a series of alleles carrying larger modifications (Fig. 3 and table S4). When a 150-kb region directly adjacent to the *HoxD* cluster and including the *Mtx2* gene was removed [Fig. 3, *del(attP-SB2)*], no detectable loss of either *Hoxd10* or any other centrally located *Hoxd* genes was scored in proximal limb buds, by using both in situ hybridization and RT-qPCR as readouts after dissection of the proximal domain (Fig. 3, white arrow, and fig. S2). In contrast, an almost complete abrogation of *Hoxd10* transcript accumulation in the proximal domain was achieved when the 525-kb *del(SB2-65)* deletion was used, which removed most of the gene desert (Fig. 3, white arrow). In this genetic configuration, *Hoxd* transcripts produced by the centrally located genes were depleted by 90 to 95% (fig. S2).

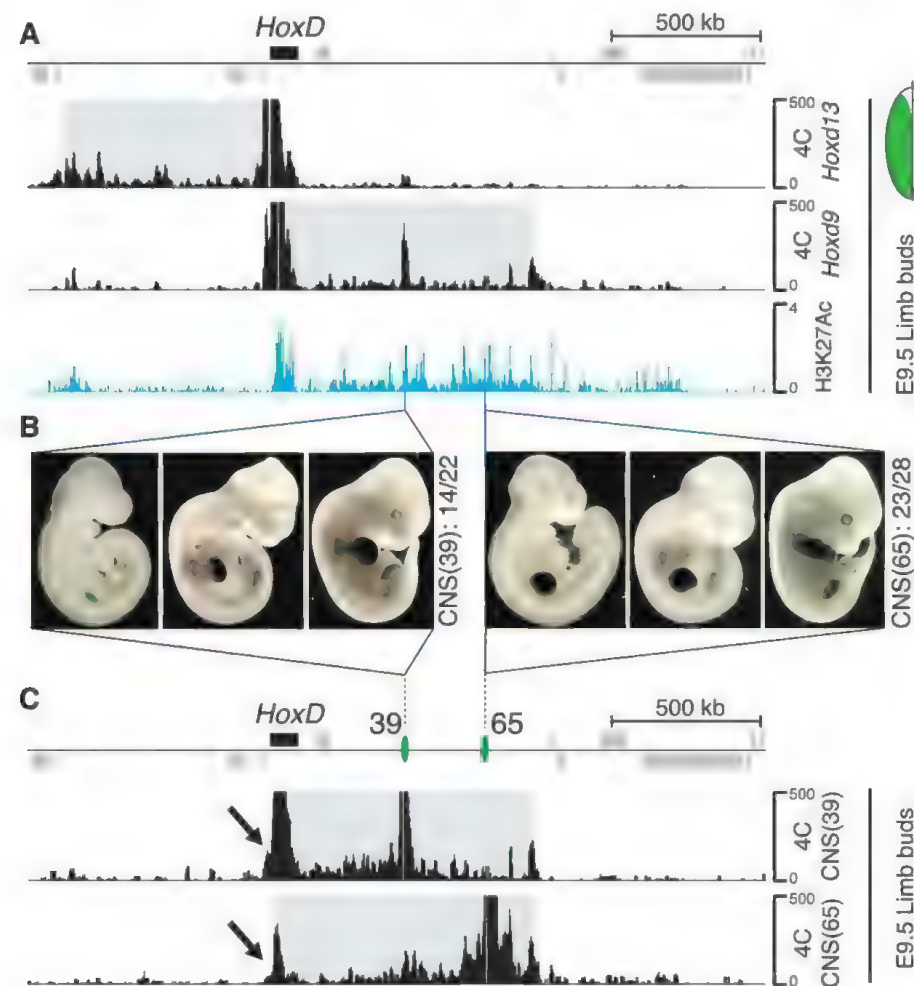


Fig. 2. Interaction profiles and forelimb bud enhancers. The 4C and H3K27Ac profiles were generated using early E9.5 limb buds. (A) The inactive *Hoxd13* gene preferentially contacts the centromeric landscape (on the left), corresponding to a topological domain according to (16) (upper track, gray-shaded area), whereas the active *Hoxd9* gene contacts the telomeric landscape with high affinity (right), also corresponding to a topological domain (middle track, gray-shaded area). The bottom track depicts the profile of H3K27 acetylation in early limb buds. The y axis represents the ChIP-enriched minus input gDNA normalized read count. (B) Two major enhancers (CNS 39 and 65) were localized within the telomeric gene desert, as shown by reporter *LacZ* patterns in transgenic embryos. The number of embryos with stained limbs over total transgenics is indicated. (C) The 4C interaction profiles (running mean, window size 11) with the CNS 39 (top) and 65 (bottom) enhancer sequences taken as viewpoints. The extents of both interaction domains (approximately covering the telomeric gene desert) are comparable when either region 39 or region 65 is used as bait. In both cases, the interaction domains match the same topological domain (gray-shaded area) as depicted in (A). In addition, both regions interact specifically with the transcribed portion of the *HoxD* cluster, with the most conspicuous peaks of interaction mapping over the *Hoxd9* to *Hoxd11* region. The frequency of interactions with both the *Hoxd13* and *Hoxd12* loci dramatically dropped down (black arrowhead) (see fig. S1).

We verified and confirmed that most of the early forelimb enhancers are located within this 525-kb DNA interval by analyzing two overlapping deletions spanning 1 Mb of telomeric DNA [Fig. 3,

del(attP-65) and *del(attP-SB3)*]. The remaining transcriptional activity completely disappeared (99% decrease) when the *inv(attP-CD44)* allele was used. In this large inversion (Fig. 3, bottom, red

arrows), the gene desert was indeed repositioned 28 Mb away from the *HoxD* cluster, and hence all potential interactions were abrogated. This also pointed to the existence of an additional remote

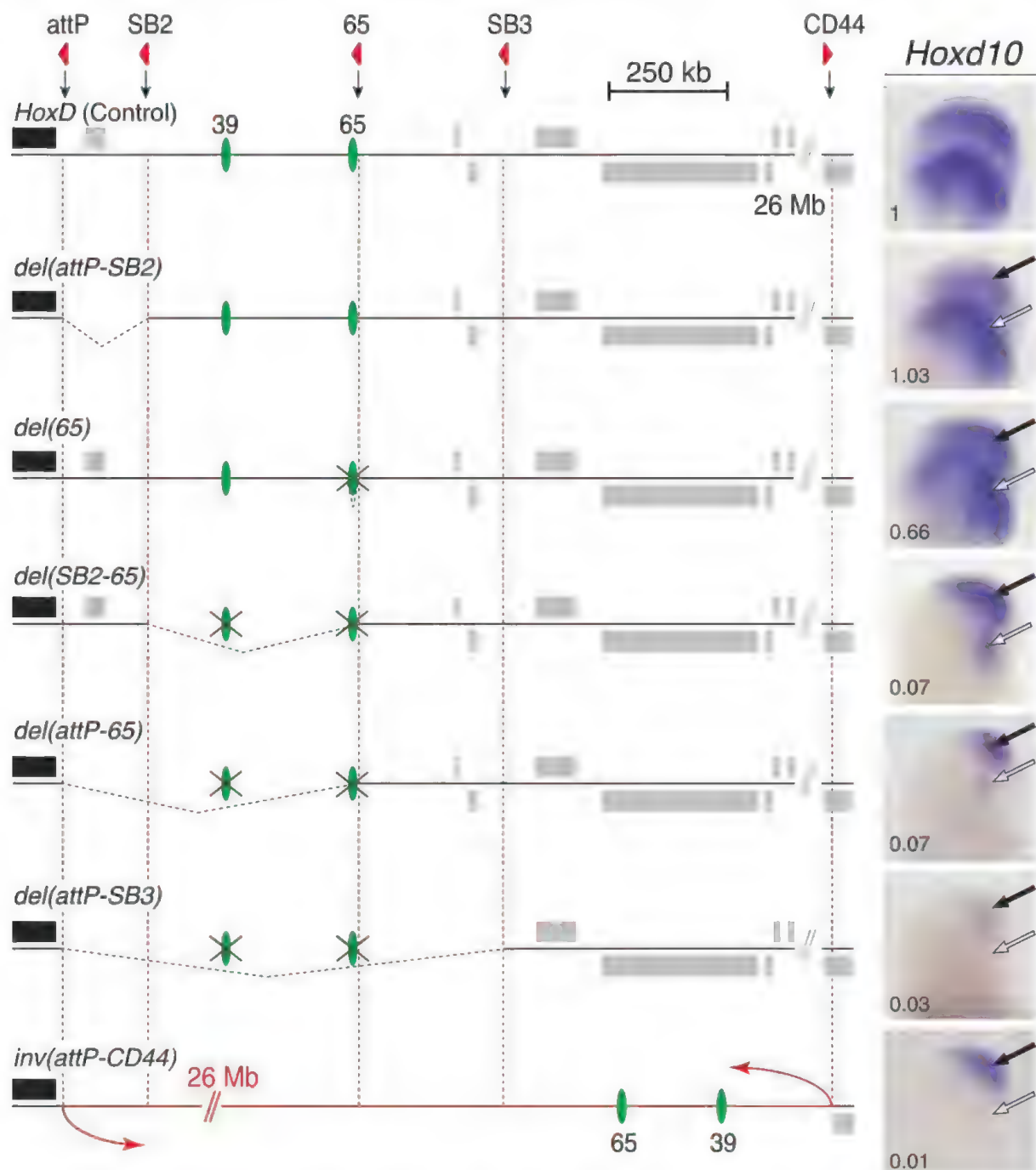


Fig. 3. Allelic series over the telomeric gene desert. This allelic series included several deletions as well as an inversion (bottom line). The CNS 39 and 65 regions are indicated with green ovals and crossed out whenever included in the deleted material in any of the mutant configuration. Animals analyzed were all heterozygotes over a balancer allele [*del(8-13)*] (13), both to ensure valid and coherent comparisons and to assess the behavior of only those *Hoxd* genes located in cis of any rearrangement. The analysis of *Hoxd10* gene expression by in situ hybridization in E11.5 embryos was used as a readout (right column). qPCR quantification of steady-state levels of *Hoxd10* mRNAs in the proximal forelimb is indicated on the bottom left corner of each panel, expressed as a fraction of the wild-type control equal to 1. In each panel, the proximal domain, resulting from the early phase of expression, is indicated with a

white arrow, whereas the late phase of expression leading to the digit domain is depicted with a black arrow. From top to bottom: A 150-kb deletion *del(attP-SB2)* had no effect on *Hoxd10* transcription ($P > 0.05$, $N = 3$ pairs of proximal limbs). The 2-kb deletion specifically removing CNS 65 significantly ($P < 0.01$, $N = 3$ pairs of proximal limbs) decreased the amount of *Hoxd10* transcript by 33%, whereas all deletions, including the *SB2-65* interval, removed more than 90% of *Hoxd10* transcripts [*del(SB2-65)*, *del(attP-65)*, and *del(attP-SB3)*; $P < 0.01$, $N = 3$ pairs of proximal limbs]. However, none of these deletions totally abrogate proximal transcription (see fig. S2). In contrast, the 28-Mb inversion *inv(attP-CD44)* (bottom) removed all traces of *Hoxd10* transcripts from the proximal forelimb, due to the dissociation between the target genes and the telomeric landscape.

enhancer(s), yet to be mapped and not included in any of the deletions used above (Fig. 3). Using this allelic series, we concluded that the early phase of *Hoxd* gene transcription in forelimb buds is controlled by enhancer sequences mostly located within the telomeric gene desert. Consequently, the two global regulations acting over the *HoxD* cluster during limb development are located in distinct topological domains, corresponding to two gene deserts present on either sides of the gene cluster.

A Transition Between Opposite Regulations

In mutant limb buds where proximal expression was almost abolished due to a telomeric deletion, we noticed a severe loss of the late expression

domain in presumptive digits, for *Hoxd9*, *Hoxd10*, and *Hoxd11* (Fig. 3 Fig. 4, A to C, black arrows, and fig. S2). Yet this was not the case for *Hoxd13*, which confirmed the presence and activity of the requested digit enhancers (12). This transcriptional down-regulation in the distal domain may have been caused by a growth defect in the distal forelimb, as induced by the absence of early *Hoxd* gene expression. We ruled out this possibility by looking at the expression of *Hoxa13*, which was used as a marker for the distal limb territory (fig. S2) (30, 31) and confirmed that these mutant embryos had normally shaped hand plates.

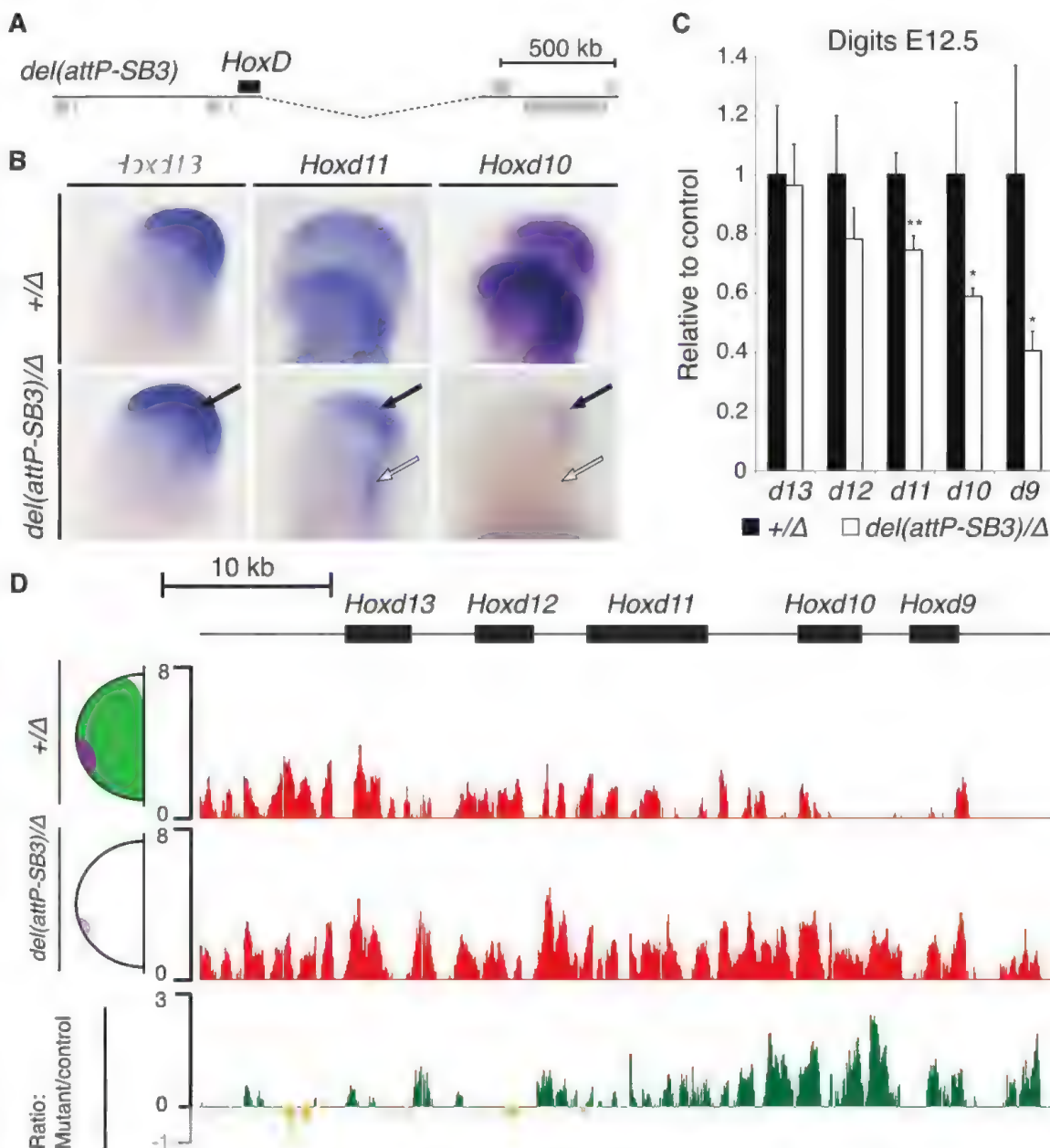
Thus, sustained transcription in the proximal domain is necessary for efficient subsequent tran-

scriptional activation of *Hoxd9* to *Hoxd11* in the digit domain. This implies that both distal and proximal *Hoxd*-expressing cells derive from the same progenitors rather than distinct progenitor populations segregated at the onset of limb development (31). Indeed, the observed effect could occur only if distal cells were derived from cells that had expressed these genes previously, during the early phase. Moreover, digit progenitor cells must go through the early expression phase to be fully licensed to activate centrally located *Hoxd* genes during the late phase, when these latter become controlled by the opposite regulatory landscape (12).

We analyzed H3K27me3 coverage over the *HoxD* cluster in *del(attP-SB3)* mutant early fore-

Fig. 4. Transcriptional connectivity of the early and late domains.

The abrogation of the early phase of transcription affects the efficiency of the subsequent transcriptional activation in digits. Δ is for the *del(8-13)* allele, used as a balancer in our crosses. (A) Scheme of the *del(attP-SB3)* deletion, removing most of the telomeric landscape. (B) This deletion strongly depletes both *Hoxd11* and *Hoxd10* transcripts from the proximal domain in E11.5 buds (white arrows). In both cases, both the intensity and extent of the distal domain was reduced too (black arrows), yet not for *Hoxd13*, which is normally not expressed in the proximal domain (left panels, black arrow). The panel showing *Hoxd10* expression is taken from Fig. 3. (C) The RT-qPCR quantifications of *Hoxd* transcripts present in the presumptive digit domain of such mutant digits show a significant decrease, from *Hoxd9* to *Hoxd11*, whereas neither *Hoxd12* nor *Hoxd13* are significantly affected. Error bars, mean \pm SD ($N = 3$ pairs of distal limbs). * $P < 0.05$, ** $P < 0.01$. (D) H3K27me3 profiles covering the centromeric part of the *HoxD* cluster in both E10.5 control (top) and mutant forelimb buds carrying a deletion of the telomeric landscape (middle). The ratio between both conditions is shown below (positive and negative values in green and orange, respectively). H3K27me3 is significantly increased over the *Hoxd9* to *Hoxd11* region in mutant limb buds, yet not over *Hoxd13*, where it remains unchanged. In the absence of *Hoxd* gene transcription, cells in the proximal domain display H3K27 trimethylation throughout this part of the cluster.



limb buds, where more than 90% of *Hoxd9*, *Hoxd10*, and *Hoxd11* transcripts were lost (fig. S2). A robust gain of H3K27me3 was scored over these three genes in the deleted configuration (Fig. 4D), coinciding with their subsequent transcriptional down-regulation in forming digits. This result suggests that in presumptive wild-type digit cells, centromeric (digit) enhancers readily access the middle part of the *HoxD* cluster due to an open chromatin configuration inherited from early limb bud cells, where this region is actively transcribed. In limbs carrying the telomeric deletions, however, this early transcription is abolished due to the absence of the appropriate enhancers. Consequently, this abnormally inactive portion of the cluster is now fully decorated with H3K27me3 chromatin marks. The unexpected presence of this *Polycomb*-associated repression likely induced the observed delay in the establishment of the second

phase of expression; when mobilized, the digit enhancers had to compete with this “negative” chromatin domain rather than interacting with a more open chromatin configuration, as in wild-type limbs. In contrast, transcription of *Hoxd13* was not modified because this gene is mostly repressed early on. H3K27me3 coverage of *Hoxd13* in mutant proximal cells was similar to what was seen in wild type, and hence its accessibility remained unchanged in the mutant.

A Regulatory Switch Between Topological Domains

From this data set, we conclude that *Hoxd9*, *Hoxd10*, and *Hoxd11* switch from telomeric regulation in early limb cells to centromeric regulation in digit cells. To confirm this hypothesis, we looked at potential modifications in three-dimensional (3D) conformations that would

occur concomitantly with the transition in regulations. We generated 4C profiles using several *Hoxd* promoters as viewpoints, in both the early and late transcription domains. In all samples analyzed, *Hoxd1* was found to interact strongly with the telomeric neighborhood, whereas *Hoxd13* was preferentially engaged toward the centromeric side. These opposite tropisms were observed regardless of the transcriptional status—i.e., whether the gene was active or inactive (Fig. 5, A and B). In contrast, both *Hoxd9* and *Hoxd11* displayed more dynamic interaction patterns. Whereas they established preferential contacts with the telomeric domain in early E9.5 forelimb cells, they both increased their interactions with the centromeric domain in E12.5 digit cells (Fig. 5, C and D), indicating that the regulatory switch is accompanied by a transition between two conformational states. This transition did not occur in

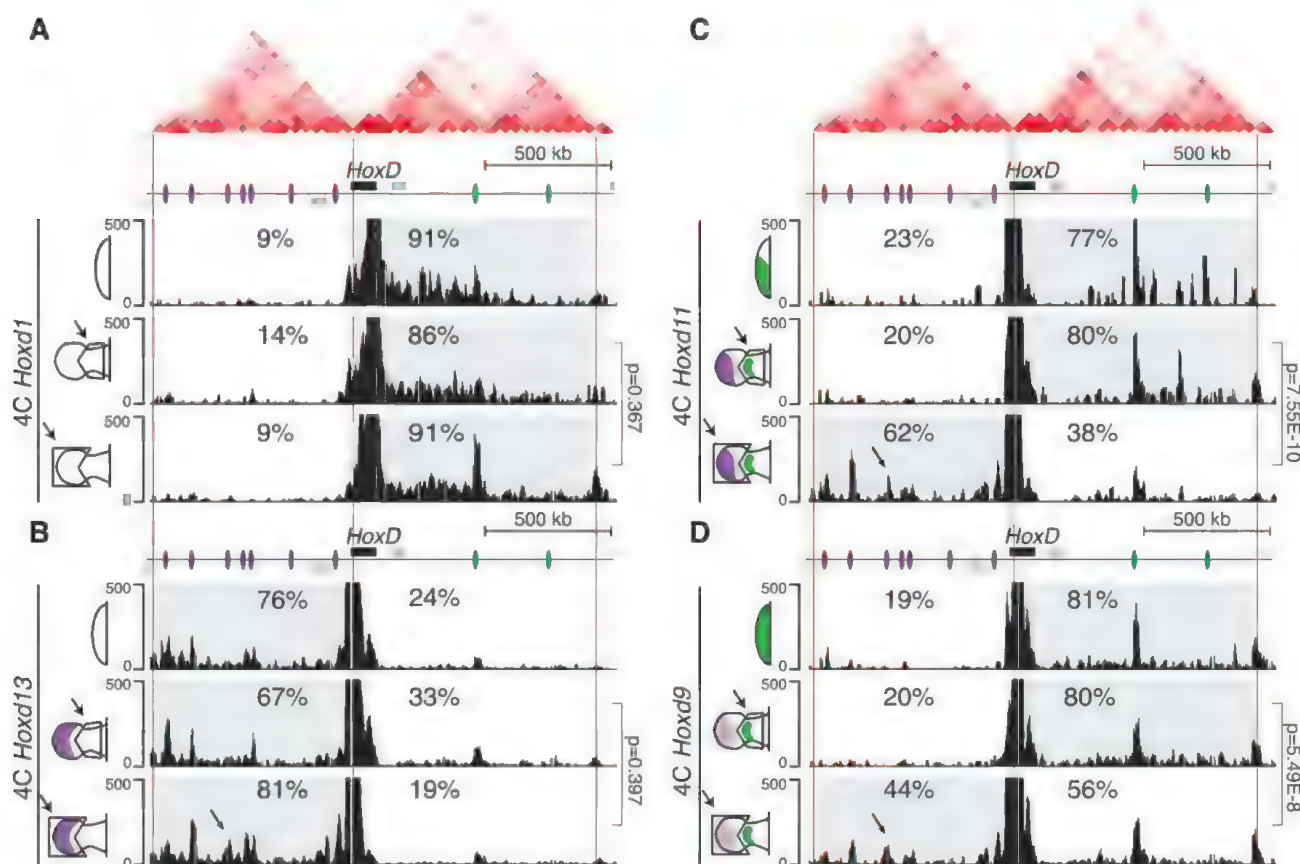


Fig. 5. A conformational switch underlies collinearity in limbs. A 4C analysis of the transition between the early and late phases of *Hoxd* gene expression in forelimb buds, as seen from different viewpoints within the gene cluster. On the left side of each track, a schematic representation of the expression pattern is shown for the corresponding gene. Green depicts the early and proximal domain, whereas the late and distal domain is shown in purple. The absence of any color reflects the absence of expression. At the top of both (A) and (C), the presence and extent of topological domains are shown, with data taken and adapted from (16). These domains, defined by HiC, reflect regions of high enhancer-promoter interactions. The red lines label their borders. The 4C interaction profiles shown below are made from a running mean. (A) *Hoxd1* is silent during the early (tracks 1 to 3) and late (track 4) expression phases. This gene establishes constitutive contacts with the telomeric domain (gray-shaded area and 86 to 91% of contacts), regardless of which regulation is implemented,

whereas 9% of the contacts are scored with the centromeric domain. (B) Likewise, *Hoxd13* strongly interacts with the centromeric landscape (gray-shaded area), regardless of whether this landscape is active or inactive, but with some differences, such as the additional contact with island 3 in digit cells, where it is transcriptionally active (arrow). (C) In contrast, *Hoxd11* can display preferential contacts with either gene desert. In the early buds and in the subsequent proximal domain, it interacts mostly with the telomeric desert (gray-shaded areas; 77 and 80%, respectively). In the distal domain, however, *Hoxd11* now switches its contacts toward the centromeric desert (62%, gray-shaded area), including a specific interaction with island 3 (arrow). (D) Likewise, *Hoxd9* mostly contacts the telomeric domain during the early phase of expression (gray-shaded area; 81 percent), yet it substantially increases its contacts with the centromeric landscape in digits, including with island 3 (arrow). In this case, however, the final balance between centromeric and telomeric interactions is almost equalized.

late proximal forelimb cells, showing that they merely maintain the early phase of transcription (Fig. 5, C and D). Notably, the conformational switch appeared more extensive for *Hoxd11* than for *Hoxd9* (Fig. 5, C and D). This may reflect the relative location of *Hoxd9* within the gene cluster, which is closer to the telomeric extremity and, as such, may have an increased preference to interact with the telomeric regulatory landscape.

The transition from the telomeric to centromeric regulation results in the strong activation of

Hoxd13 in digit cells, a gene heavily covered by H3K27me₃ in early forelimb bud cells, from where digit cells will subsequently derive. Therefore, we compared the enrichments of H3K27me₃ between the early and late transcription phases and noted a large de novo H3K27 trimethylation of the now inactive telomeric part of the cluster. This trimethylation occurred in parallel with the demethylation of the same histone H3 residue in the most centromeric—now active—part containing *Hoxd12* and *Hoxd13*, which illustrates the

antagonistic behaviors of the two topological domains (Fig. 6A).

Functional Independence of Topological Domains

We also scored a reenforced distribution of H3K27me₃ marks over the entire telomeric gene desert in digit cells (Fig. 6B). This was unexpected because a robust presence of these repressive marks was not observed previously in other contexts where *Hoxd* genes are silent, such as in

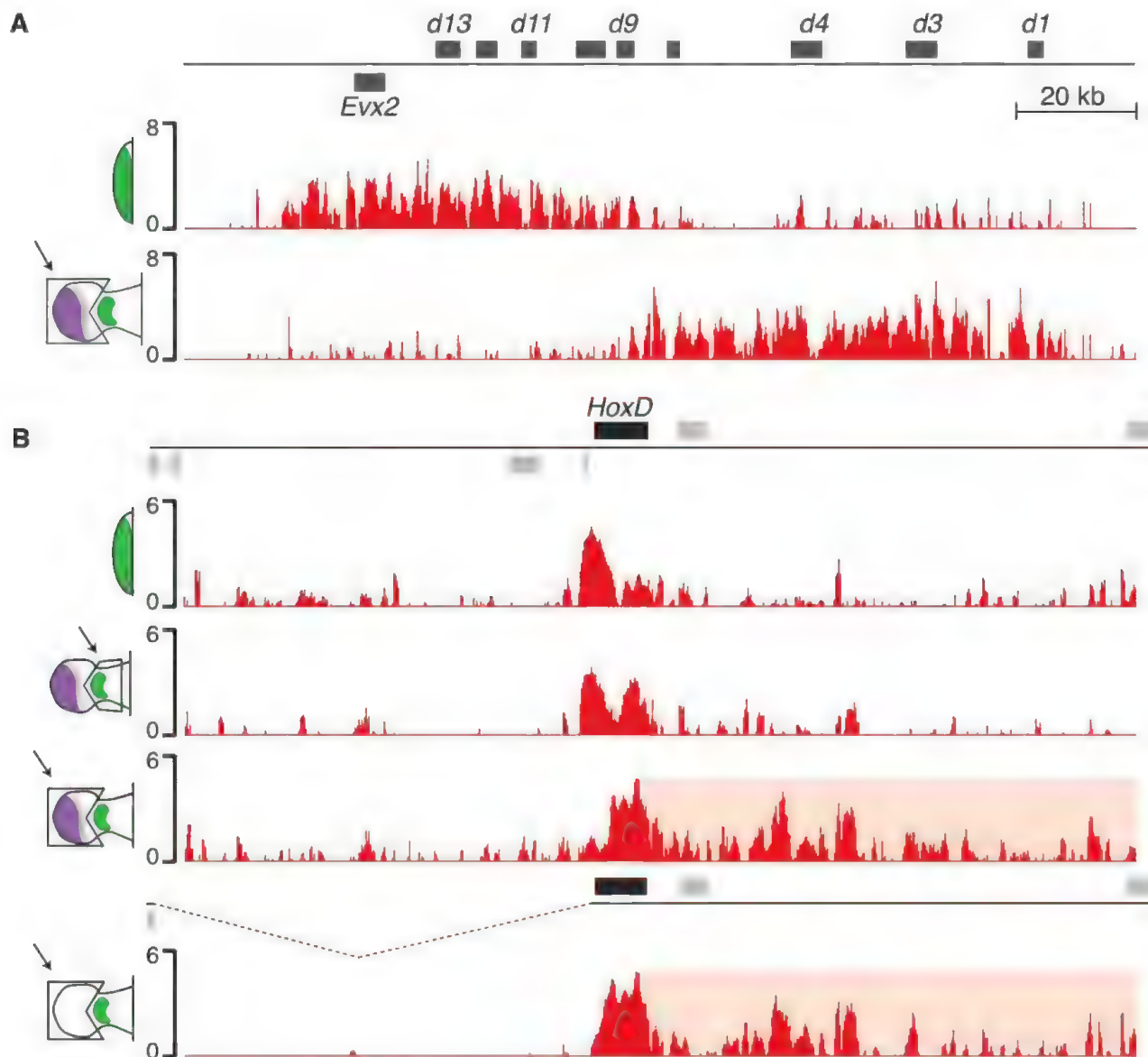


Fig. 6. Functional independence of the regulatory landscapes. (A) Dynamics of H3K27me₃ chromatin modifications covering the *HoxD* gene cluster during forelimb development. In early limb buds (upper track) where the telomeric regulation is implemented, genes located at the centromeric extremity of the cluster (e.g., *Hoxd13*) are covered by H3K27me₃ (upper track; see also Fig. 1). During the late phase of expression in the presumptive digit domain (lower track), the centromeric part of the gene cluster has now been cleared from these repression-associated marks and has become fully active. In contrast, the telomeric part of the cluster is now inactive and decorated with this posttranslational modification. The comparison between both tracks reflects the perfect complementarity of the profiles and illustrates the switch in regulations. The y axis represents a log₂ scale of ChIP-

enriched/input gDNA signal intensity. (B) The H3K27me₃ profiles over the telomeric desert show little difference between the early forelimb bud (first track) and the proximal domain of a late forelimb (second track). In contrast, this desert becomes heavily decorated with H3K27me₃ in digit cells (third track, red-shaded area), where the telomeric regulation no longer operates. In the *del(Nsi-Atf2)* deletion, which removes the centromeric gene desert (bottom track, scheme), the late phase of transcription, controlled by the centromeric regulation, is abrogated (scheme on the left). In this mutant condition, however, the trimethylation of H3K27 still occurs over the telomeric gene desert (red-shaded area), indicating that the termination of the telomeric regulation does not depend upon the start of the centromeric regulation. The y axis represents a log₂ scale of ChIP-enriched/input gDNA signal intensity.

embryonic stem cells or in the brain (10, 32). Within this gene desert, we selected those regions with the highest content of H3K27me3 modifications and compared them with another set of eleven DNA regions mapping within the desert (table S5) and showing an enrichment in the acetylation of H3K27 in early E9.5 limb buds, at a time when the telomeric regulation is fully operational. Eight out of these eleven regions were scored identically, indicating that DNA sequences heavily decorated by H3K27 acetylation in early bud cells were progressively deacetylated and trimethylated at the same H3K27 residue in digit cells. We interpret this observation as reflecting the termination of the early phase of expression (Fig. 6B) (33).

The extensive telomeric H3K27 trimethylation occurred in parallel with the acetylation of H3K27 over the opposite, centromeric gene desert (12), raising the possibility that this massive telomeric H3K27 trimethylation may be necessary to push the regulatory balance toward the active centromeric domain and secure the switch, in particular for the *Hoxd9*, *Hoxd10*, and *Hoxd11* swing genes. Alternatively, the implementation of the centromeric regulation in digits may in itself induce the switch, leading to the subsequent abrogation of the telomeric regulation and further H3K27 trimethylation of the gene desert. To discriminate between these alternatives, we looked at the H3K27me3 coverage in digits of mutant mice lacking the centromeric domain [*del(Nsi-Atf2)*] (12). In these mutant limbs, where the late regulation was no longer implemented, the telomeric

desert remained largely trimethylated at H3K27, indicating that the termination of the telomeric regulation occurred independently from the activation of the centromeric regulation (Fig. 6B).

A Fine-Tuned Balance of Interactions

These results show that the *HoxD* cluster is the target of two global and independent regulations, implemented from both flanking gene deserts. A key factor determining the activity of any gene of the cluster is its tropism toward one or the other domain, a tropism depending upon its relative position within the cluster. In early forelimb cells, the interactions with the telomeric desert are maximal for *Hoxd9*, whereas they are minimal for *Hoxd13*, correlating with their transcriptional status (fig. S3). In this tissue, a conformational insulation of *Hoxd13* from the early telomeric enhancers prevents any transcriptional leakage of this gene at this stage, a situation known to be deleterious for the limb morphology (34, 35). Conversely, the pervasive contacts established by *Hoxd13* with the centromeric desert underlie its high level of transcription in digit cells, whereas *Hoxd11* and *Hoxd9* are transcribed at progressively lower levels (fig. S3) (14), likely due to resilient contacts with the telomeric region.

We challenged this polarizing effect of the flanking gene deserts by using the 3-Mb *inv(Nsi-Ilgα6)* inversion, which completely disconnects *Hoxd13* from the centromeric gene desert (Fig. 7). We compared the interactions established by *Hoxd13* in a control proximal limb bud at E12.5 with those scored in the absence of the

neighboring gene desert and observed both a slight loss of contacts centromeric to the gene cluster (Fig. 7) (from 70 to 56%) and a concomitant increase in the interactions with the telomeric gene desert on the opposite side (from 30 to 44%). This result suggests that the disconnection between the centromeric gene desert and the *HoxD* cluster decreased the strength and/or number of contacts between *Hoxd13* and the new flanking DNA landscape, leading to a slightly increased tropism of this gene for the telomeric domain. This break in the conformational equilibrium occurred in parallel with an ectopic transcription of *Hoxd13* in the proximal limb (34), sufficient to induce a measurable shortening of forearm bones due to the suppressive effect of HOXD13 over other *Hox* gene products in the proximal limb bud (34, 36). These data illustrate that it is necessary to keep *Hoxd13* bound to the centromeric gene desert, even in the absence of transcription, to prevent its partial relocation toward the opposite regulatory domain and concurrent deleterious effects.

Discussion

Our results indicate that the correspondence between the positions of *Hoxd* genes within their genomic cluster and the proximal-to-distal sequence in the various pieces of appendicular skeleton that these genes determine is established by the antagonistic partition between two topological domains (Fig. 8A). In early limb buds, all cells are engaged into a telomeric regulation, which involves genes located centrally into the

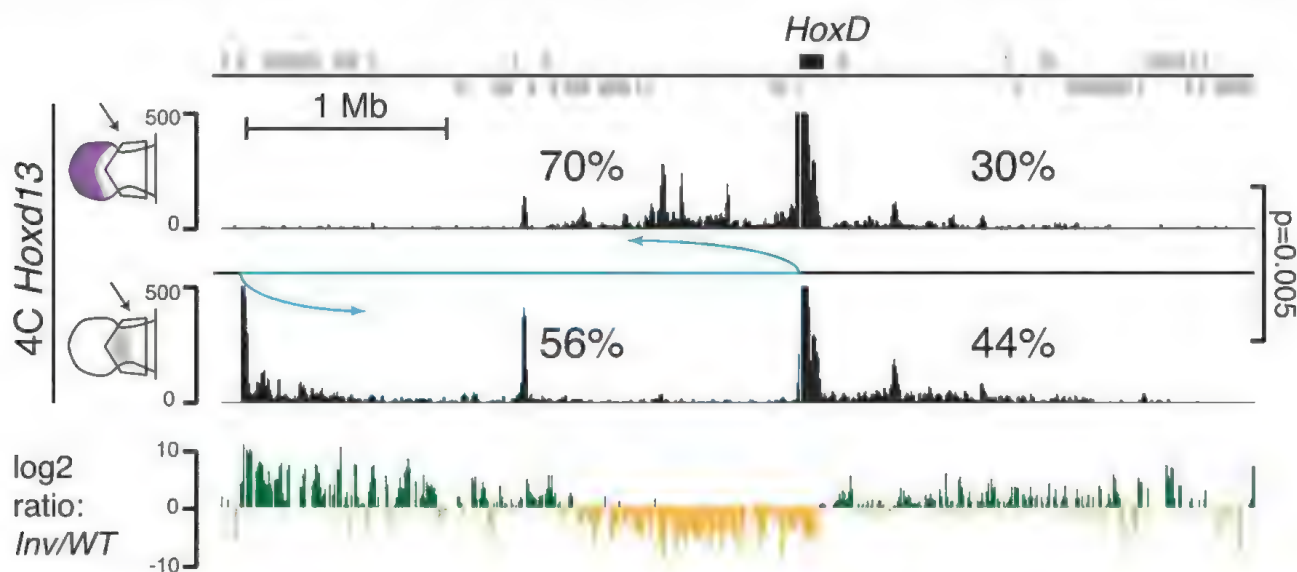


Fig. 7. Disrupting the equilibrium between telomeric and centromeric interactions. Comparison between the profiles of 4C interactions (running mean) established by *Hoxd13* in the proximal limb domain of either a control specimen (top track) or a mutant one carrying the *inv(Nsi-Ilgα6)* inversion that relocates the centromeric gene desert several megabases away from the gene cluster (middle track). In this mutant limb, the centromeric regulation can no longer operate over the *HoxD* gene cluster due to the increase distance, and hence *Hoxd13* expression is lost in digits. Because of this change in centromeric neighborhood, the interactions established by *Hoxd13* on this side are reduced (56%; green bars on the left). All contacts with the original, now displaced, centromeric domain (in

orange) are lost. In contrast, contacts are gained with the new centromeric neighborhood, which however do not fully compensate for the loss. Concomitantly, contacts are increased with the telomeric desert (44%; green bars on the right). The ratio between both conditions is shown below and illustrates the significant switch from a preference for the centromeric domain to rather equally distributed contacts between both sides ($P = 0.005$; log-likelihood ratio test for independence), suggesting that *Hoxd13* is normally prevented from responding to the telomeric regulation through its sequestering contacts with the centromeric gene desert. Animals carrying this inversion express *Hoxd13* ectopically in the proximal domain, leading to a weak mesomelic phenotype [scheme on the left and (34)].

cluster. *Hoxd13* and *Hoxd12*, to some extent, are preserved from this regulation due to their high tropism for the centromeric topological domain, which prevents them from establishing substantial telomeric contacts (Fig. 8B). Soon after the start of limb bud growth, in a subset of subapical and posterior cells, the telomeric regulation terminates, whereas the centromeric regulatory landscape becomes activated. *Hoxd13* constitutively interacts with this topological domain and is up-regulated first, followed by a set of central genes swinging from one domain to the other, with decreasing strength up to *Hoxd9*. This process accounts for the collinear expression pattern originally described in limbs (8), with a proximal-only pattern for genes closer to the telomeric part of the cluster, a distal-only pattern for *Hoxd13*, and a combined pattern for genes located at a central position, which will adopt both configurations, but at different times and in different cells.

The switch in functionality between these two constitutive topological domains may be considered as an allosteric-like transition (37), but applied to chromatin micro-architectures. Tissue-specific factors activating either of these two regulatory landscapes may act similarly to allosteric ligands, selecting between a limited number of preorganized 3D conformations and triggering the trans-

formation of a topological domain from a negative to a positive state. In this view, the recruitment of a transcription factor by enhancer sequences would not cause a complete reorganization of the 3D structure, for example by looping. Instead, a pre-formed structure may help factors to recognize their target sequences and induce minor conformational changes accompanying the formation of an active state. The fact that the transition of a topological domain from a negative to a positive configuration did not involve dramatic variations in the interaction profiles supports this view. However, although the comparison between these various profiles in active and inactive tissues indeed showed minor changes in the distribution of contacts, some of the observed differences involved DNA sequences of critical importance for the regulatory specificity. For instance, when *Hoxd13* becomes transcriptionally active, new contacts are established with one of the regulatory islands necessary for its full activity in digits (Fig. 5B, arrow, and fig. S4) (12, 16).

Thus, limb patterning by *Hoxd* genes involves a transition in the functional states of two flanking topological domains (Fig. 8, C and D). The existence of these two independent regulatory domains, one necessary to pattern the hand, the other required for patterning the forearm, fur-

ther illustrates the modular nature of our appendages. It also provides a potential explanatory framework as to how these distinct modules may have evolved at different times, in response to various environmental conditions. In this context, however, the question of the articulation between these morphological modules is critical, because the evolutionary emergence of digits without an appropriate wrist may not have represented a strong adaptive value. It is noteworthy that the subpopulation of early limb bud cells where the telomeric regulation is maintained does not participate to the further distal extension of the limb bud and will thus remain in the proximal aspect of the developing limb (Fig. 8B, green domain at E11.5). By contrast, the distal growth leading to digit development (31) will be achieved by cells implementing the centromeric regulation. Because this distal growth depends on factors released by both the apical ectodermal ridge (AER) and the zone of polarizing activity (31, 38), cells located near these signaling centers will switch toward the centromeric regulation.

Because the termination of the early phase of *Hoxd* gene expression does not require the activation of the late phase, the possibility exists for a physical separation to occur between the cells implementing the telomeric regulation, which will

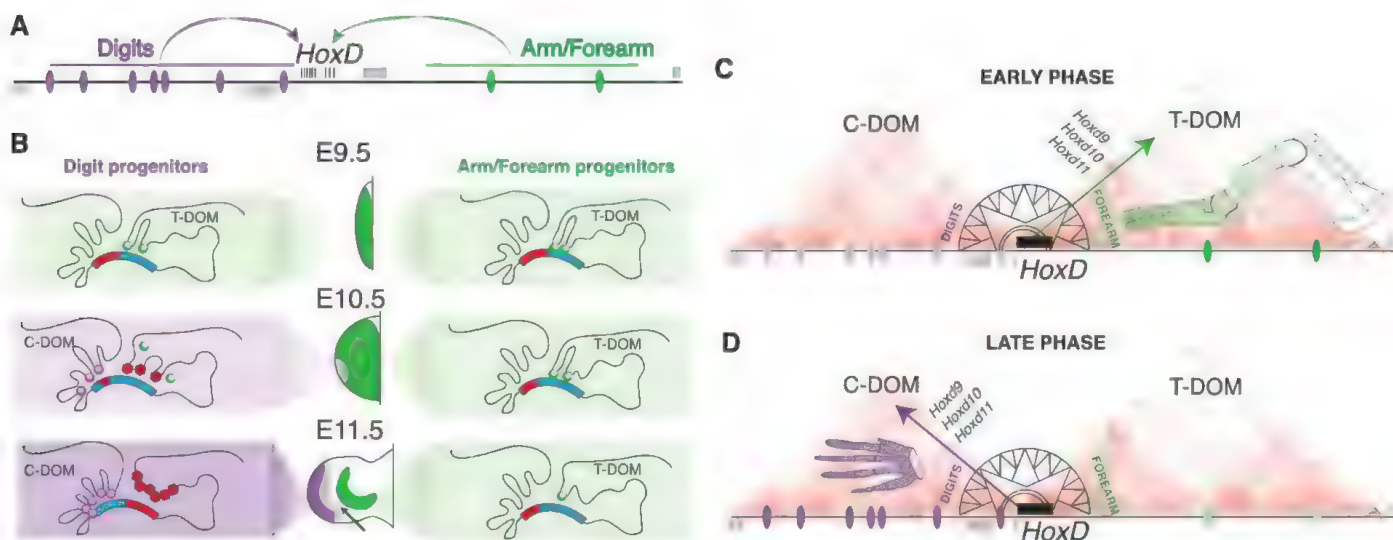


Fig. 8. A regulatory model for *Hoxd* gene collinearity in limbs. (A) Two nonoverlapping regulatory landscapes control distinct, yet partially overlapping, sets of *Hoxd* genes during limb bud development. **(B)** During early bud outgrowth (E9.5), the telomeric domain (T-DOM) and its set of early limb enhancers (green ovals) induce the first wave of gene expression in distal and proximal progenitors (green domain) with the robust activation of *Hoxd9*, followed by *Hoxd10* and *Hoxd11*, which are delayed due to their progressively increased proximity to the inactive centromeric domain (C-DOM). *Hoxd13*, which is constitutively part of the C-DOM, is closed, as illustrated by the presence of H3K27me3 (in red). The activity of these telomeric enhancers progressively decreases as the presumptive forearm grows. At E10.5, in a subset of subapical and posterior cells, the telomeric landscape becomes trimethylated at H3K27 (middle right scheme, red hexagons). At the same time, external signals activate the C-DOM (purple ovals). *Hoxd13* starts to be transcribed and concurrently demethylated at H3K27, whereas *Hoxd9*, *Hoxd10*, and *Hoxd11* change their contacts and relocate toward the active C-DOM. In presumptive digits (E11.5, left), the T-DOM and the inactive part of the cluster

become trimethylated at H3K27 (red bar and hexagons). Cells where the telomeric regulation is terminated but where the switch was not implemented, due to an increased distance to the apical signaling, do not express any *Hoxd* genes and produce a zone that will subsequently turn into the wrist (black arrow). **(C and D)** Schematic representation of the switch, as illustrated by the transition of three swing genes (*Hoxd9*, *Hoxd10*, and *Hoxd11*) from T-DOM to C-DOM, along with C-DOM becoming active and T-DOM inactive. *Hoxd13* is constitutively associated with C-DOM, whereas *Hoxd1*, *Hoxd3*, and *Hoxd4* are constitutively associated with T-DOM. The position of the boundary between these two topological domains [taken and adapted from (16)] matches the group of genes that can go either direction, depending on which landscape is activated (enhancers are colored dark and light, whether active and inactive, respectively). The set of HOX proteins produced in response to the T-DOM regulation leads to the patterning of the arm and forearm, whereas the presence of HOXD13 protein, once the regulation has switched to the C-DOM, will terminate the system and produce digits (the corresponding morphologies are schematized within each of the topological domains).

stay behind (Fig. 8B, green area), and cells implementing the centromeric regulation, which will be under the influence of the AER and hence localized at the most distal aspect of the limb bud (Fig. 8B, purple area). This segregation between the two types of *Hoxd* expressing cells leads to the appearance of an intermediate cellular territory where the global dose of HOXD proteins is minimal because cells escape both regulatory controls (Fig. 8B, arrow). This zone of low HOX protein content generates the wrist (39), which is made out of small roundish bones used to articulate the two sets of long bones found in both the forearm and the hand. Previous analyses of dominant negative mutations in both mouse and human (36, 40), which severely reduce the functional contributions of HOX proteins, have revealed a transformation of metacarpal bones into a carpal-like morphology with the loss of cortical ossification and the formation of lateral joints (40, 41). Therefore, the morphological transition between the two sets of long bones in our arms coincides with a transition between two regulatory modalities, at the boundary of topological domains. This intriguing correspondence may explain why this apparently complex system of two distinct regulations was selected and fully implemented in tetrapod species: It contained the intrinsic capacity for a built-in articulation to evolve concomitantly, which may have given a novel tetrapod appendage its full adaptive value.

References and Notes

- E. B. Lewis, A gene complex controlling segmentation in *Drosophila*. *Nature* **276**, 565 (1978). doi: 10.1038/276565a0; pmid: 1030000
- R. K. Maeda, F. Karch, The ABC of the BX-C: The bithorax complex explained. *Development* **133**, 1413 (2006). doi: 10.1242/dev.02323; pmid: 16556913
- S. J. Gaunt, P. T. Sharpe, D. Duboule, Spatially restricted domains of homeo-gene transcripts in mouse embryos: Relation to a segmented body plan. *Development* **104**, 169 (1988).
- D. Duboule, P. Dollé, The structural and functional organization of the murine HOX gene family resembles that of *Drosophila* homeotic genes. *EMBO J.* **8**, 1497 (1989). pmid: 2569969
- A. Graham, N. Papalopulu, R. Krumlauf, The murine and *Drosophila* homeobox gene complexes have common features of organization and expression. *Cell* **57**, 367 (1989). doi: 10.1016/0092-8674(89)90912-4; pmid: 2566383
- M. Minoux, F. M. Rijli, Molecular mechanisms of cranial neural crest cell migration and patterning in craniofacial development. *Development* **137**, 2605 (2010). doi: 10.1242/dev.040048; pmid: 20663816
- D. Duboule, The rise and fall of Hox gene clusters. *Development* **134**, 2549 (2007). doi: 10.1242/dev.001065; pmid: 17553908
- M. Kmita, D. Duboule, Organizing axes in time and space; 25 years of colinear tinkering. *Science* **301**, 331 (2003). doi: 10.1126/science.1085753; pmid: 12869751
- D. Noordermeer *et al.*, The dynamic architecture of Hox gene clusters. *Science* **334**, 222 (2011). doi: 10.1126/science.1207194; pmid: 21998387
- N. Soshnikova, D. Duboule, Epigenetic temporal control of mouse Hox genes in vivo. *Science* **324**, 1320 (2009). doi: 10.1126/science.1171468; pmid: 19498168
- P. Dollé, J. C. Izpisua-Belmonte, H. Falkenstein, A. Renucci, D. Duboule, Coordinate expression of the murine Hox-5 complex homeobox-containing genes during limb pattern formation. *Nature* **342**, 767 (1989). doi: 10.1038/342767a0; pmid: 2574828
- T. Montavon *et al.*, A regulatory archipelago controls Hox genes transcription in digits. *Cell* **147**, 1132 (2011). doi: 10.1016/j.cell.2011.10.023; pmid: 22118467
- B. Tarchini, D. Duboule, Control of Hox genes' collinearity during early limb development. *Dev. Cell* **10**, 93 (2006). doi: 10.1016/j.devcel.2005.11.014; pmid: 16399081
- T. Montavon, J. F. Le Garrec, M. Kerszberg, D. Duboule, Modeling Hox gene regulation in digits: Reverse collinearity and the molecular origin of thumbness. *Genes Dev.* **22**, 346 (2008). doi: 10.1101/gad.1631708; pmid: 18245448
- E. P. Nora *et al.*, Spatial partitioning of the regulatory landscape of the X-inactivation centre. *Nature* **485**, 381 (2012). doi: 10.1038/nature11049; pmid: 22495304
- J. R. Dixon *et al.*, Topological domains in mammalian genomes identified by analysis of chromatin interactions. *Nature* **485**, 376 (2012). doi: 10.1038/nature11082; pmid: 22495300
- B. E. Bernstein *et al.*, Genomic maps and comparative analysis of histone modifications in human and mouse. *Cell* **120**, 169 (2005). doi: 10.1016/j.cell.2005.01.001; pmid: 15680324
- M. P. Creighton *et al.*, Histone H3K27ac separates active from poised enhancers and predicts developmental state. *Proc. Natl. Acad. Sci. U.S.A.* **107**, 21931 (2010). doi: 10.1073/pnas.1016071107; pmid: 21106759
- A. Rada-Iglesias *et al.*, A unique chromatin signature uncovers early developmental enhancers in humans. *Nature* **470**, 279 (2011). doi: 10.1038/nature09692; pmid: 21160473
- Z. Wang *et al.*, Combinatorial patterns of histone acetylations and methylations in the human genome. *Nat. Genet.* **40**, 897 (2008). doi: 10.1038/ng.154; pmid: 18552846
- L. A. Boyer *et al.*, Polycomb complexes repress developmental regulators in murine embryonic stem cells. *Nature* **441**, 349 (2006). doi: 10.1038/nature04733; pmid: 16625203
- A. P. Bracken, N. Dietrich, D. Pasini, K. H. Hansen, K. Helin, Genome-wide mapping of Polycomb target genes unravels their roles in cell fate transitions. *Genes Dev.* **20**, 1123 (2006). doi: 10.1101/gad.381706; pmid: 16618801
- T. I. Lee *et al.*, Control of developmental regulators by Polycomb in human embryonic stem cells. *Cell* **125**, 301 (2006). doi: 10.1016/j.cell.2006.02.043; pmid: 16630818
- H. J. van de Werken *et al.*, 4C technology: Protocols and data analysis. *Methods Enzymol.* **513**, 89 (2012). doi: 10.1016/B978-0-12-391938-0.00004-5; pmid: 22929766
- Y. Shen *et al.*, A map of the cis-regulatory sequences in the mouse genome. *Nature* **488**, 116 (2012). doi: 10.1038/nature11243; pmid: 22763441
- M. Friedli *et al.*, A systematic enhancer screen using lentivector transgenesis identifies conserved and non-conserved functional elements at the Olig1 and Olig2 locus. *PLoS ONE* **5**, e15741 (2010). doi: 10.1371/journal.pone.0015741; pmid: 21206754
- C. Lois, E. J. Hong, S. Pease, E. J. Brown, D. Baltimore, Germine transmission and tissue-specific expression of transgenes delivered by lentiviral vectors. *Science* **295**, 868 (2002). doi: 10.1126/science.1067081; pmid: 11786607
- Y. Hérault, M. Rassoulzadegan, F. Cuzin, D. Duboule, Engineering chromosomes in mice through targeted meiotic recombination (TAMERE). *Nat. Genet.* **20**, 381 (1998). doi: 10.1038/3861; pmid: 9843213
- F. Spitz, C. Herkenne, M. A. Morris, D. Duboule, Inversion-induced disruption of the Hoxd cluster leads to the partition of regulatory landscapes. *Nat. Genet.* **37**, 889 (2005). doi: 10.1038/ng1597; pmid: 15995706
- Y. Yokouchi, H. Sasaki, A. Kuroiwa, Homeobox gene expression correlated with the bifurcation process of limb cartilage development. *Nature* **353**, 443 (1991). doi: 10.1038/353443a0; pmid: 1680221
- C. Tabin, L. Wolpert, Rethinking the proximodistal axis of the vertebrate limb in the molecular era. *Genes Dev.* **21**, 1433 (2007). doi: 10.1101/gad.1547407; pmid: 17575045
- B. E. Bernstein *et al.*, A bivalent chromatin structure marks key developmental genes in embryonic stem cells. *Cell* **125**, 315 (2006). doi: 10.1016/j.cell.2006.02.041; pmid: 16630819
- S. Bonn *et al.*, Tissue-specific analysis of chromatin state identifies temporal signatures of enhancer activity during embryonic development. *Nat. Genet.* **44**, 148 (2012). doi: 10.1038/ng.1064; pmid: 22231485
- P. Tschopp, D. Duboule, A regulatory 'landscape effect' over the HoxD cluster. *Dev. Biol.* **351**, 288 (2011). doi: 10.1016/j.ydbio.2010.12.034; pmid: 21195707
- Y. Hérault, N. Fraudeau, J. Zákány, D. Duboule, Unlaes (UL), a regulatory mutation inducing both loss-of-function and gain-of-function of posterior Hoxd genes. *Development* **124**, 3493 (1997). pmid: 9342042
- S. Bruneau, K. R. Johnson, M. Yamamoto, A. Kuroiwa, D. Duboule, The mouse Hoxd13(spdx) mutation, a polyalanine expansion similar to human type II synpolydactyly (SPD), disrupts the function but not the expression of other Hoxd genes. *Dev. Biol.* **237**, 345 (2001). doi: 10.1006/dbio.2001.0382; pmid: 11543619
- J. P. Changeux, 50th anniversary of the word "allosteric". *Protein Sci.* **20**, 1119 (2011). doi: 10.1002/pro.658; pmid: 21574197
- E. Laufer, C. E. Nelson, R. L. Johnson, B. A. Morgan, C. Tabin, Sonic hedgehog and Fgf-4 act through a signaling cascade and feedback loop to integrate growth and patterning of the developing limb bud. *Cell* **79**, 993 (1994). doi: 10.1016/0092-8674(94)90030-2; pmid: 8001146
- C. E. Nelson *et al.*, Analysis of Hox gene expression in the chick limb bud. *Development* **122**, 1449 (1996). pmid: 8625833
- P. Villavicencio-Lorini *et al.*, Homeobox genes d11-d13 and a13 control mouse autopod cortical bone and joint formation. *J. Clin. Invest.* **120**, 1994 (2010). doi: 10.1172/JCI41554; pmid: 20458143
- J. M. Woltering, D. Duboule, The origin of digits: Expression patterns versus regulatory mechanisms. *Dev. Cell* **18**, 526 (2010). doi: 10.1016/j.devcel.2010.04.002; pmid: 20412768

Acknowledgments: We thank I. Barde, S. Verp, and A. Quazzola, from the Ecole Polytechnique Fédérale de Lausanne transgenic platform, for their help; M. Docquier and P. Descombes, from the National Center in Genetics genomic platform; U. Gunthert and L. Thévenet for the CD44 and inv(attP-CD44) mice, respectively; B. Ren for permission to use and adapt data; and J.-P. Changeux for discussions. Computations were performed at the Vital-IT (www.vital-it.ch) computing center of the Swiss Institute of Bioinformatics using tools described in <http://bbcf.epfl.ch>. We also thank M. Friedli, N. Soshnikova, E. Joye, P. Schorderet, N. Lonfat, and other members of the Duboule laboratories for discussions and sharing reagents. This work was supported by the Ecole Polytechnique Fédérale de Lausanne, the University of Geneva, the National Center for Competence in Research Frontiers in Genetics, the Boninchi Foundation, and European Research Council grant SystemsHox.ch (to D.D.). The GEO accession number for the data is GSE45457. Authors' contributions: G.A., T.M., and D.D. designed the experiments; experiments were mostly performed by G.A., with some performed by T.M. F.G., B.M., and F.S. provided mutant mice. D.N. provided material and helped with 4C experiments. M.L. helped with data analysis, and D.T. collaborated on the transgenic screen. G.A. and D.D. wrote the manuscript with input from other coauthors.

Supplementary Materials

www.sciencemag.org/content/340/6137/1234167/suppl/DC1
Materials and Methods
Figs. S1 to S4
Tables S1 to S5
References (42–52)

17 December 2012; accepted 19 April 2013
10.1126/science.1234167

Support the sciences. **Get rewarded.**

Show your AAAS pride and reward yourself with the new AAAS Platinum Advantage Rewards Card from NASA Federal Credit Union.

Apply now and get
10,000 bonus points!

Go to nasafcu.com/AAASpromo



Get **10,000 bonus points** if you sign up for a card and spend \$3,000 within 90 days of account opening.

Learn more at
nasafcu.com/AAASpromo.

Subject to credit approval.
Membership in AAAS and NASA FCU is required.
NASA FCU is federally insured by NCUA.



Probing the Solar Magnetic Field with a Sun-Grazing Comet

Cooper Downs,^{1*} Jon A. Linker,¹ Zoran Mikić,¹ Pete Riley,¹ Carolus J. Schrijver,² Pascal Saint-Hilaire³

On 15 and 16 December 2011, Sun-grazing comet C/2011 W3 (Lovejoy) passed deep within the solar corona, effectively probing a region that has never been visited by spacecraft. Imaged from multiple perspectives, extreme ultraviolet observations of Lovejoy's tail showed substantial changes in direction, intensity, magnitude, and persistence. To understand this unique signature, we combined a state-of-the-art magnetohydrodynamic model of the solar corona and a model for the motion of emitting cometary tail ions in an embedded plasma. The observed tail motions reveal the inhomogeneous magnetic field of the solar corona. We show how these motions constrain field and plasma properties along the trajectory, and how they can be used to meaningfully distinguish between two classes of magnetic field models.

The Sun's magnetic field is of primary importance in solar and heliospheric physics. It is the energy source for solar activity, and it defines the structure of the solar corona and of the solar wind, which is largely determined

in the low solar corona (~1 to 2 solar radii, R_S , measured from Sun center). It is extremely difficult to measure the coronal magnetic field directly. Although our understanding of the corona has greatly improved with sophisticated remote sensing techniques and modeling methods, models and extrapolations explicitly depend on photospheric magnetic field observations (which provide only a partial constraint on the extended field) as a boundary condition. Because of the extremely harsh near-Sun environment, even the most ad-

vanced near-Sun exploration mission planned to date—Solar Probe Plus (1), which will take a spacecraft within 8.5 R_S of the solar surface—leaves a crucial measurement gap between the base of the solar atmosphere and the extended solar wind. It is for this reason that an opportunity to independently probe the plasma and magnetic state of the low corona is an important occurrence. In December 2011, one such opportunity came in the form of a naturally occurring celestial explorer: Sun-grazing Kreutz-family (2) comet C/2011 W3 (Lovejoy), the first Sun-grazer observed to survive its approach and reemerge from the corona (3), and the second comet observed within the corona at extreme ultraviolet (EUV) wavelengths (4).

With a perihelion of 1.2 R_S , comet Lovejoy came within 140,000 km of the visible solar surface. At heliocentric distances of 1.2 to 2.0 R_S , which are above the typical usable heights for stereoscopic or tomographic reconstructions of the coronal magnetic field and plasma state (5, 6), this passage was imaged from multiple viewpoints by three space-based EUV-imaging telescopes: the Atmospheric Imaging Assembly (AIA) aboard the NASA Solar Dynamics Observatory and the Extreme Ultraviolet Imagers (EUVI-A and EUVI-B) aboard the twin NASA STEREO spacecraft, which were located ~107° ahead and behind Earth's orbit at this time. Base ratio 171 Å images of Lovejoy's tail evolution in the corona are shown

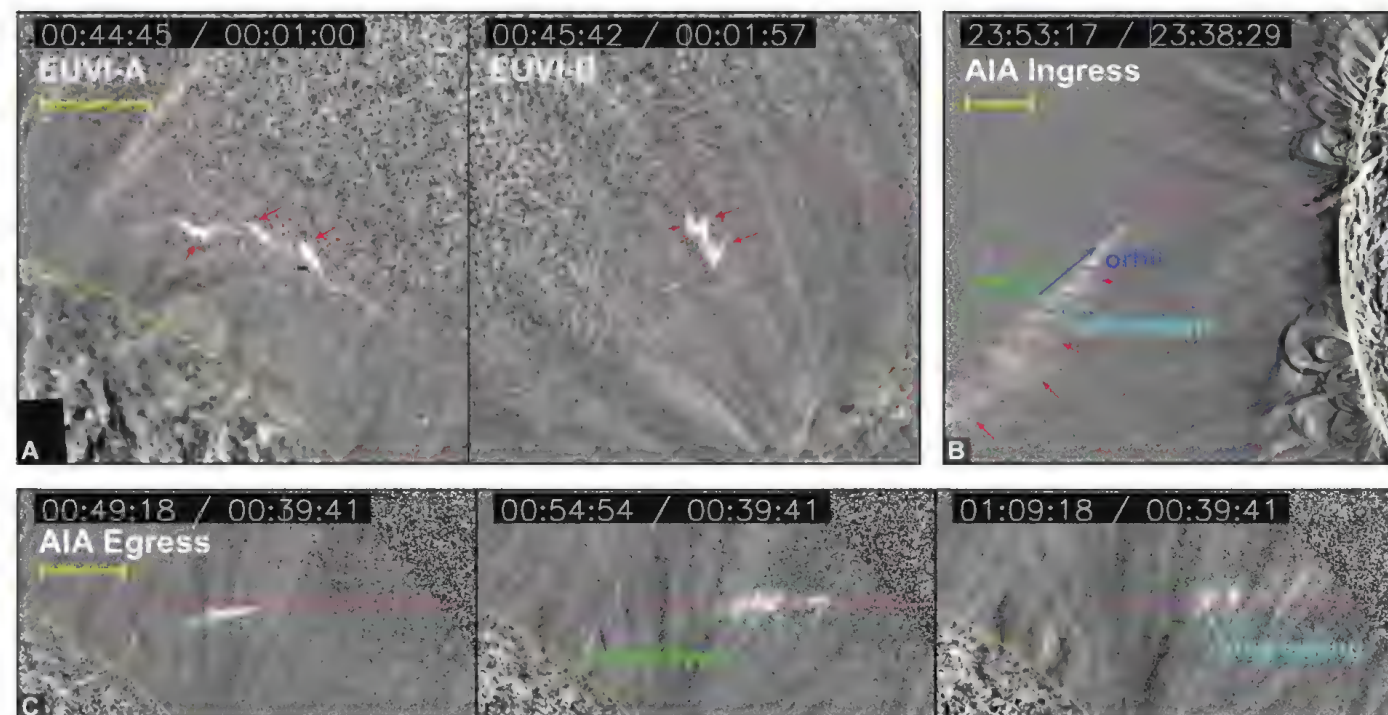


Fig. 1. Comet Lovejoy's tail dynamics in the corona. Base ratio processed 171 Å EUV observations from multiple viewpoints are shown; the white enhancements highlighted by short red arrows indicate the emitting comet tail. (A) EUVI-A and EUVI-B images that show the apparent "wiggles" out of the orbital path observed during the closest approach. (B) An AIA image before perihelion (ingress) with arrows indicating the southwest tail motion and other relevant directions. (C)

The long-lasting portions of the tail are highlighted, with a time sequence of post-perihelion AIA images (egress) that show a separation of approximately 5.5 and 15.5 min, respectively. The yellow scale bar in each panel indicates a length of 100 Mm (10^5 km) in the plane of the sky (POS), the Sun-centered plane normal to the spacecraft. See movies S1 to S4 for the full observations for each view. Image timestamps are UT between 15 and 16 December 2011.

¹Predictive Science Inc., 9990 Mesa Rim Road, Suite 170, San Diego, CA 92121, USA. ²Lockheed Martin Advanced Technology Center, 3251 Hanover Street, Palo Alto, CA 94304, USA. ³Space Sciences Laboratory, University of California, Berkeley, CA 94720, USA.

*Corresponding author. E-mail: cdowns@predsci.com

in Fig. 1. The apparent “wiggles” out of the orbital path observed by EUVI-A and EUVI-B (Fig. 1A) suggest a rapid change in the way in which comet tail ions are either channeled by or influence the ambient coronal medium. AIA observations before perihelion (ingress, Fig. 1B) show that the comet tail motion was markedly in the southwest direction. This motion corresponded neither to radial motion, which would be expected if the tail motion were dominated by solar wind outflows or radiation pressure, nor to motion tangential to the comet orbit, which would be expected if the medium had no influence at all. After perihelion (egress, Fig. 1C), observable tail emission nearer to the Sun (left half) had a relatively short lifetime ($\tau \leq 5$ min) while

the portion located farther out remained much longer ($\tau \geq 15$ min). In some of these longer-lasting regions, the projected tail emission continued to evolve anisotropically, forming contrasted linear features not aligned with the orbital path (Fig. 1C, right). This behavior was also similarly observed during ingress.

A thorough description of how EUV emission can occur from cometary material injected into the corona was given by Bryans and Pesnell (7), who modeled the comet tail as a cylinder along the orbit path and used ion outflow velocities of 10 to 100 km s⁻¹ as plausible limits on the overall width. Here, we additionally take into account the presence of the magnetic field in determining the geometrical shape and evolution

of the tail. Consider the following chain of events for a cometary oxygen (O) test particle under “standard” coronal conditions ($r < 1.2 R_S$, electron number density $n_e \sim 10^8$ cm⁻³, electron temperature $T_e \sim 1.5$ MK): A molecule containing O that was originally part of the solid comet body (the largest contributor being water ice) is sublimated via insolation from the comet surface with some outflow velocity. This molecule will quickly be photodissociated ($\tau \sim 2.9$ s) and the free neutral O atom is rapidly ionized via charge exchange with coronal protons and collisions with coronal electrons ($\tau \leq 0.07$ s for $O \rightarrow O^+$).

In the inertial frame of the Sun, this ion will initially have the vector sum of the thermal, outflow, and comet velocities ($\mathbf{v}_i = \mathbf{v}_t + \mathbf{v}_{out} + \mathbf{v}_c$).

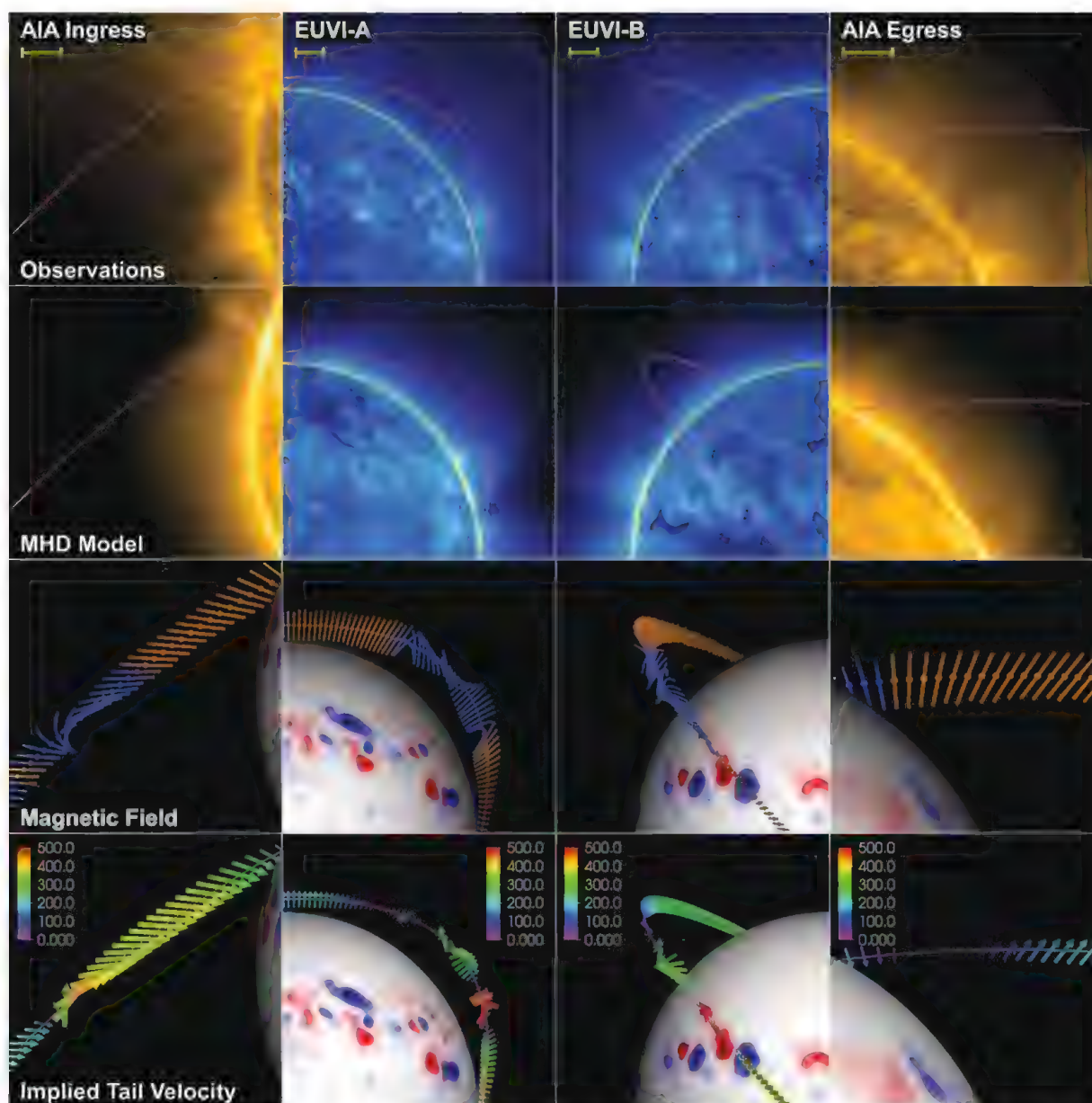


Fig. 2. Modeled coronal environment for each view of the comet flyby. The top two rows show a comparison between 171 Å imaging observations and synthesized emission from the model solution. The bottom rows show the local magnetic field along the comet trajectory (blue, closed field;

orange, open field) and the implied initial tail velocity, $(\mathbf{v}_c \cdot \hat{\mathbf{b}})\hat{\mathbf{b}}$ (arrows). The relative size and color of the arrows is proportional to the magnitude of $(\mathbf{v}_c \cdot \hat{\mathbf{b}})\hat{\mathbf{b}}$ in km s⁻¹. As in Fig. 1, the yellow scale bars in the top row indicate a length of 100 Mm in the POS.

Assuming a locally fixed magnetic field, the newly felt Lorentz force will cause the ion to gyrate about the magnetic field, effectively eliminating perpendicular flow on a macroscopic scale while leaving the parallel component unmodified; that is, $\mathbf{v}_i \rightarrow \mathbf{v}_{i,\text{macro}} = (\mathbf{v}_i \cdot \hat{\mathbf{b}})\hat{\mathbf{b}} = v_p \hat{\mathbf{b}}$, where v_p is the speed parallel to the field direction, $\hat{\mathbf{b}} = \mathbf{B}/|\mathbf{B}|$, where \mathbf{B} is the local magnetic field vector.

As the test particle flows along the given field line, it will decelerate and thermalize via collisional momentum/energy exchange with the ambient plasma (ions, protons, and electrons). As this occurs, electron impact ionization serves to successively raise the ionization state to states

where EUV emission lines are visible in the AIA channels, such as O v, O vi, and Fe ix in the case of the 171 Å channel, which occurs at successively longer time scales. Because the “tail,” as seen in the EUV, is simply a tracer for the location of emitting ions as they interact with the medium, the apparent motion of the tail can thus be approximated by considering the motion and subsequent deceleration of cometary ions flowing parallel to the coronal magnetic field (8).

This scenario opens up the possibility of testing one or more model coronae. Through their validation, we obtain information on the coronal field and on the plasma state along and around the comet’s trajectory. To do so, we used a state-

of-the-art three-dimensional (3D) thermodynamic magnetohydrodynamic (MHD) model of the global corona, tailored to best approximate the corona during perihelion (9). This massively parallel computation involved solving for the full 3D magnetic field and plasma state (flow, magnetic field, temperature, and density) in a global spherical domain from 1.0 to 20 R_S . We assessed the final thermodynamic state by comparing synthetic multiwavelength images generated from the solution directly to observational data (Fig. 2, top rows).

The local magnetic field along the comet trajectory gives a sense of the complex local magnetic geometry encountered by the comet, which

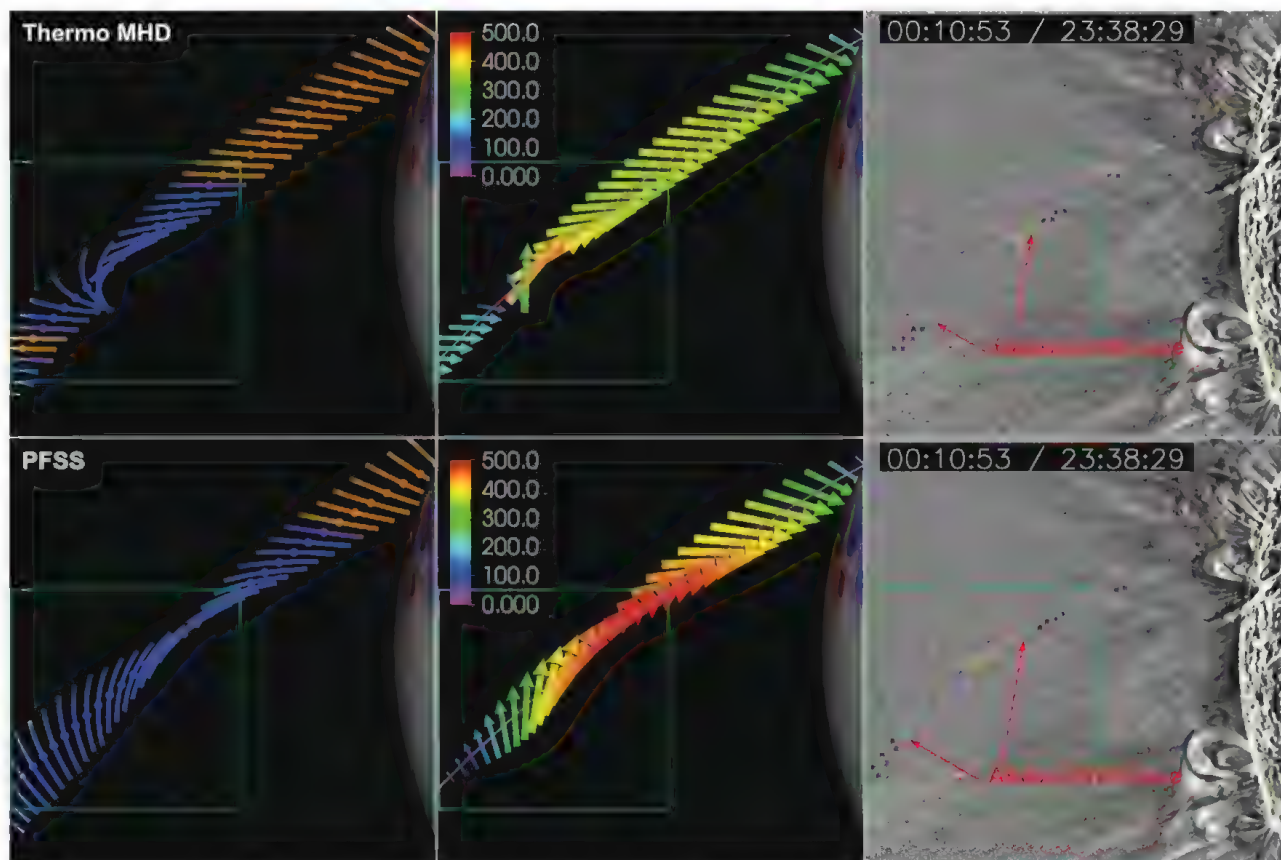


Fig. 3. Predicted tail motion for two magnetic field models. Comparison of the magnetic field (left), initial tail velocity ($\mathbf{v}_c \cdot \hat{\mathbf{b}}\hat{\mathbf{b}}$) (center), and resulting comet tail flow (right) predicted by the thermodynamic MHD model (top row) and the PFSS field model (bottom row) for the AIA ingress observations.

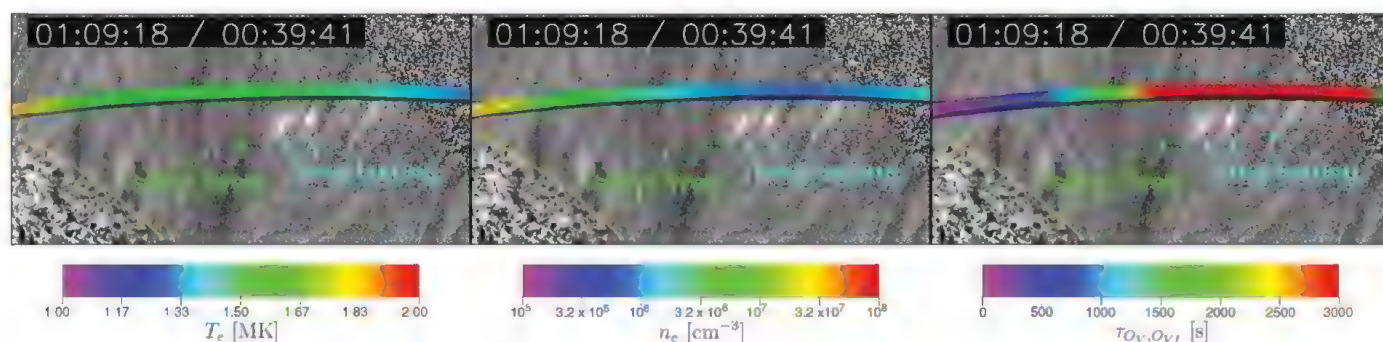


Fig. 4. Estimates of the tail lifetime from MHD model data. MHD model overlays of electron temperature (left), electron density (center), and the lifetime estimate, $\tau_{\text{OV,OVI}}$ (right), over the AIA egress observations. The MHD data along the trajectory are shown as a wide color contour placed above the orbit line.

is used to infer the initial direction and magnitude of comet tail ion velocity, $(\mathbf{v}_e \cdot \hat{\mathbf{b}})\hat{\mathbf{b}}$ (Fig. 2, bottom rows). Examining each view, we gain a sense for how the field orientation implies non-radial and nonorbital directions for tail motion, as well as rapid switching in some regions due to the changing 3D magnetic field structure. Note that the comet trajectory is interspersed with closed-field regions (blue lines) where the field orientation is changing rapidly in the comet frame, which similarly modifies $(\mathbf{v}_e \cdot \hat{\mathbf{b}})\hat{\mathbf{b}}$ over short time periods.

To fully link the MHD solution with the observations, we probed the comet tail evolution by approximating the deceleration of cometary ions along the magnetic field as an exponential decay with time constant $\tau_d = 150$ s plus flow and diffusion terms. This reduced the comet tail dynamics to the ballistic tracking of test particles within a 3D vector field and inhomogeneous medium (10).

One obvious use of the tail model applied to 3D field distributions is the comparison of results between two distinct coronal field models. We illustrate this idea by comparing the field produced by the thermodynamic MHD solution to a potential field source surface (PFSS) calculation for the same boundary conditions. Originally described by Schatten *et al.* (11), the PFSS model has become a standard tool for rapid and reasonable estimates of coronal fields. Unlike the thermodynamic MHD calculation, the PFSS solution assumes that the domain is current-free at all heights up to a source surface radius where the field becomes radial (typically $2.5 R_\odot$). However, PFSS solves only for the minimum energy state of the coronal field distribution, and therefore does not capture structures energized through sustained motions and thermodynamic forces.

There is an overall global resemblance between the thermodynamic MHD and PFSS solutions, which is not unexpected for regions with low relative electric currents (12). However, because this MHD model resolves thermodynamic forces that become non-negligible in regions where the magnetic field is weak relative to the plasma pressure, the details of the closed-field streamer regions, and hence the precise comet tail dynamics, are expected to differ. Comparing them in Fig. 3, we find that the thermodynamic MHD model captures the southwest direction of the tail during the initial ingress from 23:40 to 23:55 UT (green box). Because the curvature of the field on the east side of the streamer region (blue lines, lower left) differs between the two models, the comet flow prediction is in the opposite (northeast) direction for the PFSS model during this time period. This mismatch in tail motion may be due to missing forces in the PFSS model, although a PFSS model with a lower source surface might perform better. Neither the MHD model nor the PFSS model reproduced the southwestern motion between 23:45 and 23:48 UT, which passes through the cusp of the closed-field region. The exact location of this feature is more sensitive to

model parameters as well as the boundary conditions, which lack the most recent photospheric observations on this side of the Sun (because of solar rotation). In any case, this comparison highlights the capability of the comet tail observations to corroborate or invalidate portions of global field models—an otherwise nontrivial task fraught with ambiguity.

We also considered the long-lasting portion of the comet tail in terms of the thermodynamic state along the trajectory in the MHD model (Fig. 4). A rough lifetime estimate for O^{4+} and O^{5+} ions, and hence their emission time scale in a coronal plasma, $\tau_{OV, OVI}$, can be calculated from the electron impact ionization rates under the assumption that they scale with the local electron density (13). Using the MHD model values to compute $\tau_{OV, OVI}$, we find that this time scale is considerably lengthened relative to “typical” ($n_e = 10^8 \text{ cm}^{-3}$) coronal conditions for the later half of the view, which is qualitatively consistent with the transition from short to long lifetime in the tail observations (albeit broader and slightly offset). The longer time scales can also help to explain the relative constancy of emission from the long-lasting portions of the tail.

Extensions to the parallel flow model, such as the inclusion of perpendicular ion flow mechanisms, drifts, or coronal field modifications [e.g., (14)], could provide deep insight into the two-way coupling of the comet to the coronal field itself. Such a scenario is likely needed to explain the slow but conspicuous backward-projected motion of a portion of the tail around 00:01 UT during ingress (9). Looking forward, a higher frequency of such Sun-grazing comets is predicted for this decade (3, 15), and another large comet is predicted to pass through the solar atmosphere in November 2013 [comet C/2012 S1 (ISON) (16)]. This bolsters the exciting prospect that

coronal observations of comet flybys can offer a unique and complementary avenue toward understanding the solar atmosphere.

References and Notes

1. *Solar Probe Plus: Report of the Science and Technology Definition Team*, NASA/TM-2008-214161 (2008).
2. B. G. Marsden, *Annu. Rev. Astron. Astrophys.* **43**, 75 (2005).
3. Z. Sekanina, P. W. Chodas, *Astrophys. J.* **757**, 127 (2012).
4. C. J. Schrijver *et al.*, *Science* **335**, 324 (2012).
5. M. J. Aschwanden *et al.*, *Astrophys. J.* **756**, 124 (2012).
6. R. A. Frazin, A. M. Vázquez, F. Kamalabadi, *Astrophys. J.* **701**, 547 (2009).
7. P. Bryans, W. D. Pesnell, *Astrophys. J.* **760**, 18 (2012).
8. See supplementary text S1 for details on the relevant time scales.
9. See supplementary materials and methods.
10. See supplementary text S2 and movies S5 to S8.
11. K. H. Schatten, J. M. Wilcox, N. F. Ness, *Sol. Phys.* **6**, 442 (1969).
12. P. Riley *et al.*, *Astrophys. J.* **653**, 1510 (2006).
13. $\tau_{OV, OVI}$ is calculated using the sum of the inverse of the electron impact ionization rates for $O^{4+} \rightarrow O^{5+}$ and $O^{5+} \rightarrow O^{6+}$ at $n_e = 1 \times 10^8 \text{ cm}^{-3}$ obtained from table 2 of (7).
14. Y.-D. Jia, M. R. Combi, K. C. Hansen, T. I. Gombosi, *J. Geophys. Res.* **112**, A05223 (2007).
15. Z. Sekanina, P. W. Chodas, *Astrophys. J.* **663**, 657 (2007).
16. O. Burhonov *et al.*, *Minor Planet Electronic Circulars* 2012-S63 (2012).

Acknowledgments: Supported by NASA SDO/AIA contracts. All observational data are freely available from the NASA/SDO, AIA, HMI, STEREO, and SECCHI science teams. Simulations were conducted using the NASA Pleiades and NSF Ranger supercomputers.

Supplementary Materials

www.sciencemag.org/cgi/content/full/340/6137/1196/DC1

Materials and Methods

Supplementary Texts S1 and S2

Figs. S1 to S4

Movies S1 to S8

References (17–44)

14 February 2013; accepted 24 April 2013

10.1126/science.1236550

A Major Asymmetric Dust Trap in a Transition Disk

Nienke van der Marel,^{1*} Ewine F. van Dishoeck,^{1,2} Simon Bruderer,² Til Birnstiel,³ Paola Pinilla,⁴ Cornelis P. Dullemond,⁴ Tim A. van Kempen,^{1,5} Markus Schmalzl,¹ Joanna M. Brown,³ Gregory J. Herczeg,⁶ Geoffrey S. Mathews,¹ Vincent Geers⁷

The statistics of discovered exoplanets suggest that planets form efficiently. However, there are fundamental unsolved problems, such as excessive inward drift of particles in protoplanetary disks during planet formation. Recent theories invoke dust traps to overcome this problem. We report the detection of a dust trap in the disk around the star Oph IRS 48 using observations from the Atacama Large Millimeter/submillimeter Array (ALMA). The 0.44-millimeter-wavelength continuum map shows high-contrast crescent-shaped emission on one side of the star, originating from millimeter-sized grains, whereas both the mid-infrared image (micrometer-sized dust) and the gas traced by the carbon monoxide 6-5 rotational line suggest rings centered on the star. The difference in distribution of big grains versus small grains/gas can be modeled with a vortex-shaped dust trap triggered by a companion.

Although the ubiquity of planets is confirmed almost daily by detections of new exoplanets (1), the exact forma-

tion mechanism of planetary systems in disks of gas and dust around young stars remains a long-standing problem in astrophysics (2). In

the standard core-accretion picture, dust grains must grow from submicrometer sizes to rocky cores ~ 10 times the mass of Earth (M_{Earth}) within the ~ 10 -million-year lifetime of the circumstellar disk. However, this growth process is stymied by what is usually called the radial drift and fragmentation barrier: Particles of intermediate size [~ 1 m at 1 astronomical unit (AU) (1 AU = 1.5×10^8 km = distance from Earth to the Sun), or ~ 1 mm at 50 AU from the star] acquire high drift velocities toward the star with respect to the gas (3, 4). This leads to two major problems for further growth (5): First, high-velocity collisions between particles with different drift velocities cause fragmentation. Second, even if particles avoid this fragmentation, they will rapidly drift inward and thus be lost into the star before they have time to grow to planetesimal size. This radial drift barrier is one of the most persistent issues in planet formation theories. A possible solution is dust trapping in so-called pressure bumps: local pressure maxima where the dust piles up. One example of such a pressure bump is an anticyclonic vortex, which can trap dust particles in the azimuthal direction (6–10).

Using the Atacama Large Millimeter/submillimeter Array (ALMA), we report a highly asymmetric concentration of millimeter-sized dust grains on one side of the disk of the star Oph IRS 48 in the 0.44-mm (685 GHz) continuum emission (Fig. 1). We argue that this can be understood in the framework of dust trapping in a large anticyclonic vortex in the disk.

The young A-type star Oph IRS 48 [distance from Earth ~ 120 parsecs (pc), 1 pc = 3.1×10^{13} km] has a well-studied disk with a large inner cavity (a deficit of dust in the inner disk region), a so-called transition disk. Mid-infrared imaging at $18.7 \mu\text{m}$ reveals a disk ring in the small dust grain (size $\sim 50 \mu\text{m}$) emission at an inclination of $\sim 50^\circ$, peaking at 55 AU radius or 0.46 arc sec from the star (11). Spatially resolved observations of the $4.7\text{-}\mu\text{m}$ CO line, tracing 200 to 1000 K gas, show a ring of emission at 30 AU radius and no warm gas in the central cavity (12). This led to the proposal of a large planet clearing its orbital path as a potential cause of the central cavity. Although these observations provide information about the inner disk dynamics, they do not address the bulk cold disk material accessible in the millimeter regime.

The highly asymmetric crescent-shaped dust structure revealed by the 0.44-mm ALMA continuum (Fig. 1) traces emission from millimeter-sized dust grains and is located between 45 and 80 AU (± 9 AU) from the star. The azimuthal extent is less than one-third of the ring, with no detected flux at a 3σ level (2.4 mJy per beam) in the northern part (fig. S1). The peak emission has a very high signal-to-noise ratio of ~ 390 , and the contrast with the upper limit on the opposite side of the ring is at least a factor of 130. The complete absence of dust emission in the north of IRS 48 and resulting high contrast make the crescent-shaped feature more extreme than earlier dust asymmetries (10, 13). The spectral slope α of the millimeter fluxes F_ν [0.44 mm combined with fluxes at lower frequencies ν (14)] is only 2.67 ± 0.25 ($F_\nu \propto \nu^\alpha$), suggesting that millimeter-sized grains (15) dominate the 0.44-mm continuum emission. However, the gas traced by the ^{12}CO 6-5 line from the same ALMA data set indicates a Keplerian disk profile characteristic of a gas disk with an inner cavity around the central star (Fig. 1B). ^{12}CO 6-5 emission is detected down to a 20 AU radius, which is consistent with the hot CO ring at 30 AU (14). This indicates that there is indeed still some CO inside the dust hole, with a significant drop of the gas surface density inside of $\sim 25 \pm 5$ AU. The simultaneous ALMA line and continuum observations leave no doubt about the relative position of gas and dust.

The observations thus indicate that large millimeter-sized grains are distributed in an asymmetric structure, but that the small micrometer-sized grains are spread throughout the ring. To our knowledge, the only known mechanism that could generate this separation in the distribution of the large and small grains is a long-lived gas pressure bump in the radial and azimuthal direction. The reason that dust particles get trapped in pressure bumps is their drift with respect to the gas in the direction of the gas pressure gradient: $\vec{v}_{\text{dust}} - \vec{v}_{\text{gas}} \propto \vec{\nabla} p$ (3, 4), where \vec{v}_{dust} and \vec{v}_{gas} are the dust and gas velocities and p is the pressure. In protoplanetary disks without vortices, this gradient typically points inward, so dust particles experience the above-mentioned rapid radial drift issue. If, however, there exists (for whatever reason) a local maximum of the gas pressure in the disk (i.e., where $\vec{\nabla} p_{\text{gas}} = 0$ and $\vec{\nabla}^2 p_{\text{gas}} < 0$), then particles would converge toward this point and remain trapped there (3, 5), avoiding both inward drift and destructive collisions (14). Because small dust particles are strongly coupled to the gas, they will be substantially less concentrated toward the pressure maximum along the azimuthal direction than large particles. Various mechanisms have been proposed that could produce a local pressure maximum in disks; for instance, when there is a “dead zone” (16) or a substellar companion or planet (14, 17) in the disk, hindering accretion. Until recently, however, the presence of such dust pressure traps was purely speculative,

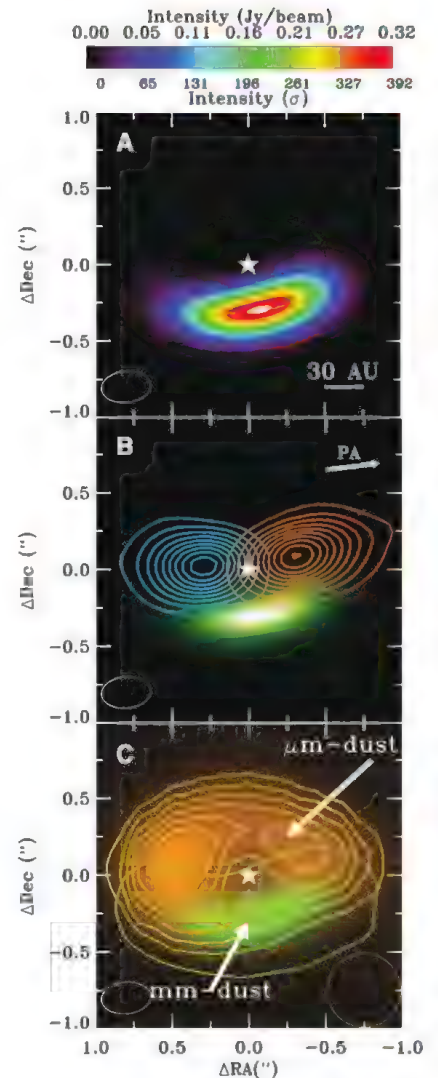


Fig. 1. IRS 48 dust and gas observations. The inclined disk around IRS 48 as observed with ALMA Band 9 observations, centered on the star (white star symbol). The ALMA beam during the observations is $0.32'' \times 0.21''$ and is indicated with a white ellipse in the lower left corner. (A) The 0.44-mm (685 GHz) continuum emission expressed both in flux density and relative to the root mean square (rms) level ($\sigma = 0.82$ mJy per beam). The 63 AU radius is indicated by a dashed ellipse. (B) The integrated CO 6-5 emission over the highest velocities in contours (6, 12, ..., 60 σ_{CO} levels, $\sigma_{\text{CO}} = 0.34$ Jy km s^{-1}); integrated over -3 to 0.8 km s^{-1} (blue) and 8.3 to 12 km s^{-1} (red), showing a symmetric gas disk with Keplerian rotation at an inclination $i = 50^\circ$. The green background shows the 0.44-mm continuum. The position angle is indicated in the upper right corner. (C) The Very Large Telescope Imager and Spectrometer for the mid-infrared (VISIR) $18.7\text{-}\mu\text{m}$ emission in orange contours (36 to $120\sigma_{\text{VISIR}}$ levels in steps of $12\sigma_{\text{VISIR}}$, $\sigma_{\text{VISIR}} = 0.2$ Jy arc sec^{-2}) and orange colors, overlaid on the 0.44-mm continuum in green colors and the 5σ contour line in green. The VISIR beam size is $0.48''$ in diameter and is indicated with an orange circle in the bottom right corner.

¹Leiden Observatory, Leiden University, Post Office Box 9513, 2300 RA Leiden, Netherlands. ²Max-Planck-Institut für Extraterrestrische Physik, Giessenbachstrasse 1, 85748 Garching, Germany. ³Harvard-Smithsonian Center for Astrophysics, 60 Garden Street, Cambridge, MA 02138, USA. ⁴Heidelberg University Center for Astronomy, Institute for Theoretical Astrophysics, Albert Ueberle Strasse 2, 69120 Heidelberg, Germany. ⁵Joint Atacama Large Millimeter/submillimeter Array (ALMA) Offices, Avenida Alonso de Cordova, Santiago, Chile. ⁶Kavli Institute for Astronomy and Astrophysics, Peking University, Yi He Yuan Lu 5, Hai Dian Qu, 100871 Beijing, People's Republic of China. ⁷Dublin Institute for Advanced Studies, 31 Fitzwilliam Place, Dublin 2, Ireland.

*Corresponding author. E-mail: nmarel@strw.leidenuniv.nl

because pre-ALMA observations did not have the spatial resolution and sensitivity necessary to constrain the distribution of gas and dust required for testing dust-trapping models (18).

Although vortices in models have an azimuthal gas contrast up to only a factor of a few (16, 19, 20), models predict that even a very minor pressure variation in the gas ring will trap the dust efficiently, leading to a strong lopsided azimuthal asymmetry in the dust ring if the vortex is long-lived. A gas contrast of only 10% can create a dust contrast of 100 for large dust particles in $\sim 10^5$ years (9), so a long-lived azimuthal pressure bump can readily explain the observed high asymmetry in the dust structure of IRS 48. Vortices created by planets have been shown to survive over at least 10^5 years (8). Even though these vortices tend to diffuse at longer time scales, $\sim 10^5$ years is enough time to create strong dust concentrations that remain even if the vortex disappears. It takes millions of years to even out these dust concentrations completely (9). More generally, vortices are expected to be long-lived if they have an elongation (an aspect ratio of arc length over width) of at least 4 (21). The accumulated dust in IRS 48 has an elongation of ~ 3.1 (± 0.6).

We present a detailed numerical model (14), showing the feasibility of our proposed scenario (Fig. 2). Given the central cavity in the Oph IRS 48 disk, we propose a substellar companion as the cause of the inner cavity, which also creates a long-lived ring of enhanced pressure outside the planetary orbit. The gas densities inside the cavity are decreased, with the level depending on the companion's mass and the disk viscosity (22, 23). The drop of the gas surface density at $\sim 25 \pm 5$ AU, in combination with the shape and steep radial drop of the millimeter dust emission at 45 AU, suggests that this substellar companion is located between the star and dust

trap around ~ 20 AU and has a mass of at least $10 M_{\text{Jupiter}}$ (17). The presented model with these parameters shows that the radial overdensity at the edge of the cavity is Rossby-unstable, leading to the production of an anticyclonic vortex (14). Dust accumulation in this pressure bump results in the spatial separation between the gas and the millimeter dust emission (17, 24). Other than the hole, the high gas velocities are symmetric in the east and west and consistent with Keplerian motion around a $2 M_{\text{Sun}}$ star (Fig. 1). Any gas density variation along the azimuthal direction cannot be observed directly in the CO 6-5 observations, because of high line optical depth within the disk and foreground absorption, but C^{17}O data are not inconsistent with a full gas ring (14).

Regardless of the formation mechanism, the ALMA observations clearly show a concentration of dust grains within a small region of the disk. The total measured dust emission corresponds to $9 M_{\text{Earth}}$, assuming a dust temperature of 60 K. The millimeter observations confirm dust growth up to a maximum grain size of $a_{\text{max}} = 4$ mm. Including larger grains, the dust mass could be a factor of $\sqrt{a_{\text{max}}(\text{mm})/4}$ larger (14). The mass is similar to the full-disk dust masses found in other young disks (25). This amount of large dust in a small area will favor grain growth up to ~ 1 m size until the fragmentation barrier (5). Further growth to planetesimal sizes is possible when additional mechanisms, such as the sweeping-up of small particles by larger seeds and bouncing effects including mass transfer, are considered (26, 27). Because these closely formed planetesimals will scatter and disperse along the ring on short time scales, it is not possible to continue growth and form a planetary core with regular orderly growth models within ~ 10 million years at this large distance from the star. On the other hand, the dust trap could in-

tiate the formation of a Kuiper Belt around IRS 48, such as that found in our own solar system at comparable radii (28). The dust trap as a "Kuiper Belt object factory" is analogous to a "planet factory" at smaller radii around other stars, where both the fragmentation barrier is higher and the collisional growth is faster (5). Thus, the possibility of dust trapping as the start of core formation could help to explain the observations of massive planets at smaller radii around A-stars such as found in HR 8799 (29) and beta Pictoris (30).

Dust asymmetries have been hinted at in other disks by Submillimeter Array (SMA) observations (13) and are clearly seen in earlier ALMA observations (10). The low image fidelity of the SMA data (low sensitivity and spatial sampling) and the lower contrast leave room for multiple interpretations, although a relation to vortices has been hinted at (10). In contrast, the ALMA observations of IRS 48, with their unprecedented spatial resolution and sensitivity, show a contrast of at least 130 in the continuum along the ring, with no indications of a highly asymmetric small dust/gas distribution. Alternative scenarios are discussed to be less likely (14). A long-lived azimuthal gas pressure bump triggered by a companion, followed by particle trapping, appears to be the most viable scenario that could produce this. The key feature is the observed separation between big and small dust grains/gas, which is a direct consequence of the dust-trapping model.

References and Notes

1. N. M. Batalha et al., *Astrophys. J. Suppl. Ser.* **204**, 24 (2013).
2. P. J. Armitage, *Annu. Rev. Astron. Astrophys.* **49**, 195 (2011).
3. F. L. Whipple, *From Plasma to Planet*, A. Elvius, Ed. (Wiley Interscience, New York, 1972).
4. S. J. Weidenschilling, *Mon. Not. R. Astron. Soc.* **180**, 57 (1977).
5. F. Brauer, C. P. Dullemond, T. Henning, *Astron. Astrophys.* **480**, 859 (2008).
6. P. Barge, J. Sommeria, *Astron. Astrophys.* **295**, L1 (1995).
7. H. H. Klahr, T. Henning, *Icarus* **128**, 213 (1997).
8. H. Meheut, R. V. E. Lovelace, D. Lai, *Mon. Not. R. Astron. Soc.* **430**, 1988 (2013).
9. T. Birnstiel, C. P. Dullemond, P. Pinilla, *Astron. Astrophys.* **550**, L8 (2013).
10. S. Casassus et al., *Nature* **493**, 191 (2013).
11. V. C. Geers et al., *Astron. Astrophys.* **469**, L35 (2007).
12. J. M. Brown, G. J. Herczeg, K. M. Pontoppidan, E. F. van Dishoeck, *Astrophys. J.* **744**, 116 (2012).
13. S. M. Andrews et al., *Astrophys. J.* **732**, 42 (2011).
14. Materials and methods are available as supplementary materials on Science Online.
15. B. T. Draine, *Astrophys. J.* **636**, 1114 (2006).
16. Z. Regály, A. Juhász, Z. Sándor, C. P. Dullemond, *Mon. Not. R. Astron. Soc.* **419**, 1701 (2012).
17. P. Pinilla, M. Benisty, T. Birnstiel, *Astron. Astrophys.* **545**, A81 (2012).
18. J. P. Williams, L. A. Cieza, *Annu. Rev. Astron. Astrophys.* **49**, 67 (2011).
19. R. V. E. Lovelace, H. Li, S. A. Colgate, A. F. Nelson, *Astrophys. J.* **513**, 805 (1999).
20. M. de Val-Borro, P. Artymowicz, G. D'Angelo, A. Peplinski, *Astron. Astrophys.* **471**, 1043 (2007).
21. G. Lesur, J. C. B. Papaloizou, *Astron. Astrophys.* **498**, 1 (2009).

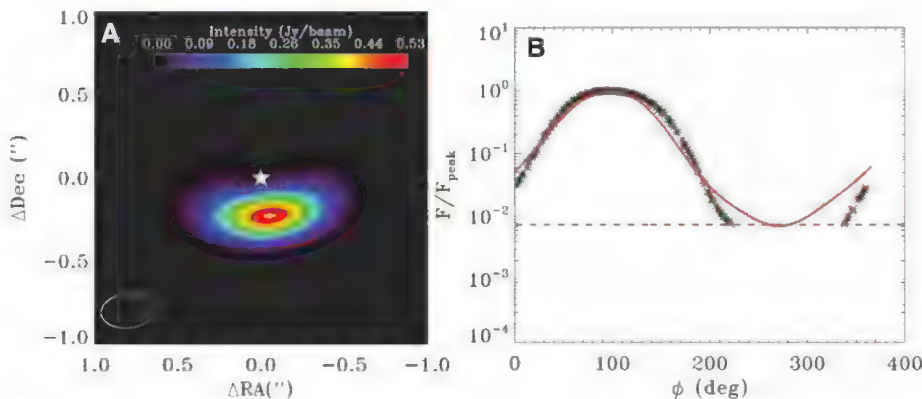


Fig. 2. Model of the dust asymmetry. (A) Simulated ALMA Band 9 dust continuum images at 0.44 mm (685 GHz) for our model using the dust-trapping scenario (9). Details of the model and model parameters are derived based on the IRS 48 properties (14). The high azimuthal contrast is similar to that found in the data. (B) Normalized logarithmic azimuthal cut at the peak emission radius through the dust ring of the observations (black) and the ALMA-simulated model (red), showing the large contrast in the millimeter dust density between the maximum and the opposite side of the ring. The (normalized) 3σ upper limit of the ALMA data is indicated with a dashed line. The data points below the normalized 3σ level have been removed for clarity.

22. A. Crida, A. Morbidelli, F. Masset, *Icarus* **181**, 587 (2006).
23. S. E. Dodson-Robinson, C. Salyk, *Astrophys. J.* **738**, 131 (2011).
24. Z. Zhu, R. P. Nelson, R. Dong, C. Espaillat, L. Hartmann, *Astrophys. J.* **755**, 6 (2012).
25. S. M. Andrews, J. P. Williams, *Astrophys. J.* **631**, 1134 (2005).
26. J.-W. Xie, M. J. Payne, P. Thébaud, J.-L. Zhou, J. Ge, *Astrophys. J.* **724**, 1153 (2010).
27. F. Windmark *et al.*, *Astron. Astrophys.* **540**, A73 (2012).
28. D. C. Jewitt, J. X. Luu, in *Protostars and Planets IV*, V. Mannings, S. S. Russell, A. Boss, Eds. (Univ. of Arizona Press, Tucson, AZ, 2000), p. 1201.

29. C. Marois *et al.*, *Science* **322**, 1348 (2008).
30. A.-M. Lagrange *et al.*, *Science* **329**, 57 (2010).

Acknowledgments: We thank M. Benisty and W. Lyra for useful discussions. This paper makes use of the following ALMA data: ADS/JAO.ALMA no. 2011.0.00635.SSB. ALMA is a partnership of the European Southern Observatory (ESO) (representing its member states), NSF (USA), and National Institutes of Natural Sciences (Japan), together with the National Research Council (Canada) and National Science Council and Academia Sinica Institute of Astronomy and Astrophysics (Taiwan), in cooperation with the Republic of Chile. The Joint ALMA Observatory is operated by the ESO, Associated Universities Inc./National Radio Astronomy Observatory, and National Astronom-

ical Observatory of Japan. The data presented here are archived at www.alma-allegro.nsl/science, and the full project data (2011.0.00635.SSB) will be publicly available at the ALMA Science Data Archive, <https://almascience.nrao.edu/alma-data/archive>.

Supplementary Materials

www.sciencemag.org/cgi/content/full/340/6137/1199/DC1
Materials and Methods
Figs. S1 to S5
References (31–54)

19 February 2013; accepted 7 May 2013
10.1126/science.1236770

Coupling a Single Trapped Atom to a Nanoscale Optical Cavity

J. D. Thompson,^{1,*} T. G. Tiecke,^{1,2,*} N. P. de Leon,^{1,3} J. Feist,^{1,4} A. V. Akimov,^{1,5} M. Gullans,¹ A. S. Zibrov,¹ V. Vuletić,² M. D. Lukin^{1†}

Hybrid quantum devices, in which dissimilar quantum systems are combined in order to attain qualities not available with either system alone, may enable far-reaching control in quantum measurement, sensing, and information processing. A paradigmatic example is trapped ultracold atoms, which offer excellent quantum coherent properties, coupled to nanoscale solid-state systems, which allow for strong interactions. We demonstrate a deterministic interface between a single trapped rubidium atom and a nanoscale photonic crystal cavity. Precise control over the atom's position allows us to probe the cavity near-field with a resolution below the diffraction limit and to observe large atom-photon coupling. This approach may enable the realization of integrated, strongly coupled quantum nano-optical circuits.

Trapped, ultracold atoms coupled to nanoscale optical cavities are exemplary hybrid quantum systems (1, 2), with potential applications ranging from single-photon nonlinear optics (3–7) to quantum networks (8, 9). However, realizing the largest interaction strengths requires placing and controlling an atom very

close to a surface, within the near field of the confined optical mode, as set by the reduced atomic resonance wavelength of $\lambda/(2\pi) \sim 125$ nm for rubidium (Rb). Position control at this level has been achieved for single atoms in free space and in micrometer-scale cavities by using standing waves (10, 11) or high numerical-aperture optics

(12, 13). Achieving similar control close to surfaces is much more challenging because attractive atom-surface forces are comparable with typical trapping forces for cold atoms in this regime. Previously, atomic ensembles have been stably trapped at distances of 500 nm from a surface by using magnetic traps formed by patterned electrodes (14, 15) and down to 215 nm by using optical dipole traps based on evanescent waves (16, 17).

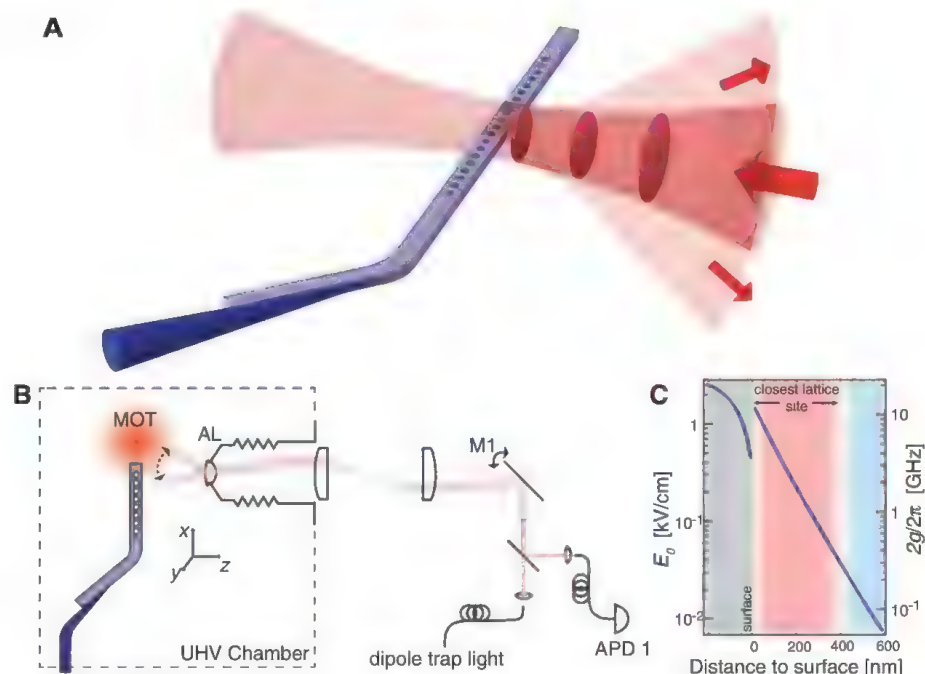
Our technique to position an atom near an arbitrary nanoscale object uses a tightly focused optical tweezer beam (18) that is retro-reflected from the nanoscale object itself (19, 20) and red-detuned from the atomic resonance (Fig. 1A).

¹Department of Physics, Harvard University, Cambridge, MA 02138, USA. ²Department of Physics, Massachusetts Institute of Technology (MIT)–Harvard Center for Ultracold Atoms, and Research Laboratory of Electronics, MIT, Cambridge, MA 02139, USA. ³Department of Chemistry and Chemical Biology, Harvard University, Cambridge, MA 02138, USA. ⁴Institute for Theoretical Atomic Molecular and Optical Physics (ITAMP), Harvard-Smithsonian Center for Astrophysics, Cambridge, MA 02138, USA. ⁵Russian Quantum Center, Skolkovo, Moscow Region 143025, Russia.

*These authors contributed equally to this work.

†Corresponding author. E-mail: lukin@physics.harvard.edu

Fig. 1. Experimental concept. (A) The atom trap near a nanoscale solid-state structure (here, a photonic crystal waveguide) arises from the interference of an optical tweezer with its reflection from the structure, which forms a standing-wave optical lattice. (B) A single atom is loaded from a free-space MOT into a dipole trap formed by an aspheric lens (AL) and steered by a galvanometer mirror (M1). Fluorescence on APD1 signals the presence of an atom and triggers the motion of the dipole trap to the nanostructure. UHV, ultrahigh vacuum. (C) The single-photon electric field strength E_0 and single-photon Rabi frequency $2g = 2E_0/\hbar$ at a given distance from the outer surface of a PWC cavity, using $\lambda_T = 815$ nm (d is the atomic dipole moment and \hbar is Planck's constant h divided by 2π). The range of distances that can be chosen for the closest lattice site is indicated. As discussed in the text, surface forces and currently realized trap depths limit the achievable distance to $z_0 \approx 100$ nm, at which point $2g/(2\pi)$ is several GHz.



The resulting standing-wave optical lattice has a local intensity maximum, corresponding to a minimum of the potential energy, at a typical distance $z_0 \sim \lambda_T/4$ from the surface, with additional maxima farther away spaced in increments of $\lambda_T/2$ (λ_T is the trap laser wavelength). The lateral position of the trap can be controlled by moving the focused incident beam, whereas the distance z_0 depends on the phase shift of the reflected light, which is determined by the geometry of the nanostructure. In certain cases, changing the structure dimensions allows z_0 to be tuned between nearly 0 and $\lambda_T/2$ (figs. S3 and S4). Crucially, the lattice site closest to the surface can be loaded with a single atom from a conventional free-space optical tweezer simply by scanning the latter onto and over the surface, provided the atom has been originally prepared at sufficiently low temperature (21). Even though the attractive van der Waals interaction between the atom and the surface limits the minimum trap distance to about 100 nm for realistic laser intensities (22), this method nevertheless allows for direct, strong, and reproducible near-field optical coupling of atoms to solid-state nanostructures of interest.

The nanostructure in the present experiment is a photonic crystal waveguide cavity (PWC) that is mounted to a tapered optical fiber tip and placed in the focal plane of a high numerical aperture lens (Fig. 1, A and B, and fig. S1). A magneto-optical trap (MOT) was formed near the fiber tip and used to load the optical tweezer ($\lambda_T = 815$ nm, beam waist $w = 900$ nm, and potential depth $U_0/k_B = 1.6$ mK, where k_B is the Boltzmann constant) with one atom at a distance of 40 μm from the nanostructure. [The presence of only a single atom is ensured by the collisional blockade effect (18).] After a period of Raman sideband cooling to the vibrational ground state in the two radial directions, and to a few vibrational quanta in the direction along the tweezer (21), we translated the optical tweezer using a scanning galvanometer mirror (Fig. 1B) until it was aimed directly at the nanostructure, loading the atom into the lattice.

We first verified that we can load the lattice site closest to the surface by positioning an atom near a bare tapered nanofiber tip (Fig. 2, A and B) without the PWC present. We distinguished the lattice sites spectroscopically by means of a

weak, off-resonant probe beam guided by the nanofiber. This beam produces a substantial differential AC Stark shift between the ground-state hyperfine levels for an atom in lattice site A, and a much smaller shift for atoms in more distant lattice sites (22). The microwave-frequency spectra on the $|F = 1, m_F = 0\rangle \leftrightarrow |2, 0\rangle$ transition is shown in Fig. 2C, obtained by focusing the tweezer in different z planes before loading the lattice (F and m_F indicate the atomic hyperfine and magnetic quantum numbers, respectively). Two distinct peaks appear: one near the unperturbed transition frequency at f_B and another shifted by 150 kHz at f_A , which we identify as the Stark-shifted resonance frequency in the lattice site closest to the fiber. This identification was made by measuring the coupling of the atomic fluorescence into the fiber. Assuming lossless propagation in the fiber taper, we expected a collection efficiency in the closest (second closest) lattice site of 4% (0.2%); the measured value in site A is $(1.5 \pm 0.6)\% \gg 0.2\%$. This confirms that site A is the closest site to the fiber. The discrepancy with the expected value is attributed to losses in the fiber taper (22). From the data in Fig. 2C, we conclude that $100^{+0}_{-12}\%$ of the atoms that survive the loading procedure are in the closest lattice site. Additional measurements show that $94 \pm 6\%$ of all atoms survive the loading process (after subtracting losses due to collisions with the background gas), so we conclude that the first lattice site may be loaded deterministically, with an unconditional fidelity of $94^{+6}_{-13}\%$.

We next describe coupling an atom to the optical resonance of a PWC (23) fabricated in silicon nitride (Fig. 3, A to C). We attached the PWC to a tapered optical fiber tip, which provides both an efficient optical interface to the cavity and mechanical support. Because of the nanoscale dimensions of the waveguide, an appreciable evanescent field resides outside the waveguide, which allows for coupling to an atom trapped in this region without the need to place the atom inside the holes (24, 25). As shown in Fig. 1C, single-photon Rabi frequencies $2g = 2\mathbf{d} \cdot \mathbf{E}/\hbar$ in the range of several gigahertz (corresponding to single-photon electric fields of several hundred volts per centimeter) are accessible for the atom-surface distances that can be realized with the present trapping technique, which is large relative to other cavity quantum electrodynamics (QED) approaches with neutral atoms. For example, $2g/(2\pi) = 430$ MHz is the current state of the art in Fabry-Perot cavities (11), and $2g/(2\pi) \approx 200$ MHz has been realized with microtoroid optical resonators (3).

To demonstrate the coupling of the atom to the cavity mode as well as the sub-wavelength position control of the atom, we mapped out the intensity distribution of the cavity mode by scanning the atom along the waveguide. The local intensity is measured by pumping the cavity weakly with a laser tuned near the $F = 2 \rightarrow F' = 2$ transition of the D2 line and measuring the optical

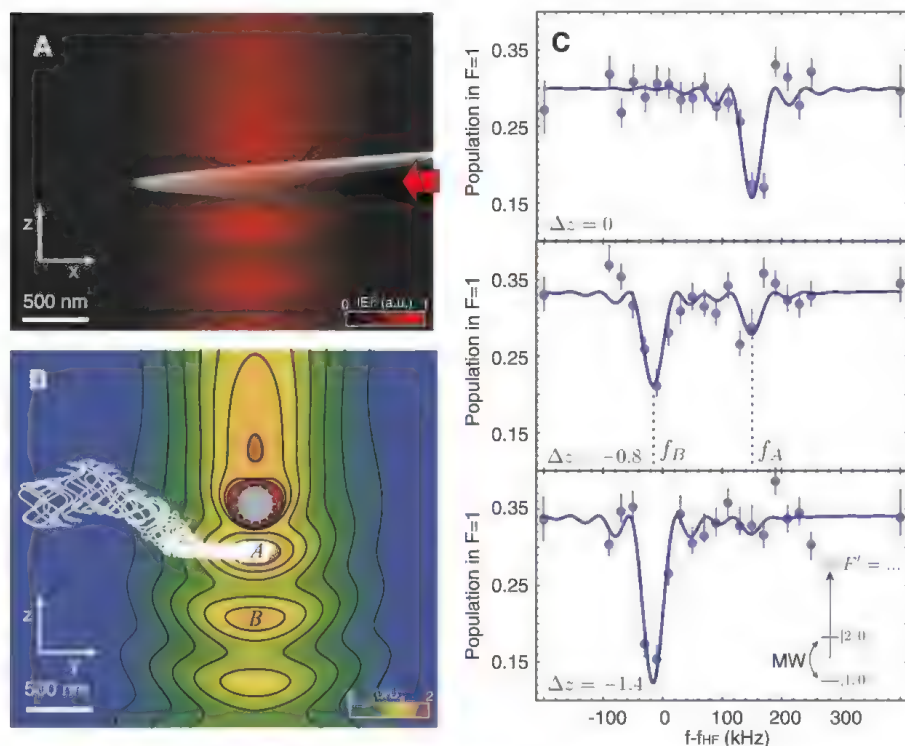


Fig. 2. Loading the optical lattice near the surface. (A) A scanning electron microscope (SEM) image of a tapered nanofiber tip, overlaid with the simulated optical tweezer intensity in the xz plane [carried out with a finite-difference time-domain (FDTD) method]. (B) Numerical simulation of loading process. Color map shows the trapping potential in the yz plane [including surface forces (22)] with the tweezer pointed directly at the nanofiber. The color scale is normalized to the potential depth of the tweezer in free space, U_0 . The white line shows the trajectory of a typical trapped atom with energy $E = 3 k_B \times 10 \mu\text{K}$ as the tweezer focus is scanned in the y direction. "A" indicates the closest lattice site, and "B" indicates the next closest lattice site. (C) Hyperfine transition spectra on the $|1, 0\rangle \leftrightarrow |2, 0\rangle$ transition, probing the atom-fiber separation. The (f_A, f_B) peaks show atoms loaded into the (A, B, and more distant) lattice sites. The focal plane of the tweezer is displaced by Δz from the fiber midplane in each graph; in this way, different lattice sites can be loaded. At $\Delta z = 0$, the absence of a peak at f_B indicates that $100^{+0}_{-12}\%$ of the atoms in the lattice are in the closest site.

pumping rate from $|F = 2, m_F = -2\rangle$ to $F = 1$ (Fig. 3D). The numerically simulated cavity mode is a standing wave (with a period given by the PWC lattice constant, $a \sim 290$ nm), modulated over several micrometers by a Gaussian-like envelope with two lobes. Both features are visible in the data. Because of the tight transverse confinement of the optical field provided by the waveguide, the standing wave is expected to have only 50% contrast: There are no real intensity nodes. The observed contrast is less than this,

so as shown in Fig. 3D, the simulation is convolved with a Gaussian with a root-mean-square (RMS) width of $\delta x_{\text{rms}} = 95$ nm. This blurring arises from drift in the tweezer alignment over the course of the measurement (32 hours), jitter in the galvanometer mirror (50 nm RMS), and motion of the atom in the trap. The RMS zero-point atomic motion is 15 to 20 nm, and the thermal motion could be somewhat larger because of heating from technical effects during the experimental sequence. Viewed as a noninvasive probe

of the cavity intensity distribution, this technique has a spatial resolution of $2 \delta x_{\text{RMS}} = 190(30)$ nm, following the Sparrow resolution criterion.

Next, we quantified the atom-cavity coupling strength by measuring the reduction of the cavity transmission induced by a single atom. Given the cooperativity $\eta \equiv (2g)^2 / (\kappa\Gamma)$ —where κ and Γ are the full linewidths of the cavity and the atomic excited $5P_{3/2}$ state, respectively—the transmission in the presence of an (unsaturated) resonant atom is given by $T = (1 + \eta)^{-2}$ (5). To

Fig. 3. Coupling a single atom to a photonic crystal cavity. (A) An SEM image of a typical PWC attached to a tapered optical fiber. The fiber serves as both a mechanical support and an optical interface to the cavity. (B) Reflection spectrum of the PWC resonance near 780 nm, measured through the optical fiber. The line is a fit to a Lorentzian plus a background of Fabry Perot modes of the waveguide, yielding $Q = 460(40)$ and $\lambda_0 = 779.5(1)$ (full spectrum is available in fig. S2). (C) Simulation of the PWC resonance at 779.5 nm, overlaid with a cross section of the structure. The simulated mode volume is $V = 0.89 \lambda^3$. (D) Measurement of the intensity distribution of the cavity using a trapped atom. Error bars reflect 1 SD in the fitted pumping rates. The red line shows a model based on simulations of the cavity mode. The systematic disagreement on the left side of the waveguide may be due to interference with background light from the fiber that is not coupled into the waveguide. (Inset) In a set of points acquired in a continuous 8-hour window so as to minimize alignment drift, the standing wave structure of the cavity mode is visible.

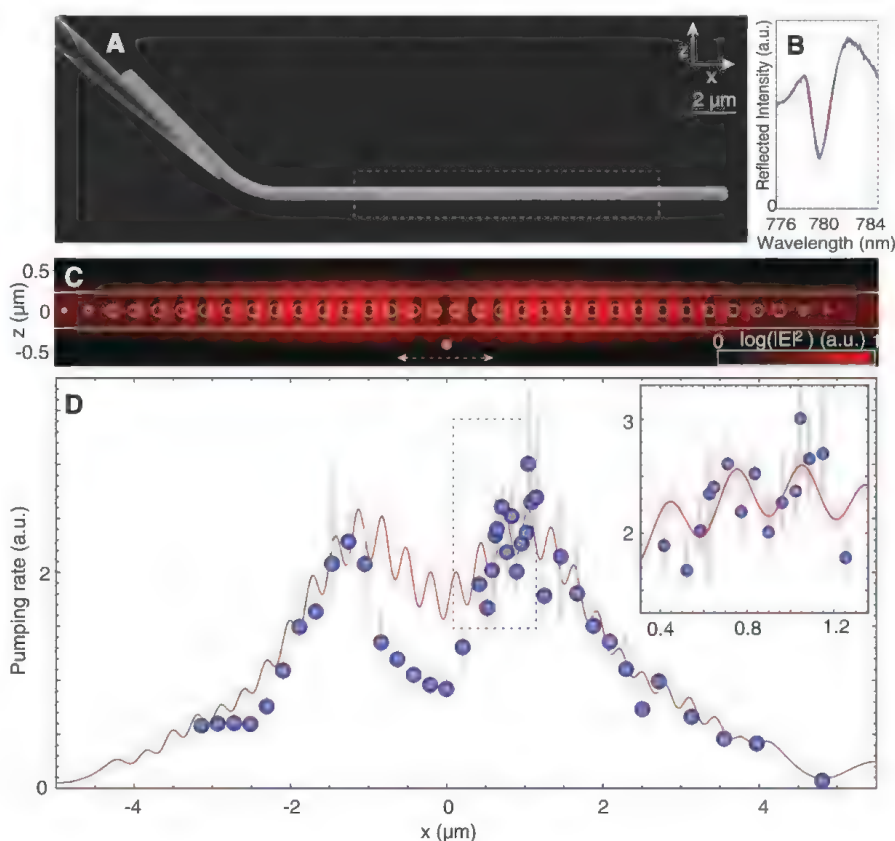
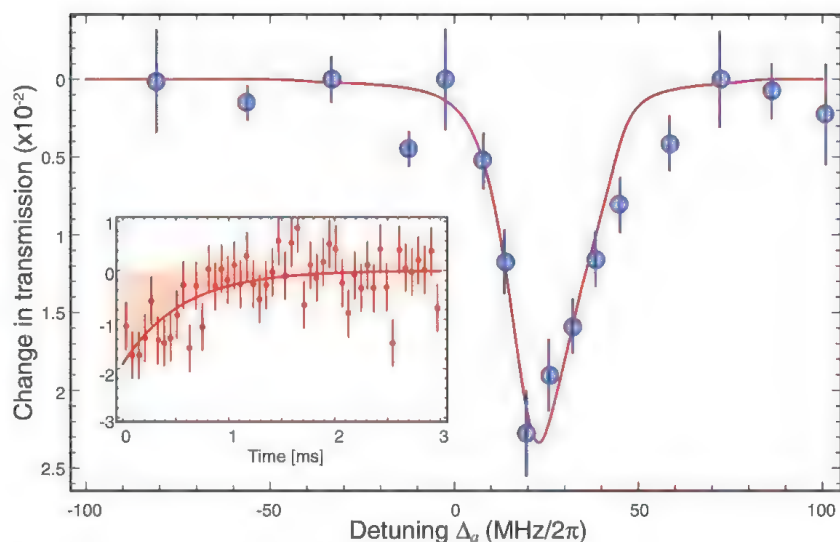


Fig. 4. Change in cavity transmission from a single atom. The transmission of a weak probe beam tuned to the $F = 2 \rightarrow F = 3$ transition is measured versus detuning from the atomic resonance $\Delta_a = \omega_l - \omega_a$, with $(\omega_l, \omega_a) =$ (laser, zero-field atomic transition) frequency. The cavity resonance remains fixed at $\omega_a + 0.3 \kappa$. Error bars reflect 1 SD in the fitted transmission reduction. The line is a fit to a numerical model described in the text, yielding $2g = 2\pi \times 600(80)$ MHz. (Inset) Transmission versus time for continuous wave probe pulse at $\Delta_a = 27$ MHz. The cavity transmission is initially suppressed; after ~ 1 ms, the atom is heated by the probe laser and lost from the trap, restoring transmission. Error bars show shot noise in the number of detected photons; the data are averaged over ~ 2500 runs with single atoms. The shaded area represents the absence of 60 photons (per atom) from the transmitted field.



measure the transmission, we coupled a weak probe field into the waveguide by scattering a focused beam off of the free-standing tip of the waveguide and collected the transmitted light through the tapered optical fiber supporting the waveguide. With the atom placed at the cavity mode maximum ($x = +0.8 \mu\text{m}$) (Fig. 3D), we recorded the transmission of light near the $F = 2 \rightarrow F' = 3$ transition, as shown in Fig. 4. The atom decreases the cavity transmission by at most 2.2%, and the full-width at half-maximum (FWHM) of the transmission dip is ~ 26 MHz, which is four times larger than the natural linewidth. The reduction lasts for ~ 1 ms before the atom is lost from the trap, during which time it scatters ~ 60 photons. The lifetime of the atom in the absence of the probe field is 250 ms; the lifetime is shortened by heating from photon scattering when the probe field is present.

The line broadening results mainly from optical pumping of the atom to other magnetic sublevels with different optical transition frequencies (fig. S6). This occurs after scattering only a few photons because the cavity field is linearly polarized and does not drive a closed cycling transition. We have modeled the line broadening using numerical simulations of the master equation for a single Rb atom, including the 12 relevant Zeeman states of the $F = 2 \rightarrow F' = 3$ transition (22), and find reasonable agreement between the model, the data, and the predicted coupling strength. The model, shown by the red line in Fig. 4, yields an estimate of $\eta = 0.07(1)$ and cavity QED parameters of $(2g, \kappa, \Gamma) = (2\pi) \times [0.60(8), 840(80), 0.006]$ GHz for the $|2, 0\rangle \rightarrow |3, 0\rangle$ transition. This Rabi frequency $2g$ is in excellent agreement with estimates based on numerical models of the optical potential and cavity geometry, which yield a trap-surface distance of $z_0 = 260$ nm and $2g/(2\pi) \sim 620$ MHz on the $|2, 0\rangle \rightarrow |3, 0\rangle$ transition.

Several straightforward improvements can be made to increase the atom-photon coupling. An optimized waveguide geometry will allow $z_0 < 130$ nm, increasing $2g/(2\pi)$ to 3 GHz (22). Additionally, quality factors as high as $Q = 3 \times 10^5$ have already been demonstrated for silicon nitride PWCs (26), which is an improvement of over 600 from our present cavity. These two improvements together give a cooperativity of $\eta > 1000$. Even stronger coupling can potentially be accessed by trapping atoms inside the holes in the waveguide by using alternative PWC geometries to create the necessary trapping potentials (25).

The present technique opens up prospects for realizing a wide variety of hybrid quantum systems. For example, the method can be used to deterministically load multiple traps on the same or different PWCs, as well as cavities forming a two-dimensional network on a chip. In combination with the parallel fabrication and integration possible with nano-photonics, this represents a promising route toward realizing complex nano-optical circuits with several atomic qubits. Poten-

tial applications range from quantum nonlinear optics to quantum networks and novel many-body systems (27, 28).

Furthermore, the demonstrated trapping technique can be applied to other systems in which it is beneficial to control atoms near surfaces, such as quantum interfaces between ultracold atoms and mechanical oscillators (15) or electromagnetic circuits on a chip (29). It can also be used for nanoscale sensing or to probe atom-surface interactions at sub-micrometer scales. By starting from a quantum-degenerate gas it may be possible to simultaneously load multiple near-field traps separated by distances considerably smaller than $\lambda/2$ (30, 31). This will allow studies of strongly correlated states to be extended into a new regime of high atomic densities and strong, long-range interactions.

References and Notes

1. C. Monroe, M. Lukin, *Phys. World* **21**, 32 (2008).
2. M. Wallquist, K. Hammerer, P. Rabl, M. Lukin, P. Zoller, *Phys. Scr.* **T137**, 014001 (2009).
3. B. Dayan et al., *Science* **319**, 1062 (2008).
4. M. Hijlkema et al., *Nature* **3**, 253 (2007).
5. D. E. Chang, A. S. Sørensen, E. A. Demler, M. Lukin, *Nat. Phys.* **3**, 807 (2007).
6. K. Hennessy et al., *Nature* **445**, 896 (2007).
7. I. Fushman et al., *Science* **320**, 769 (2008).
8. H. J. Kimble, *Nature* **453**, 1023 (2008).
9. C. Nölleke et al., *Phys. Rev. Lett.* **110**, 140403 (2013).
10. I. Dotsenko et al., *Phys. Rev. Lett.* **95**, 033002 (2005).
11. R. Gehr et al., *Phys. Rev. Lett.* **104**, 203602 (2010).
12. J. Beugnon et al., *Nat. Phys.* **3**, 696 (2007).
13. W. S. Bakr, J. I. Gillen, A. Peng, S. Fölling, M. Greiner, *Nature* **462**, 74 (2009).
14. Y. Lin, I. Teper, C. Chin, *Phys. Rev. Lett.* **92**, 050404 (2004).
15. D. Hunger et al., *Phys. Rev. Lett.* **104**, 143002 (2010).
16. E. Vetsch et al., *Phys. Rev. Lett.* **104**, 203603 (2010).
17. A. Goban et al., *Phys. Rev. Lett.* **109**, 033603 (2012).
18. N. Schlosser, G. Reymond, I. Pratsenko, P. Grangier, *Nature* **411**, 1024 (2001).

19. R. A. Cornelussen, A. H. van Amerongen, B. T. Wolschrijn, R. Spreeuw, H. B. van Linden van den Heuvell, *Eur. Phys. J. D* **21**, 347 (2002).
20. D. E. Chang et al., *Phys. Rev. Lett.* **103**, 123004 (2009).
21. J. D. Thompson, T. G. Tiecke, A. S. Zibrov, *Phys. Rev. Lett.* **110**, 133001 (2013).
22. Materials and methods are available as supplementary materials on Science Online.
23. J. S. Foresi et al., *Nature* **390**, 143 (1997).
24. B. Lev, K. Srinivasan, P. Barclay, O. Painter, H. Mabuchi, *Nanotechnology* **15**, S556 (2004).
25. C. L. Hung, S. M. Meenehan, D. E. Chang, O. Painter, H. J. Kimble, Trapped atoms in one-dimensional photonic crystals; available at <http://arxiv.org/abs/1301.5252> (2013).
26. M. Eichenfield, R. Camacho, J. Chan, K. J. Vahala, O. Painter, *Nature* **459**, 550 (2009).
27. M. J. Hartmann, F. G. S. L. Brandao, M. B. Plenio, *Nat. Phys.* **2**, 849 (2006).
28. A. D. Greentree, C. Tahan, J. H. Cole, L. C. L. Hollenberg, *Nature* **2**, 856 (2006).
29. A. André et al., *Nat. Phys.* **2**, 636 (2006).
30. M. Gullans et al., *Phys. Rev. Lett.* **109**, 235309 (2012).
31. O. Romero-Isart, C. Navau, A. Sanchez, P. Zoller, J. I. Cirac, Superconducting vortex lattices for ultracold atoms; available at <http://arxiv.org/abs/1302.3504> (2013).

Acknowledgments: We acknowledge helpful discussions with O. Painter, D. Chang, M. Loncar, Q. Quan, E. Kuznetsova, S. Yelin, H. Park, and M. Greiner. Financial support was provided by the NSF, the Center for Ultracold Atoms, the Defense Advanced Research Projects Agency (QUASAR program), the Air Force Office of Scientific Research Multidisciplinary University Research Initiative, European Union project AQUIT, and the Packard Foundation. J.D.T. acknowledges support from the Fannie and John Hertz Foundation and the NSF Graduate Research Fellowship Program, N.P.d.L. acknowledges an Element Six postdoctoral fellowship, and J.F. acknowledges a grant from the NSF through ITAMP. This work was performed in part at the Center for Nanoscale Systems (CNS), a member of the National Nanotechnology Infrastructure Network, which is supported by NSF award ECS-0335765. CNS is part of Harvard University.

Supplementary Materials

www.sciencemag.org/cgi/content/full/science.1237125/DC1
Materials and Methods
Figs. S1 to S6
References (32–38)

26 February 2013; accepted 15 April 2013
Published online 25 April 2013;
10.1126/science.1237125

Entanglement Polytopes: Multiparticle Entanglement from Single-Particle Information

Michael Walter,^{1*} Brent Doran,² David Gross,³ Matthias Christandl¹

Entangled many-body states are an essential resource for quantum computing and interferometry. Determining the type of entanglement present in a system usually requires access to an exponential number of parameters. We show that in the case of pure, multiparticle quantum states, features of the global entanglement can already be extracted from local information alone. This is achieved by associating any given class of entanglement with an entanglement polytope—a geometric object that characterizes the single-particle states compatible with that class. Our results, applicable to systems of arbitrary size and statistics, give rise to local witnesses for global pure-state entanglement and can be generalized to states affected by low levels of noise.

Entanglement is a uniquely quantum mechanical feature. It is responsible for fundamentally new effects, such as quantum

nonlocality, and constitutes the basic resource for concrete tasks such as quantum computing (1) and interferometry beyond the standard limit

(2, 3). Considerable efforts have been directed at obtaining a systematic characterization of multiparticle entanglement; however, our understanding remains limited as the complexity of entanglement scales exponentially with the number of particles (4).

In this work, we show that, for pure quantum states, single-particle information alone can serve as a powerful witness to multiparticle entanglement. In fact, we find that a finite list of linear inequalities characterizes the eigenvalues of the single-particle states in any given class of entanglement. Their violation provides a criterion for witnessing multiparticle entanglement that (i) only requires access to a linear number of degrees of freedom, (ii) applies universally to quantum systems of arbitrary size and statistics, and (iii) distinguishes among many important classes of entanglement, including genuine multiparticle entanglement. Geometrically, these inequalities cut out a hierarchy of polytopes, which captures all information about the global pure-state entanglement deducible from local information alone. Our methods are sufficiently robust to be applicable to situations where the state is affected by low levels of noise.

Formally, a pure state is said to be entangled if it cannot be written as a product $|\psi^{(1)}\rangle \otimes \dots \otimes |\psi^{(N)}\rangle$ (4). Two states can be considered to belong to the same entanglement class if they can be converted into each other with a finite probability of success using local operations and classical communication (stochastic LOCC, or SLOCC) (5, 6). For small systems, these entanglement classes are well understood. In the simplest scenario of three qubits (two-level systems), there exist two classes of genuinely entangled states of very different natures: The first contains the famous Greenberger-Horne-Zeilinger (GHZ) state $\frac{1}{\sqrt{2}}(|\uparrow\uparrow\uparrow\rangle + |\downarrow\downarrow\downarrow\rangle)$, which exhibits a particularly strong form of quantum correlations (7); the second contains the W state $\frac{1}{\sqrt{3}}(|\uparrow\uparrow\downarrow\rangle + |\uparrow\downarrow\uparrow\rangle + |\downarrow\uparrow\uparrow\rangle)$ (6). Whereas states in the W class can be approximated to arbitrary precision by states from the GHZ class, the converse is not true, implying stronger entanglement of the GHZ class (6). Already for four particles there exist infinitely many entanglement classes (8), and the number of parameters required to determine the class grows exponentially with the particle number. As a result, only sporadic results have been obtained for larger systems, despite the enormous amount of literature dedicated to the problem (4).

Our approach to multiparticle entanglement is based on establishing a connection to the one-body quantum marginal problem, or N -representability problem in quantum chemistry. This fundamental problem about quantum correlations asks which

single-particle density matrices $\rho^{(1)}, \dots, \rho^{(N)}$ can appear as the reduced-density matrices of a globally pure quantum state. Its solution is easily seen to depend only on the eigenvalues $\vec{\lambda}^{(k)}$ of the densities and allows for an elegant mathematical description: The set of possible vectors $\vec{\lambda} = (\vec{\lambda}^{(1)}, \dots, \vec{\lambda}^{(N)})$ forms a convex polytope (9–11) whose defining inequalities can be computed algorithmically (10, 11). For fermions, the most famous such inequality is the Pauli principle (12, 13).

Here, we make the crucial observation that these local eigenvalues alone can already give considerable information about the entanglement of the global state, provided that it is pure. To make this precise, we consider the set of all eigenvalue vectors $\vec{\lambda}$ of the states in the closure of a given entanglement class. Surprisingly, this set also forms a convex polytope (i.e., it is the convex hull of finitely many such vectors), and we call it the entanglement polytope of the class. Entanglement polytopes immediately lead to a local criterion for witnessing global multiparticle entanglement: If the collection of eigenvalues $\vec{\lambda} = (\vec{\lambda}^{(1)}, \dots, \vec{\lambda}^{(N)})$ of the single-particle, reduced-density matrices of a pure quantum state $|\psi\rangle$ does not lie in an entanglement polytope Δ_C , then the given state cannot belong to the corresponding entanglement class C (Fig. 1). Mathematically,

$$\vec{\lambda} = (\vec{\lambda}^{(1)}, \dots, \vec{\lambda}^{(N)}) \notin \Delta_C \Rightarrow |\psi\rangle \notin C \quad (1)$$

Phrased differently, the criterion allows us to witness the presence of a highly entangled state by showing that its local eigenvalues are incompatible with all less-entangled classes. Strikingly, there are always only finitely many entanglement polytopes, and they naturally form a hierarchy: If a state in the class C can be approximated arbitrarily well by states from D , then $\Delta_C \subseteq \Delta_D$. This reflects geometrically the fact that states in the second class are more powerful for quantum information processing.

To compute Δ_C , and to see that it is indeed a convex polytope, we use tools from algebraic geometry and group representation theory, presented in detail in (14). We use the characterization of SLOCC operations as invertible local operators $A_1 \otimes \dots \otimes A_N$ (6), which act on the class C , and therefore also on the set of polynomial functions on C . The irreducible subspaces of this action correspond to covariants, i.e., vector-valued polynomial functions transforming in a well-defined way. By the representation theory of Lie groups, each covariant is labeled by a highest-weight $\vec{\mu} = (\mu^{(1)}, \dots, \mu^{(N)})$, where the $\mu^{(k)}$ are vectors of natural numbers whose entries are ordered decreasingly and sum to the degree n of the polynomial. Thus, any normalized highest-weight $\vec{\mu}/n$ formally looks like an eigenvalue vector $\vec{\lambda}$. This formal similarity corresponds to a factual correspondence: Δ_C is essentially given by those $\vec{\mu}/n$'s whose associated covariants do not vanish on C (15). The statement that Δ_C is a convex polytope then follows from the fact that the covariants form a finitely generated algebra (15). We explain how to algorithmically compute a finite set of generators by using computational invariant theory (16), motivated in part by (17). The polytope can then be obtained as the convex hull of the normalized highest weights $\vec{\mu}/n$ of those generators that are nonzero on the class C .

In the following, we illustrate our method with a number of paradigmatic examples: For qubit systems, each single-particle reduced-density matrix $\rho^{(k)}$ has two eigenvalues, which are nonnegative and sum to one; hence, its spectrum is completely characterized by the maximal eigenvalue $\lambda_{\max}^{(k)}$, which can take values in the closed interval 0.5 to 1. In the case of three qubits, we may therefore regard the entanglement polytopes as subsets of three-dimensional (3D) space. There are two full-dimensional polytopes (18): one for the W class (the upper pyramid in Fig. 1) and the other for the GHZ class (the entire polytope, i.e., the union of both pyramids). The

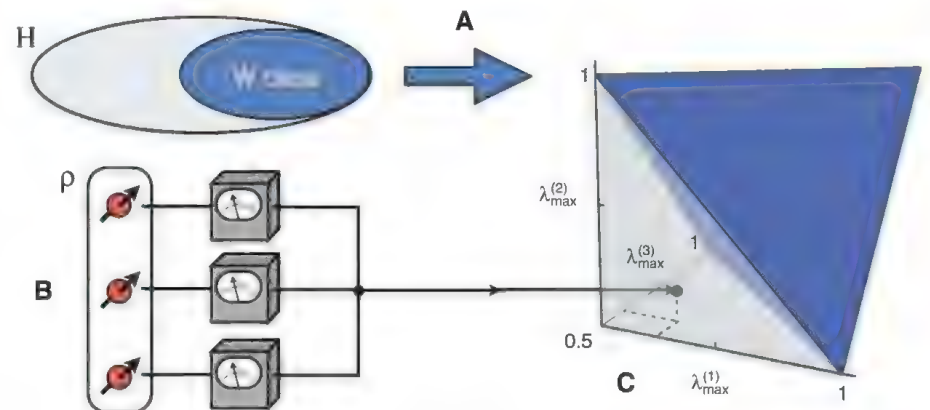


Fig. 1. Entanglement polytopes as witnesses (illustrated for three qubits). (A) An entanglement polytope contains all possible local eigenvalues of states in the entanglement class (the W class and its polytope are shown in blue; H is the set of all pure states). (B) For a sufficiently pure quantum state ρ , local tomography is performed to determine its local eigenvalues. (C) The indicated eigenvalues are not compatible with the W class nor its closure, hence ρ must have GHZ-type entanglement.

¹Institute for Theoretical Physics, Eidgenössische Technische Hochschule (ETH) Zürich, Wolfgang-Pauli-Strasse 27, 8093 Zürich, Switzerland. ²Department of Mathematics, ETH Zürich, Rämistrasse 101, 8092 Zürich, Switzerland. ³Institute for Physics, University of Freiburg, Rheinstrasse 10, 79104 Freiburg, Germany.

*Corresponding author. E-mail: mwalter@phys.ethz.ch

tip of the upper pyramid constitutes a polytope by itself, indicating a product state. Three further 1D polytopes are given by the edges emanating from this vertex. They correspond to the three possibilities of embedding a Bell state into three systems. Thus, eigenvalues in the interior of the polytope are compatible only with W and GHZ classes, i.e., genuine three-partite entanglement. Likewise, if the eigenvalues lie in the lower pyramid, then by Eq. 1 the state cannot be contained in the closure of the W class; we have witnessed GHZ-type entanglement (Fig. 1).

In systems of four qubits, there are nine infinite families of entanglement classes, each described by up to four complex parameters (8) that are not directly accessible; hence, a complete classification is too detailed to be practical. In contrast, the polytope method strikes an attractive balance between coarse-graining and preserving structure (Fig. 2): Up to permutation of the particles, there are 13 entanglement polytopes, 7 of which are full-dimensional and correspond to distinct types of genuine four-partite entanglement. One example is the four-qubit W class: In complete analogy to the previous case, its polytope is an “upper pyramid” of eigenvalues that fulfill $\lambda_{\max}^{(1)} + \lambda_{\max}^{(2)} + \lambda_{\max}^{(3)} + \lambda_{\max}^{(4)} \geq 3$.

Quantum states that are genuinely multipartite entangled are of particular interest (19). These are the states that do not factorize with respect to any partition of the qubits into two sets. We show for arbitrary qubit systems that the entanglement polytopes of the biseparable states (i.e., the states that do factorize) do not account for all possible

eigenvalues. Therefore, the presence of genuine multipartite entanglement in a pure quantum state can be certified by checking that the local eigenvalues do not lie in any biseparable polytope (Fig. 3).

Entanglement polytopes can also be constructed for quantum systems composed of bosons or fermions. Because the individual particles are indistinguishable, the reduced-density matrices $\rho^{(k)}$ and their eigenvalues $\bar{\lambda}^{(k)}$ all coincide. In the case of qubits, the entanglement polytopes are therefore intervals describing the possible values of the maximal local eigenvalue for states in the class. For bosons, the right endpoint of the interval is always equal to one, corresponding to a coherent state, while the left endpoint γ_C corresponds to the most entangled states in the class. These are the symmetric Dicke states with mean spin $m \geq 0$ per particle, for which $\gamma_C = 0.5 + m$, and they include the GHZ state for $\gamma_C = 0.5$. In (14), we also describe the entanglement polytopes for the Borland-Dennis system, which is composed of three fermions with local rank six (20).

We can also obtain quantitative information about the multipartite entanglement of a quantum state, e.g., by witnessing genuine k -partite entanglement (19) using a generalization of the argument sketched above. Furthermore, we may consider the linear entropy of entanglement $E(\psi) = 1 - \frac{1}{N} \sum_{j=1}^N \text{tr}(\rho^{(j)})^2$ used, e.g., in metrology (21). Entanglement polytopes allow us to bound the maximal linear entropy of entanglement distillable by SLOCC operations. Because $E(\psi)$ corresponds to the Euclidean length of the

vector of local eigenvalues, shorter vectors imply more entanglement. In particular, quantum states of maximal entropy of entanglement in a class C map to the point of minimal distance from the origin in the entanglement polytope Δ_C . Therefore, if the local eigenvalues of a given state lie only in polytopes with small distance to the origin, a high amount of entanglement can be distilled. In (14), we turn this observation into a quantitative statement and describe a distillation algorithm.

Quantum states prepared in the laboratory are always subject to noise and hence never perfectly pure. Our method for witnessing entanglement using Eq. 1 can be adapted to this situation as long as the noise is not too large. To make this statement precise, we assume that a lower bound $1 - \epsilon$ on the purity $\text{tr} \rho^2$ of a quantum state ρ is available (here, tr denotes the trace of a matrix). This implies that ρ has fidelity $\langle \psi | \rho | \psi \rangle \geq 1 - \epsilon$, with a pure state $|\psi\rangle$ whose local eigenvalues deviate from the measured ones by no more than a small amount $\delta(\epsilon)$. In the case of N qubits, $\delta(\epsilon) \approx N\epsilon/2$ for small ϵ . Therefore, as long as the distance of the measured eigenvalues $\bar{\lambda}$ to the entanglement polytope Δ_C is at least $\delta(\epsilon)$, the experimentally prepared state ρ has high fidelity with a pure state that is more entangled than the class C . These ideas can be further extended to show that ρ itself cannot be written as a convex combination of quantum states in a given entanglement class, as we describe in (14). Unlike the local eigenvalues, the purity $\text{tr} \rho^2$ cannot be determined by single-particle tomography alone. However, it is in general not necessary to perform full tomography of

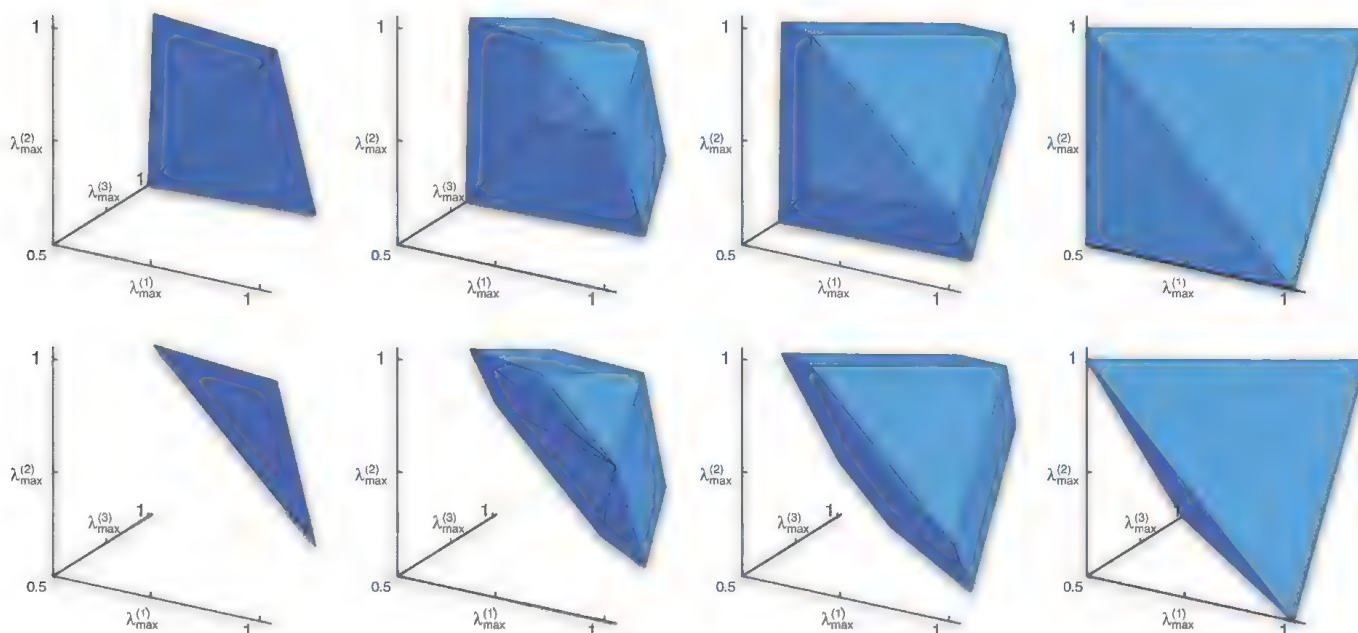


Fig. 2. Cross sections of two entanglement polytopes for four qubits. Each row shows cross sections of a 4D entanglement polytope for four values of $\lambda_{\max}^{(4)}$: 0.5, 0.66, 0.83, and 1. The first row corresponds to the entanglement class L_{04} for $a = 0$ in the characterization of (8) and the second row to the four-qubit W class; one can clearly identify the “upper-pyramid form” explained in the text. Several properties that had previously been computed algebraical-

ly (8) can be read off directly: for example, the final column corresponds to the situation when the fourth qubit has been projected onto a pure state. As apparent from the polytopes, the state of the remaining three sites is generically of GHZ type in the first row and of W type in the second row. See (26) for an interactive visualization of all four-qubit entanglement polytopes.

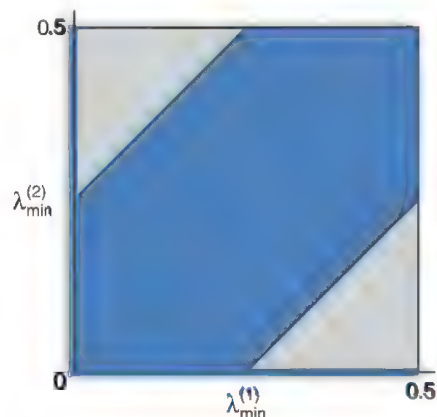


Fig. 3. Witnessing genuine multipartite entanglement. The figure displays the 2D cross section through the six-qubit eigenvalue polytope where we fix $\lambda_{\min}^{(3)} = \dots = \lambda_{\min}^{(6)} = 0.125$. If the local eigenvalues do not belong to any of the biseparable entanglement polytopes (blue region), then all corresponding pure states necessarily contain genuine six-qubit entanglement.

the global state to estimate the purity (22). Whereas it is an experimental challenge to achieve the levels of purity necessary for the application of our method, we believe that they are in the reach of current technology (23–25).

References and Notes

- G. Vidal, *Phys. Rev. Lett.* **91**, 147902 (2003).
- D. Leibfried *et al.*, *Science* **304**, 1476 (2004).
- V. Giovannetti, S. Lloyd, L. Maccone, *Science* **306**, 1330 (2004).
- R. Horodecki, P. Horodecki, M. Horodecki, K. Horodecki, *Rev. Mod. Phys.* **81**, 865 (2009).
- C. H. Bennett, S. Popescu, D. Rohrlich, J. A. Smolin, A. V. Thapliyal, *Phys. Rev. A* **63**, 012307 (2000).
- W. Dür, G. Vidal, J. I. Cirac, *Phys. Rev. A* **62**, 062314 (2000).
- D. M. Greenberger, M. A. Horne, A. Zeilinger, in *Bell's Theorem, Quantum Theory, and Conceptions of the Universe*, M. Kafatos, Ed. (Kluwer, 1989), pp. 69–72.
- F. Verstraete, J. Dehaene, B. De Moor, H. Verschelde, *Phys. Rev. A* **65**, 052112 (2002).
- M. Christandl, G. Mitchison, *Commun. Math. Phys.* **261**, 789 (2006).
- A. Klyachko, Quantum marginal problem and representations of the symmetric group, arXiv:quant-ph/0409113 (2004).
- S. Datta, P. Hayden, *Ann. Phys.* **315**, 80 (2005).
- A. J. Coleman, V. I. Yukalov, *Reduced Density Matrices: Coulson's Challenge* (Springer, 2000).
- A. Klyachko, *J. Phys. Conf. Ser.* **36**, 72 (2006).
- Further details can be found in the supplementary text on Science Online.
- M. Brion, in *Séminaire d'Algèbre P. Dubreil et M.-P. Malliavin*, M. P. Malliavin, Ed. (Springer, 1987), pp. 177–192.
- H. Derksen, G. Kemper, *Computational Invariant Theory* (Springer, 2002).
- B. Doran, F. Kirwan, *Pure Appl. Math. Q.* **3**, 61 (2007).
- Y.-J. Han, Y.-S. Zhang, G.-C. Guo, *Phys. Rev. A* **70**, 042309 (2004).

- O. Gühne, G. Toth, H. J. Briegel, *New J. Phys.* **7**, 229 (2005).
- R. E. Borland, K. Dennis, *J. Phys. B* **5**, 7 (1972).
- K. Furuya, M. C. Nemes, G. Q. Pellegrino, *Phys. Rev. Lett.* **80**, 5524 (1998).
- H. Buhrman, R. Cleve, J. Watrous, R. de Wolf, *Phys. Rev. Lett.* **87**, 167902 (2001).
- A. Rauschenbeutel *et al.*, *Science* **288**, 2024 (2000).
- J.-W. Pan, M. Daniell, S. Gasparoni, G. Weihs, A. Zeilinger, *Phys. Rev. Lett.* **86**, 4435 (2001).
- T. Monz *et al.*, *Phys. Rev. Lett.* **106**, 130506 (2011).
- M. Walter, B. Doran, D. Gross, M. Christandl, www.entanglement-polytopes.org (2012).

Acknowledgments: We thank A. Botero, F. Brandão, P. Bürgisser, C. Ikenmeyer, F. Kirwan, F. Mintert, G. Mitchison, A. Osterloh, and P. Vrana for valuable discussions. This work is supported by the German Science Foundation (grant CH 843/2-1), the Swiss National Science Foundation (grants PP00P2_128455, 20CH21_138799 (CHIST-ERA project CQC), and 200021_138071), the Swiss National Center of Competence in Research Quantum Science and Technology, and the Excellence Initiative of the German Federal and State Governments (grant ZUK 43). After completion of this work, we have learned about independent related work by Sawicki, Oszmaniec, and Kuś.

Supplementary Materials

www.sciencemag.org/cgi/content/full/340/6137/1205/DC1
Supplementary Text
Figs. S1 to S4
Tables S1 to S3
References (27–82)

19 November 2012; accepted 25 April 2013
10.1126/science.1232957

From Sub-Rayleigh to Supershear Ruptures During Stick-Slip Experiments on Crustal Rocks

François X. Passelègue,^{1*} Alexandre Schubnel,¹ Stefan Nielsen,² Harsha S. Bhat,³ Raúl Madariaga¹

Supershear earthquake ruptures propagate faster than the shear wave velocity. Although there is evidence that this occurs in nature, it has not been experimentally demonstrated with the use of crustal rocks. We performed stick-slip experiments with Westerly granite under controlled upper-crustal stress conditions. Supershear ruptures systematically occur when the normal stress exceeds 43 megapascals (MPa) with resulting stress drops on the order of 3 to 25 MPa, comparable to the stress drops inferred by seismology for crustal earthquakes. In our experiments, the sub-Rayleigh-to-supershear transition length is a few centimeters at most, suggesting that the rupture of asperities along a fault may propagate locally at supershear velocities. In turn, these sudden accelerations and decelerations could play an important role in the generation of high-frequency radiation and the overall rupture-energy budget.

Earthquake damage depends, in part, on the velocity of the rupture front (1). In 1973, Burridge demonstrated theoretically that in-plane shear ruptures (mode II) could propagate

at velocities higher than the shear wave velocity (C_s) and up to the compressional wave velocity (C_p) (2). Since then, so-called supershear ruptures ($V_r > C_s$, where V_r is rupture velocity) have been observed during large strike-slip earthquakes (3–8). The stress and geometric conditions leading to the transition between sub-Rayleigh and supershear ruptures have been investigated with photoelasticity, both theoretically (9, 10) and experimentally, on brittle polymers (11–15). Although these experiments successfully illus-

trate supershear ruptures, the lack of experiments on rock samples limits the ability to understand these rare events observed in nature. In a recent experimental study, a photoelastic setup was coupled with an acoustic high-frequency-recording multistation array during stick-slip experiments on polycarbonate sheets. This allowed Schubnel *et al.* to use high-frequency acoustics to identify unequivocally the signature of both sub-Rayleigh and supershear ruptures (15). This advance has opened the possibility of revisiting experimental work performed on rocks (16–19).

Here, we report results from stick-slip experiments conducted on saw-cut Westerly granite samples (fig. S1), which serve as proxies for crustal rocks, during triaxial loading (where the

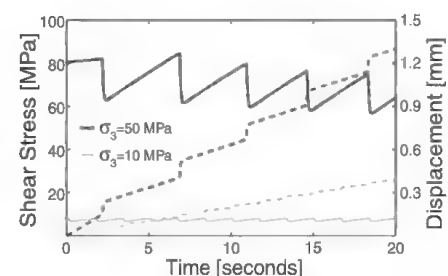


Fig. 1. Stress release during microearthquakes. Evolution of shear stress (solid lines) and displacement (dashed lines) is represented for two stick-slip experiments conducted at 10- and 50-MPa confining pressure.

¹Laboratoire de Géologie, CNRS UMR 8538, École Normale Supérieure, 75005 Paris, France. ²Istituto Nazionale di Geofisica e Vulcanologia, Roma 00143, Italy. ³Institut de Physique du Globe de Paris, 1 rue Jussieu, 75238 cedex 05 Paris, France.

*Corresponding author. E-mail: passelègue@geologie.ens.fr

principal stresses $\sigma_1 > \sigma_2 = \sigma_3$). Stick-slip experiments and earthquake mechanisms are analogous in nature because they both result from rapid frictional sliding along preexisting faults, leading to partial or total stress drop (16). In our experiments, the stress conditions were typical of the upper crust, ranging from 10 to 150 MPa in normal stress acting on the preexisting fault. In total, we recorded more than 200 stick-slip events (Fig. 1). For each event, we inverted the rupture velocity directly from our experimental records, using high-frequency acoustics as a tracking tool (fig. S2).

We used recorded accelerograms to track the Mach wavefront arrival. Theoretical arrival time of the Mach wavefront radiated away from the rupture tip was predicted using (i) the position of the rupture front determined from the inverted rupture velocity (fig. S2) and (ii) the shear wave

velocity and the distance between the Mach front antenna (MFA) sensors to the fault, as defined in Fig. 2A (15). Our calculation assumes that the rupture velocity is constant. Importantly, we looked for ruptures with V_r greater than the shear wave speed but different that $\sqrt{2}C_s$, for in this case, no Mach cone is expected (20).

We compared our calculation with waveforms recorded by the MFA array for a stick-slip event during which a supershear rupture velocity was predicted by the inversion (Fig. 2B). In agreement with theory (21), we first observed a weak P -wave arrival, which corresponds to the continuous emission of P waves by the rupture tip as it propagates. However, the signal is dominated by the arrival of a large-amplitude, coherent wavefront just after the diffuse P -wave arrival. The relative amplitude of this wavefront, when compared to the first P -wave amplitude,

increases with distance to the fault. This is expected because the geometric attenuation of a conic wavefront is smaller than that of spherical one. At each station, the arrival time of this wavefront is consistent with the predicted arrival time of the Mach wavefront.

To confirm our estimations of the rupture velocity, we used two-dimensional (2D) steady-state rupture model to conduct simulations (21). We observe an excellent fit, both in relative amplitude and for the general waveform shape, when comparing the experimental waveforms recorded on the MFA sensors during a subshear event and the synthetics obtained by our numerical simulation (Fig. 3B). We observed similar good correspondence between experimental waveforms and simulation of a supershear rupture (Fig. 3C). In both cases, we obtained the best fit between analytical and experimental records by using the rupture velocity estimated experimentally, confirming that our experimental estimate of the rupture velocity is accurate. Furthermore, we show that dynamic rupture models that can accurately simulate strong ground motions on the kilometeric scale can also simulate accelerations in the kilohertz range on centimetric sized samples. In other words, dynamic rupture propagation is truly a self-similar mechanism.

Our experimental results demonstrate that the ruptures were dominantly mode II (fig. S3). For this mode, the transition between sub-Rayleigh and supershear rupture has been extensively discussed in theoretical and experimental studies (9, 12–15). Following 2D numerical studies, this transition is generally explained in terms of the seismic ratio $S = (\tau_p - \tau_o)/(\tau_o - \tau_r)$ where τ_p , τ_o , and τ_r are the peak frictional strength, the initial shear stress, and the residual frictional strength, respectively. The ratio τ_o/σ_n (where σ_n is the normal stress), employed by Ben-David *et al.* (14), is equivalent to S , and both quantities are simply related by $\tau_o/\sigma_n = (f_s - f_d)/(1 + S) + f_d$ (where f_s and f_d are the static and dynamic friction coefficients, respectively) (Fig. 4). In our experiments, τ_o was continuously measured (Fig. 1). Taking $f_s = 0.85$ and $f_d = 0.1$, S could be estimated for each individual stick-slip. Supershear propagation may happen under both of the following conditions: (i) $S < S_c$ (where S_c , the critical value of S allowing supershear transition, is equal to 1.77 or 1.119 in 2D and 3D, respectively), which was always the case in our experiments (Fig. 4A), and (ii) when the rupture length exceeds the transition length L , estimated following the semi-empirical relation (9)

$$L = \frac{39.2}{\pi(1-\nu)} \frac{1}{(S_c - S)^3} \frac{\mu G}{\left[\sigma_n \left(\frac{f_s - f_d}{1 + S}\right)\right]^2} \quad (1)$$

where ν , μ , and G are, respectively, the Poisson ratio, the shear modulus, and the fracture energy. In our case, condition (ii) can be met only if $L < L_f$, where L_f is the finite length of the experimental fault. In our experiments, G may range from

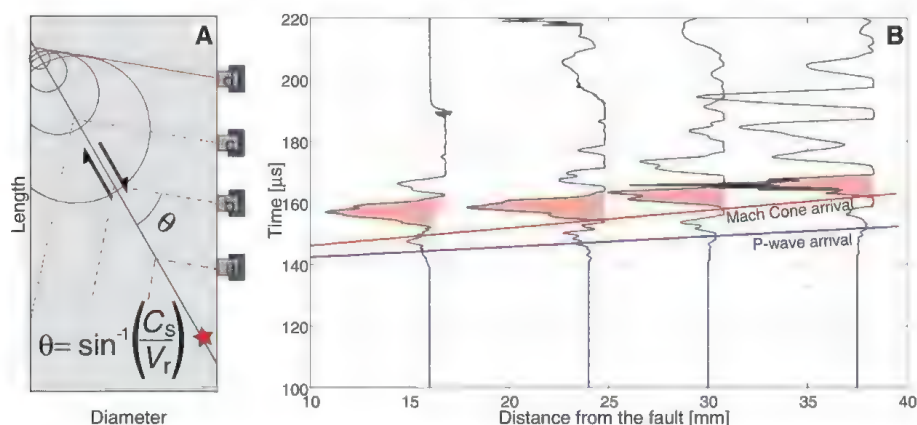


Fig. 2. Mach wavefront arrival. (A) Schematic of the Mach cone arrival at MFA stations. The red star represents the nucleation zone of the event. Arrows indicate the sense of shear (here, right lateral). The positions of the MFA stations a to d are shown relative to the fault plane. θ , is the angle of the Mach cone, a function of the ratio between the rupture and shear wave velocities. (B) Waveforms recorded on the MFA array during a supershear event that occurred at $\tau = 84$ and $\sigma_n = 99$ MPa. Blue and red solid lines represent the first P -wave front and the S -wave Mach front, respectively. The Mach front is shaded in red.

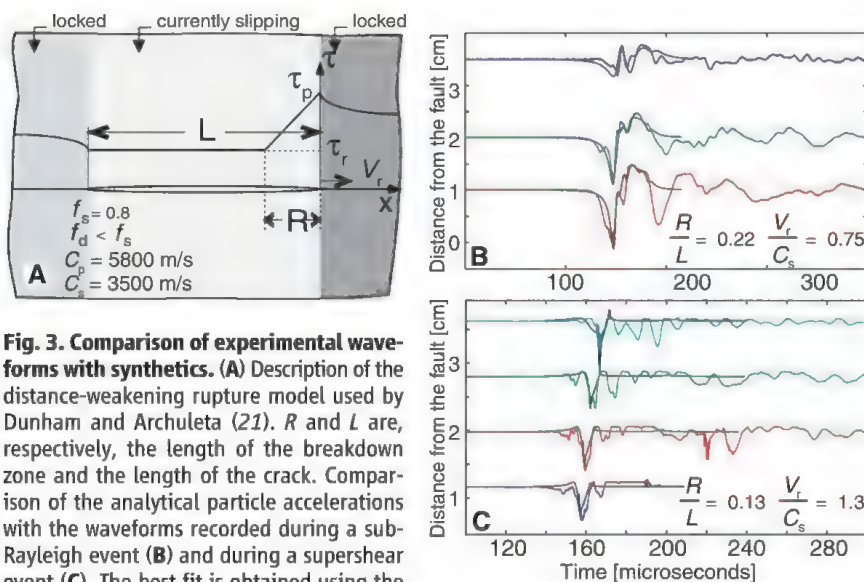


Fig. 3. Comparison of experimental waveforms with synthetics. (A) Description of the distance-weakening rupture model used by Dunham and Archuleta (21). R and L are, respectively, the length of the breakdown zone and the length of the crack. Comparison of the analytical particle accelerations with the waveforms recorded during a sub-Rayleigh event (B) and during a supershear event (C). The best fit is obtained using the inverted rupture velocity.

the lower bound 10 J/m^2 , as given by single-crystal fracture energy values and stick-slip experiments performed at low normal stress (19), to the upper bound 10^4 J/m^2 , measured for intact Westerly granite samples at high confining pressures (22). From Eq. 1, L was calculated as a function of normal stress in two cases: (i) $S = 1$ and $G = 10 \text{ J/m}^2$ and (ii) $S = 0$ and $G = 1000 \text{ J/m}^2$ (Fig. 4A). Experiments performed at the lowest normal stresses are compatible with $G \approx 10 \text{ J/m}^2$. However, experiments performed at intermediate normal stresses can be explained only by using larger fracture energy. This is consistent with our observation of an intense production of fine gouge particles at intermediate and high normal stresses. Indeed, for spherical particles, the ratio between G and surface energy of single crystals (γ) is $G/\gamma \approx 3w/d$, where w is the fault thickness and d is the average particle size. Our observation of gouge particles of $1\text{-}\mu\text{m}$ diameter and smaller is consistent with a fault roughness of less than $30 \mu\text{m}$. The match between the measured rupture velocities and the prediction that the minimum transition length L drops to a few centimeters (comparable to

our sample size) at high normal stress (Fig. 4A) explains why, in our experiments, supershear rupture becomes a “normal” phenomena for $\sigma_n > 60 \text{ MPa}$. It also explains why supershear ruptures were not clearly observed in previous experimental studies on rocks conducted at low normal stress (most often in biaxial conditions) (18, 19).

Finally, we observe a double correlation between the rupture velocity, the initial stress ratio τ_0/σ_n , and the final stress drop (Fig. 4B). Subshear ruptures occurred for stress ratios $\tau_0/\sigma_n < 0.6$ and resulted in stress drops generally lower than 1.5 MPa . Conversely, supershear ruptures occurred for stress ratios $\tau_0/\sigma_n > 0.7$ and resulted in stress drops generally larger than 3 MPa . These results not only make sense physically but are also compatible with values previously observed on brittle polymers (14) and with field observations for the Kunlunshan earthquake (23). Importantly, our findings are comparable to the average stress drops inferred by seismologists for most large crustal earthquakes. Note that our direct measurement of the stress drop is comparable to what a seismological estimate would be using the final slip u (fig. S4).

Based on our experimental results, why is there a paucity of supershear ruptures observed in nature? A first straightforward explanation is related to the difference in fault geometry between our experiments and seismogenic faults. Our experiments consisted of a perfectly planar fault geometry with very low initial roughness at high normal stress, leading to uniform and large stresses on the fault plane. Seismogenic faults, on the other hand, are most often nonplanar and exhibit self-affine roughness (24). The occurrence of kinks and dilatational jogs could slow down or even arrest locally the propagation of seismic ruptures (25). The few documented examples of supershear earthquakes are on very smooth, planar fault sections (3–8). In addition, the presence of a gouge layer along the fault interface may slow the propagation of the rupture, as well as thermo-hydro-mechanical coseismic processes within the breakdown zone [such as thermal pressurization (26), frictional melting (27), mineral reactions (28), and off fault damage, including pulverization (29)], which dissipate part of the released strain energy available, resulting in a deceleration of the rupture front. Alternatively, the paucity of supershear rupture observation in nature might also be due to limitations in instrumentation and/or spatial coverage. Nevertheless, the experimental values of L and stress drops reported here for a classical crustal lithology (Westerly granite) under upper-crustal conditions ($<150 \text{ MPa}$) demonstrate that rupture velocity may exhibit important variations at the scale of small (centimetric) asperities, so that the seismological estimate of rupture velocities over long fault segments is an average that could well have little importance at the scale of an asperity. Our experimental results strongly suggest that, despite the scarcity of compelling measurements on natural earthquakes, supershear ruptures may frequently occur at the local scale of asperities, for which the stress drop generally inferred is quite large. In turn, these sudden accelerations and decelerations of the rupture front should play an important role in generating high-frequency radiation, which will influence the total rupture-energy budget.

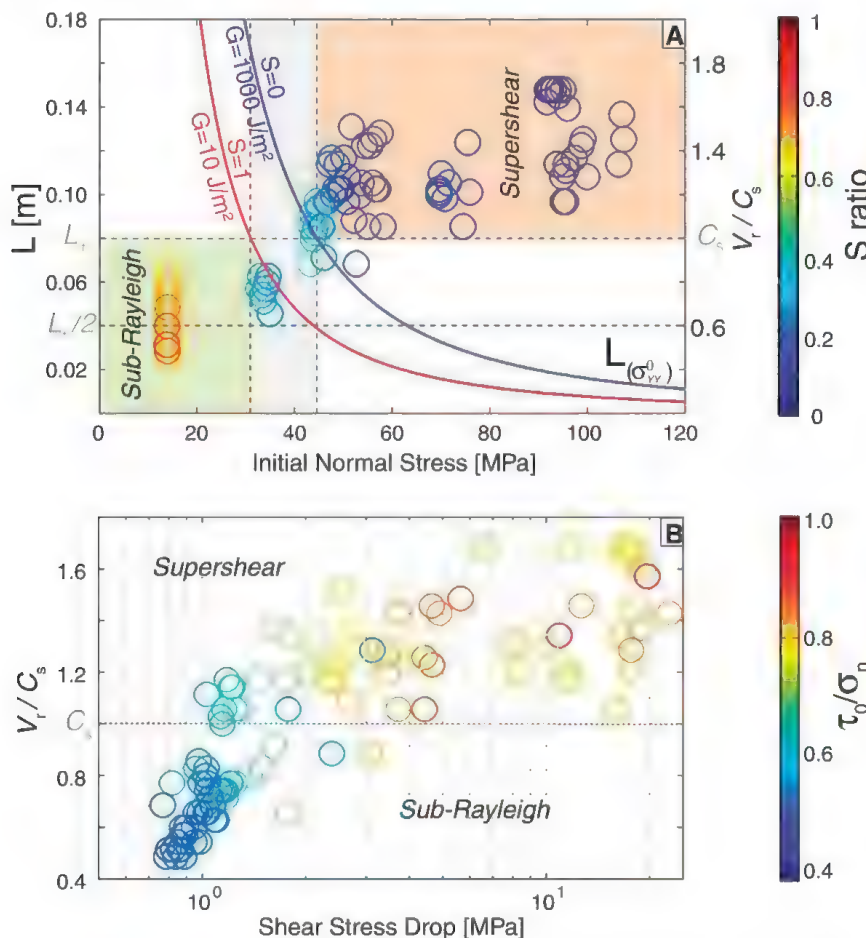


Fig. 4. The transition to supershear ruptures. (A) Correlation between normal stress and rupture velocity. Color-coding corresponds to the value of S . Red and blue solid lines represent L as a function of normal stress, assuming two combinations of S and G . **(B)** Correlation between rupture velocity and stress drop. Color-coding corresponds to the value of τ_0/σ_n . L_f is the length of the experimental fault and $L(\sigma_{yy})$ is the transition length as a function of the normal stress.

References and Notes

1. R. Madariaga, *Ann. Geophys.* **1**, 17 (1983).
2. R. Burridge, *Geophys. J. R. Astron. Soc.* **35**, 439 (1973).
3. R. J. Archuleta, *J. Geophys. Res.* **89**, 4559 (1984).
4. M. Bouchon *et al.*, *Geophys. Res. Lett.* **28**, 2723 (2001).
5. M. Bouchon, M. Vallée, *Science* **301**, 824 (2003).
6. W. L. Ellsworth *et al.*, *Earthq. Spectra* **20**, 597 (2004).
7. P. Liu, S. Custódio, R. J. Archuleta, *Bull. Seismol. Soc. Am.* **96**, S143 (2006).
8. D. Wang, J. Mori, T. Uchide, *Geophys. Res. Lett.* **39**, L21307 (2012).
9. D. J. Andrews, *J. Geophys. Res.* **81**, 5679 (1976).
10. A. Bizzarri, E. M. Dunham, P. Spudich, *J. Geophys. Res.* **115**, B08301 (2010).
11. F. T. Wu, K. C. Thomson, H. Kuenzler, *Bull. Seismol. Soc. Am.* **62**, 1621 (1972).
12. K. Xia, A. J. Rosakis, H. Kanamori, *Science* **303**, 1859 (2004).
13. S. Nielsen, J. Taddeucci, S. Vinciguerra, *Geophys. J. Int.* **180**, 697 (2010).
14. O. Ben-David, G. Cohen, J. Fineberg, *Science* **330**, 211 (2010).

15. A. Schubnel, S. Nielsen, J. Taddeucci, S. Vinciguerra, S. Rao, *Earth Planet. Sci. Lett.* **308**, 424 (2011).
16. W. F. Brace, J. D. Byerlee, *Science* **153**, 990 (1966).
17. T. L. Johnson, C. H. Scholz, *J. Geophys. Res.* **81**, 881 (1976).
18. P. G. Okubo, J. H. Dieterich, *J. Geophys. Res.* **89**, 5817 (1984).
19. M. Ohnaka, L.-f. Shen, *J. Geophys. Res.* **104**, 817 (1999).
20. M. Mello, H. S. Bhat, A. J. Rosakis, H. Kanamori, *Tectonophysics* **493**, 297 (2010).
21. E. M. Dunham, R. J. Archuleta, *Geophys. Res. Lett.* **32**, L03302 (2005).
22. T.-F. Wong, *J. Geophys. Res.* **87**, 990 (1982).
23. D. P. Robinson, C. Brough, S. Das, *J. Geophys. Res.* **111**, B08303 (2006).
24. T. Candela, F. Renard, *J. Struct. Geol.* **45**, 87 (2012).
25. R. H. Sibson, *Nature* **316**, 248 (1985).
26. J. R. Rice, *J. Geophys. Res.* **111**, B05311 (2006).
27. G. Di Toro, T. Hirose, S. Nielsen, G. Pennacchioni, T. Shimamoto, *Science* **311**, 647 (2006).
28. N. Brantut, A. Schubnel, J.-N. Rouzaud, F. Brunet, T. Shimamoto, *J. Geophys. Res.* **113**, B10401 (2008).
29. M.-L. Doan, G. Gary, *Nat. Geosci.* **2**, 709 (2009).

Acknowledgments: We thank Y. Pinquier for technical support and two reviewers and the associate editor for their constructive remarks, which helped to enhance this paper.

F.X.P., A.S., and S.N. acknowledge support from the French and Italian Ministry of Foreign affairs program GALILEO, project no. 26019WJ. This work was supported by the Institut National des Sciences de l'Univers. Data are available in the supplementary materials.

Supplementary Materials

www.sciencemag.org/cgi/content/full/340/6137/1208/DC1
Materials and Methods

Figs. S1 to S4

Table S1

References

25 January 2013; accepted 15 April 2013

10.1126/science.1235637

Stepwise Evolution of Essential Centromere Function in a *Drosophila* Neogene

Benjamin D. Ross,^{1,2} Leah Rosin,^{3*} Andreas W. Thomae,^{4*} Mary Alice Hiatt,^{2,5*} Danielle Vermaak,^{2,†} Aida Flor A. de la Cruz,^{2,6} Axel Imhof,⁴ Barbara G. Mellone,³ Harmit S. Malik^{2,6,‡}

Evolutionarily young genes that serve essential functions represent a paradox; they must perform a function that either was not required until after their birth or was redundant with another gene. How young genes rapidly acquire essential function is largely unknown. We traced the evolutionary steps by which the *Drosophila* gene *Umbrea* acquired an essential role in chromosome segregation in *D. melanogaster* since the gene's origin less than 15 million years ago. *Umbrea* neofunctionalization occurred via loss of an ancestral heterochromatin-localizing domain, followed by alterations that rewired its protein interaction network and led to species-specific centromere localization. Our evolutionary cell biology approach provides temporal and mechanistic detail about how young genes gain essential function. Such innovations may constantly alter the repertoire of centromeric proteins in eukaryotes.

Young essential genes (1) challenge longstanding dogmas about the relationship between essentiality and conservation (2). Partitioning of essential, ancestral functions (subfunctionalization) between (old) parental and (young) daughter genes (3, 4) explains one route by which young genes become essential. More difficult to understand is how new genes become essential via the emergence of novel function (neofunctionalization) (5). This could result from partial duplication of ancestral genes, novel gene fusions, or rapid amino acid changes (6). The contribution of each of these processes to the acquisition of essential function is unknown, as are the underlying molecular changes.

To gain insight into the birth and evolution of essential function, we focused on one newly evolved gene in *Drosophila*. *Umbrea* (also known as *HP6* and *CG15636*) arose via duplication of the intronless *Heterochromatin Protein 1B* (*HP1B*) gene into an intron of the *dumpy* gene (Fig. 1A) (7). *HP1B* is a chromosomal protein that predominantly localizes to heterochromatin in *D. melanogaster* cells and regulates gene expression (8). *HP1B* is dispensable for viability (8), yet RNA interference (RNAi) knockdown phenotypes show *Umbrea* to be essential in *D. melanogaster* (1, 9). The 100% late larval-pupal lethality upon *Umbrea* knockdown could be rescued by an *Umbrea*-green fluorescent protein (GFP) fusion (fig. S1). Genetic knockout experiments (fig. S1) further confirmed that *Umbrea* is essential in *D. melanogaster*.

We traced *Umbrea*'s evolutionary path after duplication from *HP1B* to understand when and how essential function was gained by comparing the localization of *HP1B* and *Umbrea* proteins in *D. melanogaster* Kc cells. GFP-tagged *HP1B* proteins from both *D. melanogaster* and *D. ananassae* [whose divergence predates the birth of *Umbrea* (7)] localized to pericentric heterochromatin and euchromatin (Fig. 1B and fig. S2). In contrast, *Umbrea*-GFP predominantly localized to interphase centromeres, but not telomeres (Fig. 1C

and fig. S3, A and B). Specific antibodies raised against *Umbrea* (fig. S4A) confirmed its centromere localization in developing spermatocytes and larval imaginal discs (Fig. 1, D and E, and fig. S4, B and C).

On the basis of its essentiality and centromere localization, we hypothesized that *Umbrea* was required for chromosome segregation. Upon depletion of *Umbrea* by RNAi knockdown (fig. S5A), relative to control cells, *D. melanogaster* S2 cells displayed increased mitotic errors, including delayed chromosome alignment, early anaphase onset, lagging anaphase chromosomes, and multipolar configurations ($P < 0.05$) (Fig. 1, F and G, fig. S5B, and movies S1 to S3). These data suggest that *Umbrea* promotes proper chromosome segregation, but is not required for the localization of the centromeric histone Cid (Fig. 1F).

To date the origin of *Umbrea* and subsequent changes, we sequenced the *Umbrea* locus from 32 *Drosophila* species (fig. S6A). Whereas *HP1B* was preserved (7), we found *Umbrea* in only 20 of 32 species, dating its monophyletic origin to 12 to 15 million years ago (Fig. 2A and fig. S6B). Using maximum likelihood methods, we observed evidence of both episodic and recurrent positive selection acting on *Umbrea* (fig. S7, A to D). These findings, together with the altered localization, lead us to conclude that neofunctionalization, not subfunctionalization, drove the divergence of *Umbrea* (10). Although *Umbrea* is essential in *D. melanogaster*, it was lost at least three independent times—in *D. fuyamai*, *D. eugracilis*, and in the *suzukii* clade (Fig. 2A)—which suggests that *Umbrea* was not essential at or immediately after its birth.

Four lineages retained full-length *Umbrea* genes, two of which encode an intact chromodomain (CD) and ancestral residues essential for binding histone H3 trimethyl Lys⁹ (H3K9me) (fig. S8) (11). However, most extant *Umbrea* genes have lost their CDs, and encode only the chromoshadow domain (CSD), which mediates protein-protein interactions (12) (Fig. 2A). We first tested how CD loss affected *HP1B* function. We found that an *HP1B*-GFP fusion lacking the CD lost heterochromatin localization (Fig. 2B), consistent with the requirement of *HP1B* CD for H3K9me binding (13). Furthermore, fusion of the *HP1B* CD and hinge to *Umbrea*-GFP reverted localization from centromeres to heterochromatin (Fig. 2C), which suggests that loss of the ancestral CD

¹Molecular and Cellular Biology Program, University of Washington, Seattle, WA 98195, USA. ²Basic Sciences Division, Fred Hutchinson Cancer Research Center, Seattle, WA 98109, USA. ³Department of Molecular and Cell Biology, University of Connecticut, Storrs, CT 06269, USA. ⁴Munich Centre of Integrated Protein Science and Adolf-Butenandt Institute, Ludwig Maximilians University of Munich, 08336 Munich, Germany. ⁵Law Firm of Fitzpatrick, Cella, Harper & Scinto, New York, NY 10104, USA. ⁶Howard Hughes Medical Institute, Fred Hutchinson Cancer Research Center, Seattle, WA 98109, USA.

*These authors contributed equally to this work.

†Present address: Science-wise Consulting, Seattle, WA 98109, USA.

‡Corresponding author. E-mail: hsmalik@fhcrcc.org

was necessary for Umbrea to gain new function. Our findings support a model of neofunctionalization that is facilitated via intermediate loss of function (14). Although CD loss was necessary, it

was not sufficient for Umbrea neofunctionalization; both full-length (*D. fuyamai*) and CSD-only (*D. eugracilis* and the *suzukii* clade) *Umbrea* genes have been lost in evolution.

We next investigated the consequences of evolution in the Umbrea-CSD. CSDs are only found in HP1-family proteins and mediate interactions with other HP1s or proteins possessing

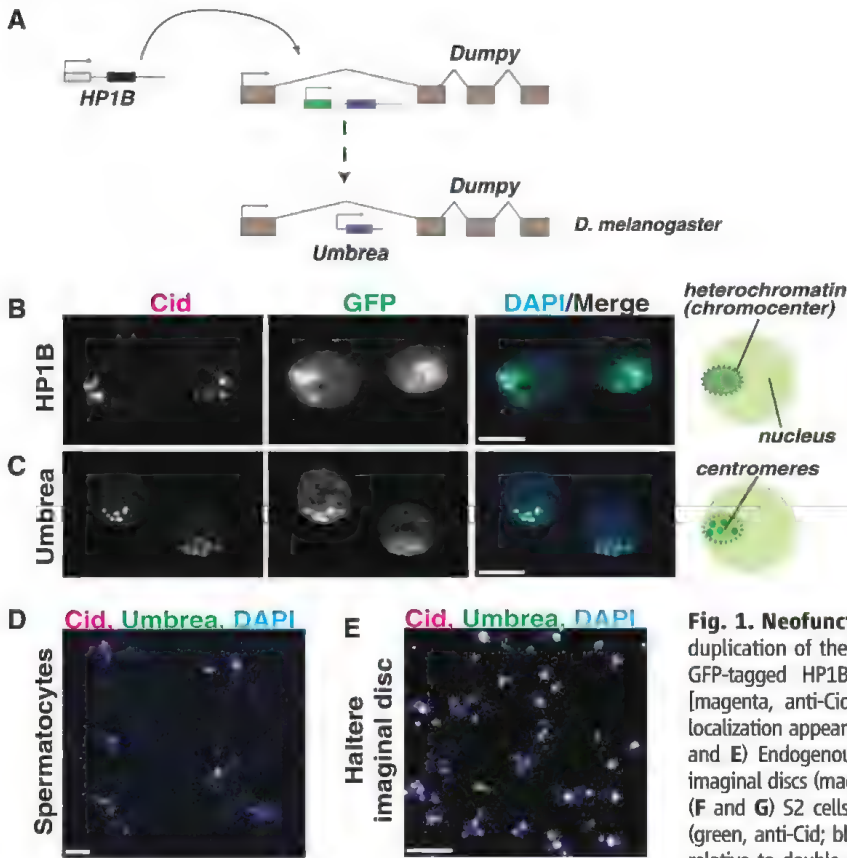


Fig. 1. Neofunctionalization of Umbrea. (A) *Umbrea* originated via gene duplication of the intronless *HP1B* gene into an intron of the *dumpy* locus. (B) GFP-tagged *HP1B* localizes to heterochromatin in *D. melanogaster* Kc cells [magenta, anti-Cid; green, GFP; blue, 4',6-diamidino-2-phenylindole (DAPI); colocalization appears white]. (C) In contrast, *Umbrea*-GFP localizes to centromeres. (D and E) Endogenous *Umbrea* colocalizes with centromeres in testes and in larval imaginal discs (magenta, anti-Cid; green, anti-*Umbrea*; blue, DAPI; scale bar, 5 μ m). (F and G) S2 cells depleted of *Umbrea* by RNAi revealed increased mitotic errors (green, anti-Cid; blue, phospho-H3-staining mitotic chromosomes; red, anti-tubulin) relative to double-stranded RNA control (** P < 0.05).

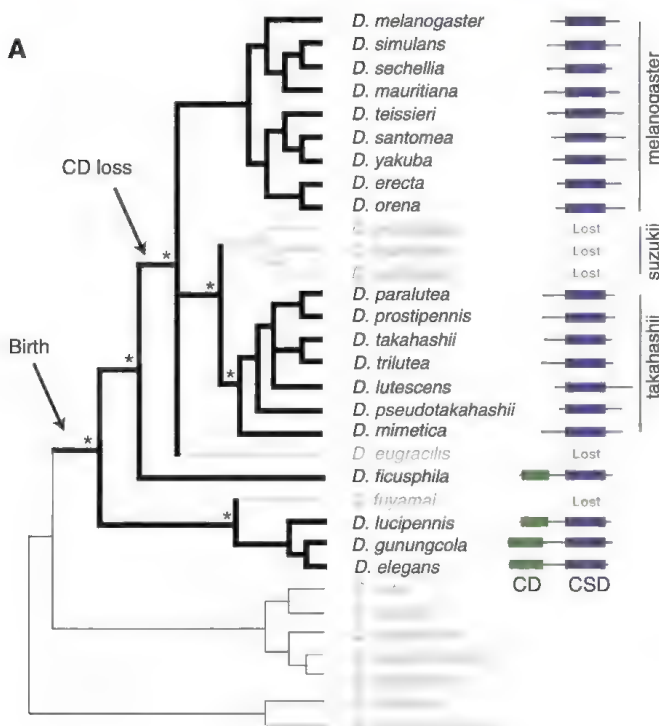


Fig. 2. Dynamic evolution of Umbrea after its birth. (A) Polymerase chain reaction to shared syntenic sites followed by sequencing (fig. S6) revealed the presence and structure of *Umbrea* genes. Asterisks indicate strong support for key branch points in the phylogeny (25), suggesting that *Umbrea* was lost at least three times. *Umbrea* is presented with HP1 canonical domains: chromodomain (CD, green) and chromoshadow domain (CSD, blue). (B) Localization of GFP-tagged *HP1B* lacking its CD is diffuse in *D. melanogaster* Kc cell nuclei (magenta, anti-Cid; green, GFP; blue, DAPI staining of DNA; scale bar, 5 μ m). (C) In contrast, *HP1B^{mel}* CD+hinge fused to *Umbrea^{mel}* delocalizes it from centromeres.

degenerate PxVxL motifs (P, Pro; V, Val; L, Leu; x, any amino acid) (15). An amino acid alignment of HP1B and Umbrea revealed conservation of residues defining the CSD structural fold (Fig. 3A). In contrast, three of the nine residues that mediate specificity for PxVxL recognition (16) changed along the branch leading to the melanogaster species subgroup (Fig. 3A and fig. S9). We found that *D. melanogaster* Umbrea CSD localized to centromeres (Fig. 3B). This property was not shared with HP1B CSD or even other Umbrea CSDs, because neither “parental” HP1B^{mel} CSD (from *D. melanogaster*) nor Umbrea^{ptak} CSD (from *D. pseudotakahashii*) could localize to centromeric regions in *D. melanogaster* cells (Fig. 3B and fig. S10B). We conclude that a discrete transition for centromere localization occurred in Umbrea CSD after divergence of the melanogaster and takahashii subgroups, co-

incident with changes in the PxVxL recognition residues. Indeed, reversion of these three residues (Cys¹⁵, Ile⁵⁷, and Phe⁵⁹; Fig. 3A and fig. S9) to the ancestral state delocalized Umbrea^{mel} CSD from centromeres (Fig. 3D). Moreover, replacement of the same residues in Umbrea^{ptak} CSD to corresponding residues in Umbrea^{mel} resulted in a gain of centromere localization (Fig. 3E). These results suggest that centromere localization by Umbrea CSD originated in the common ancestor of the melanogaster species subgroup 5 to 7 million years ago. Consistent with this, we found that GFP-Umbrea^{tei} localized to centromeres in *D. teissieri* cells (Fig. 3F). Centromeric localization may have also coincided with gain of essentiality, as Umbrea was lost three times prior to, but not after, CSD modification (Fig. 2A).

To test the prediction that mutation of PxVxL recognition resulted in CSD centromere local-

ization by alteration of protein interactions, we performed proteomic analyses to identify proteins that coimmunoprecipitate with Umbrea in S2 cells (Fig. 3G). Many chromatin factors were found in this set (table S1), including heterochromatin proteins HP4/Hip and HP5 [previously shown to be direct interactors of Umbrea (9, 17)], as well as novel interactions with the H3K9 methyltransferase Su(var)3-9 and the centromeric protein Cenp-C. We found no overlap with protein partners of HP1B, which include the euchromatic proteins HP1C, Woc, and Row (18) (Fig. 3H); this suggests a rewiring of the protein interaction network of Umbrea.

Our evolutionary analyses (fig. S7, A to D) indicated that the most recent innovations in Umbrea occurred in the short tail sequences that flank the CSD. We tested how these changes contributed to Umbrea neofunctionalization. HP1B^{mel}

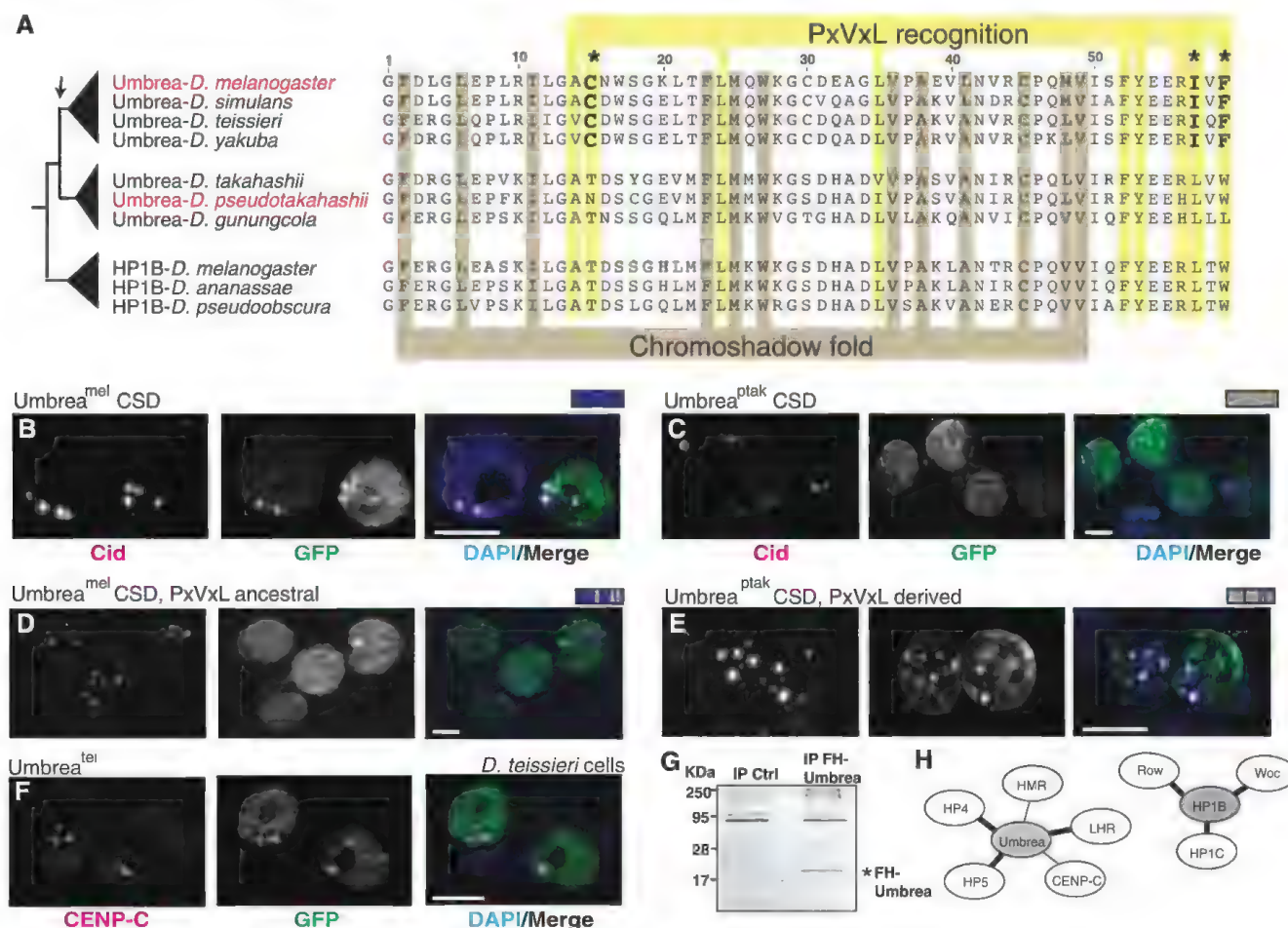
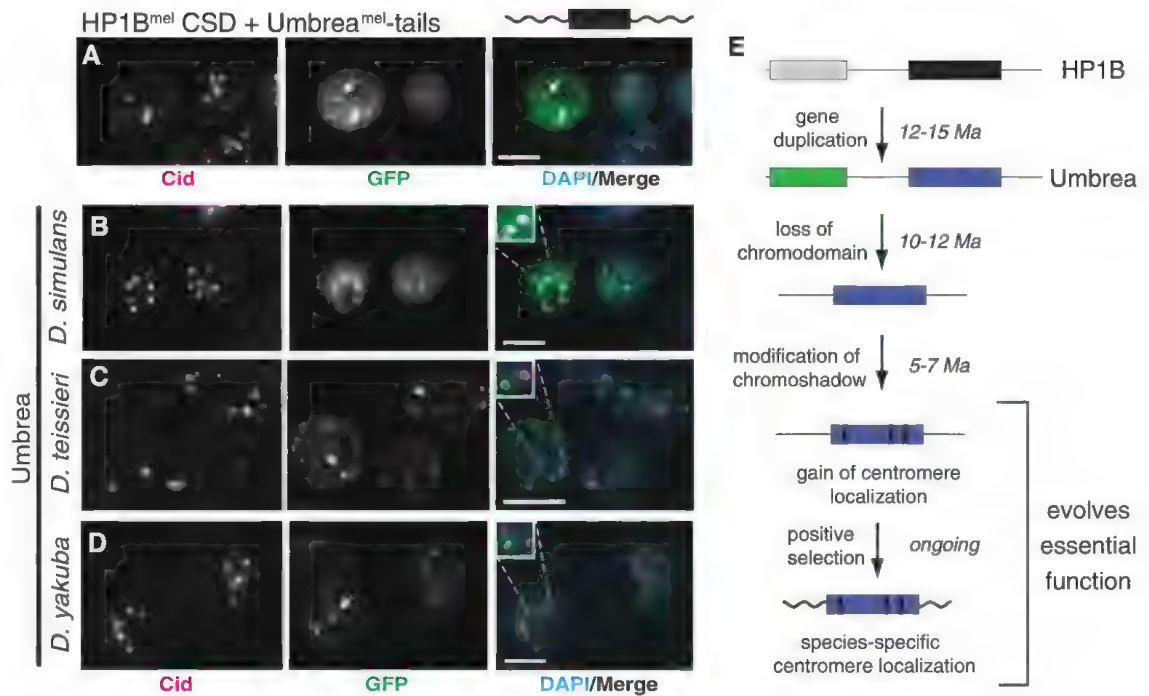


Fig. 3. Chromoshadow changes led to Umbrea centromere localization via altered protein-protein interactions. (A) An amino acid alignment of HP1B and Umbrea CSDs reveals conservation of fold-defining residues but divergence in PxVxL recognition residues. In particular, three changes (bold) are predicted to affect the binding specificity of Umbrea CSD. Abbreviations for amino acid residues: A, Ala; C, Cys; D, Asp; E, Glu; F, Phe; G, Gly; H, His; I, Ile; K, Lys; L, Leu; M, Met; N, Asn; P, Pro; Q, Gln; R, Arg; S, Ser; T, Thr; V, Val; W, Trp; Y, Tyr. (B) GFP-tagged Umbrea^{mel} CSD (green) colocalizes with Cid (magenta) at centromeres in *D. melanogaster* Kc cells (scale bar, 5 μ m, colocalization appears white). (C) However, GFP-tagged Umbrea^{ptak} CSD does not localize to centromeres. (D) Reversion of

Umbrea^{mel} PxVxL recognition residues (Cys-Ile-Phe) to ancestral states (Thr-Leu-Trp) causes delocalization from centromeres. (E) By contrast, introduction of PxVxL recognition residues (Cys-Ile-Phe) is sufficient to localize Umbrea^{ptak} CSD to centromeres (compare to Fig. 3C). (F) Umbrea^{tei} colocalizes with centromeric protein CENP-C in *D. teissieri* cells. (G) Immunoprecipitation of Flag (FH)- and hemagglutinin (HA)-tagged Umbrea pulls down protein complexes in S2 cells. (H) Analysis of these complexes reveals that Umbrea and HP1B have mutually exclusive protein-protein interactions. Umbrea interacts with centromere and heterochromatin proteins [table S2; bold lines indicate confirmation of previously reported interactions (9, 17)], but not with the primary targets of HP1B (18).

Fig. 4. Species-specific centromere targeting of *Umbrea*. (A) GFP fusion of *Umbrea*^{mel} tails with HP1B-CD (green) localizes to centromeres (magenta, anti-Cid; colocalization appears white; scale bar, 5 μ m). (B to D) *D. melanogaster* Kc cell centromere localization (magenta, Cid) of *Umbrea* orthologs (green, GFP) from *D. simulans*, *D. teissieri*, and *D. yakuba* worsens with increased divergence. (E) Steps to essential neofunctionalization by *Umbrea* after gene duplication (Ma, millions of years ago).



CSD alone showed no discrete localization (Fig. 2B), whereas the addition of *Umbrea*^{mel} tails was sufficient to confer centromere localization (Fig. 4A). These data indicate that *Umbrea* may target centromeres using both the CSD and the tails. Whereas the CSD likely mediates its localization via protein-protein interactions, *Umbrea* tails may bind centromeric nucleic acids, analogous to the hinge region of mammalian HP1 α , which binds DNA in vitro (19). Because centromeric DNA sequence diverges rapidly (20), we tested whether rapid evolution of the *Umbrea* tails resulted in species specificity. We found that *Umbrea*^{sim} localized (Fig. 4B) to centromeres in *D. melanogaster*. However, *Umbrea*^{tei} and *Umbrea*^{yak} did not (Fig. 4, C and D), localizing instead to distinct foci. Although positive selection of *Umbrea* preceded its centromere localization (fig. S7), these data suggest that positive selection in the *melanogaster* species subgroup resulted in species-specific centromere targeting, reminiscent of CenH3/Cid in *Drosophila* (21). For example, despite mislocalizing in *D. melanogaster* cells, *Umbrea*^{tei} appropriately localized to *D. teissieri* centromeres (Fig. 3F).

Our analyses suggest that gain of essential function evolved in discrete steps (Fig. 4E) (5) that involved the loss of an ancestral domain (CD), rewiring of protein interaction networks (CSD), and species-specific changes (tails). *Umbrea* was likely not essential for much of its evolutionary history; intermediate forms were lost multiple times.

Our finding that *Umbrea* rapidly became essential for the conserved process of chromosome segregation is unexpected. *Drosophila* species that never possessed or lost *Umbrea* still carry out chromosome segregation. This suggests that the essential function of *Umbrea* might be

a result of a lineage-specific requirement. Just as genetic conflicts arising during meiosis may drive rapid evolution of existing centromeric proteins (22), we propose that recurrent changes at centromeric DNA satellites could drive the retention of duplicate genes such as *Umbrea* to alleviate selective pressure on essential centromeric proteins. This is analogous to pathogen-driven genetic conflict, which promotes the diversification of existing and new antiviral immune genes (23). This process would result in idiosyncratic retention of centromeric proteins that become essential as they integrate into existing networks. Intriguingly, other HP1B-derived CSD-only genes are found in other *Drosophila* species that diverged before the birth of *Umbrea* (7), raising the possibility of convergent evolution of *Umbrea*-like centromere factors. This process may explain the broad diversity and divergence among centromeric proteins across taxa (24). Although a large fraction of the many young, essential genes identified in *Drosophila* (1) may result from subfunctionalization, others (like *Umbrea*) may illuminate other essential processes that could require recurrent genetic innovation to mitigate previously unappreciated adaptive challenges within the cell.

References and Notes

1. S. Chen, Y. E. Zhang, M. Long, *Science* **330**, 1682 (2010).
2. G. L. Miklos, G. M. Rubin, *Cell* **86**, 521 (1996).
3. A. Force et al., *Genetics* **151**, 1531 (1999).
4. A. Stoltzfus, *J. Mol. Evol.* **49**, 169 (1999).
5. H. Innan, F. Kondrashov, *Nat. Rev. Genet.* **11**, 97 (2010).
6. J. Zhang, A. M. Dean, F. Brunet, M. Long, *Proc. Natl. Acad. Sci. U.S.A.* **101**, 16246 (2004).
7. M. T. Levine et al., *PLoS Genet.* **8**, e1002729 (2012).
8. D. Zhang, D. Wang, F. Sun, *Chromosoma* **120**, 97 (2011).
9. C. Joppich, S. Scholz, G. Korge, A. Schwendemann, *Chromosome Res.* **17**, 19 (2009).

10. M. W. Hahn, *J. Hered.* **100**, 605 (2009).
11. S. A. Jacobs, S. Khorasanizadeh, *Science* **295**, 2080 (2002).
12. N. Murzina, A. Verreault, E. Laue, B. Stillman, *Mol. Cell* **4**, 529 (1999).
13. J. Nakayama, J. C. Rice, B. D. Strahl, C. D. Allis, S. I. Grewal, *Science* **292**, 110 (2001).
14. T. Ohta, *Genetics* **120**, 841 (1988).
15. J. F. Smothers, S. Henikoff, *Curr. Biol.* **10**, 27 (2000).
16. A. Thiru et al., *EMBO J.* **23**, 489 (2004).
17. L. Giot et al., *Science* **302**, 1727 (2003).
18. J. Abel, R. Eskeland, G. D. Raffa, E. Kremmer, A. Imhof, *PLoS ONE* **4**, e5089 (2009).
19. R. R. Meehan, C. F. Kao, S. Pennings, *EMBO J.* **22**, 3164 (2003).
20. A. R. Lohe, D. L. Brutlag, *J. Mol. Biol.* **194**, 161 (1987).
21. D. Vermaak, H. S. Hayden, S. Henikoff, *Mol. Cell. Biol.* **22**, 7553 (2002).
22. H. S. Malik, S. Henikoff, *Cell* **138**, 1067 (2009).
23. M. D. Daugherty, H. S. Malik, *Annu. Rev. Genet.* **46**, 677 (2012).
24. I. M. Cheeseman, A. Desai, *Nat. Rev. Mol. Cell Biol.* **9**, 33 (2008).
25. B. Prud'homme et al., *Nature* **440**, 1050 (2006).

Acknowledgments: We thank J. Bloom, M. Daugherty, M. Emerman, D. Gottschling, M. Levine, M. Patel, N. Phadnis, K. Peichel, and W. Shou for helpful comments, and *Drosophila* colleagues for generous sharing of reagents. Supported by NIH Training grant T32HG000035 and an NSF predoctoral fellowship (B.D.R.), an EU network grant (EpiGeneSys 257082, A.I.), NSF award 1024973 (B.G.M.), and a grant from the Mathers Foundation and NIH grant R01GM074108 (H.S.M.). H.S.M. is an HHMI Early Career Scientist. *Umbrea* DNA sequences have been submitted to GenBank under accession numbers KC660086 to KC660100. The mass spectrometry proteomics data have been deposited to the ProteomeXchange Consortium (PRIDE partner repository dataset identifier PXD000163).

Supplementary Materials

www.sciencemag.org/cgi/content/full/340/6137/1211/DC1
Materials and Methods
Figs. S1 to S10
Table S1
References (26–38)
Movies S1 to S3

21 December 2012; accepted 1 April 2013
10.1126/science.1234393

Density Triggers Maternal Hormones That Increase Adaptive Offspring Growth in a Wild Mammal

Ben Dantzer,^{1*} Amy E. M. Newman,² Rudy Boonstra,³ Rupert Palme,⁴ Stan Boutin,⁵ Murray M. Humphries,⁶ Andrew G. McAdam^{1,2}

In fluctuating environments, mothers may enhance the fitness of their offspring by adjusting offspring phenotypes to match the environment they will experience at independence. In free-ranging red squirrels, natural selection on offspring postnatal growth rates varies according to population density, with selection favoring faster-growing offspring under high-density conditions. We show that exposing mothers to high-density cues, accomplished via playbacks of territorial vocalizations, led to increased offspring growth rates in the absence of additional food resources. Experimental elevation of actual and perceived density induced higher maternal glucocorticoid levels, and females with naturally or experimentally increased glucocorticoids produced offspring that grew faster than controls. Therefore, social cues reflecting population density were sufficient to elicit increased offspring growth through an adaptive hormone-mediated maternal effect.

Fluctuations in food availability and the resultant changes in the population density of consumers are thought to be important ecological agents of natural selection in many animal populations (1, 2). Temporal variation in natural selection characterized by recurrent pulses in food or density can favor the evolution of adaptive phenotypic plasticity when there are reliable

cues that predict the direction or the magnitude of these agents of selection (3, 4). Phenotypic plasticity is beneficial in such changing environments because it enables individuals to track fluctuating fitness optima (5, 6). Similarly, if the parental environment or phenotype provides reliable cues of the conditions that offspring will experience, parents may induce adaptive changes in offspring that increase both parental and offspring fitness [adaptive parental effects (7, 8)].

The role of parental effects in the adaptation of offspring to changing environments is intriguing, but little is known about their importance in free-living animals. Not only do the agents of natural selection on offspring phenotype need to be identified, but the cues parents use to predict changes in the agent of selection, and the mechanism that mediates the parental effect, also need to be known. This is further complicated when considering population density as a cue because it is often confounded with food availability, which

might also relieve resource constraints and cause resource-mediated or permissive parental effects (7). Identification and experimental manipulation of the mechanisms that mediate parental effects requires a combination of field physiology, experimental ecology, and longitudinal studies of natural selection that have not been achieved to date. We identified and experimentally manipulated the social density cues and stress hormones responsible for an adaptive maternal effect in a natural population of North American red squirrels (*Tamiasciurus hudsonicus*).

Individual male and female red squirrels defend exclusive territories around a central midden (9, 10) containing cached white spruce cones [*Picea glauca* (11, 12)], and juveniles that fail to acquire a territory before their first winter do not survive (13). Red squirrels experience recurrent fluctuations in population density because of pronounced episodic fluctuations in the availability of white spruce seeds (Fig. 1A) (11, 12). Increased autumn spruce cone production is associated with increased squirrel density in the following spring (Fig. 1B) (14). In our 23-year study in the Yukon, Canada, we found that these changes in density have notable effects on red squirrels because we documented density-dependent selection on offspring postnatal growth rates. In years when spring density was high, females that produced faster-growing offspring had more offspring survive their first winter and recruit into the adult population, whereas when density was low there was no benefit to producing faster-growing offspring [$n = 463$ females, offspring growth \times density, $t_{726} = 2.15$, $P = 0.016$ (table S1)].

In such variable environments, the evolution of adaptive maternal effects may be favored, but this requires the presence of reliable cues that enable an accurate prediction of natural selection on offspring (3, 4). Therefore, cues of population density in red squirrels might induce adaptive increases in offspring growth when density is high. Red squirrels emit territorial vocalizations called rattles to defend their territories, and the

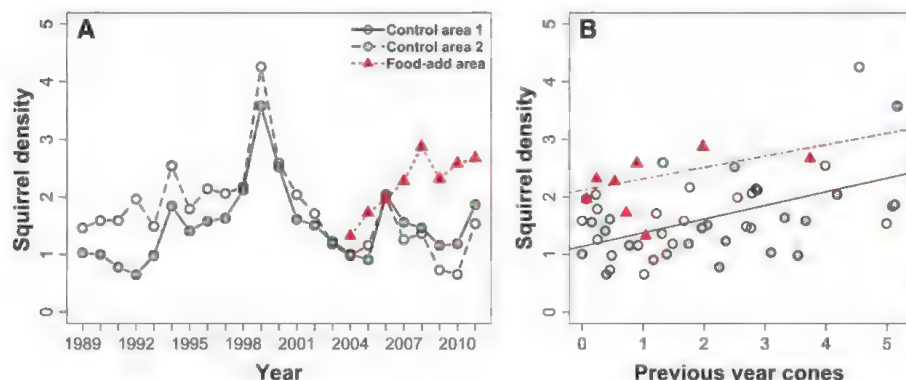


Fig. 1. Population density of North American red squirrels in the Yukon, Canada, fluctuates annually in response to the availability of spruce cones. (A) Yukon red squirrels experience recurrent fluctuations in population density (squirrels/ha) because of interannual variation in white spruce cone abundance (11, 12). **(B)** Spruce cone production in the previous autumn is associated with increased spring population density in two control

study areas ($b = 0.24 \pm 0.05$, $t_{53} = 4.3$, $P < 0.0001$) and one study area (Food-add) where squirrels have been provided with supplemental food since autumn 2004 ($b = 0.20 \pm 0.19$, $t_{53} = -0.22$, $P > 0.5$). Autumn spruce cone production is an index on a ln scale (11). Regression lines from a linear mixed-effects model. **(C)** Red squirrel extracting seeds from a white spruce cone. [Photo credit: R. W. Taylor]

frequency with which they hear rattles in their neighborhood accurately predicts density (10). We hypothesized that territorial vocalizations provide a cue of density that allows females to adaptively adjust offspring growth in anticipation of the density-dependent selection that they will experience. We tested this hypothesis by simulating high-density conditions using audio playbacks of red squirrel rattles (9, 10). This corresponded to a perceived density of 4.92 squirrels/ha, which was sixfold higher than the perceived density of females exposed to a control stimulus (bird vocalizations, 0.81 squirrel/ha) and similar to the maximum historical density (Fig. 1A) (10). Such a high-density environment would typically be associated with a strong positive relationship between offspring growth and fitness (table S1), whereas offspring growth does not affect fitness in the low-density control environment.

As predicted, offspring produced by females experiencing experimentally heightened perceived density grew significantly faster than those produced by control females (Fig. 2). Consistent with life-history theory (15), the growth rates of offspring produced by control females declined significantly as litter size increased, but this effect was attenuated by 67% in females exposed to playbacks of territorial vocalizations [playback \times litter size, $t_{186} = 1.98$, $P = 0.024$ (table S2 and Fig. 2)]. In fact, the trade-off between litter size and growth rate in females exposed to playbacks of territorial vocalizations was greatly reduced ($r = -0.12$, $t_{66} = -1.57$, $P = 0.06$) compared with that in control females ($r = -0.37$, $t_{64} = -4.43$, $P < 0.0001$). Female red squirrels, therefore, increase offspring growth in response to conspecific density because of the fitness benefits of doing so in high-density years. These growth-enhancing maternal effects in high-density years are adaptive for mothers and offspring by increasing the probability that their offspring will survive their first winter (16), which is a major component of their lifetime fitness (17). However, faster offspring growth rates are not favored under low-density conditions [≤ 1 squirrel/ha (table S1)], and in some years there is significant negative selection on offspring growth (16). Increased reproductive effort does not appear to incur a survival cost to mothers (18, 19). However, offspring born in high-density years have a reduced adult life span (20), suggesting that faster offspring growth, which enhances recruitment when density is high, might incur a cost to offspring later in life. Such conditions will promote the evolution of plasticity in maternal effects, whereby increased offspring growth coincides with the high-density conditions under which it enhances fitness.

These adaptive maternal effects on offspring were mediated by the physiological stress responses of females experiencing heightened population density. Across 6 years (2006 to 2011), we found a positive relationship between local density and concentrations of fecal cortisol metabolites [FCM; $t_{155} = 3.63$, $P = 0.0002$ (table

Fig. 2. Female red squirrels experiencing increased perceived or actual density produced faster-growing offspring than controls. Female red squirrels experiencing experimentally increased perceived population density (rattle playbacks, $n = 19$ females, 67 pups) produced offspring that grew significantly faster than those produced by controls ($n = 19$ females, 65 pups) but similar to those produced by food-supplemented females ($n = 16$ females, 55 pups) experiencing increased actual density. Values on the y axis represent residuals from a linear mixed-effects model (table S2).

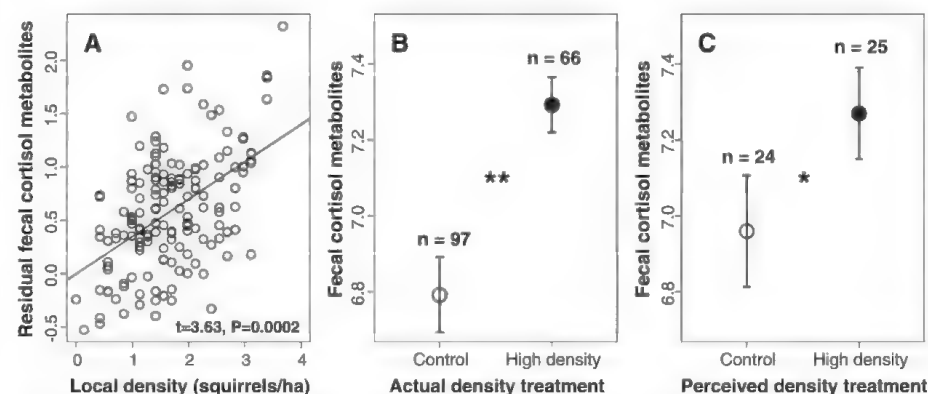
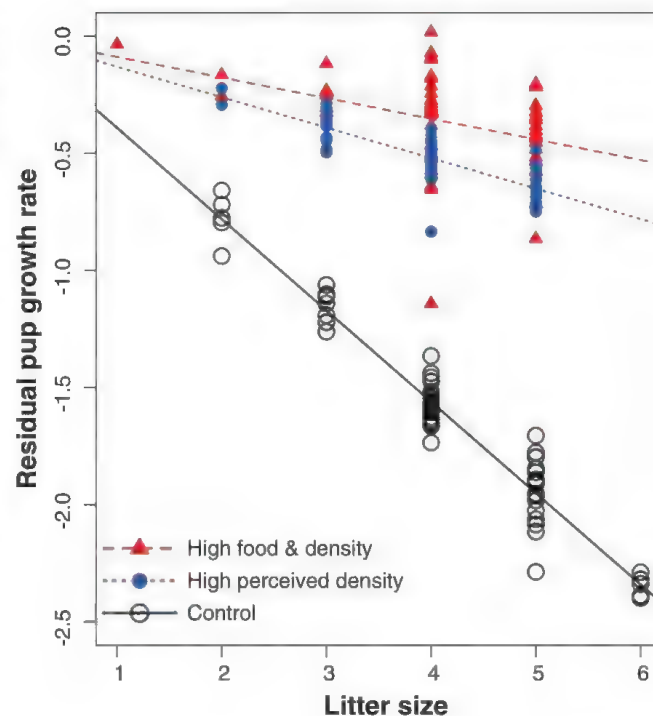


Fig. 3. Female red squirrels experiencing higher population density had higher glucocorticoid levels. (A) Female red squirrels living under high-density conditions had higher concentrations of FCM. Squirrels experiencing experimentally increased (B) actual density resulting from long-term food supplementation or (C) perceived density (rattle playbacks) had significantly higher concentrations of FCM than controls. Values on the y axis represent either (A) residuals from a linear mixed-effects model (table S4) or [(B) and (C)] raw FCM (ln ng/g of dry feces). Sample sizes refer to the number of fecal samples analyzed. ** $P < 0.01$ and * $P < 0.05$ (table S4). Error bars indicate \pm SE.

S4 and Fig. 3A)]. Females from a study area with experimentally increased density resulting from food supplementation [75% higher density than control study areas (Fig. 1)] had concentrations of FCM that were 49% higher [$t_{162} = 3.82$, $P < 0.0001$ (table S4 and Fig. 3B)] than those of females in control study areas. Females experiencing increased perceived density through the playback experiment had concentrations of FCM that were 30% higher than those of control females [$t_{48} = 2.24$, $P = 0.015$ (table S4 and Fig. 3C)]. These results confirm that increases in concentrations of FCM were driven by perceived density rather than by food abundance (21).

In mammalian species, increases in maternal glucocorticoid levels can cause profound changes in offspring phenotype (22) and may provide offspring with reliable hormonal cues about their future environment. Three lines of evidence indicate that increases in maternal glucocorticoid levels are responsible for the adaptive increase in offspring growth under high-density conditions. First, females exposed to heightened perceived density had increased concentrations of FCM during pregnancy (Fig. 3C) and also produced faster-growing offspring than controls (Fig. 2). Second, increased maternal FCM concentrations were positively associated with offspring growth in females measured over a 6-year

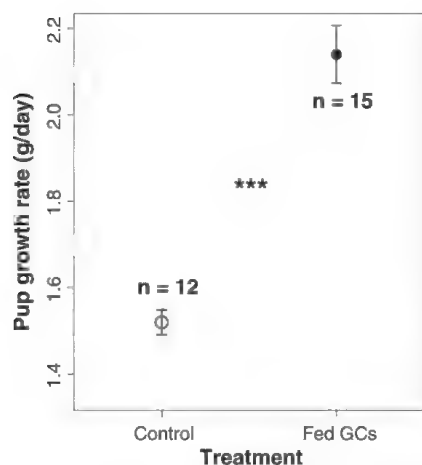


Fig. 4. Offspring produced by female red squirrels provisioned with cortisol grew significantly faster than those from controls. Raw offspring growth rates (mean \pm SE) are shown on y axis. Sample sizes denote number of pups. Fed GCs corresponds to provisioning with three different cortisol concentrations (fig. S2). *** $P < 0.0001$ (table S6).

period [$t_{98} = 1.94$, $P = 0.028$ (table S5)]. Last, offspring born to females with experimentally increased glucocorticoid levels during pregnancy [fed cortisol (fig. S1)] grew 41% faster than those produced by control females [$t_{26} = 4.98$, $P < 0.0001$ (table S6 and Fig. 4)].

Our results suggest that elevated maternal glucocorticoid levels in response to heightened population density induced an adaptive hormone-mediated maternal effect on offspring growth. In contrast to the widespread assumption that heightened maternal glucocorticoid levels are detrimental to offspring (22), our results emphasize that in free-living animals they can instead lead to adaptive adjustments in offspring (23, 24). Under high-density conditions, squirrels spend less time feeding and in the nest (10), suggesting that increased offspring growth is not a simple outcome of increased maternal care or milk provisioning. Alternatively, elevated exposure to glucocorticoids early in life (22, 25) could increase offspring growth by directly influencing offspring physiology or behavior (22, 26) and subsequent changes in growth hormone secretion in offspring (27).

For nearly 100 years, food availability has been considered to be a universal variable affecting population dynamics and life-history traits (28). Increased food availability also increases the population density of consumers, which has made it difficult to distinguish whether the plasticity in life-history traits after periods of high food availability is due to relaxation of food limitation or to adaptive reproductive adjustments to changes in density-mediated selection. Our results provide evidence that female red squirrels can produce faster-growing offspring in the absence of additional resources but only do so when the fitness prospects warrant this increased invest-

ment. In fact, offspring produced by females exposed to high-density cues but with no access to additional food grew as fast as those produced by food-supplemented females that were also experiencing increased density [1.79 ± 0.09 squirrels/ha (Fig. 2 and table S2)]. Therefore, some of the plasticity in female life history traits is due to the expected fitness benefits of producing faster-growing offspring under high-density conditions rather than only reflecting a relaxation of food limitation.

Experimental increases in food resources that result in increased reproductive output are typically interpreted as evidence for resource limitations on reproduction (29). However, if animals use food abundance as a cue of upcoming density-mediated selection, then reproductive responses to food supplementation might reflect not only relaxation of food limitation but also an adaptive adjustment to an anticipated change in natural selection resulting from an impending increase in density. Cues of population density may be a general signal that animals use to make adaptive reproductive adjustments in anticipation of density-dependent natural selection on offspring phenotypes.

References and Notes

1. M. J. Wade, S. Kalisz, *Evolution* **44**, 1947 (1990).
2. A. D. C. MacColl, *Trends Ecol. Evol.* **26**, 514 (2011).
3. R. Levins, *Evolution in Changing Environments* (Princeton Univ. Press, Princeton, NJ, 1968).
4. N. A. Moran, *Am. Nat.* **139**, 971 (1992).
5. D. Réale, A. G. McAdam, S. Boutin, D. Berteaux, *Proc. Biol. Sci.* **270**, 591 (2003).
6. A. Charmantier et al., *Science* **320**, 800 (2008).
7. T. A. Mousseau, C. A. Fox, Eds., *Maternal Effects as Adaptations* (Oxford Univ. Press, Oxford, 1998).
8. D. J. Marshall, T. Uller, *Oikos* **116**, 1957 (2007).
9. Materials and methods are available as supplementary materials on Science Online.
10. B. Dantzer, S. Boutin, M. M. Humphries, A. G. McAdam, *Behav. Ecol. Sociobiol.* **66**, 865 (2012).

11. J. M. LaMontagne, S. Boutin, *J. Ecol.* **95**, 991 (2007).
12. Q. E. Fletcher et al., *Ecology* **91**, 2673 (2010).
13. K. W. Larsen, S. Boutin, *Ecology* **75**, 214 (1994).
14. S. Boutin et al., *Science* **314**, 1928 (2006).
15. C. C. Smith, S. D. Fretwell, *Am. Nat.* **108**, 499 (1974).
16. A. G. McAdam, S. Boutin, *Evolution* **57**, 1689 (2003).
17. A. G. McAdam, S. Boutin, A. K. Sykes, M. M. Humphries, *Écoscience* **14**, 362 (2007).
18. M. M. Humphries, S. Boutin, *Ecology* **81**, 2867 (2000).
19. S. Descamps, S. Boutin, A. G. McAdam, D. Berteaux, J.-M. Gaillard, *Proc. Biol. Sci.* **276**, 1129 (2009).
20. S. Descamps, S. Boutin, D. Berteaux, A. G. McAdam, J.-M. Gaillard, *J. Anim. Ecol.* **77**, 305 (2008).
21. S. Creel, B. Dantzer, W. Goymann, D. R. Rubenstein, *Funct. Ecol.* **27**, 66 (2013).
22. A. Harris, J. Seckl, *Horm. Behav.* **59**, 279 (2011).
23. O. P. Love, T. D. Williams, *Am. Nat.* **172**, E135 (2008).
24. R. Boonstra, *Funct. Ecol.* **27**, 11 (2013).
25. A. Catalani et al., *Neuroscience* **100**, 319 (2000).
26. C. L. Moore, K. L. Power, *Dev. Psychobiol.* **19**, 235 (1986).
27. C. M. Kuhn, J. Pauk, S. M. Schanberg, *Dev. Psychobiol.* **23**, 395 (1990).
28. C. S. Elton, *Br. J. Exp. Biol.* **2**, 119 (1924).
29. S. Boutin, *Can. J. Zool.* **68**, 203 (1990).

Acknowledgments: We thank Agnes Moose and family for access to their traditional trapping area; F. E. Stewart, S. E. Evans, S. E. McFarlane, Q. E. Fletcher, S. Hossain, R. W. Taylor, and all squirrels for assistance; A. Sykes and E. Anderson for data management; and A. Charmantier, T. Getty, K. E. Holekamp, J. S. Lonstein, C. T. Williams, T. D. Williams, and three anonymous reviewers for incisive comments. Funded by Natural Sciences and Engineering Research Council of Canada, NSF (DEB-0515849 and IOS-1110436), and Ontario Ministry of Research Innovation. Data have been deposited in the Dryad Repository (<http://dx.doi.org/10.5061/dryad.b3h4q>). This is publication no. 69 of the Kluane Red Squirrel Project.

Supplementary Materials

www.sciencemag.org/cgi/content/full/science.1235765/DC1
Materials and Methods
Figs. S1 to S3
Tables S1 to S7
References (30–54)

28 January 2013; accepted 5 April 2013
Published online 18 April 2013;
[10.1126/science.1235765](http://dx.doi.org/10.1126/science.1235765)

The Cross-Bridge Spring: Can Cool Muscles Store Elastic Energy?

N. T. George,¹ T. C. Irving,² C. D. Williams,^{1,3} T. L. Daniel^{1*}

Muscles not only generate force. They may act as springs, providing energy storage to drive locomotion. Although extensible myofilaments are implicated as sites of energy storage, we show that intramuscular temperature gradients may enable molecular motors (cross-bridges) to store elastic strain energy. By using time-resolved small-angle x-ray diffraction paired with in situ measurements of mechanical energy exchange in flight muscles of *Manduca sexta*, we produced high-speed movies of x-ray equatorial reflections, indicating cross-bridge association with myofilaments. A temperature gradient within the flight muscle leads to lower cross-bridge cycling in the cooler regions. Those cross-bridges could elastically return energy at the extrema of muscle lengthening and shortening, helping drive cyclic wing motions. These results suggest that cross-bridges can perform functions other than contraction, acting as molecular links for elastic energy storage.

Elastic energy storage is heralded as a critical design characteristic of animal movement, because it promotes efficient locomotion. Canonical examples of elastic energy-storage sites include tendons of mammals and resilin, the rub-

berlike protein in insect cuticle (1, 2). Elastic energy storage is particularly important to flying insects, reducing the otherwise prohibitive inertial power costs of accelerating and decelerating the wings (3, 4). Two main sites of elastic

energy storage have been proposed for insect flight: resilin (1) and elastic myofilament proteins within flight muscles [e.g., thick and thin filaments (5, 6), cross-bridges that are attached or in rigor (7–9), collagen fibrils (7), and titin (10)]. We propose that an intramuscular temperature gradient selectively increases cross-bridge attachment time, constraining axial and radial myofilament movement and thus enabling elastic energy storage in both cross-bridges and myofilaments. This temperature gradient is an inevitable consequence of metabolic heat production combined with convective and radiative heat loss (11, 12). Because muscles' activation and deactivation rates depend on temperature, all of the kinetics associated with cross-bridge cycling are likely to vary substantially along a temperature gradient, causing higher rates of cross-bridge cycling in warmer regions of a muscle but reduced turnover and longer attachment times in cooler regions (fig. S1) (11, 13–15). Consequently the timing of cross-bridge attachment and detachment in a given length cycle will vary spatially. Thus, at any given moment in the contraction cycle, cross-bridges in the cooler region of a muscle will be less likely to detach from their actin binding sites, forming a lattice increasingly linked by these elastic elements as temperature decreases. This elastic lattice can store energy

both (i) at the extrema of the lengthening phase and (ii) at the extrema of the shortening phase. At the very end of the lengthening phase, elastic energy can be stored in the axial deformation of cross-bridges that remain bound because of the delayed activation and deactivation times associated with lower temperatures. The energy imparted to these bound cross-bridges can then be released back into the lattice as they shorten upon initiation of the shortening phase. Conversely, at the very end of the shortening phase, elastic energy can be stored in cross-bridges that remain bound as they are radially extended, orthogonal to the direction of shortening (because muscle cells are isovolumetric, they necessarily undergo radial expansion as they shorten). As the shortening phase ends and the lengthening phase begins, this elastic energy may be released back into muscle's elastic lattice, providing a restoring force to help drive cyclic wing motions (16).

We documented these events in *Manduca sexta*, a large moth known to have a significant dorsoventral temperature gradient in its dominant flight muscle, the dorsolongitudinal muscle (DLM₁) (11). We used high-speed time-resolved x-ray fiber diffraction techniques to monitor changes in myofilament lattice spacing and in the distribution of mass around the thick and thin filaments' long axes. Changes in mass distribution are due to changes in the radial position of cross-bridges and, by implication, their degree of association with the thin filaments (17). By pairing this visualization technique with simultaneous force and length measurements under controlled muscle stimulation, we coupled molecular observations with mechanical measures of whole-muscle performance (18).

We cyclically oscillated the DLM₁ at 25 Hz (wingbeat frequency) and periodically stimulated the muscle at *M. sexta*'s in vivo phase of activation while recording force and length, establishing a work-loop that measures the cyclic mechanical energy exchange of activated muscle (13, 19). Specifically, we conducted work-loops at two muscle temperatures, 25° and 35°C, to cover the range of *M. sexta*'s temperature gradient (Fig. 1 and fig. S2) (11). Additionally, to control for the regional specialization of contractile dynamics, we positioned the x-ray beam on either a ventral or a dorsal location within the DLM₁. Diffraction patterns were collected five times during each 40-ms contraction cycle. From this diffraction movie, we plotted cyclical changes in contractile dynamics by measuring variations of spacing and intensity in each diffraction pattern (movie S1 and Fig. 2). We tracked the d_{10} lattice spacing, the distance between thick filaments, as in (20). In addition, from the intensities of the 2,0; 1,1; and 1,0 equatorial reflections we found the equatorial intensity ratio, an estimate of the association of cross-bridges with the thin filament; higher ratios indicate shifts in cross-bridge mass toward the thin filament and away from the thick filament backbone (supplementary text). We expected the warmer ventral region of the DLM₁ to behave as the main power generator and therefore to have rapid cross-bridge turnover. However, in the cool dorsal region of the muscle, we expected reduced contraction rates to result in longer cross-bridge attachment times, supporting a lattice of springs that can store and return elastic energy from the axial and radial deformation of cross-bridges that remain bound at the

¹Department of Biology, University of Washington, Seattle, WA 98195–1800, USA. ²Center for Synchrotron Radiation Research and Instrumentation and Department of Biological and Chemical Sciences, Illinois Institute of Technology, Chicago, IL 60616, USA. ³Department of Organismic and Evolutionary Biology, Concord Field Station, Harvard University, Cambridge, MA 01451, USA.

*Corresponding author. E-mail: danielt@uw.edu

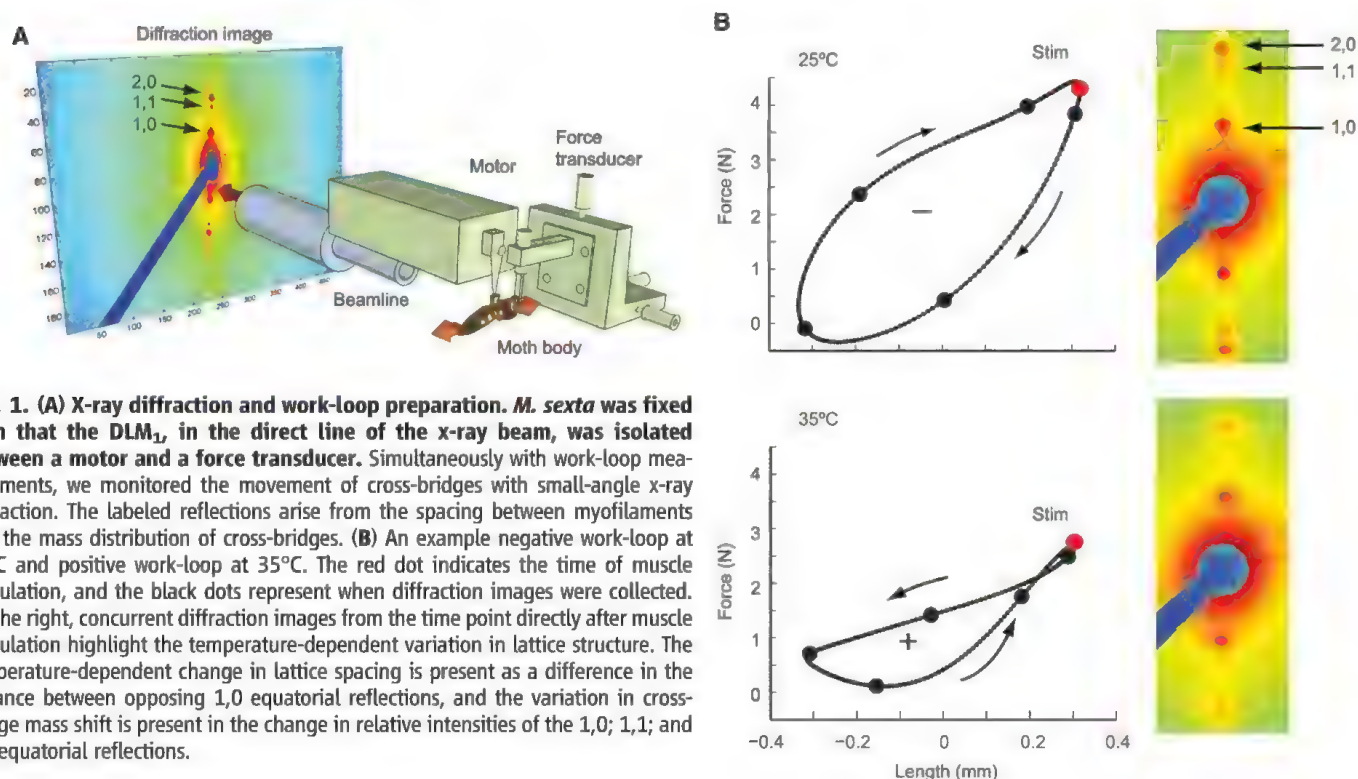


Fig. 1. (A) X-ray diffraction and work-loop preparation. *M. sexta* was fixed such that the DLM₁ in the direct line of the x-ray beam, was isolated between a motor and a force transducer. Simultaneously with work-loop measurements, we monitored the movement of cross-bridges with small-angle x-ray diffraction. The labeled reflections arise from the spacing between myofilaments and the mass distribution of cross-bridges. **(B)** An example negative work-loop at 25°C and positive work-loop at 35°C. The red dot indicates the time of muscle stimulation, and the black dots represent when diffraction images were collected. On the right, concurrent diffraction images from the time point directly after muscle stimulation highlight the temperature-dependent variation in lattice structure. The temperature-dependent change in lattice spacing is present as a difference in the distance between opposing 1,0 equatorial reflections, and the variation in cross-bridge mass shift is present in the change in relative intensities of the 1,0; 1,1; and 2,0 equatorial reflections.

extrema of the lengthening and shortening cycle, respectively.

Mean power output of the DLM₁ depends strongly on temperature. At 35°C, mean mechanical power output was $42.98 \pm 1.62 \text{ W kg}^{-1}$. In contrast, power output at 25°C was significantly negative, with a mean of $-161.20 \pm 3.20 \text{ W kg}^{-1}$ ($n = 5$ moths, mean \pm SEM; t test, $P < 0.0001$). These values are consistent with mechanical power output measures from a prior *M. sexta* work-loop study also conducted at the in vivo phase of activation (13). Lattice spacing and cross-bridge cycling dynamics were also significantly temperature dependent. For a comparison of the effect of temperature on these two factors, we first highlight results from the biologically relevant condition, the ventral region of the DLM₁ at 35°C versus the dorsal region at 25°C (11). The relationship between temperature and myofibrillar lattice spacing, as indicated by d_{10} , is shown in Fig. 2A. Although there was no significant difference in lattice spacing throughout the contraction cycle for muscle at 25° or 35°C, there was a significant difference because of muscle temperature [repeated-measures analysis of variance (ANOVA); effect of time $F(4,36) = 1.3$, $P = 0.29$; effect of temperature $F(1,36) = 13.1$, $P < 0.001$]. Because there was no effect of time, we combined the results for each temperature and found that lattice spacing was lower on average in cool dorsal muscles, with myofilaments $\sim 0.8 \text{ nm}$ closer together than in warm ventral muscle (t test, $P < 0.01$). The reduced lattice spacing in cool muscles indicates that the longer attachment times of these cross-bridges results in a higher portion remaining bound during the cycle, thus acting as molecular linkages and restraining radial expansion and axial stretch. These results are consistent with a prior study on skeletal muscles (21).

The intensity ratio, an estimate of cross-bridge association with the thin filaments, was significantly affected by both temperature and time point in the contraction cycle [repeated-measures ANOVA: effect of time $F(4,32) = 3.1$, $P < 0.05$; effect of temperature $F(1,8) = 14.1$, $P < 0.01$].

The intensity ratio across the whole contraction cycle averaged 37% higher in 35°C ventral muscles than in 25°C dorsal muscles (t test, $P < 0.0001$). The higher overall intensity ratio in warm muscles may be ascribed to the elevated cross-bridge activity expected of a power-producing muscle. Figure 2B also demonstrates the cyclical change in cross-bridge mass distribution expected of warm muscles versus the more likely bound cross-bridges in cooler muscles. This is indicated by the larger absolute percent change in the intensity ratio between progressive points in the cycle in warm muscle (mean = 17%, maximum = 29%) compared with that in cool muscle (mean = 7%, maximum = 11%). Care must be taken in interpreting the relationship between lattice spacing and intensity ratio in a muscle whose length is changing and whose temperature is spatially variable. In the isovolumetric case, lattice spacing should change as the inverse square root of length changes. At same time, however, it is possible that cross-bridge binding could influence lattice spacing. Indeed, the cooler muscle data suggest that cross-bridges do restrict lattice motion.

Controlling for the effect of location, the contractile dynamics of the DLM₁ subregions were not adapted to compensate for or enhance local temperature differences. Diffraction patterns from the ventral and dorsal locations held at the same temperature showed insufficient variation to indicate physiological compensatory mechanisms that could negate the effect of a temperature gradient on regional contractile dynamics. Lattice spacing was not significantly different between dorsal and ventral muscles at 25° or 35°C (two-way ANOVA, $P = 0.63$ at 25°C and $P = 0.45$ at 35°C; Fig. 2A). Myofibrillar spacing was similarly more restrained in ventral muscle at cold temperatures than at warm temperatures ($\sim 0.6 \text{ nm}$ less; paired t test, $P < 0.01$). Although there was an effect of location on the intensity ratio at 25° and 35°C (two-way ANOVA, $P < 0.001$ at 25°C and $P < 0.01$ at 35°C), the overall response, cyclic cross-bridge binding at 35°C versus stable cross-bridge activity at 25°C, was comparable be-

tween locations (Fig. 2B). Taken together, these data indicate that there is no effective regional specialization in molecular cycling dynamics.

Cyclical changes in the intensities and positions of major reflections in the DLM₁ of *M. sexta* suggest that a temperature gradient likely induces a gradient in cross-bridge cycling dynamics within a single muscle. Furthermore, the spatial variation in cross-bridge turnover rates appears to result in an energy-storing lattice of linked elastic elements within the cooler regions of muscles (fig. S1). Indeed, because the thick and thin filaments must be linked by cross-bridges to store energy in axial stretching, the creation of this stretching in the thick and thin filaments creates an equal store of energy in the stretching of the linked cross-bridges. Additionally, cross-bridges are able to store energy above and beyond that imparted by axial deformation, because their geometry requires them to undergo radial deformation alongside any axial stretching (16).

Temperature gradients within a single muscle inevitably result from the balance between metabolic heat production and surface heat loss. Because rates of muscle contraction are temperature dependent, this gradient has substantial implications for muscle power production and function (11, 13–15). The DLM₁ of *M. sexta* has been generally presumed to operate solely as an actuator, producing positive power to indirectly accelerate the wings downward. However, we show that, in the presence of a substantial temperature gradient, power output varies regionally from positive values (warm sectors) to negative values (cool sectors) within this single muscle. We found that significant variation in contractile dynamics (lattice spacing and intensity ratio) are associated with this decrease in power production and may provide a mechanism by which cross-bridges contribute stored elastic energy to the overall energy needed for flight. At high temperatures, rapidly cycling cross-bridges drive filament sliding and permit large length changes, but they may not be bound at the extrema of the cycle. At the coldest temperatures, accommodating large length

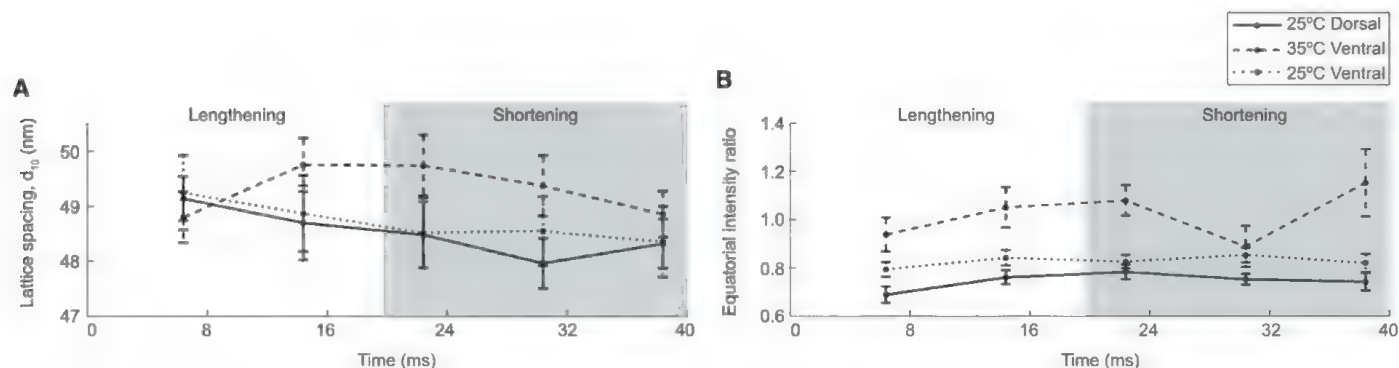


Fig. 2. Variation in lattice structure throughout the contraction cycle (mean \pm SEM; $n = 5$ moths). (A) Lattice spacing, determined by d_{10} , plotted as a function of contraction cycle for dorsal muscles at 25°C and ventral muscles at 35° and 25°C. Across the five time points, mean lattice spacing was significantly lower in 25°C muscles than in 35°C muscles, regardless of location and time point in

the contraction cycle. (B) Equatorial intensity ratio as a function of contraction cycle. Muscles at 35°C showed the expected cyclic response in intensity ratio. In contrast, muscles at 25°C showed a stable intensity ratio. The similar response of both locations at 25°C supports that the dorsal muscle's contractile dynamics are not specialized to operate at lower temperatures.

changes with bound cross-bridges requires energy to disrupt attachments, resulting in negative power production. However, intermediate temperatures permit some detachment to accommodate length changes in addition to some attachment at the extrema of the length cycle. At these intermediate temperatures, cross-bridges that remain bound at the very end of lengthening or shortening can store energy in their axial or radial extension, respectively. This stored energy may return energy into the lattice when the cross-bridges detach at the start of the subsequent phase. In doing so, the deformed cross-bridges could assist antagonistic muscles. Prior studies have shown that elastic energy storage is indeed crucial for meeting the high inertial power costs of flight (3, 4). If even a portion of these cross-bridges facilitate elastic energy savings via a temperature gradient, they would contribute to the overall energy savings in locomotion. Because temperature gradients are an inevitable consequence of internal energy generation and heat dissipation in both vertebrates and invertebrates, this mechanism of energy storage could be a general phenomenon in locomotor systems (11, 12).

References and Notes

1. M. Jensen, T. Weis-Fogh, *Philos. Trans. R. Soc. London Ser. B* **245**, 137 (1962).
2. R. M. Alexander, *Am. Zool.* **24**, 85 (1984).
3. R. M. Alexander, H. C. Bennet-Clark, *Nature* **265**, 114 (1977).
4. C. P. Ellington, *J. Exp. Biol.* **115**, 293 (1985).
5. H. E. Huxley, A. Stewart, H. Sosa, T. Irving, *Biophys. J.* **67**, 2411 (1994).
6. M. Dickinson *et al.*, *Nature* **433**, 330 (2005).
7. J. G. Tidball, T. L. Daniel, *Am. J. Physiol.* **250**, R56 (1986).
8. I. Dobbie *et al.*, *Nature* **396**, 383 (1998).
9. A. F. Huxley, R. M. Simmons, *Nature* **233**, 533 (1971).
10. K. C. Nishikawa *et al.*, *Proc. R. Soc. B* **279**, 981 (2012).
11. N. T. George, T. L. Daniel, *J. Exp. Biol.* **214**, 894 (2011).
12. F. G. Carey, J. M. Teal, *Proc. Natl. Acad. Sci. U.S.A.* **56**, 1464 (1966).
13. N. T. George, S. Sponberg, T. L. Daniel, *J. Exp. Biol.* **215**, 471 (2012).
14. R. K. Josephson, *J. Exp. Biol.* **108**, 77 (1984).
15. A. F. Bennett, *J. Exp. Biol.* **115**, 333 (1985).
16. C. D. Williams, M. Regnier, T. L. Daniel, *PLOS Comput. Biol.* **8**, e1002770 (2012).
17. A. Miller, R. T. Tregear, *Nature* **226**, 1060 (1970).
18. Information on materials and methods is available on Science Online.
19. M. S. Tu, T. L. Daniel, *J. Exp. Biol.* **207**, 2455 (2004).

20. T. C. Irving, in *Nature's Versatile Engine: Insect Flight Muscle Inside and Out*, J. O. Vigoreaux, Ed. (Springer, New York, 2006), pp. 197–213.
21. G. Wang, M. Kawai, *J. Physiol.* **531**, 219 (2001).

Acknowledgments: We thank H.-M. Hsu, E. Carrington, and R. Huey for their contributions. This research was supported by NSF Graduate Research Fellowship no. DGE-0718124 to N.T.G., NSF grant IOS-1022471 to T.L.D. and T.C.I., NSF grant EEC 1028725 to T.L.D., and the University of Washington Komen Endowed Chair to T.L.D. Use of the Advanced Photon Source was supported by the U.S. Department of Energy under contract no. DE-AC02-06CH11357. Use of BioCAT was supported by grants from the NIH (2P41RR008630-17 and 9 P41 GM103622-17). The data reported in this paper are deposited in the Dryad Repository (<http://dx.doi.org/10.5061/dryad.cg873>). For inquiries about materials, please contact N.T.G. (ntgeorge@uw.edu).

Supplementary Materials

www.sciencemag.org/cgi/content/full/science.1229573/DC1
Materials and Methods
Figs. S1 and S2
References (22, 23)
Movie S1

31 August 2012; accepted 28 March 2013
Published online 25 April 2013;
10.1126/science.1229573

Structural Systems Biology Evaluation of Metabolic Thermotolerance in *Escherichia coli*

Roger L. Chang,¹ Kathleen Andrews,² Donghyuk Kim,² Zhanwen Li,^{3,4} Adam Godzik,^{3,4} Bernhard O. Palsson^{1,2,5*}

Genome-scale network reconstruction has enabled predictive modeling of metabolism for many systems. Traditionally, protein structural information has not been represented in such reconstructions. Expansion of a genome-scale model of *Escherichia coli* metabolism by including experimental and predicted protein structures enabled the analysis of protein thermostability in a network context. This analysis allowed the prediction of protein activities that limit network function at superoptimal temperatures and mechanistic interpretations of mutations found in strains adapted to heat. Predicted growth-limiting factors for thermotolerance were validated through nutrient supplementation experiments and defined metabolic sensitivities to heat stress, providing evidence that metabolic enzyme thermostability is rate-limiting at superoptimal temperatures. Inclusion of structural information expanded the content and predictive capability of genome-scale metabolic networks that enable structural systems biology of metabolism.

Cellular thermosensitivity depends on proteome stability. Chaperones and proteases are well-characterized heat shock proteins (HSPs), and chaperones improve survival at super-

optimal temperatures (1). Protein folding and structural stability required for function are disrupted at high temperatures. Many individual proteins and their mutant variants have been studied to identify structural loci within a protein that are destabilized at high temperatures, leading to denaturation. Replacing heat-sensitive loci with more stabilizing residues has allowed engineering of thermostable proteins (2). By analogy, identifying the proteins that confer susceptibility to heat within the cellular system is critical to uncovering mechanisms for cellular thermosensitivity. Strategies for increasing thermotolerance have included introduction of chemical chaperones, overexpres-

sion of HSPs, pretreatment with moderate heat, or random mutagenesis to evolve stress tolerance (3). Instead, we sought to directly identify the particular proteins that confer thermosensitivity in the system.

The emerging discipline of structural systems biology (4) has enabled new insights into topics that include the structure-function relations in metabolism in a hyperthermophile (5), identification of causal off-target actions of drugs that cause adverse side effects (6), identification of protein-protein interactions (7, 8), and determination of causal mutations for disease susceptibility (8, 9). We used a structural systems biology approach to discover points of thermosensitivity in the mesophilic bacterium *Escherichia coli* K-12 MG1655. Metabolic thermosensitivity, affected by enzyme activity in a genome-scale model (GEM), was assessed as a function of protein thermostability, providing mechanistic explanations for effects of mutations in evolved thermotolerant strains (10, 11) and leading to the discovery of metabolic limitations to thermotolerance.

To assess protein thermostability, we integrated a genome-scale model of *E. coli* metabolism (iJO1366) (12) with protein structures (GEM-PRO) by associating metabolic reactions with structures of their catalytic enzymes (database S1), thereby enabling parameterization of the network model on the basis of protein structural properties. The main objectives of this reconstruction (Fig. 1A) were to (i) maximally cover amino acid sequence (Fig. 1B), (ii) represent the native structure of each wild-type (WT) protein (Fig. 1C), (iii) map existing amino acid functional annotations to structures (13–16) (Fig. 1C), and (iv) represent changes in functional conformation or induced fit caused by protein-substrate

¹Bioinformatics and Systems Biology Graduate Program, University of California San Diego, La Jolla, CA 92093–0412, USA.

²Department of Bioengineering, University of California San Diego, La Jolla, CA 92093–0412, USA.

³Bioinformatics and Systems Biology Program, Sanford-Burnham Medical Research Institute, La Jolla, CA 92037, USA. ⁴Joint Center for Structural Genomics (JCSG), La Jolla, CA 92037, USA. ⁵The Novo Nordisk Foundation Center for Biosustainability, Technical University of Denmark, DK-2970 Hørsholm, Denmark.

*Corresponding author. E-mail: palsson@ucsd.edu

binding (Fig. 1D). Thus, in this model a protein may be represented by zero, one, or multiple separate structures. Experimentally determined structures (17) and structures from homology modeling (fig. S1) were used to achieve 93% structural coverage of proteins in the network (Fig. 1B) and between 24 and 33% coverage of protein-substrate

binding conformations. The majority of coverage was enabled by structure-modeling techniques (5), without which such a reconstruction would not currently be possible.

Experimentally measured critical temperatures (18, 19) accounting for optimal, half-maximum, and total loss of protein activity were supple-

mented with bioinformatic predictions (20–23), based on protein three-dimensional structures, of protein melting temperatures (see table S1 for a full list and fig. S2 for a comparison of experimental and predicted melting temperatures). We used these critical temperatures to define protein activity functions that imposed temperature-dependent constraints on the metabolic model (fig. S3). In this way, temperature, by affecting protein function, became a parameter for genome-scale metabolic simulation. Simulated temperature-dependent growth showed good qualitative agreement with experimental growth data in three different nutrient media (Fig. 2A) in the range from 32° to 43°C, where growth is above 50% of maximum. Thus, thermostability of metabolic proteins appears to explain much of the thermosensitivity within this temperature range.

Our modeling framework also enabled precise prediction of points of thermosensitivity in the metabolic network (fig. S4 and table S2). The most temperature-limited protein activities cluster in cofactor synthesis pathways, identifying them as most growth limiting (Fig. 2B). We tested how temperature sensitivity of the model would change with the introduction of thermostable proteins into the network by alleviating temperature-dependent activity constraints on predicted growth-limiting proteins. For instance, optimally increasing critical temperatures of all proteins predicted to be limiting at 42.2°C produced a twofold increase in maximum growth rate and shifted the optimal temperature to 42.2°C, but narrowed the range of growth temperatures because of incompatibility of these more thermophilic activity functions with lower growth temperatures (Fig. 2B). Adjusting

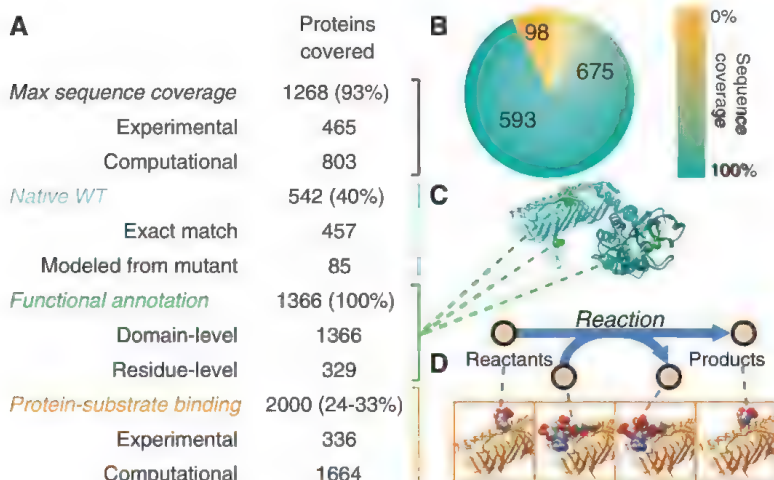


Fig. 1. Properties of the *E. coli* metabolic model integrated with protein structures. (A) The *E. coli* GEM-PRO model provides maximal amino acid sequence coverage, native WT structures, functional annotation, and protein-substrate binding for proteins included in *ijO1366*. Percentages are out of 1366 total proteins, except for the percentage of protein-substrate binding pairs, which is out of an estimated total between 6144 and 8448 such pairs. (B) The distribution of maximum amino acid sequence coverage of proteins by structures included in the GEM-PRO. Numbered wedges indicate the number of proteins with 0%, 100%, or partial sequence coverage. (C) Example of a native WT structure included in the GEM-PRO. Green highlighted residues denote annotated functional sites. (D) Protein-substrate binding is structurally represented as the pairwise interactions between each protein and the reactants or products of the catalyzed metabolic reaction.

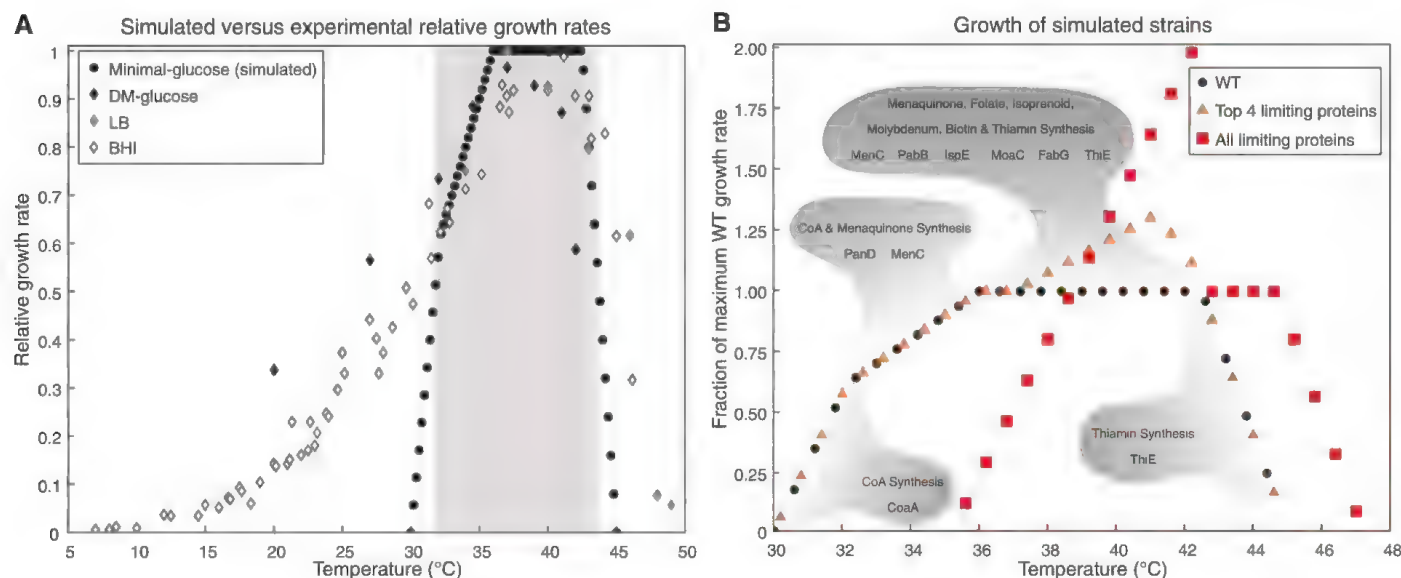


Fig. 2. Simulated and experimental growth rates as a function of temperature. (A) Growth rates relative to the maximum are depicted under each condition. Growth was simulated on minimal medium with glucose (circles) or experimentally measured (diamonds) on Davis minimal medium (DM) with glucose (29), lysogeny broth (LB) (11), or brain heart infusion (BHI) broth (30). The shaded region highlights the temperature range in which the model best predicts relative

growth rates. (B) Simulated growth rates relative to maximum WT growth rate are shown for the WT strain, a strain with critical temperatures of the four most growth-limiting proteins at 42.2°C adjusted for maximum activity at that temperature, and a strain with critical temperatures of all growth-limiting proteins at 42.2°C adjusted for maximum activity at that temperature. The gray regions indicate the predicted most growth-limiting proteins and pathways for each phase of WT growth.

activity functions for just the four most-growth-limiting proteins had similar but smaller effects on temperature-dependent growth (Fig. 2B).

Adaptive laboratory evolution experiments have yielded 119 thermotolerant *E. coli* mutants (10, 11). Investigating mutations in metabolic genes and their regulators (24) with our modeling framework yielded classification of potential causal mutations for 51 strains (supplementary text and table S3) and possible mechanistic explanations for their functionality in thermotolerance through compensating for heat-limited growth factors (Fig. 3), often consisting of cofactors. Statistical analysis (table S3) established that predicted causal mutant gene combinations conferring thermotolerance have a low probability of being identified by chance, signifying the predictive accuracy of heat-affected metabolic activities.

Mutations decreasing thermosensitivity of metabolic activities could stabilize or otherwise increase protein activity at high temperatures, for example, through increased gene expression. We thus profiled gene-expression of WT *E. coli* at 37° and 42°C (table S4) to identify genes with heat-induced transcription. Such genes participate in native heat-shock response and offer possible mechanisms for adaptive evolution of thermotolerance.

Specific susceptible proteins may be directly characterized by replacement with more thermotolerant proteins, by increasing gene expression to compensate for decreased activity (25), or by bypassing their function through nutrient supplementation. We chose metabolites produced immediately downstream of model-predicted growth-limiting proteins (fig. S4) and for which transport mechanisms are known in *E. coli* as supplements and found a set of six compounds that supplemented heat-limited growth factors (table S5). Each individual compound and a mixture combining all compounds were tested for effects on growth rate at 42° and 37°C. The mixture increased log-phase growth rate at 42°C by about 13% but yielded no benefit at 37°C (Fig. 4).

Triplicate experiments for components of the supplement mixture (table S6) were prioritized for the two compounds resulting in the highest growth rates at 42°C in single experiments (fig. S5). Pantothenate and biotin both provided heat-dependent supplementation, although to a lesser degree than the mixture (Fig. 4). Production of the coenzyme A (CoA) precursor pantothenate in WT grown at 37°C has been measured in excess of the minimum requirement for growth by as much as 15-fold, leading to excretion (26). A pathway with such excess activity at 37°C being successfully supplemented at 42°C indicates a substantial heat-dependent loss of function. This experimental result supports our predictions that this pathway has lowered activity because of thermal deactivation of PanB, PanC, PanD, and IlvC proteins. The heat dependency of this supplementation indicates that supplements do not simply alleviate the burden of synthesizing cofactors from the nutrient carbon source; it confirms the accuracy of thermosensitive metabolic activities pre-

dicted by our modeling framework and supports the precise proteins predicted to be limiting at 42°C. The supplement mixture elicited a combined benefit beyond that observed for individual compounds. The combination of pantothenate

and biotin accounts for part but not all of the benefit of the full mixture (Fig. 4). Additions to pantothenate and biotin within the mixture appear to compensate for less rate-limiting growth factor deficits.

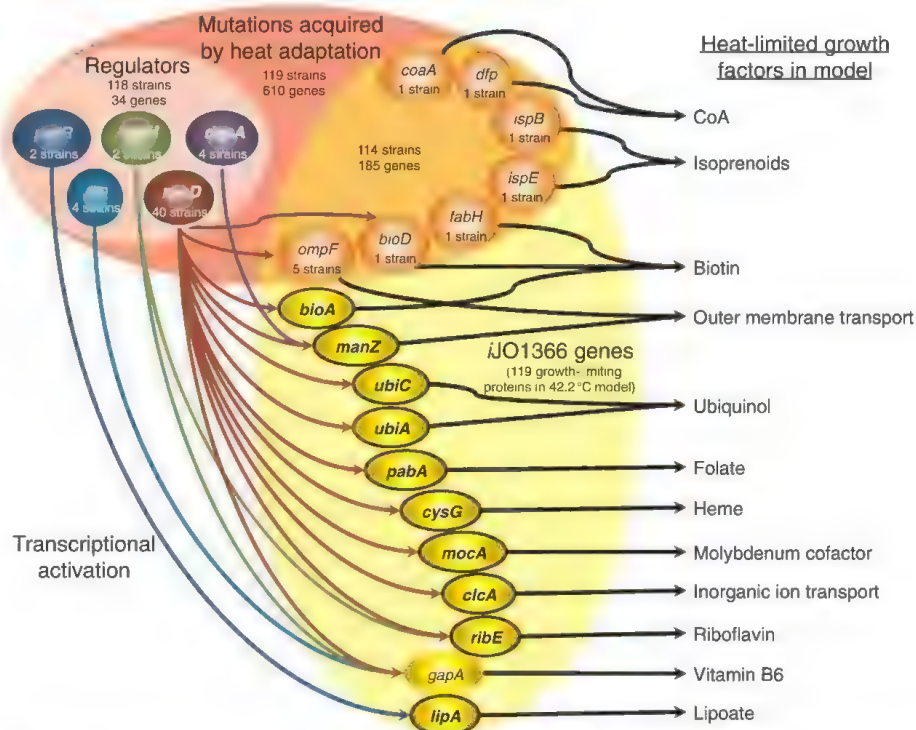
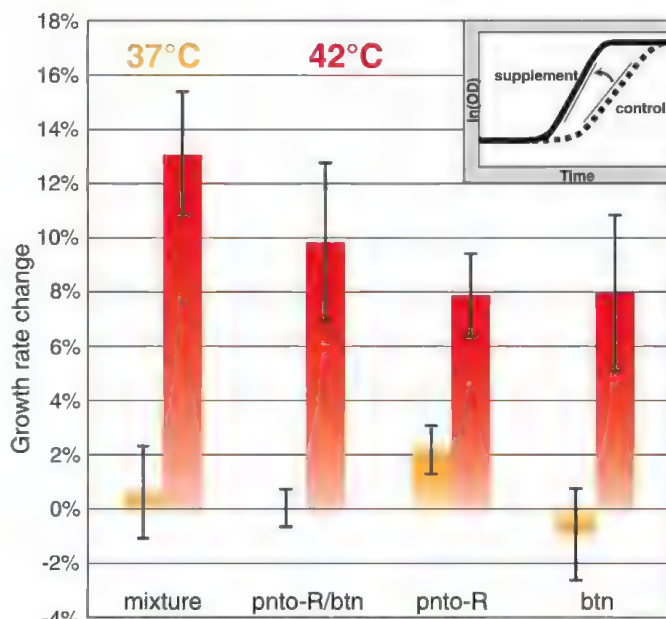


Fig. 3. Mechanisms predicted to confer thermotolerance are summarized for heat-adapted *E. coli* strains. The total number of heat-adapted strains and mutated genes is given and also noted for the regulatory and metabolic subsets of mutated genes. Only regulators acting on metabolic genes both predicted to lead to thermosensitivity and with heat-induced transcription in WT are depicted, except for *crp*. Only metabolic genes predicted to lead to thermosensitivity and either mutated in the set of evolved strains or both activated by depicted regulators and with heat-induced transcription in WT are depicted, except for *gapA*. Encircled, bolded genes show heat-induced transcription in WT. Predicted growth factors limited by heat-dependent decreases in protein activity are indicated at right.

Fig. 4. Changes in specific growth rate upon supplementation relative to a no-supplement control are depicted in orange for 37°C and red for 42°C. Error bars show standard deviations with $n = 3$ for each condition. (Inset) How growth rate changes were computed by comparing the maximum slopes of growth curves between the control and supplement condition. Mixture, combination of all six supplements; pnto-R, pantothenate; btn, biotin; OD, optical density.



The *E. coli* GEM-PRO platform reconciled disparate data types to explain fundamental properties of thermosensitivity, providing evidence that metabolic processes are growth-limiting under heat stress and providing mechanistic interpretations of complex thermotolerant mutation data. Our model suggests that these dependencies arise directly from the systemic constraints that proteome thermostability imposes upon growth, which could be relieved through exogenous supplementation of the most-limiting processes, among them CoA and biotin synthesis. Understanding thermotolerance in microbes has important implications for developing industrial microbial biocatalysts (27), probiotics, and bacterial vaccines (28). Most efficient producers of compounds of interest are not naturally thermotolerant, but the absence of a genetic system often limits the utility of native thermophiles in industrial processes. Therefore, strategies for increasing thermotolerance of production strains may be useful. Our result supports the necessity of systems biology in understanding complex stress responses. Furthermore, these findings would not have been possible with use of either protein structure data or the metabolic network in isolation, illustrating the potential of advancing the field of structural systems biology.

References and Notes

1. E. Van Derlinden, K. Bernaerts, J. F. Van Impe, *J. Appl. Microbiol.* **104**, 438 (2008).

2. A. Korkegian, M. E. Black, D. Baker, B. L. Stoddard, *Science* **308**, 857 (2005).
3. C. R. Fischer, D. Klein-Marcuschamer, G. Stephanopoulos, *Metab. Eng.* **10**, 295 (2008).
4. P. Beltrao, C. Kiel, L. Serrano, *Curr. Opin. Struct. Biol.* **17**, 378 (2007).
5. Y. Zhang *et al.*, *Science* **325**, 1544 (2009).
6. R. L. Chang, L. Xie, L. Xie, P. E. Bourne, B. Ø. Palsson, *PLoS Comput. Biol.* **6**, e1000938 (2010).
7. Q. C. Zhang *et al.*, *Nature* **490**, 556 (2012).
8. X. Wang *et al.*, *Nat. Biotechnol.* **30**, 159 (2012).
9. T. M. Cheng *et al.*, *PLoS Comput. Biol.* **8**, e1002738 (2012).
10. O. Tenaillon *et al.*, *Science* **335**, 457 (2012).
11. I. K. Blaby *et al.*, *Appl. Environ. Microbiol.* **78**, 144 (2012).
12. J. D. Orth *et al.*, *Mol. Syst. Biol.* **7**, 535 (2011).
13. C. T. Porter, G. J. Bartlett, J. M. Thornton, *Nucleic Acids Res.* **32**, D129 (2004).
14. I. M. Keseler *et al.*, *Nucleic Acids Res.* **39**, D583 (2011).
15. Z. Huang *et al.*, *Nucleic Acids Res.* **39**, D663 (2011).
16. UniProt Consortium, *Nucleic Acids Res.* **40**, D71 (2012).
17. H. M. Berman *et al.*, The Protein Data Bank, *Nucleic Acids Res.* **28**, 235 (2000).
18. M. Scheer *et al.*, *Nucleic Acids Res.* **39**, D670 (2011).
19. M. D. Kumar *et al.*, *Nucleic Acids Res.* **34**, D204 (2006).
20. T. Ku *et al.*, *Comput. Biol. Chem.* **33**, 445 (2009).
21. M. Oobatake, T. Ooi, *Prog. Biophys. Mol. Biol.* **59**, 237 (1993).
22. K. P. Murphy, E. Freire, *Pure Appl. Chem.* **65**, 1939 (1993).
23. K. A. Dill, K. Ghosh, J. D. Schmit, *Proc. Natl. Acad. Sci. U.S.A.* **108**, 17876 (2011).
24. S. Gama-Castro *et al.*, *Nucleic Acids Res.* **39**, D98 (2011).
25. T. S. Gunasekera, L. N. Csonka, O. Paliy, *J. Bacteriol.* **190**, 3712 (2008).

26. S. Jackowski, C. O. Rock, *J. Bacteriol.* **148**, 926 (1981).
27. P. Turner, G. Mamo, E. N. Karlsson, *Microb. Cell Fact.* **6**, 9 (2007).
28. B. N. Duplantier *et al.*, *Proc. Natl. Acad. Sci. U.S.A.* **107**, 13456 (2010).
29. V. S. Cooper, A. F. Bennett, R. E. Lenski, *Evolution* **55**, 889 (2001).
30. E. Van Derlinden, J. F. Van Impe, *Int. J. Food Microbiol.* **158**, 73 (2012).

Acknowledgments: We thank H. Nagarajan, A. M. Feist, P. Charusanti, P. E. Bourne, J. A. Lerman, E. T. O'Brien, D. Zielinski, Y. Zhang, and L. Jaroszewski for insightful discussion on this work and J. Orth for providing the jO1366 network map. This work was supported by NSF grant GK-12 742551 to R.L.C.; U.S. Department of Energy grant DE-SC0004917 to R.L.C., K.A., D.K., and B.O.P.; NIH grants R01GM101457, R01 GM057089, and U54GM094586 to Z.L. and A.G.; and the Novo Nordisk Foundation to B.O.P. Data reported in this report are available in the supplementary materials and the National Center for Biotechnology Information Gene Expression Omnibus (GEO) database (GSE42675). The content is solely the responsibility of the authors and does not necessarily represent the official views of the NIH. The University of California San Diego has filed a provisional patent for the method to predict proteins responsible for cellular thermosensitivity.

Supplementary Materials

www.sciencemag.org/cgi/content/full/340/6137/1220/DC1
Materials and Methods
Supplementary Text
Figs. S1 to S5
Tables S1 to S6
Database S1
References (31–53)

12 December 2012; accepted 5 April 2013
10.1126/science.1234012

Widespread Production of Extracellular Superoxide by Heterotrophic Bacteria

Julia M. Diaz,^{1*} Colleen M. Hansel,^{1,2,†‡} Bettina M. Voelker,³ Chantal M. Mendes,¹ Peter F. Andeer,² Tong Zhang²

Superoxide and other reactive oxygen species (ROS) originate from several natural sources and profoundly influence numerous elemental cycles, including carbon and trace metals. In the deep ocean, the permanent absence of light precludes currently known ROS sources, yet ROS production mysteriously occurs. Here, we show that taxonomically and ecologically diverse heterotrophic bacteria from aquatic and terrestrial environments are a vast, unrecognized, and light-independent source of superoxide, and perhaps other ROS derived from superoxide. Superoxide production by a model bacterium within the ubiquitous *Roseobacter* clade involves an extracellular oxidoreductase that is stimulated by the reduced form of nicotinamide adenine dinucleotide (NADH), suggesting a surprising homology with eukaryotic organisms. The consequences of ROS cycling in immense aphotic zones representing key sites of nutrient regeneration and carbon export must now be considered, including potential control of carbon remineralization and metal bioavailability.

Heterotrophic bacteria are ubiquitous and abundant components of natural ecosystems. These metabolically versatile organisms alter the global environment by mediating the redox transformation of many elements, including carbon, iron, and mercury. Biologically produced reactive oxygen species (ROS) may play an unrecognized role in these pathways because of the susceptibility of these elements to

redox reactions with ROS (1–4), but the ability of common heterotrophic bacteria to produce extracellular ROS has remained largely unexplored (2). Nevertheless, the recent discovery of extracellular superoxide (O₂^{•−}) production by a manganese-oxidizing marine bacterium belonging to the prolific *Roseobacter* clade (5) suggests that this capability may be present in environmentally relevant heterotrophs.

ROS production in natural waters (fig. S1) has long been linked to abiotic photooxidation of organic compounds (6). Yet, biological ROS production has been historically recognized (7), and recent field evidence indicates that biological production is likely the dominant ROS source in many marine and freshwater systems (8–10). Although all aerobic organisms produce intracellular ROS as a metabolic byproduct (11), ROS are generally toxic to living cells. Intracellular concentrations are therefore kept very low by enzymes that scavenge ROS, such as superoxide dismutase and catalase. This strict regulation of intracellular ROS and the inability of charged ROS to pass the lipid bilayer (2) point to biologically directed processes rather than adventitious cell rupture or leakage as the primary source of biogenic ROS in the environment. In fact, a number of cultivated eukaryotic phytoplankton and cyanobacteria produce extracellular

¹School of Engineering and Applied Sciences, Harvard University, Cambridge, MA 02138, USA. ²Department of Marine Chemistry and Geochemistry, Woods Hole Oceanographic Institution, Woods Hole, MA 02543, USA. ³Department of Chemistry and Geochemistry, Colorado School of Mines, Golden, CO 80401, USA.

*Present address: Biology Department, Woods Hole Oceanographic Institution, Woods Hole, MA 02543, USA.

†Present address: Department of Marine Chemistry and Geochemistry, Woods Hole Oceanographic Institution, Woods Hole, MA 02543, USA.

‡Corresponding author. E-mail: chansel@whoi.edu

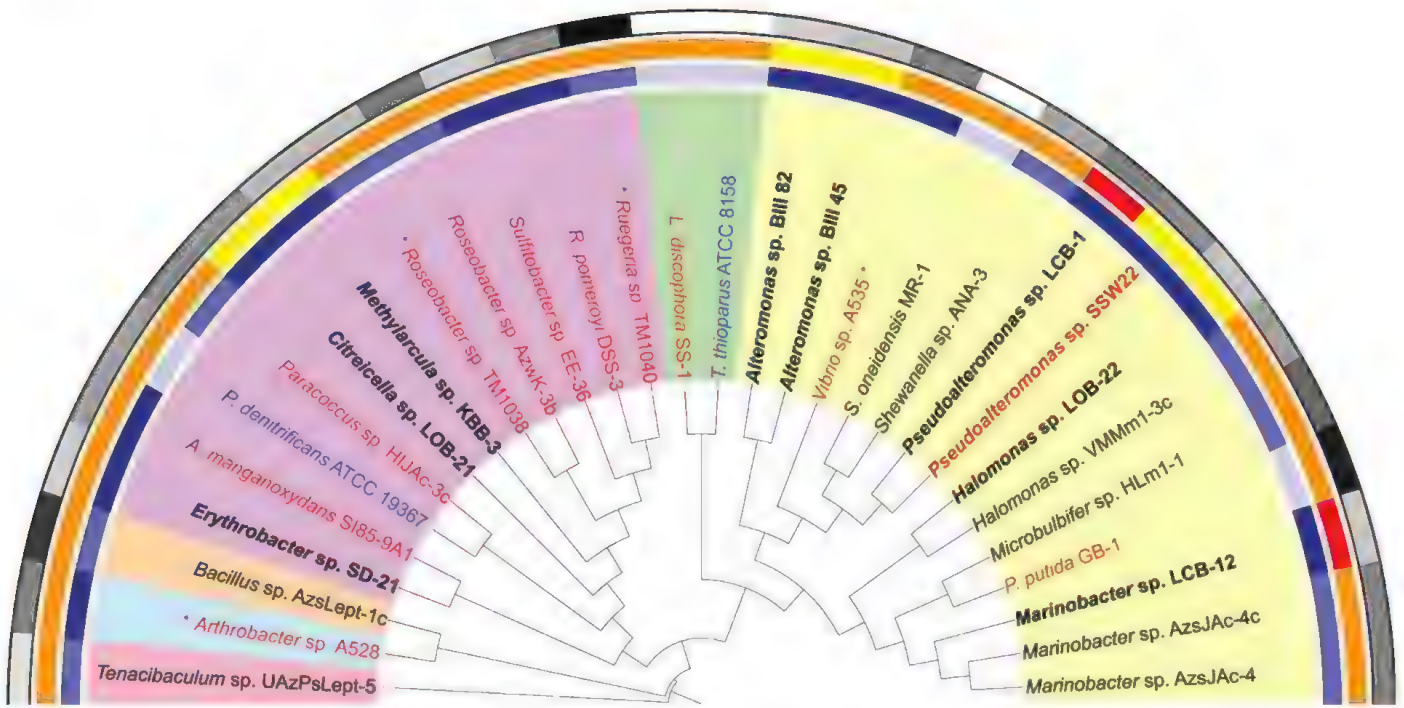
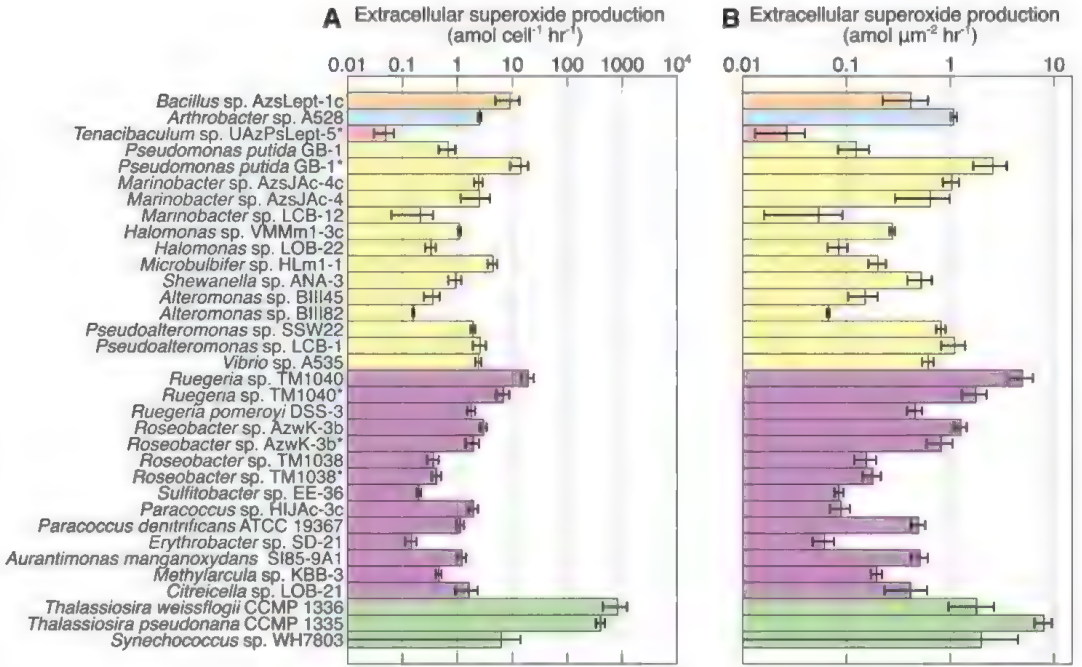


Fig. 1. Superoxide production across a broad phylogenetic and ecological diversity of bacteria. Relative superoxide production within this 16S rRNA gene tree is indicated in the outer ring and is scaled to the highest observed rate (*Ruegeria* sp. TM1040; black); white represents values below detection. The middle ring identifies psychrophiles (yellow), mesophiles (orange), and thermophiles (red). The inner ring represents freshwater (light blue), estuarine (medium blue), and marine (dark blue) habitats. Font color indicates whether the original isolate was benthic (black), planktonic (red),

or isolated from soil (blue). Organisms isolated from surface environments (<1 km) are indicated by normal font weight, whereas isolates obtained from greater than 1 km appear in bold font. Asterisks indicate that the bacterium was originally isolated from another organism or biological consortium. Leaf colors indicate phylogenetic group, including two Gram-positive isolates, one each from *Actinobacteria* (blue) and *Firmicutes* (orange), as well as Gram-negative bacteria from *Alphaproteobacteria* (purple), *Betaproteobacteria* (green), *Gammaproteobacteria* (yellow), and *Bacteroidetes* (pink).

Fig. 2. Gross rates of extracellular superoxide production by heterotrophic bacteria. (A) When normalized to abundance of metabolically active cells, rates of superoxide production by heterotrophic bacteria representing *Firmicutes* (orange), *Actinobacteria* (blue), *Bacteroidetes* (pink), *Gammaproteobacteria* (yellow), and *Alphaproteobacteria* (purple) are lower than previous estimates for phytoplankton (green). (B) However, when these active-cell rates are normalized to cell surface area, superoxide production by heterotrophs is comparable with, and in several cases greater than, previous estimates for phytoplankton. Measurements for heterotrophs represent the mean \pm SEM for biological replicates analyzed during stationary phase (indicated by asterisks) or mid-exponential growth. Phytoplankton data are from (8) and are based on the assumption that superoxide recovery is 100%. Comparing net superoxide production by heterotrophic bacteria (table S2) with these phytoplankton rates yields similar results.



superoxide under laboratory conditions (8, 12–14) for reasons equivocally related to metal nutrient acquisition (13, 15) and virulence (12). These photosynthetic organisms have been inferred as the source of total biological superoxide production in the surface ocean based only on indirect evidence, such as agreement between culture- and field-based fluxes. The ultimate source of biogenic superoxide in the environment therefore remains unclear.

We analyzed extracellular superoxide production by a broad range of ecologically and phylogenetically diverse heterotrophic bacteria (16). Using a high-sensitivity flow-through chemiluminescence approach (fig. S2) (13, 17), we detected superoxide production by 27 of 30 environmentally common isolates, including members of three *Proteobacteria* clades, *Bacteroidetes*, and two Gram-positive genera, each representing *Actinobacteria* and *Firmicutes*. The bacterial

strains selected were originally isolated from a wide variety of aquatic and terrestrial environments, including lakes, soils, hydrothermal vents, pelagic marine sediments, estuaries, and the surface and deep (>1 km) ocean. The organisms ranged from psychrophiles to thermophiles and exhibited benthic, planktonic, and symbiotic lifestyles. The three organisms that tested negative for superoxide production were *Shewanella oneidensis* MR-1 and two betaproteobacteria, *Thiobacillus thioarvus* (ATCC 8158) and *Leptothrix discophora* SS-1. As a group, these organisms exhibited no distinctively common traits to distinguish them from those that did produce extracellular superoxide. Superoxide production is thus widespread among heterotrophic bacteria, exhibiting no clear patterns with respect to ecology or phylogeny (Fig. 1).

Rates of superoxide production normalized to the proportion of metabolically active cells varied by a few orders of magnitude, between 0.02 ± 0.02 amol cell⁻¹ hour⁻¹ (mean \pm SEM) and 19.4 ± 5.2 amol cell⁻¹ hour⁻¹ (Fig. 2A and table S2). Experiments involving standard additions of superoxide to these live cultures also revealed concomitant superoxide degradation. For example, the recovery of standard superoxide additions ranged from 1 to 100%, with an average of $52 \pm 3\%$ (table S2). A clear relationship between superoxide production and standard recovery was not observed (fig. S3), indicating that enhanced production is not simply a consequence of a depressed ability to degrade superoxide.

Although cell-normalized rates of superoxide production by heterotrophic bacteria are lower than those measured previously for marine phytoplankton (Fig. 2A), rates normalized to cell surface area are comparable with, and in several cases greater than, those of phytoplankton. For instance, the most prolific heterotrophic superoxide producer, *Ruegeria* sp. TM1040, exhibited rates over two times higher than that of the cyanobacterium *Synechococcus* sp. WH7803 (Fig. 2B and table S3). This heterotrophic bacterium belongs to the highly common *Roseobacter* clade, which can account for up to 30% of marine bacterioplankton communities (18).

If we assume that bacteria producing superoxide at the rate of *Ruegeria* sp. TM1040 represent 30% of the total bacterioplankton population (18) consisting of 10^6 cells mL⁻¹, the extrapolated rate (2×10^3 fmol L⁻¹ s⁻¹) can account for 90 to >100% of biological superoxide production reported previously in the Gulf of Alaska (9) and >100% of biological superoxide production within the photic zone of the Costa Rica Dome upwelling region (table S4) (8). Similar results were obtained from an extrapolation based on the median extracellular superoxide production rate observed for heterotrophic bacteria (1.2 amol cell⁻¹ hour⁻¹) (table S4). Although extrapolated rates of superoxide production by *Synechococcus* are similar to the potential contribution of heterotrophs in the Costa Rica Dome (8), biological superoxide production in this

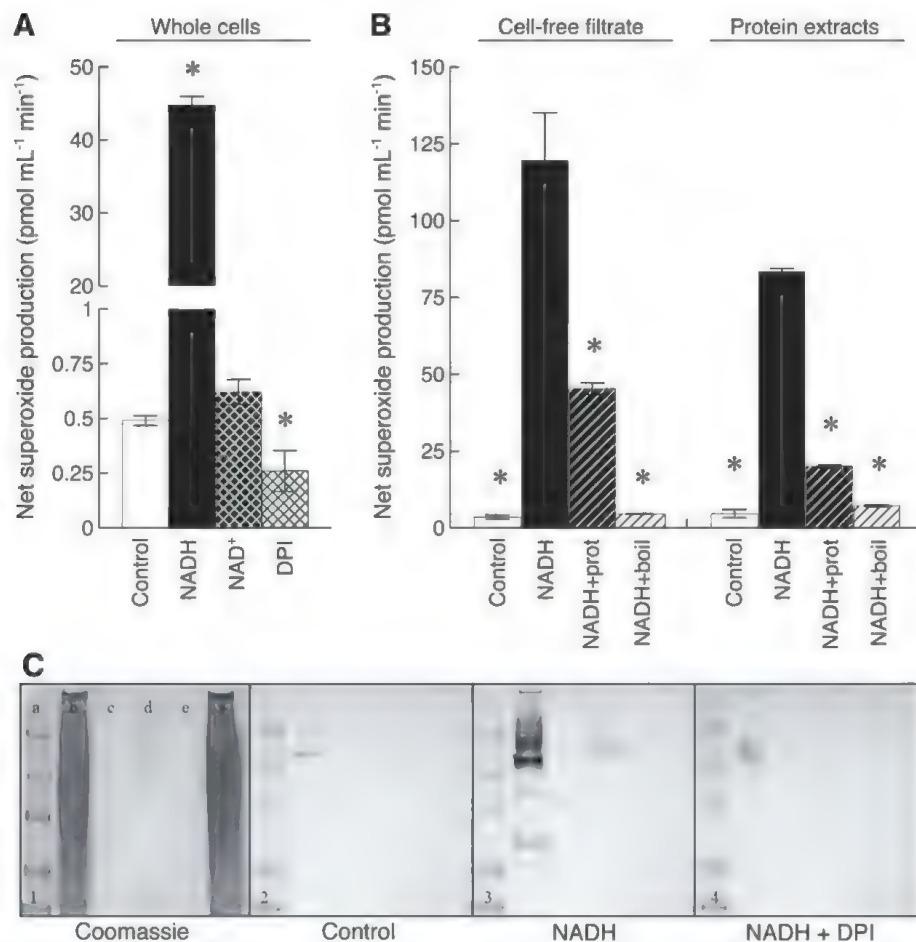


Fig. 3. Extracellular superoxide production by *Roseobacter* sp. AzwK-3b. (A and B) Addition of NADH increased superoxide production by *Roseobacter* sp. AzwK-3b in (A) whole cells and (B) (left) cell-free filtrates and (right) protein extracts, as measured with two separate methods. NAD⁺ had no significant effect (A), whereas DPI, a broad inhibitor of NAD(P)H oxidoreductases and other NAD(P)H-oxidizing enzymes, decreased superoxide production (A). Similarly, NADH-stimulated superoxide production in filtrates and protein extracts substantially decreased when protein activity was reduced (proteinase-K) or eliminated (boiling before incubation with NADH) (B). Asterisks indicate treatments that significantly differ from the control condition (A) or the NADH condition (B) ($P < 0.05$) (table S6). Measurements are means \pm SEM. (C) Proteins from *Roseobacter* sp. AzwK-3b were visible in whole-cell extracts (Coomassie gel, lane b) and also in cell-free filtrates (Coomassie gel, lane d). Reaction of the protein gel with the superoxide probe nitroblue tetrazolium (NBT) under control conditions revealed superoxide production at a single location in the separated whole-cell protein extract (Control gel, lane b). Addition of NADH stimulated superoxide production by this and other soluble whole-cell proteins (NADH gel, lane b) and also stimulated a single protein band present in the cell-free filtrate (NADH gel, lane d). Addition of DPI quenched NADH-stimulated superoxide production in whole-cell protein extracts (NADH+DPI gel, lane b) and completely inhibited it in the filtrate protein band (NADH+DPI gel, lane d). Protein ladders (lanes a) were prestained; appearance of the ladders therefore does not reflect superoxide production. Lane description for all gels (labeled in Coomassie gel) are (a) protein ladder, (b) soluble whole cell proteins, (d) cell-free filtrate proteins, (f) boiled (denatured) whole-cell soluble proteins, and (c and e) loading buffer only.

region does not correlate with *Synechococcus* abundance (8), further suggesting a role for heterotrophic bacteria.

Superoxide signals were stable (~2% coefficient of variation) over time periods of 1 to 40 min, timeframes that are comparable with or much longer than the observed half-life of superoxide (~2 min). This stability is consistent with steady-state production and would not be expected in the case of sudden superoxide release via cell lysis. In fact, for those organisms tested during mid-log and stationary phases (with the exception of *Pseudomonas putida* GB-1), superoxide production was comparable or substantially lower during stationary phase, when cell lysis would be greatest (Fig. 2). Moreover, calculations based on the superoxide content of a typical bacterial cell revealed that release of intracellular superoxide is negligible compared with any superoxide production rate observed (table S5).

The biochemical processes responsible for superoxide production may be similar between heterotrophic bacteria and eukaryotic organisms. Enzymes within the broad class of nicotinamide adenine dinucleotide (NAD⁺) and nicotinamide adenine dinucleotide phosphate (NADP⁺) [NAD(P)H] oxidoreductases, including NADPH (the reduced form of NADP⁺) oxidase and peroxidase, are thought to be involved in extracellular superoxide production by raphidophycean algae (19), diatoms (13), fungi (20), and plants (21). These conclusions are based in part on the observation that exogenous NAD(P)H stimulates extracellular superoxide production among model eukaryotic organisms, whereas diphenyleneiodonium (DPI), an inhibitor of NAD(P)H oxidoreductases and other NAD(P)H oxidizing enzymes, strongly attenuates it (13, 19, 20). For example, in the toxic eukaryotic raphidophycean flagellate *Chattonella marina*, extracellular superoxide production occurs through a loosely surface-associated putative NAD(P)H oxidase (19) that readily detaches from the cell (19). Similarly, NADH (the reduced form of NAD⁺) oxidases have been implicated in superoxide production by bacterial pathogens and *Escherichia coli* (22–24). Consistent with this previous work, addition of exogenous NAD(P)H to *Roseobacter* sp. AzwK-3b significantly increased extracellular superoxide production via an enzymatic response (Fig. 3, fig. S4, and table S6). In fact, similar to the case of *C. marina*, we detected NADH-stimulated superoxide production by protein (or proteins) collected from the cell-free filtrate of *Roseobacter* sp. AzwK-3b (Fig. 3). We thus infer that exogenous NADH is able to boost extracellular superoxide production by stimulating this extracellular protein without the need to enter the cell, as in the case of *C. marina* (19). Under natural physiological conditions, however, endogenous NADH is likely to be the primary electron donor. The physiological architecture responsible for electron flow from intracellular NADH to the surface-associated NADH oxidoreductase in *Roseobacter*

sp. AzwK-3b and *C. marina* is not yet known but may involve quinone-like electron carriers cycled within the membrane, as observed for *E. coli* (23).

Also consistent with previous results from the analysis of eukaryotic microorganisms (13, 19, 20), DPI significantly decreased enzymatic production of extracellular superoxide by *Roseobacter* sp. AzwK-3b and eliminated production by the superoxide-generating protein (or proteins) within the cell-free filtrate (Fig. 3, fig. S5, and table S6). Although NADPH oxidases have not been found in prokaryotes (20), a number of enzymes within the broad class of NADH oxidoreductases are encoded by the genome of *Roseobacter* sp. AzwK-3b. These findings reveal a widespread ability for extracellular superoxide production within prokaryotic and eukaryotic organisms, including bacteria, phytoplankton, fungi, and plants (13, 19–24), with the potential for a surprising homology in the mechanisms of formation between these disparate groups.

Given the magnitude of fluxes observed in culture (Fig. 2 and tables S2 and S3) and comparison with field-based rates (table S4), superoxide production by heterotrophic bacteria must be considered in areas conventionally regarded as important sites of ROS production by phytoplankton and abiotic photooxidation pathways, such as the surface ocean. Furthermore, superoxide production among cosmopolitan heterotrophic bacteria, whose life cycles and metabolisms do not directly depend on light, may explain ROS production in aphotic ocean regions (8, 25, 26) and provide a source of ROS to other aphotic environments, such as pelagic sediments and terrestrial soils. Because the aphotic ocean represents the largest mass of water on Earth and the largest aqueous habitat for life (27), bacterially mediated ROS cycling will undoubtedly affect global biogeochemistry. For example, given the ability of ROS to enhance carbon remineralization directly (1, 28) or indirectly (5), variations in the efficiency of the biological pump (29) may be partly attributable to wide variations in ROS production by heterotrophic bacteria. ROS cycling by heterotrophic bacteria may furthermore influence numerous metal cycles, including mercury (Hg), a bioaccumulating toxin (30). Dark redox reactions in aphotic waters, likely of biological origin, control the content of Hg in the ocean by regulating the balance between Hg(II) and Hg(0) (the latter of which is volatile and outgasses to the atmosphere) (3, 4). Because inorganic mercury cycling is canonically shaped by reactions involving ROS (3, 4), the production of ROS by abundant and ubiquitous communities of heterotrophic bacteria in the deep ocean may drive this enigmatic dark cycling of Hg and, ultimately, the content of Hg in the ocean.

References and Notes

- M. J. Pullin, S. Bertilsson, J. V. Goldstone, B. M. Voelker, *Limnol. Oceanogr.* **49**, 2011 (2004).
- A. L. Rose, *Front. Microbiol.* **3**, 124 (2012).
- H. Zhang, S. E. Lindberg, *Environ. Sci. Technol.* **35**, 928 (2001).

- S. D. Siciliano, N. J. O'Driscoll, D. R. S. Lean, *Environ. Sci. Technol.* **36**, 3064 (2002).
- D. R. Learman, B. M. Voelker, A. I. Vazquez-Rodriguez, C. M. Hansel, *Nat. Geosci.* **4**, 95 (2011).
- W. J. Cooper, R. G. Zika, R. G. Petasne, A. M. Fischer, in *Aquatic Humic Substances: Influence on Fate and Treatment of Pollutants*, I. H. Suffet, P. MacCarthy, Eds. (American Chemical Society, Washington, DC, 1989), pp. 333–362.
- B. Palenik, F. M. M. Morel, *Limnol. Oceanogr.* **33**, 1606 (1988).
- A. L. Rose, E. A. Webb, T. D. Waite, J. W. Moffett, *Environ. Sci. Technol.* **42**, 2387 (2008).
- S. P. Hansard, A. W. Vermilyea, B. M. Voelker, *Deep Sea Res. Part I Oceanogr. Res. Pap.* **57**, 1111 (2010).
- A. W. Vermilyea, T. C. Dixon, B. M. Voelker, *Environ. Sci. Technol.* **44**, 3066 (2010).
- I. Fridovich, *Annu. Rev. Biochem.* **44**, 147 (1975).
- T. Oda et al., *Biosci. Biotechnol. Biochem.* **61**, 1658 (1997).
- A. B. Kustka, Y. Shaked, A. J. Milligan, D. W. King, F. M. M. Morel, *Limnol. Oceanogr.* **50**, 1172 (2005).
- J. A. Marshall, M. de Salas, T. Oda, G. Hallegraeff, *Mar. Biol.* **147**, 533 (2005).
- A. L. Rose, T. P. Salmon, T. Lukondeh, B. A. Neilan, T. D. Waite, *Environ. Sci. Technol.* **39**, 3708 (2005).
- Materials and methods are available as supplementary materials on Science Online.
- A. L. Rose, J. W. Moffett, T. D. Waite, *Anal. Chem.* **80**, 1215 (2008).
- A. Buchan, J. M. González, M. A. Moran, *Appl. Environ. Microbiol.* **71**, 5665 (2005).
- D. Kim et al., *Biochim. Biophys. Acta* **1524**, 220 (2000).
- K. Bedard, B. Lardy, K. H. Krause, *Biochimie* **89**, 1107 (2007).
- F. V. Minibayeva, L. K. Gordon, O. P. Kolesnikov, A. V. Chasov, *Protoplasma* **217**, 125 (2001).
- M. M. Huycke et al., *Mol. Microbiol.* **42**, 729 (2001).
- S. Korshunov, J. A. Imlay, *J. Bacteriol.* **188**, 6326 (2006).
- P. C. Lin, K. Türk, C. C. Höse, G. Fritz, J. Steuber, *J. Bacteriol.* **189**, 3902 (2007).
- J. C. Yuan, A. M. Shiller, *Geophys. Res. Lett.* **31**, L01310 (2004).
- J. C. Yuan, A. M. Shiller, *Deep Sea Res. Part II Top. Stud. Oceanogr.* **48**, 2947 (2001).
- B. N. Orcutt, J. B. Sylvan, N. J. Knab, K. J. Edwards, *Microbiol. Mol. Biol. Rev.* **75**, 361 (2011).
- M. I. Heller, P. Croot, *Oceans* **115**, C12038 (2010).
- K. O. Buesseler et al., *Science* **316**, 567 (2007).
- C. Chen et al., *EcoHealth* **5**, 399 (2008).

Acknowledgments: This study was supported by the National Science Foundation under grants OCE-1129594, OCE-1131734, EAR-1024817, and EAR-1025077 and by the Radcliffe Institute for Advanced Study at Harvard University and the Ford Foundation Fellowship Program. We thank E. D. Ingall for manuscript comments, D. W. King for technical assistance, and the thoughtful comments of four anonymous reviewers. We also thank the following individuals for contributing bacterial isolates for analysis in this study: H. Ehrlich, D. Emerson, S. Fendorf, Y. Masue-Slowey, T. Mincer, M. A. Moran, B. Tebo, R. Belas, and A. Templeton. The GenBank accession numbers for 16S ribosomal RNA (rRNA) gene sequences generated in this study are as follows: *Bacillus* sp. AzsLept-1c, JX515653; *Tencibaculum* sp. UAzPsLept-5, JX515654; *Marinobacter* sp. AzsAc-4c, JX515655; *Marinobacter* sp. AzsAc-4, JX515656; *Halomonas* sp. VMm1-3c, JX515657; *Microbulbifer* sp. Hm1-1, JX515658; *Paracoccus* sp. HJAc-3c, JX515659; *Alteromonas* sp. BIII82, JX524853; *Alteromonas* sp. BIII45, JX524854; *Pseudalteromonas* sp. SSW22, JX524855; *Marinobacter* sp. LCB-12, JX524856; *Halomonas* sp. LOB-22, JX524857; and *Citirella* sp. LOB-21, JX524858.

Supplementary Materials

www.sciencemag.org/cgi/content/full/science.1237331/DC1
Materials and Methods
Figs. S1 to S6
Tables S1 to S8
References (31–51)

4 March 2013; accepted 17 April 2013

Published online 2 May 2013;

10.1126/science.1237331

Structural Basis for Effector Control and Redox Partner Recognition in Cytochrome P450

Sarvind Tripathi, Huiying Li, Thomas L. Poulos*

Cytochromes P450 catalyze a variety of monooxygenase reactions that require electron transfer from redox partners. Although the structure of many P450s and a small handful of redox partners are known, there is very little structural information available on redox complexes, thus leaving a gap in our understanding on the control of P450–redox partner interactions. We have solved the crystal structure of oxidized and reduced P450cam complexed with its redox partner, putidaredoxin (Pdx), to 2.2 and 2.09 angstroms, respectively. It was anticipated that Pdx would favor closed substrate-bound P450cam, which differs substantially from the open conformer, but instead we found that Pdx favors the open state. These new structures indicate that the effector role of Pdx is to shift P450cam toward the open conformation, which enables the establishment of a water-mediated H-bonded network, which is required for proton-coupled electron transfer.

Cytochromes P450 catalyze the oxidation of organic compounds, including drugs that require electron transfer to the P450 heme via a redox partner (Fig. 1A). Bacterial P450cam serves as a paradigm for P450 structure-function studies, including electron transfer (1). The supporting redox partners are the flavin adenine dinucleotide (FAD)-containing putidaredoxin reductase (Pdr) that shuttles the reduced form of nicotinamide adenine dinucleotide (NADH)-derived

electrons to the Fe_2S_2 center of putidaredoxin (Pdx) and Pdx that in turn delivers electrons to P450cam (Fig. 1A). The crystal structures of all three components (2–4) and the Pdr-Pdx complex are known (5), leaving the P450cam-Pdx complex as the final structure to be solved in the P450cam system. Pdx serves an effector role (6–9) by inducing structural changes in P450cam required for activity, although the details of these changes has remained unknown. Modeling studies (10) indicate that Pdx binds to the proximal side of the P450cam heme opposite from where substrate binds (Fig. 1B), yet various spectroscopic methods (11–16) show that Pdx binding results in changes in the substrate binding pocket. Therefore, Pdx binding on one side of the heme results

in changes that are transmitted to the opposite side of the heme. Some of these Pdx-induced changes defined by means of nuclear magnetic resonance (NMR) (16) include regions of P450cam that experience a large conformational change in going from the substrate-bound to -free structures, resulting in exposure of the active site (Fig. 1B) (17). It is likely that most P450s exhibit these extremes of closed substrate-bound and open substrate-free conformers.

Redox complexes are difficult to crystallize, and only two structures of P450 redox complexes are known (18, 19). We thus turned to site-specific covalent cross-linking as a method for trapping transient redox complexes (5, 20). A P450cam-Pdx model (10) served as the starting point for the design of cross-linking sites (fig. S1) and suggested that conversion of Lys^{344} to Cys in P450cam might cross-link with Cys^{73} in Pdx by using homobifunctional maleimides (fig. S1). The mutant P450cam retained full enzyme activity, and 1,6-bismaleimido-hexane generated a 1:1 covalent complex in sufficient yield and purity for crystallization. The complex crystallized in the presence of excess camphor, enabling the structure to be solved to 2.15 Å resolution (table S1), and we refer to this structure as complex 1.

Unexpectedly, $\text{Pdx}_{\text{Cys}^{73}}$ cross-linked with $\text{P450cam}_{\text{His}^{355}}$ rather than $\text{P450cam}_{\text{Cys}^{344}}$ (fig. S2), and P450cam adopted the open substrate-free conformation with no substrate bound and water coordinated to the heme iron (fig. S3). His^{355} would be inaccessible to such chemistry in the closed state but would be available in the open state. Because we were concerned that the cross-linking chemistry may have perturbed the protein-protein interface, we used the complex 1 structure

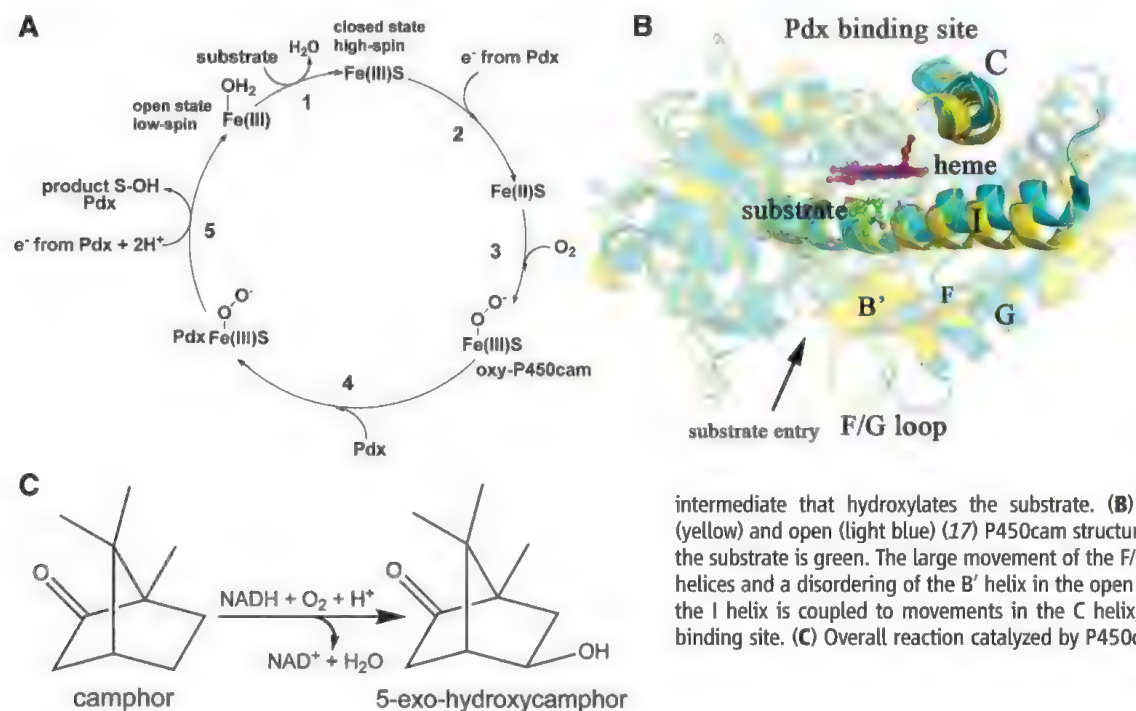


Fig. 1. Overall P450 mechanism and a comparison of the open and closed P450cam structures. (A) Substrate binding shifts P450cam from low to high spin followed by electron transfer from Pdx and O_2 binding. Step 5, the second electron transfer event, is where Pdx exerts its effector role. The binding of Pdx results in a structural switch in P450cam required for O_2 activation, leading to cleavage of the O-O bond, which leaves behind the reactive Fe(IV)=O

intermediate that hydroxylates the substrate. (B) Superposition of the closed (yellow) and open (light blue) (17) P450cam structures. The heme is in purple, and the substrate is green. The large movement of the F/G loop connecting the F and G helices and a disordering of the B' helix in the open state are shown. Movement of the I helix is coupled to movements in the C helix, which forms part of the Pdx binding site. (C) Overall reaction catalyzed by P450cam.

Departments of Molecular Biology and Biochemistry, Pharmaceutical Sciences, and Chemistry, University of California, Irvine, Irvine, CA, 92697–3900, USA.

*Corresponding author. E-mail: poulos@uci.edu

to design a second cross-linking site that involves only surface residues removed from the inter-protein interface but close enough to cross-link with the available maleimides. Asp¹⁹ in Pdx was mutated to Cys, which cross-linked with Lys³⁴⁴Cys in P450cam in good yields (Fig. 2A) and generated the spectral properties characteristic of P450s (Fig. 2B). Complex 2 also crystallized, and the structure was solved to 2.2 Å (table S1).

Complex 2 was also in the open state, and Pdx binds the same in both complexes (fig. S4), making it unlikely that the cross-linking chemistry is the cause of P450cam adopting the open conformation. We also treated complex 2 crystals with dithionite so as to reduce both proteins and solved this structure to 2.09 Å (table S1).

Because Pdx shifted P450cam to the open state, we wanted to determine whether Pdx does

the same in solution. The open conformer exhibits a low-spin spectrum owing to water coordination to the heme iron, and the cross-linked complex also exhibits a low-spin spectrum (Fig. 2B). Moreover, the addition of free Pdx to the free P450cam mutant shifts the spectrum from high- to low-spin (Fig. 2C), which is consistent with earlier studies (21). Thus, the spectral properties of cross-linked complex 2 are similar to the

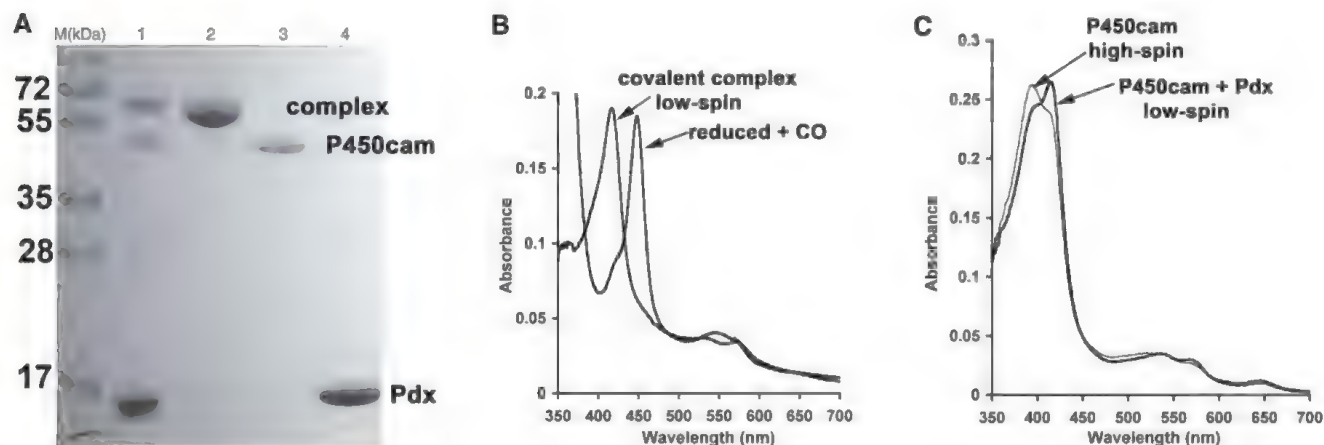
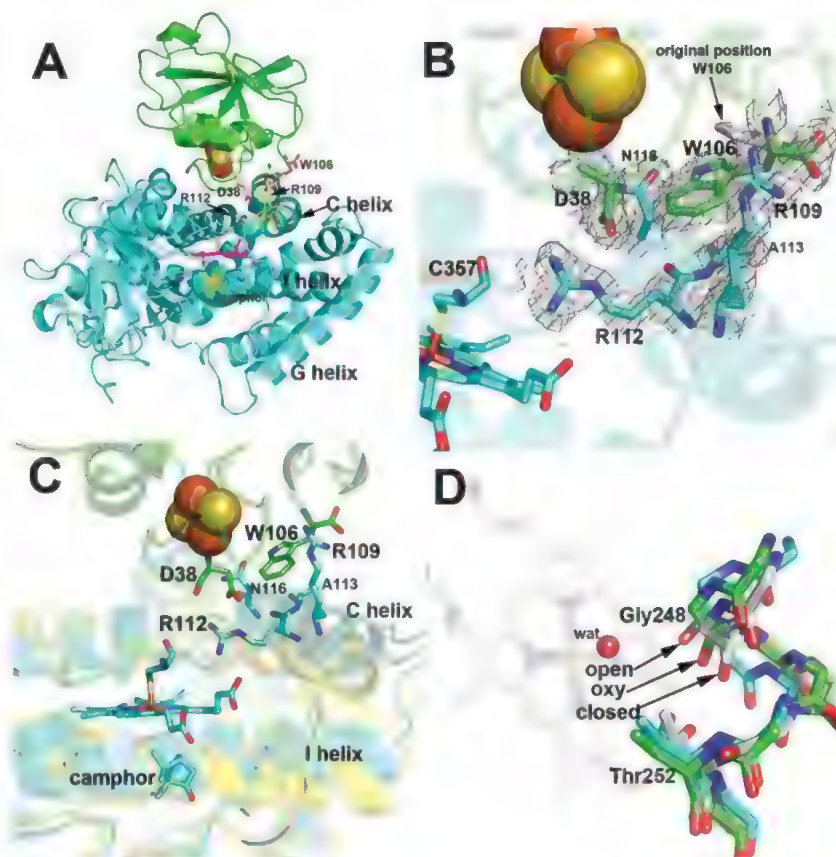


Fig. 2. Cross-linking chemistry and spectroscopy. (A) SDS gel of the cross-linked complex. Lane 1, after cross-linking with Pdx in a 10-fold excess; lane 2, purified complex; lane 3, P450cam; lane 4, Pdx. (B) Spectra of the purified oxidized covalent complex before and after reduction in the presence of carbon monoxide. The 450-nm band is characteristic of active P450 with the

expected Cys thiolate ligation. The oxidized spectrum is low-spin, even though 1 mM camphor was included. (C) Spectra of the P450cam mutant used for cross-linking in the absence and presence of a 10-fold excess of Pdx. Pdx shifts P450cam toward the low-spin state, which is consistent with earlier studies (21) and consistent with the P450cam-Pdx crystal structure.

Fig. 3. Structure of the P450cam-Pdx complex. (A) Structure of the P450cam-Pdx complex (light blue, P450cam; green, Pdx). (B) 2Fo-Fc electron density contoured at 1.0σ at the intermolecular interface. Pdx_{Trp106} forms nonbonded contacts with P450cam_{Ala113} and an H-bond with P450cam_{Asn116} that requires Pdx_{Trp106} to adopt a new rotamer conformation. P450cam_{Arg112} interacts with Pdx_{Asp38}. (C) Structural differences at the interface between the closed (yellow) and open (light blue) P450cam structures. The C helix moves up to better interact with Pdx. This movement toward Pdx is coupled with movements in the I, B', F, and G helices, which results in an opening of the active site. (D) The I helix region in the closed, oxy, and open (P450cam-Pdx complex) conformations of P450cam. In the closed substrate-bound state, the peptide carbonyl group of Gly²⁴⁸ accepts an H-bond from Thr²⁵², which weakens when O₂ binds and Gly²⁴⁸ moves away from Thr²⁵² and closer to O₂. This widens the I helix groove, which enables water molecules to enter the active site, where they participate in an H-bonded network required for promoting O-O bond cleavage. In the open conformation, Gly²⁴⁸ moves even closer to the iron, where it now can H-bond with the water coordinated to the heme iron. Thus, the I helix conformation in the oxy state is between the closed and open conformers.



noncovalent P450cam-Pdx complex, indicating that in solution, Pdx shifts P450cam to the open low-spin state, as has been previously observed (27). As expected from the spectroscopy, the structure shows that substrate is not bound, and a water molecule coordinates the heme iron (fig. S3). During turnover with excess reduced Pdx, however, the reduced and oxygenated forms of P450cam will dominate and not the oxidized low-spin form. Therefore, we also solved the structure of complex 2 reduced with dithionite. The reduced structure had either substrate, camphor, or product—5-exo-hydroxycamphor—remaining bound and thus represents the active form of the complex. In what follows, we focus on the reduced complex 2 structure.

As expected, Pdx binds on the proximal side of P450cam (Fig. 3A). The protein-protein interface is well defined (Fig. 3B), and the complex is missing only the first nine residues in P450cam. Key residues that were predicted to be involved in complex formation (22–24) in P450cam indeed form close contacts with Pdx. On the Pdx side,

two key residues are Pdx_{Asp38} and the C-terminal Pdx_{Trp106}. Pdx_{Asp38} (Fig. 3B) ion pairs with P450cam_{Arg112}, whereas Pdx_{Trp106} forms nonbonded interactions with P450cam_{Ala113} and an H-bond with P450cam_{Asn116}, which requires that Pdx_{Trp106} adopt a new rotamer conformation (Fig. 3B). In addition, P450cam_{Arg109} interacts with the Pdx_{Trp106} carboxyl group. A list of specific contacts that are consistent with mutagenesis work summarized in (24) is provided in table S2, and a possible electron transfer route is illustrated in fig. S5.

There is little change in the Pdx backbone, but in contrast, P450cam adopts the open conformation, which requires large movements involving both the Pdx docking site and the substrate access channel. The Pdx_{Asp38}-P450cam_{Arg112} ion pair requires little motion, but interactions involving Pdx_{Trp106} do. The C helix must move up toward Pdx by about 2 to 3 Å in order for Pdx_{Trp106} to form nonbonding interactions with P450cam_{Ala113} and H-bonds with P450cam_{Asn116} and P450cam_{Arg109}. Interactions involving Pdx_{Trp106} thus are critical to the closed-to-open conformational change of

P450cam. It has been known for some time that Pdx_{Trp106} is critical to the effector role of Pdx (8) and that Trp106 is especially important for the second electron transfer step (Fig. 1A) (25), in which Pdx exerts its effector function. As shown in Fig. 3C, this C helix movement up toward Pdx is coupled to movements in the I, B', F, and G helices, which opens the active site to bulk solvent.

The reduced crystals have four complex 2 molecules in the asymmetric unit, and there is clear evidence that in three of the molecules, camphor has been hydroxylated to give the product, 5-exo-hydroxycamphor (Fig. 4), whereas one complex 2 molecule has camphor bound (Fig. 4B). Although precautions were taken to remain anaerobic, crystals were rapidly frozen outside the anaerobic chamber, which may well have resulted in some exposure to O₂, thus enabling electron transfer and product formation to occur in the crystal, probably during data collection. That we observe product shows that the complex in the crystalline state is active in both electron transfer and substrate hydroxylation. As shown in Fig. 4, each molecule in the asymmetric unit provides a slightly different snapshot of the active site. A second camphor molecule binds in the open substrate access channel, and Tyr⁹⁶, which normally donates an H-bond to camphor, swings out of the active site in one of the molecules, allowing it to H-bond with the second camphor molecule (Fig. 4D). Tyr⁹⁶ thus may serve a gateway function in substrate binding and product release.

Pdx binding also promotes changes in the I helix, where the O₂ binds. The I helix regions near the O₂ binding site in closed P450cam, the P450cam-Pdx open structure, and oxy structures are compared in Fig. 3D (26, 27). When oxygen binds, the Gly²⁴⁸-Thr²⁵² H-bond weakens, and Gly²⁴⁸ moves closer to O₂, which widens the I helix groove, enabling catalytic waters to enter the active site in order to establish a proton relay network required for O-O bond heterolysis (26, 27). The I helix position in the oxy conformer is about midway between the closed and open structures, indicating that the closed-to-open motion passes through the oxy conformation. We propose that Pdx favors binding to the more open form of oxy-P450cam, which enables establishment of the water-mediated H-bonded network required for proton-coupled electron transfer and O₂ activation. Part of the catalytic machinery that also comes into play when Pdx binds includes Asp²⁵¹, which is critical for activity and has been proposed to shuttle protons from solvent to dioxygen (28). However, in the closed conformation Asp²⁵¹ cannot serve this function because it is tied up with salt bridges to Lys and Arg residues, but when Pdx binds, these salt bridges are broken, thus freeing Asp²⁵¹ to serve in the proton relay network (fig. S6).

References and Notes

1. M. Katagiri, B. N. Ganguli, I. C. Gunsalus, *J. Biol. Chem.* **243**, 3543 (1968).
2. T. L. Poulos, B. C. Finzel, A. J. Howard, *J. Mol. Biol.* **195**, 687 (1987).

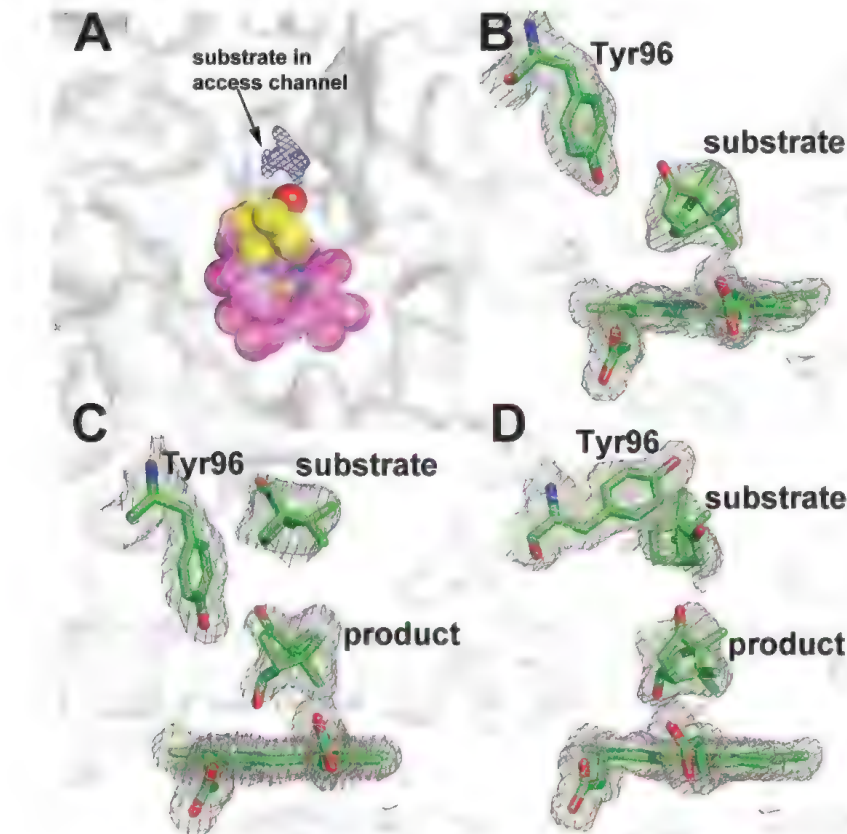


Fig. 4. Structure of the active site region of P450cam in the reduced P450cam-Pdx complex 2. Substrate binding sites in three of the complex molecules in the asymmetric unit, showing (A) Fo-Fc contoured at 3.0 σ and (B to D) 2Fo-Fc omit maps—where the substrate/product were not included in the structure factor calculation—contoured at 1.0 σ . (A) The complex with substrate bound showing the open access channel. The lobe of electron density above the camphor is most likely a second camphor molecule but is not sufficiently well defined to justify modeling in substrate. (B) The complex with camphor bound. The active site is open, but Tyr⁹⁶ remains in place and donates an H-bond to the substrate. [(C) and (D)] Molecules with product near the heme and substrate in the access channel. In (D), Tyr⁹⁶ adopts a new rotamer conformation, pointing out of the active site, where it can H-bond with the substrate bound in the access channel.

3. I. F. Sevioukova, C. Garcia, H. Li, B. Bhaskar, T. L. Poulos, *J. Mol. Biol.* **333**, 377 (2003).
4. I. F. Sevioukova, H. Li, T. L. Poulos, *J. Mol. Biol.* **336**, 889 (2004).
5. I. F. Sevioukova, T. L. Poulos, I. Y. Churbanova, *J. Biol. Chem.* **285**, 13616 (2010).
6. I. C. Gunsalus, J. R. Meeks, J. D. Lipscomb, *Ann. N. Y. Acad. Sci.* **212**, (1 Multienzyme S), 107 (1973).
7. J. D. Lipscomb, S. G. Sligar, M. J. Namtvedt, I. C. Gunsalus, *J. Biol. Chem.* **251**, 1116 (1976).
8. S. G. Sligar, P. G. Debrunner, J. D. Lipscomb, M. J. Namtvedt, I. C. Gunsalus, *Proc. Natl. Acad. Sci. U.S.A.* **71**, 3906 (1974).
9. C. A. Tyson, J. D. Lipscomb, I. C. Gunsalus, *J. Biol. Chem.* **247**, 5777 (1972).
10. T. C. Pochapsky, T. A. Lyons, S. Kazanis, T. Arakaki, G. Ratnaswamy, *Biochimie* **78**, 723 (1996).
11. S. Nagano *et al.*, *Biochemistry* **42**, 14507 (2003).
12. S. S. Pochapsky, T. C. Pochapsky, J. W. Wei, *Biochemistry* **42**, 5649 (2003).
13. Y. Shiro, T. Iizuka, R. Makino, Y. Ishimura, I. Morishima, *J. Am. Chem. Soc.* **111**, 7707 (1989).
14. T. Tosha *et al.*, *J. Biol. Chem.* **278**, 39809 (2003).
15. M. Unno *et al.*, *J. Biol. Chem.* **277**, 2547 (2002).
16. W. Zhang, S. S. Pochapsky, T. C. Pochapsky, N. U. Jain, *J. Mol. Biol.* **384**, 349 (2008).
17. Y. T. Lee, R. F. Wilson, I. Rupniewski, D. B. Goodin, *Biochemistry* **49**, 3412 (2010).
18. I. F. Sevioukova, H. Li, H. Zhang, J. A. Peterson, T. L. Poulos, *Proc. Natl. Acad. Sci. U.S.A.* **96**, 1863 (1999).
19. N. Strushkevich *et al.*, *Proc. Natl. Acad. Sci. U.S.A.* **108**, 10139 (2011).
20. M. Guo, B. Bhaskar, H. Li, T. P. Barrows, T. L. Poulos, *Proc. Natl. Acad. Sci. U.S.A.* **101**, 5940 (2004).
21. M. Unno *et al.*, *J. Am. Chem. Soc.* **119**, 6614 (1997).
22. H. Koga *et al.*, *FEBS Lett.* **331**, 109 (1993).
23. K. Nakamura *et al.*, *Biochim. Biophys. Acta* **1207**, 40 (1994).
24. H. Shimada, S. Nagano, H. Hori, Y. Ishimura, *J. Inorg. Biochem.* **83**, 255 (2001).
25. V. Y. Kuznetsov *et al.*, *J. Biol. Chem.* **280**, 16135 (2005).
26. S. Nagano, T. L. Poulos, *J. Biol. Chem.* **280**, 31659 (2005).
27. I. Schlichting *et al.*, *Science* **287**, 1615 (2000).
28. N. C. Gerber, S. G. Sligar, *J. Biol. Chem.* **269**, 4260 (1994).

Acknowledgments: This work was supported by NIH grant GM33688. Portions of this research were carried out at the Stanford Synchrotron Radiation Lightsource (SSRL), a Directorate of SLAC National Accelerator Laboratory and an Office of Science User Facility operated for the U.S.

Department of Energy (DOE) Office of Science by Stanford University. The SSRL Structural Molecular Biology Program is supported by the DOE Office of Biological and Environmental Research and by NIH, the National Institute of General Medical Sciences (NIGMS) (including P41GM103393), and the National Center for Research Resources (NCRR) (P41RR001209). The contents of this publication are solely the responsibility of the authors and do not necessarily represent the official views of NIGMS, NCRR, or NIH. We also acknowledge the Advanced Light Source supported by the Director, Office of Science, Office of Basic Energy Sciences, of the DOE under contract DE-AC02-05CH11231. We thank C. Goulding and A. Borovik for invaluable discussions and advice, D. Goodin for the low Cys P450cam expression plasmid, and Y. Meharennia for assistance in developing cross-linking protocols.

Supplementary Materials

www.sciencemag.org/cgi/content/full/340/6137/1227/DC1

Materials and Methods

Figs. S1 to S6

Tables S1 and S2

References (29–42)

29 January 2013; accepted 10 April 2013

10.1126/science.1235797

Role of Tissue Protection in Lethal Respiratory Viral-Bacterial Coinfection

Amanda M. Jamieson,^{1,2*} Lesley Pasman,^{1†} Shuang Yu,¹ Pia Gamradt,² Robert J. Homer,^{3,4} Thomas Decker,² Ruslan Medzhitov^{1*}

Secondary bacterial pneumonia leads to increased morbidity and mortality from influenza virus infections. What causes this increased susceptibility, however, is not well defined. Host defense from infection relies not only on immune resistance mechanisms but also on the ability to tolerate a given level of pathogen burden. Failure of either resistance or tolerance can contribute to disease severity, making it hard to distinguish their relative contribution. We employ a coinfection mouse model of influenza virus and *Legionella pneumophila* in which we can separate resistance and tolerance. We demonstrate that influenza virus can promote susceptibility to lethal bacterial coinfection, even when bacterial infection is controlled by the immune system. We propose that this failure of host defense is due to impaired ability to tolerate tissue damage.

Resistance and tolerance are two distinct strategies of host defense from infections: the former is based on pathogen detection and elimination, whereas the latter relies on host adaptation to a given level of pathogen burden (1–4). This distinction is important because infectious disease morbidity and mortality can be due to failed resistance or failed tolerance, which may, in turn, dictate different therapeutic options. Thus, a lethal outcome of

microbial infection is usually ascribed to either high pathogen virulence or low host resistance (for example, caused by immunosuppression or immunodeficiency). Pathogen virulence can be due to direct damage to the host by toxins and virulence factors (intrinsic virulence) or, more commonly, due to excessive inflammatory response with collateral tissue damage (extrinsic virulence). However, insufficient tissue protection and repair could also be an important contributor to infectious disease phenotypes (4).

The upper respiratory tract is exposed to numerous pathogens simultaneously, and viral-bacterial coinfection in the lung is a common clinical manifestation [reviewed in (5–8)]. Complications from secondary bacterial infection are a leading cause of morbidity and mortality associated with influenza virus infection (5–8). Influenza virus can suppress the immune response to a bacterial infection, which can lead to increased bacterial load and decreased survival. This has been shown in both clinical studies and mouse models for multiple bacterial pathogens,

including *Streptococcus pneumoniae*, *Haemophilus influenzae*, *S. pyogenes*, and *Staphylococcus aureus* [reviewed in (5–8)]. Bacterial overgrowth in these models complicates the analysis of other possible causes of morbidity and mortality. Therefore, we sought an alternative model of coinfection lacking this complication.

Legionella pneumophila has recently been recognized as a clinically relevant complication of influenza virus infection (9). When mice were infected with a sublethal dose of influenza virus and then coinfecting with a sublethal dose of *L. pneumophila*, 100% of coinfecting mice died within 1 week of coinfection, whereas all mice survived single infections (Fig. 1A). An established viral infection was necessary for lethality, because mice infected with influenza at the same time or 3 days after infection with *L. pneumophila* survived coinfection (Fig. 1A). A resolved influenza virus infection no longer affected the ability to survive coinfection with *L. pneumophila*, because mice infected with bacteria 10 or 14 days after viral infection also survived (Fig. 1A). The mice coinfecting with *L. pneumophila* 3 days after influenza virus infection also had other signs of morbidity, including decreased body weight and temperature (Fig. 1, B and C).

Importantly, despite the dramatic difference in host survival, there was no significant difference in the viral or bacterial pathogen burden after single infections or coinfections (Fig. 1, D and E). Moreover, there was no detectable systemic dissemination of influenza or *L. pneumophila* after infections (fig. S1). These results indicate that lethal synergy between influenza virus and *L. pneumophila* was not due to impaired resistance to either of these pathogens. This is in contrast to coinfections with influenza virus and opportunistic bacterial pathogens where bacterial overgrowth and systemic dissemination are commonly observed (5–8, 10–13).

¹Howard Hughes Medical Institute and Department of Immunobiology, Yale University School of Medicine, New Haven, CT 06520, USA. ²Max F. Perutz Laboratories, University of Vienna, Dr. Bohr Gasse 9/4 A-1030 Vienna, Austria. ³Department of Pathology, Yale University School of Medicine, New Haven, CT 06520, USA. ⁴VA Connecticut Healthcare System Pathology and Laboratory Medicine Service, 950 Campbell Avenue, West Haven, CT 06516, USA.

*Corresponding author. E-mail: ruslan.medzhitov@yale.edu (R.M.); amanda_jamieson@brown.edu (A.M.J.)

†Present address: Department of Molecular Microbiology and Immunology, Brown University, 171 Meeting Street, Providence, RI 02912, USA.

‡These authors contributed equally to this work.

Fig. 1. Decreased tolerance with unchanged resistance of mice coinfecting with influenza virus and *L. pneumophila*. (A) Survival of mice infected intranasally with 300 plaque-forming units (PFUs) of influenza virus and 0, 3, 6, 10, or 14 days (d) later with 1×10^6 *L. pneumophila*. To better mirror a human infection, mice were infected with a strain of *L. pneumophila* lacking the *flaA* gene (JR32Δ*flaA*), which encodes flagellin. (B) Weight of mice infected with influenza virus or *L. pneumophila* alone or coinfecting 3 days after influenza virus. (C) Body temperature of mice coinfecting 3 days after influenza virus compared with the singly infected controls. (D) Lung bacterial load in mice coinfecting 3 days after influenza virus or mice infected with *L. pneumophila* alone. Day 0 indicates colony-forming units (CFUs) in the lung 1 hour after infection. (E) Lung viral load in mice coinfecting 3 days after influenza virus or mice infected in influenza virus alone. (F) Survival of mice coinfecting 3 days after influenza virus infection with LP01Δ*dotA* or the thymidine auxotroph LP02 strains of *L. pneumophila*. (G) Survival of mice coinfecting 3 days after infection with inactivated (IA) influenza virus. Data are combined from at least three independent experiments with at least five mice in each group (* $P \leq 0.05$; ** $P \leq 0.001$). Data were analyzed with the logrank test, generalized linear model, or analysis of variance (ANOVA). Error bars represent SD from the mean.

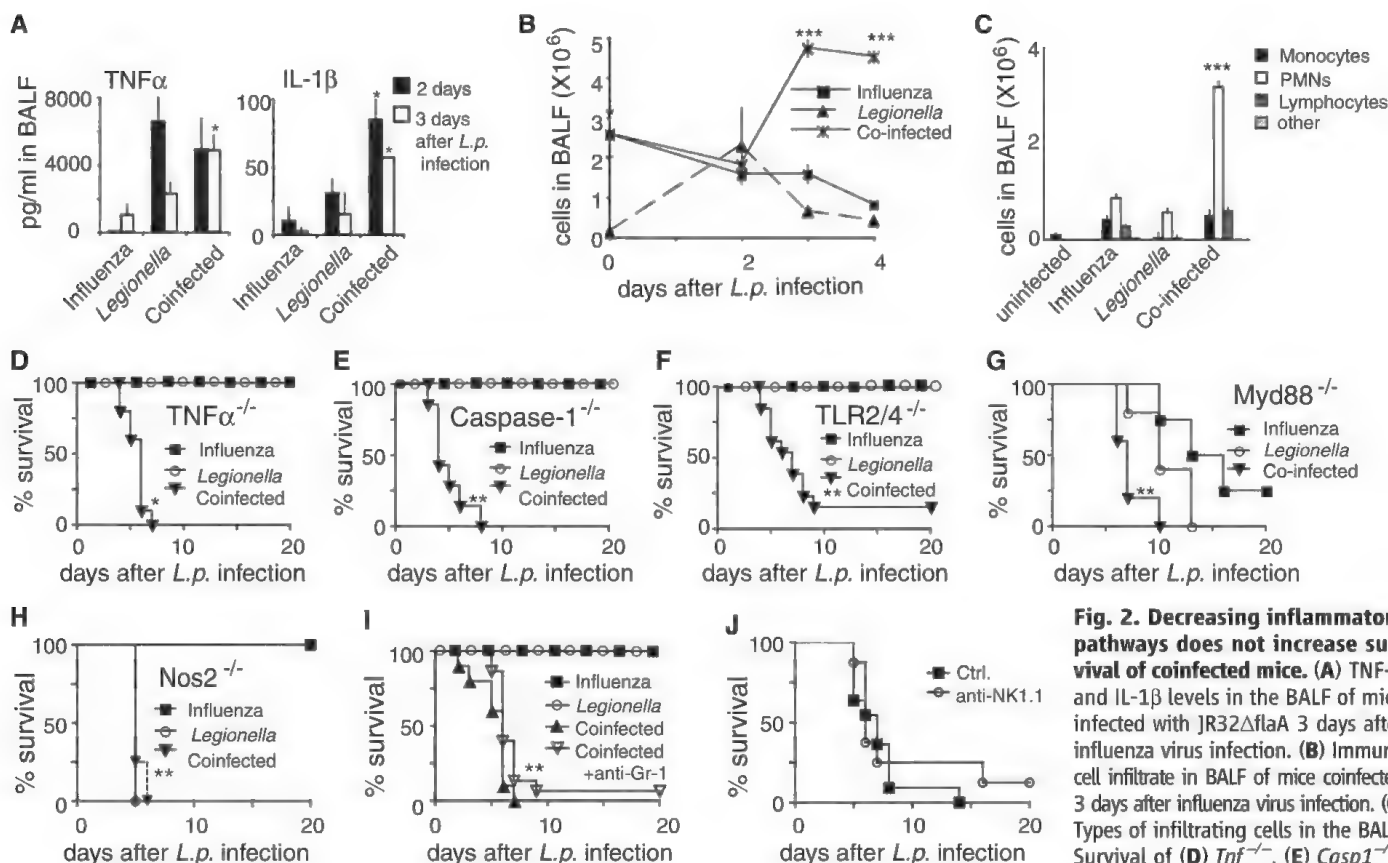
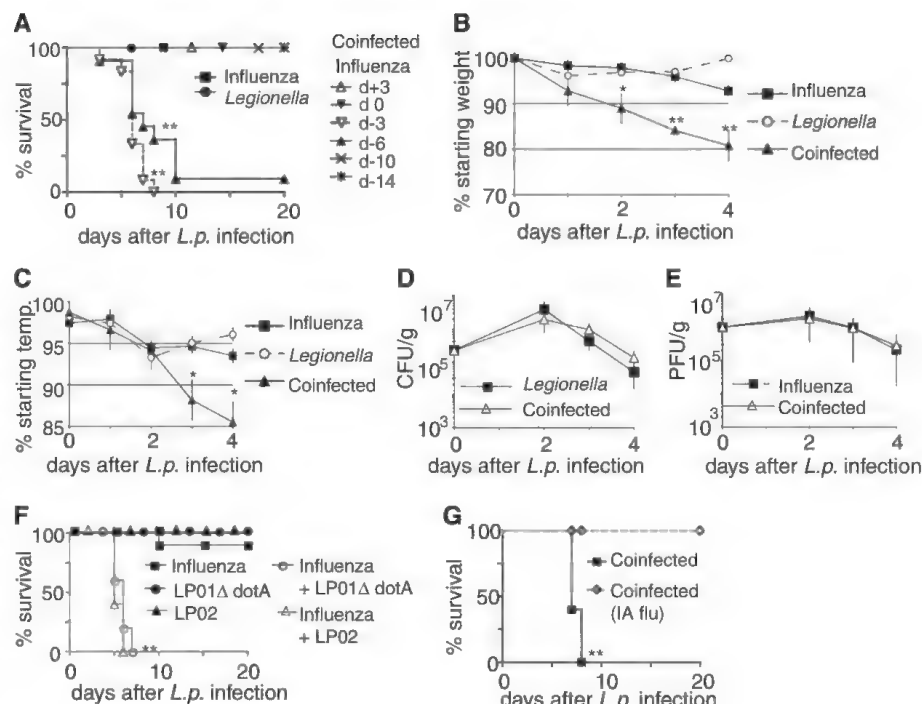


Fig. 2. Decreasing inflammatory pathways does not increase survival of coinfecting mice. (A) TNF-α and IL-1β levels in the BALF of mice infected with JR32Δ*flaA* 3 days after influenza virus infection. (B) Immune cell infiltrate in BALF of mice coinfecting 3 days after influenza virus infection. (C) Types of infiltrating cells in the BALF. Survival of (D) *Tnf*^{-/-}, (E) *Casp1*^{-/-}, (F) *Tlr2*^{-/-}*Tlr4*^{-/-}, (G) *Myd88*^{-/-}, (H) *Nos2*^{-/-}, (I) Gr-1-depleted, and (J) NK1.1-depleted mice coinfecting 3 days after infection with influenza virus compared with singly infected controls (Ctrl.). Data are combined from at least three independent experiments with at least five mice in each group (* $P \leq 0.05$; ** $P \leq 0.001$; *** $P \leq 0.0001$). Data were analyzed with the logrank test, *t* test, or ANOVA. Error bars represent SD from the mean.

Nos2^{-/-}, (I) Gr-1-depleted, and (J) NK1.1-depleted mice coinfecting 3 days after infection with influenza virus compared with singly infected controls (Ctrl.). Data are combined from at least three independent experiments with at least five mice in each group (* $P \leq 0.05$; ** $P \leq 0.001$; *** $P \leq 0.0001$). Data were analyzed with the logrank test, *t* test, or ANOVA. Error bars represent SD from the mean.

To further address the role of pathogen virulence, we used an attenuated mutant strain of *L. pneumophila*, which lacks the Dot/Icm type IV secretion system and is therefore unable to secrete virulence factors (14). Administration of *dotA* mutant or thymidine auxotroph (LP02) *L. pneumophila*, which are severely attenuated in vivo, still resulted in 100% mortality of coinfected mice (Fig. 1F and fig. S2) (14). These results indicate that bacterial virulence or growth is not essential for lethal synergy of influenza-*L. pneumophila* coinfection. Furthermore, mortality is unlikely to be due to failed immune resistance. However, administration of formalin-inactivated influenza virus did not synergize with the subsequent *L. pneumophila* coinfection (Fig. 1G), indicating that a productive virus infection is necessary to make the host sensitive to secondary bacterial infection. Moreover, treatment of mice with neuraminidase inhibitors (NAIs) increased survival and decreased weight loss and hypothermia after coinfection (fig. S3, A to C), presumably because NAIs suppressed viral load (fig. S3D) (15).

We next examined whether mortality of influenza-*L. pneumophila* coinfection was due to excessive inflammatory response. Influenza virus activates three innate immune signaling pathways: the (i) Toll-like receptor-MyD88, (ii) RIG-I-interferon- α/β , and (iii) Nlrp3-caspase-1-interleukin-1 pathways (TLR, Toll-like receptor; IFN, interferon; IL, interleukin) (16, 17).

L. pneumophila is recognized by the innate immune system via several mechanisms, including the Naip5/Birc1e-dependent pathway, which requires an intact Dot/Icm secretion system, and TLRs (18–22). Gene expression analysis of the lungs after single infection and coinfection indicated that some of the inflammatory genes, including tumor necrosis factor- α (TNF- α), nitric oxide synthase 2 (Nos2), and several chemokines, were expressed at higher levels in coinfection compared with single-infected mice (fig. S4). TNF- α and IL-1 β protein levels were also elevated in the broncho-aveolar lavage fluid (BALF) at day 3 after coinfection (Fig. 2A). Moreover, there was a significant increase in neutrophil infiltration in the lungs of coinfection mice compared with singly infected controls (Fig. 2, B and C). TNF- α , IL-1 β , Nos2, and neutrophils are all known to play important roles in immunopathology, including in the context of influenza virus infection (23–25). However, we found that genetic deletions of TNF- α , caspase-1, MyD88, TLR2/4, and Nos2 or antibody-mediated depletion of neutrophils or natural killer cells did not rescue coinfection mice from mortality (Fig. 2, D to J). Similarly, *Rag2*^{-/-} mice, which lack an adaptive immune system, also succumbed to lethal coinfection, indicating that lymphocyte-mediated immunopathology is not essential for the lethal outcome of coinfection (fig. S5A). Virus-induced IFN- α/β can interfere with antibacterial responses (26). However, IFN- α/β re-

ceptor (IFNAR)-deficient mice (*Ifnar1*^{-/-}) were still susceptible to coinfection (fig. S5B). *Rag2* and IFNAR knockout mice were also susceptible to influenza infection alone, *Nos2*^{-/-} mice were susceptible to infection with *L. pneumophila* alone, and *Myd88*^{-/-} mice were susceptible to both single infections. However, in all cases, the mortality from coinfections was kinetically distinguishable from that from single infections and was similar to the mortality kinetics of wild-type (WT) mice (Figs. 1A and 2, D to J, and fig. S5, A and B). Finally, systemic treatment of the mice with synthetic glucocorticoid dexamethasone or antioxidant *N*-acetyl cysteine did not rescue them from mortality of coinfection (fig. S5, C and D). Collectively, the elimination of all major immune and inflammatory pathways triggered by either the viral or bacterial infection did not rescue the lethal synergy. These results suggest that the lethal outcome of coinfection in our model was not solely due to excessive inflammatory response or immunopathology.

Because neither bacterial growth or virulence nor host immune responses were individually required to cause lethality in coinfection, we next combined host immunodeficiency and bacterial attenuation. We used a severely attenuated *L. pneumophila* strain LP02 Δ dotA Δ flaA, which lacks flaA and dotA and is also a thymidine auxotroph (27). This strain lacks flagellin and is unable to replicate and secrete effectors, thus lacking major immunostimulatory factors, except

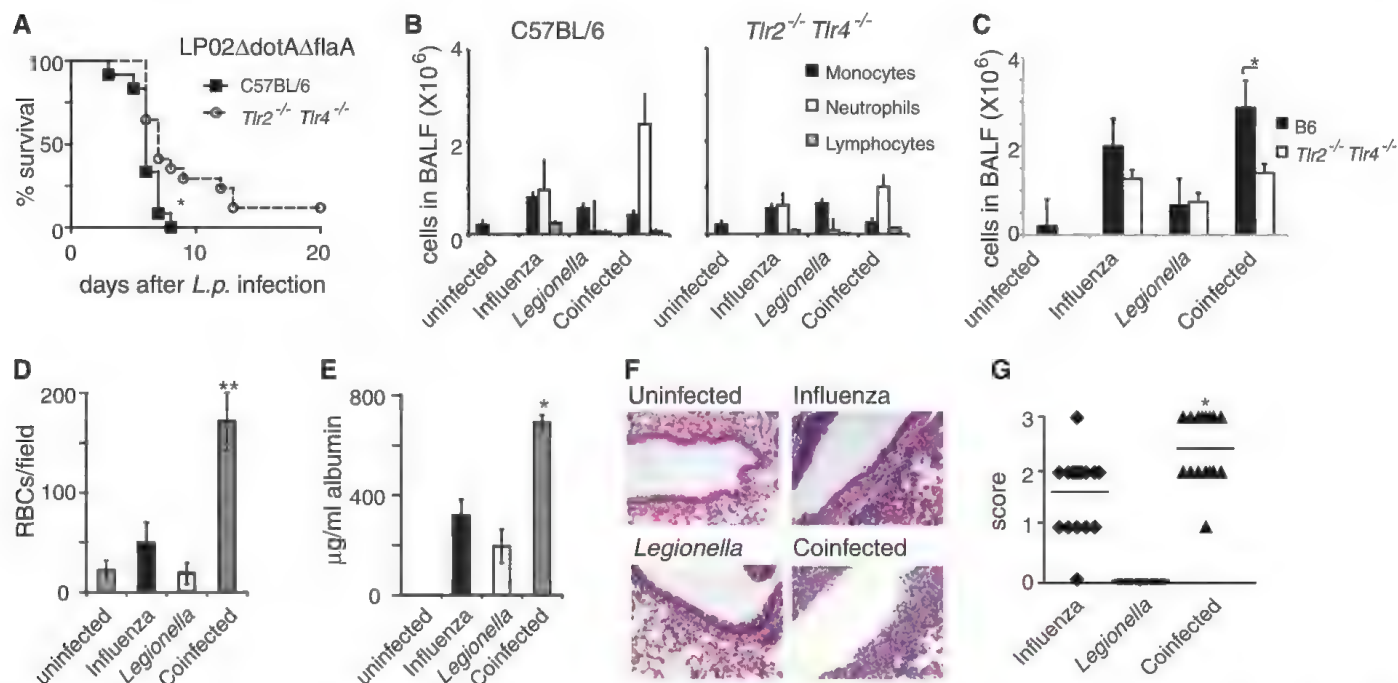


Fig. 3. Increased tissue damage in coinfection lungs. (A) Survival of *Tlr2*^{-/-}/*Tlr4*^{-/-} and C57BL/6 mice coinfection with the LP02 Δ dotA Δ flaA strain of *L. pneumophila*. (B) Types of infiltrating cells in BALF of *Tlr2*^{-/-}/*Tlr4*^{-/-} and C57BL/6 mice coinfection with strain LP02 Δ dotA Δ flaA 3 days after influenza virus infection. (C) Amount of infiltrating immune cells in BALF of *Tlr2*^{-/-}/*Tlr4*^{-/-} and C57BL/6 mice coinfection with strain LP02 Δ dotA Δ flaA 3 days after influenza virus infection. (D) Red blood cells (RBCs) and (E) albumin in the BALF day 4

after bacterial infection in C57BL/6 mice infected with influenza virus and 3 days later with the JR32 Δ flaA strain. (F) Representative images of airways and (G) histological damage scoring of lung sections 4 days after bacterial infection from C57BL/6 mice infected with influenza virus and 3 days later with the JR32 Δ flaA strain. Data are combined from at least three independent experiments with at least five mice in each group (**P* ≤ 0.05; ***P* ≤ 0.001). Data were analyzed using the logrank test, *t* test, or ANOVA. Error bars represent SD from the mean.

for cell-wall components detectable by TLR2 and TLR4. Therefore, we used this strain to coinfect TLR2/TLR4 double-deficient mice. *Tlr2*^{-/-}/*Tlr4*^{-/-} mice coinfecting with influenza virus and LP02ΔdotAΔflaA had a small increase in survival compared with WT mice infected with the same strain of bacteria (Fig. 3A); however, most mice still succumbed to coinfection. *Tlr2*^{-/-}/*Tlr4*^{-/-} mice coinfecting with LP02ΔdotAΔflaA had decreased immune cell infiltrate into the BALF at day 3 after infection, when compared with C57BL/6 mice infected with either LP02ΔdotAΔflaA or Jr32ΔflaA (Figs. 2, B and C, and 3, B and C). Thus, severely attenuated, nonreplicating *L. pneumophila* still caused mortality in coinfecting *Tlr2*^{-/-}/*Tlr4*^{-/-} mice, despite almost a complete lack of immunostimulatory signals.

The lethal outcome of influenza-*L. pneumophila* coinfection, despite normal control of pathogen growth, suggests that the mortality could be due to a failed tolerance to tissue damage caused by coinfection. Coinfected mice had high levels of red blood cells and albumin in the BALF (Fig. 3, D and E), indicating a damage to the lung

epithelial-capillary barrier (28). The lung epithelial damage was further confirmed by histological analysis (Fig. 3, F and G). The principal difference among the singly infected and coinfecting mice was in the degree of airway epithelial necrosis, with the coinfecting lungs having a significant increase in epithelial cell damage. Extensive damage to the airway epithelia, with secondary alveolar collapse (Fig. 3, D to G), is presumably responsible for the mortality of the coinfection.

Consistent with the histological evidence of lung tissue damage, a gene expression analysis revealed that a cohort of genes involved in tissue protection and repair was specifically down-regulated in coinfecting compared with singly infected or uninfected mice. This cohort included genes that are essential for tissue and cellular repair and development in the lung, such as *Mdk*, *Adams2*, *Timp4*, *Slpi*, *Mmp2*, *Mmp9*, *Vegfc*, *Itgb7*, and *Itga1* (29), as well as genes involved in stress response in lung tissue, such as *Gcnt2*, *Hif3a*, *Stra13*, *Hmox1*, and *Aifm1* (30) (fig. S6).

We next tested whether the defective expression of the tissue-repair program is responsi-

ble for mortality of coinfection. Amphiregulin (AREG), an epithelial growth factor family member, was recently found to contribute to tissue homeostasis in the lung during influenza infection (31). Although AREG did not have a significant effect in WT mice, administration of AREG to *Tlr2*^{-/-}/*Tlr4*^{-/-} mice coinfecting with influenza virus and the LP02ΔdotAΔflaA strain of *L. pneumophila* significantly increased survival while decreasing weight loss and hypothermia (Fig. 4, A to C). AREG treatment resulted in decreased lung damage, as indicated by histopathological analysis, decreased albumin level in the BALF, and decreased pulmonary infiltrate (Fig. 4, D to G). Importantly, AREG treatment significantly decreased mortality of coinfection (Fig. 4A) but did not affect the viral and bacterial burdens (Fig. 4, H and I). The reason AREG administration did not rescue WT mice from coinfection is likely because, in this case, the disease is too severe and may require a more optimal regimen of AREG administration or, perhaps, additional methods of promoting tissue protection and repair.

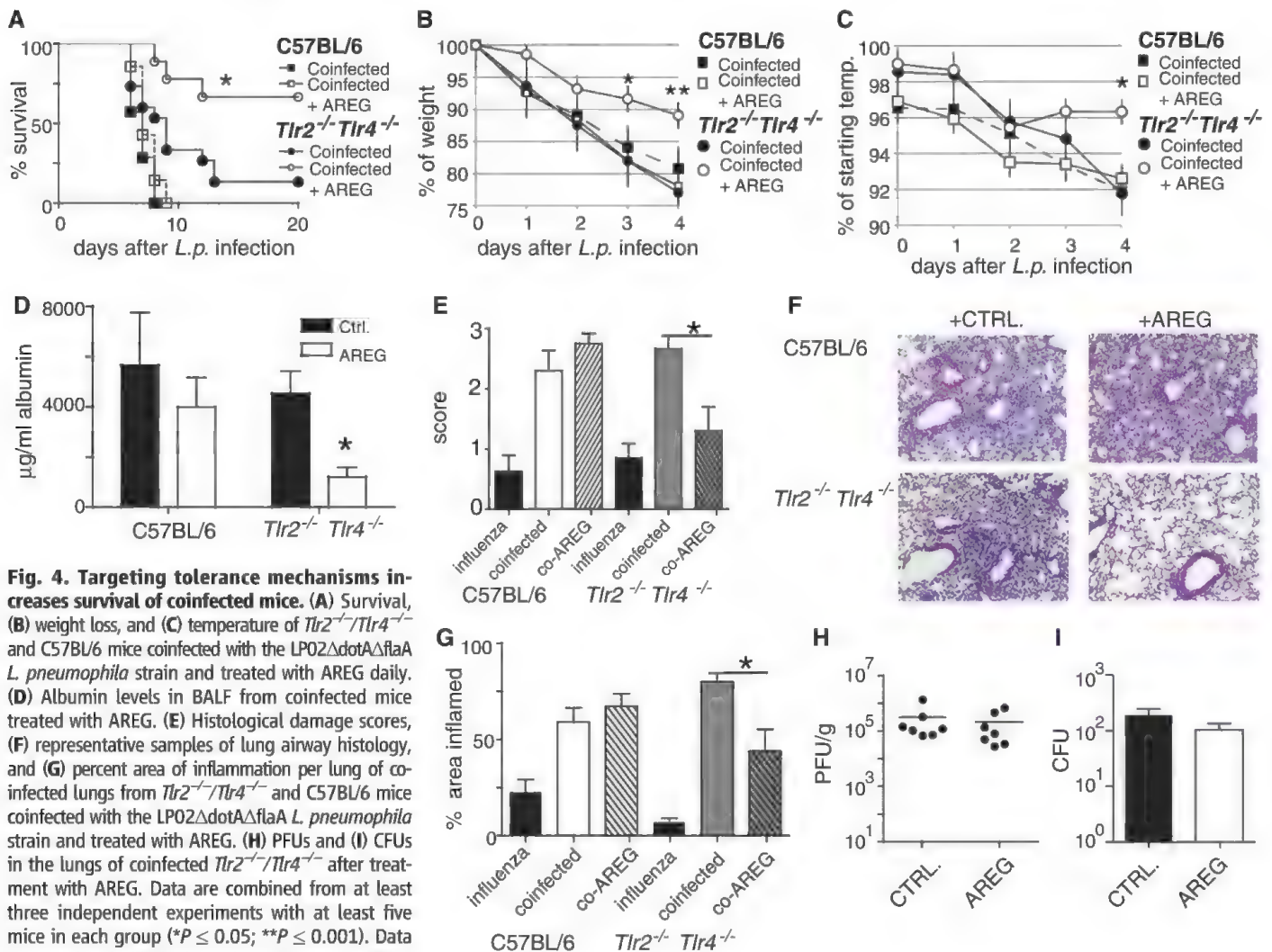


Fig. 4. Targeting tolerance mechanisms increases survival of coinfecting mice. (A) Survival, (B) weight loss, and (C) temperature of *Tlr2*^{-/-}/*Tlr4*^{-/-} and C57BL/6 mice coinfecting with the LP02ΔdotAΔflaA *L. pneumophila* strain and treated with AREG daily. (D) Albumin levels in BALF from coinfecting mice treated with AREG. (E) Histological damage scores, (F) representative samples of lung airway histology, and (G) percent area of inflammation per lung of coinfecting lungs from *Tlr2*^{-/-}/*Tlr4*^{-/-} and C57BL/6 mice coinfecting with the LP02ΔdotAΔflaA *L. pneumophila* strain and treated with AREG. (H) PFUs and (I) CFUs in the lungs of coinfecting *Tlr2*^{-/-}/*Tlr4*^{-/-} after treatment with AREG. Data are combined from at least three independent experiments with at least five mice in each group (**P* ≤ 0.05; ***P* ≤ 0.001). Data were analyzed with the logrank test, *t* test, or ANOVA. Error bars represent SD from the mean.

Collectively, these results demonstrate that (i) lethal synergy of influenza virus and bacterial coinfection can result from loss of tolerance to infection-induced tissue damage, (ii) morbidity and mortality of coinfection can be independent of pathogen burden or excessive inflammatory response, and (iii) promoting tissue repair can, in principle, rescue coinfecting animals from morbidity and mortality, even without affecting pathogen burden. Finally, our influenza-*L. pneumophila* coinfection model demonstrates the distinction between resistance and tolerance as separate host defense strategies that can both contribute to morbidity and mortality of infectious disease.

References and Notes

1. L. Råberg, D. Sim, A. F. Read, *Science* **318**, 812 (2007).
2. L. Råberg, A. L. Graham, A. F. Read, *Philos. Trans. R. Soc. London Ser. B Biol. Sci.* **364**, 37 (2009).
3. D. S. Schneider, J. S. Ayres, *Nat. Rev. Immunol.* **8**, 889 (2008).
4. R. Medzhitov, D. S. Schneider, M. P. Soares, *Science* **335**, 936 (2012).
5. C. Beadling, M. K. Slifka, *Curr. Opin. Infect. Dis.* **17**, 185 (2004).
6. J. A. McCullers, *Clin. Microbiol. Rev.* **19**, 571 (2006).
7. J. M. Hament, J. L. Kimpen, A. Fleer, T. F. Wolfs, *FEMS Immunol. Med. Microbiol.* **26**, 189 (1999).
8. V. T. Peltola, J. A. McCullers, *Pediatr. Infect. Dis. J.* **23** (suppl.), S87 (2004).
9. M. Iannuzzi et al., *J. Med. Case Rep.* **5**, 520 (2011).
10. A. Shahangian et al., *J. Clin. Invest.* **119**, 1910 (2009).
11. A. R. Iverson et al., *J. Infect. Dis.* **203**, 880 (2011).
12. K. Sun, D. W. Metzger, *Nat. Med.* **14**, 558 (2008).
13. A. Didierlaurent et al., *J. Exp. Med.* **205**, 323 (2008).
14. K. H. Berger, R. R. Isberg, *Mol. Microbiol.* **7**, 7 (1993).
15. D. B. Mendel et al., *Antimicrob. Agents Chemother.* **42**, 640 (1998).
16. T. Ichinohe, *Expert Rev. Vaccines* **9**, 1315 (2010).
17. A. García-Sastre, C. A. Biron, *Science* **312**, 879 (2006).
18. T. Ren, D. S. Zamboni, C. R. Roy, W. F. Dietrich, R. E. Vance, *PLoS Pathog.* **2**, e18 (2006).
19. A. B. Molofsky et al., *J. Exp. Med.* **203**, 1093 (2006).
20. D. S. Zamboni et al., *Nat. Immunol.* **7**, 318 (2006).
21. K. A. Archer, C. R. Roy, *Infect. Immun.* **74**, 3325 (2006).
22. R. Spörri, N. Joller, U. Albers, H. Hilbi, A. Oxenius, *J. Immunol.* **176**, 6162 (2006).
23. N. L. La Gruta, K. Kedzierska, J. Stambas, P. C. Doherty, *Immunol. Cell Biol.* **85**, 85 (2007).
24. J. S. M. Peiris, K. P. Y. Hui, H.-L. Yen, *Curr. Opin. Immunol.* **22**, 475 (2010).
25. N. Schmitz, M. Kurrer, M. F. Bachmann, M. Kopf, *J. Virol.* **79**, 6441 (2005).
26. T. Decker, M. Müller, S. Stockinger, *Nat. Rev. Immunol.* **5**, 675 (2005).
27. M. F. Fontana, S. Shin, R. E. Vance, *Infect. Immun.* **80**, 3570 (2012).
28. D. K. Bhalla, *J. Toxicol. Environ. Health B Crit. Rev.* **2**, 31 (1999).
29. L. M. Crosby, C. M. Waters, *Am. J. Physiol. Lung Cell. Mol. Physiol.* **298**, L715 (2010).
30. H. R. Wong, J. R. Wispé, *Am. J. Physiol.* **273**, L1 (1997).
31. L. A. Monticelli et al., *Nat. Immunol.* **12**, 1045 (2011).

Acknowledgments: We thank S. Holley and C. Annicelli for technical assistance; T. Ichinohe, M. Linehan, and A. Iwasaki for viral strains and advice; T. Ren, M. Fontana, R. Vance, K. Archer, S. Shin, and C. Roy for *L. pneumophila* strains and advice; M. Gillum for assistance with experiments; and M. Mueller and C. Lassing for mouse infection infrastructure. The data presented in the manuscript are tabulated in the main paper and in the supplementary materials. This work was supported by the Howard Hughes Medical Institute (R.M.), NIH grants R01 046688 and AI R01 055502 (R.M.), the Ellison Foundation (R.M.), the New England Regional Center of Excellence (R.M.), and FWF (Austrian Science Fund) grant P25235-B13 (A.M.). A.M.J. was a Berger Foundation fellow of the Damon Runyon Cancer Research Foundation. The authors have no conflicts of interest.

Supplementary Materials

www.sciencemag.org/cgi/content/full/science.1233632/DC1
Supplementary Text
Figs. S1 to S6
References (32, 33)

4 December 2012; accepted 15 April 2013
Published online 25 April 2013;
10.1126/science.1233632

Repeated Cortico-Striatal Stimulation Generates Persistent OCD-Like Behavior

Susanne E. Ahmari,^{1,2,3,4*} Timothy Spellman,⁵ Neria L. Douglass,^{1,2} Mazen A. Kheirbek,^{1,2} H. Blair Simpson,^{1,3,4} Karl Deisseroth,⁶ Joshua A. Gordon,^{1,2} René Hen^{1,2}

Although cortico-striato-thalamo-cortical (CSTC) circuit dysregulation is correlated with obsessive compulsive disorder (OCD), causation cannot be tested in humans. We used optogenetics in mice to simulate CSTC hyperactivation observed in OCD patients. Whereas acute orbitofrontal cortex (OFC)–ventromedial striatum (VMS) stimulation did not produce repetitive behaviors, repeated hyperactivation over multiple days generated a progressive increase in grooming, a mouse behavior related to OCD. Increased grooming persisted for 2 weeks after stimulation cessation. The grooming increase was temporally coupled with a progressive increase in light-evoked firing of postsynaptic VMS cells. Both increased grooming and evoked firing were reversed by chronic fluoxetine, a first-line OCD treatment. Brief but repeated episodes of abnormal circuit activity may thus set the stage for the development of persistent psychopathology.

OCD is characterized by intrusive distressing thoughts (obsessions) and/or repetitive mental or behavioral acts (compulsions) and is a leading cause of illness-related disability (1, 2). Although the pathophysiology underlying OCD is unclear, multiple lines of evidence implicate dysregulation within cortico-striato-thalamo-cortical (CSTC) circuits (3–6). Specifically, functional imaging studies suggest that hyperactivity in orbitofrontal cortex (OFC) and ventromedial striatum (VMS) is associated with OCD pathology (5, 7, 8). Furthermore, successful treatments are associated with reductions in hyperactivity (9, 10). However, it is not known if OFC-VMS

hyperactivity can directly cause OCD symptoms, because increased activity could represent adaptive, homeostatic, or unrelated processes compensating for other primary abnormalities. We therefore used an optogenetic strategy to directly test whether hyperstimulation of glutamatergic OFC-VMS projections leads to OCD-like behaviors in mice.

A Cre-inducible adenovirus-associated vector (AAV) carrying the gene encoding channel-rhodopsin (ChR2) fused to enhanced yellow fluorescent protein (EYFP) [pAAV-Ef1a-DIO-ChR2 (H134R)-EYFP; referred to as DIO-ChR2] (11) was stereotactically injected into OFC of

EMX-Cre transgenic mice to ensure specific ChR2 expression in cortical glutamatergic neurons (Fig. 1A) (12). Cortical Cre expression led to sustained expression of ChR2-EYFP (Fig. 1B). Unilateral 473-nm stimulation through chronic fiber-optic implants in OFC yielded lateralized increased activation of the immediate early gene *c-fos* ($P < 0.009$) (Fig. 1, C and D), which demonstrated *in vivo* cellular activation by laser stimulation. Two weeks postinjection, EYFP staining was seen in OFC cell bodies and axons projecting to VMS (Fig. 1E), which indicated targeting of OFC-VMS projections. *In vitro* recordings in cortico-striatal slices demonstrated VMS field responses after 473-nm laser stimulation of OFC axon terminals in striatum (Fig. 1F). To verify adequate stimulation of ChR2-expressing OFC-VMS terminals *in vivo*, we implanted stereo-optrodes (optrodes) into VMS that permit combined fiber-optic stimulation and 32-channel simultaneous recording of multiple single units (Fig. 1G). In awake behaving mice, *in vivo* recordings demonstrated robust VMS field responses after 473-nm laser stimulation of OFC axon terminals in striatum (Fig. 1, H and I), which showed

¹Department of Psychiatry, Columbia University College of Physicians and Surgeons, New York, NY 10032, USA. ²Division of Integrative Neuroscience, New York State Psychiatric Institute, New York, NY 10032, USA. ³Division of Clinical Therapeutics, New York State Psychiatric Institute, New York, NY 10032, USA. ⁴Anxiety Disorders Clinic and OCD Research Program, New York State Psychiatric Institute, New York, NY 10032, USA. ⁵Department of Physiology, Columbia University College of Physicians and Surgeons, New York, NY 10032, USA. ⁶Departments of Psychiatry and Bioengineering, Stanford University School of Medicine, Stanford, CA 94305, USA.

*Corresponding author. E-mail: sea2103@columbia.edu

feasibility of activation of specific cortical-VMS projections.

Because patients with OCD have hyperactivity in OFC-striatal circuits (3–6), we predicted that direct elevation of OFC-VMS activity would lead to increases in OCD-related behaviors including grooming, anxiety, and prepulse inhibition (PPI) deficits (13). We injected DIO-ChR2 into the left OFC of EMX-Cre mice and implanted fiber-optic probes unilaterally in left VMS (Fig. 2A). After waiting 3 to 4 weeks for surgical recovery and stable viral expression, we habituated mice to the open field and fiber-optic stimulation apparatus. We then repeatedly elevated activity in OFC-VMS projections by stimulating for 5 min at 10 Hz for five consecutive days (10 ms, 1 to 5 mW) (14). Grooming behavior was recorded with digital video and scored by blind raters for

5 min before (Pre), during (Stim), and after (Post) stimulation (Fig. 2B). Whereas acute OFC-VMS stimulation did not produce grooming, a small but significant progressive increase in grooming time was noted during the prestimulation period on consecutive days (Fig. 2C) [repeated measures analysis of variance (ANOVA), main effect: $P < 0.048$; $F = 4.43$; Fisher's protected least significant difference (PLSD): for day 3, $P < 0.03$; for day 5, $P < 0.047$]. Because the prestimulation measurement on days 2 to 5 served as a 24-hour time stamp for effects of stimulation the day before, this suggested that repeated stimulation led to chronic circuit changes that ultimately resulted in sustained, stimulation-independent OCD-like behavior. Although it is possible that stress from handling contributed to the grooming increase in the prestimulation period, stress was

minimized by habituation to fiber-optic tethering daily for a week before data collection and was identical for controls and ChR2+ mice. To resolve the time-course of the grooming increase, we examined a new cohort an hour after stimulation ($\text{Groom}_{1 \text{ hour post}}$) (Fig. 2D). We observed a dramatic progressive increase in grooming over consecutive days using this measure (main effect: $P < 0.02$; $F = 7.32$) (Fig. 2E). Although total grooming time increased, there was not a significant increase in stereotyped syntactic grooming chains in ChR2+ animals on day 5 of stimulation (table S1). No differences in grooming time were observed between controls and ChR2+ animals on day 1 of stimulation, which indicated that ChR2 expression without laser stimulation did not lead to an increase in grooming. Notably, increased grooming persisted even

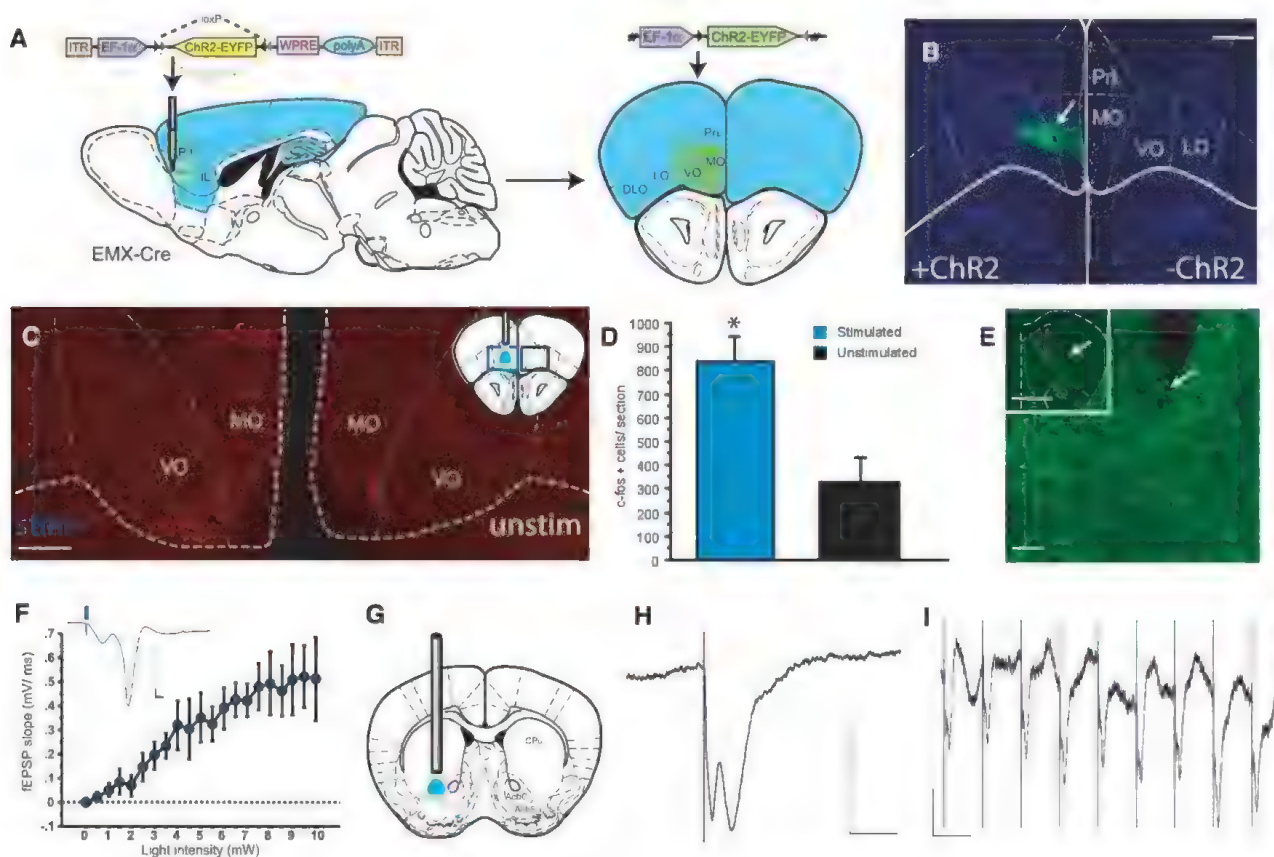


Fig. 1. Injection of ChR2-EYFP AAV into OFC leads to functional ChR2 expression in projections from OFC to VMS. (A) Schematic diagram of DIO-ChR2 injections. (Left) Reference sagittal section indicates injection position in ventromedial OFC (VO/MO) of EMX-Cre mice (2.6 mm AP, 1.7 mm DV, 0.5 mm ML). Blue shading: Cre expression in cortex and hippocampus. (Right) Cre-expressing glutamatergic cells in OFC irreversibly invert the ChR2-EYFP open reading frame, which leads to cell type-specific ChR2-EYFP expression (green shading). EF-1 α , elongation factor 1 α ; ITR, inverted terminal repeat; WPRE, woodchuck hepatitis virus posttranslational regulatory element; DLO, dorsolateral orbitofrontal cortex; LO, lateral orbitofrontal cortex; PrL, prelimbic cortex. (B) Confocal image of YFP-immunostaining shows unilateral ChR2 expression at OFC injection site. Scale bar, 500 μ m. (C) c-Fos immunostaining demonstrates 473-nm light-induced activation of OFC in awake behaving mice through chronic fiber-optic implant. (Inset) Reference coronal section. Blue square, stimulated; black, unstimulated. (D) Quantifica-

tion of c-Fos-positive cells in stimulated versus unstimulated OFC ($P < 0.009$) ($n = 4$ controls; 4 ChR2 mice; five sections each). (E) Targeting of OFC-VMS projections evidenced by axonal YFP staining under fiber-optic implant site (arrow). Scale bar, 100 μ m. (Inset) Low magnification. Scale bar, 500 μ m. (F) Extracellular field recordings from striatal slices. Increased population spike amplitude with increasing laser power. (Inset) Individual population spike after 0.1-ms light pulse (3 mW); calibration bars: vertical 0.5 mV, horizontal 1 ms. $n = 4$ slices from each of three animals. (G) Schematic diagram of stereo-optrode implant in VMS. (Stereotaxic coordinates: 0.98 mm AP, 3.5 mm DV, 1.25 mm ML). CPu, caudate putamen; AcbC, accumbens core; AcbSh, accumbens shell. (H) In vivo recordings in awake behaving animals show field responses to 473-nm stimulation of VMS terminals. Mean response to 20 flashes delivered at 0.5 Hz. Calibration bars: vertical 0.5 mV, horizontal 20 ms. (I) Raw responses to train of 10 flashes at 10 Hz. Calibration bar: vertical 0.5 mV, horizontal 100 ms.

in the absence of stimulation up to 2 weeks later ($P < 0.03$) (Fig. 2F).

Acute OFC-VMS stimulation led immediately to a large but transient increase in locomotion compared with controls; no differences were observed pre- or poststimulation (fig. S1A). To ensure that increased grooming was not simply a consequence of increased locomotion, we injected DIO-ChR2 and implanted fiber optics in motor cortex (M2) of EMX-Cre mice (fig. S1B). The 5-day stimulation paradigm described above led to increased locomotion (fig. S1C) but not to increased grooming (fig. S1D), which suggested that increased grooming was not simply a side effect of overall increased activity. To determine the specificity of OFC-VMS pathway hyperactivation in induction of persistent grooming, we injected AAV-ChR2 into infralimbic and prelimbic cortex (IL/PrL) (fig. S2A) and stimulated IL/PrL-VMS projections using our 5-day stimulation paradigm. Repeated stimulation of IL/PrL-VMS projections did not lead to a progressive increase in grooming behavior (fig. S2, B to D).

Other OCD-associated behavioral measures were tested after completion of the 5-day stimu-

lation paradigm. No differences were seen in PPI (13) or anxiety levels (in open field and elevated plus maze) compared with testing before stimulation (fig. S3); in addition, no changes in open field anxiety were observed during acute stimulation (fig. S4). Together, these results suggest that repeated stimulation of OFC-VMS projections led to specific induction of repetitive behavior.

We next examined electrophysiologic changes correlated with the progressive grooming increase using VMS stereo-optrodes (Fig. 3A and fig. S5). In awake behaving mice, recordings of multiple single units in the VMS were obtained during the 15-min stimulation protocol and 1 hour post grooming assessment (Fig. 3B). Light-evoked responses were observed in individual units in response to 10 Hz stimuli (Stim) or 0.1 Hz probe pulses (used to measure light-evoked activity during pre-, post-, and 1 hour poststimulation) over 5 days of repeated stimulation. Cells displayed a range of responses to light pulses, including activation (Fig. 3C), suppression (Fig. 3D), and no effect (Fig. 3E); we therefore used each cell's stimulation-induced change in firing rate (ex-

pressed as a Z-score; see supplementary methods) to assess responsiveness to afferent stimulation. Across 5 days of stimulation, mean responses increased both during stimulation and 1 hour poststimulation (Fig. 3F; $R = 0.21$ and 0.28 ; $P < 0.002$ and < 0.001 , respectively). Z-scores were greater on day 5 than on day 1, which indicated increased evoked firing (at 10 Hz: $P < 0.02$; at 0.1 Hz: $P < 0.004$). Thus, repeated hyperstimulation led to a marked progressive increase in light-evoked firing paralleling the increase in repetitive behavior.

Finally, we determined whether a medication regimen used to treat OCD would reverse the increases in repetitive behavior and evoked VMS activity. After 7-day grooming induction, we initiated fluoxetine treatment (18 mg/kg body weight per day) while continuing daily stimulation (Fig. 4A). Fluoxetine was chosen because serotonin reuptake inhibitors (SRIs) are the only proven monotherapy for OCD (15). Although there was no effect of fluoxetine after 1 week, 2 weeks of treatment led to a reversal of grooming behavior to control levels (Fig. 4B) (main effect: $P < 0.009$, $F = 9.53$; Fisher's PLSD: baseline versus week 2,

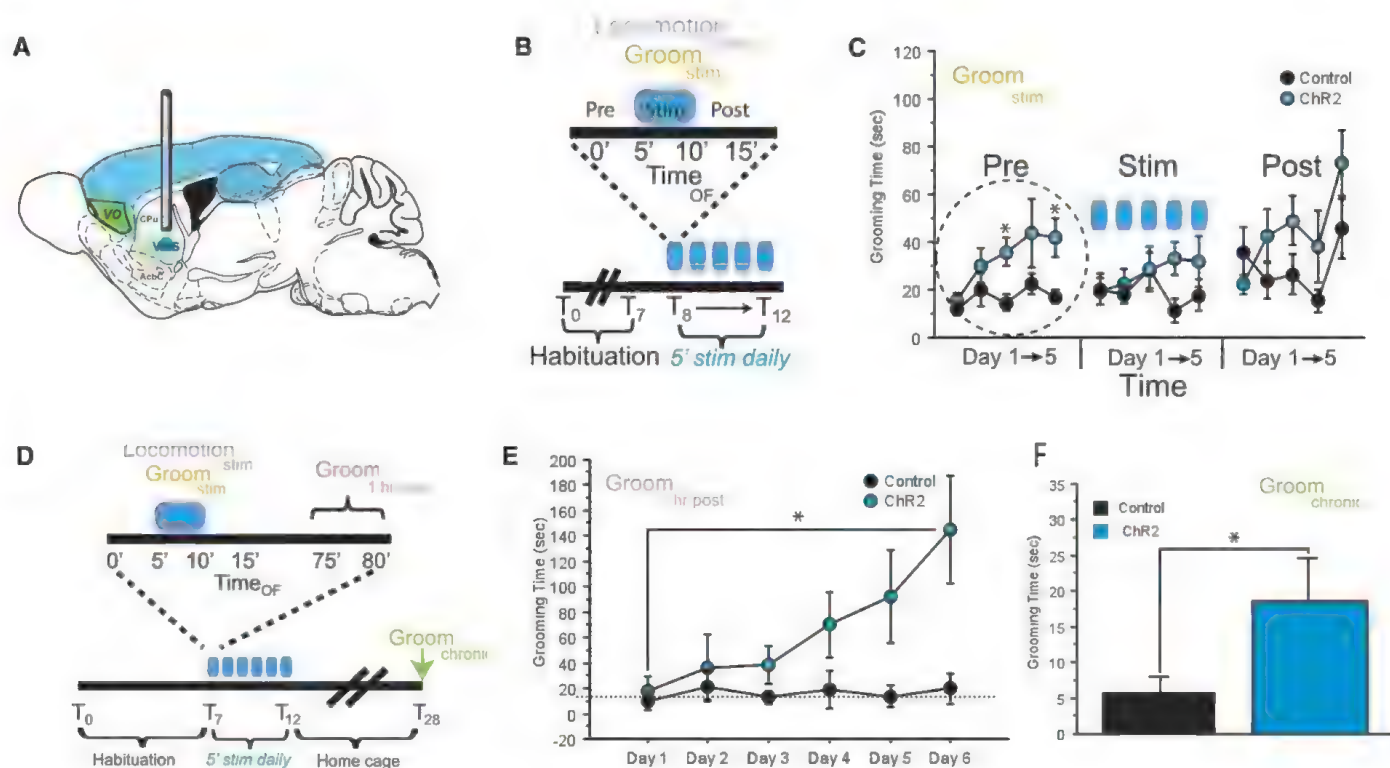


Fig. 2. Brief repeated hyperstimulation of OFC-VMS projections leads to progressively increased grooming behavior. (A) Localization of viral injection and fiber-optic implant. ChR2 (green) is expressed in ventromedial OFC. Fiber-optic implant is placed into VMS to stimulate ChR2 in axon terminals projecting from OFC. (B) Time line for chronic stimulation of OFC-VMS projections. After habituation to the tethering procedure for 7 days (T_1 to T_7), mice underwent the stimulation protocol. Time_{OF} = Time in open field. (C) Grooming behavior over five consecutive days of stimulation. Total time grooming was assessed for 5 min before (Pre), during (Stim), and after stimulation (Post) for five consecutive days. Data are grouped into Pre, Stim, and Post categories for days 1 to 5 to facilitate exam-

ination of changes in behavior over time. Stimulation (10 Hz) led to a significant increase in grooming time in ChR2 animals before stimulation (Pre) (main effect: $P < 0.048$, $F = 4.43$; post hoc test: day 3, $*P < 0.03$; day 5, $*P < 0.047$; $n = 8$ ChR2 mice, 7 controls). (D) Time line for examination of chronic impact of stimulation. (E) After 6 days of stimulation, ChR2+ animals had significantly elevated grooming during Groom_{1 hour post} (main effect $*P < 0.02$; $F = 7.32$; n count: ChR2 = 6; control = 5). (F) Two weeks after repeated stimulation (T_{28}), ChR2+ animals continued to demonstrate significantly increased grooming (Groom_{chronic} $*P < 0.03$; one-tailed t test), although absolute grooming time was decreased compared with times immediately after stimulation paradigm (T_{12}).

$P < 0.003$). This delayed response is consistent with the delayed onset of effective SRI treatment in OCD patients. We also repeated this experiment using a vehicle control group (Fig. 4C). Again, 2 weeks of fluoxetine led to reversal of induced grooming (Fig. 4D). Moreover, in a separate cohort of stereo-optrode-implanted animals, the increase in light-evoked activity induced by repeated 10 Hz stimulation was normalized after chronic fluoxetine (Fig. 4, E and F).

Repeated hyperactivation of OFC-VMS projections generates a progressive increase in grooming, temporally linked to a cumulative increase in VMS light-evoked firing. Acute stimulation of the OFC-VMS pathway was not sufficient to produce OCD-relevant excessive grooming (3, 16–18). The behavioral change was persistent, becoming stimulation-independent within 6 days. Although classic theories suggest that abnormal repetitive behaviors, including

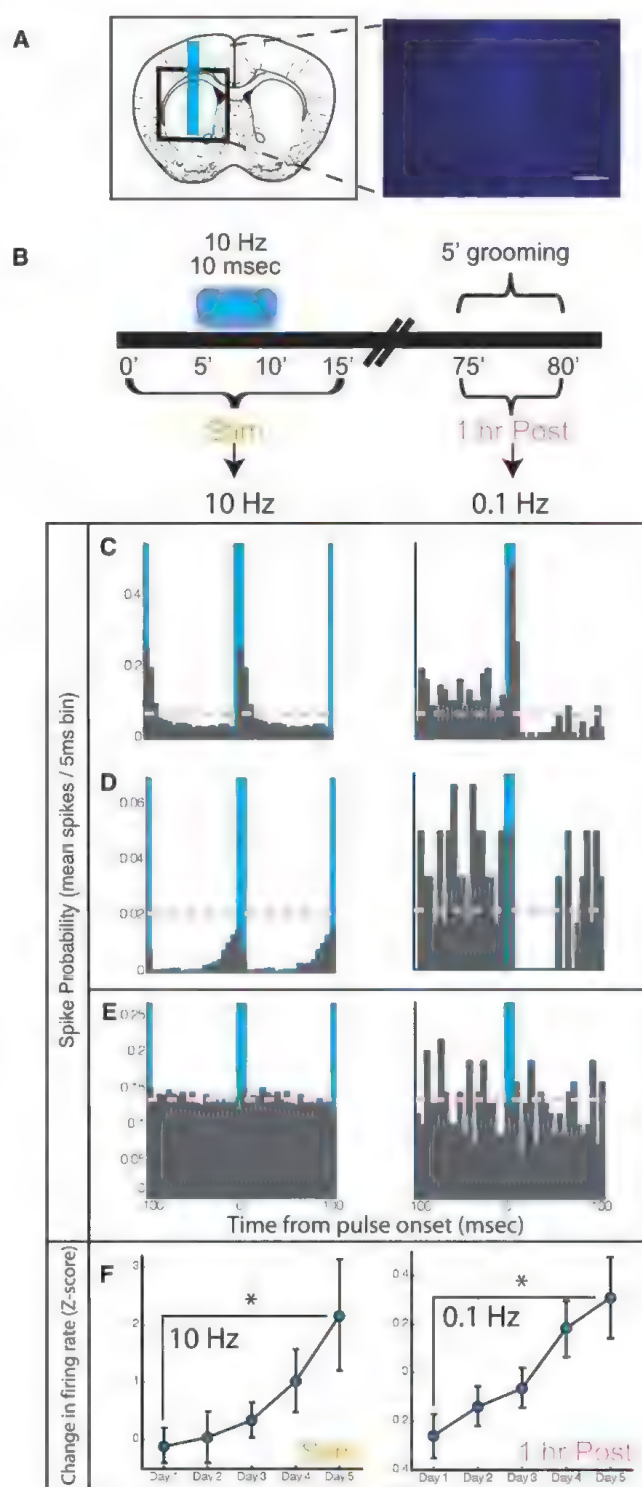
OCD symptoms, directly result from hyperactivity in CSTC loops (19–21), causation has been difficult to prove. Though genetic and pharmacologic manipulations of norepinephrine and dopamine can lead to transient increases in repetitive behaviors (22), the interventions were not limited to specific circuits, and associated electrophysiologic changes were observed in multiple brain regions. Our optogenetic system permits activation of specific cortico-striatal circuits and genetic definition of the activated cell-type as cortical glutamatergic projection neurons.

Our *in vivo* electrophysiology data suggest a circuit-based mechanism for establishment of repetitive behaviors. Repeated hyperstimulation led to a marked progressive increase in light-evoked firing paralleling the increase in grooming, suggesting plasticity at OFC-VMS synapses that builds over consecutive days. We speculate that brief episodes of light-induced activity lead to long-lasting changes that prime OFC-VMS synapses, decreasing the activation threshold during subsequent bouts of stimulation. In turn, increased activity at OFC-VMS synapses may transmit information through the CSTC circuit (23–25) and lead to multiple downstream events that ultimately reinforce repetitive behaviors, including (i) plasticity in downstream structures such as thalamus and prefrontal cortex (26), and (ii) increased motivational saliency mediated by the ventral tegmental area (22). This mechanism would be consistent with the observed fluoxetine effects, since selective SRIs have been shown to reduce primary reward processing (27, 28).

OCD is a heterogeneous disorder. Our study therefore may have greater relevance for particular OCD subtypes. For example, dimensional models of OCD have been proposed in which different types of obsessions and compulsions are associated with different circuits (29, 30). Because our results suggest that repeated stimulation of OFC-VMS projections led to specific induction of repetitive grooming, our model may be of particular importance for OCD patients with predominant contamination concerns.

Our findings yield new insight into how psychopathology could develop. Only 5 min of stimulation per day was sufficient to lead to sustained significant behavioral effects. This raises the possibility that pathological changes, including compulsions in OCD, may result from small but repeated bursts of abnormal neuronal activity and also offers suggestions for new treatment approaches or refinements of existing therapies for disorders characterized by repetitive behaviors. For example, our data are consistent with recent clinical studies demonstrating efficacy of ventral capsule-ventral striatum deep brain stimulation in OCD (31, 32), which is thought to act via inhibition of OFC hyperactivity. Optogenetic approaches could be used to dissect circuit mechanisms underlying deep brain stimulation and other treatments, with a goal of identifying new treatment targets.

Fig. 3. Repeated daily stimulation of OFC-VMS projections leads to increased evoked firing. (A) (Left) Schematic diagram of stereo-optrode implant site. (Right) Placement visualized via implanting a stereo-optrode dipped in Hoechst stain (1:1000). Scale bar, 500 μ m. (B) Stimulation protocol used for *in vivo* recording. (C to E) Representative peristimulus spike histograms (5-ms time bins) of three neurons recorded during 10 Hz stimulation (left) and 0.1 Hz probe pulses (1 hour poststimulation on right). Baseline spontaneous firing rate for each cell is shown as pink dashed line. Cells exhibited varied stimulus responsiveness, including evoked activation (C), evoked suppression (D), and no response (E). (F) Light-evoked firing (measured by peristimulus z-scores) across 5 days of stimulation both during 10 Hz stimulation (Stim) and during 0.1 Hz probe pulses 1 hour after stimulation (1 hour post) (* $P < 0.021$ and $P < 0.004$). Negative Z-scores for 0.1 Hz on days 1 and 2 indicate net suppression of evoked firing rate during Groom_{1 hour post} after the first two epochs of 10 Hz stimulation.



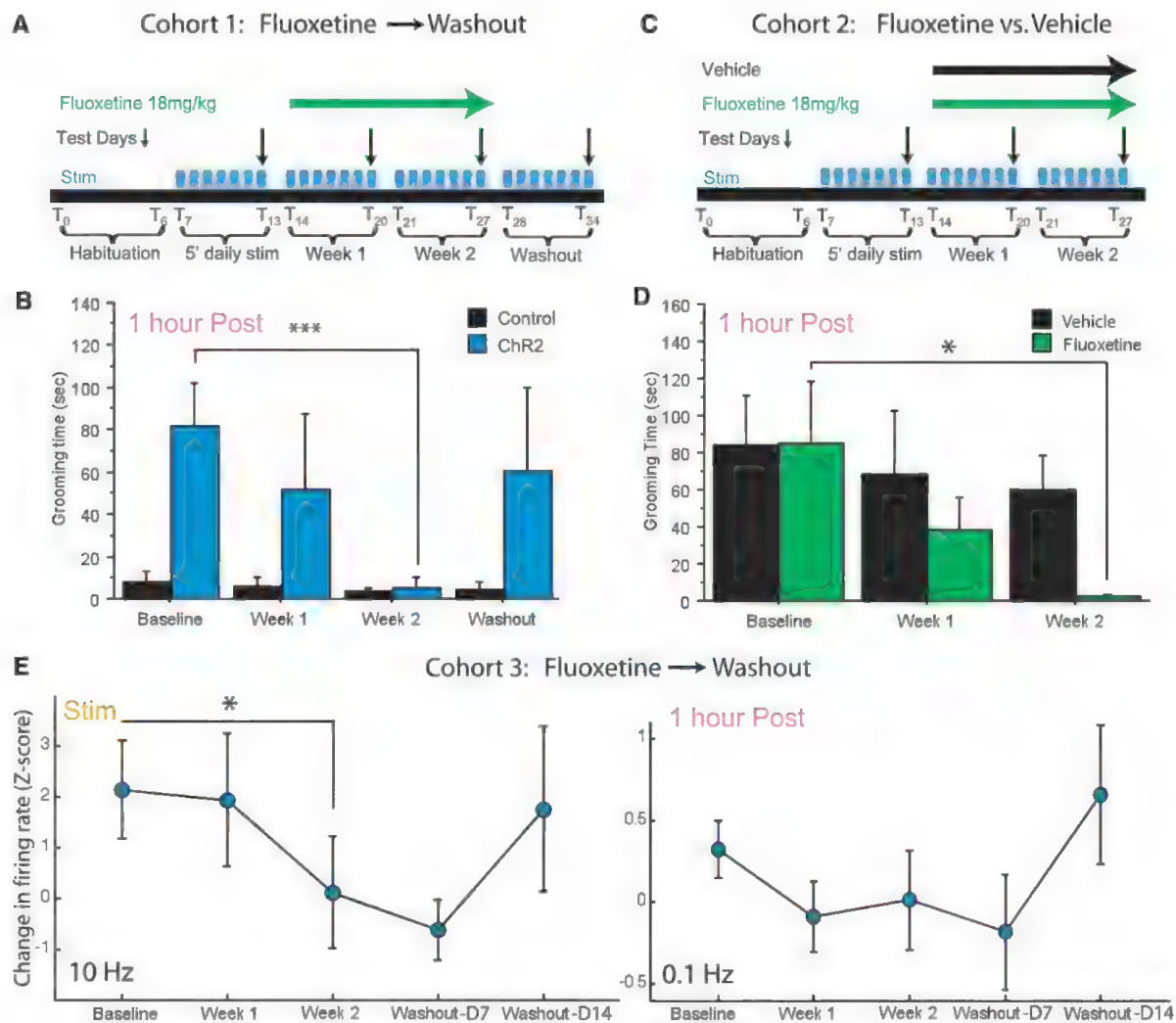


Fig. 4. Perseverative grooming and elevated evoked firing rate are resolved by chronic, but not acute, fluoxetine treatment. (A) Experimental time line for fluoxetine wash-out experiment. (B) Two weeks of fluoxetine treatment reduced grooming to level of controls. Main effect: $P < 0.009$; $F = 9.53$; Fisher's PLSD: baseline versus week 2, $***P < 0.003$. Increased grooming was reestablished after a 1-week fluoxetine wash-out. Main effect: $P < 0.09$; $F = 3.58$. n values: Chr2⁺ mice = 8; controls = 7. (C) Experimental time line for fluoxetine versus vehicle experiment. (D) Two

weeks of fluoxetine treatment reduced grooming to levels of vehicle-treated animals. Main effect: $P < 0.14$; $F = 2.59$; Fisher's PLSD: baseline versus week 2, $*P < 0.04$. Fluoxetine: $n = 7$; vehicle: $n = 6$. (E) (Left) In stereoptrode-implanted animals, peristimulus Z-scores for 10 Hz stimuli normalized after 2 weeks of fluoxetine ($P < 0.028$); after 2-week wash-out, Z-scores returned to pretreatment levels. (Right) Peristimulus Z-scores for 0.1 Hz probe pulses showed a nonsignificant decrease after fluoxetine treatment, which returned to pretreatment levels after wash-out.

References and Notes

- C. J. L. Murray, A. D. Lopez, *The Global Burden of Disease: A Comprehensive Assessment of Mortality and Disability from Diseases, Injuries, and Risk Factors in 1990 and Projected to 2020*, Global burden of disease and injury series; vol. 1 (Harvard School of Public Health, Harvard Univ. Press, Cambridge, MA, 1996).
- R. C. Kessler et al., *Arch. Gen. Psychiatry* **62**, 593 (2005).
- J. T. Ting, G. Feng, *Curr. Opin. Neurobiol.* **21**, 842 (2011).
- R. Marsh, T. V. Maia, B. S. Peterson, *Am. J. Psychiatry* **166**, 664 (2009).
- M. R. Milad, S. L. Rauch, *Trends Cogn. Sci.* **16**, 43 (2012).
- C. Pittenger, M. H. Bloch, K. Williams, *Pharmacol. Ther.* **132**, 314 (2011).
- S. Saxena, R. G. Bota, A. L. Brody, *Semin. Clin. Neuropsychiatry* **6**, 82 (2001).
- J. Y. Rotge et al., *Biol. Psychiatry* **65**, 75 (2009).
- S. L. Rauch, C. R. Savage, N. M. Alpert, A. J. Fischman, M. A. Jenike, *Biol. Psychiatry* **42**, 446 (1997).
- J. L. Abelson et al., *Biol. Psychiatry* **57**, 510 (2005).
- H. C. Tsai et al., *Science* **324**, 1080 (2009).
- J. A. Gorski et al., *J. Neurosci.* **22**, 6309 (2002).
- S. E. Ahmari, V. B. Risbrough, M. A. Geyer, H. B. Simpson, *Neuropsychopharmacology* **37**, 1216 (2012).
- J. Mattis et al., *Nat. Methods* **9**, 159 (2012).
- L. M. Koran, G. L. Hanna, E. Hollander, G. Nestadt, H. B. Simpson; American Psychiatric Association, *Am. J. Psychiatry* **164** (suppl.), 5 (2007).
- S. V. Shmelkov et al., *Nat. Med.* **16**, 598, 1p, 602 (2010).
- J. M. Welch et al., *Nature* **448**, 894 (2007).
- S. K. Chen et al., *Cell* **141**, 775 (2010).
- T. R. Insel, J. T. Winslow, *Psychiatr. Clin. North Am.* **15**, 813 (1992).
- D. R. Rosenberg, M. S. Keshavan, *Biol. Psychiatry* **43**, 623 (1998).
- L. R. Baxter Jr. et al., *Am. J. Psychiatry* **145**, 1560 (1988).
- K. Dzirasa et al., *J. Neurosci.* **30**, 6387 (2010).
- S. K. Bourne, C. A. Eckhardt, S. A. Sheth, E. N. Eskandar, *Front Integr Neurosci* **6**, 29 (2012).
- A. M. Graybiel, S. L. Rauch, *Neuron* **28**, 343 (2000).
- S. N. Haber, S. L. Rauch, *Neuropsychopharmacology* **35**, 1 (2010).
- E. G. Antzoulatos, E. K. Miller, *Neuron* **71**, 243 (2011).
- B. Abler, G. Grön, A. Hartmann, C. Metzger, M. Walter, *J. Neurosci.* **32**, 1329 (2012).
- C. McCabe, Z. Mishor, P. J. Cowen, C. J. Harmer, *Biol. Psychiatry* **67**, 439 (2010).
- D. Mataix-Cols et al., *Arch. Gen. Psychiatry* **61**, 564 (2004).
- J. F. Leckman et al., *Depress. Anxiety* **27**, 507 (2010).
- B. D. Greenberg et al., *Mol. Psychiatry* **15**, 64 (2010).
- P. P. de Koning, M. Figue, P. van den Munckhof, P. R. Schuurman, D. Denys, *Curr. Psychiatry Rep.* **13**, 274 (2011).

Acknowledgments: We thank H. B. Simpson and C. Kellendonk for critical discussions and reading of the manuscript and D. Flicker and M. Cloidt for behavioral scoring assistance. S.E.A. is supported by National Institute of Mental Health (NIMH) K08MH087718; the Louis V. Gerstner, Jr., Scholars Program; the Irving Institute for Clinical and Translational Research; the Gray Matters Foundation; the Leon Levy Foundation; and a Brain and Behavior Research Foundation NARSAD Young Investigator Award. M.A.K. is supported by

NIMH K01MH099371, the Sackler Institute, and a NARSAD Young Investigator Award. K.D. is supported by the Howard Hughes Medical Institute, NIH, California Institute for Regenerative Medicine, and the Defense Advance Research Projects Agency The Reorganization and Plasticity to Accelerate Injury Recovery (REPAIR) Program. J.G. is supported by NIH R01 MH096274, the Hope for Depression Research

Foundation, and the International Mental Health Research Organization. R.H. is supported by the Hope for Depression Research Foundation.

Supplementary Materials

www.sciencemag.org/cgi/content/full/340/6137/1234/DC1
Materials and Methods

Figs. S1 to S5
Table S1
References (33–43)

3 January 2013; accepted 3 April 2013
10.1126/science.1234733

Geniculocortical Input Drives Genetic Distinctions Between Primary and Higher-Order Visual Areas

Shen-Ju Chou,^{1,*†} Zoila Babot,^{1,*} Axel Leingärtner,^{1,‡} Michele Studer,^{2,§}
Yasushi Nakagawa,^{1||} Dennis D. M. O'Leary^{1¶}

Studies of area patterning of the neocortex have focused on primary areas, concluding that the primary visual area, V1, is specified by transcription factors (TFs) expressed by progenitors. Mechanisms that determine higher-order visual areas (V^{HO}) and distinguish them from V1 are unknown. We demonstrated a requirement for thalamocortical axon (TCA) input by genetically deleting geniculocortical TCAs and showed that they drive differentiation of patterned gene expression that distinguishes V1 and V^{HO} . Our findings suggest a multistage process for area patterning: TFs expressed by progenitors specify an occipital visual cortical field that differentiates into V1 and V^{HO} ; this latter phase requires geniculocortical TCA input to the nascent V1 that determines genetic distinctions between V1 and V^{HO} for all layers and ultimately determines their area-specific functional properties.

The neocortex is patterned into functionally distinct fields that include primary sensory areas, which receive modality-specific sensory input from thalamocortical axons (TCAs) that originate from the principal sensory nuclei of the dorsal thalamus (dTh), and higher-order sensory areas that are connected with the primary areas through intracortical projections (1). Studies of mechanisms that pattern the neocortex into areas, known as arealization, have focused on primary areas and have led to the prevailing model that genetic mechanisms intrinsic to the neocortex are predominant in arealization (2). Transcription factors (TFs) expressed in neocortical progenitors determine the size and position of primary areas (2–5) and regulate guidance information that governs the area-specific targeting of TCAs (6). However, roles for TCAs in arealization remain vague (7–10), and important features of arealization, such as differential gene

expression in the embryonic neocortex that relates to nascent areas, develop independently of TCA input (9, 10).

Higher-order areas outnumber primary areas by roughly 10-fold; for example, in mouse, nine higher-order visual areas (V^{HO}) are positioned around the primary visual area (V1) within the occipital neocortex (11). However, mechanisms that specify and regulate differentiation of the particular properties of higher-order areas and distinguish them from primary areas have yet to be explored (11, 12). To perform genetic manipulations of dTh neurons required for these studies, we created $ROR\alpha$ -IRES-Cre mice ($ROR\alpha^{Cre}$; fig. S1, A and B) with $ROR\alpha$ function intact and expression of Cre recombinase driven by $ROR\alpha$ regulatory elements (13). Crossing this $ROR\alpha^{Cre}$ mouse to conditional reporter lines (fig. S1) revealed Cre-mediated recombination in neurons of the principal sensory nuclei in dTh at embryonic day 14.5 (E14.5), shortly after they become postmitotic (14), with robust recombination in the dorsal lateral geniculate nucleus (dLG) (fig. S1, C to K), which forms the geniculocortical TCA projection that relays visual information from the eyes selectively to V1. Little or no recombination was detected in the neocortex through the end of the first postnatal week, encompassing the differentiation of cortical areas and the time frame of our study (fig. S1, C to K).

We crossed $ROR\alpha^{Cre}$ mice to mice in which the third exon of the COUP-TF1 gene is flanked by loxP sites, i.e. floxed (fl) COUP-TF1 [COUP-TF1^{fl/fl} is described in (5)], because COUP-TF1 is strongly expressed in dLG, COUP-TF1 deletion

diminishes axon growth (15), and most TCAs fail to reach the cortex in COUP-TF1-null mice (16). COUP-TF1-null mice are not useful for our studies because of viability issues and defects in cortical development (16). In contrast, the conditional knockout (cKO) mice ($ROR\alpha^{Cre/+}$ or $ROR\alpha^{Cre/Cre}$; COUP-TF1^{fl/fl}) were viable and retained robust COUP-TF1 expression in the neocortex (fig. S2, A and B), but COUP-TF1 was deleted from dLG by E15.5 (fig. S2, A and B), and dLG size in cKO mice progressively decreased from the wild-type (WT) size embryonically to virtually absent by postnatal day 7 (P7) (figs. S2, C and D, and S3).

To visualize TCA projections in the cortex, we first used serotonin [5-hydroxytryptamine (5-HT)] immunostaining on tangential sections of flattened P7 cortices. In P7 WT mice, 5-HT staining revealed the geniculocortical TCA projection from dLG to V1, as well as TCA projections from the ventroposterior nucleus (VP) to the primary somatosensory area (S1) and from the medial geniculate nucleus (MG) to the primary auditory area (A1) (Fig. 1A). In P7 cKO mice, 5-HT staining showed that TCA projections to S1 and A1 were intact, but the geniculocortical TCA projection to V1 was absent (Fig. 1A). The loss of geniculocortical input to V1 in P7 cKO mice was confirmed by anterograde and retrograde axon tracing from dLG and V1 (fig. S4, A and B) and by crossing the cKO mice to a ROSA26-GAP43-eGFP reporter line that labels TCAs by $ROR\alpha^{Cre}$ reporter activation (fig. S5A). Thus, conditional deletion of COUP-TF1 from dLG using the $ROR\alpha^{Cre}$ line resulted in deletion of the geniculocortical TCA projection by P7, but COUP-TF1 remained intact in the cortex.

To determine the time course of the geniculocortical TCA projection in cKO mice as compared to WT mice, we bred $ROR\alpha^{Cre}$ mice on either a WT (COUP-TF1^{fl/+}; $ROR\alpha^{Cre/+}$) or cKO (COUP-TF1^{fl/fl}; $ROR\alpha^{Cre/+}$ or COUP-TF1^{fl/fl}; $ROR\alpha^{Cre/Cre}$) background, to a conditional reporter line (Ai14 tdTomato) (17). Activation of the tdTomato reporter with the $ROR\alpha^{Cre}$ line labeled, at high resolution, geniculocortical TCAs from the dLG and TCAs from VP and MG projecting to S1 and A1 (Fig. 1B). Genulocortical TCAs extend tangentially in the subplate and underlie the cortical plate (CP) of nascent V1 by E16.5, invade after birth the overlying V1 CP, and over the first postnatal week arborize in V1 layer 4, their predominant target layer (18). At E16.5, before TCAs invade the CP, the appearance of tdTomato-labeled TCAs was indistinguishable between WT and cKO mice, with

¹Molecular Neurobiology Laboratory, The Salk Institute for Biological Studies, La Jolla, CA, USA. ²Institute of Biology Valrose, INSERM, Nice, France.

*These authors contributed equally to this work.

†Present address: Institute of Cellular and Organismic Biology, Academia Sinica, Taipei, Taiwan.

‡Present address: University Cancer Center Hamburg, University Medical Center Hamburg-Eppendorf, Hamburg, Germany.

§Present address: Institute of Biology Valrose, iBV, UMR INSERM1091/CNRS7277/UNS, Nice, F-06108, France; and University of Nice Sophia-Antipolis, UFR Sciences, Nice, F-06108, France.

||Present address: Department of Neuroscience, Stem Cell Institute and Developmental Biology Center, University of Minnesota, Minneapolis, MN 55455, USA.

¶Corresponding author. E-mail: doleary@salk.edu

a high density of labeled TCAs present in the occipital cortex of both (Fig. 1B). At P1, when geniculocortical TCAs normally invade the CP of V1, the density of labeled axons in the occipital cortex was substantially decreased in cKO mice as compared to WT mice (Fig. 1B). By P3, labeled geniculocortical TCAs were robustly arborizing in layer 4 of V1 of WT mice but were virtually absent from V1 and from the entire occipital cortex of cKO mice (Fig. 1B). These findings were corroborated by retrograde axon tracing from V1 and S1 (figs. S4 and S6). Thus, geniculocortical TCAs appeared WT in embryonic cKO mice but were eliminated early postnatally before significantly invading the CP or arborizing in layer 4 of V1.

Retrograde labeling from V1 and S1 showed that the area specificity of TCA input in the cKO mice was similar to that in the WT mice (19, 20) (figs. S4 and S6). Overall size, surface area, and tangential dimensions of the cortex were also similar between WT and cKO mice, as was S1 position in the cortex and occipital cortex size, which in WT mice is primarily V1 and V^{HO} (fig. S5). Other features of the occipital cortex, including thickness, cell density, and lamination, had similar appearances in adult cKO and WT mice (fig. S7). Thus, mechanisms intrinsic to the cortex determine the overall size of the occipital visual cortical field and of S1 relative to it, independent of geniculocortical TCA input.

This cKO line provided a model to address whether geniculocortical TCA input to V1 differentiates the occipital visual cortical field into V1 and V^{HO} and whether its early postnatal deletion disturbs this patterning. The distinct properties and functions that distinguish V1 from V^{HO} are largely determined by their genetic profiles; i.e., differences in their patterned expression of sets of genes. Therefore, we developed gene markers that distinguished V1 and V^{HO} and were exemplary of their distinct genetic profiles. We assessed in WT mice when area patterning is mature, at P7 and later, the expression of candidate genes to identify those that marked V1 or V^{HO} in patterns that distinguished them and fully delineated one or the other, or both uniquely, using tangential sections of flattened cortices and cortical whole mounts, augmented with sagittal sections to also assess laminar expression. The majority of genes expressed in visual areas did not delineate nor distinguish V1 and/or V^{HO} , but we identified a set of genes that did, and by definition they are among those that generate the distinct properties that define and distinguish V1 and V^{HO} (21–27).

Figure 2A illustrates the two types of expression patterns that delineated V1 and 5-HT staining to mark geniculocortical TCAs terminating in layer 4 of V1. In P7 WT mice, ROR β was highly expressed in V1 layer-4 neurons but at low levels in V^{HO} , whereas in P14 WT mice, Igfbp4 expression was not detected in V1 but was robust in layers 2/3 of V^{HO} . The relationship of these expression patterns to geniculocortical TCA input to V1 suggests that this input induces

the patterned expression of genes such as ROR β and represses the patterned expression of genes such as Igfbp4. In P7 cKO mice, coincident with loss of geniculocortical TCA input to V1, ROR β expression exhibited a significant reduction in V1, complemented by a significant increase of ROR β expression in V^{HO} , whereas Igfbp4 expression exhibited a strong up-regulation in V1 of P14 cKO mice (Fig. 2A). We performed densitometry of ROR β expression to quantify its areal expression in P7 WT and cKO mice (Fig. 2B). In P7 WT mice, V1 and S1 had similar high levels of ROR β expression and significantly lower expression in V^{HO} , resulting in a trough in expression intensity coincident with V^{HO} (Fig. 2C). In P7 cKO mice, S1 had high expression similar to that in WT mice, but the high expression in V1 and the low expression trough coincident with V^{HO} were replaced by flattened ROR β expression across the occipital visual cortical field of V^{HO} and V1. The absence in cKO mice of ROR β expression differences between V^{HO} and V1 characteristic of WT mice was due to both increased expression in V^{HO} and decreased expression in V1, and unlike WT mice, no significant difference was evident in expression levels between V^{HO} and V1 in the cKO mice (Fig. 2C,D).

Gene markers in our panel suitable for whole-mount in situ hybridization (WMISH) at P7 delineated V1 and V^{HO} in the intact brain, while retaining the natural shapes and positions of areas. In P7 WT cortices, moderate expression of Igfbp5 selectively marked the entire V1 and distinguished it from V^{HO} , which had nondetectable levels of Igfbp5. In P7 cKO cortices, Igfbp5 expression in V1 was diminished to a level indistinguishable from that in V^{HO} , and the entire occipital visual cortical field had low or nondetectable Igfbp5 expression. In P7 WT mice, both cadherin8 (Cad8) and Lmo4 showed opposing expression patterns as compared to Igfbp5, with higher expression in V^{HO} than V1, in distinct patterns that fully delineated V1 and V^{HO} independently. In cKO mice, the patterned expression of Cad8 and Lmo4 was lost, and neither distinguished V^{HO} from V1; instead, the occipital visual cortical field exhibited a homogeneous expression across its full extent, due in large part to increased expression of both genes throughout V1 to a level equivalent to that in V^{HO} (Fig. 3).

The expression of the type 2 muscarinic acetylcholine receptor (m2AChR) and distinct phosphorylation forms of neurofilaments (SMI-32) in adult WT mice delineate and distinguish V1 and

Fig. 1. Selective deletion of geniculocortical TCA projection to V1 in ROR α -IRES-Cre floxed COUP-TF1 cKO mice occurs early postnatally. (A) Genulocortical projection to V1 is selectively absent in P7 cKO mice. 5-HT immunostaining on tangential sections through layer 4 of P7 WT (COUP-TF1^{fl/+}; ROR α ^{Cre/+}) and cKO (COUP-TF1^{fl/fl}; ROR α ^{Cre/+}) flattened cortices is shown. Rostral is at left and medial at the top. 5-HT staining reveals TCA input from principal sensory thalamic nuclei to primary sensory areas: dLG to V1, VP to S1, and MG to the primary auditory area (A). The 5-HT-negative region surrounding V1 is composed of V^{HO} . In P7 cKO mice, 5-HT immunostained geniculocortical TCA input to V1 is absent. 5-HT staining of S1 appeared modestly diminished in cKO as compared to WT mice probably because COUP-TF1 may influence TCA input from VP, which expresses Cre (fig. S1) and exhibits COUP-TF1 deletion (fig. S2), but VP is less affected than dLG by COUP-TF1 deletion (figs. S2 and S4 to S6). (B) Time course of the deletion of geniculocortical TCA projection from dLG to V1 revealed in WT (COUP-TF1^{fl/+}; ROR α ^{Cre/+}; Ai14) and cKO (COUP-TF1^{fl/fl}; ROR α ^{Cre/+}; Ai14) mice crossed to the Ai14 line with the Cre-inducible axon reporter tdTomato. Sagittal sections from E16.5, P1, and P3 WT and cKO cortices, showing TCAs labeled by tdTomato reporter activated by Cre expressed in dLG and VP (anterior to the left, dorsal at the top) are shown. At E16.5, labeled TCAs (arrows) are densely packed in the subplate underlying the cortical plate of nascent V1, with the TCA projection being indistinguishable between WT and cKO mice. At P1, the geniculocortical TCA projection is beginning to invade the overlying CP of V1 in WT mice but is retarded in the cKO mice. By P3, the geniculocortical TCA projection is densely terminating in V1 of WT mice but is virtually absent from V1 in cKO mice. Abbreviations are as follows: 4, layer 4; ic, internal capsule; arrowheads approximate the anterior (A) – posterior (P) extent of nascent V1. Scale bars, 0.5 mm in (A) and 0.2 mm in (B).

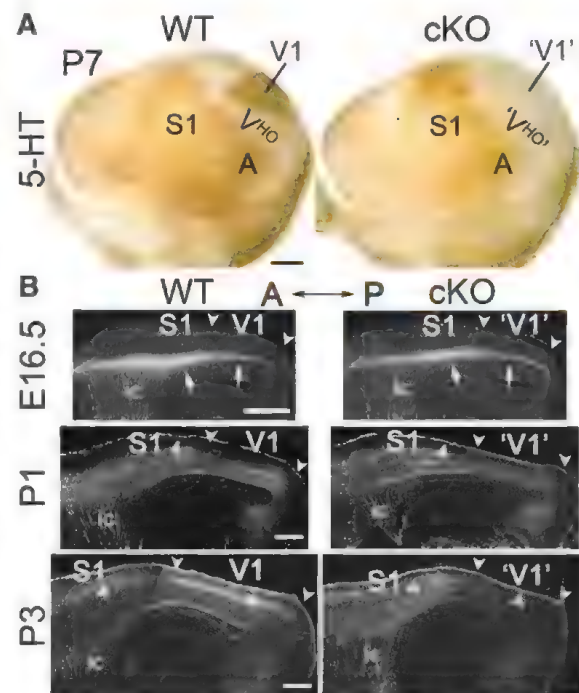


Figure 1B illustrates the time course of the deletion of geniculocortical TCA projection from dLG to V1 revealed in WT (COUP-TF1^{fl/+}; ROR α ^{Cre/+}; Ai14) and cKO (COUP-TF1^{fl/fl}; ROR α ^{Cre/+}; Ai14) mice crossed to the Ai14 line with the Cre-inducible axon reporter tdTomato. Sagittal sections from E16.5, P1, and P3 WT and cKO cortices, showing TCAs labeled by tdTomato reporter activated by Cre expressed in dLG and VP (anterior to the left, dorsal at the top) are shown. At E16.5, labeled TCAs (arrows) are densely packed in the subplate underlying the cortical plate of nascent V1, with the TCA projection being indistinguishable between WT and cKO mice. At P1, the geniculocortical TCA projection is beginning to invade the overlying CP of V1 in WT mice but is retarded in the cKO mice. By P3, the geniculocortical TCA projection is densely terminating in V1 of WT mice but is virtually absent from V1 in cKO mice. Abbreviations are as follows: 4, layer 4; ic, internal capsule; arrowheads approximate the anterior (A) – posterior (P) extent of nascent V1. Scale bars, 0.5 mm in (A) and 0.2 mm in (B).

V^{HO} and contribute to their specific functional properties (11, 26, 27). Immunostaining for m2AChR revealed low or nondetectable labeling of V^{HO} between the strongly labeled V1 and S1 (Fig. 4A). In adult cKO mice, immunostaining for m2AChR was substantially diminished in layer 4 throughout V1, coupled with significantly increased staining of layer 4 in V^{HO} , resulting in homogeneous low staining across the entire occipital visual cortical field normally composed of V1 and V^{HO} (Fig. 4B). In situ hybridization for m2AChR recapitulated both the WT and cKO expression patterns observed with m2AChR staining patterns (Fig. 4B), showing that the changes in the cKO mice reflected a reduction of

m2AChR expression by V1 layer 4 neurons rather than the loss of presynaptic m2AChR protein (27). Immunostaining for SMI-32 in adult WT mice also delineated V1 from V^{HO} with robust staining of V1 and low staining of V^{HO} , but with staining predominantly localized to projection neurons in layers 3 and 5. Deletion of geniculocortical TCAs to V1 in the cKO mice produced a substantial reduction in SMI-32 staining of both layer-3 and -5 projection neurons in V1 of adult cKO mice as compared to WT mice, resulting in homogeneous staining of layers 3 and 5 across the occipital visual cortical field and an inability to distinguish V1 from V^{HO} (Fig. 4, A and B).

We have shown a prominent role for TCA input and redefined the role of intrinsic genetic regulation of the differentiation of higher-order sensory areas from primary sensory areas (fig. S8A). We selectively deleted geniculocortical TCA input to V1 early in postnatal development to accomplish two goals: (i) to assess the requirement of geniculocortical TCA input for the differentiation of genetic profiles that distinguish V1 from V^{HO} and establish their specific functional properties; and (ii) to isolate the function of intrinsic genetic mechanisms to assess their role relative to geniculocortical TCAs in the specification and differentiation of V1 and V^{HO} . Isolating

Fig. 2. Differentiation of complementary gene markers that distinguish V1 from V^{HO} requires the postnatal influence of geniculocortical TCA projection. (A) 5-HT immunostained tangential sections of flattened cortices to reveal TCA input and ROR β and Igfbp4 in situ hybridization (ISH) from WT (COUP-TF1^{fl/+}; ROR α ^{Cre/+}) and cKO (COUP-TF1^{fl/fl}; ROR α ^{Cre/+}) mice; the field shown is indicated in the schematic. 5-HT and ROR β labeling were performed on sections through layer 4 of P7 cortices; Igfbp4 labeling was done on sections through layers 2/3 of P14 cortices. In WT mice, ROR β is strongly expressed in V1 and low in V^{HO} , whereas Igfbp4 expression is low in V1 and high in V^{HO} . The lack of TCA input in cKO V1 (*) is accompanied by a loss in differential expression patterns of ROR β and Igfbp4 that distinguish V1 from V^{HO} in WT mice. Scale bar, 1 mm. (B) ROR β expression at P7 from collapsing all tangential sections through layer 4. The rectangles are 100 μ m wide and 2700 μ m long and indicate the area used for pixel intensity measurements shown in (C) and (D). (C) Plot of the normalized pixel intensity (mean \pm SEM) in the rectangular field shown in (B). Each bin is 100 μ m wide and 20 μ m long and encompasses expression throughout layer 4 (z axis). The expression of ROR β in barrel B1 in the posterior medial barrel subfield of S1 is set at 100; other data are normalized to it. In WT (black, $n = 4$) mice, the ROR β expression is high in S1 and V1 and low in V^{HO} , whereas in cKO mice (red, $n = 4$), expression is flattened across the occipital visual cortical field due to up-regulation in V^{HO} and down-regulation in V1. (D) Bar graph of the statistical analysis performed with data from (C). Significant difference in ROR β expression intensity between V^{HO} (white) and V1 (black) was observed in WT mice (* $P < 0.0001$), but not in cKO mice (n.s., not significant).

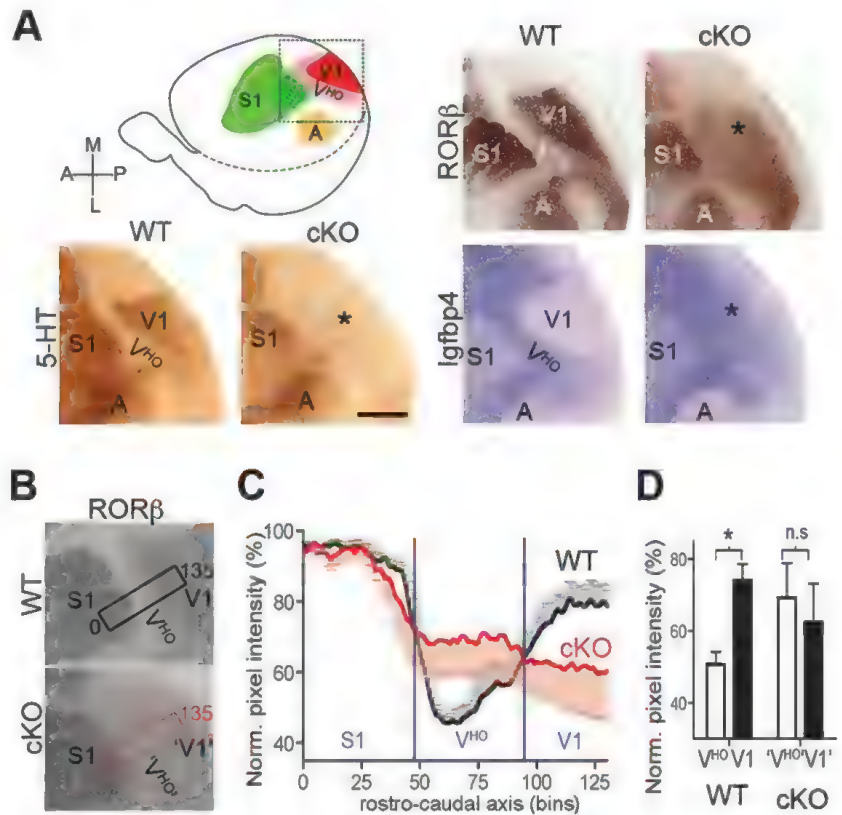


Fig. 3. V1 and V^{HO} delineated by complementary gene expression patterns are replaced with a uniform occipital visual cortical field after deletion of geniculocortical TCA input. Photos show the posterior part of P7 WT (COUP-TF1^{fl/+}; ROR α ^{Cre/+}) and cKO (COUP-TF1^{fl/fl}; ROR α ^{Cre/+}) cortices, as in the schematic at top left, processed using whole-mount in situ hybridization (WMISH) for Igfbp5, Cad8, and Lmo4. Igfbp5 expression specifically delineates V1; Cad8 and Lmo4 show lower expression in V1 and higher expression in V^{HO} and delineate both. These differential expression patterns in WT mice are lost in the cKO cortex and replaced with a uniform expression field that encompasses the entire occipital visual cortical field (marked with *). Scale bar, 0.5 mm.

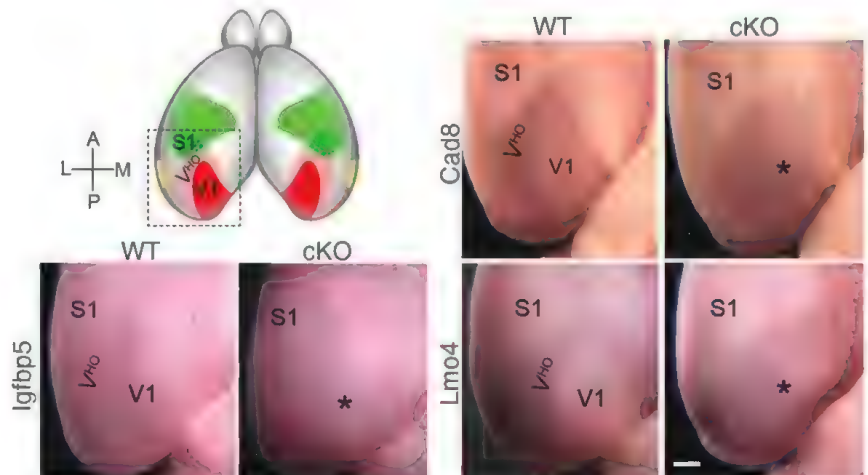
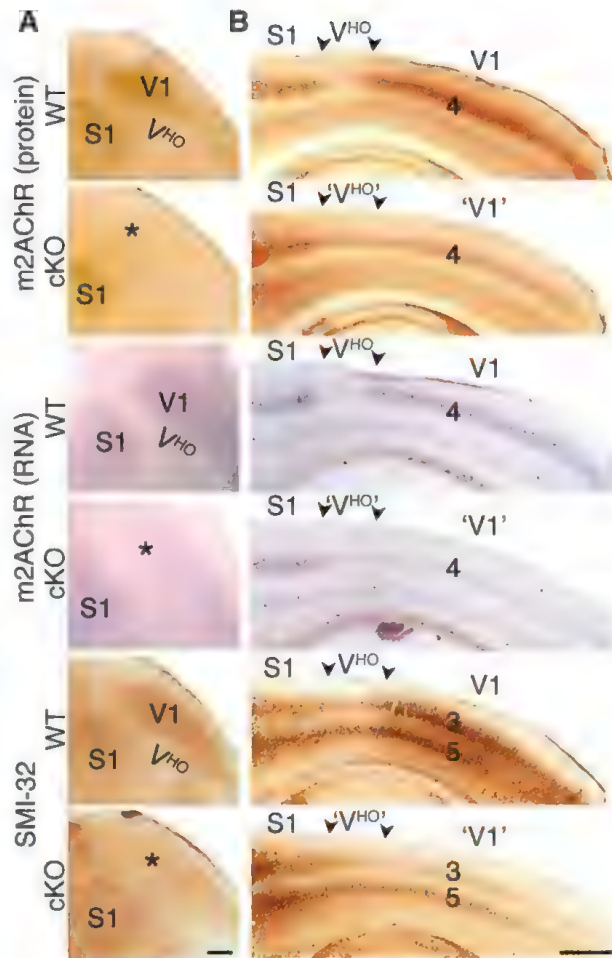


Fig. 4. Geniculocortical input drives differential patterning of genes and proteins that contribute to functional distinctions between V1 and V^{HO} in the adult cortex. Immunostaining for m2AChR and the SMI-32 epitope (a nonphosphorylated epitope on medium and heavy chains of neurofilaments that distinguishes functionally different forms) and ISH with an m2AChR probe on flattened tangential (A) and sagittal sections (B) of WT (COUP-TF1^{fl/+}, ROR α ^{Cre/+}) and cKO (COUP-TF1^{fl/fl}, ROR α ^{Cre/+}) cortices from adult (3-month-old) mice is shown. Rostral is to the left. In WT mice, m2AChR is highly expressed in layer 4 of V1, and SMI-32 is highly expressed in layers 3 and 5 of V1; both are expressed at low or nondetectable levels in V^{HO} of WT mice. In the cKO occipital cortex, m2AChR and SMI-32 are greatly down-regulated in V1 and modestly up-regulated in V^{HO}, resulting in uniform expression across the occipital visual cortical field (marked with *) posterior to S1 that would normally differentiate into V1 and V^{HO}. Scale bars, 0.5 mm.



in cKO mice the function of intrinsic genetic mechanisms in patterning V1 and V^{HO} redefined their roles in arealization and showed that they specify an occipital visual cortical field that has a similar genetic profile over its extent. Geniculocortical TCA input is required postnatally to differentiate the visual cortical field into V1 and V^{HO} and establish the genetic profiles that delineate and distinguish them. Regardless of whether in WT mice the gene and protein markers were more highly expressed in V1 than V^{HO}, or vice versa, they exhibited significant changes in their patterned expression in cKO mice in which geniculocortical TCA input was deleted, resulting in a uniform intermediate level of expression across the occipital visual cortical field that would normally differentiate into V1 and V^{HO} (fig. S8B). The change from patterned to uniform expression occurred through bidirectional changes in expression, with both down-regulation of expression in V1 and up-regulation in V^{HO}, or vice versa, to produce intermediate expression levels across the occipital visual cortical field despite the selective targeting in WT mice of geniculocortical TCAs to only part of the occipital visual cortical field; i.e., the nascent V1. These changes in patterned gene expression occurred not only in the primary TCA target layer 4, but also in layers 2, 3, and 5, which receive little or no direct TCA input.

Our findings require a revision of the prevailing model of arealization and indicate a working model with distinct stages: Intrinsic genetic mechanisms specify an occipital visual cortical field with a relatively uniform genetic profile, followed by its differentiation into V1 and V^{HO} driven by geniculocortical TCA input targeted selectively to the nascent V1 (fig. S9). This multistage process of arealization creates the hierarchical cortical organization of primary and higher-order visual areas that is required for proper visual perception and behavior.

References and Notes

- D. J. Felleman, D. C. Van Essen, *Cereb. Cortex* **1**, 1 (1991).
- D. D. O'Leary, S. J. Chou, S. Sahara, *Neuron* **56**, 252 (2007).
- K. M. Bishop, G. Goudreau, D. D. O'Leary, *Science* **288**, 344 (2000).
- T. Hamasaki, A. Leingärtner, T. Ringstedt, D. D. O'Leary, *Neuron* **43**, 359 (2004).
- M. Armentano et al., *Nat. Neurosci.* **10**, 1277 (2007).
- A. Leingärtner, L. J. Richards, R. H. Dyck, C. Akazawa, D. D. O'Leary, *Cereb. Cortex* **13**, 648 (2003).
- P. Rakic, I. Suñer, R. W. Williams, *Proc. Natl. Acad. Sci. U.S.A.* **88**, 2803 (1991).
- C. Dehay, P. Giroud, M. Berland, H. Killackey, H. Kennedy, *J. Comp. Neurol.* **367**, 70 (1996).
- E. M. Miyashita-Lin, R. Hevner, K. M. Wassarman, S. Martinez, J. L. Rubenstein, *Science* **285**, 906 (1999).
- Y. Nakagawa, J. E. Johnson, D. D. O'Leary, *J. Neurosci.* **19**, 10877 (1999).

- Q. Wang, A. Burkhalter, *J. Comp. Neurol.* **502**, 339 (2007).
- J. H. Marshel, M. E. Garrett, I. Nauhaus, E. M. Callaway, *Neuron* **72**, 1040 (2011).
- Y. Nakagawa, D. D. O'Leary, *Dev. Neurosci.* **25**, 234 (2003).
- R. D. Lund, M. J. Mustari, *J. Comp. Neurol.* **173**, 289 (1977).
- M. Armentano, A. Filosa, G. Andolfi, M. Studer, *Development* **133**, 4151 (2006).
- C. Zhou et al., *Neuron* **24**, 847 (1999).
- L. Madisen et al., *Nat. Neurosci.* **13**, 133 (2010).
- G. López-Bendito, Z. Molnár, *Nat. Rev. Neurosci.* **4**, 276 (2003).
- Bilateral enucleation in marsupials, which leads to decreased dLg size because of loss of retinal input, results in aberrant TCA input to V1 from dTh nuclei that normally project exclusively to other primary areas (20). Despite the selective deletion of the geniculocortical TCA projection in cKO mice, Dil injections into the putative V1 of the cKO mice did not aberrantly label neurons in VP, MG, or elsewhere in dTh (figs. S4 and S6). Injections of a second, retrograde tracer, DiD, targeted to nascent V1 of the same mice, labeled a similar-appearing high density of VP neurons in WT and cKO mice at both P0 and P7, and at late embryonic ages, but in neither WT nor cKO mice did S1 injections label neurons in dLg (figs. S4 and S6).
- S. J. Karlen, D. M. Kahn, L. Krubitzer, *Neuroscience* **142**, 843 (2006).
- The marker genes identified that met our criteria included those encoding the TFs, Lmo4 and ROR β , and the cell adhesion molecule Cad8, all of which function in cortical development (10, 13, 22–24); insulin-like growth factor-binding proteins Igfbp4 and Igfbp5 (25); and m2AChR and neurofilament subunits with the nonphosphorylated epitope SMI-32 that contribute to functional distinctions between V1 and V^{HO} (11, 26, 27). One subset of marker genes had more robust expression in V1 than V^{HO} (ROR β , Igfbp5, m2AChR, and SMI-32) and the other in V^{HO} than V1 (Igfbp4, Lmo4, and Cad8). Each clearly identified the border between V1 and V^{HO} and was expressed more-or-less uniformly throughout either V1 or V^{HO}.
- S. Bulchand, L. Subramanian, S. Tole, *Dev. Dyn.* **226**, 460 (2003).
- A. H. Kashani et al., *J. Neurosci.* **26**, 8398 (2006).
- D. Jabaudon, S. J. Snider, D. J. Tischfield, M. J. Galazo, J. D. Macklis, *Cereb. Cortex* **22**, 996 (2012).
- S. M. Firth, R. C. Baxter, *Endocr. Rev.* **23**, 824 (2002).
- E. Van der Gucht, P. R. Hof, L. Van Brussel, K. Burnat, L. Arckens, *Cereb. Cortex* **17**, 2805 (2007).
- E. A. van der Zee, T. Matsuyama, A. D. Strosberg, J. Traber, P. G. M. Luiten, *Histochemistry* **92**, 475 (1989).

Acknowledgments: We thank members of the O'Leary lab for discussion, including S. May for developing Igfbp5 as a V1 marker using WMISH, and B. Higgins and H. Gutierrez for maintaining mice. We thank M. Goulding (Salk Institute) for the ROSA-GAP43-eGFP reporter line, K.-F. Lee (Salk Institute) for the IRES/Cre/FRT/neo/FRT construct, A. Nagy (Mount Sinai Hospital) for the R1 ES cells, J. Simon (Salk MultiMedia Relations) for help making Adobe Illustrator schematics, and C. Peto (Salk Institute Neuroscience Imaging Core) for help using ImageJ software. Support was provided by NIH R01 grants NS31558 and MH086147 and the Vincent J. Coates Chair of Molecular Neurobiology (D.D.M.O.). M.S. is supported by the ANR "2009 Chaires d'Excellence" Program, France, grant number R09125AA. Z.B. was a recipient of postdoctoral fellowships from the Spanish Ministry of Education and Science and from the Generalitat de Catalunya (Spain).

Supplementary Materials

www.sciencemag.org/cgi/content/full/340/6137/1239/DC1
Materials and Methods
Figs. S1 to S9
References (28–31)

15 November 2012; accepted 10 April 2013
10.1126/science.1232806

Optogenetic Stimulation of Lateral Orbitofronto-Striatal Pathway Suppresses Compulsive Behaviors

Eric Burguière,¹ Patrícia Monteiro,¹ Guoping Feng,¹ Ann M. Graybiel^{1*}

Dysfunctions in frontostriatal brain circuits have been implicated in neuropsychiatric disorders, including those characterized by the presence of repetitive behaviors. We developed an optogenetic approach to block repetitive, compulsive behavior in a mouse model in which deletion of the synaptic scaffolding gene, *Sapap3*, results in excessive grooming. With a delay-conditioning task, we identified in the mutants a selective deficit in behavioral response inhibition and found this to be associated with defective down-regulation of striatal projection neuron activity. Focused optogenetic stimulation of the lateral orbitofrontal cortex and its terminals in the striatum restored the behavioral response inhibition, restored the defective down-regulation, and compensated for impaired fast-spiking neuron striatal microcircuits. These findings raise promising potential for the design of targeted therapy for disorders involving excessive repetitive behavior.

Repetitive behaviors are cardinal features of a number of neuropsychiatric conditions (1, 2). Single behaviors and ritualistic sequences of behavior can be repeated compulsively to the point of seriously interfering with daily functioning (3). Attempts to find efficacious

therapies for such conditions have been challenging (4, 5). Neuroimaging studies have identified abnormalities in cortico-basal ganglia circuits, particularly those involving the orbitofrontal cortex, implicated in the expression of repetitive, compulsive, and impulsive behaviors (6, 7). Dis-

abling the lateral part of the orbitofrontal cortex (IOFC) reduces response inhibition and increases impulsive choice, and this deficit in response inhibition is likely related to abnormalities in orbitofrontal interactions with the striatum and associated basal ganglia circuits (7–10). We targeted this orbito-fronto-striatal system to examine its function and to develop an optogenetic, therapeutic approach to treat compulsive behavior. As a model, we focused on the compulsive behavioral responses exhibited by *Sapap3* mutant mice (11, 12), which exhibit spontaneous, repetitive facial overgrooming and anxiety, behaviors that could be considered analogous to pathological repetitive behaviors in obsessive-compulsive disorder–spectrum disorders (13).

We first asked whether, as is thought to be the case in some human conditions, repetitive behavior in the *Sapap3* mutants could be triggered as an excessive reaction to a neutral stimulus that has been associated with a natural behavioral response. We designed a conditioning paradigm in which a neutral stimulus (a water drop applied to the

¹McGovern Institute for Brain Research and Department of Brain and Cognitive Sciences, Massachusetts Institute of Technology, Cambridge, MA 02139, USA.

*Corresponding author. E-mail: graybiel@mit.edu

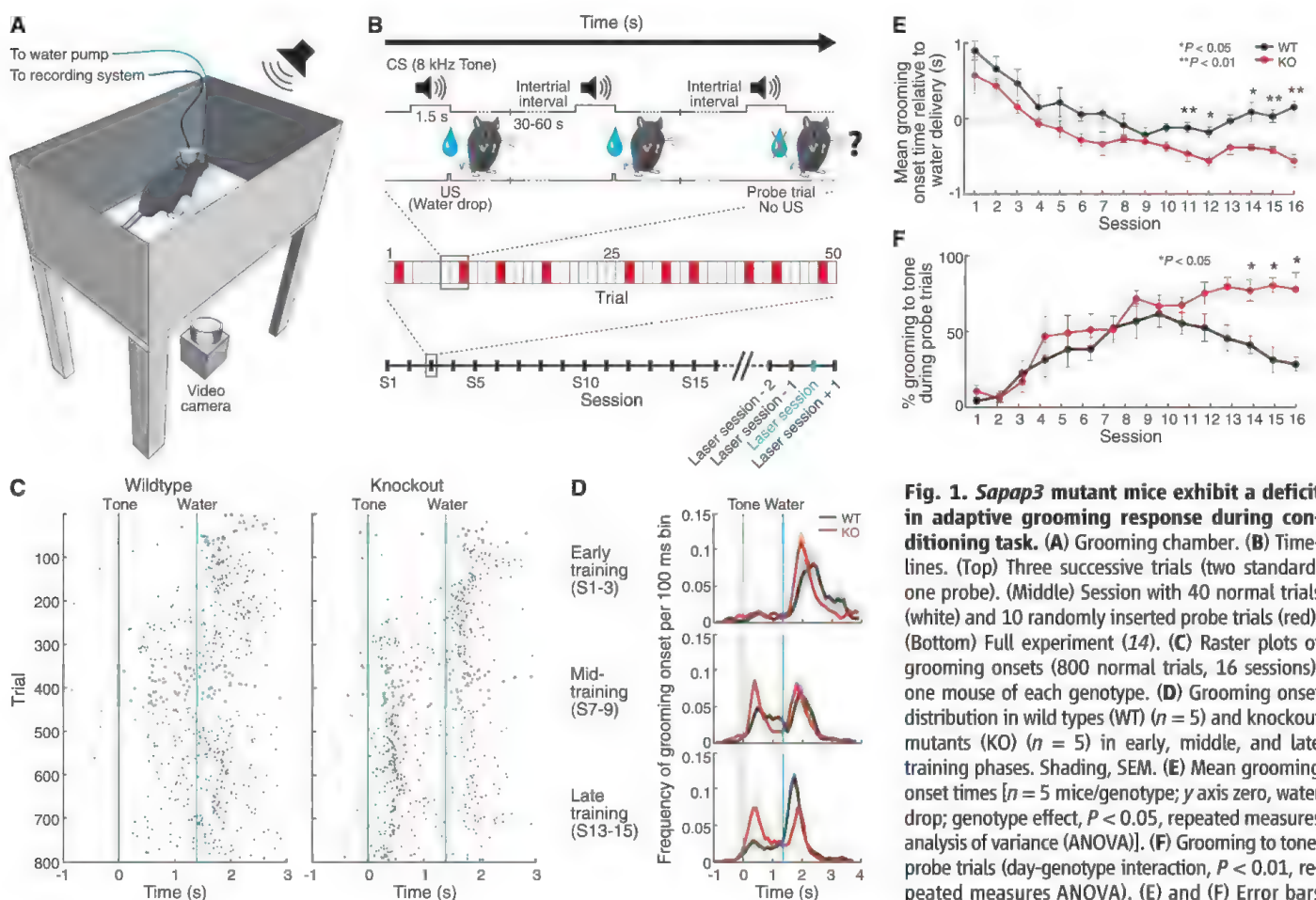


Fig. 1. *Sapap3* mutant mice exhibit a deficit in adaptive grooming response during conditioning task. (A) Grooming chamber. (B) Time-lines. (Top) Three successive trials (two standard, one probe). (Middle) Session with 40 normal trials (white) and 10 randomly inserted probe trials (red). (Bottom) Full experiment (14). (C) Raster plots of grooming onsets (800 normal trials, 16 sessions), one mouse of each genotype. (D) Grooming onset distribution in wild types (WT) ($n = 5$) and knockout mutants (KO) ($n = 5$) in early, middle, and late training phases. Shading, SEM. (E) Mean grooming onset times [$n = 5$ mice/genotype; y axis zero, water drop; genotype effect, $P < 0.05$, repeated measures analysis of variance (ANOVA)]. (F) Grooming to tone, probe trials (day-genotype interaction, $P < 0.01$, repeated measures ANOVA). (E) and (F) Error bars show SEM.

forehead) provoked a grooming response that could be clearly identified, which allowed us to pair a tone with the water drop in a delay-conditioning paradigm (Fig. 1, A and B, and fig. S1) (14).

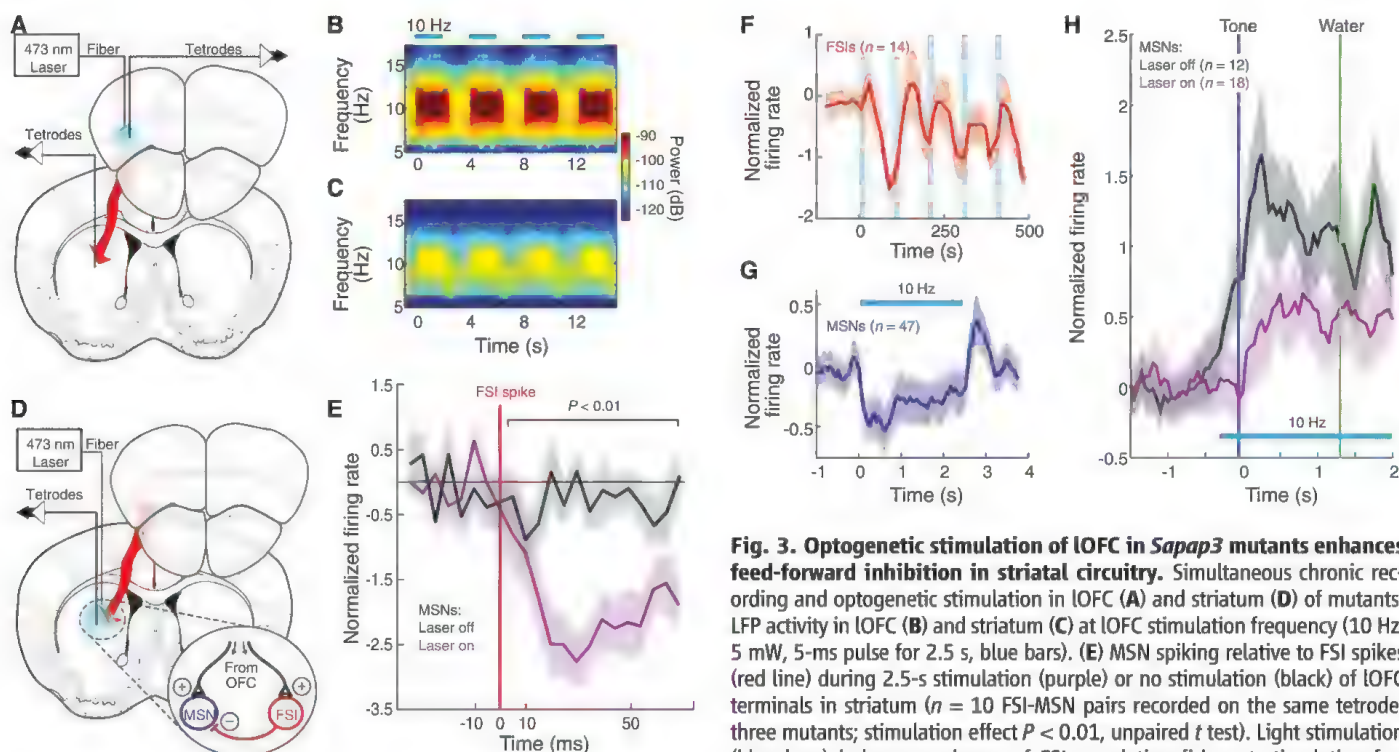
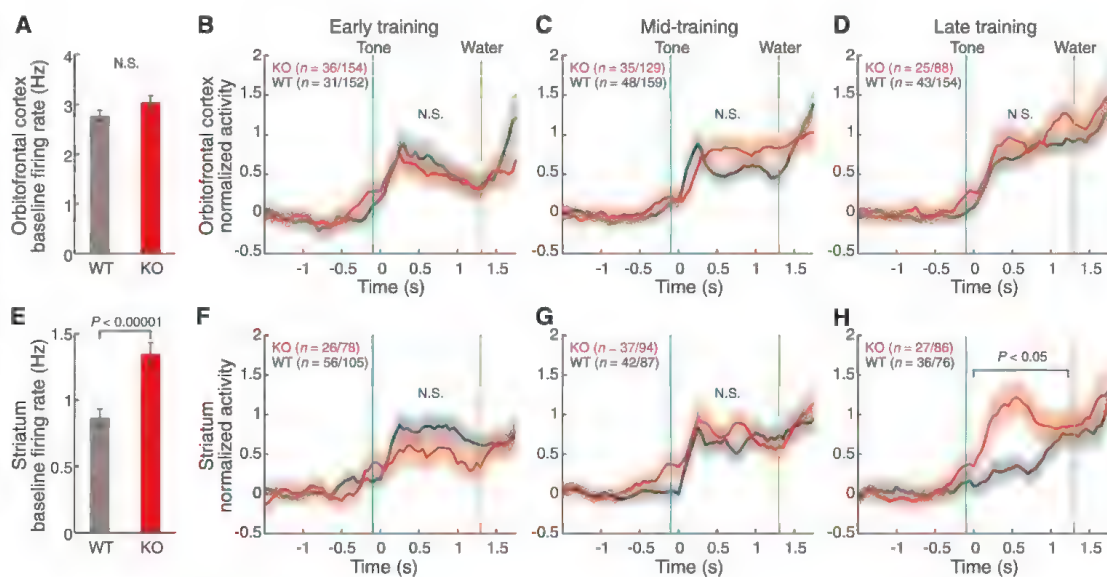
The behavior of the *Sapap3* mutant mice and their wild-type littermates diverged sharply during the course of conditioning. Early on, both mutants ($n = 7$) and littermate controls ($n = 7$) readily became conditioned, grooming when the conditioning tone was played (Fig. 1, C and D). Later in training, the wild types began to inhibit

this early grooming to the tone onset and to respond immediately after the water-drop release. The *Sapap3* mutants, by contrast, having once acquired the conditioned responses, kept responding to the tones with short-latency grooming, even in probe trials lacking water-drop delivery (Fig. 1, C to F; figs. S2 and S3; and table S1). This emergence of excessive short-latency responses was not accompanied by increased general grooming behavior or by hypersensitivity to the tone (figs. S4 and S5 and supplementary

text). The *Sapap3* mutant mice thus expressed an acquired maladaptive behavior characterized by defective inhibition of their conditioned responses to the originally neutral tone stimuli.

Learning theories of human compulsive behavior suggest that repetitive behaviors can result from malfunction of a learning process that leads to loss of the ability to repress sensorimotor associations (3, 15, 16). To identify the neuronal basis of such a deficit, we recorded spike and local field potential (LFP) activity simultaneously

Fig. 2. Dynamic learning-related changes in IOFC and striatal ensemble activity differ in wild-type and *Sapap3* mutant mice. Average baseline firing rates of IOFC (A) and striatal (E) units. Average activity of IOFC (B to D) and striatal (F to H) units classified as task-responsive (i.e., firing preferentially between tone and water events relative to baseline activity). Mean z-scores normalized for each neuron relative to baseline activity for wild-type (WT) ($n = 7$) and *Sapap3* mutant (KO) ($n = 7$) mice during training. Above, ratios of task-responsive units to total units per genotype. Shading, SEM.



frequency (**F**) ($n = 14$ units, three mutants) and long-lasting inhibition of MSNs during stimulation (**G**) ($n = 47$ units, three mutants). (**H**) Same stimulation protocol applied at the end of the training significantly decreased MSNs firing (purple) relative to no-stimulation condition (black). Shading, SEM.

with tetrodes in the IOFC and centromedial striatum as the mice acquired and then performed the task (fig. S6) (14). The baseline raw firing rates of putative pyramidal cells in the IOFC were similar in mutants ($n = 7$) and wild types ($n = 7$) throughout training, but the baseline firing rates of putative medium spiny neurons (MSNs) in the striatum were significantly elevated in the *Sapap3* mutants (Fig. 2, A and E).

During the early stages of training, subpopulations of pyramidal neurons in the IOFC in both genotypes exhibited a significant increase of activity between the tone and water events (Fig. 2B, fig. S7A, and table S2) (14). These IOFC responses remained similar throughout training; activity after the tone became progressively sustained up to the time of water-drop delivery (Fig. 2, B to D). By contrast, striatal task-related MSN activity patterns diverged markedly during training for the mutant and wild-type mice (Fig. 2, F to H, and fig. S7B) (14). Early on, MSNs in both geno-

types exhibited a phasic increase in response to the tone; but the slope of this increase steadily declined in the wild types but did not in the *Sapap3* mutants (Fig. 2H). This tuning of MSN activity in the wild types occurred as their grooming onset times shifted toward the time of water-drop delivery (fig. S8).

The lack of such learning-related MSN tuning in the mutants could have reflected increased excitation or decreased inhibition of activity after the tone (see supplementary text). We considered one powerful source of MSN inhibition, deriving from fast-spiking striatal interneurons (FSIs), which mediate fast feed-forward inhibition of MSNs in response to cortical activation (17) and largely correspond to parvalbumin (PV)-containing interneurons. In cell counts of PV-immunostained sections, we found significantly fewer PV-positive striatal neurons in the mutants than in the wild types ($n = 8$ mice per genotype, chi-square test, $P < 0.05$) (fig. S9) (14).

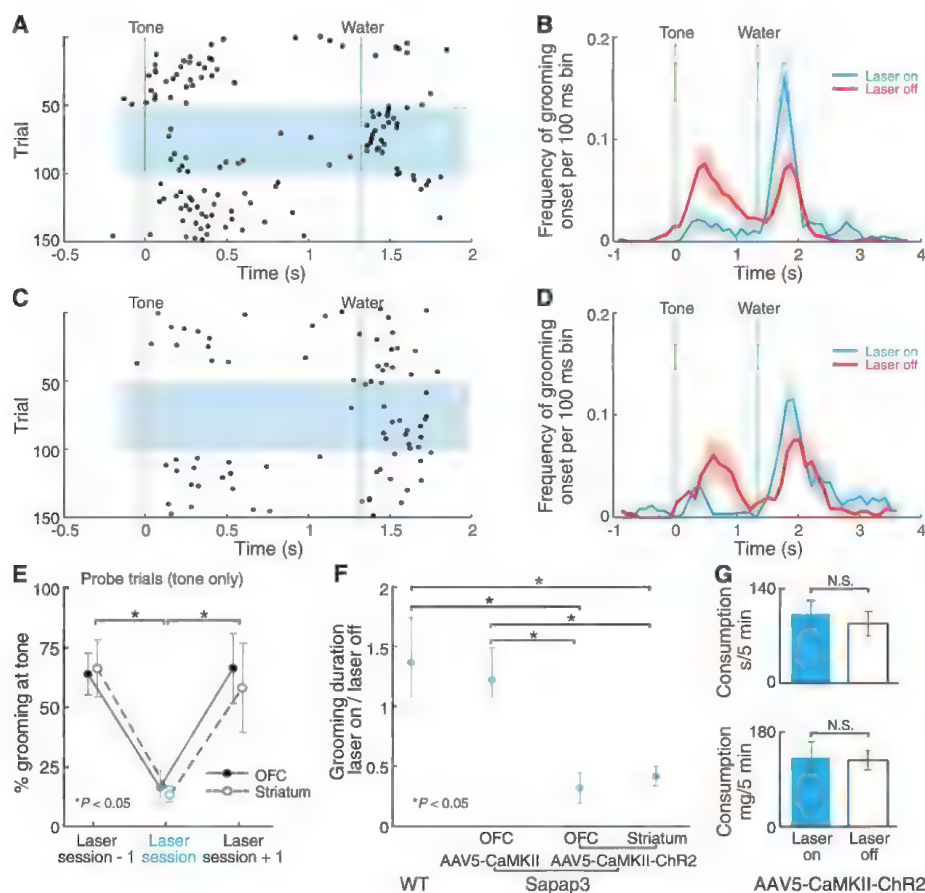


Fig. 4. Optogenetic stimulation of IOFC alleviates compulsive grooming of *Sapap3* mutant mice. Rasters of grooming onsets before, during (blue shading), and after bilateral IOFC (A) or striatal (C) stimulation (10 Hz, 5 mW, 5-ms light pulses) in a *Sapap3* mutant, late in training. Grooming onsets for the *Sapap3* population during session with laser stimulation (blue) in IOFC (B) ($n = 4$) or striatum (D) ($n = 3$) compared with preceding laser-off session (red). Shading, SEM. (E) Suppression of tone-evoked grooming by IOFC or striatal stimulation during probe trials ($P < 0.01$, unpaired t test). (F) Alleviation of compulsive grooming in *Sapap3* mutants ($n = 4$) by IOFC or striatal stimulation (5 Hz, 5 mW, 5-ms light pulses) during 3-min free-movement periods, and control virus ($n = 3$) and wild-type ($n = 3$) comparisons ($P < 0.05$, unpaired t test). (G) Lack of effect of same out-of-task IOFC stimulation in mutants ($n = 4$) on time spent eating (top) or food consumed (bottom) during 5-min free-feeding periods. Error bars in (E to G), SEM.

This result suggested that a defect in intra-striatal inhibition could contribute to the *Sapap3* mutant phenotype but did not identify the source of the abnormality. In the light of clinical evidence (6, 9), we asked whether we could restore the striatal inhibition by optogenetically altering IOFC input to the striatum. We injected the IOFC bilaterally with adeno-associated virus (AAV5) to express a fusion protein of channelrhodopsin-2 and enhanced yellow fluorescent protein (ChR2-EYFP) under the calcium- and calmodulin-dependent protein kinase II (CaMKII) promoter (18) to target cortical pyramidal neurons of *Sapap3* mutant mice (fig. S10). We delivered pulses of blue light (473 nm, 5 mW, 10 Hz pulses) through two independently movable optical fibers and simultaneously recorded neural activity in the IOFC and striatum (Fig. 3, A and D, and fig. S11) (14). We confirmed expression of ChR2 and spike and LFP modulation at the stimulation frequency (Fig. 3, B and C, and figs. S10 and S11). Control experiments with ineffective laser stimulation and with control virus were negative (fig. S12).

We stimulated the ChR2-containing IOFC axon terminals within the striatum while we recorded from ensembles of striatal neurons (Fig. 3D). To assess specifically the direct effect of IOFC stimulation on FSIs and MSNs in the *Sapap3* mutants, we isolated 10 FSI-MSN pairs in which both members of the pair were recorded on the same tetrad (Fig. 3E and figs. S7B and S13) (14). In these recordings, MSN spiking was inhibited after FSI spikes, and this inhibition was greatly increased during optogenetic stimulation of IOFC terminals in the striatum (unpaired t test, $P < 0.01$). This effect could also be seen at the population level (Fig. 3, F and G). These dynamics suggest that activation of the IOFC-striatal pathway in the *Sapap3* mutants compensated for their abnormally high MSN activity at the end of the training by eliciting a powerful feed-forward inhibition of MSNs driven by the cortical activation of FSIs (19).

We applied this IOFC-striatal optogenetic stimulation at the end of training and showed that it could restore MSN tone-response inhibition in the *Sapap3* mutants (Fig. 3H). We then asked whether such stimulation could also ameliorate the behavior of the *Sapap3* mutant mice (Fig. 4, A to D). At the end of the training, we excited either projection neurons in the IOFC or their terminals in the striatum in different experiments, triggering the laser at tone onset and continuing it for 2.5 s at 10 Hz. When the *Sapap3* mutants were under optical stimulation, their early grooming responses to the tones were almost completely abolished, both by IOFC stimulation ($n = 4$) (Fig. 4, A, B, and E) and by striatal stimulation ($n = 3$) (Fig. 4, C to E). Yet the mutants groomed normally as soon as the water drop was delivered. The abnormal stimulus-evoked compulsive behavior in the *Sapap3* mutants thus could have resulted from a deficit of behavioral inhibition that was restored by optogenetically stimulating the IOFC-striatal pathway.

We next tested whether we could also rescue the spontaneous compulsive phenotype of the *Sapap3* mutants by optogenetically stimulating in IOFC ($n = 6$) or striatum ($n = 4$) during their unconditioned, natural behavior, which is typified by excessive grooming, but for which the triggers impelling the grooming behavior are unknown (Fig. 4F) (14). Stimulation (5 Hz, 5 mW, 5-ms pulse for 3 min) almost fully alleviated their compulsive grooming (Fig. 4F), leaving intact other out-of-task behaviors requiring fine motor coordination and motivation ($n = 5$) (Fig. 4G). Wild types expressing CaMKII-ChR2 ($n = 3$) and *Sapap3* mutants expressing control virus ($n = 3$) showed no difference in grooming with the laser on or off (Fig. 4F).

Our findings demonstrate that selective stimulation of the IOFC-striatal pathway can restore a behavioral inhibition signal in an animal model expressing pathological repetitive behaviors and can prevent overexpression of both conditioned and spontaneous repetitive grooming. Optogenetic stimulation increased inhibition of striatal MSNs in the mutants, and it specifically activated striatal FSIs and affected FSI-MSN striatal microcircuitry. The abnormally elevated MSN baseline firing rates in the *Sapap3* mutant striatum and reduced numbers of PV-immunostained striatal interneurons, likely corresponding to physiologically identified FSIs, suggest that the microcircuit necessary for inhibiting MSN responses through FSI excitation may not have been fully functional (supplementary text) (11, 13).

A pathologic decrease of PV-containing striatal neurons has been observed in Tourette's syndrome, and FSI microcircuits have been implicated in other extrapyramidal disorders (20, 21). Our findings suggest that a key role of the IOFC in

underpinning response inhibition could include specific effects on FSI-MSN microcircuitry by which the IOFC controls striatal neurons (supplementary text).

Our finding that optogenetic control of this IOFC-striatal pathway can alleviate repetitive behaviors in a genetic model of compulsive behavior raises important questions for future work (supplementary text). Are subsystems of striatal MSNs (e.g., D1 and D2 dopamine receptor-expressing neurons or striosome and matrix neurons) differentially affected (22–25)? Can this targeted optogenetic therapy alleviate repetitive behaviors in other models? What microcircuits underlie the normal orbitofronto-striatal pathway neuroplasticity and behavioral adaptation evident in the wild types? Our findings should provide a platform for exploring these differential influences and for developing new potential therapeutic targets to alleviate conditions characterized by abnormally repetitive behavior.

References and Notes

1. J. F. Leckman, *Lancet* **360**, 1577 (2002).
2. R. M. Ridley, *Prog. Neurobiol.* **44**, 221 (1994).
3. M. E. Franklin, E. B. Foa, *Annu. Rev. Clin. Psychol.* **7**, 229 (2011).
4. C. Otte, *Dialogues Clin. Neurosci.* **13**, 413 (2011).
5. W. K. Goodman, R. B. Lydiard, *J. Clin. Psychiatry* **68**, e30 (2007).
6. S. R. Chamberlain et al., *Science* **321**, 421 (2008).
7. M. R. Milad, S. L. Rauch, *Trends Cogn. Sci.* **16**, 43 (2012).
8. D. M. Eagle, C. Baunez, *Neurosci. Biobehav. Rev.* **34**, 50 (2010).
9. A. C. Mar, A. L. Walker, D. E. Theobald, D. M. Eagle, T. W. Robbins, *J. Neurosci.* **31**, 6398 (2011).
10. A. M. Graybiel, S. L. Rauch, *Neuron* **28**, 343 (2000).
11. M. Chen et al., *J. Neurosci.* **31**, 9563 (2011).
12. J. M. Welch et al., *Nature* **448**, 894 (2007).
13. S. Züchner et al., *Mol. Psychiatry* **14**, 6 (2009).
14. Materials and methods are available as supplementary materials on Science Online.
15. S. Morein-Zamir, N. A. Fineberg, T. W. Robbins, B. J. Sahakian, *Psychol. Med.* **40**, 263 (2010).
16. J. E. Steinmetz, J. A. Tracy, J. T. Green, *Integr. Physiol. Behav. Sci.* **36**, 220 (2001).
17. G. J. Gage, C. R. Stoezner, A. B. Wiltchko, J. D. Berke, *Neuron* **67**, 466 (2010).
18. F. Zhang, L. P. Wang, E. S. Boyden, K. Deisseroth, *Nat. Methods* **3**, 785 (2006).
19. N. Mallet, C. Le Moine, S. Charpier, F. Gonon, *J. Neurosci.* **25**, 3857 (2005).
20. P. S. Kalanithi et al., *Proc. Natl. Acad. Sci. U.S.A.* **102**, 13307 (2005).
21. A. H. Gitis, A. C. Kreitzer, *Trends Neurosci.* **35**, 557 (2012).
22. J. R. Crittenden, A. M. Graybiel, *Front. Neuroanat.* **5**, 59 (2011).
23. J. J. Canales, A. M. Graybiel, *Nat. Neurosci.* **3**, 377 (2000).
24. E. Saka, C. Goodrich, P. Harlan, B. K. Madras, A. M. Graybiel, *J. Neurosci.* **24**, 7557 (2004).
25. D. M. Eagle et al., *J. Neurosci.* **31**, 7349 (2011).

Acknowledgments: The authors thank D. Hu, H. F. Hall, C. Keller-McGandy, J. Lee, Y. Kubota, R. MacRae, and D. J. Gibson for their generous help. Funded by the Simons Initiative on Autism and the Brain at MIT (A.M.G. and E.B.); National Institute of Child Health and Development, NIH, R37 HD028341 and Defense Advanced Research Projects Agency, W911NF1010059 (A.M.G.); and National Institute on Mental Health, NIH, R01 MH081201 and Simons Foundation Autism Research Initiative (G.F.). E.B. and A.M.G. designed the experiments, performed data analysis, and wrote the manuscript; E.B. conducted the experiments; P.M. conducted the cell counts; G.F. provided the *Sapap3* mutant mouse model and read the manuscript. The authors declare no competing financial interest. Correspondence and requests for materials should be addressed to A.M.G. (graybiel@mit.edu).

Supplementary Materials

www.sciencemag.org/cgi/content/full/340/6137/1243/DC1
Materials and Methods
Supplementary Text
Figs. S1 to S13
Tables S1 and S2
References (26–32)

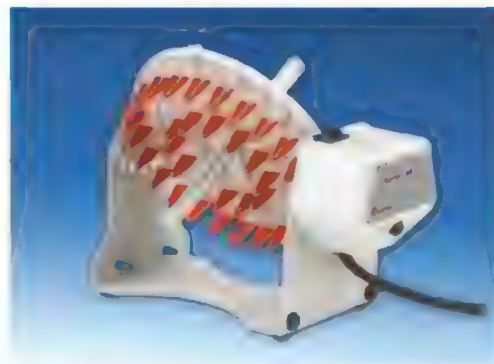
5 November 2012; accepted 3 April 2013
10.1126/science.1232380

ROTATING MIXER

The Sarmix MR 1 is a versatile and economic rotating mixer. It has three rotisserie configurations, two rotisserie positions, and can be placed in various positions to produce a wide range of motions. When the rotisserie is mounted in the vertical position, a gentle rolling motion is produced. For more vigorous mixing, the rotisserie can be placed horizontally. The same rotisserie position is used to create a tumbling movement by tilting the unit to rest on either end. Any of the three rotisseries can be used as a rocking platform.

Sarstedt

For info: 800-257-5101 | www.sarstedt.com

**ION CHROMATOGRAPHY SYSTEM**

The new Dionex ICS-5000⁺ Reagent-Free HPIC system is designed to elevate ion chromatography separation capabilities to new levels of resolution, speed, and flexibility. The new Dionex ICS-5000⁺ Reagent-Free HPIC system is designed to operate at continuous pressures up to 5,000 psi at analytical flow rates and extend the benefits of high-pressure ion chromatography to standard bore and microbore as well as capillary format separations. High backpressure tolerance is intended to let users increase flow rates to maximize throughput while still providing the advantages of electrolytic eluent generation and suppression. The Dionex ICS 5000⁺ HPIC system features a proprietary all-PEEK polymer flow path for metal-free inertness with the strength to operate continuously at 5,000 psi. The Dionex ICS-5000⁺ HPIC system can use the new high-efficiency 4 μ m-particle-size IC columns at high pressures, which may enable users to discover peaks they have been missing.

Thermo Fisher Scientific

For info: 781-933-4689 | www.thermofisher.com

FLAME PHOTOMETER

The groundbreaking BWB XP is the only five-channel flame photometer in the world offering simultaneous detection and display of all five elements. The incorporation of high-quality build and unparalleled performance with state-of-the-art technology provides improved accuracy and stability while significantly reducing analysis time. BWB flame photometers have been designed to combat the challenge traditionally faced in photometry such as maintaining flame intensity, consistency in liquid to flame flow rate, and pressure to fuel gas flow rate, all of which affect the photometers ability to determine the concentration of metal ions. Benefits include analysis in parts per million and a clear, intuitive LCD display—which eliminates the need for specialized training, saving time and money. In addition to logical simplicity, the BWB flame photometers include everything required to use the product straight from the box—just add gas. The built-in air compressor greatly reduces noise and laboratory footprint while increasing instrument stability, accuracy, and reproducibility.

BWB

For info: +44-(0)-1787-273451 | www.bwbtech.com

THERMAL CYCLER ALTERNATIVE

The Hyb-Ice Thermal Profiling System is an affordable and flexible alternative to a standard thermal cycler for performing everyday temperature profiles. The system consists of a programmable heating/cooling base and removable block that heat and cool samples from 4°C to 99°C. The system accommodates a variety of quick-change blocks to fit nearly any tube or plate. The Hyb-Ice System provides excellent temperature regulation, uniformity, and ramp rates and performs polymerase chain reaction in either standard- or large-volume tubes. A non-contact heated lid controls condensation. Programs can be stored or run via an onboard USB drive.

SciGene

For info: 408-733-7337 | www.scigene.com

CONTAINMENT ENCLOSURES

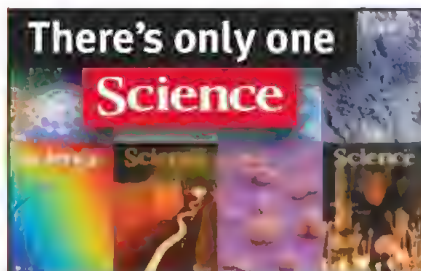
The PowderSafe Type B Enclosures usher in a new era of powder weighing and containment technology. PowderSafe Type B enclosures provide a controlled negative pressure HEPA-filtered environment for professionals to work with and weigh powders. PowderSafe Type B is fabricated with polypropylene, which is a chemically resistant, high-mass polymer. The innate chemical resistance of polypropylene allows users to easily clean the enclosure without the worry of degradation, while the high-mass construction alleviates the threat of vibration and balance disturbance during weighing. Exclusive to PowderSafe enclosures, HepaSafe technology allows the operator to safely and easily change both the prefilter and the primary HEPA filter while the enclosure remains under negative pressure. Furthermore, FlowSmooth technology provides even, horizontal air distribution throughout the enclosure, preventing turbulence. This laminar horizontal air movement is also key to operator protection from hazardous chemical and compounds being manipulated within the enclosure.

AirClean Systems

For info: 800-849-0472 | www.aircleansystems.com

Electronically submit your new product description or product literature information! Go to www.sciencemag.org/products/newproducts.dtl for more information.

Newly offered instrumentation, apparatus, and laboratory materials of interest to researchers in all disciplines in academic, industrial, and governmental organizations are featured in this space. Emphasis is given to purpose, chief characteristics, and availability of products and materials. Endorsement by *Science* or AAAS of any products or materials mentioned is not implied. Additional information may be obtained from the manufacturer or supplier.



Science Careers Advertising

For full advertising details, go to ScienceCareers.org and click For Employers, or call one of our representatives.

Tracy Holmes
Worldwide Associate Director
Science Careers
Phone: +44 (0) 1223 326525

THE AMERICAS

E-mail: advertise@sciencecareers.org
Fax: 202-289-6742

Tina Burks
East Coast/West Coast/South America
Phone: 202-326-6577

Marci Gallun
Midwest/Canada
Phone: 202-326-6582

Candice Nulsen
Corporate
Phone: 202-256-1528

Online Job Posting Questions
Phone: 202-312-6375

EUROPE / INDIA / AUSTRALIA / NEW ZEALAND / REST OF WORLD

E-mail: ads@science-int.co.uk
Fax: +44 (0) 1223 326532

Axel Gesatzki
Phone: +44 (0)1223 326529

Lucy Nelson
Phone: +44 (0)1223 326527

Kelly Grace
Phone: +44 (0) 1223 326528

JAPAN

Yuri Kobayashi
Phone: +81-(0)90-9110-1719
E-mail: ykobayas@aaas.org

CHINA / KOREA / SINGAPORE / TAIWAN / THAILAND

Ruolei Wu
Phone: +86-1367-1015-294
E-mail: rwu@aaas.org

All ads submitted for publication must comply with applicable U.S. and non-U.S. laws. Science reserves the right to refuse any advertisement at its sole discretion for any reason, including without limitation for offensive language or inappropriate content, and all advertising is subject to publisher approval. Science encourages our readers to alert us to any ads that they feel may be discriminatory or offensive.



ScienceCareers.org

FACULTY POSITIONS Physiology & Pharmacology

The Department of Physiology & Pharmacology at Des Moines University invites applicants for open-rank, tenure-track faculty positions. Qualifications include preparation and expertise in one or more of the following areas:

**Cardiovascular Physiology; Respiratory Physiology;
Endocrine Physiology; or Medical Pharmacology.**

We are committed to advancing our research enterprise and fostering an environment conducive to scholarly success through cultivation of distinctive faculty and student researchers who discover and disseminate new knowledge. Applicants should demonstrate the potential to develop an innovative and extramurally funded research program. Applicants must have an earned Ph.D. or equivalent plus minimum of two years postdoctoral experience.

Please submit a letter of application, CV and a concise statement of teaching interests and educational philosophy, a well-defined research plan including specific aims and objectives and contact information for three references using the online applicant tracking system at www.dmu.edu/employment. Review of applications will begin immediately and continue until the positions are filled.

Job description, faculty benefit summary and/or information on Des Moines University are available at www.dmu.edu/employment.



Des Moines University is an equal opportunity/affirmative action employer. The University seeks excellence through diversity among its administrators, faculty, employees and students. The University prohibits discrimination on the basis of race, color, national origin, creed, religion, age, disability, sex, gender identity, sexual orientation, veteran status, genetic information or any other legally protected status. Applications by members of all underrepresented groups are encouraged.



CEPLAS

Cluster of Excellence on Plant Sciences

From Complex Traits towards Synthetic Modules

The Cluster of Excellence on Plant Sciences announces a faculty position as

Full Professor of Microbiology at the University of Cologne

The Cluster of Excellence on Plant Sciences (www.ceplas.eu) invites applications for a Full Professorship (W3) in Microbiology with emphasis on environmental microbiology at the University of Cologne (UoC).

CEPLAS holds a unique position within the German Excellence Initiative as the only cluster focusing on plant sciences and plant-associated microbes. It applies a new approach driven by evolutionary analysis and synthetic biology. CEPLAS currently establishes overall 9 faculty positions affiliated either to the UoC or the Heinrich Heine University of Düsseldorf (HHU).

The new professor is expected to establish an outstanding research program in microbial sciences, preferably working on fundamental principles governing microbe-plant and/or microbe-microbe interactions. The announced professorship will be established together with two new professorships in Ecological Genetics of Microbes (W2; UoC) and in Synthetic Microbiology (W2; HHU). To facilitate implementation of the research program, the teaching load will be reduced during the first 5 years.

Applications should include a curriculum vitae, a list of refereed publications as well as a statement of research and teaching interests, and names of three referees as one PDF file. The letter of application should be addressed to the Dean of the Faculty of Mathematics and Natural Sciences and sent electronically to bewerbung@ceplas.de. The closing date for applications is June 28, 2013.

UoC is an equal opportunity and affirmative action employer. In order to increase the number of women in leading academic positions, we specifically encourage women to apply. UoC is further responsive to the needs of dual career couples and qualifies as a family friendly employer. University of Cologne offers a Dual Career Service and is a member of the Dual Career Network Rhineland. Further information can be found under: www.dualcareer-rheinland.de

www.uni-koeln.de

Universität
zu Köln





SLAC Associate Laboratory Director

Director of the Stanford Synchrotron Radiation Lightsource

SLAC National Accelerator Laboratory is a U.S. Department of Energy Office of Science, multi-program laboratory operated by Stanford University. SLAC's cutting-edge research facilities attract thousands of scientists from around the world each year working in the areas of photon science, particle physics, cosmology, accelerator technology, materials and energy science, chemistry and biology.

The Stanford Synchrotron Radiation Lightsource (SSRL), a directorate of SLAC, is inviting applications for the position of Associate Lab Director. As one of five light sources funded by the DOE Office of Science, SSRL enables research that leads to major advances in energy production, environmental remediation, nanotechnology, new materials and medicine. SSRL also serves as a vital training ground for graduate students and postdoctoral scholars.

SLAC seeks a scientist with an extraordinary combination of scientific vision, accomplishment and leadership to assume responsibility for all aspects of the SSRL Directorate. Reporting to the SLAC Laboratory Director, the Associate Laboratory Director for the SSRL program will:

- Lead and manage a directorate of accomplished scientists, technical staff and administrators to deliver outstanding user operations and innovative, state-of-the-art science and technology.
- Manage and oversee strategic planning, budgets, operational and R&D functions for the directorate.
- Lead the development of future generation light sources.
- Serve as a member of the SLAC Executive Council. Collaborate with the Laboratory Director and other program directors to realize the full potential of SSRL.
- Represent SLAC and the Lab Director in communications with Congress, DOE, industry, local government and citizens groups, and Stanford University.
- Leverage SLAC capabilities and resources to create opportunities that address the needs of industry.

The SSRL Associate Laboratory Director will be an internationally recognized scientist with established leadership credentials, strategic thinking and execution skills, excellent communication skills, commitment to excellence and capability to expand the capacities of SLAC's pioneering synchrotron facilities. The successful candidate is expected to assume a tenured position on the Stanford/SLAC faculty.

For more information visit the career section at slac.stanford.edu or contact:

Lisa Mongetta, Manager, SLAC Staffing Services
2575 Sand Hill Road, Menlo Park, CA 94025
650-926-2733, mongetta@slac.stanford.edu

Stanford University is an equal opportunity employer and is committed to increasing the diversity of its faculty. It welcomes nominations of, and applications from, women and members of minority groups, as well as others who would bring additional dimensions to the University's research and teaching missions.



SLAC Associate Laboratory Director

Director of the Linac Coherent Light Source

SLAC National Accelerator Laboratory is a U.S. Department of Energy Office of Science, multi-program laboratory operated by Stanford University. SLAC's cutting-edge research facilities attract thousands of scientists from around the world each year working in the areas of photon science, particle physics, cosmology, accelerator technology, materials and energy science, chemistry and biology.

The Linac Coherent Light Source (LCLS), a directorate of SLAC, is inviting applications for the position of Associate Lab Director. LCLS is the world's most powerful X-ray laser and the first free electron laser to operate in the wavelength range of 0.15-1.5 nanometers. The LCLS's highly focused beam and ultrafast pulses allow researchers to probe complex, ultra-small structures and capture atomic motions, thus shedding light on the fundamental processes of chemistry, biology, materials and energy science and technology.

SLAC seeks a scientist with an extraordinary combination of scientific vision, accomplishment and leadership to assume responsibility for all aspects of the LCLS Directorate. Reporting to the SLAC Laboratory Director, the Associate Laboratory Director for the LCLS program will:

- Lead and manage a directorate of accomplished scientists, technical staff and administrators to deliver outstanding user operations and innovative, state-of-the-art science and technology.
- Manage and oversee strategic planning, budgets, operational and R&D functions for the directorate.
- Sponsor and lead free electron laser R&D programs.
- Serve as a member of the SLAC Executive Council. Collaborate with the Laboratory Director and other program directors to realize the full potential of LCLS.
- Represent SLAC and the Lab Director in communications with Congress, DOE, industry, local government and citizens groups, and Stanford University.
- Leverage SLAC capabilities and resources to create opportunities that address the needs of industry.

The LCLS Associate Laboratory Director will be an internationally recognized scientist with established leadership credentials, strategic thinking and execution skills, excellent communication skills, commitment to excellence and capability to expand the capacities of SLAC's world class free electron laser program. The successful candidate is expected to assume a tenured position on the Stanford/SLAC faculty.

For more information visit the career section at slac.stanford.edu or contact:

Lisa Mongetta, Manager, SLAC Staffing Services
2575 Sand Hill Road, Menlo Park, CA 94025
650-926-2733, mongetta@slac.stanford.edu

Stanford University is an equal opportunity employer and is committed to increasing the diversity of its faculty. It welcomes nominations of, and applications from, women and members of minority groups, as well as others who would bring additional dimensions to the University's research and teaching missions.



廣東工業大學
Guangdong University of Technology

**Invites Applications and Nominations for
"Deans of five different schools"& "One-Hundred Talents" Chair
Professors & "One-Hundred Young Talents" Associate Professors**

Guangdong University of Technology, located in Guangzhou, a beautiful city in southern China, is a key multi-disciplinary university of Guangdong Province with a history of over 50 years. With the advantage of bordering on Hong Kong and the benefits of Guangdong's prosperous economic development, the university's research and competitive power has been remarkably improved in recent years.

The "School Deans" Program

The university plans to invite scholars, experts and entrepreneurs who are competent to build first-class schools to work as deans of the following schools:

(1) School of Electromechanical Engineering (2) School of Automation (3) School of Chemical Engineering and Light Industry (4) School of Materials and Energy (5) School of Physics and Optoelectronic Engineering

The applicants for The "School Deans" Program shall have good capacity in organization and coordination to lead the school for further development.

The "One-Hundred Talents" Chair Professors:

The eligible candidates should hold a doctoral degree(s), no older than 50 in general; and have obtained at least associate professor titles or equivalent, and have all-round knowledge of related key technologies or work in urgently needed fields; and already have achievements in relevant academic fields, or work as technological leaders and have experiences in organizing world-class technological projects.

The "One-Hundred Young Talents" Associate Professors:

Age below 35, hold a doctoral degree(s), graduated from a famous overseas university or a National Key University, have working experiences in famous overseas laboratories, research institute, national key research platform and achieved satisfactory initial results.

More information on requirements and disciplines, please visit university's website: www.gdut.edu.cn

Salaries and Benefits:

We offer competitive compensation package and benefits for the qualified candidates. The annual compensation can be up to 1 million RMB; the startup R&D funding can be up to 10 million RMB. Laboratory space will be provided. We also provide qualified candidates with a temporary apartment and housing allowance.

Candidates should provide a cover letter and a resume to:

Ms Zhiying Zeng Email: gduyzzp@gdut.edu.cn Telephone: 86-20-39322509

FACULTY POSITIONS AT TIANJIN UNIVERSITY

Founded in 1895 as Peiyang University, Tianjin University is regarded as the pioneer of modern higher education in China. Supported by Chinese Ministry of Education, Tianjin University is among the first group of universities to be included in the "985", "211" and "2011" Projects of national investment for developing world recognized universities. Over the years, Tianjin University has grown into a world prestigious research university with distinctive quality and strength in education, research and social services. (www.tju.edu.cn)

Positions

Tianjin University invites applications for full-time professorship, covering engineering, natural science, management, pedagogy and some newly emerging inter-discipline. Applicants with research background of multi-disciplinary and non-traditional approach are highly expected.

Qualifications

Academic faculties and postdoctoral fellows with outstanding academic performance will be deemed as competitive applicants. Relevant research field with a proven record of research excellence and outstanding communication skills are essential.

Responsibilities

Responsibilities include establishing a vigorous research program, participating in teaching at the undergraduate and graduate levels, and providing professional/institutional services.

Salary and Support

Tianjin University offers an attractive remuneration package, including an annual pre-tax salary range from 400K to 600K RMB. The salary will be commensurate with the candidate's qualifications and experience. An additional salary increment is promised if applicants are ranked in the official high-level talent program of China. In addition, a start-up package will be provided which includes adequate start-up financial support, ample working space and research assistants.

Application Procedure

Please send the electronic version of the following mandatory materials to oplan@tju.edu.cn. As for the detailed application procedure and application form, please download from <http://hr.tju.edu.cn/zpxx/js/>. The application deadline is **30th July 2013**.

- (1) Application form
- (2) Detailed curriculum vitae
- (3) Publications list and five full representative papers

Contact Methods

Contact Persons: Ms LIU Na (Ph.D.), Ms ZHANG Yinlu
Human Resource Department, Tianjin University, China

E-mail: oplan@tju.edu.cn **Tel:** (+) 86-022-27403932, (+)86-022-27402079 **Fax:** (+)86-022-27404177

Add: 223/Building 9, 92 Weijin Road, Nankai District, Tianjin, 300072

WOMEN IN SCIENCE

forging
new pathways in
green
science



Read inspiring stories
of women working in
"Green Science"
who are blending
a unique combination of
enthusiasm for science
and concern for others
to make the world
a better place.

Download this
free booklet
[ScienceCareers.org/
LOrealWiS](http://ScienceCareers.org/LOréalWiS)



This booklet is brought to you by the
AAAS/Science Business Office
in partnership with the
L'Oréal Foundation



The Alberta Prion Research Institute congratulates Dr. Fei Wang, The Ohio State University, winner of the APRI International Young Researcher Prize.



FOR MORE INFORMATION, VISIT
prioninstitute.ca

Tokyo University of Agriculture and Technology



東京農工大学

Tenure-track positions at the associate professor level

Tokyo University of Agriculture and Technology (TUAT) invites applications for six (6) tenure-track positions at the rank of Associate Professor. The appointee will be provided with an independent laboratory, startup budget and research fund with fewer duties on the administration and lecture side. There will be two evaluations at the 3rd and 5th years after the appointment. If the outcome of the evaluation indicates that the appointee has made promising or significant research, he or she will be promoted to the status of a tenured position.

Area of Research - (A) Biotechnology and Life Science, (B) Organic and Polymer Materials Chemistry, (C) Mechanical Systems Engineering, (D) Applied Physics, (E) Computer Science and Information Technology, (F) Environment Symbiotic Production System, (G) Science of Biological Production, (H) Applied Biological Chemistry, (I) Eco-material Science, (J) Environmental Science on Biosphere, (K) Environment Conservation, (L) Plant Pathology, (M) Applied Entomology.

Salary - Annual salary is approximately from JPY5,500,000 to 7,500,000 depending on education, teaching experiences etc.

Duration of appointment - The contract is for five years.

Details and Inquiries - Details on the application and e-mail addresses for inquiries are shown in the following URL.

<http://www.tuat.ac.jp/~senryaku/koubo/tt/ttkoubo-en.html>



IHU-A-ICM PARIS INSTITUTE OF TRANSLATIONAL NEUROSCIENCES CALL FOR APPLICATIONS - GROUP LEADER POSITIONS

The Brain and Spine Institute (ICM) with the Institut Hospitalo Universitaire - (IHU - Paris Institute of Translational Neurosciences) brings together more than 450 researchers, 300 physicians and 900 nursing and paramedical staff, as well as a large network of public and industrial partners. It is dedicated to basic, translational and clinical research in neuroscience as well as to the improvement of the quality of care and education. The ICM comprises 23 selected research teams, innovative technological platforms - molecular & cellular research, animal facilities, neuroimaging -, an in-house neuroscience clinical research center, and has a floor reserved for spin-off and companies. The ICM is located within the Pitié-Salpêtrière hospital, whose cohorts of neurological patients are the largest in France, thus offering a unique opportunity for translational research. Additionally, 13 National Reference Centers for rare diseases are also located at the Pitié-Salpêtrière, alongside the largest number of separate, rare neurological disease units in the country.

The ICM was one of the six candidates selected to be financed by the french investment for the future program and was granted University Hospital Institute (IHU) status. It brings together teams of researchers and physicians, of all origins, to promote excellence in research, training, patient care, and technology transfer in the field of the nervous system diseases.

The institute is welcoming applications for group leader positions and wishes to reinforce three research axes:

- Neurodegenerative disorders with a focus on cellular biology
- Neuroimmunology
- Modeling of behavior and diseases

but also strongly encourage applicants with open proposals in the field of neuroscience.

The candidates should be dynamic investigators with a strong track record. Applications from both Junior investigators (to start a new group) and Senior investigators (to move with a preexisting group) will be considered. New groups are expected to start as soon as 2014.

Successful candidates will benefit of lab spaces in the institutes, state-of-the-art platforms and core facilities. A stimulating international environment and graduate programs from the Université Pierre et Marie Curie (UPMC) are well established. A start-up package will be provided to the appointed group leaders. Assistance for applications to national and european programs will be provided (CNRS, Inserm, ANR, ATIP-Avenir, Equipes FRM, ERC) for their long-term insertion in France.

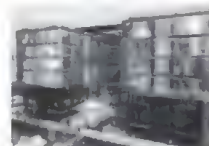
Expression of interest will include a short CV, a short list of publications, a brief description of past achievements and future research (2 pages). **The EoI must be send by July 15th, 2013** at the following address: researchleader-ihu@icm-institute.org

Short-listed applicants will be requested to send the full application proposal including:

- Title, summary and five main publications (limited 2 pages)
- CV (limited to 2 pages),
- Description of the research project (no more than 10 pages)
- List of publications and conferences
- Names and contacts of three referees

Full applications must be sent by November 15th, 2013 at the following address researchleader-ihu@icm-institute.org. The applications will be reviewed by the International Scientific Advisory Board of the institute. Short-listed applicants will be invited for an interview and oral presentation in Paris in late January 2014.

Expression of Interest Deadline (2 pages maximum)	First Selections Announcement	Full Application Proposal Deadline	Finalists Oral Presentation
July 15th, 2013	September 15th, 2013	November 15th, 2013	End January, 2014





Learning with Purpose

Careers with **Mass Appeal**

Assistant Dean College of Sciences

The Assistant Dean of the College of Sciences will provide comprehensive support to the Dean and Faculty in managing various aspects of the College including day-to-day operations, student services, and aspects of department management. Responsibilities include identifying and advising students at risk; helping to administer college events; working with departments to manage scheduling and enrollments and to facilitate employment searches; assist in strategic planning, resource allocation, curriculum planning, and data acquisition; manage freshmen co-ops, the college website, and the college newsletter and brochures; preside over student grade and academic dishonesty appeals; conduct general administrative duties and manage college projects as assigned. This is a full-time, benefited position, and salary is commensurate with experience.

Minimum Qualifications: Master's degree in a science or math discipline; 5 years administrative leadership in higher education; the ability to work effectively with diverse groups.

Preferred Qualifications: Strong communication and interpersonal skills; ability to exercise discretion and confidentiality; ability to work with diverse groups; experience advising students.

To view the full job description and apply, please visit <https://jobs.uml.edu>. Please submit a cover letter, curriculum vitae, and names and contact information of three references. Review of applications will begin June 17, 2013 and continue until the positions are filled. However, the position may close when an adequate number of qualified applications are received. Thank you for considering the University of Massachusetts Lowell as an employer of choice. We look forward to receiving your application.

The University of Massachusetts Lowell is committed to increasing diversity in its faculty, staff, and student populations, as well as curriculum and support programs, while promoting an inclusive environment. We seek candidates who can contribute to that goal and encourage you to apply and to identify your strengths in this area. The University of Massachusetts Lowell is an EO/AA/IRCA/ADA employer.



UNIVERSITY OF ILLINOIS
COLLEGE OF MEDICINE AT PEORIA

Head – Department of Cancer Biology and Pharmacology Director, Program of Cancer Biology

The University of Illinois College of Medicine at Peoria (UICOMP) is recruiting an exceptional MD or PhD cancer researcher for the dual position of Head of the Department of Cancer Biology and Pharmacology and Director of the Program of Cancer Biology. The new Head will be charged with enhancing his/her own cancer research program, recruiting additional cancer researchers, developing collaborations and advancing translational research with our large clinical community. The successful candidate will have a collaborative mind frame, be at the rank of Associate Professor or Professor, and be able to mentor junior faculty. This is an opportunity to further develop a cancer biology research program as well as create an innovative, community-oriented, translational cancer research program.

UICOMP is one of the regional campuses of the University of Illinois College of Medicine, and is part of a 900-bed hospital district containing two major hospital systems as well as the medical school. UICOMP's educational programs include 150 medical students and 240 residents/fellows in 20 different post-graduate programs. This regional campus has made cancer the focus of its basic science research, and has the support of community, clinical and corporate partners. A new 24,000 square foot Cancer Research building provides exceptional laboratory space and is well equipped with state-of-the art research equipment and core facilities.

The University offers a highly competitive salary, benefits and recruitment package. This leadership position offers an opportunity to strengthen a strong collaborative research environment, and capitalize on many such opportunities in both basic and clinical research.

For fullest consideration please respond by **August 1, 2013**. Applicants should apply online at: <http://jobs.uic.edu/job-board/job-details?jobID=32244>.

The University of Illinois is an EO/AA Employer.



BROWN

Postdoctoral Research Fellow NIEHS Training Program in Environmental Pathology The Warren Alpert Medical School of Brown University

This training provides the opportunity to develop an independent research project using the tools of cell biology, biochemistry, molecular biology, and molecular epidemiology to study the basic mechanisms of disease related to environmental exposures. Strong emphasis is placed on career development, communication skills, grantsmanship, interdisciplinary research, and implications of basic research for diagnosis and prevention of human disease. Opportunities are provided for clinical and translational research collaborations at Rhode Island Hospital and Women & Infants Hospital, as well as field work and community outreach in Rhode Island in collaboration with the Brown Superfund Basic Research Program. The faculty have active, well-funded research programs and access to modern research facilities equipped for quantitative imaging; laser capture microdissection; genomics, epigenomics, and proteomics; flow cytometry; and transgenic animal models. Eligible candidates will be considered for training grant support provided by the NIEHS Training Program in Environmental Pathology.

Interested candidates can apply on line at <https://secure.interfolio.com/apply/21697> and the following documents should be uploaded: a letter of application, curriculum vitae, and three letters of recommendation addressed to:

**Kim Boekelheide, M.D., Ph.D., Professor and
Search Committee Chair
Co-Director, NIEHS Training Program in
Environmental Pathology
Department of Pathology and Laboratory Medicine
The Warren Alpert Medical School of Brown University
Box G-E5
Providence, Rhode Island 02912**

Brown University is an EEO/AA Employer and invites applications from women and minorities.

Science Careers is the forum
that answers questions.



Science Careers is dedicated to opening new doors and providing timely answers to the career questions that matter to you.

Science Careers Forum:

- » Relevant Career Topics
- » Timely Advice and Answers
- » Community, Connections, and More!

Your Future Awaits.

Visit the forum and join the conversation today!



ScienceCareers.org



北京航空航天大学
BEIHANG UNIVERSITY

Faculty Positions Available in Beihang University, China

Established in 1952, located in Haidian District, Beijing, Beihang University is one of the top research-oriented universities in China, focusing on fundamental cutting edge research and high-level education, covering such diverse fields as science, engineering, technology, humanities, economics, management and law. One of the first universities funded by China's "211" and "985" programs, it has seven national key laboratories and twenty-five provincial and ministerial key laboratories. At present, the university has a total area of two million square meters, and over 3800 faculty and staff.

Beihang University is on a clear path to become a world-class university in many engineering and science disciplines. As part of Beihang's further pursuit for excellence in research and education, we have expanded our global search for the best research talent to join our International Research Institute for Multidisciplinary Science (IRIMS). Five independent international research centers (IRC) were established recently under the name of IRIMS. As the core part of IRIMS, IRCs are devoted to establish a world-class, advanced and multidisciplinary research platform.

Beihang University invites applications for full-time Professors, Associate Professors and excellent scientists. Preference will be given to candidates whose research emphasis demonstrates the potential to complement and advance the IRIMS existing research strengths. Successful candidates will be provided competitive salaries and start-up funds.

Positions Available

- Position offered by the Recruitment Program of Global Experts (1000 Plan Professorship)
- Position offered by the Chang Jiang Scholars Program
- Position offered by the Recruitment Program of Global Young Experts (1000 Plan Professorship for Young Talents)
- Position offered by Beihang University's Zhuoyue Program of Professors
- Position offered by Beihang University's Zhuoyue Program of Associate Professors.

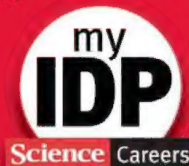
Interested individuals should send curriculum vitae by email to rscreb@buaa.edu.cn, with "Faculty Application from *Science*" in the title. For more information, please visit the university's Human Resource Department website <http://rsc.buaa.edu.cn/>, or contact us by email rscreb@buaa.edu.cn or by telephone 86-010-82317779.

For your career in science, there's only one

Science

Introducing myIDP: A career plan customized for you, by you.

- The first and only online app that helps scientists prepare their very own individual development plan.
- Recommended by leading professional societies and the NIH.
- Developed by scientists at FASEB, UCSF, and the Medical College of Wisconsin in collaboration with AAAS and Science Careers, with support from the Burroughs Wellcome Fund.



Visit the website and
start planning today!
myIDP.sciencecareers.org

AAAS In partnership with:



FASEB
Federation of American Societies
for Experimental Biology



University of California
San Francisco



BURROUGHS
WELLCOME
FUND

**Download
your free copy
today.**

ScienceCareers.org/booklets



From technology specialists to patent attorneys to policy advisers, learn more about the types of careers that scientists can pursue and the skills needed in order to succeed in nonresearch careers.



POSITIONS OPEN

CAREER OPPORTUNITY—Doctor of Optometry (OD) degree in 27 months for Ph.D.s in science and M.D.s. Excellent career opportunities for O.D.-Ph.D.s and O.D.-M.D.s in research, education, industry and clinical practice. This unique program starts in March of each year, features small classes, and 12 months devoted to clinical care.

Contact the Admissions Office, telephone: 800-824-5526 at The New England College of Optometry, 424 Beacon Street, Boston, MA 02115. Additional information, website: <http://www.neco.edu>; e-mail: admissions@neco.edu.

**Your
career
is our
cause.**

Get help
from the
experts.

**www.
sciencecareers.org**

- Job Postings
- Job Alerts
- Resume/CV Database
- Career Advice
- Career Forum

Science Careers

From the journal *Science* AAAS

ProMab Biotechnologies, Inc.

**Custom Monoclonal
Antibody \$3,900**

> 3,000 CLONES WILL BE SCREENED

1-866-339-0871

www.ProMab.com | info@promab.com

Widely
Recognized
Original &
Guaranteed

KlenTaq1™

8c/u
Truncated
Taq DNA
Polymerase

Withstand 99°C

e-mail: order@JEMBIO.com www.JEMBIO.com

Call: **JEM BIO Home of KlenTaq-5**

Ph: 1•866•493•3464 Fax: 636•465•3979

PURIFIED HBsAg AVAILABLE

Supplies of purified hepatitis B surface antigen (HBsAg) subtype ayw available. Currently the antigen is in use for production of commercial diagnostic reagents. For inquiries please use the following e-mail address:
gvnek@optimum.net

AAAS|2014 ANNUAL MEETING

13-17 FEBRUARY • CHICAGO

MEETING GLOBAL CHALLENGES:
DISCOVERY AND INNOVATION

The 2014 Annual Meeting will focus on finding sustainable solutions through inclusive, international, and interdisciplinary efforts that are most useful to society and enhance economic growth.

Save the Date: 13-17 February 2014

You are invited to attend the AAAS Annual Meeting in Chicago. Thousands of leading scientists, engineers, educators, policymakers, and journalists will gather from around the world to discuss recent developments in science and technology.

The Annual Meeting has a diverse scientific program and also features:

- Career development workshops
- Exhibit hall with international exhibitors
- Family Science Days, a free public event

Registration and housing open in early August.

www.aaas.org/meetings

